

Special Issue Reprint

---

# CFD Applications in Energy Engineering Research and Simulation

Volume II

---

Edited by  
Alfredo Iranzo

[mdpi.com/journal/processes](https://mdpi.com/journal/processes)

**CFD Applications in Energy  
Engineering Research and  
Simulation—Volume II**



# CFD Applications in Energy Engineering Research and Simulation—Volume II

Editor

**Alfredo Iranzo**



Basel • Beijing • Wuhan • Barcelona • Belgrade • Novi Sad • Cluj • Manchester

*Editor*

Alfredo Iranzo  
University of Sevilla  
Sevilla  
Spain

*Editorial Office*

MDPI AG  
Grosspeteranlage 5  
4052 Basel, Switzerland

This is a reprint of articles from the Special Issue published online in the open access journal *Processes* (ISSN 2227-9717) (available at: [https://www.mdpi.com/journal/processes/special\\_issues/CFD\\_Energy\\_Engineering](https://www.mdpi.com/journal/processes/special_issues/CFD_Energy_Engineering)).

For citation purposes, cite each article independently as indicated on the article page online and as indicated below:

Lastname, A.A.; Lastname, B.B. Article Title. <i>Journal Name</i> <b>Year</b> , Volume Number, Page Range.
--

**Volume II**

ISBN 978-3-7258-2317-8 (Hbk)

ISBN 978-3-7258-2318-5 (PDF)

[doi.org/10.3390/books978-3-7258-2318-5](https://doi.org/10.3390/books978-3-7258-2318-5)

**Set**

ISBN 978-3-7258-2221-8 (Hbk)

ISBN 978-3-7258-2222-5 (PDF)

© 2024 by the authors. Articles in this book are Open Access and distributed under the Creative Commons Attribution (CC BY) license. The book as a whole is distributed by MDPI under the terms and conditions of the Creative Commons Attribution-NonCommercial-NoDerivs (CC BY-NC-ND) license.

# Contents

<b>About the Editor</b> . . . . .	<b>ix</b>
<b>Fei Wang, Lin Wang and Guoding Chen</b> Analysis of Oil Droplet Deposition Characteristics and Determination of Impact State Criterion in Aero-Engine Bearing Chamber Reprinted from: <i>Processes</i> <b>2020</b> , <i>8</i> , 741, doi:10.3390/pr8060741 . . . . .	<b>1</b>
<b>Jie Fang, Weiqiu Huang, Fengyu Huang, Lipei Fu and Gao Zhang</b> Investigation of the Superposition Effect of Oil Vapor Leakage and Diffusion from External Floating-Roof Tanks Using CFD Numerical Simulations and Wind-Tunnel Experiments Reprinted from: <i>Processes</i> <b>2020</b> , <i>8</i> , 299, doi:10.3390/pr8030299 . . . . .	<b>14</b>
<b>Francisco Burgos-Florez, Antonio Bula, John Marquez, Alberto Ferrer and Marco Sanjuan</b> CFD-DEM Modeling and Simulation Coupled to a Global Thermodynamic Analysis Methodology for Evaluating Energy Performance: Biofertilizer Industry Reprinted from: <i>Processes</i> <b>2019</b> , <i>7</i> , 673, doi:10.3390/pr7100673 . . . . .	<b>36</b>
<b>Héctor Redal, Jaime Carpio, Pablo A. García-Salaberri and Marcos Vera</b> DynamFluid: Development and Validation of a New GUI-Based CFD Tool for the Analysis of Incompressible Non-Isothermal Flows Reprinted from: <i>Processes</i> <b>2019</b> , <i>7</i> , 777, doi:10.3390/pr7110777 . . . . .	<b>56</b>
<b>Rasheed Atif, Madeleine Combrinck, Jibrán Khaliq, James Martin, Ahmed H. Hassanin, Nader Shehata, et al.</b> Study of Air Pressure and Velocity for Solution Blow Spinning of Polyvinylidene Fluoride Nanofibres Reprinted from: <i>Processes</i> <b>2021</b> , <i>9</i> , 1014, doi:10.3390/pr9061014 . . . . .	<b>83</b>
<b>Tao Zhang, Bin Chen, Kun Sun and Wenjie Chang</b> Study on the Law of Diesel Oil Carrying Water in Lanzhou–Chengdu–Chongqing Product Oil Pipeline Based on Large Eddy Simulation Reprinted from: <i>Processes</i> <b>2020</b> , <i>8</i> , 1049, doi:10.3390/pr8091049 . . . . .	<b>93</b>
<b>Gao Zhang, Fengyu Huang, Weiqiu Huang, Zhongquan Zhu, Jie Fang, Hong Ji, et al.</b> Analysis of Influence of Floating-Deck Height on Oil-Vapor Migration and Emission of Internal Floating-Roof Tank Based on Numerical Simulation and Wind-Tunnel Experiment Reprinted from: <i>Processes</i> <b>2020</b> , <i>8</i> , 1026, doi:10.3390/pr8091026 . . . . .	<b>114</b>
<b>Chuan Wang, Xiaoke He, Li Cheng, Can Luo, Jing Xu, Kun Chen and Weixuan Jiao</b> Numerical Simulation on Hydraulic Characteristics of Nozzle in Waterjet Propulsion System Reprinted from: <i>Processes</i> <b>2019</b> , <i>7</i> , 915, doi:10.3390/pr7120915 . . . . .	<b>129</b>
<b>Mohamed Gadalla, Mehdi Ghommem and George Bourantas</b> Modeling and Thermal Analysis of a Moving Spacecraft Subject to Solar Radiation Effect Reprinted from: <i>Processes</i> <b>2019</b> , <i>7</i> , 807, doi:10.3390/pr7110807 . . . . .	<b>150</b>
<b>Harith Jayakody, Raya Al-Dadah and Saad Mahmoud</b> Cryogenic Energy for Indirect Freeze Desalination—Numerical and Experimental Investigation Reprinted from: <i>Processes</i> <b>2020</b> , <i>8</i> , 19, doi:10.3390/pr8010019 . . . . .	<b>165</b>

<b>Santiago Céspedes, Alejandro Molina, Betiana Lerner, Maximiliano S. Pérez, Camilo A. Franco and Farid B. Cortés</b> A Selection Flowchart for Micromodel Experiments Based on Computational Fluid Dynamic Simulations of Surfactant Flooding in Enhanced Oil Recovery Reprinted from: <i>Processes</i> <b>2021</b> , <i>9</i> , 1887, doi:10.3390/pr9111887 . . . . .	191
<b>Hassan F. Elattar, Eckehard Specht, Ali Fouda, Saeed Rubaiee, Ahmed Al-Zahrani and Sameh A. Nada</b> Swirled Jet Flame Simulation and Flow Visualization Inside Rotary Kiln—CFD with PDF Approach Reprinted from: <i>Processes</i> <b>2020</b> , <i>8</i> , 159, doi:10.3390/pr8020159 . . . . .	215
<b>Pablo A. García-Salaberri, Tugba Ceren Gokoglan, Santiago E. Ibáñez, Ertan Agar and Marcos Vera</b> Modeling the Effect of Channel Tapering on the Pressure Drop and Flow Distribution Characteristics of Interdigitated Flow Fields in Redox Flow Batteries Reprinted from: <i>Processes</i> <b>2020</b> , <i>8</i> , 775, doi:10.3390/pr8070775 . . . . .	230
<b>Jesús Rodríguez and Ernesto Amores</b> CFD Modeling and Experimental Validation of an Alkaline Water Electrolysis Cell for Hydrogen Production Reprinted from: <i>Processes</i> <b>2020</b> , <i>8</i> , 1634, doi:10.3390/pr8121634 . . . . .	256
<b>Sen Li, Jinxing Guo, Xin Lv, Teng Deng, Bo Cao and Juan Wang</b> Research on High-Pressure Hydrogen Pre-Cooling Based on CFD Technology in Fast Filling Process Reprinted from: <i>Processes</i> <b>2021</b> , <i>9</i> , 2208, doi:10.3390/pr9122208 . . . . .	273
<b>Adriana Rojas-Rishor, Jorge Flores-Velazquez, Edwin Villagran and Cruz Ernesto Aguilar-Rodríguez</b> Valuation of Climate Performance of a Low-Tech Greenhouse in Costa Rica Reprinted from: <i>Processes</i> <b>2022</b> , <i>10</i> , 693, doi:10.3390/pr10040693 . . . . .	289
<b>Cruz Ernesto Aguilar-Rodríguez, Jorge Flores-Velázquez, Fernando Rojano, Hector Flores-Magdaleno and Enrique Rubiños Panta</b> Simulation of Water Vapor and Near Infrared Radiation to Predict Vapor Pressure Deficit in a Greenhouse Using CFD Reprinted from: <i>Processes</i> <b>2021</b> , <i>9</i> , 1587, doi:10.3390/pr9091587 . . . . .	301
<b>Payam Nejat, Hasanen Mohammed Hussen, Fodil Fadli, Hassam Nasarullah Chaudhry, John Calautit and Fatemeh Jomehzadeh</b> Indoor Environmental Quality (IEQ) Analysis of a Two-Sided Windcatcher Integrated with Anti-Short-Circuit Device for Low Wind Conditions Reprinted from: <i>Processes</i> <b>2020</b> , <i>8</i> , 840, doi:10.3390/pr8070840 . . . . .	315
<b>Cruz Ernesto Aguilar-Rodríguez, Jorge Flores-Velazquez, Waldo Ojeda-Bustamante, Fernando Rojano and Mauro Iñiguez-Covarrubias</b> Valuation of the Energy Performance of a Greenhouse with an Electric Heater Using Numerical Simulations Reprinted from: <i>Processes</i> <b>2020</b> , <i>8</i> , 600, doi:10.3390/pr8050600 . . . . .	336
<b>Zhenjie Yang, Adnan Abbas, Xiaochan Wang, Muhammad Ameen, Haihui Yang and Shakeel Ahmed Soomro</b> Influence of Soil Particle Size on the Temperature Field and Energy Consumption of Injected Steam Soil Disinfection Reprinted from: <i>Processes</i> <b>2020</b> , <i>8</i> , 241, doi:10.3390/pr8020241 . . . . .	349

<b>Xuejun Qian, Seong W. Lee and Yulai Yang</b> Heat Transfer Coefficient Estimation and Performance Evaluation of Shell and Tube Heat Exchanger Using Flue Gas Reprinted from: <i>Processes</i> <b>2021</b> , <i>9</i> , 939, doi:10.3390/pr9060939 . . . . .	<b>378</b>
<b>Bo Zhang, Ziqiang Lin, Jun Zhang, Sheng Yang and Honghu Ji</b> Numerical Investigation of the Flow and Infrared Radiation Characteristics of Nozzles with Transverse Jets of Different Shapes Reprinted from: <i>Processes</i> <b>2022</b> , <i>10</i> , 763, doi:10.3390/pr10040763 . . . . .	<b>397</b>
<b>Junan Jiang, Ning Yang, Hanyang Liu, Jianxin Tang, Chenfeng Wang, Rije Wang and Xiaoxia Yang</b> Modification of Meso-Micromixing Interaction Reaction Model in Continuous Reactors Reprinted from: <i>Processes</i> <b>2023</b> , <i>11</i> , 1576, doi:10.3390/pr11051576 . . . . .	<b>409</b>
<b>Alfredo Iranzo</b> CFD Applications in Energy Engineering Research and Simulation: An Introduction to Published Reviews Reprinted from: <i>Processes</i> <b>2019</b> , <i>7</i> , 883, doi:10.3390/pr7120883 . . . . .	<b>428</b>





# About the Editor

## **Alfredo Iranzo**

Alfredo Iranzo is a Chemical Engineer from the University of Zaragoza (2000), MSc in Thermal Energy Systems from the University of Seville (2010), and PhD from the University of Seville (2011). He worked at ANSYS Germany as Customer Support for CFD software. His research activity focuses on Computational Fluid Dynamics applications in energy and chemical engineering, hydrogen technologies, green hydrogen production, and, in particular, PEM fuel cell technology, including CFD (computational fluid dynamics) models and simulations and experimental research.

He has published 70 articles in JCR journals with high international impact (h index = 25). He has participated in several public and private funded projects in CFD and hydrogen technologies. He is currently CSO (Chief Scientific Officer) of the Innovation Hub of the University of Seville, within the European University Ulysseus, in Sustainable Energy, Transport, and Mobility for Smart Cities. He is member of the Editorial Board of the journal *Engineering Applications of Computational Fluid Mechanics* and Assistant Editor of the *International Journal of Hydrogen Energy*.



Article

# Analysis of Oil Droplet Deposition Characteristics and Determination of Impact State Criterion in Aero-Engine Bearing Chamber

Fei Wang \*, Lin Wang \* and Guoding Chen

School of Mechanical Engineering, Northwestern Polytechnical University, Xi'an 710072, China; gdchen@nwpu.edu.cn

\* Correspondence: wfei@mail.nwpu.edu.cn (F.W.); wanglin@nwpu.edu.cn (L.W.); Tel.: +86-187-2900-1815 (F.W.)

Received: 31 May 2020; Accepted: 24 June 2020; Published: 25 June 2020

**Abstract:** The research of oil/air two-phase flow and heat transfer is the fundamental work of the design of lubrication and heat transfer in aero-engine bearing chamber. The determination of impact state criterion of the moving oil droplets with the wall and the analysis of oil droplet deposition characteristics are important components. In this paper, the numerical analysis model of the impact between the moving oil droplet and the wall is established by using the finite volume method, and the simulation of oil droplet impingement on the wall is carried out. Then the effects of oil droplet diameter, impact velocity, and incident angle on the characteristic parameters of impact state are discussed. The characteristic parameters include the maximum spreading length, the maximum spreading width, and the number of splashing oil droplets. Lastly the calculation results are verified through comparing with the experimental results in the literature. The results show as follows: (1) The maximum spreading width of oil droplet firstly increases and then slows down with the incident angle and the oil droplet diameter increasing; (2) when the oil droplet diameter becomes small, the influence of the incident angle on the maximum spreading length of oil droplet is obvious and vice versa; (3) with the impact velocity and diameter of oil droplet increasing, the maximum spreading width of oil droplet increases firstly and then slows down, and the maximum spreading length increased gradually; (4) the number of splashing oil droplets increases with the incident angle and impact velocity increasing; and (5) compared with the experimental data in literature, the critical dimensionless splashing coefficient  $Kc$  proposed in this paper can better distinguish the impact state of oil droplet.

**Keywords:** aero-engine; bearing chamber; oil droplet; numerical simulation; criterion; splash; deposition; impact; process

---

## 1. Introduction

Lubrication oil is supplied to roller or ball bearings via an under-race lubrication method and then sheds into aero-engine bearing chamber in the form of oil droplets. The high-speed moving oil droplets impact with the chamber wall at different incident angles, the diameter of oil droplets is in the range of 1–500  $\mu\text{m}$ , and the impingement time is only a few microseconds. Then the oil droplet or deposits on the wall surface to form oil film, or disintegrates many smaller secondary oil droplets to suspend in the bearing chamber. Thus air, oil droplet, and oil film coexist in the bearing chamber. The whole impingement process can be simplified as the impact of oil droplet with the oblique wall. Meanwhile, the real aero-engine operating conditions are complicated, and the experimental studies are limited. It is very difficult to accurately analyze the air-oil two-phase flow, and restricts the precise design of aero-engine lubrication system. So, the numerical simulation can make up the deficiency of the experiment method to a large extent. In this paper, the determination of impact state criterion

between oil droplet and wall and the analysis of oil droplet disposition characteristics are performed, which can provide more reasonable initial condition for the further research of multiphase flow and heat transfer in the bearing chamber.

The phenomenon of liquid drop impacting with solid wall was firstly observed by Worthin et al. [1] by means of the experiment that water droplet and mercury droplet impact with metal surface. Subsequently, more comprehensive and extensive experimental research had been carried out by many scholars under different parameter conditions. Early research focused on the observation of the droplet shape change after the impact, and the analysis of the influence of droplet physical parameters, impact velocity, and wall roughness. Mundo et al. [2] observed the impact phenomenon of alcohol, water, and solid wall through experimental research, analyzed the influence of physical parameter of solution, impact parameter and droplet diameter on the collision, and introduced the characteristic parameter as the criterion for judging whether the droplet splashes or not. Glahn et al. [3] measured oil droplet sizes and velocities by utilizing a Phase Doppler Particle Analyzer (PDPA) technique for the first time under the real engine conditions, and calculated the droplet trajectories and velocities by using numerical method. Simmons et al. [4] calculated the dispersion oil droplets motions using the two-way coupling method, where the oil droplet diameter is in the range of 1~500 microns. Cossali et al. [5] studied the splashing phenomenon of droplets after impinging on the liquid film by experiments, proposed the definition of splashing, and summarized the critical parameters of splashing. Sikalo et al. [6,7] carried out an experimental study on the impact between the droplet and the inclined wall, found the phenomenon of spread, rebound, and splash appeared after the impact between the droplet and the solid surface, and analyzed the influence of the incident angle and impact velocity of the droplet on the spreading characteristics and rebound rate of the liquid film. Rioboo et al. [8,9] put forward six kinds of impact phenomena between liquid droplet and solid wall based on the observation results of collision test using water and alcohol mixture, and analyzed the influence of the liquid droplet, impact velocity, and the roughness of solid wall on the shape change of splashed liquid droplet and liquid film after collision. Hitoshi and Yu et al. [10] combining experimental and numerical simulation methods, studied the form of spreading water film formed by water droplet after colliding with inclined wall. Shen et al. [11] used a two-dimensional numerical simulation method to compute the dynamic process of water droplet impacting the inclined wall, and analyzed the influence of impact velocity and incident angle of water droplet under the condition of low impact energy on the spreading length. Wang et al. [12] established the collision model of oil droplet and chamber wall based on the motion state before the collision between oil droplet and bearing chamber wall in the aero-engine, and obtained the influence rule of oil droplet diameter on the deposition rate and momentum transfer rate of oil droplet. Fujimoto and Ogino et al. [13] calculated the deformation, velocity, and pressure distribution of liquid droplet when hit the horizontal and inclined surface, and compared them with the experimental results. Fukai et al. [14] used the two-dimensional finite element method to simulate the deformation behavior after the collision of droplet and plates, and analyzed the influence of impacting velocity and contact angle. Lu et al. [15] used the high-speed photography technology to establish the relationship between the spreading characteristics of liquid film, the weber number, and impact incident angle. Vladimir et al. [16] studied the collision of droplet and the oil tank surface by theoretical analysis method, and analyzed the change rule of the adhesion and splashing of a single droplet impact with the oil tank surface. Gorse et al. [17] carried out an experimental study on the oil droplet generation by roller bearing in a wide range of engine conditions, the results revealed that the pressure across the bearing and the structure of the bearing support had strong influence on the generation of oil droplets. Farrall et al. [18] used CFD technique to determine the outcome of droplet impact with a wall film, and the results show that the behavior of oil in bearing chamber is strongly influenced by the conditions with which it leaves the bearing. Chen et al. [19] established the oil droplet movement model in the air fluid by Lagrangian method, and analyzed the deposition characteristics of the moving oil droplet after colliding with the bearing chamber wall. Chen et al. also analyzed the collision between the deformed oil droplet and the wall, and obtained the change rule of the flow characteristics of the oil

film on the wall. Tembely et al. [20] discussed the effect of substrates' wettability on the droplet impact droplet spreading, and the evolution of spreading diameter was determined. Adenyi et al. [21] carried out numerical and experimental study of a customized shallow sump aero-engine bearing chamber with inserts to improve oil residence volume. Bristot et al. [22] identified a Volume of Fluid (VOF) approach with turbulence damping for the transient simulation of air/gas two-phase flows in bearing chamber, which improve the accuracy of bearing chamber flows modelling.

Although there are many researches on the impact between droplet and solid wall, most of them focus on spreading characteristics after the impact between droplet and solid wall. However, the determination of impact state criteria for the adhesion and splashing state of droplet and the variation of the number of secondary droplets after the impact is rarely discussed. Meanwhile, compared with the water droplet, the high viscosity coefficient makes it show inherent characteristics when an oil droplet impacts with the wall. Therefore, it is very necessary to carry out the research on the determination of impact state criteria and the deposition characteristics of moving oil droplets in the bearing chamber.

The VOF method is used to establish the numerical model of oblique collision between moving oil droplet and solid wall. The impact state and the deposition characteristic of oil droplet is calculated under the different oil droplet diameter, incident angle, and impact velocity. Single factor analysis method is employed to analyze oil droplet impact state. The determination of impact state criterion between the dimensionless splashing coefficient and oil droplet impact state is acquired. The results can be applied to the impact analysis of oil droplet and wall in aero-engine bearing chamber. And the quantitative analysis of the number of splashing secondary oil droplets could provide the initial condition for further research on coalescence and breakup of the secondary oil droplet in the bearing chamber.

## 2. Theory and Calculation Model

### 2.1. The Governing Equation of Oil Droplet Impacting with the Wall

There are two kinds of fluids involved in the process of impact between oil droplet and the wall: Lubricating oil and air. Both of them are assumed incompressible fluid and no mass and momentum exchanged with each other. The mass and momentum conservation equation of each phase are as follows:

$$\nabla \cdot \mathbf{V} = 0 \quad (1)$$

$$\frac{d\mathbf{V}}{dt} + \nabla \cdot (\mathbf{V}\mathbf{V}) = g - \frac{1}{\rho} [\nabla p - \mu \nabla^2 \mathbf{V}] + \frac{1}{\rho} F \quad (2)$$

where  $\mathbf{V}$  is the fluid velocity;  $p$  is the fluid pressure;  $g$  is the gravity acceleration;  $\rho$  and  $\mu$  are the average density and average dynamic viscosity of fluid respectively;  $F$  is the momentum source term generated by oil surface.

VOF method [23,24] is used to trace the free interface between oil droplet and air, and the volume fraction of oil in grid cell is calculated. The oil volume fraction equation is given by

$$\frac{\partial \Omega}{\partial t} + \mathbf{V} \cdot \nabla \Omega = 0 \quad (3)$$

where  $\Omega$  is the oil volume fraction,  $\Omega = 0$  and  $\Omega = 1$  indicate that there is no oil or full oil in the grid cell respectively;  $0 < \Omega < 1$  indicates that oil and air coexist in the grid cell at the same time.

The average density and dynamic viscosity of the fluid in the grid cell are

$$\rho = \Omega \rho_l + (1 - \Omega) \rho_g \quad (4)$$

$$\mu = \Omega \mu_l + (1 - \Omega) \mu_g \quad (5)$$

where subscript *l* and *g* represent oil and air respectively.

According to the continuous surface tension model proposed by Bracketbill et al. [25], the momentum source term in Equation (2) is given by

$$F = \sigma \frac{\rho \kappa \nabla \Omega}{(\rho_l + \rho_g)/2} \tag{6}$$

where  $\kappa$  is the surface curvature,  $\kappa = \nabla(n/|n|)$ ,  $n$  is the normal direction of the free interface between oil droplet and air,  $n = \nabla \Omega$ .

### 2.2. Numerical Model of Oil Droplet Impacting with Wall

The schematic diagram of the impacting between oil droplet and the solid wall is shown in Figure 1. The diameter of the incident oil droplet is *D*, the incident angle of the oil droplet is  $\theta$ , and the impacting velocity is *v*. The width and length of the wall are *W* and *L* respectively.

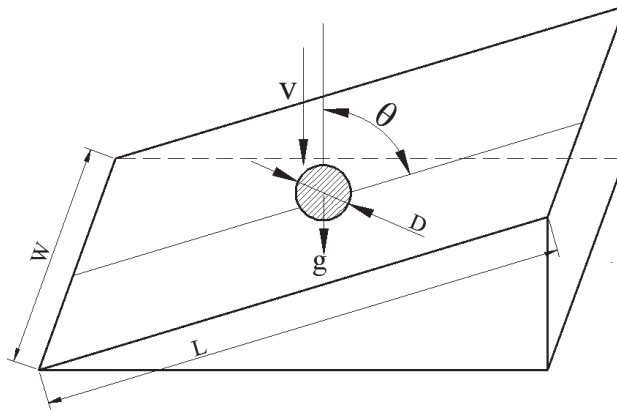


Figure 1. Oil droplet impact with solid wall.

The grid model of oil droplet impacting with solid wall is shown in Figure 2, and the calculation region is  $W \times L \times H = 2 \text{ mm} \times 2 \text{ mm} \times 0.4 \text{ mm}$ . The boundary conditions of calculation are as follows:

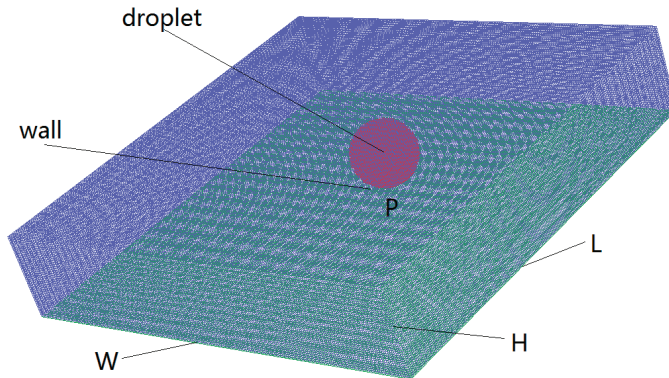


Figure 2. Grid model of moving oil droplet impacting with the wall.

- (1) In the calculation area of oil droplet, the volume fraction of oil is set as 1, the initial oil droplet velocity is the impacting velocity;

- (2) in the other calculation area, the volume fraction of oil is set as 0; and
- (3) the wall adopts the no-slip velocity boundary condition.

The impact point of oil droplet and the wall is P. Hexahedral structured grids are generated in the entire computational domain. In order to ensure the calculation accuracy,  $W$  and  $L$  are divided into 200 segments respectively, and  $H$  is divided into 40 segments. The volume cell is  $1\ \mu\text{m} \times 1\ \mu\text{m} \times 1\ \mu\text{m}$ , and the total grid number is 1,600,000. The mesh quality is quite fine, which completely meets the computing requirement. Considering the accuracy and sharpness, the Geo-Reconstruct is employed for interface reconstruction. And the second-order upwind scheme is employed for discretization of fluid mass and momentum conservation equation. The transient solver is used to solve the equations, in which Presto algorithm is employed for the pressure term, PISO algorithm is used for coupling the pressure and velocity term: where oil density  $\rho_l$  is  $926\ \text{kg/m}^3$ , dynamic viscosity  $\mu_l$  is  $0.007\ \text{P}\cdot\text{s}$ , and surface tension coefficient  $\sigma_l$  is  $0.035\ \text{N/m}$ . Gas density  $\rho_g$  is  $1.225\ \text{kg/m}^3$ , dynamic viscosity  $\mu_g$  is  $1.789 \times 10^{-5}\ \text{P}\cdot\text{s}$ .

### 3. Results and Discussion

In this paper, the deposition characteristics of oil droplet are calculated under different operating condition. The impacting velocity, incident angle and oil droplet diameter chosen are derived from the literature [3,12,19]. The specific parameters and values are shown in Table 1.

**Table 1.** Operating condition.

Parameters	Value
Impacting velocity $v$ (m/s)	10,15,20,25,30
Incident angle $\theta$ ( $^\circ$ )	30,45,60,75
Oil droplet diameter $D$ ( $\mu\text{m}$ )	100,150,200,250,300

#### 3.1. Deposition Characteristics of Oil Droplet under Different Oil Droplet Diameter, Velocity, and Incident Angle

The adhesion and spreading process of oil droplet in  $60\ \mu\text{s}$  is shown in Figure 3 when the diameter is  $150\ \mu\text{m}$ , the impacting velocity is  $15\ \text{m/s}$  and the incident angle is  $30^\circ$ . The adhesion and spread indicates that there are no secondary oil droplets appeared after the oil droplet impacting the wall. After impacting with the solid wall, the oil droplet spread along the wall under the combined action of gravity, inertial force, surface tension, and viscous force. It can be seen from the figure that the spreading length and spreading width of the oil film are quite different, and the oil film distribution is asymmetrical in the direction  $W$  and  $L$ . The oscillation and accumulation phenomenon occurred at the bottom of the oil film, accompanied by the appearance of “dry out spots”. The reason is that the force of oil droplet is uneven in the direction of spreading length and width. Due to that the incident angle is small, the effect of gravity and viscous force on the direction of spreading length are more significant, but the spread in the direction of width is only affected by viscous force.

The adhesion and spreading process of oil droplet in  $60\ \mu\text{s}$  is shown in Figure 4 when the diameter is  $200\ \mu\text{m}$ , the impacting velocity is  $10\ \text{m/s}$  and the incident angle is  $60^\circ$ . Compared with Figure 3, the spread of oil droplet on the wall is quite different. Under this condition, the spread shape of oil droplet on the wall is approximately circular, and the spread is relatively uniform in the direction of length and width. The reason is that the effect of gravity on the oil droplet become small with the incident angle increasing, and surface tension and viscous force plays a leading role.



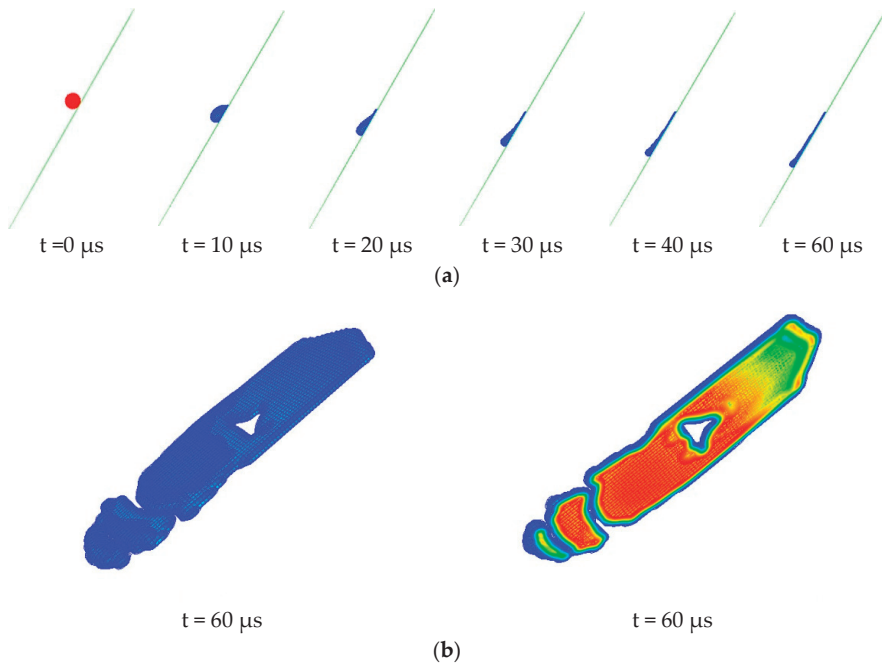


**Figure 3.** Spreading process of oil droplet ( $D = 150 \mu\text{m}$ ,  $v = 15 \text{ m/s}$ ,  $\theta = 30^\circ$ ), where the contour plots represent the volume fraction of oil droplet. (a) Spreading process of oil droplet in  $60 \mu\text{s}$ . (b) Spreading of oil droplet at  $60 \mu\text{s}$ .

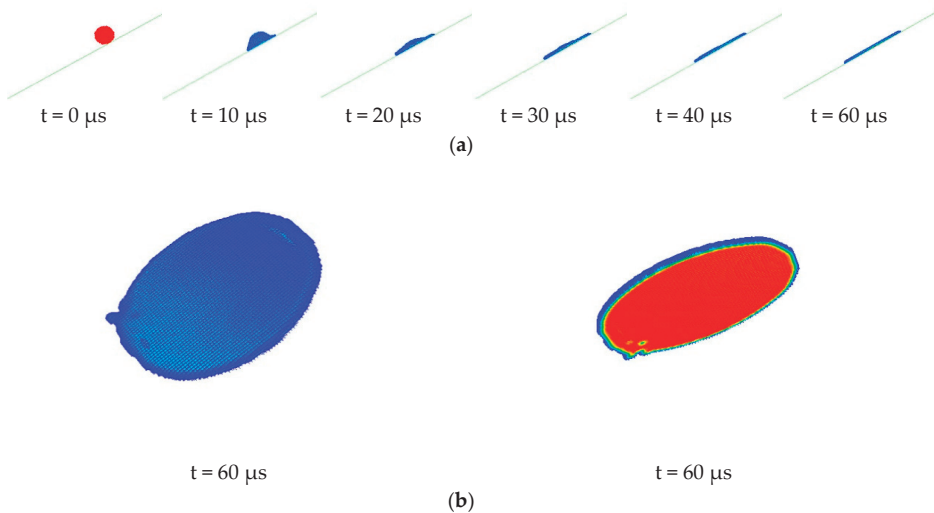


**Figure 4.** Spreading process of oil droplet ( $D = 200 \mu\text{m}$ ,  $v = 10 \text{ m/s}$ ,  $\theta = 60^\circ$ ), where the contour plots represent the volume fraction of oil droplet. (a) Spreading process of oil droplet in  $60 \mu\text{s}$ . (b) Spreading of oil droplet at  $60 \mu\text{s}$ .

The adhesion and spreading process of oil droplet in  $60 \mu\text{s}$  is shown in Figure 5 when the diameter is  $250 \mu\text{m}$ , the impacting velocity is  $25 \text{ m/s}$  and the incident angle is  $60^\circ$ . It can be seen that the oil

droplet splashed after impacting with the wall. Due to that the diameter of the oil droplet is large and the impacting velocity is high, so the momentum of the impacting oil droplet is larger. But a large incident angle reduced the flow velocity of the deposited oil film along the wall, and the propagation velocity of the internal shock wave of the oil film is faster than that of the oil film along the wall, so “small oil column” appears at the edge of the spreading oil film. With the aid of the propagation of the shock wave, the energy accumulated at the edge, and “small oil column” extends upward, thus the “small oil column” breaks up and forms the second small splashing oil droplet. Meanwhile, it can be seen that the oil film also breaks up under the action of shock wave, which results in uneven spreading thickness of oil film on the wall, and accompanies by the appearance of dry out spots.

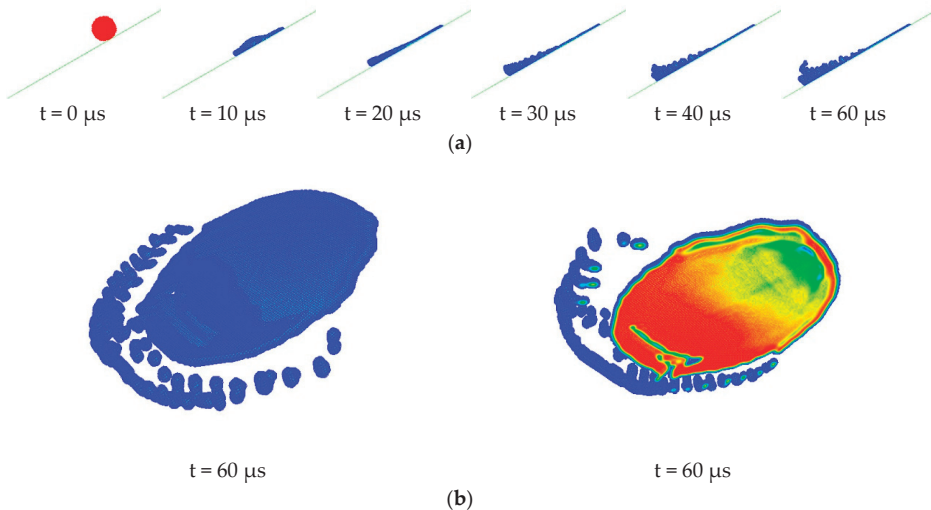


**Figure 5.** Splashing process of oil droplet ( $D = 250 \mu\text{m}$ ,  $v = 25 \text{ m/s}$ ,  $\theta = 60^\circ$ ), where the contour plots represent the volume fraction of oil droplet. (a) Splashing process of oil droplet in  $60 \mu\text{s}$ . (b) Splashing of oil droplet at  $60 \mu\text{s}$ .

The characteristic parameters include the maximum spreading length, the maximum spreading width, and the number of splashed secondary oil droplet, which are used to characterize the change rule of the impact state between the oil droplet and the solid wall. Figure 6 shows the relationship of the maximum spreading length and the maximum spreading width of the deposited oil film with the diameter of oil droplet under different incident angles when the impacting velocity is  $20 \text{ m/s}$ . The maximum spreading width of the oil film increases with the diameter and incident angle of oil droplet increasing, and the spreading width of the oil film increases firstly and then gradually slows down. With the diameter and incident angle of oil droplet increasing, the splash phenomenon occurs after the oil droplet impacting with the wall. The relationship between the maximum spreading length of the oil film, the diameter and the incident angle of the oil droplet is complicated. When the incident angle is small, the oil droplet is significantly affected by gravity. So, the maximum spreading length of the oil film is large. However, with the diameter of oil droplet increasing, the influence of incident angle on maximum spreading length of oil film weakens.

In Figure 7, the relationship of the maximum spreading length and width of deposited oil film with the diameter of impacting oil droplet under different impacting velocity when the incident angle is  $60^\circ$  and the spreading time is  $60 \mu\text{s}$ . It can be seen that with the impacting velocity increasing, the maximum spreading width of oil film increases firstly and then slows down, while the maximum spreading width of oil film increases with the impacting velocity and oil droplet diameter increasing. The larger impacting velocity and kinetic energy of oil droplet, the greater remaining energy after the

oil droplet overcomes the energy dissipation in the spreading process, which is conducive to the further spreading. However, due to the splashing phenomenon on the edge of spreading, the spreading width slows down.

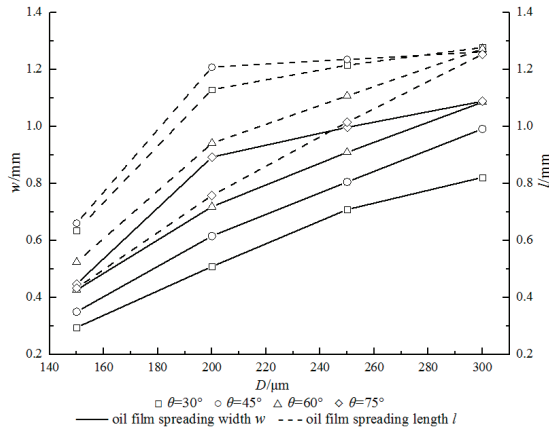


Figure 6. Effect of incident angle on spreading characteristics of deposited oil film when the impacting velocity is 20 m/s.

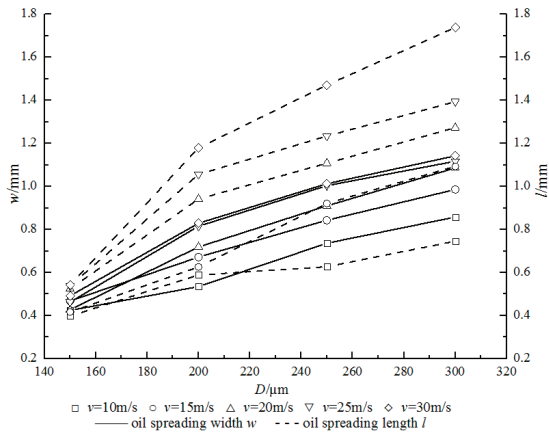
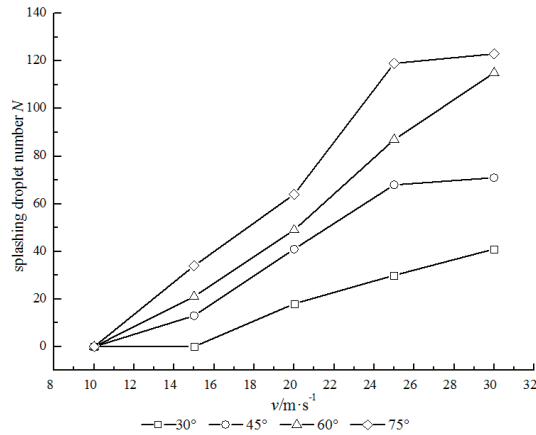


Figure 7. Effect of impacting velocity on spreading characteristics of deposited oil film when the incident angle is 60°.

The trend of oil droplet impacting velocity and the number of splashed oil droplet under different incident angles is shown in Figure 8 when the oil droplet diameter is 300  $\mu\text{m}$  and the spreading time is 60  $\mu\text{s}$ . It can be seen that when the impacting velocity of oil droplet is low, no splash occurs after the impact between oil droplet and the wall. With the impacting velocity of oil droplet increasing, the number of splashed oil droplet increases. Obviously, the reason is that the higher impacting momentum of oil droplet with larger impacting velocity, the more splashing oil droplet produced. Meanwhile, with the incident angle increasing, more splashing oil droplets are born at the same impacting velocity. The oil film is more evenly stressed in the length and width direction with the incident angle increasing. And more small oil columns emerge at the edge of the oil film, then occurs fracture, so more splashing oil droplets are produced.



**Figure 8.** Effect of impact velocity on the number of splashed oil droplets when the oil droplet diameter is 300  $\mu\text{m}$ .

### 3.2. Determination of Impact State Criterion

The determination of impact state criterion of moving oil droplet and the wall indicates that the criterion can judge whether the critical state of oil droplet splashing occurred after the impacting with the wall. According to the previous analysis, whether the splashing phenomenon occurs is depended on the geometric and motion parameters such as the diameter, impacting velocity and incident angle of oil droplet. The relevant parameters are derived from the literature [9,14]. In order to determine whether the splashing phenomenon occurred after oil droplet impacted with the wall in the bearing chamber, the single factor analysis method is employed in a wide range of parameter. The numerical simulation of impact state between oil droplet and the wall are carried out to compute the deposition and splashing of oil droplet under the combination of several influence parameters. The value of the combination of geometric and motion parameter are recorded under corresponding conditions. In order to establish the criterion for judge the critical state of moving oil droplet impacting the wall, the dimensionless splashing coefficient  $K$  is introduced, and the expression is given by

$$K = We^{0.5} Re^{0.25} \quad (7)$$

where

$$We = \rho_l v^2 D / \sigma_l \quad (8)$$

$$Re = \rho_l v D / \mu_l \quad (9)$$

where  $\rho_l$  is oil droplet density;  $v$  is oil droplet impacting velocity;  $D$  is oil droplet diameter;  $\sigma_l$  is surface tension of oil droplet;  $\mu_l$  is dynamic viscosity of oil droplet.  $We$  is the Weber number.  $Re$  is Reynolds number.

The distribution relationship between the combination of geometric and operating parameters and the dimensionless splashing coefficient  $K$  which correspond to the oil droplet deposition and splashing state is shown in Figure 9. In the figure, the deposition and splashing of oil droplet are divided into two parts. The dimensionless splashing coefficient corresponding to the fitted curve was known as critical dimensionless splashing coefficient, which was represented by  $K_c$ . The fitting relationship between the dimensionless splashing coefficient and the incident angle of oil droplet obtained by univariate nonlinear regression analysis, which is given by

$$K_c = 182.657 \times \theta^{-0.5543} \quad (10)$$

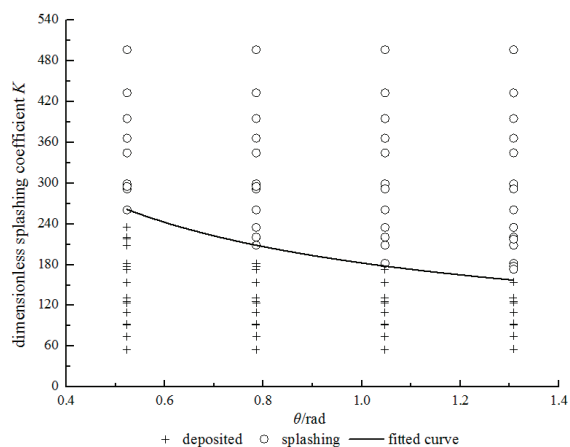


**Figure 9.** Distribution relationship between oil droplet deposition or splashing state and dimensionless splashing coefficient  $K$ .

The significance of the critical dimensionless splashing coefficient is that: (1) when  $K < K_c$ , the moving oil droplet will deposit after impacting with the solid wall, and no secondary oil droplet will be produced; (2) when  $K > K_c$ , the moving oil droplet will splash after impacting with the wall, and secondary oil droplet will be produced. The critical dimensionless splashing coefficient can be used as a criterion to judge the impact state between the oil droplet and the wall in the aero-engine bearing chamber.

### 3.3. Verification and Comparison of Impact State between Oil Droplet and the Wall

The dimensionless splashing coefficient can be used as the judgment criterion for the impact state of moving oil droplet and solid wall. In order to verify the rationality and validity, the critical dimensionless splashing coefficient and the judgment results provided in this paper are compared with the relevant experimental results in the literature [2,6,26], as shown in Table 2. Through comparison, it is found that the results of this paper are consistent with experimental results in the literature, and the critical dimensionless splashing coefficient proposed in this paper can better distinguish the impact state of oil droplet. The criterion for determining the impact state between moving oil droplet and the wall can be applied to the aero-engine bearing chamber, which has not been achieved in the existing research work.

**Table 2.** Comparison with the experimental results.

D (mm)	$\rho_l$ (kg/m <sup>3</sup> )	$\mu_l$ (Pa·s)	$\sigma_l$ (N/m)	$\theta$ (°)	v (m/s)	Experimental Results of [2,6,26]	Dimensionless Splashing Coefficient K of This Paper	Judgement Results of This Paper
0.132	786	0.0024	0.021	54°	17	splashing [2]	196.74	splashing
0.5	1000	0.000894	0.072	90°	18.81	splashing [26]	502.02	splashing
0.5	1000	0.000894	0.072	90°	32.54	splashing [26]	995.98	splashing
0.5	1000	0.0021	0.069	90°	18.27	splashing [26]	399.41	splashing
0.5	1050	0.0021	0.069	90°	32.92	splashing [26]	864.90	splashing
0.5	684	0.000387	0.020	90°	14.23	splashing [26]	623.14	splashing
0.5	684	0.000387	0.020	90°	8.93	splashing [26]	348.05	splashing
0.5	714	0.000720	0.022	90°	7.56	splashing [26]	238.29	splashing
0.5	714	0.000720	0.022	90°	13.28	splashing [26]	481.90	splashing
2.45	1220	0.116	0.063	90°	1.04	deposited [6]	16.30	deposited
2.72	996	0.001	0.072	10°	3.25	deposited [6]	193.119	deposited
2.72	996	0.001	0.072	45°	3.25	splashing [6]	193.11	splashing
2.72	996	0.001	0.072	45°	1.55	deposited [6]	76.54	deposited
3.3	786	0.0024	0.021	45°	2.1	splashing [6]	161.08	splashing

#### 4. Conclusions

- (1) The influence of incident angle on the maximum spreading length of oil droplet is large when the diameter of oil droplet is small; the influence of incident angle on the maximum spreading length of oil droplet is small when the diameter of the oil droplet is large; while the maximum spreading width of the oil droplet increases firstly and then slows down with the incident angle increasing.
- (2) With the oil droplet diameter and impacting velocity increasing, the maximum spreading width increasing firstly and then slows down, while the maximum spreading length shows an increasing trend.
- (3) With impacting velocity and incident increases, the number of splashing oil droplet presents an increasing trend under the condition of splashing caused by oil droplet impacting with the wall.
- (4) Compared with the physical experiments in the literature, the rationality and validity of the critical dimensionless splashing coefficient proposed in this paper is verified. It is shown that the dimensionless splashing coefficient is feasible as a criterion for judging the impact between the moving oil droplet and the solid wall in the bearing chamber.

**Author Contributions:** Conceptualization, F.W.; Methodology, F.W.; Software, F.W.; Validation, F.W.; Formal Analysis, F.W. Investigation, F.W. and L.W. Writing—original draft preparation, F.W.; Writing—Review and Editing, F.W., L.W., G.C.; Supervision, G.C.; Project Administration, G.C.; Funding Acquisition, L.W. All authors have read and agreed to the published version of the manuscript.

**Funding:** This research was funded by the National Natural Science Foundation of China, grant number 51975475.

**Conflicts of Interest:** The authors declare no conflicts of interest.

#### Nomenclature

$\rho$	average density of fluid
$\mu$	average dynamic viscosity of fluid
$\rho_l$	oil density
$\rho_g$	gas density
$\mu_l$	oil dynamic viscosity
$\sigma_l$	oil surface tension coefficient
$\mu_g$	air dynamic viscosity
$\theta$	incident angle of oil droplet
$\kappa$	surface curvature
$\Omega$	oil volume fraction
$p$	fluid pressure
$D$	diameter of oil droplet
$F$	momentum source term generated by oil surface
$g$	gravity acceleration
$n$	normal direction of the free interface between oil droplet and air
$v$	impacting velocity of oil droplet
$We$	Weber number
$Re$	Reynolds number
$K$	dimensionless splashing coefficient
$Kc$	Critical dimensionless splashing coefficient

#### References

1. Worthington, A.M. On the forms assumed by drops of liquids falling vertically on a horizontal plate. *Proc. R. Soc. Lond.* **1876**, *25*, 171–178.
2. Mundo, C.; Sommerfeld, M.; Tropea, C. Droplet wall collisions: Experimental studies of the deformation and breakup process. *Int. J. Multiph. Flow* **1995**, *21*, 151–173. [CrossRef]

3. Glahn, A.; Kurreck, M.; Willmann, M.; Wittig, S. Feasibility study on oil droplet flow investigations inside aero engine bearing chambers—PDDPA techniques in combination with numerical approaches. *J. Eng. Gas Turbines Power* **1996**, *118*, 749–755. [CrossRef]
4. Simmons, K.; Hibberd, S.; Wang, Y.; Care, I. Numerical study of the two-phase air/oil flow within an aero-engine bearing chamber model using a coupled Lagrangian droplet tracking method. In Proceedings of the ASME Pressure Vessels and Piping Conference, Vancouver, BC, Canada, 5–9 August 2002.
5. Cossali, G.E.; Coghe, A.; Marengo, M. The impact of a single drop on a wetted solid surface. *Exp. Fluids* **1997**, *22*, 463–473. [CrossRef]
6. Sikalo, S.; Tropea, C.; Ganic, E.N. Impact of droplets onto inclined surfaces. *J. Colloid Interface Sci.* **2005**, *286*, 661–669. [CrossRef]
7. Sikalo, S.; Ganic, E.N. Phenomena of droplet surface interactions. *Exp. Therm. Fluid Sci.* **2006**, *31*, 97–110. [CrossRef]
8. Rioboo, R.; Tropea, C.; Marengo, M. Outcomes from a drop impact on solid surfaces. *At. Sprays* **2001**, *11*, 155–165. [CrossRef]
9. Rioboo, R.; Marengo, M.; Tropea, C. Time evaluation of liquid drop impact onto solid dry surfaces. *Exp. Fluids* **2002**, *33*, 112–121. [CrossRef]
10. Hitoshi, F.; Yu, S. Three-dimensional numerical analysis of the deformation behavior of droplets impinging onto a solid substrate. *Int. J. Multiph. Flow* **2007**, *33*, 317–332.
11. Shen, S.Q.; Cui, Y.Y.; Guo, Y.L. Numerical simulation of droplet striking on inclined isothermal surface. *J. Therm. Sci. Technol.* **2009**, *8*, 194–197. (In Chinese)
12. Wang, J.; Chen, G.D.; Liu, Y.J. Analysis of the oil droplet motion and deposition Characteristics in an aeroengine bearing chamber. *Tribology* **2010**, *30*, 362–366. (In Chinese)
13. Fujimoto, H.; Ogino, T. Collision of a droplet with a hemispherical static droplet on a solid. *Int. J. Multiph. Flow* **2001**, *27*, 1227–1245. [CrossRef]
14. Fukai, J.; Tanaka, M.; Miyatake, O. Maximum spreading of liquid droplets upon impact on flat surface. *J. Chem. Eng. Jpn.* **1998**, *31*, 456–461. [CrossRef]
15. Lu, J.; Chen, X.L.; Cao, X.K. Characteristic phenomenon and analysis of a single liquid droplet impacting on a dry surface. *Chem. React. Eng. Technol.* **2007**, *12*, 505–511. (In Chinese)
16. Weinstock, V.D.; Heister, S.D. Modeling oil flows in engine sumps: Drop dynamics and wall impact simulation. *J. Eng. Gas Turbines Power Trans. ASME* **2006**, *128*, 163–172. [CrossRef]
17. Gorse, P.; Dullenkopf, K.; Bauer, H.-J.; Wittig, S. An Experimental Study on Droplet Generation in Bearing Chambers Caused by Roller Bearings. In Proceedings of the ASME Turbo Expo 2008: Power for Land, Sea, and Air, Berlin, Germany, 9–13 June 2008.
18. Farrall, M.; Simmons, S.; Hibberd, S.; Gorse, P. Modeling Oil Droplet/Film Interaction in an Aero-Engine Bearing Chamber and Comparison with Experimental Data. ASME Paper No. GT2004–53698. In Proceedings of the ASME Turbo Expo 2004: Power for Land, Sea, and Air, Vienna, Austria, 14–17 June 2004.
19. Chen, B.; Chen, G.D.; Wang, T. Flow characteristics analysis of wall oil film with consideration of oil droplet deformation and secondary oil droplet deposition in aeroengine bearing chamber. *Acta Aeronaut. Astronaut. Sin.* **2013**, *34*, 1980–1989.
20. Tembely, M.; Vadillo, D.; Soucemarianadin, A.; Dolatabadi, A. Numerical Simulations of Polymer Solution Droplet Impact on Surfaces of Different Wettabilities. *Processes* **2019**, *7*, 798. [CrossRef]
21. Adeniyi, A.A.; Morvan, H.P.; Simmons, K.A. A Transient CFD Simulation of the Flow in a Test Rig of an Aeroengine Bearing Chamber. In Proceedings of the ASME Turbo Expo 2014: Turbine Technical Conference and Exposition, Düsseldorf, Germany, 16–20 June 2014.
22. Bristot, A.; Morvan, H.; Simmons, K. Evaluation of a volume of fluid CFD methodology for the oil film thickness estimation in an aero-engine bearing chamber. In Proceedings of the ASME Turbo Expo 2016: Turbomachinery Technical Conference and Exposition, Seoul, Korea, 13–17 June 2016.
23. Hirt, C.W.; Nichols, B.D. Volume of fluid (VOF) method for the dynamics of free boundaries. *J. Comput. Phys.* **1981**, *39*, 201–225. [CrossRef]
24. Youngs, D.L. Time dependent multi-material flow with large fluid distortion. In *Numerical Methods for Fluid Dynamics*; Morton, K.W., Baines M.J., Eds.; Academic Press: New York, NY, USA, 1982; pp. 273–285.

25. Brackbill, J.U.; Kothe, D.B.; Zemach, C. A continuum method for modeling surface-tension. *J. Comput. Phys.* **1992**, *100*, 335–354. [CrossRef]
26. Pan, K.L.; Tseng, K.C.; Wang, C.H. Breakup of a droplet at high velocity impacting a solid surface. *Exp. Fluids* **2010**, *48*, 143–156. [CrossRef]



© 2020 by the authors. Licensee MDPI, Basel, Switzerland. This article is an open access article distributed under the terms and conditions of the Creative Commons Attribution (CC BY) license (<http://creativecommons.org/licenses/by/4.0/>).



Article

# Investigation of the Superposition Effect of Oil Vapor Leakage and Diffusion from External Floating-Roof Tanks Using CFD Numerical Simulations and Wind-Tunnel Experiments

Jie Fang, Weiqiu Huang \*, Fengyu Huang, Lipai Fu and Gao Zhang

Jiangsu Key Laboratory of Oil & Gas Storage and Transportation Technology, Changzhou University, Changzhou 213164, China; fangxyjoyce@sina.com (J.F.); 17000271@smail.cczu.edu.cn (F.H.); fulipeiupc@163.com (L.F.); e9940610@Gmail.com (G.Z.)

\* Correspondence: hwq213@cczu.edu.cn

Received: 31 January 2020; Accepted: 3 March 2020; Published: 5 March 2020

**Abstract:** Based on computational fluid dynamics (CFD) and Realizable  $k-\epsilon$  turbulence model, we established a numerical simulation method for wind and vapor-concentration fields of various external floating-roof tanks (EFRTs) (single, two, and four) and verified its feasibility using wind-tunnel experiments. Subsequently, we analysed superposition effects of wind speed and concentration fields for different types of EFRTs. The results show that high concentrations of vapor are found near the rim gap of the floating deck and above the floating deck surface. At different ambient wind speeds, interference between tanks is different. When the ambient wind speed is greater than 2 m/s, vapor concentration in leeward area of the rear tank is greater than that between two tanks, which makes it easy to reach explosion limit. It is suggested that more monitoring should be conducted near the bottom area of the rear tank and upper area on the left of the floating deck. Superposition in a downwind direction from the EFRTs becomes more obvious with an increase in the number of EFRTs; vapor superposition occurs behind two leeward tanks after leakage from four large EFRTs. Considering safety, environmental protection, and personnel health, appropriate measures should be taken at these positions for timely monitoring, and control.

**Keywords:** external floating-roof tank; oil vapor superposition effect; numerical simulation; leakage and diffusion; wind tunnel

## 1. Introduction

External floating-roof tanks (EFRTs) are widely used for crude oil storage [1]. With the development of petroleum reserve strategies, different types of EFRTs have been developed. However, the floating deck in an EFRT cannot seal a tank wall absolutely as it needs to float up and down freely [2]. In other words, there is an annular rim gap between the floating deck and tank wall. As the elasticity of the rim seal gradually decreases with long-term usage, the rim gap widens. Especially, improper operation or poor maintenance will aggravate the attrition of the sealing device. Under such conditions, oil evaporation from the rim gap and oil vapor diffusion into the atmosphere increase simultaneously. The discharged vapor typically contains volatile organic compounds (VOCs), which can cause several safety and environmental problems [3–5]. When air flows through storage tanks, vortices are generated and an improper layout will produce some ‘dead angles of the vortices’ [6], and these dead angles adversely affect air flow and oil-vapor discharge. In this case, the concentration of oil vapor in these dead angles is superimposed, which increases the likelihood of accidents, such as fire. Therefore, analysing the effect of superposition on VOC leakage and diffusion in EFRTs has obvious practical significance and theoretical value [7–9].

Numerical simulation methods are widely used to describe oil-vapor diffusion in storage tanks [10–12]. Sharma et al. [13] investigated static breathing evaporation loss from two horizontal storage tanks on the ground and underground and found that higher the concentration of n-butane and i-pentane, higher is the breathing loss. Huang et al. [14] and Wang et al. [15] investigated the effects of oil loading rate and the initial oil-vapor concentration on the oil-vapor mass transfer and the evaporation loss in the large dome roof tank by using the phase-interface convection mass transfer model. The results revealed the variation rules of the oil-vapor concentration, the speed ratio of gas to liquid, and the evaporation loss rates of oil products in the tank and at the discharge ports. Hou et al. [16] investigated the heat and mass transfer mechanisms in refueling process by using two-dimensional unsteady state model of the vehicle refueling process. The results showed that as the refueling velocity increases, the gas-liquid mixing is increased, and the free surface of liquid is gradually blurred. Hassanvand et al. [17,18] used the volume-of-fluid (VOF) model of CFD to simulate the various influence factors in the process of gasoline tank loading, and studied the effects of the temperature, the oil loading speed, the initial oil-vapor concentration of the tank on the oil loss rate of the tank. Hao et al. [19] carried out numerical simulation methods and experimental verification for the oil vapor leakage and diffusion from the large and small EFRT at different leakage locations and pore sizes. The results showed that when there is a rim leakage between the floating deck and tank wall, oil vapor diffuses along the tank wall to the upper space of the floating deck. Ai and Mak [20] used CFD methods under the hypothesis that infectious respiratory aerosols exhausted from a unit can reenter into another unit in the same building through opened windows, and found that the distribution of the polluted gas is highly dependent on the wind direction, and the diffusion is more intense when the wind deviation angle is not  $0^\circ$ .

Several researchers used the wind-tunnel test platform to study oil leakage and diffusion from storage tanks [21–23]. Liu et al. [24] studied the diffusion behaviour of heavy gases in the case of instantaneous leakage and continuous release in wind tunnels. Using this methodology, the influence of different obstacles on the diffusion of heavy gases was also studied. Macdonald et al. [25] used the wind-tunnel test platform to study wind loads on tank walls and roofs of different types, tank sizes, and Reynolds numbers. Poterla and Godoy [26] carried out experimental studies on cylindrical shells with different height-diameter ratios and roof forms in a wind tunnel and obtained the corresponding wind-pressure distribution law. Wang et al. [27] measured the volume fraction of carbon dioxide, ethyne and propylene in a flammable gas-leak accident on direct-current wind-tunnel test platform, analysed the concentration distribution using a meteorological chromatograph, and measured the wind speed distribution using an anemometer. A range of hazardous gas volume fraction was obtained at different wind speeds and different leakage rates.

The diffusion of oil vapors is highly dependent on the ambient wind speed. At different wind speeds, vapor distribution trends in a tank vary, resulting in different concentration distributions and vapor-accumulation locations. Furthermore, there may appear superposition effects of wind speed and concentration fields in different EFRT groups. Therefore, in this study, we conducted wind-tunnel experiments and numerical simulations on a single EFRT and two EFRTs at different ambient wind speeds of 2, 4, and 6 m/s. Subsequently, numerical simulations were conducted on vapor leakage and diffusion from four 10000 m<sup>3</sup> EFRTs.

## 2. Methodology

### 2.1. Experimental Protocol

A self-made direct-flow wind tunnel was used to generate steady wind fields, as shown in Figure 1. The wind tunnel (DFWT-10) included gas-gathering, stable, contraction, test, first diffusion, power, and second diffusion sections. The size of the test section is 1.5 m (H) × 1.5 m (W) × 3 m (L) and the turbulence intensity of the designed wind field in the test section is 30–40% to simulate a wind field (0–20 m·s<sup>-1</sup>). The ambient wind speed, the temperature, and the humidity can be measured by the

hot-wire anemometer (TES-1341, Taishi, the wind speed range of  $0\text{--}30\text{ m}\cdot\text{s}^{-1}$  and the resolution of  $0.01\text{ m}\cdot\text{s}^{-1}$ , the temperature range of  $-10\text{--}60\text{ }^{\circ}\text{C}$  and the resolution of  $0.01\text{ }^{\circ}\text{C}$ , and the humidity range of  $10\text{--}95\%$  RH and the resolution of  $0.1\%$  RH). The evaporation loss can be automatically measured by the high-precision electronic balance (WT-30000-1B, Wantai Electronic Balance with the range of  $0\text{--}30\text{ kg}$  and the resolution of  $0.1\text{ g}$ ). The mass difference method was used to measure the mass change of n-hexane in a period of time. N-hexane mass was measured before and after the experiment and the mass change can be calculated as the mass loss of n-hexane during an hour, which is measured for 5 times. Then, the variation of the mass per unit time can also be calculated as the loss rate of n-hexane. In addition, the evaporation loss rate of the EFRT from the annular rim gap were measured by the wind tunnel test, and then the evaporation loss rate was set as the mass-flow-inlet of the boundary conditions of the annular rim gap in the FLUENT software. The gas sampler (QC-4S) with a rate range of  $0.1\text{--}1.5\text{ L}\cdot\text{min}^{-1}$  was chosen to sample the vapor around the tank. The vapor components and concentrations can be analysed using a gas chromatography (GC-2010 Plus, Shimadzu International Trading Co., Limited, Japan) with FID and capillary column of Rtx-1 ( $30\text{ m} \times 0.25\text{ mm} \times 0.25\text{ }\mu\text{m}$ ).



Figure 1. Wind tunnel for the experiments.

The small EFRT represents a scaled model (35:1) of a  $1000\text{ m}^3$  field EFRT [28]. This ratio guarantees the blocking rate of the tank in the wind tunnel. The diameter, wall height, and rim gap width of the small EFRT were 344, 272, and 6 mm, respectively. A schematic diagram of the wind-tunnel experiment is shown in Figure 2. Because the volatility of n-hexane is moderate, it was used as a representative of conventional oil in the numerical calculation of the leakage and diffusion from EFRTs. When the wind speed is  $2\text{ m/s}$ ,  $Re$  for the field in the wind tunnel is 257566, which is more than 4000, so it can be seen as turbulence.

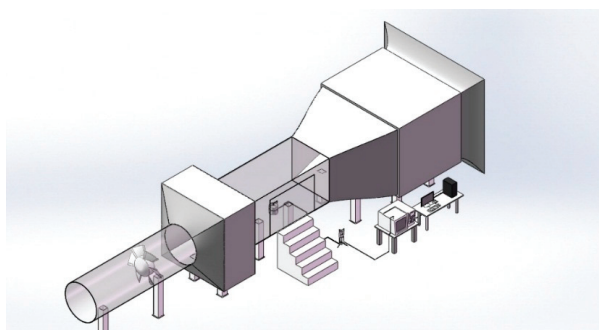
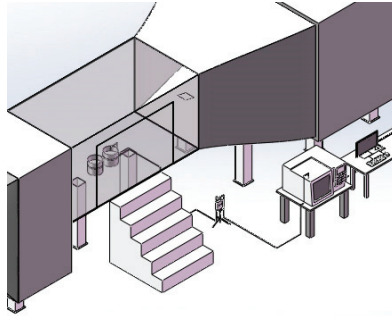


Figure 2. Cont.



**Figure 2.** Schematic representation of the wind-tunnel experiment.

## 2.2. Numerical Calculation Method

### 2.2.1. Governing Equations

An EFRT is affected by external wind and the gas space above the floating deck and around the tank wall will produce a pressure difference. Due to this pressure difference, oil vapor under the seal rim of the floating deck will diffuse into the atmosphere. To describe this fluid motion, the following governing equations and turbulence model were used.

(1) The continuity equation,

$$\operatorname{div}(u) = \frac{\partial \rho}{\partial t} + \frac{\partial}{\partial x_j}(\rho u_j) = 0 \quad (1)$$

where  $\rho$  ( $\text{kg}\cdot\text{m}^{-3}$ ) is the fluid density,  $t$  (s) is the time,  $x_j$  (m) represent the moving distance on X, Y, and Z axes, and  $u_j$  ( $\text{m}\cdot\text{s}^{-1}$ ) represents velocity vectors on X, Y, and Z axes. For the incompressible fluid, the density is the constant.

(2) The momentum equation,

$$\frac{\partial(\rho u_i)}{\partial t} + \frac{\partial}{\partial x_j}(\rho u_i u_j) = -\frac{\partial p}{\partial x_i} + \frac{\partial}{\partial x_j}(\mu_t \frac{\partial u_i}{\partial x_j}) + (\rho - \rho_a)g_i \quad (2)$$

where  $p$  (Pa) is the absolute pressure of the atmosphere,  $\mu_t$  (Pa·s) is the eddy viscosity,  $\rho_a$  ( $\text{kg}\cdot\text{m}^{-3}$ ) is the density of the atmosphere, and  $g$  represents gravitational acceleration. The subscript  $i$  in  $x_i$ ,  $u_i$  and  $g_i$  indicates the values on X, Y, and Z axes, respectively.

(3) The energy equation,

$$\frac{\partial(\rho E)}{\partial t} + \frac{\partial(\rho u_j E)}{\partial x_j} = \rho f_j u_j - \frac{\partial(p u_j)}{\partial x_j} + \frac{\partial(\tau_{ij} u_j)}{\partial x_i} + \frac{\partial}{\partial x_j} \left( k \frac{\partial T}{\partial x_j} \right) + S_h \quad (3)$$

Here,

$$E = h - \frac{p}{\rho} + \frac{u^2}{2}$$

where  $T$  (K) is the temperature of the fluid,  $f_j$  ( $\text{N}/(\text{m}^{-3}\cdot\text{s})$ ) is the volume force,  $\tau$  is the stress tensor,  $S_h$  includes the heat of the chemical reaction, and any other volumetric heat sources.

(4) The component transport equation,

$$\frac{\partial(\rho\omega)}{\partial t} + \frac{\partial}{\partial x_j}(\rho u_j \omega) = \frac{\partial}{\partial x_j}(\rho D_1 \frac{\partial \omega}{\partial x_j}) \quad (4)$$

Here,

$$\omega = \frac{CM_{mol}}{1000\rho} = \frac{nM_{mol}}{1000\rho V}$$

where  $D_1$  (m<sup>2</sup>/s) is the turbulent diffusion coefficient.  $\omega$  is the mass fraction of the vapor to the gas mixture of the vapor-air.  $C$  (mol/L) is the molar concentration of the vapor,  $M_{mol}$  (g/mol) is the molar mass of the vapor,  $n$  (mol) is the amount of the vapor,  $V$  (m<sup>3</sup>) is the volume of the vapor-air mixture. This equation is applied to systems with mass exchange or multiple chemical components.

(5) The turbulence model

In general, an EFRT is located in the atmospheric boundary layer above the ground in industrial applications. Flow field in the boundary layer is affected by air pressure, temperature, ground friction, obstacles, and other parameters and hence, the flow is turbulent. Both the standard  $k$ - $\varepsilon$  model and realizable  $k$ - $\varepsilon$  turbulence model can be employed to simulate fully-developed turbulent flow; however, the latter better represents flow separation and vortices than the former; furthermore, the realizable  $k$ - $\varepsilon$  turbulence model yields a more accurate concentration distribution than the RNG  $k$ - $\varepsilon$  turbulence model [29]. Thus, the realizable  $k$ - $\varepsilon$  turbulence model was chosen for numerical calculations; the turbulent kinetic energy and dissipation rate equations of the model are shown in Equations (5) and (6), respectively.

$$\frac{\partial(\rho K)}{\partial t} + \frac{\partial(\rho u_y K)}{\partial x_y} = \frac{\partial}{\partial x_y} \left[ \left( \mu + \frac{\mu_t}{\sigma_K} \right) \frac{\partial K}{\partial x_y} \right] + P_K + G_b - \rho \varepsilon - Y_M \quad (5)$$

$$\frac{\partial(\rho \varepsilon)}{\partial t} + \frac{\partial(\rho u_y \varepsilon)}{\partial x_y} = \frac{\partial}{\partial x_y} \left[ \left( \mu + \frac{\mu_t}{\sigma_\varepsilon} \right) \frac{\partial \varepsilon}{\partial x_y} \right] + \rho C_1 S \varepsilon - C_2 \rho \frac{\varepsilon^2}{K + \sqrt{v \varepsilon}} + C_{\varepsilon 1} \frac{\varepsilon}{K} C_{\varepsilon 3} G_b \quad (6)$$

Here,

$$\mu_t = C_\mu \rho \frac{K^2}{\varepsilon}, C_{\varepsilon 1} = 1.44, C_2 = 1.9, \sigma_\varepsilon = 1.2, \sigma_K = 1.0, C_1 = \max\left(0.43, \frac{\eta}{\eta + 5}\right)$$

$$\eta = \frac{K}{\varepsilon} S, S = \sqrt{2S_{xy}S_{xy}}, C_\mu = \frac{1}{A_0 + A_s \frac{U^* K}{\varepsilon}}$$

$$A_0 = 4.04, A_s = \sqrt{6} \cos \varphi, \varphi = \frac{1}{3} \arccos(\sqrt{6}W), W = \frac{S_{xy}S_{yz}S_{zy}}{\sqrt{S_{xy}S_{xy}}}, S_{ij} = \frac{1}{2} \left( \frac{\partial u_x}{\partial x_y} + \frac{\partial u_y}{\partial x_x} \right)$$

$$U^* = \sqrt{S_{xy}S_{xy} + \tilde{\Omega}_{xy}\tilde{\Omega}_{xy}}, \tilde{\Omega}_{xy} = \Omega_{xy} - 2\varepsilon_{xyz}\omega_z, \Omega_{xy} = \bar{R}_{xy} - \varepsilon_{xyz}\omega_z, \bar{R}_{xy} = \frac{1}{2} \left( \frac{\partial u_x}{\partial x_y} - \frac{\partial u_y}{\partial x_x} \right)$$

In these equations,  $\rho$  (kg·m<sup>-3</sup>) represents fluid density,  $f_x$  (N·m<sup>-3</sup>) represents volume force,  $\mu$  (Pa·s) is the kinetic viscosity,  $K$  (m<sup>2</sup>·s<sup>-2</sup>) is the turbulent kinetic energy,  $\varepsilon$  (m<sup>2</sup>·s<sup>-3</sup>) is the dissipation rate,  $P_k$  (m·s<sup>-2</sup>) is the turbulent kinetic energy generation term,  $G_b$  is the buoyancy generation term,  $Y_M$  is the compressibility corrected term,  $\nu$  (m<sup>2</sup>·s<sup>-1</sup>) indicates kinematic viscosity, and  $\omega_z$  (rad·s<sup>-1</sup>) indicates angular velocity. When the direction of shear flow is the same as the gravitational direction,  $C_{\varepsilon 3} = 1$  and when the shear flow is perpendicular to the direction of gravity,  $C_{\varepsilon 3} = 0$ .  $\sigma_k$  and  $\sigma_\varepsilon$  are the Prandtl

numbers corresponding to the turbulent kinetic energy and dissipation rate, respectively;  $S_k$  and  $S_\epsilon$  are user-defined values.

### 2.2.2. Computational Domain and Boundary Conditions

The computational domain size setting should take into account both the calculation time and the accuracy of calculation results. In computational wind engineering, the blocking ratio is often used to set the cross-sectional area of the computational domain. If the blocking ratio is less than 3% to 5%, it is considered that the flow field near and in the tank is not affected by the boundaries of the computational domain [30]. Considering the computational accuracy, blocking ratio, and calculation time, as shown in Figure 3, a three-dimensional computational domain was selected in this study. The size of the region was  $15D$  (X)  $\times$   $5H$  (Y)  $\times$   $10D$  (Z) (D: tank diameter, H: total height of the tank). Figure 3a shows the computational domain of a single small EFRT and Figure 3b shows the domain corresponding to two small EFRTs. Large EFRTs are commonly used in industrial applications; as shown as Figure 3c, four  $10000\text{ m}^3$  EFRTs were chosen to investigate the effect of oil vapor superposition between EFRTs. Structured mesh division was selected. The total number of cells for the single, double and four EFRTs was about 1.10 million, 1.74 million and 2.44 million, and the independence of cells were validated.

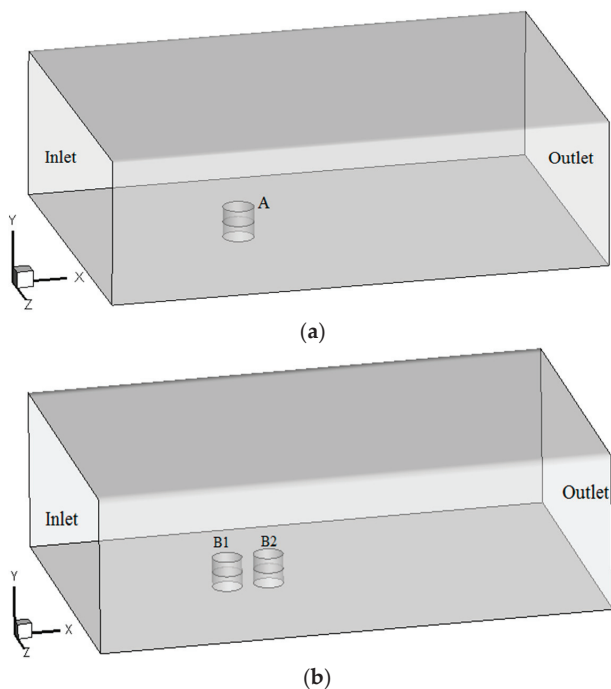
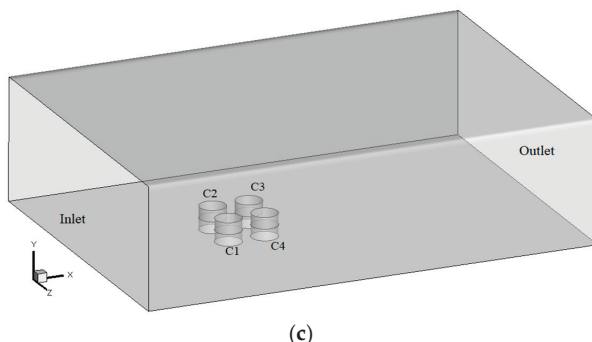


Figure 3. Cont.



**Figure 3.** Computational domain of (a) a single external floating-roof tank (EFRT), (b) two EFRTs, and (c) four large EFRTs.

The inlet boundary of the flow field was set as the velocity inlet boundary condition and the ambient wind speed represents an exponential distribution. Wind speed was introduced using the FLUENT User Defined Function (UDF). The direction of wind speed was positive along the X axis. The outlet boundary of the flow field was set as the pressure outlet boundary condition while the gap between the floating deck and the tank wall was set as the mass-flow boundary condition and mass-flow rates were determined experimentally. The tank bottom, tank wall, and floating deck were all set as no-slip boundaries and the ambient temperature was set at 13.5 °C. The mass-flow rate of the single tank at 2 m/s is  $2.37 \times 10^{-5} \text{ kg}\cdot\text{s}^{-1}$ , at 4 m/s is  $4.30 \times 10^{-5} \text{ kg}\cdot\text{s}^{-1}$  and at 6 m/s is  $5.13 \times 10^{-5} \text{ kg}\cdot\text{s}^{-1}$ . The mass-flow rates of the double tanks at 2 m/s are  $3.52 \times 10^{-5} \text{ kg}\cdot\text{s}^{-1}$  (B1) and  $2.42 \times 10^{-5} \text{ kg}\cdot\text{s}^{-1}$  (B2). The mass-flow rates of the double tanks at 4 m/s are  $5.08 \times 10^{-5} \text{ kg}\cdot\text{s}^{-1}$  (B1) and  $4.30 \times 10^{-5} \text{ kg}\cdot\text{s}^{-1}$  (B2). The mass-flow rates of the double tanks at 6 m/s are  $6.25 \times 10^{-5} \text{ kg}\cdot\text{s}^{-1}$  (B1) and  $5.03 \times 10^{-5} \text{ kg}\cdot\text{s}^{-1}$  (B2). The parameter properties in the calculation process are shown in Table 1.

**Table 1.** The properties of material parameters in the calculation process.

Material	Test Temperature/°C	Density/kg·m <sup>-3</sup>	Mole Mass/g·mol <sup>-1</sup>	Saturated Vapor Pressure/kPa	Diffusion Coefficient in Air/10 <sup>-6</sup> m <sup>2</sup> ·s <sup>-1</sup>
n-hexane vapor	13.5	663.5	86.2	11.9	7.4
atmosphere	13.5	1.29	29	/	/

### 3. The Wind-Tunnel Test Validation

There are many factors affecting leakage and diffusion from EFRTs, including the position of the floating deck, ambient wind speed, and temperature. At present, there are few experimental studies on the leakage and diffusion laws of EFRTs. To understand evaporation loss from EFRTs at different ambient wind speeds (2, 4, and 6 m/s) and oil vapor distribution inside or outside EFRTs and to verify the rationality of the simulation and EFRT geometric models applied to oil-evaporation loss, a wind-tunnel test platform was used for experimental research and data analysis under leaking conditions in the rim gaps of the floating decks of EFRTs. Herein, the floating deck height was defined as the distance of the floating deck position to the tank bottom and it was set at 136 mm. Since n-hexane is the main component of gasoline vapor, and its physical properties are relatively mild, it is feasible and convenient to use n-hexane instead of gasoline for experiment and simulation.

Firstly, the height of the floating deck was set at 136 mm, i.e., the space below this height was filled with n-hexane. Later, the ambient wind speed was varied from 2 to 6 m/s. The wind speed and concentration-field distributions at the same position of the floating deck height but at different ambient wind speeds were measured. The measuring positions for the single EFRT were located at the centre of the single EFRT (A) (W1), 0.2D behind the single EFRT (A) (W2), 0.9D behind the single EFRT

(A) (W3), and 1.6D behind the single EFRT (A) (W4). The measuring point positions of the two EFRTs were the centre of the windward EFRT (B1) (P1), 0.2D behind the windward EFRT (B1) (P2), centre of the leeward EFRT (B2) (P3), and 0.2D behind the leeward EFRT (B2) (P4). Herein, the position of W3 corresponded to that of P3 and the position of W4 corresponded to that of P4. In these stated values, D represents tank diameter.

From the above experiments, the wind- and concentration-field distributions at different ambient wind speeds were obtained, as shown in Figures 4–6. In these figures, as gas chromatographic measurements were calibrated using methane, the values of concentration fields were based on methane concentration.

According to Figures 4–6, the larger the ambient wind speed, the greater is the disturbance from the leeward EFRT (B2) to the windward EFRT (B1), which is mainly reflected in the larger the maximum wind speed above the windward EFRT (B1) than that above the leeward EFRT (B2). The concentration distribution at 2 m/s is different from that at 4 and 6 m/s. Vapor concentration above the windward EFRT (B1) is lower than that above the centre of the two EFRTs at a wind speed of 2 m/s, which shows that most of the vapor is still in B1; the vortex current above the centre of the two EFRTs leads to a higher vapor concentration than that just above the windward tank (B1).

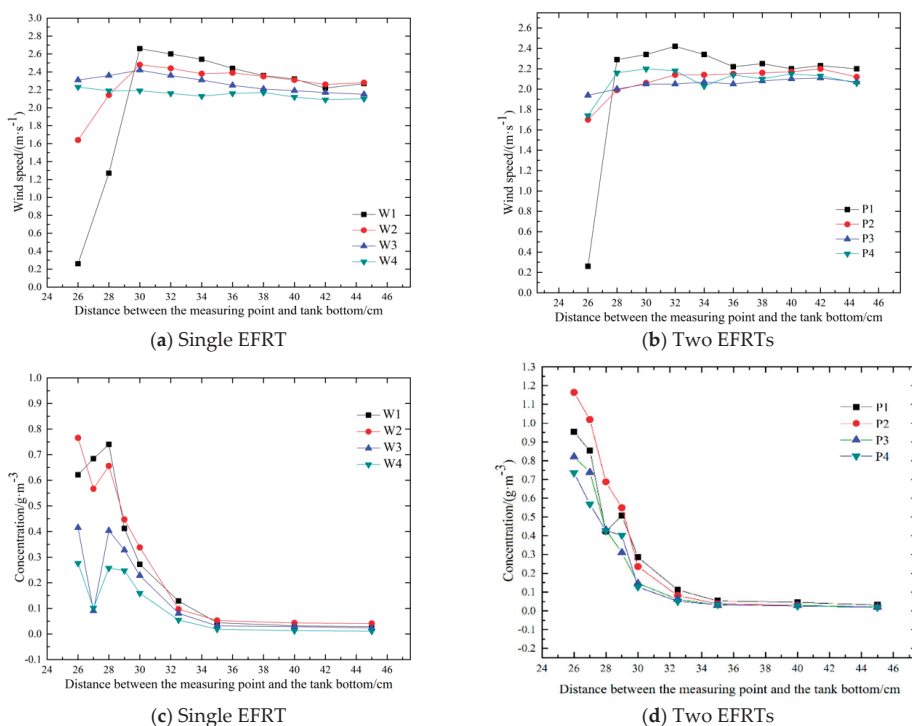


**Figure 4.** Wind speed distribution and concentration distribution above the floating deck surface at an ambient wind speed of 2 m/s.



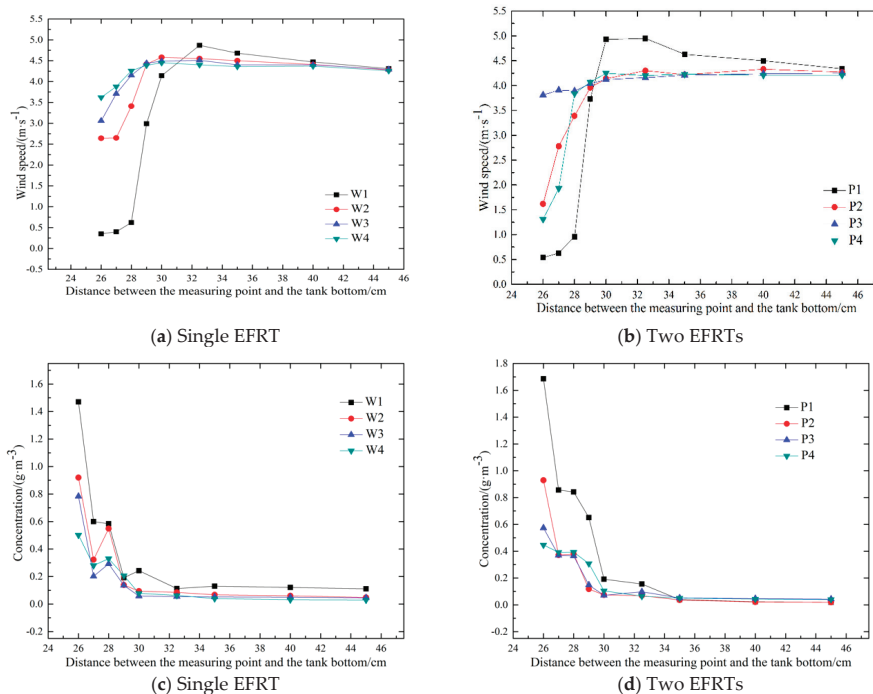


Figure 5. Wind speed distribution and concentration distribution above the floating deck surface at an ambient wind speed of 4 m/s.

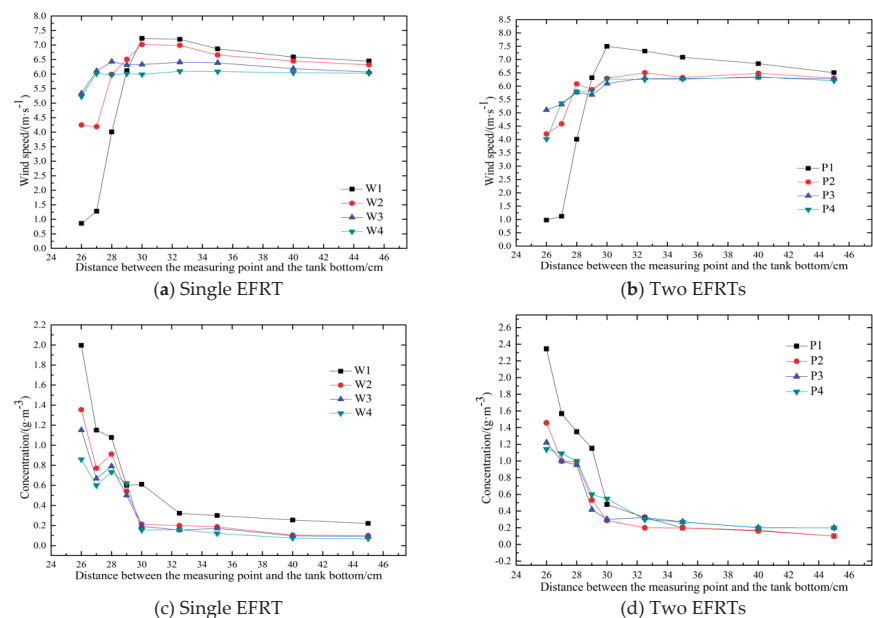


Figure 6. Wind speed distribution and concentration distribution above the floating deck surface at an ambient wind speed of 6 m/s.

At an ambient wind speed of 2 m/s, the values of wind speed and vapor concentration at each point in the vertical wind direction above the centre of the floating deck of the single EFRT (A) and above the centre of the floating decks of the two EFRTs (B1 and B2) were measured and they were then compared with the simulated values. The results are shown in Figures 7 and 8. From these figures, it can be inferred that the simulated values are consistent with the experimental values with only a small error between them, which proves that the construction of the geometric model and settings used for the numerical calculation method are reasonable. The deviations in wind speed are mainly due to errors in measurement. The probe of an anemometer affects the flow field to a certain extent when it enters into the tank. The deviation in concentration is mainly due to the destruction of some concentration fields around the sampler when it extracts vapor. Improper cleaning of the sampler also affects the measurement results.

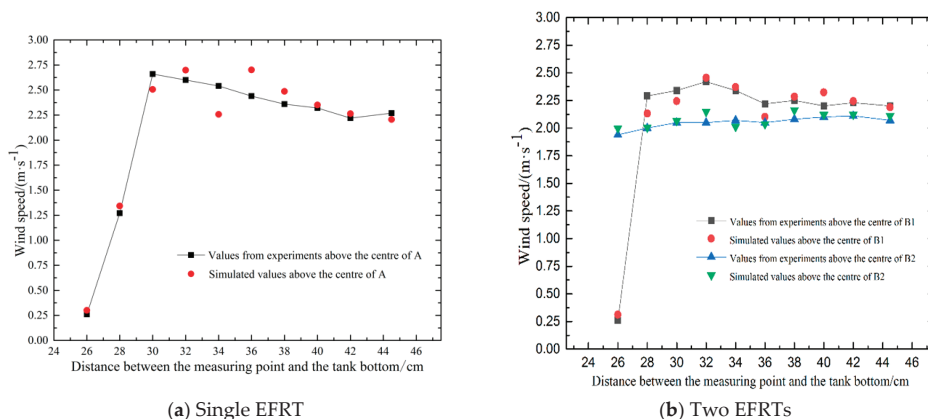


Figure 7. Comparison between experimental and simulated wind speed distribution values.

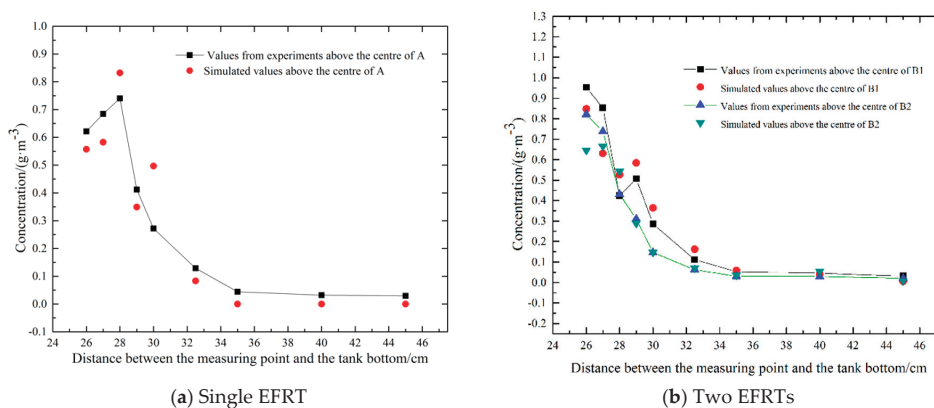


Figure 8. Comparison between experimental and simulated vapor-concentration distribution values.

## 4. Results and Analysis

### 4.1. The Wind Speed Distribution of Different EFRTs

Based on CFD numerical computations, the wind speed distributions of various EFRTs (single, two, and four) were analysed at a floating deck height of 122 mm. Wind speed cloud diagrams of the single EFRT and two EFRTs on the XY plane along the X-axis were simulated (Figure 9). To conveniently compare velocity distributions at different ambient wind speeds, Figure 9a,d represent

the values obtained at 2 m/s. Figure 9b,e show the values corresponding to a wind speed of 4 m/s while Figure 9c,f show the values corresponding to a wind speed of 6 m/s.

Wind speed cloud diagrams of the single EFRT on the XY plane along the X axis were simulated (Figure 9a–c). It can be seen in the figures that irrespective of the ambient wind speed, the following phenomena occur. On the windward side of the tank, due to blocking, airflow speed decreases gradually to 0 m/s; there is a light blue area close to the tank wall due to the reverse airflow caused by wind hitting the tank wall. At the bottom area of the windward side, there is a blue area with a negative wind speed, indicating backflow in this area and the danger of vapor superposition. On the leeward side of the tank, a large blue area with a negative wind speed appears on the right side of the tank, which indicates that the leeward area of the tank has a strong backflow and the wind speed isopleth is not as close to the tank wall as that on the windward side and the entire airflow-speed isopleth inclines along the lower right side. In the area above the tank, there is a high airflow-speed area (red area), where the wind speed exceeds the ambient wind speed. This is because the airflow area above the tank is smaller, leading to an accelerated airflow rate.

Wind speed cloud diagrams of the two EFRTs on the XY plane along the X axis were simulated (Figure 9d–f). It can be noted in these figures that wind speed distribution on the windward side is basically similar to that of the single EFRT. Although the airflow-speed values are different in the back area, the entire airflow-speed isopleth inclines along the upper right side. The space of the blue backflow zone at the back becomes larger and more complex. This is due to mutual blocking between tanks, which aggravates turbulence. The above-described phenomena occur irrespective of the ambient wind speed.

Combining with the wind fields measured experimentally, it can be found that the wind speed at 2 m/s is slightly different from that at 4 and 6 m/s. When the ambient wind speed is 2 m/s, the maximum wind speed above B1 is lesser than that above A but at 4 and 6 m/s, the maximum wind speed above B1 is approximately similar to or larger than that above A.

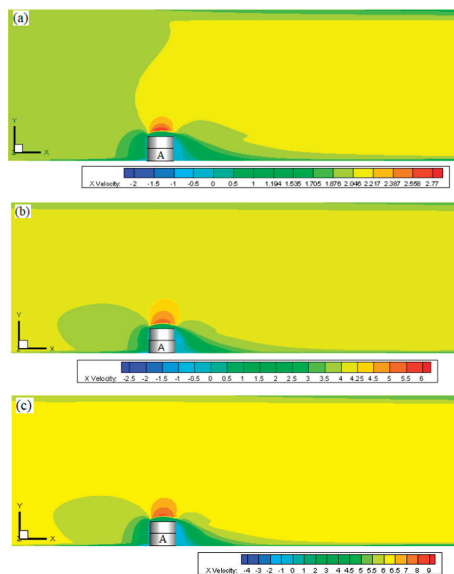
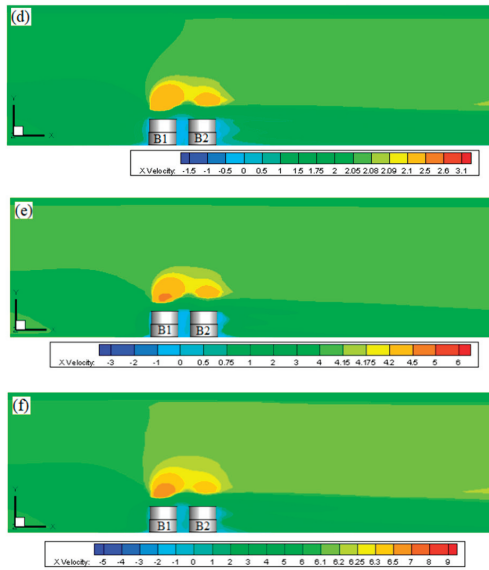
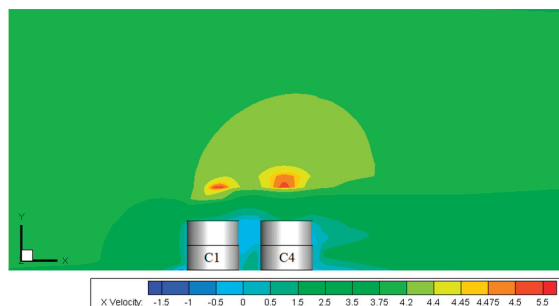


Figure 9. Cont.



**Figure 9.** Wind speed cloud diagrams of a single EFRT and two EFRTs on the XY plane along the X axis at ambient wind speeds of (a,d) 2, (b,e) 4, and (c,f) 6 m/s.

The wind speed cloud diagrams of the four large EFRTs on the XY plane along the X axis were simulated (Figures 10 and 11) at an ambient wind speed of 4 m/s. Figure 10 shows the wind speed cloud diagrams of C1 and C4 and Figure 11 shows the wind speed cloud diagrams of C2 and C3. According to these figures, wind speed distribution on the windward side is similar to that observed in the case of the single EFRT and two EFRTs. The rule of area between C1 and C4 (C2 and C3) is different from that of the two EFRTs, but the entire wind speed isopleth inclines along the right side. Comparing the wind fields of the three cases at the same ambient wind speed, it can be seen that the area corresponding to a higher airflow speed becomes larger and the space of the blue backflow zone on the back becomes larger and more complex with an increase in the number of tanks. This is due to mutual blocking between tanks, which aggravates turbulence. In addition, due to interaction between the four large EFRTs, there is no longer a high-speed vortex over C3 on the leeward side.



**Figure 10.** Wind speed cloud diagrams of C1 and C4 on the XY plane along the X axis (4 m/s).

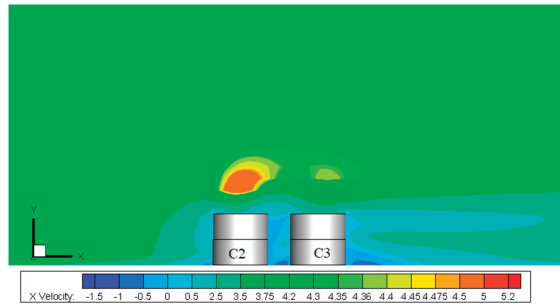


**Figure 11.** Wind speed cloud diagrams of C2 and C3 on the XY plane along the X axis (4 m/s).

4.2. Streamline Distribution Inside and Outside EFRTs

The streamline diagrams of gas movement in the single EFRT on the XZ plane at ambient wind speeds of 2 and 4 m/s are shown in Figure 12. Figure 13 illustrates the velocity vector diagrams of the single EFRT on the XY plane. The airflow follows a mirror distribution along the central axis of the floating deck. The vortex of the airflow is clockwise in the upper half and counter-clockwise in the lower half. Combining with the streamline diagrams of gas movement in the XY plane in Figure 13, the centre of the vortex is close to the middle of the floating deck. Comparing Figure 12a,b and Figure 13a,b, it can be inferred that the trend of gas movement in the single EFRT is almost constant.

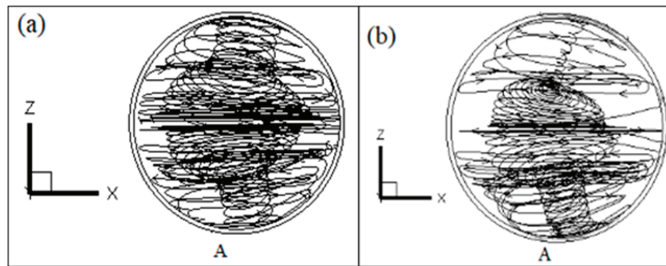


**Figure 12.** Flow diagrams of vapor movement in the single EFRT on the XZ plane at ambient wind speeds of (a) 2 and (b) 4 m/s.

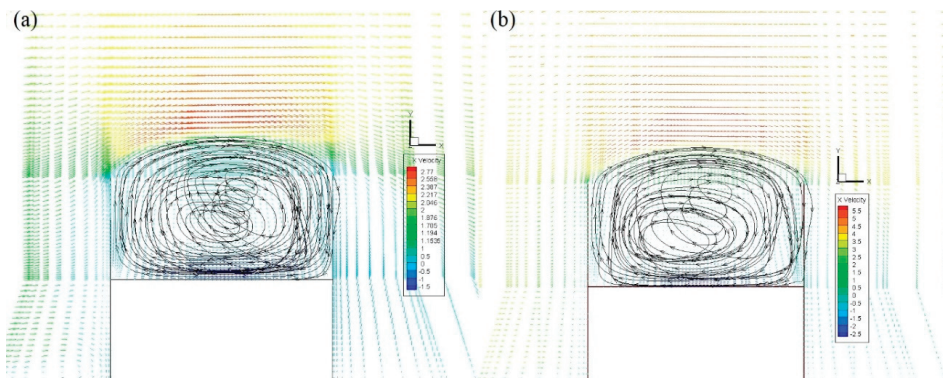


**Figure 13.** Flow diagrams of the vapor movement in the single EFRT on the XY plane at ambient wind speeds of (a) 2 and (b) 4 m/s.

The streamline diagrams of gas movement in the double EFRTs on the XZ plane at ambient wind speeds of 2 and 4 m/s are shown in Figures 14 and 15, respectively. Figure 16 shows the velocity-vector diagrams of the two EFRTs on the XY plane, in which the gas movement is more complicated. The front tank (B1) has two gas vortices that are similar to the single tank (A). Because of the blocking of B1 and disturbance in the airflow from B1, vortices in the rear tank (B2) are disturbed and no longer form recirculating vortices. According to Figures 14–16, gas movement in the single EFRT and two EFRTs is similar at ambient wind speeds of 2 and 4 m/s and hence we shall discuss the situation observed at 4 m/s later.

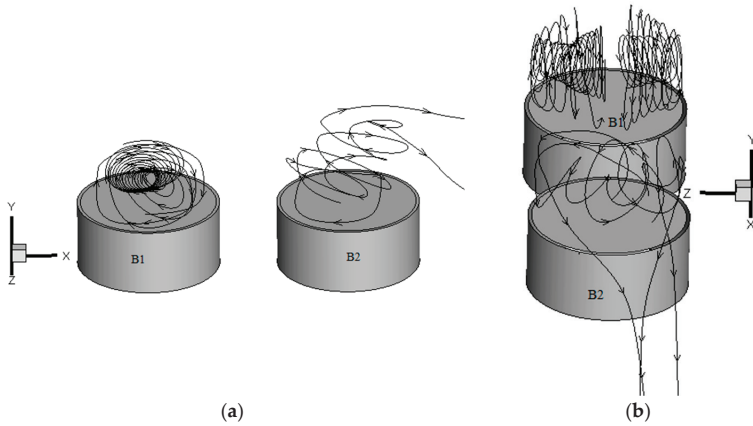


**Figure 14.** Flow diagrams of vapor movement in the two EFRTs at 2 m/s. (a) Positive angle and (b) side angle.

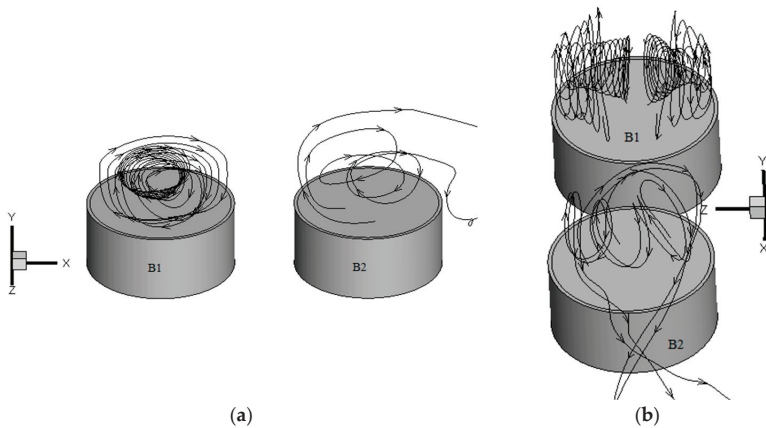


**Figure 15.** Flow diagrams of vapor movement in the two EFRTs at 4 m/s. (a) Positive angle and (b) side angle.

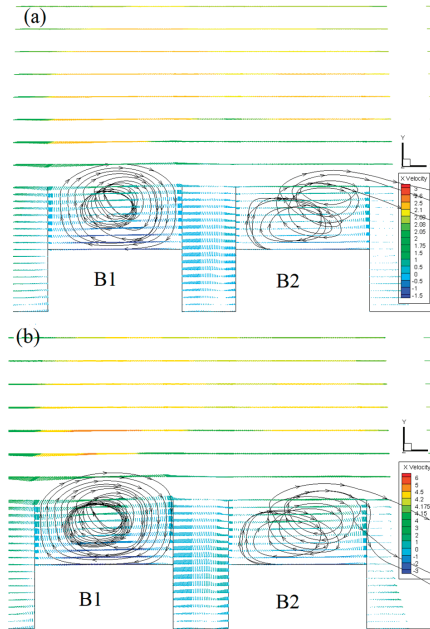


**Figure 16.** Flow diagrams of vapor movement in the two EFRTs on the XY plane at ambient wind speeds of (a) 2 and (b) 4 m/s.

The streamline diagrams of gas movement in the four large EFRTs on the XZ plane are shown in Figure 17. Here, the gas movement is highly complicated because apart from the interaction between the front and rear tanks, left and right EFRTs also exert some influence. The gas movement in C1 and C2 on the windward side is more regular and there are relatively complete airflow vortices in the tanks. In Figures 17 and 18, because of the effect of the Karman Vortex Street, airflow moves to the rear EFRTs periodically along a similar ‘S’ trajectory after bypassing the front EFRTs. Combining with the pressure cloud diagram in Figure 18, it can be seen that the pressure on the left side of C4 is higher than that observed for C3, which leads to a greater internal wind speed in C4 and large circular vortices. However, because the wind speed in C3 is too small to drive all the airflow in the tank, two symmetrical small circular vortices are formed on the left side.

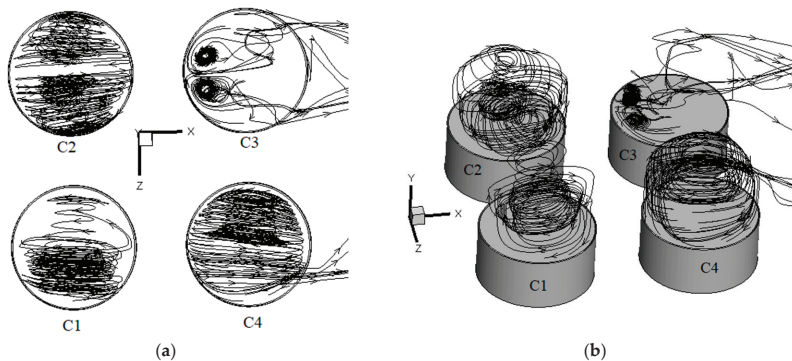


**Figure 17.** Flow diagrams of vapor movement in the four large EFRTs at an ambient wind speed of 4 m/s. (a) Top view and (b) main view.

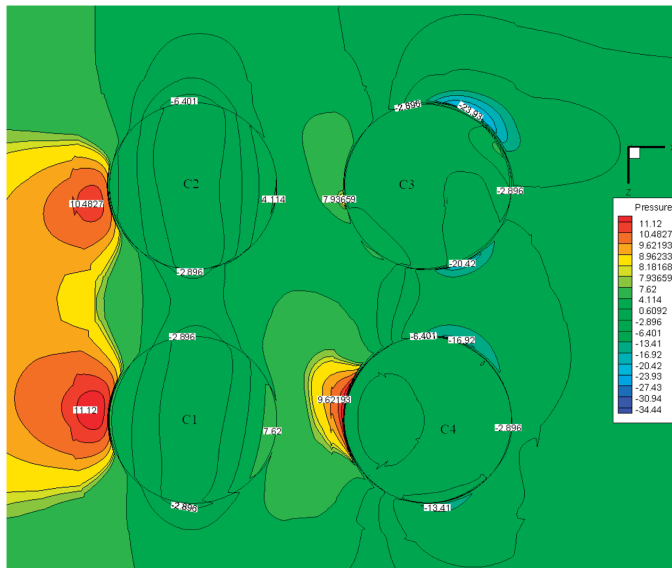


**Figure 18.** Pressure cloud diagram of the four large EFRTs at a height equal to the tank top on the XZ plane at an ambient wind speed of 4 m/s.

The flow diagrams of vapor movement outside different EFRTs (single, two, and four) at an ambient wind speed of 4 m/s are shown in Figures 19–21, respectively. Similar to the case of gas movement in EFRTs, as the number of tanks increases, the interaction between EFRTs increases and the trajectory of airflow becomes more complex. Vortices are formed but the vortex area of the two EFRTs and four large EFRTs is larger than that of the single EFRT. For the coupled and four large EFRTs, because the rear tanks block the backward movement of airflow, a backflow is also formed between them, resulting in vortices. This area also experiences vapor superposition and hence is a key monitoring area.

In addition, comparing Figures 19b, 20b and 21b, it can be seen that the vortex at the rear of the single tank (A) is stacked on one side but the vortex currents behind tanks B1, C1, and C2 accumulate symmetrically. Meanwhile, gas streamlines from the front tank (B1) and rear tank (B2) intersect behind the rear tank (B2). Similarly, gas streamlines from the front tank (C2) and rear tank (C4) intersect behind the rear tank (C4). Gas streamlines from the front tank (C2) and rear tank (C3) intersect behind the rear tank (C3). The area in which gas intersection occurs will also experience vapor superposition.

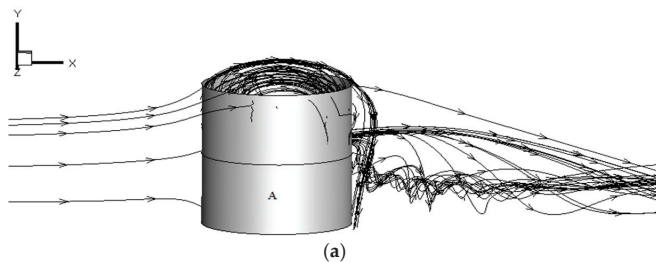


**Figure 19.** Cont.



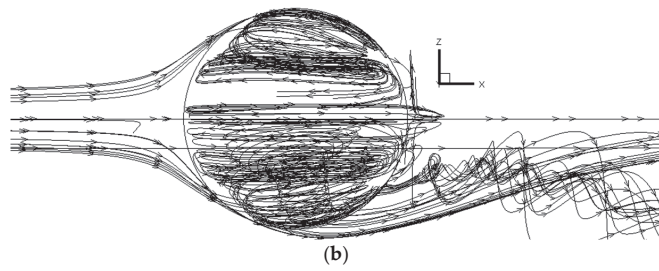


**Figure 19.** Flow diagrams of vapor movement outside the single EFRT at an ambient wind speed of 4 m/s. (a) Main view and (b) top view.

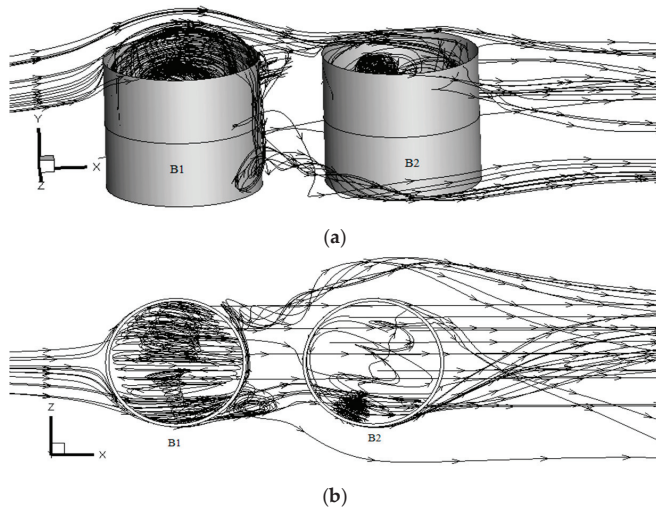


**Figure 20.** Flow diagrams of vapor movement outside the two EFRTs at an ambient wind speed of 4 m/s. (a) Main view and (b) top view.

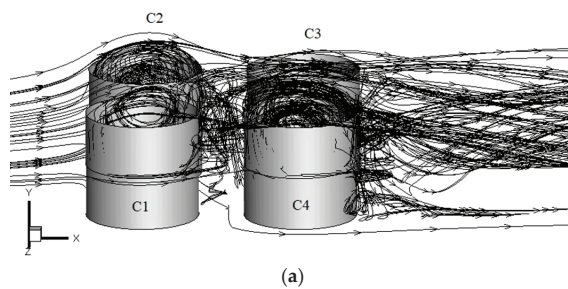


**Figure 21.** *Cont.*

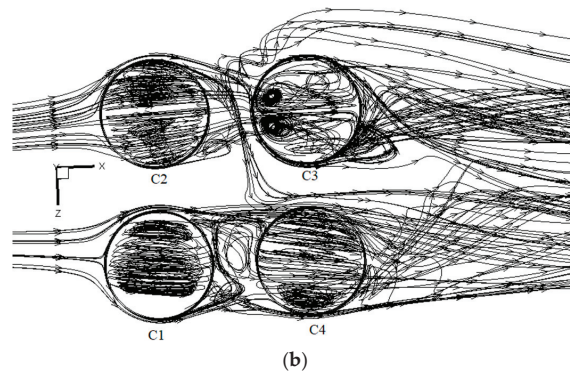


**Figure 21.** Flow diagrams of vapor movement outside the four large EFRTs at an ambient wind speed of 4 m/s. (a) Main view and (b) top view.

#### 4.3. Concentration Distribution for Various EFRTs

Vapor mass-fraction distribution cloud diagrams corresponding to single EFRT on the XY plane are shown in Figure 22. It can be seen that when the floating deck rim leaks, vapors are mainly located near the rim and upper part of the floating deck surface, leading to vapor concentration and potential safety hazards. Combining these inferences with Figure 13, it can be stated that because the gas in the tank rotates upwards in a large vortex, vapor accumulates at the centre of the vortex and upper part of the gap between the floating deck and tank wall. The main reason is that airflow in the tank rotates clockwise and wind speed is very low near the floating deck surface, owing to which the vapor can easily accumulate. Comparing Figure 22a,b, it can be seen that when the ambient wind speed increases, turbulence in the airflow in the tank increases when the floating deck rim leaks and subsequently, vapor concentration above the floating deck increases.

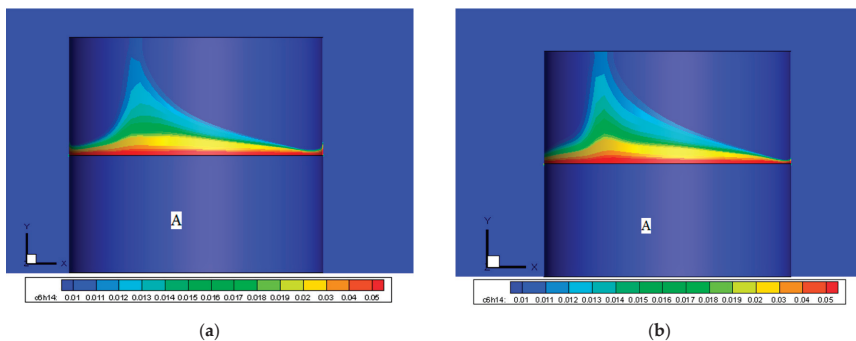


**Figure 22.** Vapor concentration-distribution cloud diagrams in the single EFRT on the XY plane at ambient wind speeds of (a) 2 and (b) 4 m/s.

Vapor concentration-distribution cloud diagrams in the two EFRTs above the floating deck and at the tank wall are shown in Figures 23 and 24, respectively. The highest vapor concentration is found at the rim gap of the floating deck. Because the front tank (B1) blocks the rear tank (B2) and some ambient wind bypasses B1 and enters into B2 directly from the rear of B2 resulting in right-to-left vortices, it leads to vapor accumulation on the left side of the rim gap. At a low ambient wind speed of 2 m/s, the leaked vapor from B1 cannot be blown out of the tank and hence vapor concentration in this tank is very high. Due to the blocking of the front tank (B1), airflow speed in the rear tank (B2) is close to the ambient wind speed and hence vapor concentration in B2 is smaller than that at 4 m/s. Combining Figures 15 and 20, it

can be seen that vapor in the front tank (B1) moves upwards along the windward side of the tank wall due to the front airflow vortices and hence vapor concentration is higher on the left side than on the right side. After vapor in the rear tank (B2) leaks out from the gap of the floating deck, it mainly moves towards the tank top along the windward side of the tank wall and eventually accumulates in the left half of B2.

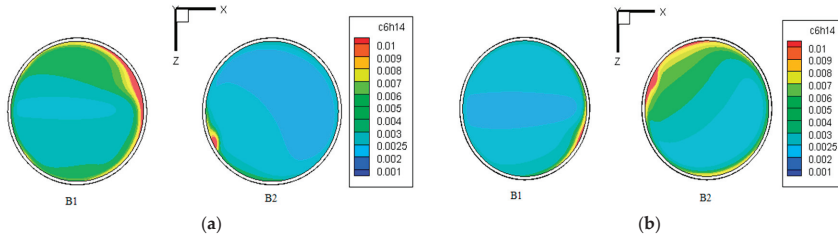


**Figure 23.** Vapor concentration-distribution cloud diagrams of the two EFRTs on the XZ plane at ambient wind speeds of (a) 2 and (b) 4 m/s.

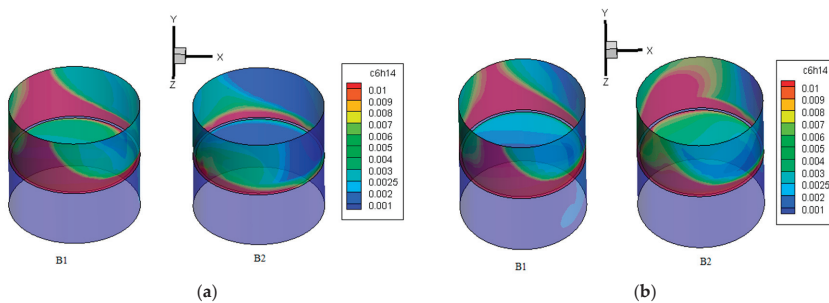


**Figure 24.** Vapor concentration-distribution cloud diagrams of the two EFRTs at ambient wind speeds of (a) 2 and (b) 4 m/s.

Vapor concentration-distribution cloud diagrams above the floating deck in the four large EFRTs on the XY plane at an ambient wind speed of 4 m/s are shown in Figure 25. It can be observed that vapor concentration in C2 is the lowest. This is because there are high-speed vortices above C2, which drive airflow in C2 in a clockwise manner and remove the leaked vapor. Figure 26 shows the vapor-concentration cloud diagram of the four large EFRTs near the ground on the XZ plane and Figure 27 depicts the vapor-concentration cloud diagram of the four large EFRTs at a height equal to the tank top on the XZ plane. Vapor concentration is relatively higher between C2 and C3 and after C3 and C4. From Figure 27, it can be inferred that vapor concentration in C4 is the highest, followed by C3; further, vapor concentration in C3 and C4 is larger than that in C1 and C2. In addition, according to Figures 21, 26 and 27, vapor superposition occurs behind C3 and C4 after leakage. Therefore, EFRTs in the downwind direction and the rear of these EFRTs should be considered as key areas for monitoring.

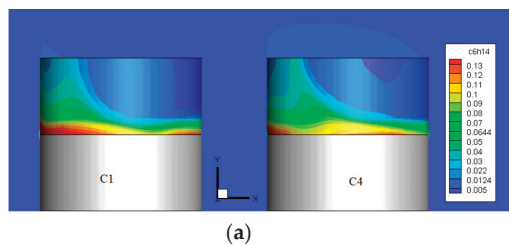


**Figure 25.** Cont.

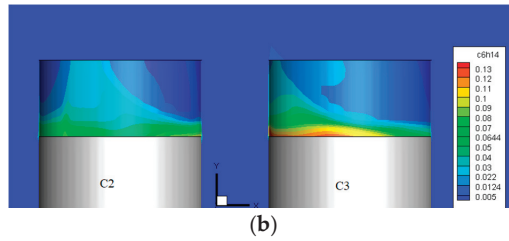


**Figure 25.** Vapor concentration-distribution cloud diagrams in the four large EFRTs on the XY plane of (a) C1 and C4, (b) C2 and C3.

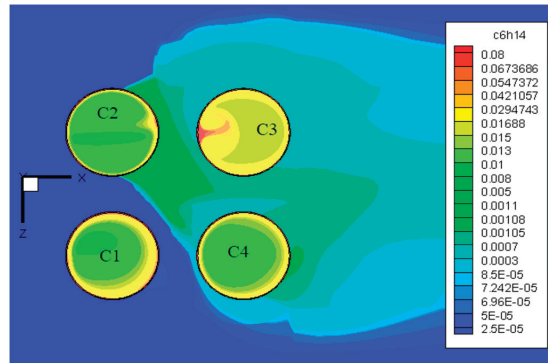


**Figure 26.** Vapor-concentration cloud diagram of the four large EFRTs near the ground on the XZ plane at 4 m/s.

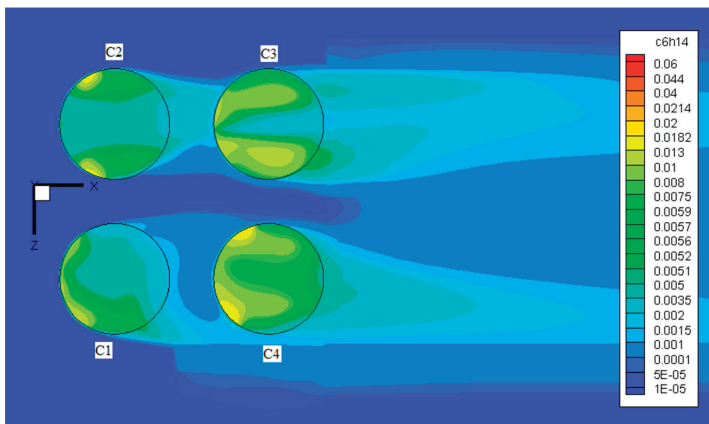


**Figure 27.** Vapor-concentration cloud diagram of the four large EFRTs at a height equal to that of the tank top on the XZ plane at 4 m/s.

## 5. Conclusions

In this study, we conducted numerical simulations and wind-tunnel experiments on vapor leakage and diffusion from a single EFRT and two EFRTs as well as numerical simulations on vapor leakage and diffusion from four large EFRTs. Based on wind-tunnel experiments, the physical model and numerical simulation model were verified. Furthermore, we discussed the distribution of wind speed and concentration fields in different types of EFRTs. Vapor diffusion after leakage from the rim gap of

the floating deck was studied and the superposition effect of the two tanks and four large tanks was investigated. The main features and conclusions of this work can be summarised as follows:

- (1) A numerical simulation method for leakage in and diffusion from tank groups is proposed and verified by wind-tunnel experiments and it can be used to simulate leakage in and diffusion from tank groups of different numbers under different working conditions.
- (2) For different EFRTs (single, two, and four), distributions on the windward side are similar. There is a large backflow area where the overall trend moves downwards on the leeward side. The two and four EFRTs also form gas vortices between the tanks and vapor tends to accumulate in them.
- (3) At different ambient wind speeds, the interference between the two tanks is different. At 2 m/s, vapor concentration in the rear tank is smaller than that in the front tank. However, at 4 m/s, vapor concentration in the rear tank is higher than that in the front tank. Combining experimental and simulation results, when the ambient wind speed is greater than 2 m/s, vapor concentration in the leeward area of the rear tank is greater than that between the two tanks. It is suggested that more monitoring should be carried out at the bottom area of the rear tank and upper area on the left of the floating deck.
- (4) The superposition effect becomes more obvious with an increase in the number of EFRTs. Vapor superposition occurs behind C3 and C4 after leakage from four large EFRTs. Therefore, EFRTs in the downwind direction and the area behind the EFRTs should be monitored frequently.

**Author Contributions:** Conceptualization, J.F., W.H.; software, J.F.; formal analysis, W.H., J.F., F.H., L.F. and G.Z.; investigation, F.H.; data curation, W.H., J.F., and G.Z.; writing—original draft preparation, J.F., W.H., F.H.; writing—review and editing, J.F., W.H., F.H., L.F. and G.Z.; supervision, W.H.; funding acquisition, W.H. All authors have read and agreed to the published version of the manuscript.

**Funding:** This research was funded by the National Natural Science Foundation of China (No. 51574044 and No. 51804045), the Key Research and Development Program of Jiangsu Province (Industry Foresight and Common Key Technology) (No. BE2018065), the Sci & Tech Program of Changzhou (No. CJ20180053) and Postgraduate Research & Practice Innovation Program of Jiangsu Province (NO. KYCX19\_1786 and NO. SJCX19\_0668).

**Conflicts of Interest:** The authors declare no conflict of interest.

## References

1. Yang, J.Y.; Zhu, S.J.; Chen, P. Leakage loss and emission calculation of VOCs in outer floating crude oil tank. *Saf. Health Environ.* **2017**, *17*, 37–40.
2. Shi, L.; Huang, W.Q. Sensitivity analysis and optimization for gasoline vapor condensation recovery. *Process Saf. Environ. Prot.* **2014**, *92*, 807–814. [CrossRef]
3. Si, H.T. Accident's type and cause of large-scale floating roof tank. *Oil Gas Storage Transp.* **2013**, *32*, 1029–1033.
4. Huang, W.Q.; Bai, J.; Zhao, S.H. Investigation of oil vapor emission and its evaluation methods. *J. Loss Prev. Process Ind.* **2011**, *24*, 178–186. [CrossRef]
5. Feng, L. Analysis of existing problems and discussion of countermeasures for sealing devices of large-scale external floating roof tanks. *Oil Gas Field Surf. Eng.* **2017**, *36*, 79–83.
6. Carlos, A.B.; Rossana, C.J.; Jorge, L.L. Wind buckling of tanks with conical roof considering shielding by another tank. *Thin Walled Struct.* **2014**, *84*, 226–240.
7. Jia, M.Y. Numerical Simulation on Wind Environment of Oil Tank Group Based on CFD. *Sci. Technol. Eng.* **2011**, *11*, 1881–1883.
8. Wu, C.F.; Wu, T.G.; Hashmonay, R.A. Measurement of fugitive volatile organic compound emissions from a petrochemical tank farm using open-path Fourier transform infrared spectrometry. *Atmos. Environ.* **2014**, *82*, 335–342. [CrossRef]
9. Tamaddon, M.; Sotudeh-Gharebagh, R.; Nario, S. Experimental study of the VOC emitted from crude oil tankers. *Process Saf. Environ. Prot.* **2014**, *92*, 929–937. [CrossRef]
10. Stamoudis, N.; Chryssakis, C.; Kaitsus, L. A two-component heavy fuel oil evaporation model for CFD studies in marine Diesel engines. *Fuel* **2014**, *115*, 145–153. [CrossRef]

11. Abianeh, O.S.; Chen, C.P.; Mahalingam, S. Numerical modeling of multi-component fuel spray evaporation process. *Int. J. Heat Mass Transf.* **2014**, *69*, 44–53. [CrossRef]
12. Sun, W.; Cheng, Q.L. Research on coupled characteristics of heat transfer and flow in the oil static storage process under periodic boundary conditions. *Int. J. Heat Mass Transf.* **2018**, *122*, 719–731. [CrossRef]
13. Sharma, Y.K.; Majhi, A.; Kukreti, V.S. Stock loss studies on breathing loss of gasoline. *Fuel* **2010**, *89*, 1695–1699. [CrossRef]
14. Huang, W.Q.; Wang, Z.L.; Ji, H. Experimental determination and numerical simulation of vapor diffusion and emission in loading gasoline into tank. *CIESC J.* **2016**, *67*, 4994–5005.
15. Wang, Z.L.; Huang, W.Q.; Ji, H. Numerical simulation of vapor diffusion and emission in loading gasoline into dome roof tank. *Acta. Petrol. Sin.* **2017**, *33*, 26–33.
16. Hou, Y.; Chen, J.Q.; Zhu, L. Numerical simulation of gasoline evaporation in refueling process. *J. Adv. Mech. Eng.* **2017**, *9*, 1–8. [CrossRef]
17. Hassanvand, A.; Hashemabadi, S.H.; Bayat, M. Evaluation of gasoline evaporation during the tank splash loading by CFD techniques. *Int. Commun. Heat Mass Transf.* **2010**, *7*, 907–913. [CrossRef]
18. Hassanvand, A.; Hashemabadi, S.H. Direct numerical simulation of interphase mass transfer in gas-liquid multiphase systems. *Int. Commun. Heat Mass Transf.* **2011**, *7*, 943–950. [CrossRef]
19. Hao, Q.F.; Huang, W.Q.; Jing, H.B. Numerical simulation of oil vapor leakage and diffusion from different pores of external floating-roof tank. *Chem. Ind. Eng. Prog.* **2019**, *38*, 1226–1235.
20. Ai, Z.T.; Mak, C.M. A study of interunit dispersion around multistory buildings with single-sided ventilation under different wind directions. *Atmos. Environ.* **2014**, *88*, 1–13. [CrossRef]
21. Saathoff, P.J.; Melbourne, W.H. Freestream turbulence and wind tunnel blockage effects on streamwise surface pressures. *J. Wind Eng. Ind. Aerodyn.* **1987**, *26*, 353–370. [CrossRef]
22. Jing, H.B.; Huang, W.Q. Study on similarity criteria number of wind tunnel experiment for oil vapor diffusion based on numerical simulation technology. *J. Changzhou Univ.* **2019**, *31*, 25–34.
23. Huang, W.Q.; Fang, J. Numerical simulation and applications of equivalent film thickness in oil evaporation loss evaluation of internal floating-roof tank. *Process Saf. Environ. Prot.* **2019**, *129*, 74–88. [CrossRef]
24. Liu, G.L.; Xuan, J.; Du, K. Wind tunnel experiments on dense gas plume dispersion. *J. Saf. Environ.* **2004**, *4*, 27–32.
25. Macdonald, P.A.; Kwok, K.C.S.; Holmes, J.D. Wind loads on circular storage bins, silos and tanks: I. Point pressure measurements on isolated structures. *J. Wind Eng. Ind. Aerodyn.* **1988**, *31*, 165–187. [CrossRef]
26. Portela, G.; Godoy, L.A. Wind pressures and buckling of cylindrical steel tanks with a dome roof. *J. Constr. Steel Res.* **2005**, *61*, 808–824. [CrossRef]
27. Wang, S.L.; Bi, M.S.; Yu, X.W. Experimental study on the diffusion volume fraction of flammable gas. *Chem. Eng.* **2003**, *31*, 62–65.
28. MHUDPRC (Ministry of Housing and Urban-Rural Development of the People's Republic of China), & GAQSIQPRC (General Administration of Quality Supervision, Inspection and Quarantine of the People's Republic of China). *Code for Design of Oil Depot (GB 50074-2014)*; China Planning Press: Beijing, China, 2014.
29. Lateb, M.; Masson, C.; Stathopoulos, T. Comparison of various types of  $k-\epsilon$  models for pollutant emissions around a two-building configuration. *J. Wind Eng. Ind. Aerodyn.* **2013**, *115*, 9–21. [CrossRef]
30. Bekele, S.A.; Hangan, H. A comparative investigation of the TTU pressure envelope - Numerical versus laboratory and full scale results. *Wind Struct.* **2002**, *5*, 337–346. [CrossRef]



© 2020 by the authors. Licensee MDPI, Basel, Switzerland. This article is an open access article distributed under the terms and conditions of the Creative Commons Attribution (CC BY) license (<http://creativecommons.org/licenses/by/4.0/>).

Article

# CFD-DEM Modeling and Simulation Coupled to a Global Thermodynamic Analysis Methodology for Evaluating Energy Performance: Biofertilizer Industry

Francisco Burgos-Florez <sup>1</sup>, Antonio Bula <sup>1,\*</sup>, John Marquez <sup>2</sup>, Alberto Ferrer <sup>2</sup> and Marco Sanjuan <sup>1</sup>

<sup>1</sup> Department of Mechanical Engineering, Universidad del Norte, Barranquilla 081007, Colombia; fjburos@uninorte.edu.co (F.B.-F.); msanjuan@uninorte.edu.co (M.S.)

<sup>2</sup> Engineering Department, Monomeros Colombo-Venezolanos, Vía 40 Las Flores, Barranquilla 080001, Colombia; jmarquez@monomeros.com.co (J.M.); aferrer@monomeros.com.co (A.F.)

\* Correspondence: abula@uninorte.edu.co; Tel.: +575-350-9229

Received: 24 August 2019; Accepted: 25 September 2019; Published: 29 September 2019

**Abstract:** This work develops a methodology based on real chemical plant data collected from a Nitrogen-Phosphorus-Potassium fertilizer (NPK) cooling rotary drum. By blending thermodynamic variables given by global energy and mass balances with computational fluid dynamics-discrete element method (CFD-DEM) modeling and simulation, the methodology provides an initial approximation to the understanding of heat transfer inside industry rotary coolers. The NPK cooling process was modeled in CFD software Simcenter STAR – CCM + 13.06.011 using a Eulerian–Lagrangian scheme through a coupled CFD-DEM method using one-way coupling. The average temperature of the NPK particles was obtained as well as the average mass flow of the particles dropping as the drum was rotating. The analysis was performed for two-particle diameters (8 and 20 mm) during 17.5 s. The average heat transfer coefficient between the fluid and the NPK particles during the simulated time was obtained. A thermodynamic analysis was carried out using instantaneous energy and mass balances. Prandtl, Nusselt, and Reynolds numbers were obtained for each simulated time step. Finally, through a non-linear regression using the Marquardt method, a correlation between Prandtl, Nusselt, and Reynolds number was developed that allowed analyzing the rotating drum. Results showed that the proposed methodology could serve as a useful tool during the design and analysis of any given rotary cooler, allowing calculation of the heat transfer coefficient and obtaining the process variables that could expand the machine operational capabilities due to the knowledge of the Nusselt number as a function of the drum working parameters.

**Keywords:** rotary cooler; rotating drum; multiphase flow; fertilizer industry; CFD-DEM

## 1. Introduction

Countercurrent rotary drums are commonly used in the bio-organic fertilizer industry for cooling of granular solids that have high internal moisture retention, low thermal conductivity, and hygroscopicity, such as the case of organic fertilizers. They are often made of a long cylindrical shell that rotates upon bearings along its longitudinal axis, which is inclined to the horizontal to induce product motion from the inlet towards the outlet of the cylinder (Figure 1a) [1]. A blower is placed above the product outlet to provide the cold countercurrent airflow needed for cooling. Besides, to promote air-material contact, most drums have lifters, which are fin-like structures placed along the cylinder length that lift the material from the bed and showers it through the air stream as the drum rotates, creating a cross-flow heat transfer scheme (Figure 1a) [1].

The design of a rotary drum relies on designer expertise and experience with the product and the process and the application of certain theoretical principles and empirical correction factors [2]. Drum flights and shells design have an essential effect on the cooling process [3]. During operation, some particles are sliding and rolling along with the drum, while others are being lifted or falling in spreading cascades through the air stream and re-entering the bed at the bottom, giving rise to complex particle dynamics which affect fluid–solid interactions (Figure 1b) [4]. Nevertheless, a better understanding of the heat transfer phenomena in these processes is still needed for process optimization.

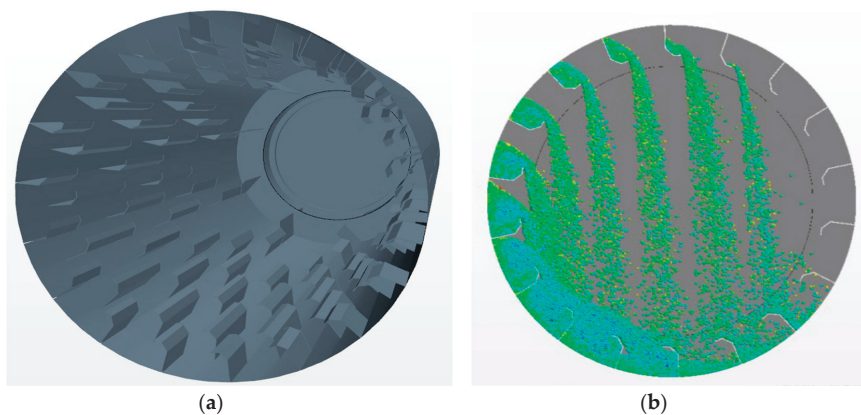


**Figure 1.** (a) Internal view of an industrial rotary drier (Schematic). (b) Particle motion inside a rotary drum.

NPK grade 15–15–15 (Fertilizer with 15% Nitrogen, 15% Phosphorus, 15% Potassium) is a water-soluble granular fertilizer of 2.7 mm average particle diameter commonly produced in the Colombian biofertilizer industry. After drying, NPK enters a countercurrent rotary cooler at circa 90 °C and must be below 45 °C at the outlet to decrease the likelihood of compaction and agglomeration during curing and packaging, which negatively affects the quality of the product. Operators often achieve outlet temperatures by adjusting operating conditions such as reducing drum inclination angle, drum rotation, NPK feed rate, and fuel mass flow. Once an industrial rotary drum is manufactured and put into operation, however, further geometrical and operational modifications for process optimization are harder to incorporate, since they generally require long plant downtimes not previously accounted for in maintenance schedules, as well as additional design and manufacturing costs for geometry changes. Thus, these measures ensure a decrease in product throughput and an increase in process costs, which ultimately diminish overall company profits. For these reasons, the industry permanently demands alternate low-cost approaches for process optimization.

Computational techniques have been increasingly employed for understanding complex solid–fluid interactions in multiphase flows. Among them, the discrete element method (DEM) has been widely accepted as an effective method in addressing complex inter particle phenomena in problems involving granular materials, such as granular flows and powder mechanics [5]. In recent years, coupled DEM and computational fluid dynamics (CFD) have been used for modeling the interaction between highly packed low-diameter granulated solids and gas/liquid fluids in fluidized beds, tumbling mills, and particle impaction in water reservoirs, among others [6–11]. Nevertheless, real industrial processes such as NPK cooling in a rotary drum involve billions of particles which require vast computational power, which is unfeasible in most research centers [12]. Also, the effects of discontinuous or granulated materials on fluid properties (also known as two-way coupling) requires additional convective terms in the fluid’s conservation of mass, momentum, and energy equations. Hence, simulations become much more computationally intensive [13].



To overcome the above difficulties, a methodology was developed that blends thermodynamic variables given by global energy and mass balances with CFD-DEM modeling and simulation that permits an initial approximation to the understanding of heat transfer inside industrial rotary coolers. Initially, the process is modeled as the cooling process of NPK 15–15–15 inside a  $50 \frac{T}{h}$  countercurrent rotary cooler located in a Colombian biofertilizer industry. The drum geometry and lifting flights were based on the industrial-scale design. The rotating drum was analyzed with a Eulerian–Lagrangian scheme using a CFD-DEM one-way coupled physics model corresponding to the airflow and the NPK granulated solid, respectively. Two particle sizes were analyzed: 20 mm and 8 mm diameter NPK spherical particles inside the rotating cooler in a 1 m and 0.1 m drum section length, respectively. The novelties of this work are presented below:

- A CFD-DEM computational model for NPK in the rotary cooler was developed to study the influence of NPK particle diameter on its average temperature along the drum section length; 17.5 s of simulated cooling time was required to validate the results.
- The process average heat transfer coefficient throughout the simulated time was obtained.
- A thermodynamic model of the drum operation was developed using a heat exchanger model, which was fed by the previously found average heat transfer coefficient of the process.
- Through a non-linear regression method, a correlation of dimensionless numbers was obtained which determines, in a given interval, the process operation characteristics.

CFD-DEM models have been used to study many different complex problems involving particle–fluid flow interaction [14,15] and have been found useful to model fluidized beds. The first study using this approach [16] simulated plug flow through horizontal pipes. Since then, many different problems have been solved with this method [17–19].

This paper offers a novel approach that mixes thermodynamic analysis (boundary conditions for the cooler), knowledge about the rotary system (geometry, rotational speed), as well as transport phenomena conditions (air velocity, particle size), to develop a methodology able to solve complex problems in the chemical industry. We expect this work to serve as a quick supporting tool for the design or modification of countercurrent rotary coolers in the biofertilizer industry, particularly in cases where new granulated materials are to be employed, or additional product requirements are placed which require changes in the process current operational conditions.

## 2. Materials and Methods

The NPK cooling process was simulated in CFD software Simcenter STAR – CCM + V.13.06.011 using a Eulerian–Lagrangian scheme through a coupled CFD-DEM method. Momentum, heat, and mass transfer, were exchanged in only one direction to reduce computational costs, also known as one-way coupling. In this method, only the continuous Eulerian phase (air) influences the solid particles. Hence, the effects of the granulated solid on the air, such as displacement, interphase momentum, mass, and heat transfer, are not initially considered in the methodology. The average temperature of NPK particles, as well as their average mass flow falling from the top of the rotating drum during 17.5 s for two-particle diameters (8 and 20 mm), is obtained. These results were then used to calculate the average heat transfer coefficient between the fluid and the NPK particles during the simulated time. Afterward, a thermodynamic analysis was performed using energy, and mass balances of the simulated section of the rotating cooler to obtain the heat transfer coefficient of the process. Also, the instantaneous Prandtl, Nusselt, and Reynolds numbers of the process for each simulated time step were calculated. Finally, through a non-linear regression using the Marquardt method, a correlation between Prandtl, Nusselt, and Reynolds numbers was obtained for the analyzed rotating cooler.

## 2.1. Mathematical Models

### 2.1.1. Particle Dynamics

Linear motion description for the NPK granular flow with spherical solid particles is modeled using the DEM since it extends the Lagrangian formulation to account for inter-particle interactions in the particle equations of motion, which are essential in highly loaded flows. The equation of conservation of linear momentum for a DEM particle of mass  $m_p$  is given by Equation (1), where  $V_p$  denotes the instantaneous particle velocity,  $F_s$  is the resultant of the forces acting on the surface particle, and  $F_b$  is the resultant of the body forces. These forces are also decomposed according to Equation (2), where  $F_d$  is the drag force,  $F_p$  is the pressure gradient force,  $F_g$  is the gravity force,  $F_c$  is the contact force from the DEM, and  $F_{MRF}$  is the force produced by the rotating reference frame.

$$m_p \frac{dV_p}{dt} = F_s + F_b \quad (1)$$

$$\begin{aligned} F_s &= F_d + F_p \\ F_b &= F_g + F_c + F_{MRF} \end{aligned} \quad (2)$$

For the solid-fluid interactions, the resultant  $F_s$  forces represent the momentum transfer from the continuous phase to the particle. The drag force is given by Equation (3), where  $\rho$  is the density of the continuous phase,  $A_p$  is the projected area of the particle,  $V_s$  is the particle slip velocity, and  $C_d$  is the drag coefficient of the particle given by the Schiller–Naumann correlation, which is suitable for spherical solid particles. The pressure gradient force  $F_p$  is defined according to Equation (4), where  $V_p$  is the volume of the particle and  $\nabla p_{static}$  is the gradient of the static pressure in the continuous phase.

$$F_d = \frac{1}{2} C_d \rho A_p |V_s| V_s \quad (3)$$

$$F_p = -V_p \nabla p_{static} \quad (4)$$

For the particle body forces, the gravity force is given by Equation (5), where  $g$  is the gravitational acceleration vector. The contact force  $F_c$  represents inter-particle and particle-boundary interaction and is presented in Equation (6), where  $F_{cm}$  is the contact force model. A modification of the linear spring contact model developed by Cundall and Strack was used [20].

$$F_g = m_p g \quad (5)$$

$$F_c = \sum_{contact} F_{cm} \quad (6)$$

The normal and tangential forces are defined by Equation (7), where  $K_n$  is the normal spring constant,  $K_t$  is the tangential spring constant,  $N_n$  is the normal damping,  $v_n$  is the normal velocity component of the relative sphere surface velocity at the contact point,  $C_{fs}$  is the static friction coefficient, and  $d_n$  and  $d_t$  are overlaps in the normal and tangential directions at contact points.

$$\begin{aligned} F_n &= -K_n d_n - N_n v_n \\ F_t &= -K_t d_t - N_t v_t \text{ if } K_t d_t < K_n d_n C_{fs}, \text{ otherwise } F_t = -\frac{|K_n d_n| C_{fs} d_t}{|d_t|} \end{aligned} \quad (7)$$

The normal and tangential spring stiffness is given by Equation (8).  $E_{eq}$ ,  $G_{eq}$ , and  $R_{eq}$  are the equivalent Young's modulus, shear modulus, and radius of the interacting particles, and they are

calculated according to Equation (9), where  $E_A$  and  $E_B$  are Young's modulus of the particles,  $\nu_A$ , and  $\nu_B$  their Poisson's ratios, and  $R_A$  and  $R_B$  their radii.

$$\begin{aligned} K_n &= \frac{4}{3} E_{eq} \sqrt{d_n} R_{eq} \\ K_t &= 8 G_{eq} \sqrt{d_t} R_{eq} \end{aligned} \quad (8)$$

$$\begin{aligned} E_{eq} &= \frac{1}{\frac{1-\nu_A^2}{E_A} + \frac{1-\nu_B^2}{E_B}} \\ G_{eq} &= \frac{1}{\frac{2(2-\nu_A)(1+\nu_A)}{E_A} + \frac{2(2-\nu_B)(1+\nu_B)}{E_B}} \\ R_{eq} &= \frac{1}{\frac{1}{R_A} + \frac{1}{R_B}} \end{aligned} \quad (9)$$

The normal and tangential damping is given by Equation (10), where  $N_n damp$  and  $N_t damp$  are the normal and tangential damping coefficient, and  $M_{eq}$  is the equivalent particle mass. The normal and tangential coefficients and equivalent particle mass are given by Equation (11), where  $C_{nrest}$  and  $C_{trest}$  are the normal and tangential coefficients of restitution defined by the physical properties of the material, and  $M_A$  and  $M_B$  the mass of each colliding particle.

$$\begin{aligned} N_n &= 2 N_n damp \sqrt{K_n} M_{eq} \\ N_t &= 2 N_t damp \sqrt{K_t} M_{eq} \end{aligned} \quad (10)$$

$$\begin{aligned} N_n damp &= \frac{-\ln(C_{nrest})}{\sqrt{\pi^2 + \ln(C_{nrest})^2}} \\ N_t damp &= \frac{-\ln(C_{trest})}{\sqrt{\pi^2 + \ln(C_{trest})^2}} \\ M_{eq} &= \frac{1}{\frac{1}{M_A} + \frac{1}{M_B}} \end{aligned} \quad (11)$$

The force produced by the moving reference frame is given by Equation (12), where  $\omega$  is the angular velocity vector of the rotating reference frame and  $\mathbf{r}$  is the distance vector to the axis of rotation.

$$F_{MRF} = m_p [\omega \times (\omega \times \mathbf{r}) + 2(\omega \times \mathbf{V}_p)] \quad (12)$$

Rotational motion for DEM particles is described by orientations and, therefore, their angular momentum must also be conserved, and it is represented by Equation (13), where  $I_p$  is the particle moment of inertia described by a second-order tensor,  $\omega_p$  is the particle angular velocity,  $M_b$  is the drag torque, that is, the moment that acts on the particle due to rotational drag, and  $M_c$  is the total moment from contact forces.

$$I_p \frac{d\omega_p}{dt} = M_b + M_c \quad (13)$$

The drag torque reduces the difference between a particle and the fluid in which it is immersed, and is defined by Equation (14), where  $C_R$  is the rotational drag coefficient.  $\Omega$  is the relative angular velocity of the particle to the fluid and is given by Equation (15), where  $\mathbf{v}$  is the fluid velocity, and  $\omega_p$  is the angular velocity of the particle. The rotational drag coefficient is defined by Equation (16) where  $Re_R$  is the rotational Reynolds number defined by Equation (17).

$$M_b = \frac{\rho}{2} \left(\frac{D}{2}\right)^5 C_R |\Omega| \Omega \quad (14)$$

$$\Omega = \frac{1}{2} \nabla \times \mathbf{v} - \omega_p \quad (15)$$

$$C_R = \frac{64\pi}{Re_R} \quad (16)$$

$$Re_R = \frac{\rho D^2 |\Omega|}{\mu} \quad (17)$$

The total moment from contact forces is defined according to Equation (18), where  $r_c$  is the position vector from the particle center of gravity to the contact point, and  $M_{cm}$  is the moment that acts on the particle from rolling resistance. Rolling resistance was modeled with the proportional force method with a defined coefficient of rolling resistance  $\mu_r$ .

$$M_c = \sum_{contacts} (r_c \times F_{cm} + M_{cm}) \quad (18)$$

In order to study the heat and mass transfer process inside the cooling rotary drum, the solid-fluid heat transfer needs to be defined properly. The equation of conservation of mass of a material particle is given by Equation (19), where  $\dot{m}_p$  is the rate of mass transfer to the particle. This term is zero since no evaporation occurs. The particle energy balance is shown in Equation (20), where  $Q_{rad}$  represents heat transfer by radiation and  $Q_s$  represents heat transfer by other sources, and both of them are negligible in this process.

$$\frac{dm_p}{dt} = \dot{m}_p \quad (19)$$

$$m_p c_p \frac{dT_p}{dt} = Q_t + Q_{rad} + Q_s \quad (20)$$

Convective heat transfer  $Q_t$  is calculated according to Equation (21), where  $h$  is the heat transfer coefficient, and  $A_s$  is the particle surface area. The heat transfer coefficient was obtained from the particle Nusselt number presented in Equation (22), where  $k$  is the thermal conductivity of the fluid. Nusselt number was obtained using the Ranz–Marshall correlation defined by Equation (23), where  $Pr$  is the Prandtl number of the air.

$$Q_t = h A_s (T - T_p) \quad (21)$$

$$Nu_p = h \frac{D_p}{k_f} \quad (22)$$

$$Nu_p = 2 \left( 1 + 0.3 Re_p^{0.5} Pr^{1/3} \right) \quad (23)$$

The solid-solid heat transfer process is taken into consideration. When particles make contact with each other or with the wall, heat is transferred through conduction. In this work, the drum wall was considered adiabatic. Thus, conductive heat transfer was only considered between particles. Particle–particle heat transfer is given by Equation (24), where  $r_c$  is the contact radius and  $k$  is the equivalent thermal conductivity of the two particles and  $T_i$ ,  $T_j$  the temperatures of particle  $i$  and  $j$ . The equivalent thermal conductivity is calculated according to Equation (25), where  $k_i$  and  $k_j$  are the thermal conductivities for particles  $i$  and  $j$ .

$$q_{ij} = 4 r_c k_m (T_j - T_i) \quad (24)$$

$$\frac{1}{k} = \frac{1}{k_i} + \frac{1}{k_j} \quad (25)$$

The impact heat model was employed for calculating the heat production that results from friction and damping in DEM particles. This model has a linear formulation given by Equation (26), where  $c_t$  and  $c_n$  are the fractions of frictional and damping work that are converted to heat,  $f_t$  and  $f_n$  are the frictional and damping forces on the particle, and  $v_t$  and  $v_n$  are the relative tangential and normal impact velocities.

$$q_r = c_t f_t v_t + c_n f_n v_n \quad (26)$$

### 2.1.2. Fluid Dynamics

Air was modeled as a constant density gas using a Eulerian scheme. The equations of conservation of mass, momentum, and energy were solved with mesh motion, which provides an additional flux in the convective terms. This set of equations is defined by Equation (27), where  $\mathbf{v}_g$  is the grid velocity in the reference frame and  $\mathbf{v}_r$  is the relative velocity with respect to the reference frame,  $\boldsymbol{\sigma}$  is the stress tensor,  $\mathbf{f}_b$  is the resultant body forces (gravity),  $E$  is the total energy per unit mass,  $\mathbf{q}$  is the heat flux and  $S_u$  and  $S_e$  are mass and energy sources

$$\begin{aligned} \frac{\partial}{\partial t} \int_V \rho dV + \oint_A \rho(\mathbf{v}_r - \mathbf{v}_g) \cdot d\mathbf{a} &= \int_V S_u dV \\ \frac{\partial}{\partial t} \int_V \rho \mathbf{v} dV + \oint_A \rho \mathbf{v} \otimes (\mathbf{v}_r - \mathbf{v}_g) \cdot d\mathbf{a} &= \oint_A \boldsymbol{\sigma} \cdot d\mathbf{a} + \int_V \mathbf{f}_b dV - \int_V \rho \boldsymbol{\omega} \times \mathbf{v} dV \\ \frac{\partial}{\partial t} \int_V \rho E dV + \oint_A \rho E (\mathbf{v}_r - \mathbf{v}_g) \cdot d\mathbf{a} &= - \oint_A \mathbf{q} \cdot d\mathbf{a} + \oint_A (\mathbf{v} \cdot \boldsymbol{\sigma}) \cdot d\mathbf{a} + \int_V \mathbf{f}_b \cdot \mathbf{v} dV + \int_V S_e dV \end{aligned} \quad (27)$$

When the mesh is moving, cells shape and position change with time. Hence, an additional equation was solved to enforce space conservation, described by Equation (28).

$$\frac{d}{dt} \int_V dV = \int_A \mathbf{v}_g \cdot d\mathbf{a} \quad (28)$$

### 2.1.3. Turbulence Model

Turbulence was modeled with the realizable k- $\epsilon$  model, which exhibits superior performance for flows involving rotation than the k- $\epsilon$  turbulence model. This model added two equations which solve the turbulent kinetic energy  $k_e$  and turbulent energy dissipation rate  $\epsilon$  [21], which are given by Equation (29):

$$\begin{aligned} \frac{\partial}{\partial t} (\rho k_e) + \frac{\partial}{\partial x_j} (\rho k_e u_j) &= \frac{\partial}{\partial x_j} \left[ \left( \mu + \frac{\mu_t}{\sigma_k} \right) \frac{\partial k_e}{\partial x_j} \right] + P_k + P_b - \rho \epsilon - Y_M + S_k \\ \frac{\partial}{\partial t} (\rho \epsilon) + \frac{\partial}{\partial x_j} (\rho \epsilon u_j) &= \frac{\partial}{\partial x_j} \left[ \left( \mu + \frac{\mu_t}{\sigma_\epsilon} \right) \frac{\partial \epsilon}{\partial x_j} \right] + \rho C_1 S_\epsilon - \rho C_2 \frac{\epsilon^2}{k_e + \sqrt{\nu \epsilon}} + C_{1\epsilon} \frac{\epsilon}{k_e} C_{3\epsilon} P_b + S_\epsilon \end{aligned} \quad (29)$$

In these equations,  $S$  is the modulus of the mean rate-of-strain tensor,  $P_k$  represents the generation of turbulence kinetic energy due to the mean velocity gradients, calculated in the same manner as standard k- $\epsilon$  model, and  $P_b$  is the generation of turbulence kinetic energy due to buoyancy, calculated in the same way as standard k- $\epsilon$  model [21,22].  $C_1$ ,  $\eta$  and  $S$  and  $\mu$  are given Equation (30), while the turbulent viscosity is defined by Equation (31) and the terms required are defined in Equation (32).

$$\begin{aligned} C_1 &= \max \left[ 0.43, \frac{\eta}{\eta + 5} \right] \\ \eta &= \max \left[ S \frac{k_e}{\epsilon} \right] \\ S &= \sqrt{2 S_{ij} S_{ij}} \end{aligned} \quad (30)$$

$$\mu_t = \rho C_\mu \frac{k_e^2}{\epsilon} \quad (31)$$

$$\begin{aligned} C_\mu &= \frac{1}{A_0 + A_s \frac{k_e U^*}{\epsilon}} \\ U^* &= \sqrt{S_{ij} S_{ij} + \widetilde{\Omega}_{ij} \widetilde{\Omega}_{ij}} \\ \widetilde{\Omega}_{ij} &= \Omega_{ij} - 2 \epsilon_{ijk} \omega_k \\ \Omega_{ij} &= \Omega_{ij} - \epsilon_{ijk} \omega_k \end{aligned} \quad (32)$$

The final terms defining the turbulence model are presented in Equation (32), where  $\overline{\Omega_{ij}}$  is the mean rate-of-rotation tensor viewed in a rotating reference frame with the angular velocity  $\omega_k$ , and the model constants  $A_0$  and  $A_s$  are given by Equation (33).

$$\begin{aligned}
 A_0 &= 4.04 \\
 A_s &= \sqrt{6}\cos(\phi) \\
 \phi &= \frac{1}{3}\cos^{-1}(\sqrt{6}W) \\
 W &= \frac{S_{ij}S_{jk}S_{ki}}{S^3} \\
 \tilde{S} &= \sqrt{S_{ij}S_{ij}} \\
 S_{ij} &= \frac{1}{2}\left(\frac{\partial u_i}{\partial x_j} + \frac{\partial u_j}{\partial x_i}\right) \\
 C_{1\epsilon} &= 1.44 \\
 C_2 &= 1.8 \\
 \sigma_k &= 1.0 \\
 \sigma_\epsilon &= 1.2
 \end{aligned}
 \tag{33}$$

### 2.2. Heat-Transfer Model

The average NPK temperature is used for each time step to obtain the heat-transfer coefficient between air and solid particles. NPK average temperature differential is given by Equation (34), where  $dt$  is the simulation timestep,  $\overline{T}_{t+dt}$  is the average NPK temperature in time  $t + dt$  and  $\overline{T}_t$  is the average NPK temperature in time  $t$ .

$$d\overline{T}_{t+dt} = \overline{T}_{t+dt} - \overline{T}_t \tag{34}$$

Heat transfer between NPK and air is assumed to occur mostly during PK falling from the flights during drum rotation. Hence, NPK thermal energy is defined by Equation (35), where  $\overline{m}_{mf}$  is the average NPK mass that falls during one time step. It is assumed that this energy is given to the flowing air, increasing its temperature accordingly. Thus, the air temperature differential is defined by Equation (36), where  $\overline{m}_a$  is the air mass passing during one time step, and  $Cp_a$  is the air-specific heat. The final expression for air temperature after one time step is given by Equation (37), where  $T_{ai}$  is the air temperature at the inlet.

$$Qm_{t+dt} = \overline{m}_{mf}Cp_m d\overline{T}_{t+dt} \tag{35}$$

$$dT_{a_{t+dt}} = \frac{Qm_{t+dt}}{m_a Cp_a} \tag{36}$$

$$T_{a_{t+dt}} = T_{ai} + d\overline{T}_{a_{t+dt}} \tag{37}$$

In order to obtain the average heat-transfer coefficient  $h$ , the process was modeled as a counter-current heat exchanger. This method is suitable in cases where flow rates and heat transfer area are constant. Thus, a generic heat exchanger was employed with two ends: A, at which the hot material enters, and hot air leaves the system, and B, where cold material leaves and cold air enters the system. The logarithmic mean temperature difference *LMTD* is defined as the difference between the hot and cold feeds at each end of the countercurrent heat exchanger and is given by Equation (38).

$$LMTD = \frac{(\overline{T}_t - T_{a_{t+dt}}) - (\overline{T}_{t+dt} - T_{ai})}{\ln\left(\frac{\overline{T}_t - T_{a_{t+dt}}}{\overline{T}_{t+dt} - T_{ai}}\right)} \tag{38}$$

The *LMTD* was used to determine the heat transfer coefficient  $h$  for each timestep in the heat exchanger model, and it is calculated according to Equation (39), where  $\frac{dQ_m}{dt}$  is the heat exchanged between NPK and the air during the defined timestep in the heat exchanger model, and  $A_{fp}$  is the area

of heat exchange corresponding to the total area of the particles falling during one timestep. This term, the rate of heat transfer  $\frac{dQ_m}{dt}$  during the time step  $dt$  is given by Equation (40).

$$h = \frac{\frac{dQ_m}{dt}}{A_{fp}LTMD} \quad (39)$$

$$\frac{dQ_m}{dt} = \frac{Q_{m_{t+dt}}}{dt} \quad (40)$$

The area of heat exchange  $A_{fp}$  is given by Equation (41).

$$A_{fp} = \frac{4\pi\left(\frac{D_p}{2}\right)^2}{m_p} \bar{m}_{mf} \quad (41)$$

The average heat transfer coefficient for each simulation was found by averaging the heat transfer coefficients of each timestep during the entire simulated time.

### 2.3. Thermodynamic Model

A global energy balance was used to obtain a generalized thermodynamic model of the cooler. First, the heat was assumed to transfer from the NPK material to the air without losses. Hence, the energy balance is presented by Equation (42), where  $\dot{m}_a$  and  $\dot{m}_m$  are the mass flows of air and material entering the rotating cooler, respectively,  $T_{ai}$  and  $T_{ao}$  the air temperatures at the inlet and outlet, and  $T_{mi}$  and  $T_{mo}$  the material temperatures at the inlet and outlet. Since NPK inlet and outlet temperatures were known, thermal power is given by Equation (43).

$$\dot{m}_a C_p a (T_{ao} - T_{ai}) = \dot{m}_m C_p m (T_{mo} - T_{mi}) \quad (42)$$

$$Q_m = \dot{m}_m C_p m (T_{mo} - T_{mi}) \quad (43)$$

The air outlet temperature was then obtained from Equation (44).

$$T_{ao} = T_{ai} + \frac{Q_m}{\dot{m}_a C_p a} \quad (44)$$

The heat-transfer coefficient from Section 2.2 was used for both particle diameters in a counter-current heat exchanger model of the entire NPK industrial cooler. The inlet–outlet temperatures were used to in the thermodynamic model to find the exchanged heat in the cooling process, which is calculated from Equation (45).

$$Q_{he} = h A_{he} LTMD_{he} \quad (45)$$

$A_{he}$  is the total area for heat exchange, and  $LTMD_{he}$  is the logarithmic mean temperature difference of the heat exchanger. The total area of heat exchange is defined by Equation (46), where  $L$  is the rotating cooler length, and  $l$  is the length of the simulated drum model.

$$A_{he} = \frac{4\pi\left(\frac{D_p}{2}\right)^2 \bar{m}_{mf} L}{dt m_p l} \quad (46)$$

The logarithmic mean temperature difference is given by Equation (47).

$$LMTD_{he} = \frac{(T_{mi} - T_{ao}) - (T_{mo} - T_{ai})}{\ln\left(\frac{T_{mi} - T_{ao}}{T_{mo} - T_{ai}}\right)} \quad (47)$$

Both  $Q_m$  and  $Q_{he}$  should be equal. Thus, Equation (48) is used as check point.

$$Q_{he} = hA_{he}LMTD_{he} = Q_m = \dot{m}_m C p_m (T_{mo} - T_{mi}) \quad (48)$$

Through trial and error, NPK outlet temperature that makes  $Q_{he} = Q_m$  was calculated. NPK and air inlet and outlet temperatures obtained from this model were validated with the ones given as boundary conditions in the real industrial rotary cooler.

#### 2.4. Dimensionless Numbers

The Nusselt number and Reynolds number for the NPK material, as well as the Prandtl number for the air for each particle diameter during each time step, were obtained. Particle Nusselt is given by Equation (49).

$$Nu_m = \frac{hD_p}{k} \quad (49)$$

The Prandtl number of the air was found by linear interpolation of published Prandtl numbers for given air temperatures. The average air temperature was defined according to Equation (50).

$$T_{ma} = \frac{T_{ai} + T_{a_{l+dt}}}{2} \quad (50)$$

NPK Reynolds number was obtained from Equation (51), where  $v_{max}$  is the maximum air velocity throughout the drum, and  $\nu$  is the air kinematic viscosity at the average air temperature. Air kinematic viscosity was obtained by linear interpolation of published kinematic viscosities for given air temperatures. The maximum air velocity is given by Equation (52), where  $V_{ai}$  is the average air inlet velocity and  $Vf$  is the void factor, which is defined by Equation (53).  $V_d$  is the drum volume, and  $V_m$  is the volume occupied by the NPK. The drum volume is calculated according to Equation (54), where  $D$  is the drum diameter, and  $l$  is the drum length in the simulation.

$$Re_m = \frac{v_{max} D_p}{\nu\{T = T_{ma}\}} \quad (51)$$

$$v_{max} = \frac{V_{ai}}{Vf} \quad (52)$$

$$Vf = \frac{V_d - V_m}{V_d} \quad (53)$$

$$V_d = \pi \left(\frac{D}{2}\right)^2 l \quad (54)$$

The volume occupied by the NPK material is given by Equation (55), where  $N$  is the number of NPK particles in the model.

$$V_m = \frac{4}{3} \pi \left(\frac{D_p}{2}\right)^3 N \quad (55)$$

#### 2.5. Non-Linear Regression for Dimensionless Numbers Correlation

The values of the dimensionless numbers obtained for each particle diameter at each time step were used to find a correlation of the form given by Equation (56), where  $a$ ,  $b$ , and  $c$  are constants that relate the dimensionless numbers. The Marquardt non-linear regression method was used in the software Statgraphics Centurion V16.1 to obtain the values of these constants.

$$Nu = a Re^b Pr^c \quad (56)$$



### 3. Computational Implementation

#### 3.1. Rotary Cooler Characteristics

A fully operating Colombian industrial NPK rotary cooler was used as a case study for the proposed methodology. The cooler has a diameter of three meters, is 19 meters long, rotates at 5 rpm, and is tilted down  $1.5^\circ$  to the horizontal. Four different flight designs are employed in the industrial drum. The flights are arranged in a defined order along the drum length to complete a total of 13 sections. Atmospheric air is used as cooling fluid and enters the drum using a blower which generates a mass flow of  $25 \frac{\text{Kg}}{\text{s}}$  at  $30^\circ\text{C}$  and leaves it at approximately  $59^\circ\text{C}$ . NPK particles enter the drum with a mass flow of  $13.88889 \frac{\text{Kg}}{\text{s}}$  at a temperature of  $90^\circ\text{C}$  and leave it at  $46.5^\circ\text{C}$ . Outlet mass flows were measured to be equal to inlet ones. Solid NPK particles have an average diameter of 2.7 mm in the industrial cooler and have a residence time of 30 min. With these values, a total mass of 25,000 kg is found inside the drum at any given time. That amounts to approximately  $2.3 \times 10^9$  solid NPK particles. Process parameters are shown in Table 1.

#### 3.2. Model Description

Considering that computational resources for simulating NPK cooling of such a large number of solid particles were unfeasible to acquire, the drum length was reduced, and particle diameter was increased to obtain a total mass that achieved less than a million particles but still was representative of the cooling process. Hence, two models were developed, one of a one-meter drum section length with 20 mm diameter NPK spherical particles, and one of a 0.1 m section length with 8 mm diameter NPK spherical particles, both tilted down  $1.5^\circ$  to the horizontal.

For 20 mm particles, drum length was reduced considering fluid dynamic conditions, particularly Reynolds number and Pressure coefficient. Reynolds number remained constant and was independent from the length of the drum. Since Reynolds was turbulent, the hydrodynamic entry region was 10 times the drum diameter, resulting in 30 m. With this condition, fully developed turbulent flow could not be achieved. For pressure coefficient, the pressure drop is proportional to the length of the drum presenting a linear behavior. Since a developing region will dominate the phenomenon inside, the length of the drum to be analyzed was dropped to 1 m, which represented 5.2% of the total length, which is well inside the developing region of the process. For 8 mm particles, Fourier number was considered because of the transient situation to be analyzed during the cooling process. For both particle sizes, 20 and 8 mm, Fourier number was held at  $4 \times 10^{-3}$ . This allowed the calculation of drum length for 8 mm particles' size.

For these lengths, masses of 1315.789 kg and 131.578 kg of NPK were obtained, formed by 299,164 and 467,443 spheres. Both models used one of the four given types of lifters, which were chosen since they allowed the highest particle dispersion angle (angle between the first and last particle showering from the top of the drum). The geometry of the 0.1 m long rotating cooler and its lifters is shown in Figure 2.

Air inlet and outlet conditions were defined as mass flow inlet and pressure outlet in the software. Values for mass flows, pressures, and temperatures were defined as equal to those currently employed in the industrial cooler. Nevertheless, solid NPK particles did not flow from defined inlet and outlet boundaries. Instead, a random particle injector, a tool inside STAR-CCM+, was used to place particles inside the drum's fluid region in a randomized fashion with a defined initial temperature equal to the NPK inlet temperature of the industrial cooler. Hence, even though no NPK inlet flow was used, NPK particles were initially set with the industrial cooler NPK inlet temperature.

Wall boundary conditions were chosen for the drum carcass and phase-impermeable conditions for the air inlet and outlet boundaries, so particles could not escape the drum during cooling once they have been randomly injected (Figure 3). Thus, a constant number of particles were randomly positioned inside the drum at the start of the simulation and could not leave the drum. Particle

dynamics were obtained by solving the equations found in Section 2.1.1 for the constant number of particles defined in Table 1.

**Table 1.** Process parameters. N.r. means not reported, d.a. means do not apply.

	Industry Rotating Cooler	Model One	Model Two
Drum properties			
Drum diameter $D(m)$	3	3	3
Drum length $L(m), l(m)$	19	0.1	1
Flight design	four different designs (not shown)		Figure 2
Flight material	Stainless steel		Carbon steel
Wall material	Carbon steel		Carbon steel
Angular velocity $\omega(rpm)$	5		
Fluid properties and flow conditions			
Fluid			
Air			
Inlet pressure $P_i(kPa)$	101.3		
Outlet pressure $P_o(kPa)$	101.3		
Inlet temperature $T_{ai}(^{\circ}C)$	30		
Outlet temperature $T_{ao}(^{\circ}C)$	59		d.a.
Inlet mass flow $\dot{m}_{ai}(\frac{kg}{s})$	25		25
Outlet mass flow $\dot{m}_{ao}(\frac{kg}{s})$	25		25
Particle properties			
Material			
NPK granulated solid			
Diameter $D_p(mm)$	2.7	8	20
Young's Modulus $E_{eq}(kPa)$	n.r.		517
Poisson's ratio $\nu$	n.r.		0.45
Specific heat $C_p(\frac{J}{kg \cdot K})$		1465.38	
Thermal conductivity $k_m(\frac{W}{m \cdot K})$		0.18596	
Density $\rho(\frac{kg}{m^3})$		1050	
Residence time $rs(min)$		30	
Total mass $MT(kg)$	25,000	131.57	1315.78
Number of particles $N$	$2.31 \times 10^9$	$4.67 \times 10^5$	$2.99 \times 10^5$
Inlet mass flow $\dot{m}_{mi}(\frac{kg}{s})$	13.88		d.a.
Outlet mass flow $\dot{m}_{mo}(\frac{kg}{s})$	13.88		d.a.
Inlet temperature $T_{mi}(^{\circ}C)$		90	
Outlet temperature $T_{mo}(^{\circ}C)$	46.5		d.a.
Phase Interactions			
Particle-particle			
Static friction coefficient $C_{fsp}$	n.r.		0.4
Normal restitution coefficient $C_{nrestp}$	n.r.		0.1
Tangential restitution coefficient $C_{trestp}$	n.r.		0.1
Frictional work fraction $c_{tp}$	n.r.		0.1
Damping work fraction $c_{np}$	n.r.		0.1
Particle-wall			
Static friction coefficient $C_{fstw}$	n.r.		0.2
Normal restitution coefficient $C_{nrestw}$	n.r.		0.3
Tangential restitution coefficient $C_{trestw}$	n.r.		0.3
Frictional work fraction $c_{tw}$	n.r.		0.4
Damping work fraction $c_{nw}$	n.r.		0.1

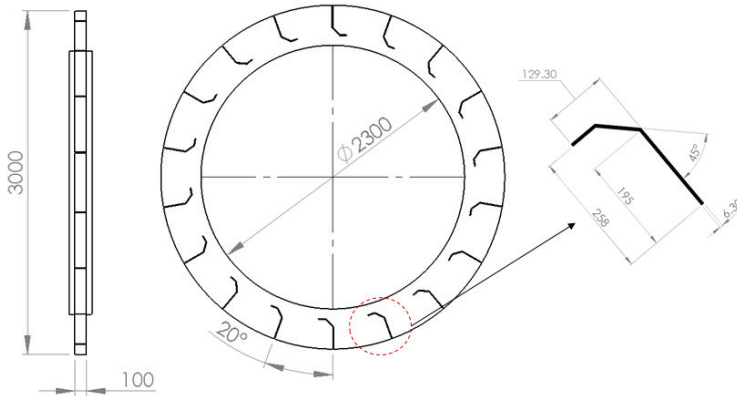


**Figure 2.** Rotating drum and flights geometry. Dimensions are in millimeters (mm).

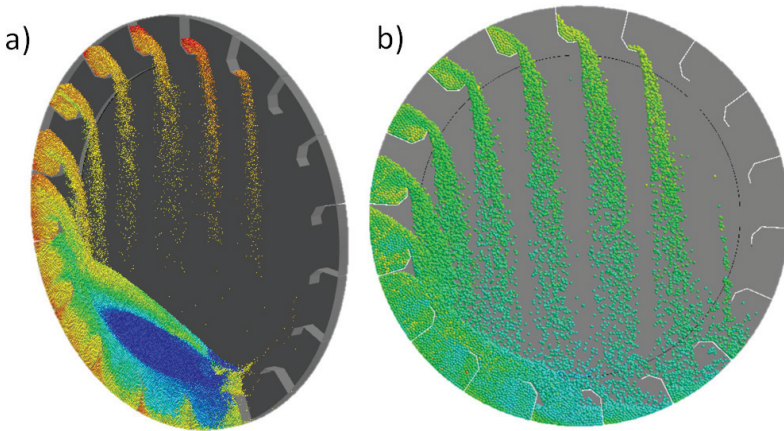


**Figure 3.** Rotating drum models. (a) 0.1 m section length with 8 mm-diameter particles falling. (b) 1 m section length with 20 mm-diameter particles falling.

### 3.3. Simulation

The simulation was run for 17.5 s for each model, which corresponded to 1.45 rotations of NPK particles inside the drum. Longer simulation times did not provide additional information regarding NPK temperature drop dynamics since no considerable differences in average heat transfer coefficients were found. Furthermore, the logarithmic mean temperature difference behavior is well defined at this point, allowing the calculations of the heat to be removed inside the drum during the cooling process. The average air inlet velocity  $V_{ai}$  was used for calculating the maximum air velocity  $v_{max}$ . Average NPK falling mass flow was calculated using the track model in STAR-CCM+, which allowed the tracking of each moving particle throughout time. A plane cutting the drum in half in the y-axis was defined, and the tracked particles which cross it throughout a specified time frame were plotted (Figure 4). The data was then exported to a CSV file, where each row corresponded to each crossing particle and each column to the crossing time and z- position. Particle falling mass flow for each model is given by Equation (57), where  $\Delta t$  is the time frame between the first and last particle that passes through the defined plane section. Measurements for  $\overline{\dot{m}_{mf}}$  were performed in time frames positioned after one

second of real simulated time since this time was enough for the initially randomly localized particles to position inside the flights of the rotating drum and produce a quasi-steady falling mass flow.

$$\bar{m}_{mf} = \frac{\#ofparticles}{\Delta t} m_p \tag{57}$$

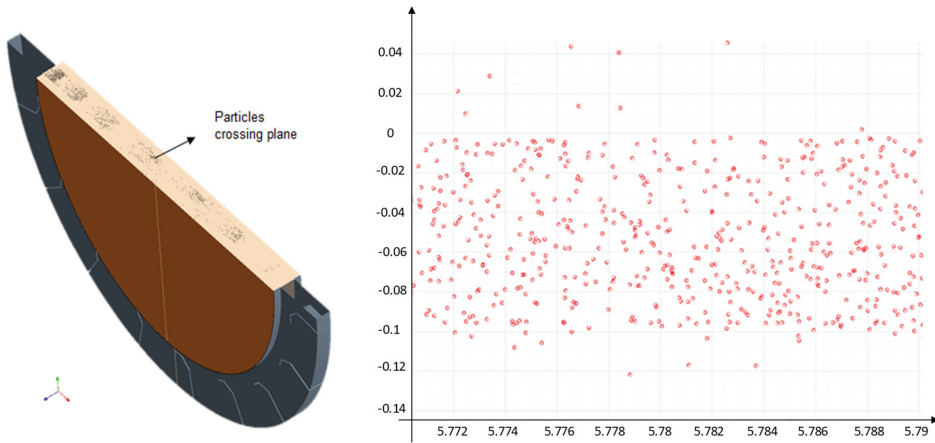


**Figure 4.** Particle tracking in the transverse plane section of model one. Each circle corresponds to one particle passing through the defined plane in a given time point.

### 3.4. Domain Discretization

#### 3.4.1. Mesh Generation

The fluid domain was discretized using three models: surface remesher, trimmer, and prism layer mesher. The first one resulted in a good quality surface mesh by adequately maintaining the drum and flights geometry. Trimmer mesh was employed for generating a predominantly hexahedral mesh with minimal cell skewness and a low number of trimmed cells. This method was sufficient for producing a mesh with appropriate curvature and alignment with the z-direction corresponding to the drum length (Figure 5). Prism layer mesher was used to model the inclusion of a prism layer along the borders of the fluid domain to capture boundary layer flow. Mesh properties are shown in Table 2.

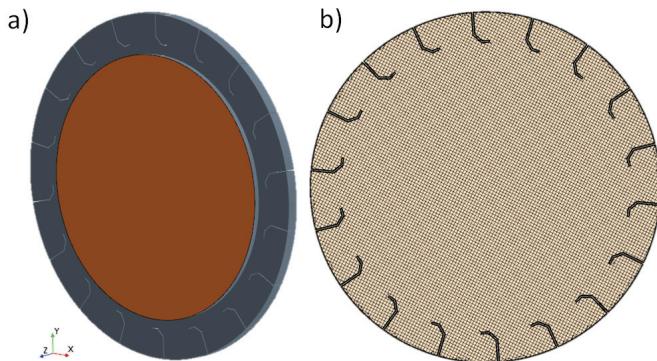


**Figure 5.** Rotating drum model and mesh. (a) Isometric view of 0.1 m section length drum, the air outlet is shown in orange. (b) X-Y plane of 0.1 m section length drum showing mesh with 0.03 m base size.

**Table 2.** Mesh characteristics for each model.

Model	One			Two		
Particle diameter (mm)	8			20		
Mesh number	1	2	3	1	2	3
base size (m)	0.0368	0.0300	0.0245	0.0480	0.0400	0.0338
Cells	91,952	146,144	226,565	216,008	336,351	504,635
Faces	264,569	422,248	654,658	632,931	988,663	1,485,106
Vertices	102,434	160,771	244,976	228,135	353,909	526,248
Prism layers				5		
Prism layer thickness (m)				0.009		
Prism layer stretching				1.5		

### 3.4.2. Time and Mesh Independence Analysis

Three different mesh sizes were generated for each model. Each finer mesh had 1.5 times the number of cells of the coarser ones. Convergence criteria were set to  $10^{-4}$  for momentum, energy, turbulent kinetic energy and turbulent energy rate of dissipation. Initially, a time independence analysis was performed. For it, Mesh number 1 was chosen for each model (Table 3). The time step was decreased to half for each simulation, beginning with 0.01 and 0.05 for models one and two, respectively. Average NPK temperature was recorded at time  $t = 3.5$  s for each simulation. Timesteps of 0.005 and 0.01 were chosen for model one and two since they showed relative errors lower than 1%. A mesh independence analysis was then performed using the chosen timesteps (Table 4). Average NPK temperature was again captured at time  $t = 3.5$  s for each simulation with each finer mesh, and the relative error was calculated. Mesh number 2 was chosen for each model since it had a relative error lower than 1%. Table 5 shows the chosen meshes and timesteps for each model.

**Table 3.** Time independence analysis.

Model	One			Two		
Particle diameter (mm)	8			20		
Timestep (s)	0.010	0.005	0.001	0.050	0.010	0.005
Average solid temperature $\bar{T}_{3.5s}$ (°C)	80.86	82.42	82.43	85.30	86.85	86.86
Relative error (%)	1.93	0.02		1.83	0.02	
Mesh number	1			1		

**Table 4.** Mesh independence analysis.

Model	One			Two		
Particle diameter (mm)	8			20		
Mesh number	1	2	3	1	2	3
Average solid temperature $\bar{T}_{3.5s}$ (°C)	82.42	83.98	84.66	86.85	88.41	89.04
Relative error (%)	1.89	0.81		1.80	0.72	
Timestep (s)	0.005			0.010		

**Table 5.** Mesh and timestep for each model.

Model	One	Two
Particle diameter (mm)	8	20
Mesh number	2	2
Number of cells	146144	336351
Timestep (s)	0.005	0.010

## 4. Results and Discussion

### 4.1. Average Particle Temperature

Figure 6 shows NPK 8 mm particles cooling inside a 0.1 m drum section during 4.5 s. Particles are lifted by the drum flights which move due to the angular rotation of the drum and fall at a given mass flow rate which is constant in the central plane defined in Section 3.3 of this work. From the figure, it can be seen that particles located in the middle of the lower bulk of NPK material show the lowest temperature (around 71 °C in blue), while particles near the flights and drum surface exhibit the highest temperature. This circumstance can be explained by the fact that air–particle interactions taking place near the center of the rotating drum achieve higher heat transfer rates due to airflow being fastest in this area as in near the rotating drum edges. Besides, these particles seemed to experience little movement compared to those in other drum regions. Even though some of them appear to add filling mass to the lower moving flights, most of them are not capable of entering the flights and move as a bulk material to the left by the action of contact forces by particles already inside the flights. Therefore, once they start going upwards, they end up falling again to lower flights already being filled by falling particles from the top flights of the drum. This phenomenon is not desirable since it could cause high temperature drops in some particles, while others could not achieve the desired outlet temperature, hence altering the overall quality of the product at the outlet.

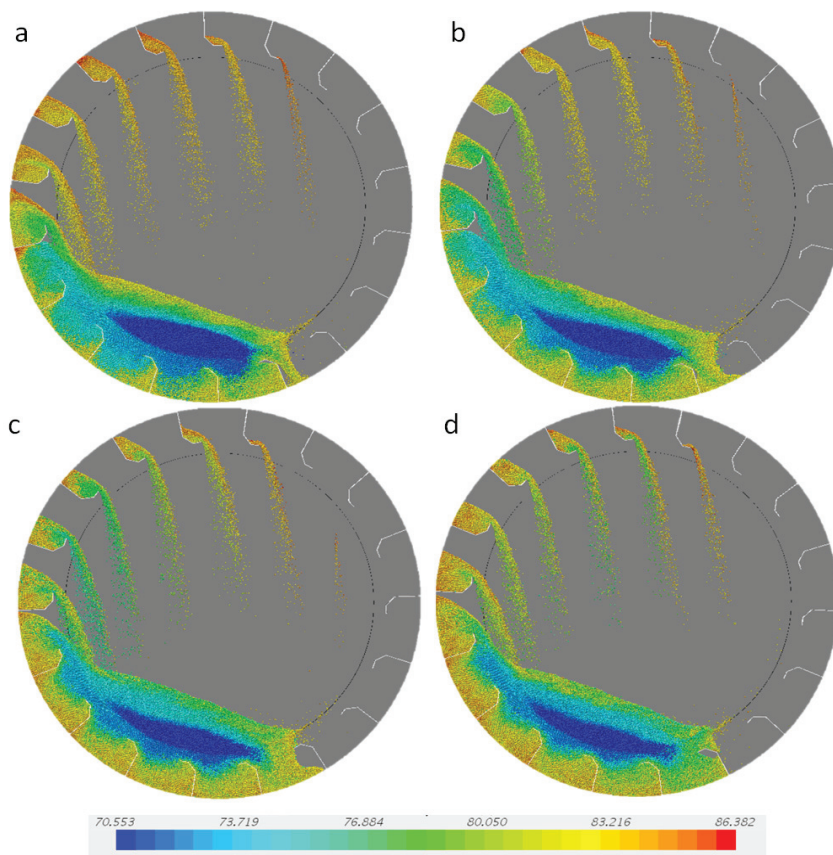


**Figure 6.** NPK particles of 8 mm diameter cooling at different times. (a) 6 s, (b) 7.5 s, (c) 9 s and (d) 10.5 s. Temperature bar is in °C.

Figures 7 and 8 provide the average NPK temperature variation in 17 s of simulated time for 8 mm and 20 mm diameter NPK particles. The differences in the cooling behavior could be explained by differences in total NPK mass, considering that model one has 1/10th of the section length of model two. Nevertheless, both figures show a decaying exponential behavior, which is expected in heat-transfer processes.

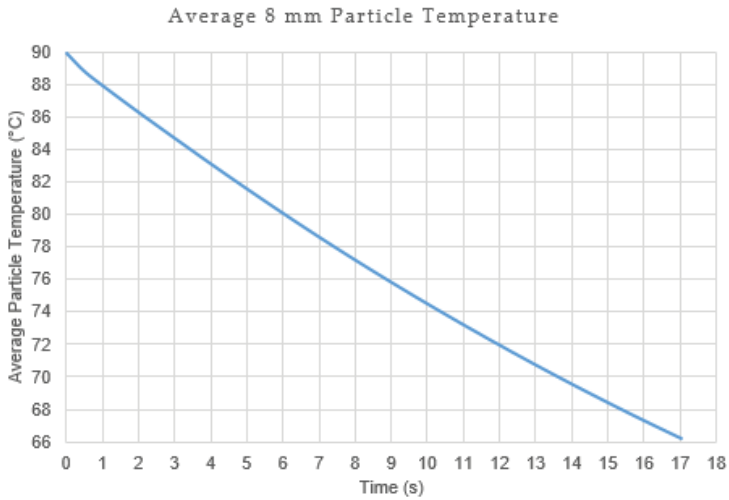


Figure 7. NPK particles of 8 mm diameter, average temperature during the simulated time.

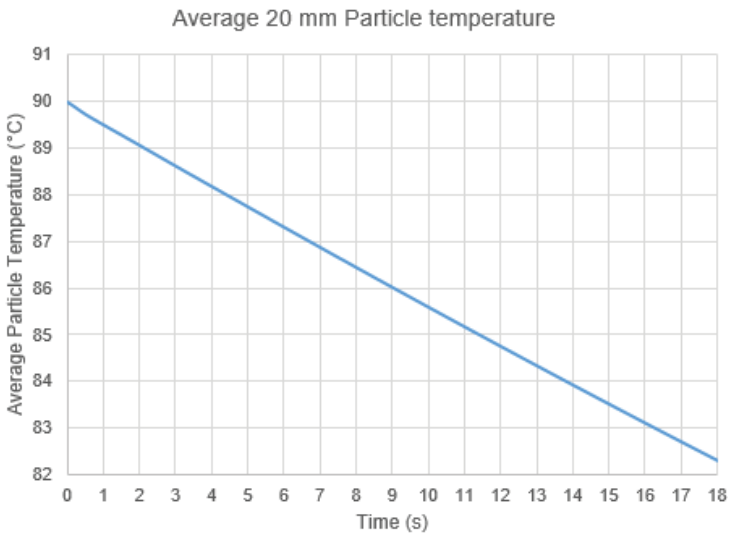


Figure 8. NPK particles of 20 mm diameter, average temperature during the simulated time.

#### 4.2. Average Heat-Transfer Coefficient

Table 6 shows the heat transfer variables calculated for obtaining the model’s heat transfer coefficient. Air masses are different due to different time steps, which is also expected for falling material mass. However, if timestep  $dt$  and length  $l$  are made equal to model one in model two, material falling mass remains almost identical in both:  $(dt = 0.01; \bar{m}_{aM1} = 0.04(2)(10) = 0.8 \text{ Kg} \approx 0.82 = \bar{m}_{aM2})$ . Hence, the falling behavior is essentially the same for both particle diameters. The heat transfer

coefficient is significantly increased for lower diameter particles, due to a greater area of heat exchange when the particle diameter is made smaller.

**Table 6.** Heat transfer variables for each model during the given time step.

Model	One	Two
Particle diameter $D_p$ (mm)	8	20
Timestep $dt$ (s)	0.005	0.010
Air mass $\bar{m}_a$ (kg)	0.125	0.250
Material falling mass $\bar{m}_{mf}$ (kg)	0.04	0.82
Area of heat exchange $A_{fp}$ (m <sup>2</sup> )	0.029	0.233
Average heat transfer coefficient $h$ ( $\frac{W}{m^2 \cdot C}$ )	60.15	38.93

#### 4.3. Thermodynamic Model

Table 7 shows the comparison between the thermodynamic models obtained for each simulated model and that found for the industry cooler. The thermodynamic behavior of model one provides a close approximation to air and NPK temperature boundary conditions when model one is used in the calculations. The calculated area of heat exchange for model one shows that its cooling capabilities are higher than the one found on the industry cooler. Thus, heat losses should be taken into account, as the simulation is set with adiabatic wall boundary conditions.

**Table 7.** Comparison of Thermodynamic and Counter-current Heat exchanger models results with industry cooler analysis.

Properties	Model One	Model Two	Industry Cooler
Particle diameter $D_p$ (mm)	8	20	2.7
Thermodynamic model			
Material outlet temperature $T_{mo}$ (°C)	40.90	61.23	45.00
Thermal power $Q_m$ (kW)	998.40	584.87	915.04
Air outlet temperature $T_{ao}$ (°C)	69.73	53.27	66.42
Counter-current Heat exchanger model			
Material inlet temperature $T_{mi}$ (°C)	90.00	90.00	90.00
Air inlet temperature $T_{ai}$ (°C)	69.73	53.27	66.42
Material outlet temperature $T_{mo}$ (°C)	40.90	61.23	45.00
Air outlet temperature $T_{ao}$ (°C)	30.00	30.00	30.00
Logarithmic mean temperature difference $LMTD_{he}$ (°C)	15.10	33.90	18.97
Heat transfer coefficient $h$ ( $\frac{W}{m^2 \cdot C}$ )	60.15	38.92	60.15
Exchanged heat $Q_{he}$ (kW)	998.48	584.88	915.04
The total area of heat exchange $A_{he}$ (m <sup>2</sup> )	1099.28	443.13	802.01

#### 4.4. Correlation

Equation (58) shows the correlation found using the Marquardt method. Table 8 shows the analysis of variance performed on the model. The p-value states that the model parameters can explain the variation seen in the data. Therefore, the model is suitable for reproducing the data obtained from the thermodynamic balance and the DEM-CFD simulation.

$$Nu_m = 0.0531283 Re_m^{0.523707} Pr_a^{1.00824} \quad (58)$$



**Table 8.** Analysis of variance of non-linear correlation.

Source of Variance	Sum of Squares	Degrees of Freedom	Mean Square	F Observed	P-Value
Model	58466.6	3	19488.87	23,086,378	0.0000
Error	4.05118	4799	0.000844		
Total	58470.6	4802			
Adjusted R-squared (%)	99.8634				

Figure 9 shows the Nusselt vs. Reynolds for a fixed value of Prandtl. Note that Nusselt and Reynolds grow as particle diameter is increased.

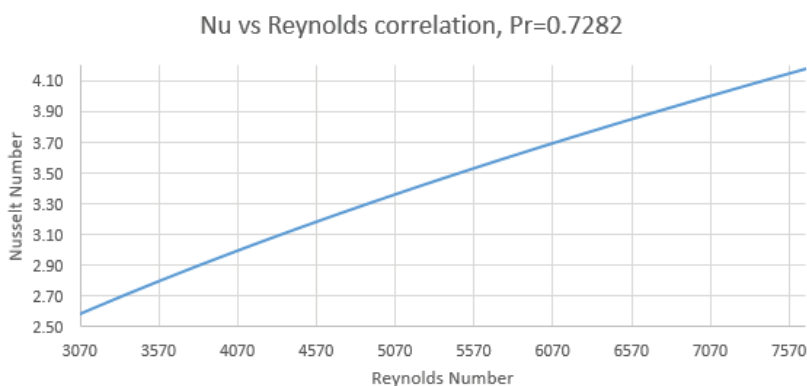


**Figure 9.** Nusselt vs. Reynolds correlation for industry cooler at Pr = 0.7282. Valid if  $3073 < Re < 7686$ .

## 5. Conclusions

This work describes and employs a new methodology that blends CFD-DEM modeling and global energy and mass balances to obtain an initial approximation of the heat-transfer phenomena taking place inside an industry-scale  $50 \frac{T}{h}$  counter-current rotary drum during the cooling process of NPK 15–15–15 biofertilizer. The low computational effort needed for simulating the proposed CFD-DEM model and the ease of the methodology offers a fast, concise method to elucidate process heat transfer dynamics in the current operating point. Besides, by the calculation of process dimensionless numbers and correlations, heat-transfer coefficients and overall process operating characteristics can be predicted when process variables such as drum angular velocity, air velocity, material inlet-outlet temperatures, and the average particle diameter are changed inside the range of valid Reynolds numbers for the defined correlation. Hence, process optimization and design modifications can be achieved without long plant downtimes given by the execution of new experimental designs. In this way, overall company profits are not severely affected.

Consequently, results from our simulation could be useful in many different cases. One scenario could be the following: There is a current rotating cooler operating at set parameters and the company wants to change variables such as cooler rotation, tilt angle, feeding rate, and particle diameter. After applying the methodology, the user can predict how these variables should be reprogrammed for achieving any given set of outlet boundary conditions, such as outlet temperature and outlet mass flow of granulated solid after cooling.

**Author Contributions:** Conceptualization, M.S.; Methodology, A.B. and F.B.-F.; Software, A.B. and F.B.-F.; Validation, A.B. and F.B.-F.; Formal Analysis, A.B. and F.B.-F.; Investigation, M.S.; Resources, J.M. and A.F.; Data Curation, F.B.-F.; Writing-Original Draft Preparation, F.B.-F.; Writing-Review & Editing, A.B.; Visualization, A.B. and F.B.-F.; Supervision, M.S.; Project Administration, M.S.; Funding Acquisition, J.M. and A.F.

**Funding:** This work was funded by COLCIENCIAS Research Call 757 and the Office of Management and Academic Development at Universidad del Norte.

**Conflicts of Interest:** The authors declare no conflict of interest.

## References

1. Lisboa, M.H.; Vitorino, D.S.; Delaiba, W.B.; Finzer, J.R.D.; Barrozo, M.A.S. A study of particle motion in rotary dryer. *Braz. J. Chem. Eng.* **2007**, *24*, 365–374. [CrossRef]
2. Silvério, B.C.; Arruda, E.B.; Duarte, C.R.; Barrozo, M.A.S. A novel rotary dryer for drying fertilizer: Comparison of performance with conventional configurations. *Powder Technol.* **2015**, *270*, 135–140. [CrossRef]
3. Fernandes, N.J.; Ataíde, C.H.; Barrozo, M.A.S. Modeling and experimental study of hydrodynamic and drying characteristics of an industrial rotary dryer. *Braz. J. Chem. Eng.* **2009**, *26*, 331–341. [CrossRef]
4. Kemp, I.C. Comparison of Particles Motion Correlations for Cascading Rotary Dryers. In Proceedings of the 14th International Drying Symposium (IDS), São Paulo, Brazil, 22–25 August 2004; pp. 790–797.
5. Zhu, H.P.; Zhou, Z.Y.; Yang, R.Y.; Yu, A.B. Discrete particle simulation of particulate systems: Theoretical developments. *Chem. Eng. Sci.* **2007**, *62*, 3378–3396. [CrossRef]
6. Fries, L.; Antonyuk, S.; Heinrich, S.; Palzer, S. DEM–CFD modeling of a fluidized bed spray granulator. *Chem. Eng. Sci.* **2011**, *66*, 2340–2355. [CrossRef]
7. Tsuji, T.; Yabumoto, K.; Tanaka, T. Spontaneous structures in three-dimensional bubbling gas–fluidized bed by parallel DEM–CFD coupling simulation. *Powder Technol.* **2008**, *184*, 132–140. [CrossRef]
8. di Renzo, A.; di Maio, F.P. Homogeneous and bubbling fluidization regimes in DEM–CFD simulations: Hydrodynamic stability of gas and liquid fluidized beds. *Chem. Eng. Sci.* **2007**, *62*, 116–130. [CrossRef]
9. Fries, L.; Antonyuk, S.; Heinrich, S.; Dopfer, D.; Palzer, S. Collision dynamics in fluidised bed granulators: A DEM–CFD study. *Chem. Eng. Sci.* **2013**, *86*, 108–123. [CrossRef]
10. Mayank, K.; Malahe, M.; Govender, I.; Mangadoddy, N. Coupled DEM–CFD Model to Predict the Tumbling Mill Dynamics. *Procedia IUTAM* **2015**, *15*, 139–149. [CrossRef]
11. Shan, T.; Zhao, J. A coupled CFD–DEM analysis of granular flow impacting on a water reservoir. *Acta Mech.* **2014**, *225*, 2449–2470. [CrossRef]
12. Feng, Y.T.; Owen, D.R.J. Discrete element modelling of large scale particle systems—I: Exact scaling laws. *Comput. Part. Mech.* **2014**, *1*, 159–168. [CrossRef]
13. Tomac, I.; Gutierrez, M. Discrete element modeling of non-linear submerged particle collisions. *Granul. Matter* **2013**, *15*, 759–769. [CrossRef]
14. Chu, K.W.; Yu, A.B. Numerical simulation of the gas–solid flow in three-dimensional pneumatic conveying bends. *Ind. Eng. Chem. Res.* **2008**, *47*, 7058–7071. [CrossRef]
15. Ibsen, C.H.; Helland, E.; Hjertager, B.H.; Solberg, T.; Tadríst, L.; Occelli, R. Comparison of multifluid and discrete particle modelling in numerical predictions of gas particle flow in circulating fluidised beds. *Powder Technol.* **2004**, *149*, 29–41. [CrossRef]
16. Tsuji, Y.; Tanaka, T.; Ishida, T. Lagrangian numerical simulation of plug flow of cohesionless particles in a horizontal pipe. *Powder Technol.* **1992**, *71*, 239–250. [CrossRef]
17. Sen, M.; Barrasso, D.; Singh, R.; Ramachandran, R. A multi-scale hybrid CFD–DEM–PBM description of a fluid-bed granulation process. *Processes* **2014**, *2*, 89–111. [CrossRef]
18. Grimard, J.; Dewasme, L.; Wouwer, A.V. A review of dynamic models of hot-melt extrusion. *Processes* **2016**, *4*, 19. [CrossRef]
19. Muddu, S.; Tamrakar, A.; Pandey, P.; Ramachandran, R. Model development and validation of fluid bed wet granulation with dry binder addition using a population balance model methodology. *Processes* **2018**, *6*, 154. [CrossRef]
20. Cundall, O.D.L.; Strack, A.P. A discrete numerical model for granular assemblies. *Geotechnique* **1979**, *29*, 47–65. [CrossRef]
21. Jones, W.P.; Launder, B.E. The prediction of laminarization with a two-equation model of turbulence. *Int. J. Heat Mass Transf.* **1972**, *15*, 301–314. [CrossRef]
22. Wilcox, D.C. *Turbulence Modeling for CFD*; DCW Industries: Anaheim, CA, USA, 1998.



© 2019 by the authors. Licensee MDPI, Basel, Switzerland. This article is an open access article distributed under the terms and conditions of the Creative Commons Attribution (CC BY) license (<http://creativecommons.org/licenses/by/4.0/>).

Article

# DynamFluid: Development and Validation of a New GUI-Based CFD Tool for the Analysis of Incompressible Non-Isothermal Flows

Héctor Redal <sup>1</sup>, Jaime Carpio <sup>2</sup>, Pablo A. García-Salaberri <sup>1</sup> and Marcos Vera <sup>1,\*</sup>

<sup>1</sup> Departamento de Ingeniería Térmica y de Fluidos, Universidad Carlos III de Madrid, 28911 Leganés, Spain; hector.redal@gmail.com (H.R.); pagsalab@ing.uc3m.es (P.A.G.-S.)

<sup>2</sup> Departamento de Ingeniería Energética, E.T.S. Ingenieros Industriales, Universidad Politécnica de Madrid, 28006 Madrid, Spain; jaime.carpio@upm.es

\* Correspondence: marcos.vera@uc3m.es; Tel.: +34-91624-9987; Fax: +34-91624-9430

Received: 9 October 2019; Accepted: 24 October 2019; Published: 27 October 2019

**Abstract:** A computational fluid dynamics software (DynamFluid) based on the application of the finite element method with the characteristic-based-split algorithm is presented and validated. The software is used to numerically integrate the steady and unsteady Navier–Stokes equations for both constant-density and Boussinesq non-isothermal flows. Benchmark two-dimensional computations carried out with DynamFluid show good agreement with previous results reported in the literature. Test cases used for validation include (i) the lid-driven cavity flow, (ii) mixed convection flow in a vertical channel with asymmetric wall temperatures, (iii) unsteady incompressible flow past a circular cylinder, and (iv) steady non-isothermal flow past a circular cylinder with negligible buoyancy effects. The new software is equipped with a graphical user interface that facilitates the definition of the fluid properties, the discretization of the physical domain, the definition of the boundary conditions, and the post-processing of the computed velocity, pressure and temperature fields.

**Keywords:** finite element method; characteristic-based-split algorithm; benchmark problems; lid-driven cavity flow; non-isothermal vertical channel; flow past a circular cylinder; Boussinesq approximation

## 1. Introduction

The science of fluid mechanics involves a broad spectrum of techniques for the study of fluid flows [1,2]. Experimental fluid mechanics plays an important role in the validation of theoretical models and the determination of their limits of application. Moreover, laboratory-scale experiments (e.g., wind tunnel model testing) combined with dimensional analysis [3,4] provides the science with an effective way of studying complex flows, saving the time and money that would otherwise be employed in full-scale experimental studies. On the other hand, computational fluid dynamics (CFD) is the art of substituting the set of partial differential equations governing the flow by a set of algebraic equations that can be solved with computers [5–10]. As a result, CFD can be regarded as the connection between theory and experiments, providing an economical alternative to experimental model testing. The ever growing importance of CFD has driven the development of a large variety of commercial software (ANSYS Fluent [11], Star-CCM+ [12], COMSOL's CFD [13], Altair AcuSolve [14], to name a few) and open source solutions (OpenFOAM [15–17], FreeFEM++ [18], FEniCS [19], for example) in the last decades.

This paper presents a new CFD software tool (DynamFluid) based on the finite element method (FEM) for the analysis of incompressible flows. The finite element method has been selected in favour

of other options, such as the finite difference method (FDM) or the finite volume method (FVM), because of its higher adaptability to arbitrarily shaped domains, as other methods require complex curvilinear transformation when trying to solve problems in complex geometries represented in regular Cartesian coordinates. This and other advantages are already exploited in a variety of commercial and open-source codes, such as the above mentioned COMSOL's CFD [13], FreeFEM++ [18] or FEniCS [19]. Although the developed code has the capability of solving fully three-dimensional (3D) problems with arbitrary density variations and the general form of the gravitational term (body force), the validation process in this work will be restricted to two-dimensional (2D) flows where the fluid density undergoes tiny variations, so that the Boussinesq approximation can be employed. Further validation in 3D geometries with large density variations is left for future work. DynamFluid is implemented in C++.

The main characteristics of the DynamFluid tool can be summarized as follows:

1. Windows-based software, which can be run in any Windows Operating System: both 32- and 64-bit architectures are supported. When run in a 64-bit architecture, the software leverages on the larger word-size when performing computations.
2. Graphical user interface for defining the geometric domain, physical model, boundary conditions, and displaying the results obtained in any simulation.
3. Custom database for storing both the project domain definition and all the information generated during the simulation. The database provides the user with ODBC (Open DataBase Connectivity) interface for interacting with any ODBC client.
4. Support for NASTRAN format file importing, which allows the user to import any geometry and physical definition in DMAP (Direct Matrix Abstraction Programming) language.
5. Vtk file format capabilities, to export generated simulations into ASCII text Vtk files that can be visualized using Paraview [20].
6. Basic meshing capabilities to sample the geometric domain. Two methods have been implemented: (a) structured meshing (linear, logarithmic) using both quadrangular elements (QUAD) and triangular elements (TRIA) for regular geometric domains, and (b) Delaunay–Voronoi meshing for irregular geometric domains.
7. Software designed to run in a computer with a motherboard that may have one or several multi-core processors. This includes parallel computation of the finite element matrices, parallel assembly of the global matrices and parallel computation of the right hand side of each step of the algorithm. The software uses the conjugate gradient stabilized algorithm provided by the Eigen library [21] to solve the linear systems, and it has been compiled with the openmp compiler flag so that the Eigen library exploits the multiple cores available in the hardware.
8. Custom user language for post-processing the results (velocity, pressure and temperature), with basic algebra functions and support for different coordinate reference systems. Internal compiler for translating this user language into machine code that can be applied in parallel to every node and/or finite element.
9. Support for different types of finite elements (both Lagrangian and Serendipity): (a) linear TRIA elements and (b) linear and quadratic QUAD elements.
10. DynamFluid is a freeware CFD tool available at <https://sites.google.com/view/dynamfluid>.

Four benchmark 2D problems have been selected in this work for validation purposes, namely (i) the lid-driven cavity flow, (ii) mixed convection flow in a vertical channel with asymmetric wall temperatures, (iii) unsteady incompressible flow past a circular cylinder, and (iv) steady non-isothermal flow past a circular cylinder with negligible buoyancy effects. These problems are briefly outlined below.

- (i) The lid-driven cavity flow. This is a classical benchmark problem that has been widely used since the early days of CFD to assess and validate new techniques and methods. This test case is easy to set and simulate because its boundary conditions are particularly simple. However, the fully developed flow displays almost all fluid mechanical phenomena, with

increasingly complex aspects emerging as the Reynolds number is increased, such as corner eddies, laminar to turbulence regime transition, and even turbulence at high Reynolds number. A recent comprehensive review of the literature on the subject can be found in [22], where the work of several authors is presented and discussed [23–28]. Available benchmark results have been tabulated to provide a comprehensive source of validation data [29].

- (ii) Mixed convection flow in a vertical channel with asymmetric wall temperatures. In this mixed convection heat transfer problem, an initially uniform flow develops in a slender vertical channel whose walls are at different temperatures. The cold and hot wall temperatures may also differ from the incoming flow temperature. As a result of the upward buoyancy force that appears near the hot wall, the velocity increases in the near-wall region. As the fluid accelerates downstream, the fluid near the cold wall may suffer flow reversal so as to maintain the imposed fixed flow rate. One of the most interesting features exhibited by this flow is thus the possibility of flow reversal at the cold wall as the flow develops. The occurrence (or not) of flow reversal depends on the length of the vertical channel and the buoyancy effect induced by the temperature difference between the hot and cold walls. Previous studies have shown that for the flow reversal to occur, in high Reynolds number flows the ratio of the Grashof number to the Reynolds number must be higher than a critical value that depends on the wall temperature difference ratio [30–43].
- (iii) Unsteady incompressible flow past a circular cylinder. The flow of a constant density fluid past a bluff body is another classical problem that has been widely studied in the literature. Understanding the flow regimes past bluff bodies poses a daunting challenge, so that 2D and 3D vortical structures in wakes of different bodies have been analyzed by scientists and engineers for decades. The reason for this interest is the vast range of applications of external flow past round bluff bodies: aerodynamics (planes, rockets, ground vehicles), hydrodynamics (ships, submarines) or wind energy (wind turbines), to name the few. At very low Reynolds numbers (creeping flow) the flow past a non-heated circular cylinder is symmetric in the streamwise direction [44–47]. As the Reynolds number grows to values of order unity the symmetry is lost, and when it exceeds a critical value the non-linear convective effects trigger the onset of steady flow separation, accompanied by the appearance of steady recirculation bubbles behind the cylinder. One important aspect of these flows is the so-called vortex shedding, which is an oscillating flow pattern that emerges for even larger Reynolds numbers. This regime has been thoroughly studied experimentally [48–52] and numerically [53–57]. The alternate shedding of vortices in the wake leads to the well known Kármán vortex street, which originates large fluctuating pressure forces in the direction transverse to the flow and may cause structural vibrations, acoustic noise, or resonance, which in some cases may lead to structural damage or even collapse.
- (iv) Steady non-isothermal flow past a circular cylinder with negligible buoyancy effects. This case is similar to the previous one but with the particularity that the temperature of the cylinder differs from the temperature of the incoming fluid, which causes the flow past a circular cylinder to exhibit interesting heat transfer features. This problem is of interest for the design of cylinder-shaped sensors located in fluid streams, hot-wire anemometers, tube heat exchangers, nuclear reactor fuel rods and chimneys. In this work, attention will be restricted to steady flow with negligible buoyancy effects, with the aim of characterizing the local Nusselt number at the cylinder wall for different Reynolds numbers [44,54,58,59].

## 2. Governing Equations

Let  $\mathbf{x} = (x, y, z)^T \in \Omega_t \subset R^3$  be the spatial domain at time  $t \in (0, T)$ , with  $x_i$  denoting the  $i$ -th cartesian coordinate. Using the Einstein summation convention, the governing equations for three-dimensional unsteady flow with variable density (due, e.g., to temperature variations) can be written as follows

$$\frac{\partial \rho}{\partial t} + \frac{\partial(\rho u_j)}{\partial x_j} = 0 \quad (1)$$

$$\left[ \frac{\partial(\rho u_i)}{\partial t} + \frac{\partial(\rho u_j u_i)}{\partial x_j} \right] = -\frac{\partial p}{\partial x_i} + \frac{\partial \tau_{ij}}{\partial x_j} + \rho g_i, \quad i = \{1, 2, 3\} \quad (2)$$

$$\left[ \frac{\partial(\rho e_T)}{\partial t} + \frac{\partial(\rho u_j e_T)}{\partial x_j} \right] = -\frac{\partial(\rho u_j)}{\partial x_j} + \frac{\partial(\tau_{ij} u_i)}{\partial x_j} + \rho g_j u_j + \frac{\partial}{\partial x_j} \left( k \frac{\partial T}{\partial x_j} \right), \quad (3)$$

where  $\rho$  is the fluid density,  $u_i$  the  $i$ -th component of the velocity vector  $\mathbf{u} = (u, v, w)^T$ ,  $e_T = e + u_i u_i / 2$  the total energy per unit mass (with  $e = c_v T$  the specific internal energy per unit mass, assuming a calorically perfect fluid),  $p$  the pressure,  $T$  the absolute temperature,  $g_i$  the  $i$ -th component of the acceleration of gravity, and  $k$  the thermal conductivity. In the above equations  $\tau_{ij}$  represent the deviatoric stress components

$$\tau_{ij} = \mu \left( \frac{\partial u_i}{\partial x_j} + \frac{\partial u_j}{\partial x_i} - \frac{2}{3} \delta_{ij} \frac{\partial u_k}{\partial x_k} \right), \quad (4)$$

where  $\mu$  is the dynamic viscosity and  $\delta_{ij}$  the Kronecker delta.

In non-isothermal flows where the density variations are small but the flow is driven by buoyancy forces, such as in natural or mixed convection problems, one may simplify the equations by means of the Boussinesq approximation. This approximation assumes that variations in density have no effect on the flow field other than to give rise to buoyancy forces. In this case, the continuity and momentum equations take the simplified form

$$\frac{\partial u_j}{\partial x_j} = 0 \quad (5)$$

$$\rho_\infty \left[ \frac{\partial u_i}{\partial t} + \frac{\partial(u_j u_i)}{\partial x_j} \right] = -\frac{\partial p}{\partial x_i} + \frac{\partial \tau_{ij}}{\partial x_j} + \rho_\infty (1 - \beta(T - T_\infty)) g_i, \quad i = \{1, 2, 3\} \quad (6)$$

where  $\rho_\infty$  is the reference fluid density,  $T_\infty$  the reference temperature, and  $\beta = -\rho^{-1}(\partial \rho / \partial T)_p$  the thermal expansion coefficient.

In the Boussinesq approximation, the energy equation is often simplified by also ignoring the density variations. However, in this work, the energy equation will be kept in its general form, without any further simplification. The reason for this approach is to minimize the approximation error when computing the temperature field in a fluid that undergoes tiny variations of density, and to give a unified treatment to the energy equation independently of the way density is computed. In the range of Reynolds number considered here, the different treatments of the energy equation, and the assumption of constant specific heats, do not make a significant difference. Leaving the general form allows validating the implementation of the energy equation when the Boussinesq approximation is used in the Navier–Stokes equations but not in the energy equation.

Let  $L_\infty$  be the characteristic length,  $U_\infty$  the characteristic velocity,  $L_\infty / U_\infty$  the characteristic residence time of the problem,  $\rho_\infty$  the reference density,  $\mu_\infty$  the reference dynamic viscosity, and  $k_\infty$  the reference thermal conductivity. With these scales, the following dimensionless variables can be introduced

$$\begin{aligned} x_i^* &= \frac{x_i}{L_\infty}, & t^* &= \frac{U_\infty t}{L_\infty}, & \rho^* &= \frac{\rho}{\rho_\infty}, & u_i^* &= \frac{u_i}{U_\infty}, & p^* &= \frac{p - p_\infty}{\rho_\infty U_\infty^2}, & \tau_{ij}^* &= \frac{\tau_{ij} L_\infty}{\mu_\infty U_\infty}, \\ g_i^* &= \frac{g_i}{g}, & \mu^* &= \frac{\mu}{\mu_\infty}, & e_T^* &= \frac{e_T}{U_\infty^2}, & T^* &= \frac{c_p T}{U_\infty^2}, & k^* &= \frac{k}{k_\infty} \end{aligned} \quad (7)$$

where  $p_\infty$  represents a convenient pressure datum, and  $g \simeq 9.81 \text{ m/s}^2$  is the acceleration of gravity.

The asterisk will be dropped in the following for simplicity, so that all variables will be assumed to be non-dimensional. Thus, the general governing Equations (1)–(3) can be rewritten as follows

$$\frac{\partial \rho}{\partial t} + \frac{\partial(\rho u_j)}{\partial x_j} = 0 \quad (8)$$

$$\left[ \frac{\partial(\rho u_i)}{\partial t} + \frac{\partial(\rho u_j u_i)}{\partial x_j} \right] = -\frac{\partial p}{\partial x_i} + \frac{1}{\text{Re}} \frac{\partial \tau_{ij}}{\partial x_j} + \frac{1}{\text{Fr}} \rho g_i, \quad i = \{1, 2, 3\} \quad (9)$$

$$\left[ \frac{\partial(\rho e_T)}{\partial t} + \frac{\partial(\rho u_j e_T)}{\partial x_j} \right] = -\frac{\partial(p u_j)}{\partial x_j} + \frac{1}{\text{Re}} \frac{\partial(\tau_{ij} u_j)}{\partial x_i} + \frac{1}{\text{Fr}} \rho g_j u_j + \frac{1}{\text{Re Pr}} \frac{\partial}{\partial x_j} \left( k \frac{\partial T}{\partial x_j} \right), \quad (10)$$

where  $\text{Re} = \rho_\infty U_\infty L_\infty / \mu_\infty$  is the Reynolds number,  $\text{Fr} = U_\infty^2 / (L_\infty g)$  is the Froude number, and  $\text{Pr} = \mu_\infty c_p / k_\infty$  is the Prandtl number, defined in terms of the specific heat at constant pressure  $c_p$ , assumed here to be constant. Note that for liquids both specific heats are equal  $c_p = c_v$ , whereas for gases  $c_p = c_v + R_g$ , where  $R_g = R^\circ / W$  is the gas constant, defined as the ratio between the universal gas constant  $R^\circ = 8.314 \text{ J}/(\text{mol} \cdot \text{K})$  and the molecular mass of the gas  $W$  that is constant for gases of uniform composition.

Under the Boussinesq approximation, it is convenient to define the normalized dimensionless temperature

$$\Theta = \frac{T - T_\infty}{T_w - T_\infty}, \quad (11)$$

in terms of the reference temperature  $T_\infty$  and a characteristic temperature  $T_w$  (e.g., that of a hot or cold wall, thereby the subscript  $w$ ) that determines the characteristic temperature difference of the problem,  $T_w - T_\infty$ . In this case, the momentum conservation Equation (6) and the energy conservation Equation (3) can be rewritten as follows, where the asterisks are dropped again so that all variables are non-dimensional

$$\frac{\partial u_i}{\partial t} + \frac{\partial(u_j u_i)}{\partial x_j} = -\frac{\partial p}{\partial x_i} + \frac{1}{\text{Re}} \frac{\partial \tau_{ij}}{\partial x_j} + \frac{1}{\text{Fr}} g_i - \frac{\text{Gr}}{\text{Re}^2} g_i \Theta, \quad i = \{1, 2, 3\} \quad (12)$$

$$\rho \left[ \frac{\partial e_T}{\partial t} + \frac{\partial(u_j e_T)}{\partial x_j} \right] = -\frac{\partial(p u_j)}{\partial x_j} + \frac{1}{\text{Re}} \frac{\partial(\tau_{ij} u_j)}{\partial x_i} + \frac{1}{\text{Fr}} \rho g_j u_j + \frac{1}{\text{Re Pr}} \frac{\partial}{\partial x_j} \left( k \frac{\partial T}{\partial x_j} \right), \quad (13)$$

while the continuity Equation (5) remains unchanged, implying the divergence-free nature of the velocity field. The simplified form of the continuity equation has been used, in particular, to rewrite the convective term in the energy Equation (13) including the velocity  $u_j$  into the spatial derivative. Note that, following standard practice, in the momentum conservation Equation (12) the dimensionless density has been assumed to be constant ( $\rho = 1$ ) except in the buoyancy term, which is written in terms of the Grashof number

$$\text{Gr} = \frac{\beta g (T_w - T_\infty) L_\infty^3}{\nu_\infty^2}, \quad (14)$$

and the normalized dimensionless temperature  $\Theta$ , given by (11) in terms of the dimensionless temperature  $T$  computed from (13).

Finally, to be well posed, the mathematical problem also requires appropriate boundary conditions and a set of initial conditions for all the variables to be solved.

### 3. Numerical Method

#### 3.1. Temporal Discretization: The Characteristics-Based-Split Algorithm

Following Zienkiewicz's et al. [60–64], the Navier-Stokes equations can be sampled in time using a characteristic method, the so-called characteristic-based-split (CBS) scheme. To obtain the numerical solution, the time interval will be divided into  $N_t$  subintervals  $I_n := (t_n, t_{n+1}]$  with constant time step

size  $\Delta t = t_{n+1} - t_n$ . Then, a variable  $\phi$  at time  $n + \theta$  can be approximated as  $\phi^{n+\theta} = (1 - \theta)\phi^n + \theta\phi^{n+1}$ , where the superscript denotes the time at which the variable is evaluated. As a result, it can be written that

$$\phi^{n+\theta} = (1 - \theta)\phi^n + \theta\phi^{n+1} = \phi^n + \theta\Delta\phi, \quad (15)$$

with  $\Delta\phi = \phi^{n+1} - \phi^n$ .

Consequently, the CBS scheme, proposed by Zienkiewicz and Codina [61], applied to the governing Equations (1), (12) and (13) can be sampled in time as follows

$$\frac{u_i^{n+1} - u_i^n}{\Delta t} = \frac{\Delta u_i}{\Delta t} = \left[ -\frac{\partial(u_j u_i)}{\partial x_j} + \frac{1}{\text{Re}} \frac{\partial \tau_{ij}}{\partial x_j} + \frac{1}{\text{Fr}} g_i - \frac{\text{Gr}}{\text{Re}^2} g_i \Theta \right]^n - \frac{\partial p^{n+\theta_2}}{\partial x_i}, \quad i = \{1, 2, 3\} \quad (16)$$

$$\frac{\rho^{n+1} - \rho^n}{\Delta t} = \frac{\Delta \rho}{\Delta t} = \left( \frac{1}{a^2} \right)^n \frac{\Delta p}{\Delta t} = -\frac{\partial(\rho u_j^{n+\theta_1})}{\partial x_j} \quad (17)$$

$$\rho^n \frac{e_T^{n+1} - e_T^n}{\Delta t} = \rho^n \frac{\Delta e_T}{\Delta t} = \left[ -\rho \frac{\partial(u_j e_T)}{\partial x_j} - \frac{\partial(p u_j)}{\partial x_j} + \frac{1}{\text{Re}} \frac{\partial(\tau_{ij} u_j)}{\partial x_i} + \frac{1}{\text{Fr}} \rho g_j u_j + \frac{1}{\text{RePr}} \frac{\partial}{\partial x_j} \left( k \frac{\partial T}{\partial x_j} \right) \right]^n \quad (18)$$

where the continuity equation for incompressible fluids has been substituted by an equation of conservation of mass (17) that includes an artificial compressibility [65]. In that equation  $a$  represents the speed of sound in the fluid, which in the incompressible limit tends to infinity. The principal asset of this split algorithm is that it does not only apply to compressible flows, but also to incompressible flows, which makes it suitable for a wide variety of applications. In the above equations,  $\theta_1$  and  $\theta_2$  represent, respectively, the velocity and pressure relaxation factors. The explicit form of the algorithm is  $\theta_2 = 0$ , whereas in the semi-implicit form  $\theta_2 \in [0.5, 1]$ . In both cases the value of  $\theta_1 \in [0.5, 1]$ . In the numerical simulations presented in this paper we have considered the semi-implicit algorithm, setting the velocity relaxation factor to  $\theta_1 = 1.0$ , and the pressure relaxation factor to  $\theta_2 = 1.0$ . For this parameter choice, second-order accuracy in time is expected [61]. Moreover, the algorithm imposes a restriction to the time step size  $\Delta t$  and it is conditionally stable, as reported by [61]. In its semi-implicit form [66], the time step size must be  $\Delta t \leq \min\{h/|\mathbf{u}_i|, h^2/(2\nu)\}$ , whereas in the explicit form,  $\Delta t \leq h/|\mathbf{a}|$ , leading to a more stringent time step in incompressible fluids. That is the reason why, for incompressible fluids, the semi-implicit form is cheaper in terms of computational cost, providing the required results in less time.

Equation (16) is coupled to Equation (17) and for this reason it cannot be used explicitly. To overcome this limitation, an auxiliary variable  $\Delta u^{**}$  is introduced, defined by

$$\Delta u_i^{**} = u_i^{**} - u_i^n = \Delta t \left[ -\frac{\partial(u_j u_i)}{\partial x_j} + \frac{1}{\text{Re}} \frac{\partial \tau_{ij}}{\partial x_j} + \frac{1}{\text{Fr}} g_i - \frac{\text{Gr}}{\text{Re}^2} g_i \Theta + \frac{\Delta t}{2} u_k \frac{\partial}{\partial x_k} \left( \frac{\partial(u_j u_i)}{\partial x_j} - \frac{1}{\text{Fr}} g_i + \frac{\text{Gr}}{\text{Re}^2} g_i \Theta \right) \right]^n \quad (19)$$

This equation does not contain the pressure term and the variable  $u_i^{**}$  can thus be computed explicitly. When the pressure term is available, the following correction is applied

$$\Delta u_i = u_i^{n+1} - u_i^n = \Delta u_i^{**} - \Delta t \frac{\partial p^{n+\theta_2}}{\partial x_i} - \frac{\Delta t^2}{2} u_k \frac{\partial}{\partial x_k} \left( -\frac{\partial p^{n+\theta_2}}{\partial x_i} \right). \quad (20)$$

Expressing  $\Delta u_i^{n+1}$  as a function of  $\Delta u_i^{**}$  using (20) and substituting the result in (17) yields

$$\Delta \rho = \left( \frac{1}{a^2} \right)^n \Delta p = -\Delta t \left[ \frac{\partial u_i^n}{\partial x_i} + \theta_1 \frac{\partial \Delta u_i^{**}}{\partial x_i} - \Delta t \theta_1 \left( \frac{\partial^2 p^n}{\partial x_i \partial x_i} + \theta_2 \frac{\partial^2 \Delta p}{\partial x_i \partial x_i} \right) \right]. \quad (21)$$

Finally, expressing  $\Delta e_T$  as a function of  $e_T^n$  gives



$$\rho \Delta e_T = \Delta t \left[ -\frac{\partial(u_j(\rho e_T + p))}{\partial x_j} + \frac{1}{\text{Re}} \frac{\partial(\tau_{ij} u_j)}{\partial x_i} + \frac{1}{\text{Fr}} \rho g_j u_j + \frac{1}{\text{RePr}} \frac{\partial}{\partial x_j} \left( k \frac{\partial T}{\partial x_j} \right) + \frac{\Delta t}{2} u_j \frac{\partial}{\partial x_j} \left( \frac{\partial(-u_i(\rho e_T + p))}{\partial x_i} \right) \right]^n \quad (22)$$

The way the variables of the problem are solved is summarized in the following step sequence:

- Step 1.** Calculate  $\Delta u_i^{**}$  from Equation (19).
- Step 2.** Calculate  $\Delta \rho$  or  $\Delta p$  from Equation (21).
- Step 3.** Calculate  $\Delta u_i$  from Equation (20), which yields the velocity at time  $t_{n+1}$ .
- Step 4.** Calculate  $\Delta e$  from Equation (22), which can be calculated in parallel with the other steps since the right hand side of Equation (22) does not depend on the variables at time  $t_{n+1}$ . Step 4 allows obtaining the value of the energy at time  $t_{n+1}$ .

The reason for choosing the CBS algorithm instead of others is to achieve second order convergence in both time and space using linear finite elements (TRIA and/or QUAD). Additionally, since the right hand side of the different equations of the algorithm are treated explicitly, they are easy to parallelize, as it has been done in the implementation of the algorithm.

### 3.2. Spatial Discretization

Following the characteristics-Galerkin approximation, Equations (19)–(22) are discretized in space using the finite element method [67–69]. To this end, the spatial domain is divided into a regular, unstructured triangulation  $\mathbb{T}_h$  of non-overlapping elements. Associated with that triangulation, a conforming finite element space  $V_h$  is defined composed of continuous, piecewise polynomials over each mesh element. The current implementation of the software uses only linear polynomials for all fluid variables, so higher order elements are not considered. Therefore, the numerical method is expected to be second order in space for smooth solutions in the  $L^2$ -norm. The advantage of the finite element method, as spatial discretization method, is that it allows to work with complex geometries, and to use fine or coarse finite elements in different zones of the domain (local mesh refinement) [70]. Moreover, the implemented code supports both TRIA and QUAD finite elements.

Hence, if  $m$  is the number of mesh points (or nodal points) of the triangulation  $\mathbb{T}_h$ , the numerical solution  $\phi_h$  belonging to the finite element space  $V_h$  can be written as

$$\phi_h = \sum_{k=1}^m N_h^k \phi^k, \quad (23)$$

where the summation spans over the set of nodes comprising the sampled domain, being  $k$  the index of the node, for  $1 \leq k \leq m$ .  $\phi^k$  is the unknown variable evaluated at node  $k$ , and  $\{N_h^k\}_{k=1}^m$  is the set of basis functions of  $V_h$  satisfying  $N_h^k(x_j) = \delta_{kj}$ , with  $\delta_{kj}$  the Kronecker delta. Moreover, Equation (23) may be expressed in matricial form as

$$\phi_h = \mathbf{N}_h \overline{\mathbf{C}} \quad (24)$$

with

$$\overline{\mathbf{C}} = [\phi^1, \dots, \phi^k, \dots, \phi^m]^T \quad \text{and} \quad \mathbf{N}_h = [N_h^1, \dots, N_h^k, \dots, N_h^m]. \quad (25)$$

In this problem the generic variable  $\phi_h$  will be replaced by the unknown fluid variables: the pressure,  $p$ , the velocity components,  $u_i$ , the total energy,  $\rho e_T$ , and the temperature,  $T$ .

As a final step to apply the standard Galerkin approximation via the Finite Element method, the weak formulation of Equations (19)–(22) must be obtained. Thus, equations can be weighted and integrated over the sampled domain using the basis functions  $N_{h\phi}^k \in V_{h0}^\phi$ , where  $V_{h0}^\phi$  is the finite element space of functions that take null values in the dirichlet boundary associated with the variable

$\phi_h = \{u_i, p, T\}$  (which means that it does not include the basis functions associated with the dirichlet nodes, whose values for the variable  $\phi_h$  are known).

The weak formulation of Equation (19) (Step 1 of the algorithm to compute  $\Delta u_i^{**}$  for  $i = \{1, 2, 3\}$ ) in the standard Galerkin approximation is the following

$$\int_{\Omega} N_h^k \Delta u_i^{**} d\Omega = \Delta t \left[ - \int_{\Omega} N_h^k \frac{\partial(u_j u_i)}{\partial x_j} d\Omega - \frac{1}{\text{Re}} \int_{\Omega} \frac{\partial N_h^k}{\partial x_j} \tau_{ij} d\Omega - \int_{\Omega} N_h^k \left( \frac{\text{Gr}}{\text{Re}^2} g_i \Theta - \frac{1}{\text{Fr}} g_i \right) d\Omega \right]^n + \Delta t \left[ \frac{1}{\text{Re}} \int_{\Gamma} N_h^k \tau_{ij} n_j d\Gamma \right]^n - \left[ \frac{\Delta t^2}{2} \int_{\Omega} \frac{\partial}{\partial x_j} (u_j N_h^k) \left( \frac{\text{Gr}}{\text{Re}^2} g_i \Theta - \frac{1}{\text{Fr}} g_i + \frac{\partial(u_j u_i)}{\partial x_j} \right) d\Omega \right]^n, \quad (26)$$

where  $n_j$  denotes the  $j$ -th component of the unit outward normal vector to the boundary surface and  $N_h^k \in V_h$ , since it does not impose dirichlet boundary condition over  $\Delta u_i^{**}$ .

To obtain the weak formulation of Equation (21) (Step 2 of the algorithm to compute  $\Delta p = p^{n+1} - p^n$ ), the equation should be multiplied by the  $N_{hp}^k$  basis functions not associated with the dirichlet boundary nodes where pressure is prescribed  $p = \tilde{p}^{n+1}$  at  $\Gamma_p$ . This gives

$$\int_{\Omega} N_{hp}^k \Delta p d\Omega = \int_{\Omega} N_{hp}^k \left( \frac{1}{a^2} \right) \Delta p d\Omega = \Delta t \int_{\Omega} \frac{\partial N_{hp}^k}{\partial x_j} \left[ u_j^n + \theta_1 \Delta u_j^{**} - \theta_1 \Delta t \frac{\partial p^n}{\partial x_j} - \theta_1 \theta_2 \Delta t \frac{\partial \Delta p}{\partial x_j} \right] d\Omega - \Delta t \int_{\Gamma_p \setminus \Gamma} N_{hp}^k \left[ u_j^n + \theta_1 \Delta u_j^{**} - \theta_1 \Delta t \frac{\partial p^n}{\partial x_j} - \theta_1 \theta_2 \Delta t \frac{\partial \Delta p}{\partial x_j} \right] n_j d\Gamma, \quad (27)$$

where the boundary  $\Gamma_p \setminus \Gamma$  is the entire boundary of the domain minus the dirichlet pressure boundary. In the computation of the boundary integral on  $\Gamma_p \setminus \Gamma$ , the Dirichlet condition for the velocity component,  $u_i$ , may also be specified, in which case, the integrand will match the prescribed velocity,  $u_i^n + \theta_1 \Delta u_i^{**} - \theta_1 \Delta t \partial p^n / \partial x_i - \theta_1 \theta_2 \Delta t \partial \Delta p / \partial x_i = \tilde{u}_i$ , at  $\Gamma_u$ .

In the same way, to build the weak formulation of Equation (20) (Step 3 of the algorithm to compute  $\Delta u_i = u_i^{n+1} - u_i^n$  for  $i = \{1, 2, 3\}$ ), the basis functions  $N_{hu}^k$  not associated with the dirichlet boundary nodes where velocity is prescribed,  $u_i^{n+1} = \tilde{u}_i$  at  $\Gamma_u$ , must be considered. This results in

$$\int_{\Omega} N_{hu}^k \Delta u_i d\Omega = \int_{\Omega} N_{hu}^k \Delta u_i^{**} d\Omega - \Delta t \int_{\Omega} N_{hu}^k \frac{\partial p^{n+\theta_2}}{\partial x_i} d\Omega - \frac{1}{2} \Delta t^2 \int_{\Omega} \frac{\partial (u_j^n N_{hu}^k)}{\partial x_j} \frac{\partial p^n}{\partial x_i} d\Omega \quad (28)$$

Finally, the weak formulation of the energy conservation Equation (22) (Step 4 of the algorithm to compute  $T^{n+1}$  through  $\Delta e_T = e_T^{n+1} - e_T^n$ ) takes the form

$$\int_{\Omega} N_{hT}^k \rho \Delta e_T d\Omega = \Delta t \left[ - \int_{\Omega} N_{hT}^k \frac{\partial}{\partial x_j} (u_j (\rho e_T + p)) d\Omega - \frac{1}{\text{Re}} \int_{\Omega} \frac{\partial N_{hT}^k}{\partial x_j} \left( \tau_{ij} u_j + \frac{1}{\text{Pr}} k \frac{\partial T}{\partial x_j} \right) d\Omega + \int_{\Omega} N_{hT}^k \frac{1}{\text{Fr}} \rho g_j u_j d\Omega \right]^n + \frac{\Delta t^2}{2} \left[ \int_{\Omega} \frac{\partial}{\partial x_j} (u_j N_{hT}^k) \frac{\partial}{\partial x_j} (-u_j (\rho e_T + p)) d\Omega \right]^n + \Delta t \frac{1}{\text{Re}} \left[ \int_{\Gamma_T \setminus \Gamma} N_{hT}^k \left( \tau_{ij} u_j + \frac{1}{\text{Pr}} k \frac{\partial h}{\partial x_i} \right) n_i d\Gamma \right]^n, \quad (29)$$

where  $N_{hT}^k$  are the basis functions not associated with the dirichlet boundary nodes where temperature (energy) is prescribed,  $T^{n+1} = \tilde{T}$  at  $\Gamma_T$ . Moreover, in the computation of the boundary integral on  $\Gamma_T \setminus \Gamma$ , the value of the temperature gradient (heat flux) can be specified on some part of it (neumann boundary) as boundary condition.

#### 4. Software Validation

In order to validate the implementation of the CBS algorithm described above, four test cases have been selected for study. Although the implementation of DynamFluid allows the integration of the Navier–Stokes equations in their general form (1)–(3), it can also be applied to fluid dynamics problems

within the Boussinesq approximation (5) and (6). This is the approach chosen for the validation with the test cases presented in this section. All simulations are two-dimensional, hence we shall restrict our attention to cases with  $x_i = (x, y)^T$ ,  $u_i = (u, v)^T$ , and  $g_i = (g_x, g_y)^T$ . As discussed in the numerical section, in all test cases the velocity and pressure relaxation factors  $\theta_1$  and  $\theta_2$  have been set to unity.

#### 4.1. Lid-Driven Cavity Flow

The first step in the validation of a new CFD tool is to check if it is able to predict the flow behaviour in confined domains with simple boundary conditions. The flow in a cavity with an upper mobile lid, shown schematically in Figure 1, is considered as a standard software validation case for steady incompressible flows in confined geometries. In the lid-driven cavity, the fluid is confined in a 2D square cavity of side length  $L$  ( $\equiv L_\infty$ ), with a zero velocity enforced by the no-slip condition in all the walls of the square cavity except in the top wall, where a uniform slip velocity  $U$  ( $\equiv U_\infty$ ) is imposed. Additional parameters of the problem include the density,  $\rho$  ( $\equiv \rho_\infty$ ), and viscosity,  $\mu$  ( $\equiv \mu_\infty$ ), of the fluid, assumed here to be constant. Under isothermal conditions, the only governing parameter is the Reynolds number  $Re = UL/\nu$ , based on the lid velocity, the side length of the squared cavity, and the kinematic viscosity of the fluid,  $\nu = \mu/\rho$  ( $\equiv \nu_\infty$ ).

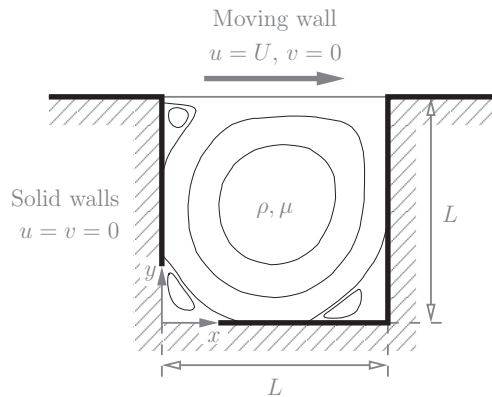


**Figure 1.** Schematic representation of the lid-driven cavity flow showing the coordinate system, dimensional parameters, and boundary conditions.

##### 4.1.1. Literature Review

The lid-driven cavity flow has been extensively addressed by many authors [23–28]. Erturk et al. [23] performed numerical calculations of the two-dimensional steady incompressible lid-driven cavity flow for Reynolds number up to 21,000 with an extremely small residual error of the steady solution, finding a fourth vortex at the bottom left corner and a third vortex at the top left corner as the Reynolds number was increased, and obtaining a solution free of spurious oscillations despite the high Reynolds number.

Erturk [24] studied in detail the two-dimensional lid-driven cavity flow considering all physical, mathematical and numerical aspects, concluding that physically this flow is not two-dimensional but three-dimensional above a certain Reynolds number when the two-dimensional solution becomes unstable to small three-dimensional perturbations. Thus, while numerical solutions for the planar lid-driven cavity flow for high Reynolds numbers can be obtained, this flow can be considered fictitious. One important point for obtaining a solution at high Reynolds number is that a sufficiently fine mesh is needed so as to rule out any spurious oscillatory solution provided by the numerical method that prevents reaching the steady-state solution.

Yapici et al. [25] managed to perform several simulations up to Reynolds number 65,000, obtaining a steady solution with two new vortices in the bottom left and right corners of the square cavity for Reynolds number larger than 25,000.

Erturk et al. [29] also studied the benchmark problem of a driven skewed cavity flow for skew angles of  $30^\circ$  and  $45^\circ$ . Using a very fine grid and highly accurate numerical solvers, they obtained numerical results for Reynolds number varying from 100 to 1000.

#### 4.1.2. Boundary and Initial Conditions

In dimensionless form, a unit horizontal velocity is imposed at the upper wall,  $u - 1 = v = 0$ , whereas the non-slip condition is imposed at the left, bottom and right walls,  $u = v = 0$ . As an initial condition, both components of the velocity are set to 0 in all the points of the domain, except at the upper wall (lid) where the horizontal component is set to 1. The pressure is arbitrarily set to zero,  $p = 0$ , at the lower-left corner of the cavity.

#### 4.1.3. Convergence Analysis

In this section, we study the influence of the mesh in the numerical solution, which includes analyzing the influence of the mesh space discretization and cell size in the convergence of the solution. The method for estimating the convergence order of an algorithm requires to obtain a solution for different meshes with different element sizes. The meshes used for the convergence analysis are three uniform (i.e., equispaced) meshes using TRIA elements for the discretization of the domain with (mesh #1)  $20 \times 20$ , (mesh #2)  $50 \times 50$  and (mesh #3)  $100 \times 100$  points, respectively. The coarser mesh is shown in Figure 2 for illustrative purposes.

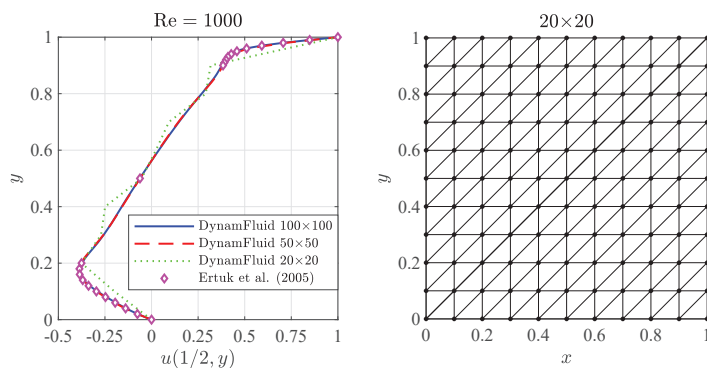


**Figure 2.** Convergence analysis for the horizontal velocity along the vertical mid line corresponding to  $Re = 1000$  (left) and triangular elements (TRIA)  $20 \times 20$  element mesh used in the computations with DynamFluid (right). The  $50 \times 50$  and  $100 \times 100$  meshes are finer meshes with the same topology.

The boundary conditions are applied to the mesh assuming the ramp condition: the velocity in the top of the cavity (moving lid) grows from zero in the corners of the cavity (left and right) until the non-dimensional value in the span of a cell/element. Alternatively, other researchers use the leaking lid formulation, where the velocity in the top lid is constant and equal to the imposed velocity and zero in the rest of the walls.

The Reynolds number used for showing the influence of the mesh element size in the accuracy of the solution is  $Re = 1000$ . The variable chosen for the convergence analysis is the horizontal velocity component  $u$  along the vertical line that goes through the center of the cavity. The steady-state solution is obtained by means of a transient simulation. It is assumed that the steady-state is reached when the relative value of the horizontal velocity in two successive time steps differ less than  $10^{-9}$ , that is,  $\sum_{k=1}^N |u_k^{n+1} - u_k^n| / |u_k^n| \leq 10^{-9}$ , the sum going through all  $N$  nodes in the mesh for the horizontal

velocity component. Figure 2 shows that as the mesh is refined the solution tends to that obtained by Erturk et al. [23]. There is no appreciable difference between the results obtained with the  $50 \times 50$  point and  $100 \times 100$  point meshes.

For a TRIA element mesh composed by two-dimensional elements, as the one shown in Figure 3, an equivalent length for node  $k$  can be defined according to  $h_k = \min(2A_j/l_j)$ , where  $j$  spans from 1 to the number of adjacent elements connected to node  $k$ ,  $A_j$  is the area of the  $j$ -th element adjacent to node  $k$ , and  $l_j$  is the length of the opposite edge belonging to the  $j$ -th element adjacent to node  $k$  [71].

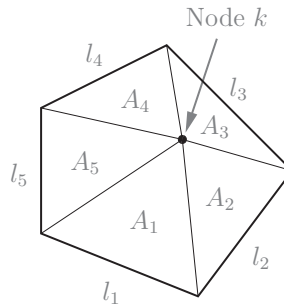


**Figure 3.** Two-dimensional finite elements adjacent to node  $k$  used to compute the equivalent element size  $h_k = \min(2A_j/l_j)$ .

The convergence order of the algorithm has been estimated using the well-known grid convergence index calculation. Following Roache [72], the order of convergence for the algorithm is obtained solving the following equations iteratively for the three different meshes, starting from the coarse mesh #1 ( $20 \times 20$ ) to the more refined mesh #3 ( $100 \times 100$ )

$$p = \frac{|\ln |Er_{32}/Er_{21}| + q(p)|}{\ln r_{21}} \tag{30}$$

$$q(p) = \ln \left( \frac{r_{21}^p - s}{r_{32}^p - s} \right) \tag{31}$$

$$s = \text{sign}(Er_{32}/Er_{21}), \tag{32}$$

where  $Er_{ij} = u_i - u_j$  and  $r_{ij} = h_i/h_j$ , with  $u_i$  the horizontal velocity at mesh  $i$  and  $u_j$  the horizontal velocity at mesh  $j$ , and  $h_i$  the equivalent length for mesh  $i$  and  $h_j$  the equivalent length for mesh  $j$ . This is translated into  $Er_{32}$  being the difference in the estimating function between mesh #3 ( $100 \times 100$ ) and mesh #2 ( $50 \times 50$ ), and  $Er_{21}$  between mesh #2 ( $50 \times 50$ ) and mesh #1 ( $20 \times 20$ ). Similarly,  $r_{32}$  is the mesh ratio between mesh #3 and mesh #2, and  $r_{21}$  between mesh #2 and mesh #1.

The iterative process starts with an initial guess for  $q(p)$ , e.g.,  $q(p) = 0$  in this case. Using the value of  $q$  at a given iteration step, the value of  $p$  is calculated at the next iteration step. After a few iterations, the convergence order  $p$  is obtained. Table 1 shows the maximum norm of the error  $Er_{L_\infty} = \max|u_i - u_j|$  ( $p = 2.71$ ), and the mean norm of the error  $Er_{L_1} = (1/N) \sum_{i=1}^N |u_i - u_j|$  ( $p = 1.98$ ) for the implementation of the CBS algorithm discussed here applied to the lid-driven cavity flow.

**Table 1.** Mean and max error for the horizontal velocity.

Grid Comparison	$Er_{L_1}$	$Er_{L_\infty}$	$r_{ij}$
$50 \times 50$ vs. $20 \times 20$	0.00176	0.00748	2.0
$100 \times 100$ vs. $50 \times 50$	0.0138	0.0969	2.5

#### 4.1.4. Results for Re up to 10,000

Figure 4 compares numerical integrations of the lid-driven cavity flow carried out with DynamFluid with those obtained by Erturk [24] and Ghia et al. [26] for Reynolds number up to 10,000. Erturk et al. [23] reported that a  $257 \times 257$  mesh is needed in order to get a steady solution for Reynolds number up to 10,000, thus a refined mesh of  $257 \times 257$  elements was used for the simulations. As it can be seen, the agreement with previous results is excellent for  $Re \leq 10,000$ , showing a slightly better agreement at low Reynolds number than at high Reynolds number.

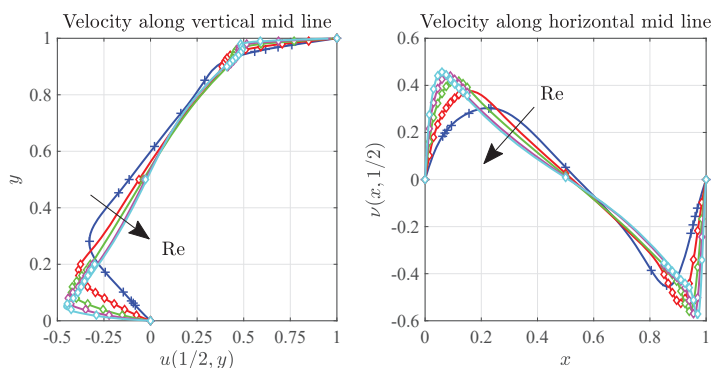


**Figure 4.** Horizontal velocity along the vertical mid line (left) and vertical velocity along the horizontal mid line (right) as predicted by DynamFluid (solid lines) and reported by Erturk [24] ( $\diamond$ ) and Ghia et al. [26] (+) for  $Re = \{400, 1000, 25,000, 5000, 10,000\}$ .

#### 4.2. Mixed Convection Flow in a Vertical Channel with Asymmetric Wall Temperatures

This is a mixed convection heat transfer problem in which an initially uniform flow develops in a slender vertical channel whose walls are at different temperatures. The flow is assumed to be two dimensional. The cold wall temperature,  $T_c$ , and hot wall temperature,  $T_h$  ( $\equiv T_w$ ), are also different from the incoming flow temperature,  $T_\infty$ , as illustrated in Figure 5. The parameters characterizing the flow are the channel width  $H$  ( $\equiv L_\infty$ ) and length  $L \gg H$ , the cold and hot wall temperature differences,  $T_c - T_\infty$  and  $T_h - T_\infty$ , and the uniform velocity of the fluid entering the rectangular channel,  $U$  ( $\equiv U_\infty$ ). Additional parameters include the density,  $\rho$  ( $\equiv \rho_\infty$ ), viscosity,  $\mu$  ( $\equiv \mu_\infty$ ), and thermal conductivity,  $k$  ( $\equiv k_\infty$ ), of the fluid. The non-dimensional numbers that emerge in this problem are the Reynolds number,  $Re = UH/\nu$ , based on the inlet velocity and the channel width, the Grashof number,  $Gr = g\beta(T_h - T_\infty)H^3/\nu^2$ , defined in terms of the channel width and the hot wall temperature difference, and the wall temperature difference ratio  $\Theta_c = (T_c - T_\infty)/(T_h - T_\infty)$ . The Prandtl number is assumed to be constant,  $Pr = 0.72$ . As shown in Figure 5, the acceleration of gravity is assumed to point opposite to the direction of the incoming flow. When the height of the channel is large compared to the channel width, the flow becomes fully developed far downstream, where the streamlines are parallel to each other and point vertically upwards.

##### 4.2.1. Literature Review

The mixed convection flow in a vertical channel has been investigated by several authors. In a series of papers, Aung and Worku [30–32] studied the effects of buoyancy on the laminar vertical upward flow between parallel plates subject to two types of boundary conditions: (i) uniform wall temperatures, where the vertical walls may be at equal or different temperatures, and (ii) uniform heat fluxes, where the vertical walls may be subject to the same or different heat fluxes. They used the boundary layer approximation for their analysis when the dimensionless buoyancy parameter becomes  $Gr/Re$  instead of  $Gr/Re^2$ . As a result, the controlling parameters are  $Gr/Re$ , the wall temperature difference ratio  $\Theta_c$ , and the Prandtl number,  $Pr = 0.72$ , assumed to be constant. Aung and Worku [30]

considered a set of values of  $Gr/Re$  in the range 0, 25, 50, 100 and 250, founding that buoyancy extends the hydrodynamic entry length whereas it reduces the thermal entry length. As a general rule, no flow reversal was observed for sufficiently small values of  $Gr/Re$ , while it appeared for small values of  $\Theta_c$  and large values of  $Gr/Re$  (the larger value of  $Gr/Re$ , the larger the downwards velocity in the flow reversal region). Aung and Worku [31] predicted that with constant heat fluxes the ratio  $Gr/Re$  for flow reversal to happen is higher than with constant wall temperatures. In particular, for values of  $Gr/Re$  up to 500 no flow reversal was observed when uniform heat flux boundary conditions are used. Flow reversal did not occur either for symmetrically heated walls. As part of their study, they developed an analytical theory [32] for fully developed mixed convection flow including flow reversal, obtaining analytical expressions for the velocity profile and the temperature profile that will be used below for validation purposes.

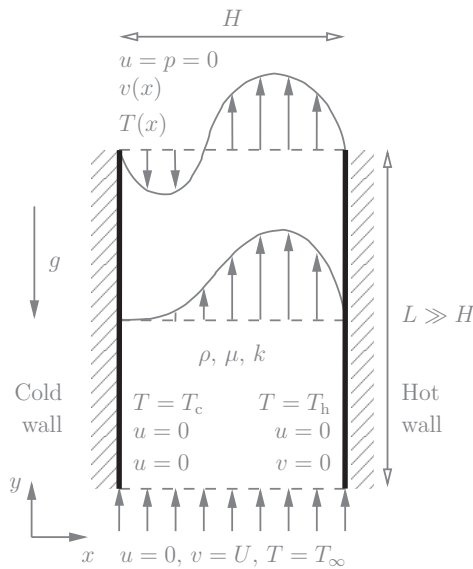


**Figure 5.** Schematic representation of the non-isothermal flow in a vertical channel with asymmetric wall temperatures showing the coordinate system, dimensional parameters, and boundary conditions.

Ingham et al. [40] found that infinite duct walls also bring about flow reversal in the vicinity of the cold wall, while Ingham et al. [41] obtained numerical solutions of the problem for a steady laminar mixed convection flow in a vertical duct with parallel plates. They compared this flow with the case of pure forced convection finding that large values of  $Gr/Re$  cause reverse flow in the channel (similar to Aung and Worku [30,32]). Kim et al. [43] used an implicit finite difference scheme to solve the governing equations in the conjugate heat transfer flow established between two vertical plates subject to asymmetric wall temperatures. They found that the independent parameters are the Grashof number, the Prandtl number, the solid to fluid thermal conductivity ratio, the wall thickness to channel width ratio, the channel height to channel width ratio and the asymmetric heating parameter.

Gau et al. [38] studied experimentally the heat transfer process in a vertical channel comprised of two parallel plates (one heated uniformly and the opposite wall insulated), having a very large buoyancy parameter  $Gr/Re^2$ . From flow visualizations, they concluded that the reversal of the flow happened to be a V-shaped recirculating flow near the channel exit when  $Gr/Re^2$  is greater than a critical value, although the reversal occurs initially downstream, but advances gradually downwards when  $Gr/Re^2$  increases. El-Din [37], studied the flow development between two vertical plates with uniform heat and mass fluxes studying the effect of the thermal and mass transfer buoyancies.

Cheng et al. [36] also studied this type of flow taking into account different boundary conditions (walls with constant temperature or with constant heat flux). Hamadah and Wirtz [39] investigated the effect of thermal buoyancy opposing the flow between two vertical plates with different boundary conditions (uniform asymmetric temperatures, uniform asymmetric heat fluxes, and the case of one wall at a uniform temperature and the other with uniform heat flux). Boulama and Galanis [35] provided analytical solutions for the fully-developed steady-state mixed convection flow past two vertical plates at constant temperatures and at constant heat flux (the two walls with the same type of boundary conditions or one with uniform temperature and the other with uniform heat flux).

Barletta et al. [34] studied the problem of a fully developed mixed convection flow with frictional heat generation in a vertical channel bounded by isothermal plane walls having the same temperature. Barletta [33] carried out an study of a laminar and fully developed flow with mixed convection in a rectangular and vertical duct where at least one of the two walls was isothermal, providing an analytical solution for the velocity and temperature fields. Desrayaud and Lauriat [73] investigated the flow reversal phenomena in a vertical channel with two parallel plates at symmetrically uniform heated walls when air is used as the fluid, for a laminar, mixed-convection flow with Reynolds number in the range  $300 \leq Re \leq 1300$ . The velocity and temperature profiles caused by the buoyancy forces were analyzed. Finally, Jeng et al. [42] investigated the mixed convection flow in a vertical channel with parallel walls at different temperatures:  $\Theta_c$  was in the range of  $0 \leq \Theta_c \leq 1$ , the Reynolds number was in the range of  $1 \leq Re \leq 1000$ , and the ratio  $Gr/Re$  in the range of  $0 \leq Gr/Re \leq 500$ . They found that when the streamwise coordinate was scaled out using the Reynolds number, the velocity and the temperature profile were independent of the Reynolds number for  $Re \geq 50$ .

#### 4.2.2. Boundary and Initial Conditions

In the simulations presented below, the right wall is assumed to be at a higher temperature than the left wall,  $T_h > T_c$ . Two cases are considered in the study. In the first one the cold wall is at the same temperature than the incoming fluid,  $T_c = T_\infty$ , or  $\Theta_c = 0$ , and in the second case the cold wall is at a temperature halfway between the incoming fluid and the hot wall,  $T_c - T_\infty = 0.5(T_h - T_\infty)$ , or  $\Theta_c = 0.5$ . The dimensionless boundary condition for the velocity, pressure and normalized temperature are

- Left, cold non-slip wall:  $u = v = \Theta - \Theta_c = 0$ .
- Right, hot non-slip wall:  $u = v = \Theta - 1 = 0$ .
- Bottom side, incoming flow:  $u = v - 1 = \Theta = 0$ .
- Top side, outgoing flow:  $p = u = \partial v / \partial y = \partial \theta / \partial y = 0$ .

Since the channel width is taken as length scale, the dimensionless width of the channel is one. By contrast, the dimensionless length of the channel is set to  $H/L = 80 \gg 1$ , which is long enough to ensure that the flow is fully developed in the outflow boundary (see Figure 5 for details; note that the height and width are not to scale).

#### 4.2.3. Discussion of Results

As previously discussed, Aung and Worku [32] obtained analytical expressions for the velocity profile and the temperature profile in the fully developed mixed convection flow established far downstream the channel, namely

$$\left. \begin{aligned} v(x) &= \frac{Gr}{Re} (1 - \Theta_c) \left( -\frac{x^3}{6} + \frac{x^2}{4} - \frac{x}{12} \right) - 6x^2 + 6x \\ \Theta(x) &= x \end{aligned} \right\} 0 < x < 1 \quad (33)$$



the later corresponding to a linear temperature profile (i.e., a purely conductive heat flux) between the hot and cold walls. It is interesting to note that the analytical problem solved by Aung and Worku [30–32] included a simplified form of the energy equation that accounted only for thermal energy convection and heat conduction. As a consequence, the numerical results obtained with DynamFluid, which incorporates the general form of the energy Equation (10) or (13), can not be expected to match exactly the fully developed profiles given above.

Figure 6 shows the comparison between the fully developed profiles (33) with the numerical profiles predicted by DynamFluid in the outflow boundary corresponding to  $Re = 100$ ,  $Gr = 25,000$ , and two values of  $\Theta_c = \{0, 0.5\}$ . In both cases the flow reversed near the cold wall ( $x = 0$ ) with higher downward velocities for  $\Theta_c = 0$ , and the temperature profiles are very close to linear. The minor differences observed between the numerical and analytical predictions can be attributed to the differences in the treatment of the energy equation. In summary, the figure shows an excellent agreement between the numerical profiles and the analytical solution for both values of  $\Theta_c$ . This indicates that DynamFluid is able to predict accurately the velocity and temperature profiles in mixed convection problems under different conditions.

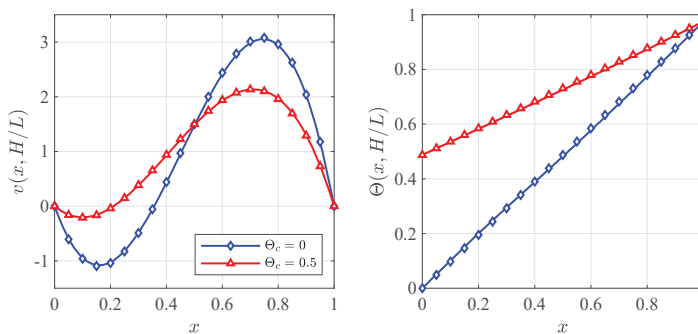


**Figure 6.** Comparison between the fully developed velocity (left) and temperature (right) profiles as predicted by DynamFluid (solid lines) and by the fully developed theory of Aung and Worku [32] (symbols) corresponding to  $Re = 100$ ,  $Gr = 25,000$ , and  $\Theta_c = \{0, 0.5\}$ .

#### 4.3. Isothermal Flow Past a Circular Cylinder

The flow past a circular cylinder is the prototypical benchmark case for the validation of external flows: either steady (the flow does not vary with time) or unsteady (the flow varies with time exhibiting either a transient or oscillatory behavior). Figure 7 shows a schematic representation of the flow: a circular cylinder of diameter  $D$  ( $\equiv L_\infty$ ) surrounded by an unbounded fluid of density  $\rho$  ( $\equiv \rho_\infty$ ) and viscosity  $\mu$  ( $\equiv \mu_\infty$ ) with an uniform incoming velocity  $U$  ( $\equiv U_\infty$ ). In the non-isothermal flow past a circular cylinder, to be considered in the next section, the cylinder is assumed to be at a uniform temperature  $T_w$  different from that of the incoming stream  $T_\infty$ . In both cases, the only non-dimensional parameter that appears in the limit of non-buoyant flows ( $Ri = Gr/Re^2 \rightarrow 0$ ) to be considered here is the Reynolds number,  $Re = UD/\nu$ , based on the incoming flow velocity, the diameter of the cylinder, and the kinematic viscosity of the fluid.

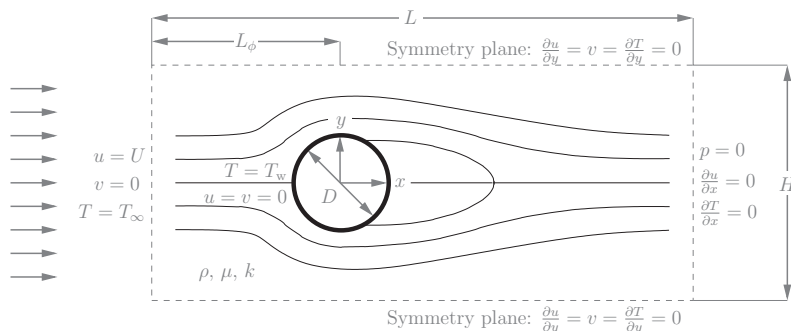


**Figure 7.** Schematic representation of the flow past a circular cylinder showing the coordinate system, dimensional parameters, and boundary conditions. The size of the computational domain is determined by the parameters  $L$ ,  $L_\phi$  and  $H$ .

#### 4.3.1. Literature Review

The flow past a non-heated circular cylinder at moderate Reynolds numbers exhibits flow separation and vortex shedding and has been studied numerically by many authors. De Sampaio et al. [56] obtained the solution of the incompressible Navier-Stokes equations with a Petrov-Galerkin method using an adaptive remeshing strategy applied to transient viscous flows. Ding et al. [54] used a mesh-free least square-based finite difference method to study the steady and unsteady viscous flow past a circular cylinder up to  $Re = 200$ . Park et al. [55] computed several flow properties such as the Strouhal number, the drag and lift coefficients, the pressure and vorticity distributions, the separation angle and the bubble separation length as a function of the Reynolds number up to  $Re = 160$ .

Nithiarasu [74] used the CBS algorithm in its fully explicit form and with artificial compressibility to predict the flow past a circular cylinder for a wide range of Reynolds numbers. Massarotti et al. [75] performed a comparison between the explicit and semi-implicit form of the CBS algorithm using benchmark test cases for both steady and unsteady flows, founding only slightly differences between both schemes for transient flows and identical results for steady flows. They concluded that the fully explicit version of the algorithm was an interesting option. Selvam [76] used an implicit CBS scheme with large eddy simulation in a 2D domain to compute the Strouhal number for high Reynolds numbers  $Re = \{10^4, 10^5, 5 \times 10^5, 10^6\}$  and compared his results with the available experimental and numerical data. He reported that the measured reduction in the drag coefficient with the Reynolds number was not appropriately captured numerically and needed to be double-checked using a 3D model.

Qu et al. [77] performed several simulations using a FVM-based code for a wide range of Reynolds numbers ( $Re = 50\text{--}200$ ) and studied the effect of the blockage ratio and the grid density in the vicinity of the cylinder wall, concluding that at lower Reynolds numbers the simulation requires a more uniform grid whereas at higher Reynolds number a finer grid near the vicinity of the cylinder wall is needed to resolve the thin viscous boundary layer that develops around the cylinder and eventually separates from it. Subhankar et al. [57] studied the critical Reynolds number that first causes flow separation from the cylinder wall, founding that for non-confined flows the value is  $Re = 6.29$ . Other authors that have addresses this problem include Sahin and Owens [78], Posdziech and Grundmann [79], Mittal and Raghuvanshi [80], Mittal and Kumar [81], Kieft et al. [82], and Jordan and Ragab [83].

#### 4.3.2. Computational Domain, Boundary and Initial Conditions and Mesh Generation

The domain used for the simulations is shown in Figure 7. The cylinder is located a distance  $L_\phi$  from the inlet. The total length in the streamwise direction,  $L > L_\phi$ , must be large enough so that the perturbations introduced by the cylinder become sufficiently small at the right limit of the domain for an outflow boundary condition to be used. In the simulations, the domain had a dimensionless

size of  $L/D = 64$  with  $L_\phi/D = 16$ . Behr et al. [84] studied the influence of the distance of the lateral boundaries on the computation of two-dimensional unsteady incompressible flow past a circular cylinder. They concluded that the distance between the center of the cylinder and the lateral boundaries has a significant effect on the Strouhal number and other flow properties. In particular, they found that the minimum distance at which this influence vanishes for  $Re = 100$  is 32 cylinder diameters. For this reason, in our simulations we chose also  $H/D = 64$  in order to rule out any influence of the boundary conditions in the solution obtained. The Reynolds numbers chosen for the validation campaign are 100 [56,85,86] and 200 [54,77], so that the lateral boundaries are expected not to perturb the results in either case.

The boundary conditions are schematized in dimensional form in Figure 7 for non-isothermal flow past a circular cylinder at uniform temperature, to be considered in the next section. For the isothermal flow considered here, the dimensionless boundary condition for the velocity and pressure are

- Left boundary, uniform incoming flow:  $u - 1 = v = 0$ .
- Right boundary, outflow boundary condition:  $p = \partial u / \partial x = v = 0$ .
- Top and bottom boundaries, symmetry boundary condition:  $\partial u / \partial y = v = 0$ .
- Cylinder wall, non-slip condition:  $u = v = 0$ .

As initial condition, the components of the velocity are set to 0 in all the points of the domain, except at the inflow boundary, where  $u$  is set to 1. The non-dimensional vertical velocity component  $v$  is set to 0 everywhere.

The strategy followed for the generation of the mesh was to use small elements in the vicinity of the cylinder and in the cylinder wake, whereas a coarser mesh was used in the rest of the domain, with the size of the elements varying gradually from the finest to the coarser regions as shown schematically in Figure 8. Several grids have been tested, from coarse to fine grids. The final grid used for the computations did not provide significantly different results than the previous coarser grid, but it was selected in order to get better estimates. In the final grid, the number of nodes was 77,011 and the number of TRIA elements was 153 318. Being  $D$  the cylinder diameter, the mesh size in the vicinity of the cylinder up to a concentric cylinder of diameter  $1.1D$  was  $0.01D$ . The mesh size in the vicinity of the previous inner cylinder up to a concentric cylinder of radius  $2D$  was less than  $0.05D$ . In a rectangular region with height  $2D$ , continuous to the outer concentric cylinder, the mesh size was less than  $0.05D$ . In the rest of the domain, the mesh size was less than  $0.5D$ .

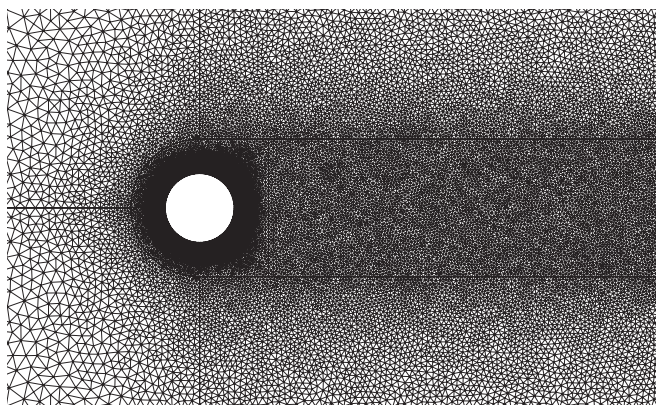
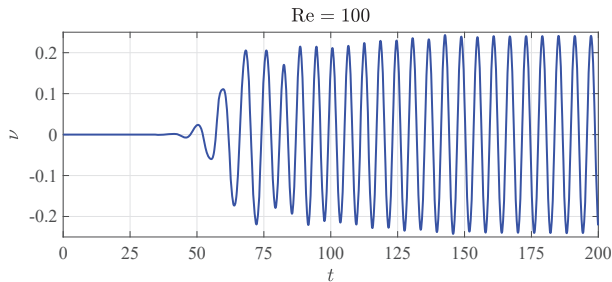


Figure 8. Close-up view of the mesh in the vicinity of the cylinder and in the wake.

#### 4.3.3. Discussion of Results

The flow past a circular cylinder is periodic for  $Re = 100$ . Figure 9 shows the long-term variation of the vertical velocity  $v$  in a point located at the wake of the cylinder just in the middle of the outflow

boundary ( $x = 64, y = 32$ ). As can be seen, after an initial transient the flow becomes periodic with a given frequency  $f$ . As can be seen in Figure 10, counter rotating eddies are shed periodically with period  $T = 1/f$ , giving rise to the well-known Karman vortex street in the cylinder wake.



**Figure 9.** Vertical velocity  $v$  in the mid plane far downstream the cylinder for  $Re = 100$ .

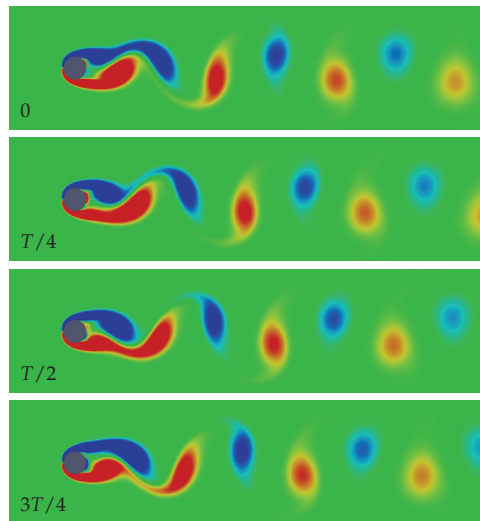


**Figure 10.** Vorticity field of the flow past a circular cylinder for  $Re = 100$  at four successive instants during the vortex shedding cycle.

Table 2 shows the variation of the Strouhal number ( $St = fD/U_\infty$ ) associated with the vortex shedding process corresponding to  $Re = 100$  and different blockage ratios ( $D/H$ ). For the smallest blockage ratio, the predicted Strouhal number perfectly matches that obtained by De Sampaio [56] (0.165), while it deviates only 0.01% from the value obtained by Ding et al. [54] and by Rahman et al. [85] (0.164). As the Reynolds number increases the influence of the blockage ratio becomes less important, hence the mesh with blockage ratio equal to  $1/64$  has been used in the computations presented below for both  $Re = 100$  and  $200$ . For  $Re = 200$  the computed Strouhal number is 0.1954, which deviates only  $-0.18\%$  from the value obtained by Qu et al. [77] (0.1958) and  $-0.3\%$  from the value obtained by Ding et al. [54] (0.196).

Table 3 compares the results obtained with DynamFluid with those of previous references. As can be seen, the Strouhal number obtained for the two Reynolds numbers considered in the study show very good agreement with the existing literature, which validates the performance of DynamFluid for the prediction of unsteady flows.

**Table 2.** Strouhal number as a function of the blockage ratio for  $Re = 100$ .

$D/H$	St
1/16	0.1792
1/32	0.1703
1/64	0.1650

**Table 3.** Comparison between the Strouhal number for  $Re = \{100, 200\}$  as predicted by DynamFluid and reported by previous authors.

Re	[56]	[77]	[86]	[85]	[54]	Present Work
100	0.165	0.1649	0.1569	0.164	0.164	0.165
200	—	0.1958	0.1957	—	0.196	0.1954

#### 4.4. Flow Past a Heated Circular Cylinder with Forced Convection

The non-isothermal flow past a heated circular cylinder is similar to that past a non-heated cylinder with the particularity that the temperature of the cylinder,  $T_w$ , is now different from the temperature of the bulk fluid,  $T_\infty$ . In the presence of buoyancy forces, the temperature variations that cause the flow to exhibit additional features due to the effects of aiding or opposing buoyancy, but for simplicity attention will be restricted here to the case where the effects of buoyancy can be neglected. As the main difference with the mixed convection problem in a vertical channel, the Prandtl number is assumed here to be  $Pr = 0.71$  (instead of 0.72) in order to match the value used in previous works used here for validation.

##### 4.4.1. Literature Review

Flow and heat transfer in forced convection past a circular cylinder has been studied by Apelt and Ledwith [87], Dennis et al. [46] and Rashid and Ahmad [88] up to  $Re = 40$ . Bitwas et al. [58] showed that in the absence of thermal buoyancy, the separation angle and the length of the recirculation bubble increase with the Reynolds number. They also showed that the average Nusselt number increases with increasing Reynolds number and the predicted results were in accordance with well-known experimental observations. Badr [89] studied numerically the influence of the flow direction, vertically upwards (parallel flow) vs. vertically downwards (opposing flow), accounting for buoyancy effects.

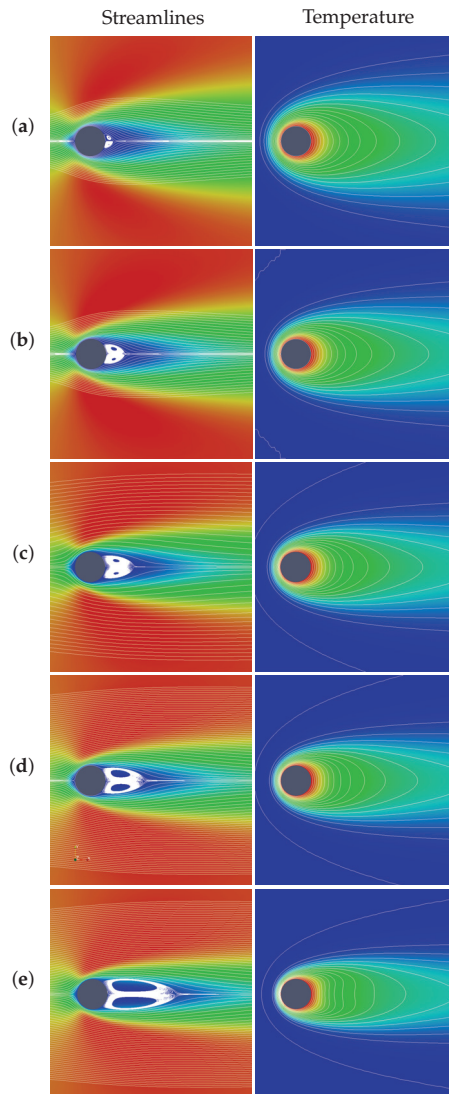
##### 4.4.2. Computational Domain and Boundary Conditions

The computational domain used for the simulations is similar to that used in previous section, but in this case the length of the domain was reduced to  $L/D = 25$  cylinder diameters, and the height of the domain was reduced to  $H/D = 20$  cylinder diameters, which gives a blockage ratio of 0.05. The center of the cylinder is located at  $L_\phi/D = 10$  diameters from the inlet. As a result, the outflow boundary is located 15 diameters downstream the center of the cylinder. The boundary conditions imposed to the velocity and pressure fields are the same as in the previous section, with additional Dirichlet boundary conditions for the temperature ( $\Theta = 0$ ) at the inlet and at the cylinder wall ( $\Theta = 1$ ), zero heat flux boundary conditions at the upper and lower boundaries ( $\partial\Theta/\partial y = 0$ ) as well as the outflow boundary ( $\partial\Theta/\partial x = 0$ ).

##### 4.4.3. Discussion of Results

Several simulations were carried out for increasing Reynolds numbers ranging from  $Re = 10$  to 40 in the limit of non-buoyant flows ( $Ri = Gr/Re^2 \rightarrow 0$ ). Figure 11 shows the steady-state solution reached in each simulation, including the streamlines and temperature contours obtained for the different Reynolds numbers under study. As previously reported by Williamson [90], for low Reynolds numbers ( $Re < 49$ ) a vertically symmetric steady wake is formed with the structure shown schematically in Figure 12. The nomenclature used to describe the flow behind the cylinder is:  $A$  is the front stagnation point,  $B$  the rear stagnation point,  $C$  the stagnation point in the cylinder wake,  $E$  and  $F$  the upper and lower

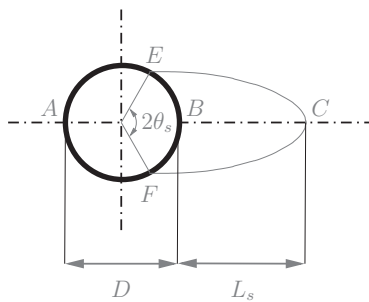
separation points,  $L_s$  the eddy length of the recirculation region  $E-C-F-B-E$  and  $\phi_s$  the angle with respect to the horizontal line where the fluid detaches from the cylinder. The plots in the left panels of Figure 11 show a perfect symmetry with respect to the horizontal mid-line which passes through the center of the cylinder as previously reported by Williamson [90]. The temperature gradient at the front stagnation point, the eddy length, and the separation angle all increase monotonically with the Reynolds number. For reference purposes, Table 4 shows the variation with the Reynolds number of the non-dimensional eddy length and the separation angle. Note that the eddy length is made non-dimensional with the cylinder radius ( $D/2$ ) to be consistent with previous references, and that the angles are measured from the rear stagnation point. As can be seen, the results obtained with DynamFluid show excellent agreement with the values obtained by other authors [44,54,58,59] for all Reynolds numbers under study.



**Figure 11.** Streamlines and temperature contours of the steady state solution for several Reynolds numbers and  $Ri = 0$ : (a)  $Re = 10$ , (b)  $Re = 15$ , (c)  $Re = 20$ , (d)  $Re = 25$ , and (e)  $Re = 40$ . The color map in the left plots represents the modulus of the velocity vector.

**Table 4.** Comparison between the eddy length ( $L_s$ ) and the separation angle ( $\theta_s$ ) for several Reynolds numbers as predicted by DynamFluid and reported by previous authors.

Variable	Re	[44]	[59]	[58]	[54]	[55]	DynamFluid
$2L_s/D$	10	0.504	0.498	0.52	0.504	0.51	0.512
	15	—	1.162	1.189	—	—	1.227
	20	1.88	1.844	1.865	1.86	1.87	1.866
	25	—	—	2.517	—	—	2.548
	40	4.69	4.65	4.424	4.4	4.59	4.480
Variable	Re	[44]	[59]	[58]	[54]	[55]	DynamFluid
$\theta_s$ (°)	10	29.6	29.3	29.12	30.0	—	28.57
	15	—	38.6	38.57	—	—	38.57
	20	43.7	43.65	43.64	44.1	—	43.58
	25	—	—	46.89	—	—	47.14
	40	53.8	53.55	53.1	53.5	—	51.43

**Figure 12.** Schematic description of the recirculation region showing the dimensionless eddy length ( $L_s$ ) and the separation angle ( $\theta_s$ ).

The local heat lost from the cylinder by heat conduction to the fluid is given by the local Nusselt number

$$\text{Nu} = -\frac{\partial \Theta}{\partial n}, \quad (34)$$

where  $n$  denotes the outward normal to the cylinder surface. The local value of Nu along the cylinder surface was computed and compared with previous results taken from the literature [46,58,89], as can be seen in Figure 13. The Nusselt number computed with DynamFluid shows good agreement with the results by Biswas et al. [58] for all Reynolds number under study, showing also good agreement in the rear stagnation point with other authors [46,89]. However, it deviates slightly in the front stagnation point from the value computed by Bard [89] and Dennis et al. [46]. The results shown in Figure 13 indicate that Badr [89] overestimated the value of the Nusselt number in the range  $\text{Re} = 20\text{--}40$ , while Dennis et al. [46] overestimated the value of the Nusselt number in the range  $\text{Re} = 10\text{--}40$ . Note that the works by Dennis et al. [46] and Bard [89] were published in 1968 and 1984, when the precision of numerical computations was still far from that of today. These results indicate that DynamFluid is able to reproduce with good agreement results of forced convection heat transfer problems, particularly those published more recently, exhibiting only local small variations that can be attributed to the imprecision of the numerical results reported decades ago.

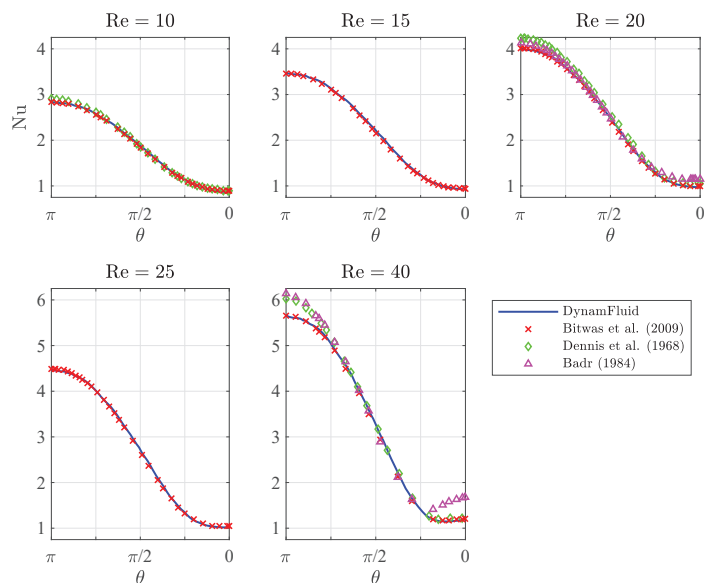


**Figure 13.** Variation of the local Nusselt number on the surface of the cylinder at different Reynolds number as predicted by DynamFluid (solid lines) and by previous authors.

## 5. Conclusions

A new CFD software tool (DynamFluid) based on the finite element method and the characteristic-based-split algorithm has been presented and validated against four benchmark constant-density and Boussinesq-type non-isothermal two-dimensional flows, showing excellent agreement with previous results taken from the literature. The test cases have comprised both stationary problems, such as the lid-driven cavity flow, mixed convection in a vertical channel, or flow past a heated circular cylinder at low Reynolds numbers, as well as unsteady problems, such as isothermal flow past a circular cylinder at moderate Reynolds numbers, covering a wide range of Reynolds, Grashof and Richardson numbers. The results provide the prospect users high confidence for the application of this software to other 2D fluid dynamic problems of interest, particularly those involving isothermal and non-isothermal incompressible flows under the Boussinesq approximation. In the near future, DynamFluid is expected to cover a broader scope of flow regimes, including fully compressible three-dimensional flows, non-constant density flows, and general non-isothermal flows.

**Author Contributions:** Conceptualization, H.R. and M.V.; data curation, H.R.; formal analysis, H.R., J.C. and M.V.; funding acquisition, M.V.; investigation, H.R. and M.V.; methodology, H.R. and M.V.; project administration, H.R., J.C. and M.V.; resources, H.R., P.A.G.-S. and M.V.; software, H.R. and J.C.; supervision, J.C. and M.V.; validation, H.R., P.A.G.-S. and M.V.; visualization, H.R., P.A.G.-S. and M.V.; writing—original draft, H.R. and M.V.; writing—review & editing, J.C., P.A.G.-S. and M.V.

**Funding:** This research was funded by FEDER/Ministerio de Ciencia, Innovación y Universidades grant numbers ENE2015-68703-C2-1-R and RTC-2017-5955-3.

**Conflicts of Interest:** The authors declare no conflict of interest.

## Nomenclature

$a$	Speed of sound
$B$	Blockage ratio ( $D/H$ )
$c_p$	Specific heat at constant pressure
$c_v$	Specific heat at constant volume
$D$	Cylinder diameter



$e$	Internal energy per unit mass, $e = c_v T$
$e_T$	Total energy per unit mass, $e_T = e + u_i u_i / 2$
$\bar{E}$	Energy tensor containing the values of $\rho e_T$ in every node of the mesh
$Er_{ij}$	Difference in the estimating function between mesh # $i$ and mesh # $j$
$f$	Frequency
$g$	Acceleration of gravity
Gr	Grashof number
$h$	element size
$H$	Characteristic height of the problem
$I_{ij}$	Identity tensor
$k$	Thermal conductivity
$L$	Characteristic length of the problem
$L_\phi$	Distance from the inlet to the center of the cylinder
$L_s$	Eddy length
$n$	outward normal coordinate
$\mathbf{N}$	Shape functions
Nu	Local Nusselt number
$p$	Pressure
$\bar{p}$	Pressure tensor containing the values of $p$ in every node of the mesh
Pr	Prandtl number, $\nu / \alpha$
Re	Reynolds number
Ri	Richardson number, $Gr / Re^2$
St	Strouhal number
$t$	Time
$\tilde{t}_i$	$i$ -th component of the prescribed stress
$T$	Temperature
$\tilde{T}$	Prescribed Temperature
$\bar{T}$	Temperature tensor containing the values of $T$ in every node of the mesh
$\widetilde{\nabla T}_i$	$i$ -th component of the prescribed temperature gradient
$u_i$	$i$ -th component of the velocity vector, $(u, v, w)^T$
$\bar{u}_i$	Velocity tensor containing the $i$ -th component of the velocity vector in every node of the mesh
$\tilde{u}_i$	$i$ -th component of the prescribed velocity
$x_i$	$i$ -th Cartesian coordinate, $(x, y, z)^T$

### Greek letters

$\alpha$	Thermal diffusivity, $k / (\rho c_p)$
$\beta$	Thermal expansion coefficient, $-\rho^{-1}(\partial \rho / \partial T)_p$
$\mu$	Dynamic viscosity
$\phi$	Variable to approximate using the finite element method
$\phi_s$	Angle of detachment
$\rho$	Density
$\nu$	Kinematic viscosity, $\mu / \rho$
$\tau_{ij}$	deviatoric viscous stress tensor
$\theta_1$	velocity relaxation factor
$\theta_2$	pressure relaxation factor
$\Theta_c$	the wall temperature difference ratio, $(T_c - T_\infty) / (T_h - T_\infty)$
$\mathbb{T}_h$	unstructured triangulation composed by non-overlapping elements

### Subscripts

$c$	Cold boundary
-----	---------------

$h$	Hot boundary
$w$	Wall
$\infty$	Reference value

## References

1. Batchelor, C.K. *An Introduction to Fluid Dynamics*; Cambridge University Press: Cambridge, UK, 2000; ISBN 0-521-66396-2.
2. Van Dyke, M. *An Album of Fluid Motion*; The Parabolic Press: Stanford, CA, USA, 1982; ISBN 978-0915760022.
3. Barenblatt, G.I. *Dimensional Analysis*; CRC Press: Amsterdam, The Netherlands, 1987; ISBN 3-7186-0438-8.
4. Bridgman, P.W. *Dimensional Analysis*; Yale University Press: New Haven, CT, USA, 1922.
5. Anderson, J.D.; Wendt, J. *Computational Fluid Dynamics*; McGraw-Hill: New York, NY, USA, 1995; Volume 206.
6. Ferziger, J.H.; Peric, M. *Computational Methods for Fluid Dynamics*, 3rd ed.; Springer Science Business Media: New York, NY, USA, 2012; ISBN 978-540-42074-3.
7. Fletcher, C. *Computational Techniques for Fluid Dynamics 1. Fundamental and General Techniques*; Springer Science Business Media: New York, NY, USA, 1998; ISBN 978-3-642-97037-5.
8. Fletcher, C.A. *Computational Techniques for Fluid Dynamics 2: Specific Techniques for Different Flow Categories*; Springer Science Business Media: New York, NY, USA, 2012; ISBN 978-3-642-97073-3.
9. Pironneau, O. *Finite Element Methods for Fluids*; John Wiley & Sons: New York, NY, USA, 1989; ISBN 0-471-92255-2.
10. Versteeg, H.K.; Malalasekera, W. *An Introduction to Computational Fluid Dynamics: the Finite Volume Method*; Pearson Education: Harlow, UK, 2007; ISBN 978-0-13-127498-3.
11. ANSYS Fluent: 2019 ANSYS, Inc. Available online: <https://www.ansys.com/products/fluids/ansys-fluent> (accessed on 9 October 2019).
12. Star-CCM+: 2019 Siemens Product Lifecycle Management Software Inc., All Rights Reserved. Available online: <https://mdx.plm.automation.siemens.com/star-ccm-plus> (accessed on 9 October 2019).
13. COMSOL Multiphysics® v. 5.4. Available online: <https://www.comsol.com> (accessed on 9 October 2019).
14. Altair AcuSolve™ ©: 2019 Altair Engineering, Inc. Available online: <https://altairhyperworks.com/product/AcuSolve> (accessed on 9 October 2019).
15. Weller, H.G.; Tabor, G.; Jasak, H.; Fureby, C. A tensorial approach to computational continuum mechanics using object-oriented techniques. *Comput. Phys.* **1998**, *12*, 620–631. [CrossRef]
16. Jasak, H.; Jemcov, A.; Tukovic, Z. OpenFOAM: A C++ library for complex physics simulations. In Proceedings of the International Workshop on Coupled Methods in Numerical Dynamics, IUC, Dubrovnik, Croatia, 19–21 September 2007.
17. OpenFOAM: OpenCFD Ltd (ESI Group). Available online: <https://www.openfoam.com> (accessed on 9 October 2019).
18. Hecht, F. New development in FreeFem++. *J. Numer. Math.* **2012**, *20*, 251–266. [CrossRef]
19. Alnaes, M.S.; Blechta, J.; Hake, J.; Johansson, A.; Kehlet, B.; Logg, A.; Richardson, C.; Ring, J.; Rognes, M.E.; Wells, G.N. The FEniCS Project Version 1.5. *Arch. Numer. Soft.* **2015**, *3*, 9–23. [CrossRef]
20. Ahrens, J.; Geveci, B.; Law, C. ParaView: An End-User Tool for Large-Data Visualization. In *The Visualization Handbook*; Hansen, C.D., Johnson, C.R., Eds.; Elsevier Butterworth-Heinemann: Amsterdam, The Netherlands, 2005; pp. 717–731. ISBN: 978-0-12-387582-2.
21. Eigen: GNU Free Documentation License 1.2. Available online: <http://eigen.tuxfamily.org> (accessed on 9 October 2019).
22. AbdelMigid, T.A.; Saqr, K.M.; Kotb, M.A.; Aboelfarag, A.A. Revisiting the lid-driven cavity flow problem: Review and new steady state benchmarking results using GPU accelerated code. *Alex. Eng. J.* **2017**, *56*, 123–135. [CrossRef]
23. Erturk, E.; Corke, T.C.; Gökçöl, C. Numerical solutions of 2D steady incompressible driven cavity flow at high Reynolds numbers. *Int. J. Numer. Methods Fluids* **2005**, *48*, 747–774. [CrossRef]
24. Erturk, E. Discussions on driven cavity flow. *Int. J. Numer. Methods Fluids* **2009**, *60*, 275–294. [CrossRef]
25. Yapici, K.; Uludag, Y. Finite volume simulation of 2-D steady square lid-driven cavity flow at high Reynolds numbers. *Braz. J. Chem. Eng.* **2013**, *30*, 923–937. [CrossRef]

26. Ghia, U.; Ghia, K.N.; Shin, C.T. High-Re Solutions for incompressible flow using the Navier-Stokes equations and a multigrid method. *J. Comput. Phys.* **1982**, *48*, 387–411. [CrossRef]
27. Marchi, C.H.; Suero, R.; Araki, L.K. The lid-driven square cavity flow: Numerical solution with a 1024 x 1024 grid. *J. Braz. Soc. Mech. Sci.* **2009**, *31*, 186–198. [CrossRef]
28. Zhen-Hua, C.; Bao-Chang, S.; Lin, Z. Simulating high Reynolds number flow in two-dimensional lid-driven cavity by multi-relaxation-time lattice Boltzmann method. *Chin. Phys.* **2006**, *15*, 1855. [CrossRef]
29. Erturk, E.; Dursun, B. Numerical solutions of 2-D steady incompressible flow in a driven skewed cavity. *ZAMM Z. Angew. Math. Mech.* **2007**, *87*, 377–392. [CrossRef]
30. Aung, W.; Worku, G. Developing flow and flow reversal in a vertical channel with asymmetric wall temperatures. *J. Heat Transf.* **1986**, *108*, 299–304. [CrossRef]
31. Aung, W.; Worku, G. Mixed convection in ducts with asymmetric wall heat fluxes. *J. Heat Transf.* **1987**, *109*, 947–951. [CrossRef]
32. Aung, W.; Worku, G. Theory of fully developed, combined convection including flow reversal. *J. Heat Transf.* **1986**, *108*, 485–488. [CrossRef]
33. Barletta, A. Analysis of flow reversal for laminar mixed convection in a vertical rectangular duct with one or more isothermal walls. *Int. J. Heat Mass Transf.* **2001**, *44*, 3481–3497. [CrossRef]
34. Barletta, A.; Magyari, E.; Keller, B. Dual mixed convection flows in a vertical channel. *Int. J. Heat Mass Transf.* **2005**, *48*, 4835–4845. [CrossRef]
35. Boulama, K.; Galanis, N. Analytical solution for fully developed mixed convection between parallel vertical plates with heat and mass transfer. *J. Heat Transf.* **2004**, *126*, 381–388. [CrossRef]
36. Cheng, C.H.; Kou, H.S.; Huang, W.H. Flow reversal and heat transfer of fully developed mixed convection in vertical channels. *J. Thermophys. Heat Transf.* **1990**, *4*, 375–383. [CrossRef]
37. El-Din, M.S. Effect of thermal and mass buoyancy forces on the development of laminar mixed convection between vertical parallel plates with uniform wall heat and mass fluxes. *Int. J. Therm. Sci.* **2003**, *42*, 447–453. [CrossRef]
38. Gau, C.; Yih, K.A.; Aung, W. Reversed flow structure and heat transfer measurements for buoyancy-assisted convection in a heated vertical duct. *J. Heat Transf.* **1992**, *114*, 928–935. [CrossRef]
39. Hamadah, T.T.; Wirtz, R.A. Analysis of laminar fully developed mixed convection in a vertical channel with opposing buoyancy. *J. Heat Transf.* **1991**, *113*, 507–510. [CrossRef]
40. Ingham, D.B.; Keen, D.J.; Heggs, P.J. Flows in vertical channels with asymmetric wall temperatures and including situations where reverse flows occur. *J. Heat Transf.* **1988**, *110*, 910–917. [CrossRef]
41. Ingham, D.B.; Keen, D.J.; Heggs, P.J. Two dimensional combined convection in vertical parallel plate ducts, including situations of flow reversal. *Int. J. Numer. Methods Eng.* **1988**, *26*, 1645–1664. [CrossRef]
42. Jeng, Y.N.; Chen, J.L.; Aung, W. On the Reynolds-number independence of mixed convection in a vertical channel subjected to asymmetric wall temperatures with and without flow reversal. *Int. J. Heat Fluid Flow* **1992**, *13*, 329–339. [CrossRef]
43. Kim, S.H.; Anand, N.K.; Aung, W. Effect of wall conduction on free convection between asymmetrically heated vertical plates: Uniform wall heat flux. *Int. J. Heat Mass Transf.* **1990**, *33*, 1013–1023. [CrossRef]
44. Dennis, S.C.R.; Chang, G.-Z. Numerical solutions for steady flow past a circular cylinder at Reynolds number up to 100. *J. Fluid Mech.* **1970**, *42*, 471–489. [CrossRef]
45. Dennis, S.C.R.; Hudson, J.D. An  $h^4$  accurate vorticity-velocity formulation for calculating flow past circular cylinder. *Int J. Numer. Methods Fluids* **1995**, *21*, 489–497. [CrossRef]
46. Dennis, S.C.R.; Hudson, J.D.; Smith, N. Steady laminar forced convection from a circular cylinder at low Reynolds numbers. *Phys. Fluids* **1968**, *11*, 933–940. [CrossRef]
47. Grove, A.S.; Shair, F.H.; Petersen, E.E. An experimental investigation of the steady separated flow past a circular cylinder. *J. Fluid Mech.* **1964**, *19*, 60–80. [CrossRef]
48. Norberg, C. Pressure forces on a circular cylinder in cross flow. In *Bluff-Body Wakes, Dynamics and Instabilities*; Eckelmann, H., Graham, J.M.R., Huerre, P., Monkewitz, P.A., Eds.; Springer: Berlin/Heidelberg, Germany, 1993; pp. 275–278. ISBN: 978-3-662-00414-2.
49. Norberg, C. An experimental investigation of the flow around a circular cylinder: influence of aspect ratio. *J. Fluid Mech.* **1994**, *258*, 287–316. [CrossRef]
50. Norberg, C. Flow around a circular cylinder: Aspects of fluctuating lift. *J. Fluid Struct.* **2001**, *15*, 459–469. [CrossRef]

51. Norberg, C. Fluctuating lift on a circular cylinder: Review and new measurements. *J. Fluid Struct.* **2003**, *17*, 57–96. [CrossRef]
52. Triton, D.J. Experiments on the flow past a circular cylinder at low Reynolds number. *J. Fluid Mech.* **1959**, *6*, 547–567. [CrossRef]
53. Chakraborty, J.; Verma, N.; Chhabra, R.P. Wall effects in the flow past a circular cylinder in a plane channel: A numerical study. *Chem. Eng. Process.* **2004**, *43*, 1529–1537. [CrossRef]
54. Ding, H.; Shu, C.; Yeo, K.S.; Xu, D. Simulation of incompressible viscous flows past a circular cylinder by hybrid FD scheme and meshless least square-based finite difference scheme. *Comput. Methods Appl. Mech.* **2004**, *193*, 727–744. [CrossRef]
55. Park, J.; Kwon, K.; Choi, H. Numerical solutions of flow past a circular cylinder at Reynolds numbers up to 160. *KSME Int. J.* **1998**, *12*, 1200–1205. [CrossRef]
56. De Sampaio, P.A.B.; Lyra, P.R.M.; Morgan, K.; Weatherill, N.P. Petrov-Galerkin solutions of the incompressible Navier-Stokes equations in primitive variables with adaptive remeshing. *Comput. Methods Appl. Mech.* **1993**, *106*, 143–178. [CrossRef]
57. Subhankar, S.; Sanjay, M.; Gautam, B. Numerical Simulation of Steady Flow Past a Circular Cylinder. In Proceedings of the 37th National and 4th International Conference on Fluid Mechanics and Fluid Power, IIT Madras, Chennai, India, 16–18 December 2010.
58. Bitwas, G.; Sarkar, S. Effect of thermal buoyancy on vortex shedding past a circular cylinder in cross-flow at low Reynolds numbers. *Int. J. Heat Mass Transf.* **2009**, *52*, 1897–1912. [CrossRef]
59. Takami, H.; Keller, H.B. Steady two-dimensional viscous flow of an incompressible fluid past a circular cylinder. *Phys. Fluids* **1969**, *12*, II-51–II-56. [CrossRef]
60. Zienkiewicz, O.C.; Morgan, K.; Satya Sai, B.V.K.; Codina, R.; Vazquez, M. A general algorithm for compressible and incompressible flow—Part II. Tests on the explicit form. *Int. J. Numer. Methods Fluids* **1995**, *20*, 887–913. [CrossRef]
61. Zienkiewicz, O.C.; Codina, R. A general algorithm for compressible and incompressible flow - Part I. The split, characteristic based scheme. *Int. J. Numer. Methods Fluids* **1996**, *20*, 869–885. [CrossRef]
62. Zienkiewicz, O.C.; Nithiarasu, P.; Codina, R.; Vazquez, M.; Ortiz, P. The characteristic-based-split procedure: An efficient and accurate algorithm for fluid problems. *Int. J. Numer. Methods Fluids* **1999**, *31*, 359–392. [CrossRef]
63. Zienkiewicz, O.C.; Taylor, R.L. *The Finite Element Method. Volume 3: Fluid Dynamics*, 6th ed.; Elsevier Butterworth-Heinemann: Amsterdam, The Netherlands, 2005; ISBN 0-7506-6322-7.
64. Nithiarasu, P.; Codina, R.; Zienkiewicz, O.C. The Characteristic-Based Split (CBS) scheme—A unified approach to fluid dynamics. *Int. J. Numer. Methods Eng.* **2006**, *66*, 1514–1546. [CrossRef]
65. Chorin, A.J. A numerical method for solving incompressible viscous flow problems. *J. Comput. Phys.* **1967**, *2*, 12–26. [CrossRef]
66. Codina, R.; Vazquez, M.; Zienkiewicz, O.C. A general algorithm for compressible and incompressible flows. Part III: The semi-implicit form. *Int. J. Numer. Methods Fluids* **1998**, *27*. [CrossRef]
67. Editorial Board. Georgii Ivanovich Petrov (on his 100th birthday). *Fluid Dyn.* **2012**, *47*, 289–291. [CrossRef]
68. Ern, A.; Guermond, J.L. *Theory and Practice of Finite Elements*; Springer: New York, NY, USA, 2004; ISBN 9780387205748.
69. Mikhlin, S.G. *Variational Methods in Mathematical Physics*; Pergamon Press: New York, NY, USA, 1964.
70. Carpio, J.; Prieto, J.L.; Vera, M. A local anisotropic adaptive algorithm for the solution of low-Mach transient combustion problems. *J. Comput. Phys.* **2016**, *306*, 19–42. [CrossRef]
71. Lewis, R.W.; Nithiarasu, P.; Seetharamu, K.N. *Fundamentals of the Finite Element Method for Heat and Fluid Flow*; Wiley: West Sussex, UK, 2004; ISBN 978-0-470-02081-4.
72. Roache, P.J. Quantification of uncertainty in computational fluid dynamics. *Annu. Rev. Fluid Mech.* **1997**, *29*, 123–160. [CrossRef]
73. Desrayaud, G.; Lauriat, G. Flow reversal of laminar mixed convection in the entry region of symmetrically heated, vertical plate channels. *Int. J. Therm. Sci.* **2009**, *48*, 2036–2045. [CrossRef]
74. Nithiarasu, P. An efficient artificial compressibility (AC) scheme based on the characteristic based split (CBS) method for incompressible flows. *Int. J. Numer. Methods Eng.* **2003**, *5*, 1815–1845. [CrossRef]
75. Massarotti, N.; Arpino, F.; Lewis, R.W.; Nithiarasu, P. Explicit and semi-implicit CBS procedures for incompressible viscous flows. *Int. J. Numer. Methods Eng.* **2006**, *66*, 1618–1640. [CrossRef]

76. Selvam, R.P. Finite element modelling of flow around a circular cylinder using LES. *J. Wind Eng. Ind. Aerod.* **1997**, *67*, 129–139. [CrossRef]
77. Qu, L.; Norgerg, C.; Davidson, L.; Peng, S.; Wang, F. Quantitive numerical analysis of flow past a circular cylinder at Reynolds number between 50 and 200. *J. Fluid Struct.* **2013**, *39*, 347–370. [CrossRef]
78. Sahin, M.; Owens, R.G. A numerical investigation of wall effects up to high blockage ratios on two-dimensional flow past a confined circular cylinder. *Phys. Fluids* **2004**, *16*, 1305–1320. [CrossRef]
79. Posdziech, O.; Grundmann, R. A systematic approach to the numerical calculation of fundamental quantities of the two-dimensional flow over a circular cylinder. *J. Fluid Struct.* **2007**, *23*, 479–499. [CrossRef]
80. Mittal, S.; Raghuvanshi, A. Control of vortex shedding behind circular cylinder for flows at low Reynolds numbers. *Int. J. Numer. Methods Fluids* **2001**, *35*, 421–447. [CrossRef]
81. Mittal, S.; Kumar, V. Finite element study of vortex-induced cross-flow and in-line oscillations of a circular cylinder at low Reynolds numbers. *Int. J. Numer. Methods Fluids* **1999**, *31*, 1087–1120. [CrossRef]
82. Kieft, R.; Rindt, C.C.M.; van Steenhoven A.A. Near-weak effects of a heat input on the vortex-shedding mechanism. *Int. J. Heat Fluid Flow* **2007**, *28*, 938–947. [CrossRef]
83. Jordan, S.A.; Ragab, S.A. A large-eddy simulation of the near wake of a circular cylinder. *J. Fluid Eng.* **1998**, *120*, 243–252. [CrossRef]
84. Behr, M.; Hastreiter, D.; Mittal, S.; Tezduyar, T.E. Incompressible flow past a circular cylinder: Dependence of the computed flow field on the location of the lateral boundaries. *Comput. Methods Appl. Mech.* **1995**, *123*, 309–316. [CrossRef]
85. Rahman, M.; Karim, M.; Alim, A. Numerical investigation of unsteady flow past a circular cylinder using 2-D Finite Volume Method. *JNAME* **2007**, *4*, 27–42. [CrossRef]
86. Rajani, B.N.; Kandasamy, A.; Majumdar, S. Numerical simulation of laminar flow past a circular cylinder. *Appl. Math. Model.* **2009**, *33*, 1228–1247. [CrossRef]
87. Apelt, C.J.; Ledwich, M.A. Heat transfer in transient and unsteady flows past a circular cylinder in the range  $1 < R < 40$ . *J. Fluid Mech.* **1979**, *95*, 761–777. [CrossRef]
88. Rashid A.; Ahmad, P.H. Steady-State Numerical Solution of the Navier-Stokes and Energy Equations around a Horizontal Cylinder at Moderate Reynolds Numbers from 100 to 500. *Heat Transf. Eng.* **1996**, *17*, 31–81. [CrossRef]
89. Badr, H.M. Laminar combined convection from a horizontal cylinder—Parallel and contra flow regimes. *Int. J. Heat Mass Transf.* **1984**, *27*, 15–27. [CrossRef]
90. Williamson, C.H.K. Vortex dynamics in the cylinder wake. *Annu. Rev. Fluid Mech.* **1996**, *28*, 477–539. [CrossRef]



© 2019 by the authors. Licensee MDPI, Basel, Switzerland. This article is an open access article distributed under the terms and conditions of the Creative Commons Attribution (CC BY) license (<http://creativecommons.org/licenses/by/4.0/>).

## Article

# Study of Air Pressure and Velocity for Solution Blow Spinning of Polyvinylidene Fluoride Nanofibres

Rasheed Atif <sup>1</sup>, Madeleine Combrinck <sup>2</sup>, Jibran Khaliq <sup>2</sup>, James Martin <sup>2</sup>, Ahmed H. Hassanin <sup>3,4,5</sup>, Nader Shehata <sup>3,6,7,8</sup>, Eman Elnabawy <sup>3</sup> and Islam Shyha <sup>1,\*</sup>

- <sup>1</sup> Mechanical Engineering and Design, School of Engineering and the Built Environment, Merchiston Campus, Edinburgh Napier University, Edinburgh EH10 5DT, UK; A.Rasheed@napier.ac.uk
- <sup>2</sup> Department of Mechanical and Construction Engineering, Faculty of Engineering and Environment, Northumbria University, Newcastle upon Tyne NE1 8ST, UK; madeleine.combrinck@northumbria.ac.uk (M.C.); jibran.khaliq@northumbria.ac.uk (J.K.); james.e.martin@northumbria.ac.uk (J.M.)
- <sup>3</sup> Centre of Smart Nanotechnology and Photonics (CSNP), SmartCI Research Centre, Alexandria University, Alexandria 21544, Egypt; ahmed.hassanin@ejust.edu.eg (A.H.H.); nader83@vt.edu (N.S.); eman.elnabawy@smartci.alexu.edu.eg (E.E.)
- <sup>4</sup> Department of Textile Engineering, Faculty of Engineering, Alexandria University, Alexandria 21544, Egypt
- <sup>5</sup> Materials Science & Engineering Department, School of Innovative Design Engineering, Egypt-Japan University of Science and Technology (E-JUST), 179 New Borg El-Arab City, Alexandria 21934, Egypt
- <sup>6</sup> Department of Engineering Mathematics and Physics, Faculty of Engineering, Alexandria University, Alexandria 21544, Egypt
- <sup>7</sup> USTAR Bioinnovations Centre, Faculty of Science, Utah State University, Logan, UT 84341, USA
- <sup>8</sup> Kuwait College of Science and Technology (KCST), Doha District 13133, Kuwait
- \* Correspondence: I.Shyha@napier.ac.uk; Tel.: +44-(0)1-314-552-624

**Citation:** Atif, R.; Combrinck, M.; Khaliq, J.; Martin, J.; Hassanin, A.H.; Shehata, N.; Elnabawy, E.; Shyha, I. Study of Air Pressure and Velocity for Solution Blow Spinning of Polyvinylidene Fluoride Nanofibres. *Processes* **2021**, *9*, 1014. <https://doi.org/10.3390/pr9061014>

Academic Editor: Alfredo Iranzo

Received: 30 April 2021  
Accepted: 2 June 2021  
Published: 8 June 2021

**Publisher's Note:** MDPI stays neutral with regard to jurisdictional claims in published maps and institutional affiliations.

**Abstract:** Solution blow spinning (SBS) is gaining popularity for producing fibres for smart textiles and energy harvesting due to its operational simplicity and high throughput. The whole SBS process is significantly dependent on the characteristics of the attenuation force, i.e., compressed air. Although variation in the fibre morphology with varying air input pressure has been widely investigated, there is no available literature on the experimentally determined flow characteristics. Here, we have experimentally measured and calculated airflow parameters, namely, output air pressure and velocity in the nozzle wake at 12 different pressure values between 1 and 6 bar and 11 different positions (retracted 5 mm to 30 mm) along the centreline. The results obtained in this work will answer many critical questions about optimum protrusion length for the polymer solution syringe and approximate mean fibre diameter for polyvinylidene fluoride (PVDF) at given output air pressure and velocity. The highest output air pressure and velocity were achieved at a distance of 3–5 mm away from the nozzle wake and should be an ideal location for the apex of the polymer solution syringe. We achieved 250 nm PVDF fibres when output air pressure and velocity were 123 kPa and 387 m/s, respectively.

**Keywords:** solution blow spinning (SBS); air pressure and velocity; computational fluid dynamics (CFD); polyvinylidene fluoride (PVDF); energy harvesting



**Copyright:** © 2021 by the authors. Licensee MDPI, Basel, Switzerland. This article is an open access article distributed under the terms and conditions of the Creative Commons Attribution (CC BY) license (<https://creativecommons.org/licenses/by/4.0/>).

## 1. Introduction

The solution blow spinning (SBS) technique has two main advantages over its competitor electrospinning: Firstly, it does not require an electric field, and secondly, its throughput can be two orders of magnitude higher than that of electrospinning [1–5]. SBS process is also very simple since it mainly contains compressed air that passes through a nozzle and attenuates polymer solution droplet converting it into a fibre. The fluid flow characteristics are significantly dependent on the nozzle design. Park and Reitz [6] employed a jet superposition modelling approach using an equation they derived based on the law of

conservation of momentum and then used that equation as a sub-grid-scale sub-model in a Lagrangian Drop–Eulerian Gas CFD model. They reported that when the angle of convergence increases, spray cross section becomes ellipsoidal, and the air entrainment becomes more conspicuous. The air entrainment can affect the droplets' size range since it can favour collision, resulting in either division or coalescence. The droplet size is an essential parameter in fibre spinning because it dictates the diameter of the produced fibre.

Similarly, nozzle diameter also influences the fibre spinning process. Morrall et al. carried out Reynolds-averaged Navier–Stokes (RANS) simulations based on  $k-\omega$  shear stress transport and the Reynolds stress models [7]. They reported that nozzle diameter significantly influences the flow swirl and head losses in the nozzle. A stronger flow swirl retains jet energy for a longer duration that helps in the thorough mixing of the fluids coming out of the nozzle. The prolonged interaction time can aid in more extensive stretching in the fibre resulting in thinner fibres and can help in rapid evaporation of the solvent in the polymer solution, resulting in comparatively dry fibres. They further reported that although both tested models predict flow characteristics that are in good agreement with the experimental results; however, at higher flow swirls, the Reynolds stress model appears to be more accurate.

Although the SBS process has been mainly carried out at room temperature, the inflow temperature can be an interesting parameter to investigate. Xue et al. carried out CFD simulations of spray nozzles using mixture models and reported that the discharge coefficient is dependent on the inflow temperature, and as the inflow temperature increases, the discharge coefficient decreases [8]. They further observed that higher inflow temperatures lead to higher cavitation intensity, higher saturation pressure, and an increased vapour phase concentration at the nozzle's exit point. Such factors can significantly reduce the mass flow rate. The heating of the compressed gas interacting with the polymer solution can cause it to dry quickly. In the case of polyvinylidene fluoride (PVDF), the polymer solution is generally comprised of 10–20 wt/vol%, which means that there is 80–90% of organic solvent that needs to be removed entirely from the spun fibres since any retained solvent or volatiles can degrade both mechanical and piezoelectric properties [9]. Hot compressed air can aid in obtaining solvent-free dry fibres.

Since air is the only attenuation force, the fibre morphology is significantly dependent on the airflow characteristics. If air does not have significant pressure and velocity to overcome surface tension, the polymer droplet will not elongate but rather solidify as a spherical particle [10–13]. Therefore, the input air pressure and related velocity should be above a specific threshold value depending on the polymer type, viscosity of the polymer solution, and diameter of the droplet. The mean fibre diameter should then intuitively decrease with increasing input air pressure and related velocity. However, the more the input air pressure and corresponding velocity are, the more turbulent the flow will be. This turbulence might cause random and localised variations in the fibre diameter or even break the fibres [14]. Therefore, it is important to determine an optimum input air pressure and related velocity under a given set of conditions. This makes the investigation of the airflow fields important.

In this work, we have investigated the airflow field using a pitot tube and a manometer and compared the results with computational fluid dynamics (CFD) results based on the  $k-\epsilon$  turbulence model. We have then approximated the flow characteristics with the mean fibre diameter based on experimentally produced PVDF nanofibres.

## 2. Materials and Methods

A schematic diagram showing the procedure to measure dynamic pressure and data logging is presented in Figure 1, and the experimental setup is shown in Figure 2. Two different datasets were acquired with the central nozzle hole, as shown in Figure 2 (inset) where polymer solution syringe was stationed, completely blocked for the first dataset, and fully opened for the other dataset. A Bambi air compressor (VTS 150D, Bambi, Newcastle upon Tyne, UK) was used to provide oil-free dry air. An SBS nozzle was clamped on a stand

and air was supplied through a 6 mm internal diameter hose. To measure the centreline dynamic air pressure coming out of the nozzle, a pitot tube with an inner diameter of 0.4 mm and an external diameter of 0.7 mm was positioned right in front of the nozzle end. The distance between the tip of the pitot tube and the nozzle was varied and pressure was measured at 11 different locations, as shown in Figure 3. Due to its small size, the pitot tube could be inserted into the nozzle (Figure 3a). It was positioned 5 mm inside the nozzle and called  $-5$  mm, where the minus sign indicates retraction. The second measurement was made right at the tip of the nozzle end with a distance of 0 mm. The following nine readings were made at distances of 1, 2, 3, 5, 7, 10, 15, 20, and 30 mm. The pitot tube was connected to the positive terminal of the manometer (TPI 665), while the negative terminal was exposed to the atmosphere and hence dynamic pressure was recorded. To achieve continuous digital values, a manometer was connected to a laptop, and the frequency of data logging was 1 Hz. From the dynamic pressure, air velocity was calculated using Equation (1).

$$\frac{1}{2}\rho v^2 = \frac{\gamma}{\gamma - 1} p \left[ \left( \frac{p_0}{p} \right)^{(\gamma - 1)/\gamma} - 1 \right] \quad (1)$$

where  $\rho$  is air density ( $1.225 \text{ kg/m}^3$ ),  $v$  is the air velocity,  $\gamma$  is the ratio of specific heats (1.4 for air),  $p$  is the dynamic pressure, and  $p_0$  is the total pressure. The values obtained were compared with the  $k-\epsilon$  turbulence model based on CFD results and the mean fibre diameter of PVDF. A detailed description of the CFD method and production of PVDF nanofibres is provided elsewhere [15] and will not be repeated here for the sake of brevity.

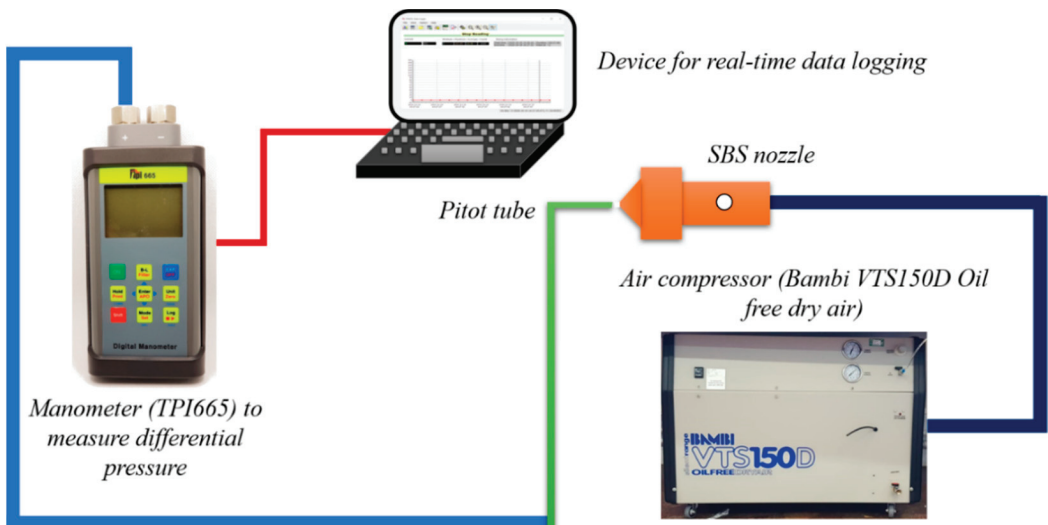


**Figure 1.** A schematic diagram showing the setup to measure the airflow field as it exists the SBS nozzle.



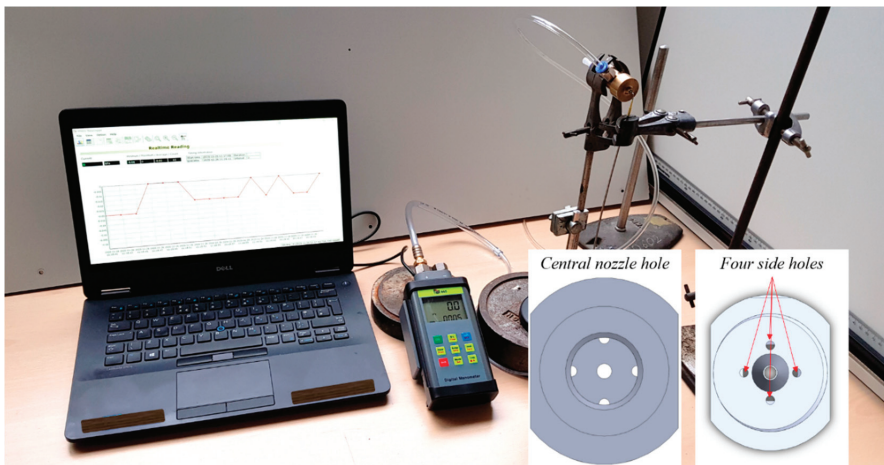


**Figure 2.** The experimental setup consisting of the pitot tube, SBS nozzle, manometer, and laptop for data logging. Inset shows the central nozzle hole and four side holes for air.

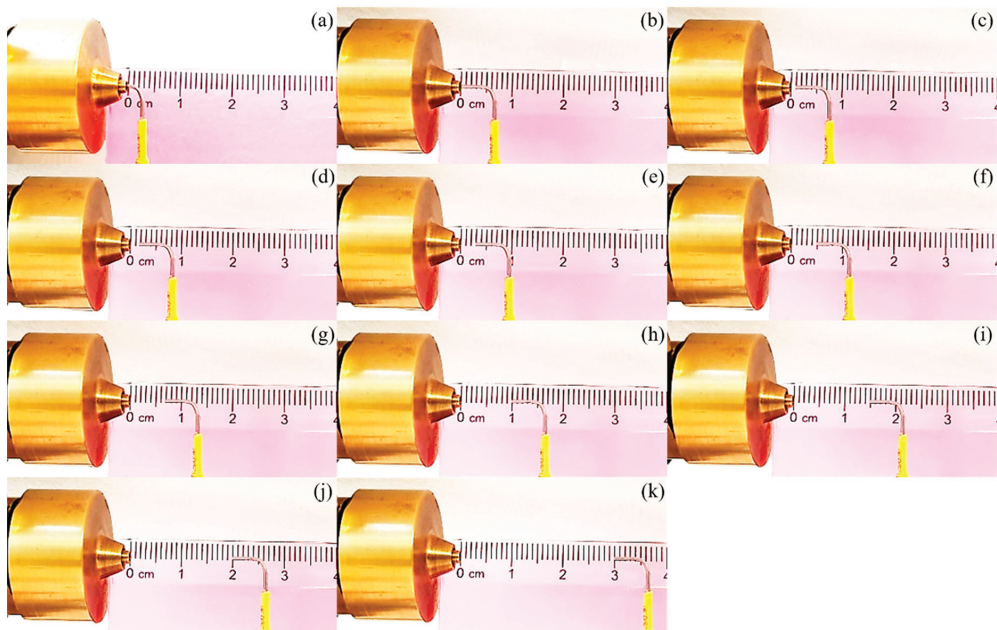


**Figure 3.** Varying distance between pitot tube and the nozzle outlet: (a)  $-5$  mm (negative sign shows that the pitot tube is inside the nozzle), (b)  $0$  mm, (c)  $1$  mm, (d)  $2$  mm, (e)  $3$  mm, (f)  $5$  mm, (g)  $7$  mm, (h)  $10$  mm, (i)  $15$  mm, (j)  $20$  mm, and (k)  $30$  mm.

### 3. Results and Discussion

When the pitot tube was inside the nozzle, only negative pressure values were recorded, confirming that no air passed through the central hole. The air coming out through the annulus around the central hole caused a negative air pressure, and CFD demonstrated this phenomenon as reverse flow [15]. The variation in output air pressure

along the centreline at different input air pressure values with the central hole completely blocked is shown in Figure 4. The central nozzle hole was blocked in the experimental work and simulations; therefore, the comparison charts presented are under the same conditions. At 1 bar input air pressure, CFD predicted that output air pressure would fluctuate between 0 and 5 kPa as we move away from the nozzle end to a distance of 5 mm. The first four readings (i.e., up to 3 mm distance away from the nozzle end) of the experimentally measured output air pressure were relatively closer to CFD values. However, the experimental value at a distance of 5 mm showed a considerable jump and recorded a value of ~80 kPa, nearly equal to 0.8 bar. This value suggested that about 80% of the input air pressure was transmitted through the nozzle. A decrease of 20% can be attributed to pressure losses at the junctions, reverse flow, and turbulence.

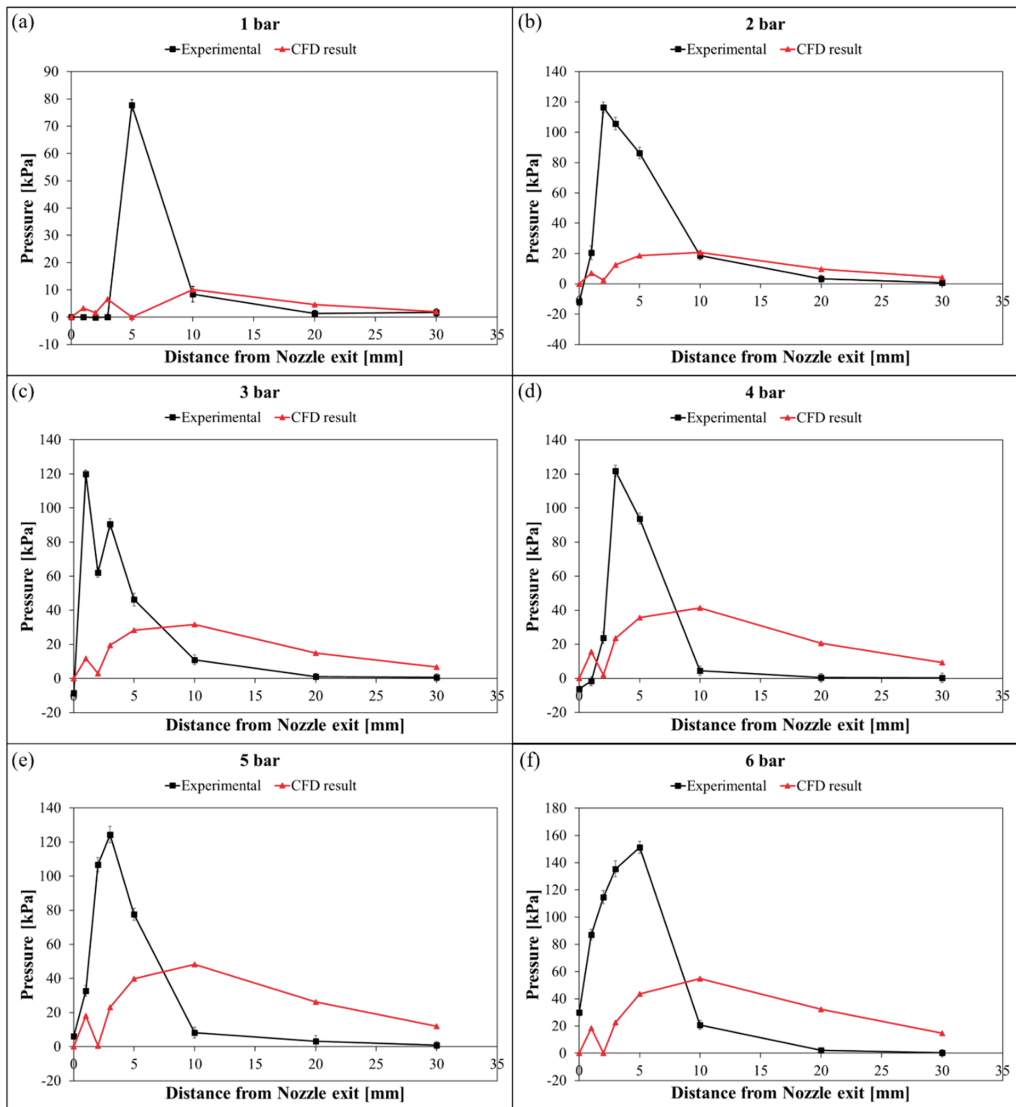


**Figure 4.** Comparison between CFD and experimental results for output air pressure at different input pressure values: (a) 1 bar, (b) 2 bar, (c) 3 bar, (d) 4 bar, (e) 5 bar, and (f) 6 bar.

Although achieving 80% of the input as output seemed reasonable, CFD prediction of  $\sim 0$  kPa seemed highly unlikely. However, such a difference can be easily explained based on reverse flow and the limitation of the pitot tube diameter.

When a fluid exited through a convergent nozzle, a reverse flow developed in the proximity of the exit point. If we were to place a pitot tube in that region, the pressure recorded could either be negative or close to zero. However, if some part of the opening of the pitot tube was outside of the reverse flow region, a positive value of pressure would be recorded. Since we observed a negative value of output air pressure (at 2, 3, and 4 bar input air pressure), it suggested that the diameter of the pitot tube was smaller than the reverse flow region. This left us assuming that the reverse flow region did not extend to 5 mm away from the nozzle end. At a distance of 10 mm away from the nozzle end, the output air pressure values plummeted to  $\sim 10$  kPa. Both CFD and experimental values showed a remarkable match.

At 2 bar input air pressure, CFD predicted output air pressure value close to zero. However, the experimental value was  $\sim -12$  kPa, indicating the pitot tube was inside the reverse flow region. At a distance of 2 mm, CFD predicted a value of  $\sim 1$  kPa. On the contrary, the pitot tube recorded a value of  $\sim 117$  kPa, which is the highest value recorded at 2 bar. At 3 mm and 5 mm, the recorded values decreased to  $\sim 105$  kPa and  $\sim 84$  kPa, respectively. The CFD and experimental values remained in agreement at a distance of  $\geq 10$  mm. The comparative trends remained similar at higher pressures, except that CFD overestimated output air pressure values at a distance of  $\geq 10$  mm. This indicated that pressure decayed more rapidly in reality than that predicted by CFD. Although the  $k-\epsilon$  turbulence model predicted a slow decay in the air velocity, some other theoretical studies suggest a rapid decay. Zhang et al. [16] carried out CFD of a sharp-edged nozzle using the OpenFOAM source code and reported that the axial velocity showed a rapid decay at the jet centre (within the axial distance).

The trends suggested that CFD underestimated the values of air pressure and velocity. The discrepancy resulted from the underestimation of the turbulence intensity of the nozzle in CFD simulations. Turbulence intensity represents the intensity of velocity fluctuation of a fluid. It is defined as the ratio of the standard deviation of fluctuating fluid velocity to the mean fluid speed. Some work has been recently carried out to optimise the role of turbulence intensity to better predict the overall flow characteristics [17]. The exploration into the modification of the influential parameters has led to the development of various turbulence models that can be traversed for a more accurate prediction of the flow characteristics [18,19].

The highest output pressure values were recorded outside the nozzle at around 5 mm away from the nozzle end. This is an important result since the protrusion length of the polymer solution syringe is critical in achieving a smooth and continuous process as flow is hindered in the retracted syringes and causes disruption in the process. Lou et al. [20] showed that a protrusion length of 4 mm is optimum, and our results were in close agreement.

The variation in output air velocity with input air pressure is shown in Figure 5. The air velocity could reach as high as 600 m/s. Compared to firearm muzzle velocities that range from  $\sim 100$  m/s to 350 m/s, a velocity of 600 m/s can be lethal. This much high velocity can rupture the eardrum and knock the eye out of its socket. Therefore, care had to be exercised while the SBS nozzle was in operation.

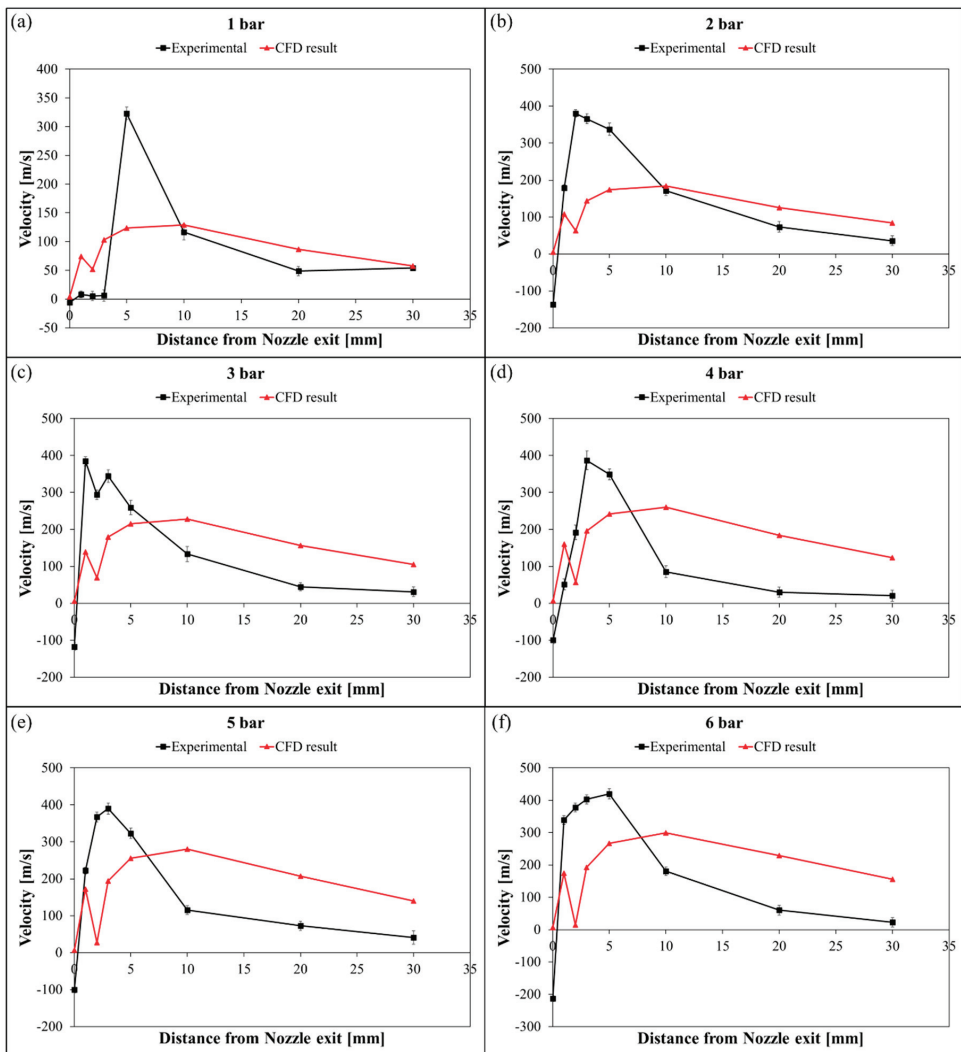


**Figure 5.** Comparison between CFD and experimental results for output air velocity at different input pressure values: (a) 1 bar, (b) 2 bar, (c) 3 bar, (d) 4 bar, (e) 5 bar, and (f) 6 bar.

The mean fibre diameters achieved experimentally at 2, 3, and 4 bar input air pressure were 530, 420, and 250 nm, respectively. The achieved air pressure and velocity can be correlated with the mean fibre diameter as listed in Table 1. When the air output pressure was around 117 kPa, the mean fibre diameter (15 wt% PVDF in DMF at a feed rate of 10 mL/h) was around 530 nm. Similarly, if the output air velocity was around 380 m/s, the mean fibre diameter was around 530 nm. A similar discussion extends to other pressure and velocity values, as presented in Table 1.

**Table 1.** Various airflow parameters and resultant mean fibre diameter.

Sr.	Input Air Pressure (bar)	Output Air Pressure (kPa)	Output Air Velocity (m/s)	Mean Fibre Diameter (nm)
1	2	117	379.9	530
2	3	121	384.4	420
3	4	123	386.9	250

At input air pressure values of  $\geq 5$  bar, we observed intertwined fibres rather than individual fibres separated from each other. Such variation in fibre morphology could be explained based on turbulence. When the flow rate exceeded a certain limit, it behaved more turbulent than laminar. The variation in output pressure and velocity became prominent at elevated flow rates, and input pressure  $\geq 5$  bar provided such conditions. This suggested that any nozzle design would limit the maximum allowable input pressure since fibre morphology depended on the air pressure or velocity as well as on the turbulence. Therefore, a trade-off was essential between pressure and turbulence to achieve fibres with suitable morphology.

The pressure values were also measured by removing the blockage from the central hole, and the manometer readings for all locations have been shown in the Supplementary Materials (Figures S1–S9). In general, the pressure values recorded were higher than those achieved with a blocked central hole. For example, at 5 bar input air pressure, the output air pressure was 124 kPa (with blocked central hole), increasing to 157 kPa after opening the central hole. Although this could be easily explained on the basis of increased mass flow rate, it suggested that the clearance between nozzle and polymer solution syringe could be an important influential factor in defining the fibre morphology. This factor has been ignored in the reviewed literature.

#### 4. Conclusions

In this work, we built a setup to determine air pressure and velocity as the air comes out of a solution blow spinning (SBS) nozzle. The setup comprised an air compressor, SBS nozzle, pitot tube, manometer, and a laptop for real-time data logging with a frequency of 1 Hz. We determined output air pressure and calculated air velocity and compared them with computational fluid dynamics (CFD) results based on the  $k-\epsilon$  turbulence model. We investigated two variables: input pressure up to 6 bar with increments of 0.5 bar and distance from the nozzle end and the selected range was  $-5$  mm to 30 mm (minus sign shows retraction). We investigated pressure and velocity with the central hole either completely blocked or fully opened for the polymer solution syringe. When the central hole block was blocked, the maximum output air pressure was recorded at a 3–5 mm distance. On the other hand, in the case of the central hole fully opened, the maximum output air pressure mainly was recorded at a  $-5$  mm distance. This difference in the location of maximum pressure suggested that the clearance between the nozzle and polymer solution syringe is an important influential factor. We observed that when output air pressure (velocity) values were 117 kPa (380 m/s), 121 kPa (384 m/s), and 123 kPa (387 m/s), the mean fibre diameters of produced PVDF nanofibres were 530 nm, 420 nm, and 250 nm, respectively. By comparing the values of output air pressure (velocity), one can infer that turbulence plays a crucial role in defining fibre morphology. The obtained results will help in achieving a more tailored morphology of the fibres. The data presented here have been limited to PVDF but can be extended to other polymers with similar rheological properties.

**Supplementary Materials:** The following are available online at <https://www.mdpi.com/article/10.3390/pr9061014/s1>, Figure S1: (a–l) Air compressor dial gauge readings showing the input pressure values and the corresponding manometer output dynamic pressure values are shown immediately below, Figure S2: (a–l) Manometer readings when pitot tube was placed at a distance of 0 mm from the nozzle end along the centreline, Figure S3: (a–l) Manometer readings when pitot tube was placed at a distance of 1 mm from the nozzle end along the centreline, Figure S4: (a–l) Manometer readings

when pitot tube was placed at a distance of 2 mm from the nozzle end along the centreline, Figure S5: (a–l) Manometer readings when pitot tube was placed at a distance of 3 mm from the nozzle end along the centreline, Figure S6: (a–l) Manometer readings when pitot tube was placed at a distance of 5 mm from the nozzle end along the centreline, Figure S7: (a–l) Manometer readings when pitot tube was placed at a distance of 10 mm from the nozzle end along the centreline, Figure S8: (a–l) Manometer readings when pitot tube was placed at a distance of 20 mm from the nozzle end along the centreline, Figure S9: (a–l) Manometer readings when pitot tube was placed at a distance of 30 mm from the nozzle end along the centreline.

**Author Contributions:** Conceptualisation, I.S. and A.H.H.; methodology, R.A. and M.C.; software, M.C. and R.A.; validation, R.A., M.C. and J.M.; data curation, R.A. and M.C.; writing—original draft preparation, R.A.; writing—review and editing, R.A., M.C., J.K., J.M., A.H.H., N.S., E.E. and I.S.; supervision, I.S.; project administration, I.S.; funding acquisition, I.S. and A.H.H. All authors have read and agreed to the published version of the manuscript.

**Funding:** This research was funded by the British Council Grant Number 352360451 and Newton-Mosharafa Call between UK and Egypt, ID: 30886.

**Institutional Review Board Statement:** Not applicable.

**Informed Consent Statement:** Not applicable.

**Data Availability Statement:** Project data is stored at Edinburgh Napier University repository.

**Acknowledgments:** The authors would like to thank the British Council for providing funding for the Institutional Links Project (Project ID: 352360451) between Alexandria University, Egypt, and Northumbria University, Newcastle upon Tyne, UK. This work is part of the project (Newton-Mosharafa Call between UK and Egypt, ID: 30886) funded by the Science, Technology, and Innovation Funding Authority (STIFA), Egypt.

**Conflicts of Interest:** The authors declare no conflict of interest.

## References

- Atif, R.; Khaliq, J.; Combrinck, M.; Hassanin, A.H.; Shehata, N.; Elnabawy, E.; Shyha, I. Solution Blow Spinning of Polyvinylidene Fluoride Based Fibers for Energy Harvesting Applications: A Review. *Polymers* **2020**, *12*, 1304. [CrossRef] [PubMed]
- Tandon, B.; Kamble, P.; Olsson, R.T.; Blaker, J.J.; Cartmell, S.H. Fabrication and characterisation of stimuli responsive piezoelectric PVDF and hydroxyapatite-filled PVDF fibrous membranes. *Molecules* **2019**, *24*, 1903. [CrossRef] [PubMed]
- Medeiros, E.S.; Glenn, G.M.; Klamczynski, A.P.; Orts, W.J.; Mattoso, L.H.C. Solution Blow Spinning: A New Method to Produce Micro- and Nanofibers from Polymer Solutions. *J. Appl. Polym. Sci.* **2009**, *113*, 2322–2330. [CrossRef]
- Vural, M.; Behrens, A.M.; Ayyub, O.B.; Ayoub, J.J.; Kofinas, P. Sprayable elastic conductors based on block copolymer silver nanoparticle composites. *ACS Nano* **2015**, *9*, 336–344. [CrossRef] [PubMed]
- Behrens, A.M.; Casey, B.J.; Sikorski, M.J.; Wu, K.L.; Tutak, W.; Sandler, A.D.; Kofinas, P. In situ deposition of PLGA nanofibers via solution blow spinning. *ACS Macro Lett.* **2014**, *3*, 249–254. [CrossRef]
- Park, S.W.; Reitz, R.D. A gas jet superposition model for CFD modeling of group-hole nozzle sprays. *Int. J. Heat Fluid Flow* **2009**, *30*, 1193–1201. [CrossRef]
- Morrall, A.; Quayle, S.; Campobasso, M.S. Turbulence modelling for RANS CFD analyses of multi-nozzle annular jet pump swirling flows. *Int. J. Heat Fluid Flow* **2020**, *85*, 108652. [CrossRef]
- Xue, R.; Ruan, Y.; Liu, X.; Cao, F.; Hou, Y. The influence of cavitation on the flow characteristics of liquid nitrogen through spray nozzles: A CFD study. *Cryogenics* **2017**, *86*, 42–56. [CrossRef]
- Atif, R.; Shyha, I.; Inam, F. The degradation of mechanical properties due to stress concentration caused by retained acetone in epoxy nanocomposites. *RSC Adv.* **2016**, *6*, 34188–34197. [CrossRef]
- Drabek, J.; Zatloukal, M. Meltblown technology for production of polymeric microfibers/nanofibers: A review. *Phys. Fluids* **2019**, *31*, 091301. [CrossRef]
- Hassan, M.A.; Anantharamaiah, N.; Khan, S.A.; Pourdeyhimi, B. Computational Fluid Dynamics Simulations and Experiments of Meltblown Fibrous Media: New Die Designs to Enhance Fiber Attenuation and Filtration Quality. *Ind. Eng. Chem. Res.* **2016**, *55*, 2049–2058. [CrossRef]
- Wang, Y.; Wang, X. Investigation on a new annular melt-blowing die using numerical simulation. *Ind. Eng. Chem. Res.* **2013**, *52*, 4597–4605. [CrossRef]
- Moore, E.M.; Shambaugh, R.L.; Papavassiliou, D.V. Analysis of isothermal annular jets: Comparison of computational fluid dynamics and experimental data. *J. Appl. Polym. Sci.* **2004**, *94*, 909–922. [CrossRef]
- Han, W.; Xie, S.; Sun, X.; Wang, X.; Yan, Z. Optimization of airflow field via solution blowing for chitosan/PEO nanofiber formation. *Fibers Polym.* **2017**, *18*, 1554–1560. [CrossRef]

15. Atif, R.; Combrinck, M.; Khaliq, J.; Hassanin, A.H.; Shehata, N.; Elnabawy, E.; Shyha, I. Solution Blow Spinning of High-Performance Submicron Polyvinylidene Fluoride Fibres: Computational Fluid Mechanics Modelling and Experimental Results. *Polymers* **2020**, *12*, 1140. [CrossRef] [PubMed]
16. Zhang, L.; Shao, J.; Chen, X. CFD simulation of nozzle characteristics in a gas aggregation cluster source. *Vacuum* **2016**, *129*, 105–110. [CrossRef]
17. Kimura, K. Chapter 3—Wind loads. In *Innovative Bridge Design Handbook*; Pipinato, A., Ed.; Butterworth-Heinemann: Boston, MA, USA, 2016; pp. 37–48.
18. Ren, G.; Liu, J.; Wan, J.; Li, F.; Guo, Y.; Yu, D. The analysis of turbulence intensity based on wind speed data in onshore wind farms. *Renew. Energy* **2018**, *123*, 756–766. [CrossRef]
19. Arenas-López, J.P.; Badaoui, M. Stochastic modelling of wind speeds based on turbulence intensity. *Renew. Energy* **2020**, *155*, 10–22. [CrossRef]
20. Lou, H.; Han, W.; Wang, X. Numerical study on the solution blowing annular jet and its correlation with fiber morphology. *Ind. Eng. Chem. Res.* **2014**, *53*, 2830–2838. [CrossRef]

Article

# Study on the Law of Diesel Oil Carrying Water in Lanzhou–Chengdu–Chongqing Product Oil Pipeline Based on Large Eddy Simulation

Tao Zhang \*, Bin Chen, Kun Sun and Wenjie Chang

Petroleum Engineering School, Southwest Petroleum University, Chengdu 610500, China; 201821000774@stu.swpu.edu.cn (B.C.); 201821000526@stu.swpu.edu.cn (K.S.); changwjz@163.com (W.C.)

\* Correspondence: zhangt@swpu.edu.cn; Tel.: +86-139-8229-1124

Received: 12 August 2020; Accepted: 24 August 2020; Published: 27 August 2020

**Abstract:** Water accumulation at the bottom of the product oil pipeline will lead to corrosion damage to the pipeline. The study on water carrying laws of refined oil could provide a reference for the safe operation of the pipeline. In this paper, the actual size of Lanzhou–Jiangyou section of Lanzhou–Chengdu–Chongqing pipeline was taken as the pipeline size. The volume of fluid (VOF) model of oil–water two–phase flow based on large eddy simulation (LES) was established. The numerical simulation of the water–carrying behavior of the product oil in the inclined pipeline was carried out. The LES–based two–phase flow model can capture the characteristics of stratified flow, wavy stratified flow, and dispersed flow under various operating conditions. The model was applied to simulate the water carrying process under various oil inlet velocities and the inclined pipe angles. The results show that as the pipeline inclined angle is  $10\sim 20^\circ$  and the oil inlet velocity is 0.66 m/s, the flow patterns in the pipeline mainly include stratified flow and wavy stratified flow. As the oil inlet velocity is 0.88~1.55 m/s, the flow patterns in the pipe are mainly stratified flow, wavy stratified flow, and dispersed flow. As the inclined angle of the pipeline is  $30\sim 40^\circ$ , the flow patterns in the pipeline mainly include stratified flows, wavy stratified flows, and dispersed flows. Finally, with the increase of flow time, water can be carried completely from the pipeline through the oil. With the increase of oil inlet velocity, the water carrying capacity of oil gradually increases. With the increase of pipeline inclination, the water carrying capacity of oil firstly increases and then decreases.

**Keywords:** Lanzhou–Chengdu–Chongqing product oil pipeline; water carrying capacity of oil; VOF; LES; flow pattern

## 1. Introduction

Lanzhou–Chengdu–Chongqing (Lan–Cheng–Yu) product oil pipeline is a typical pipeline with many ups and downs and large drops with complex terrain [1–3]. The pipeline is put into production by water combined transport. During the production process, due to the large fluctuation of the pipeline, part of the water phase may not be able to climb over the high point, and the water accumulates in the low–lying area along the inclined pipe and forms water in the pipe. Sulfur in the product oil dissolves in accumulated water to form an acidic environment and impurities such as  $O_2$ ,  $CO_2$ ,  $CaCO_3$ , and  $SiO_2$  in the pipe form electrochemical internal corrosion in this environment [4,5]. Corrosion of product oil pipeline occurs from time to time and corrosion products do exist in the pigging process of Lan–Cheng–Yu product oil pipeline. Up to now, accidents caused by corrosion products in the product oil pipeline have occurred frequently [6,7]. Since the refined oil pipeline has a certain carrying effect on the water when transporting oil, if the water in the low–lying part of the pipeline can be carried out by oil flow, the corrosion problem caused by the water in the pipeline can be solved [8,9].



The water-carrying process of oil flow in the product oil pipeline is affected by many factors, such as the apparent velocity of oil phase [10,11], physical properties of oil products [12,13], pipeline inclined angle [14,15], accumulated water amount [16], and pipeline diameter [17,18]. It can also be observed through experiments [19,20], numerical simulation [21,22], and theoretical analysis [23]. Based on the above influencing factors, different researchers have studied the influence of water accumulation on pipeline corrosion, interface distribution [24,25], influencing factors of oil flow carrying capacity [26,27], flow pattern characteristics [19,28], and oil-water interface fluctuation characteristics, etc. [14] However, the turbulence models based on Reynolds average method are mostly used in the above simulation studies, which cannot identify the small-scale turbulence information. After average processing, the instantaneous information representing turbulence pulsation is smoothed out, which makes the oil-water interface in the pipeline evenly distributed without any mixing phenomenon. Only stratified flows with the smooth oil-water interface can be identified. Tao Zhang et al. [29] established a multiphase flow model based on the LES method through mutual verification of simulation and experiment. Compared with Reynolds average method, this method adopts the modeling method for small-scale pulsation and direct simulation methods for large-scale pulsation, which shows more flow information. However, all the above studies were carried out under the experimental scale, and the experimental pipe diameter is small, which is quite different from the engineering pipe diameter.

Therefore, a VOF model based on LES was applied to study the laws of diesel oil carrying water in the engineering pipe. The actual size of Lanzhou–Jiangyou section of Lan–Cheng–Yu pipeline was taken as the model size to study the oil carrying water law. All simulation parameters were set strictly according to the actual operating parameters of this section and the numerical calculation method was extended from the experimental scale to engineering practice.

## 2. Mathematical Model

### 2.1. Governing Equation of VOF Model

A set of momentum equations is used for different fluid components in VOF. The phase interface of each computing unit can be tracked by introducing the variable of phase volume fraction [30].

Continuity:

$$\frac{\partial u_i}{\partial x_i} = 0 \quad (1)$$

Momentum:

$$\frac{\partial u_i}{\partial t} + \frac{\partial}{\partial x_j} (u_i u_j) = -\frac{1}{\rho} \frac{\partial p}{\partial x_i} + \frac{\partial}{\partial x_j} \left[ \nu \left( \frac{\partial u_i}{\partial x_j} + \frac{\partial u_j}{\partial x_i} \right) \right] + g + F_S \quad (2)$$

Volume fraction:

$$\frac{\partial \alpha}{\partial t} + u_i \frac{\partial \alpha}{\partial x_i} = 0 \quad (3)$$

where  $u_i$  and  $u_j$  are the velocities in  $i$  and  $j$  directions, m/s;  $p$  is pressure, Pa;  $\rho$  is density, kg/m<sup>3</sup>;  $\nu$  is the kinematic viscosity of the mixture, m<sup>2</sup>/s;  $F_S$  means the unit mass force under surface tension, m/s<sup>2</sup>;  $\alpha$  indicates the dimensionless volume fraction in the liquid phase.

### 2.2. LES and Sub-Grid Scale Model

Filters are used to deal with the N-S equation in LES. Large-scale vortices are stimulated directly by the unsteady N-S equation. The effects of small vortices on large vortices are modeled through a sub-grid scale (SGS) model [31].

The velocity is divided into the filtered velocity  $u_i$  and the sub-grid velocity  $u_{i,sgs}$ .

$$u_i = \bar{u}_i + u_{i,sgs} \quad (4)$$

A spatial filtering function is used for the filtering process. The filtered N-S equation is shown in Equation (5):

$$\frac{\partial \bar{u}_j}{\partial t} + \rho \bar{u}_i \frac{\partial \bar{u}_j}{\partial x_i} = -\frac{\partial \bar{p}}{\partial x_j} + \frac{\partial}{\partial x_i} \left( \mu \frac{\partial \bar{u}_j}{\partial x_i} - \tau_{ij} \right) \quad (5)$$

where  $u_i, \bar{u}_j$  are the filtered velocity in the  $i$  and  $j$  directions, m/s;  $t$  is called time, s;  $\bar{p}$  is defined the filtered pressure, Pa; the superscript “—” means filtered;  $\rho$  is the density, kg/m<sup>3</sup>;  $\tau_{ij}$  is the sub-grid stress and is shown in formula Equation (6):

$$\tau_{ij} = \overline{u_i u_j} - \bar{u}_i \bar{u}_j \quad (6)$$

In the sub-grid model,  $\tau_{ij}$  is the sub-grid stress tensor, as shown below:

$$\tau_{ij} = (\overline{u_i u_j} - \bar{u}_i \bar{u}_j) = \frac{1}{3} \tau_{kk} \delta_{ij} - 2\mu_{sgs} \left( \overline{S_{ij}} - \frac{1}{3} \overline{S_{kk}} \delta_{ij} \right) \quad (7)$$

where  $\overline{S_{ij}} = \frac{1}{2} \left( \frac{\partial \bar{u}_i}{\partial x_j} + \frac{\partial \bar{u}_j}{\partial x_i} \right)$  is the strain rate tensor,  $\mu_{sgs} = \bar{\rho} (C_s \Delta)^2 |\overline{S}|$  is called eddy viscosity in the Smagorinsky model,  $\Delta$  is the filter width and  $|\overline{S}| = \sqrt{2 \overline{S_{ij} S_{ij}}}$  is the strain rate, and  $C_s$  indicates the Smagorinsky coefficient.

### 2.3. Surface Tension Model

The continuous surface force model (CSF) and the continuous surface stress model (CSS) are applied to modeling for surface tension in Fluent. The CSF is calculated in Equation (8) [30]:

$$\vec{F}_S = \sigma \lambda(l) \delta(\vec{r}) \vec{n} \quad (8)$$

where  $\sigma$  is the surface tension coefficient;  $\delta(\vec{r})$  is the Dirac delta function;  $\lambda(l)$  is the curvature at the position of  $l$ ;  $\vec{n}$  is the unit normal vector at the interface.

$$\vec{n} = \nabla c(a) \quad (9)$$

where  $c(a)$  is the color scale function.  $\lambda(l)$  is calculated as:

$$\lambda(l) = -(\nabla \cdot \vec{n}) \quad (10)$$

## 3. Numerical Model

### 3.1. Geometrical Model

The actual size of Lanzhou–Jiangyou section of Lan–Cheng–Yu pipeline is taken as the model size, and a pipeline with a diameter of 508 mm is adopted. As shown in Figure 1, the actual wall thickness is  $\delta$ , the length of the horizontal pipe section is  $L_1$ , the inclined pipe section is  $L_2$ , the angle between the horizontal pipe and inclined pipe is  $\alpha$ , and the radius of curvature is  $R$ . The specific parameters of the model are listed in Table 1. The left side of the horizontal section is an oil phase inlet, and the right side of the inclined section is the oil-water outlet.

**Table 1.** Parameters of the geometrical model.

$L_1$ (m)	$L_2$ (m)	$D$ (mm)	$\delta$	$R$ (mm)
10	10	508	9	2450

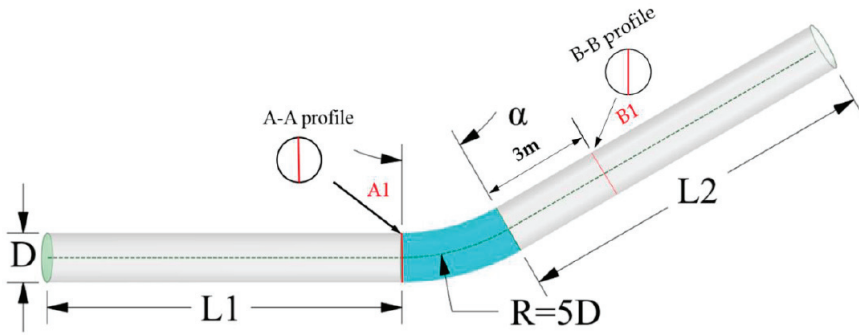


Figure 1. Geometrical model of the pipeline.

### 3.2. Mesh Generation

In order to ensure the calculation accuracy, the model in Figure 1 is divided into a block-structured mesh. The mesh division and mesh quality inspection results are listed in Figures 2 and 3, respectively.

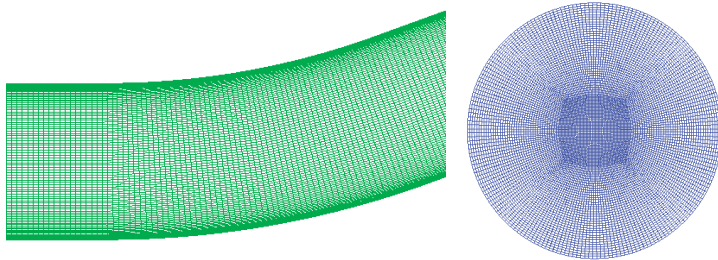
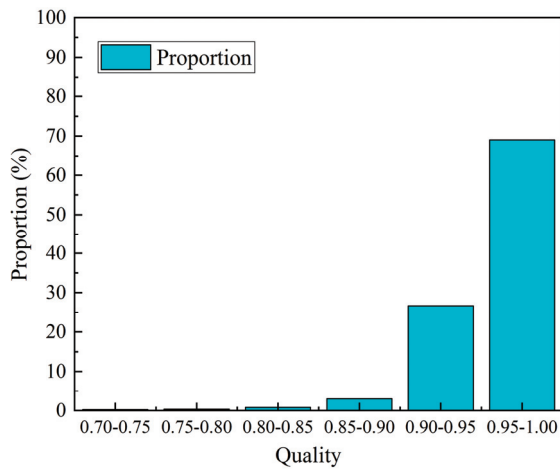
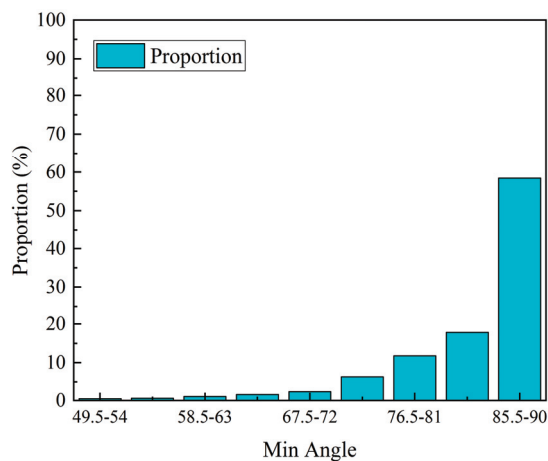


Figure 2. Mesh generation.

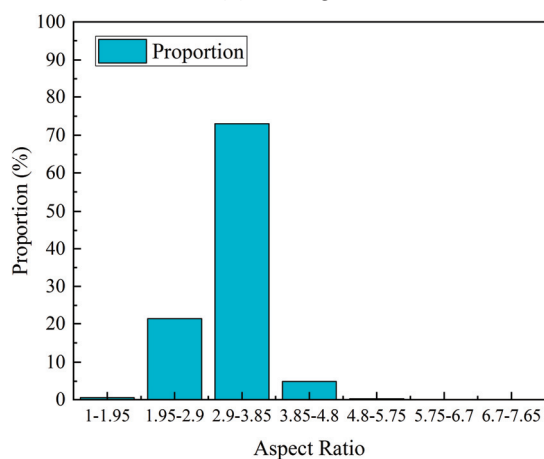


(a) Quality

Figure 3. Cont.



(b) Min Angle



(c) Aspect Ratio

Figure 3. Results of mesh quality inspection.

### 3.3. Parameter Settings

The oil phase inlet is set to the velocity inlet. Since the annual oil transportation volume of Lanzhou–Jiangyou section in recent years is between  $304\text{--}608 \times 10^4$  t [10], the speeds are 0.66, 0.88, 1.11, 1.33, and 1.55 m/s, with an interval of 0.22 m/s. All velocities at the inlet section of the pipe are the same. The turbulent intensity at the inlet of the pipe is 5% considering the inlet pulsation. The oil-water outlet is set as an outflow. The part around the pipe adopts the no-slip wall boundary. The initial water content is set as shown in Figure 4 and  $h$  is 150 mm. The length of the assumed water region is 5 m along the pipe length. At the beginning of the simulation, the initial velocities of the water phase and the oil phase in the pipeline are assumed to be 0 m/s. This is an ideal hypothesis. However, since both fluids are incompressible, the state in the pipe is consistent with the actual flow when the flow begins. In addition, the pipeline in the Lanzhou–Jiang oil section is highly undulating, with inclined angles ranging from  $10^\circ$  to  $40^\circ$ , so four sets of inclined angles of  $10^\circ$ ,  $20^\circ$ ,  $30^\circ$ , and  $40^\circ$  are selected. The physical properties of diesel oil and water at  $20^\circ\text{C}$  are listed in Table 2.

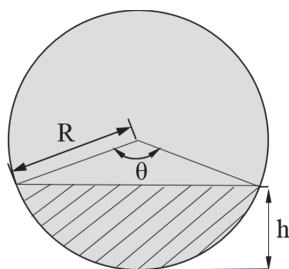


Figure 4. Initial water content.

Table 2. Physical parameters.

Medium	Dynamic Viscosity/mPa·s	Density/kg·m <sup>-3</sup>
Diesel oil	3.575	908.2
Water	1.03	1000
Surface tension	0.01795 N/m	

### 3.4. Numerical Methods

Numerical methods play an important role in simulation research and different methods often get different simulation results. LES method was used for numerical simulation and the specific model and solution method was shown in Table 3.

Table 3. Model and numerical solution methods.

Specification	Category	Methods
Turbulence model	LES	Smagorinsky–Lilly
Pressure-velocity coupling	Scheme	PISO
Spatial discretization	Gradient	Least square cell based
	Pressure	PRESTO!
	Momentum	Bounded central differencing
	Volume fraction	First order upwind

### 3.5. Mesh Independence Verification

Under the same operating conditions, five grids with the model inclination of 30° and the number of meshes of 1,754,910, 2,889,432, 3,849,120, 4,368,125, and 5,706,880 were simulated to verify the mesh independence. The time step size is 0.005 s. The velocity distribution at B1 of the B-B profile in Figure 1 was extracted for comparative analysis to determine the appropriate mesh model.

The inlet velocity of the oil was set at 1.11 m/s, and other settings were consistent. The above five meshes were used to simulate the process. As the flow time is 8 s, the velocity magnitude curve at B1 is shown in Figure 5. This velocity is the instantaneous velocity magnitude at B1 in Figure 1. As shown in the figure, when the number of meshes gradually increases, the change in velocity decreases. As the mesh numbers are 4,368,125 and 5,706,880, the velocities are basically the same. To improve the efficiency and accuracy of calculation, the mesh model with 4,368,125 is taken as the final calculation model.

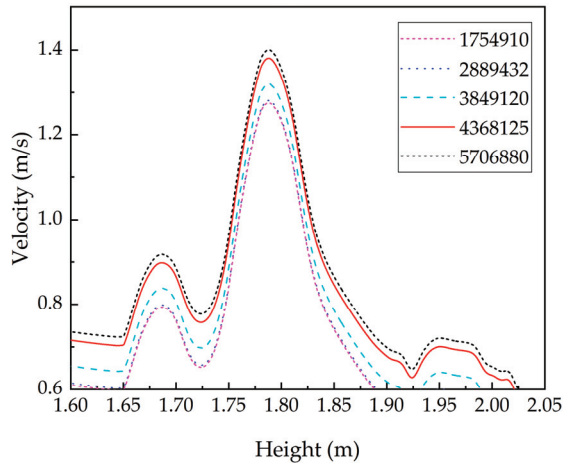


Figure 5. Mesh independence verification.

### 3.6. Analysis of $y^+$

The results have shown that the calculation results of  $y^+$  between 0 and 30 in the LES method are the most accurate [32,33]. Therefore, the distribution of the  $y^+$  value in the pipeline direction when the flow time is 15 s is extracted in Figure 6. The value of  $y^+$  along the pipeline is between 2 and 50, which meets the requirements of calculation accuracy required for LES.

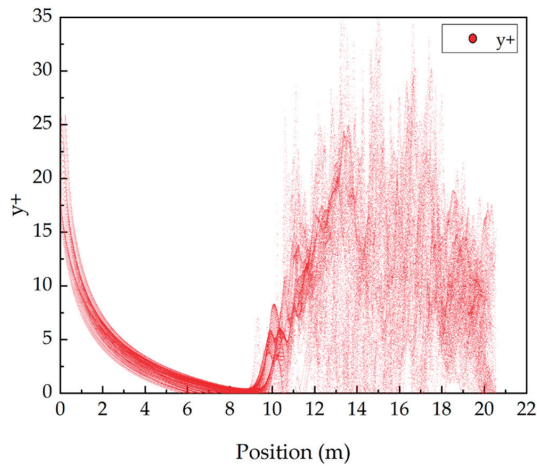


Figure 6.  $y^+$  along the pipeline.

## 4. Analysis of Simulation Results

### 4.1. Method Verification

An inclined pipe model was established by Tao Zhang et al. [29] to verify the application of the LES method with diameter  $D = 50$  mm, horizontal part  $L_1 = 1000$  mm, inclined part  $L_2 = 1000$  mm, and curvature radius  $R = 5D = 250$  mm. Under the conditions of corresponding parameters, the LES simulations are compared with the experimental data by means of experimental observation and simulation verification. The results show that the experimental and simulation results of the oil carrying water process are highly consistent, which proves that LES can be applied to the simulation

of carrying water. Figure 7 shows the oil-water distribution of experimental results and simulation results with  $v = 0.25$  m/s,  $\alpha = 10^\circ$  and  $40^\circ$ .

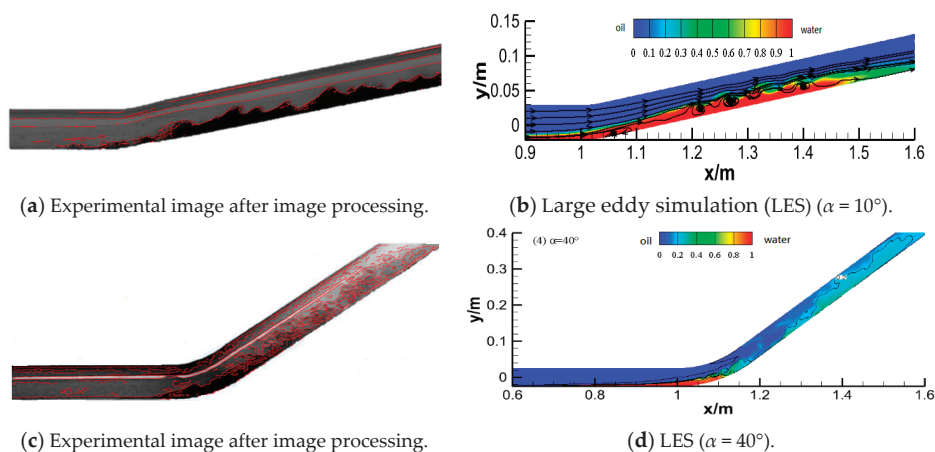


**Figure 7.** Comparison of two methods ( $t = 3$  s) [29].

The flow pattern presents a wavy stratified flow in Figure 7a. The water in the horizontal section gradually enters the inclined section, and most of the water is mainly concentrated in the lower part of the inclined pipe, and obvious wavy stratification appears at the oil-water interface. In Figure 7b, the contour of the LES method shows a wavy stratified flow, the oil-water interface is evenly distributed and there is a phenomenon of mutual mixing at the interface, which is consistent with the experimental results. In addition, the streamline was distorted and formed a vortex, and then formed a wave structure in the process of oil carrying water. As shown in Figure 7d, there is a smooth stratified flow pattern in the horizontal section. As the water is carried to the inclined part of the pipeline by oil, the water is quickly dispersed into the oil to form a dispersed flow pattern, which basically conforms to the Figure 7c flow pattern characteristics.

The comparative analysis of the experimental and simulation results under the two operating conditions proves that the LES method can identify the flow characteristics of oil carrying water. It is in good agreement with the experimental results, which can be used for the study of the law of oil and water.

#### 4.2. Processes of Oil Carrying Water

The water-carrying process of oil is a typical transient flow process. The LES is used to simulate the dynamic water carrying process of Lan–Cheng–Yu pipeline. As the inclined angle  $\alpha$  is  $10^\circ$  and the oil inlet velocity  $v$  is 1.33 m/s, the contours of the water-carrying process are shown in Figure 8.

As shown in Figure 8, the flow in the pipe is at the initial stage of 1–8 s, the oil-water interface is smooth, and there is no mixing phenomenon. The water flows to the inclined section in a smooth stratified flow pattern with the displacement function of the oil. As the time is between 9–14 s, the water is carried by the oil phase into the inclined section. The kinetic energy of water is gradually transformed into potential energy, velocity decreases, oil-water velocity difference increases, shear effect increases, and the stratified flow transforms into a wave-like stratified flow. As flow time is 15–19 s, the oil-water is mixed, the oil flow area decreases and the velocity increases at the crest, while the oil flow area increases and the velocity decreases at the trough. The fluctuation between crest and trough gradually develops into a vortex, resulting in more severe disturbance of the oil-water interface. Then the flow pattern appears as a dispersed flow.

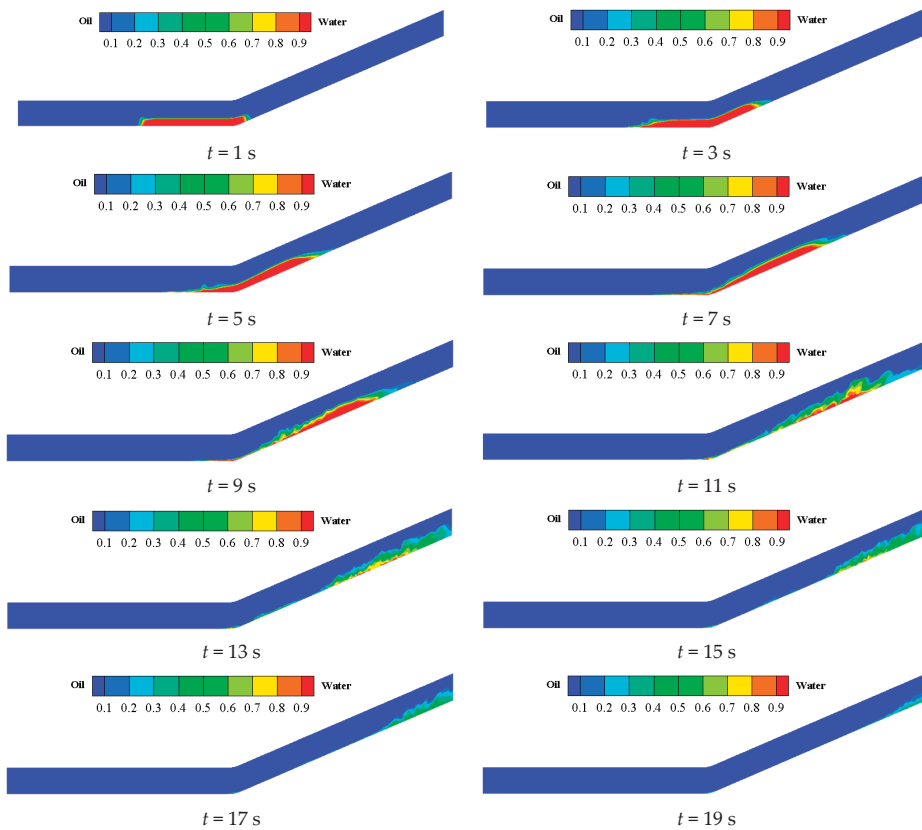


**Figure 8.** Phase distribution of water-carrying process ( $\alpha = 10^\circ$ ).

Figure 9 is the contours of the water-carrying process of the oil as the inclined angle  $\alpha$  is  $30^\circ$  and the inlet velocity is 1.33 m/s. As the flow time is 1~8 s, the oil phase has just entered the pipeline. The inclined section presents a smooth stratified flow, and the oil-water interface is evenly distributed with little disturbance. As the flow time is 9 s, the flow time increases, the oil-water velocity difference increases, the front end of the water and the oil phase are mixed with each other, and the water content decreases. At this time, the stratified flow becomes a wavy stratified flow. As flow time is 10~19 s, the flow state is turbulent, the fluid in the pipe pulsates violently, the oil-water mixing in the inclined pipe is serious, the shearing action is great, and the flow pattern develops into a dispersed flow.

The Lan-Cheng-Yu product oil pipeline fluctuates greatly in Figures 8 and 9. The flow patterns in the pipeline are mainly stratified flow, wavy stratified flow, and dispersed flow. In addition, the transition time of flow patterns is different under various operating conditions.



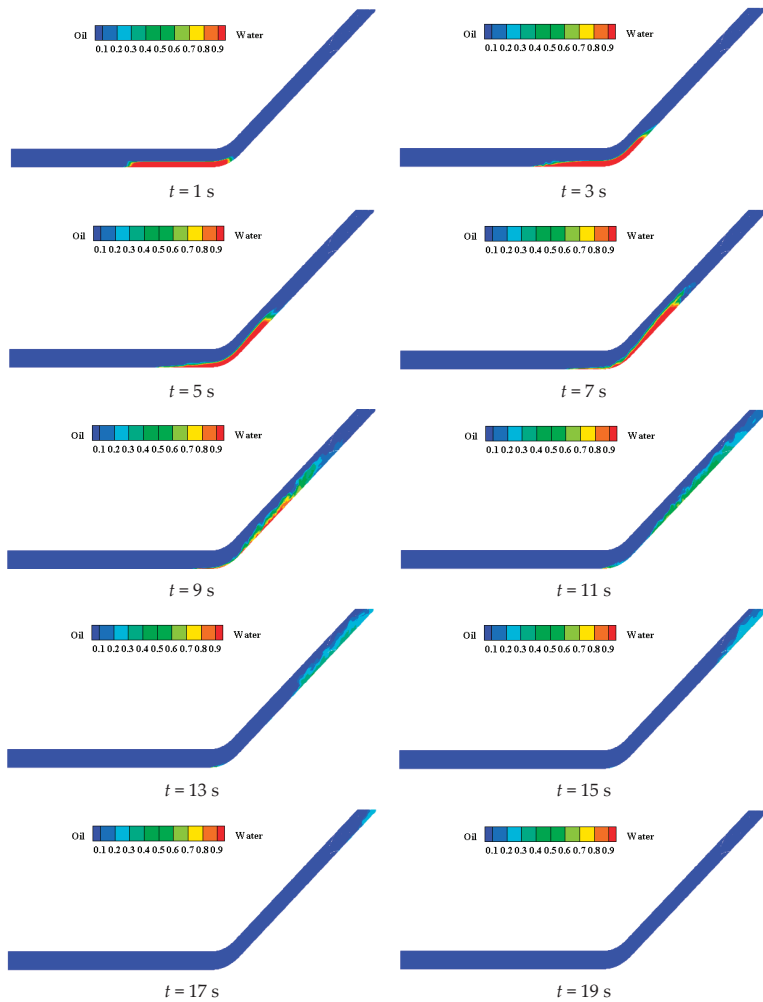


**Figure 9.** Phase distribution of water-carrying process ( $\alpha = 30^\circ$ ).

### 4.3. The Transition of Flow Patterns

#### 4.3.1. Distribution of Two Phases

The variation laws of flow pattern in the process of oil carrying water in Lan–Cheng–Yu pipeline under variable oil inlet velocities and angles were studied with the above-mentioned numerical model.

Figure 10 shows the oil-water distribution and streamline diagram under different oil phase inlet flow rates as the flow time is  $t = 11$  s and the pipeline inclined angle is  $\alpha = 10^\circ$ . In Figure 10, as the velocity is 0.66~1.11 m/s, the water gradually flows from the bottom of the horizontal section to the inclined section. At this time, the oil-water velocity difference is small, the shear effect is small, the oil-water two-phase interface fluctuates little, and the streamline is less affected by the fluctuation, showing a smooth stratified flow pattern. As the velocity is 1.33~1.55 m/s, the oil-water velocity difference increases, the shearing effect is greater, the oil-water two-phase interface begins to fluctuate, and the oil-water intermixes with each other. The streamlines of the oil-water interface are slightly distorted. The oil and water present a wavy stratified flow and moves to the bottom of the inclined pipe.

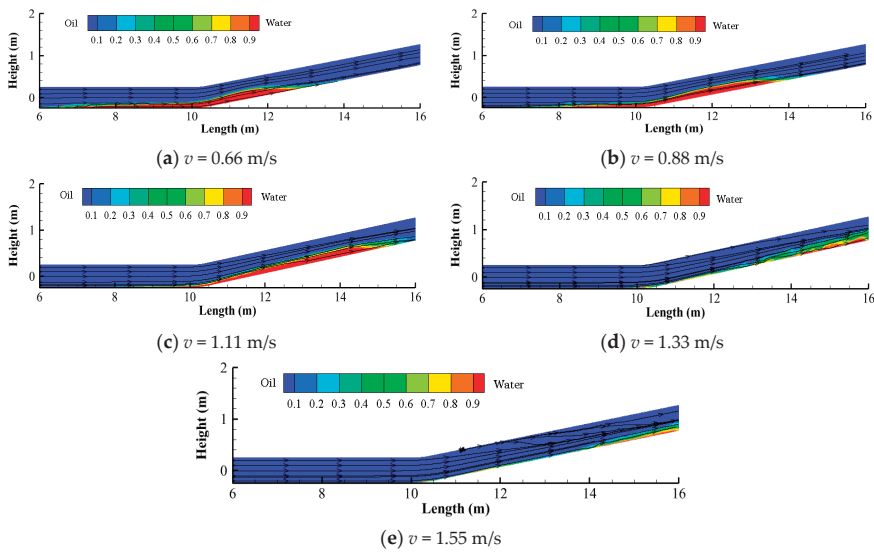


Figure 10. Distribution of oil and water ( $\alpha = 10^\circ$ ,  $t = 11.0$  s).

Figure 11 shows the oil-water distribution and streamline diagram at different oil-phase inlet velocities as  $t$  is 11 s and  $\alpha$  is  $20^\circ$ . As the velocity is  $0.66\text{--}0.88$  m/s, the water phase has not completely entered the bottom of the inclined section, the flow pattern in the horizontal part is stratified flow, and the flow pattern at the bottom of the inclined section has a tendency to transition to wavy stratified flow. As the velocity is  $1.11$  m/s, the flow of oil and water presents a wavy stratified flow. As the velocity is  $1.33\text{--}1.55$  m/s, the oil-water two phases are mixed with each other, the wavy stratified flow disappears, and the flow flows to the inclined pipe in the form of dispersed flow.

Figure 12 shows the oil-water two-phase distribution and streamline diagram at different oil-phase inlet flow velocities as the flow time  $t$  is 11 s and the pipe inclination  $\alpha$  is  $30^\circ$ . As the velocity is  $0.66\text{--}0.88$  m/s, the tube presents a smooth stratified flow pattern. The streamline is relatively stable at the oil-water interface. It is seriously distorted at the water phase, forming vortices at the bottom and top of the inclined tube. As the velocity is  $1.11$  m/s, the stratified flow gradually changes into a wavy stratified flow, and a vortex is performed at the bottom of the inclined tube. When the velocity continues to increase, the vortex disappears and the flow pattern eventually develops into a dispersed flow.

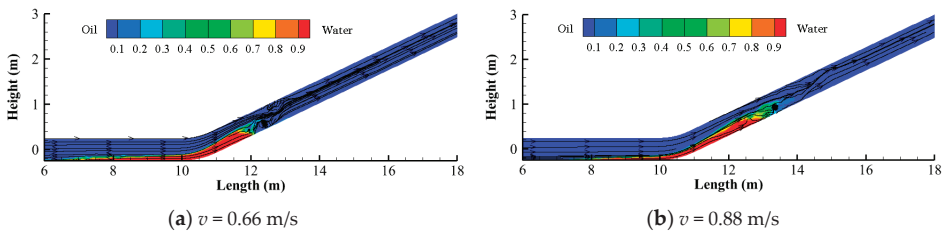


Figure 11. Cont.

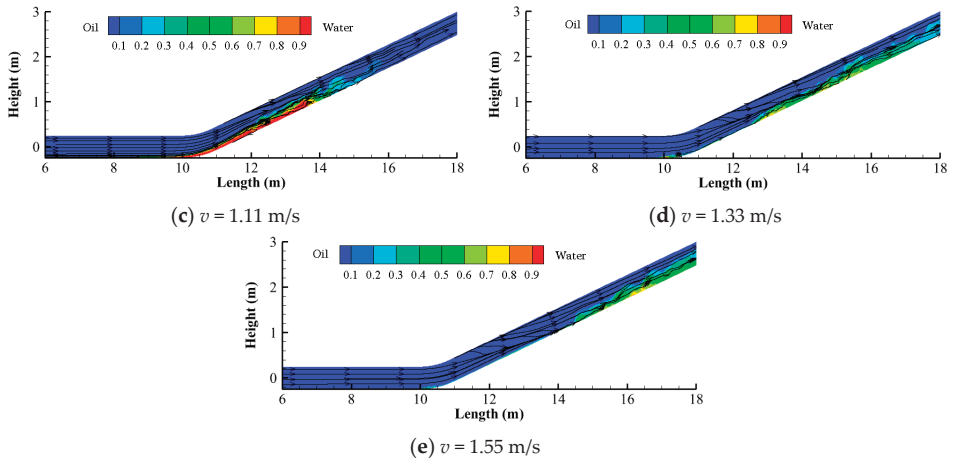


Figure 11. Distribution of oil and water ( $\alpha = 20^\circ$ ,  $t = 11.0$  s).

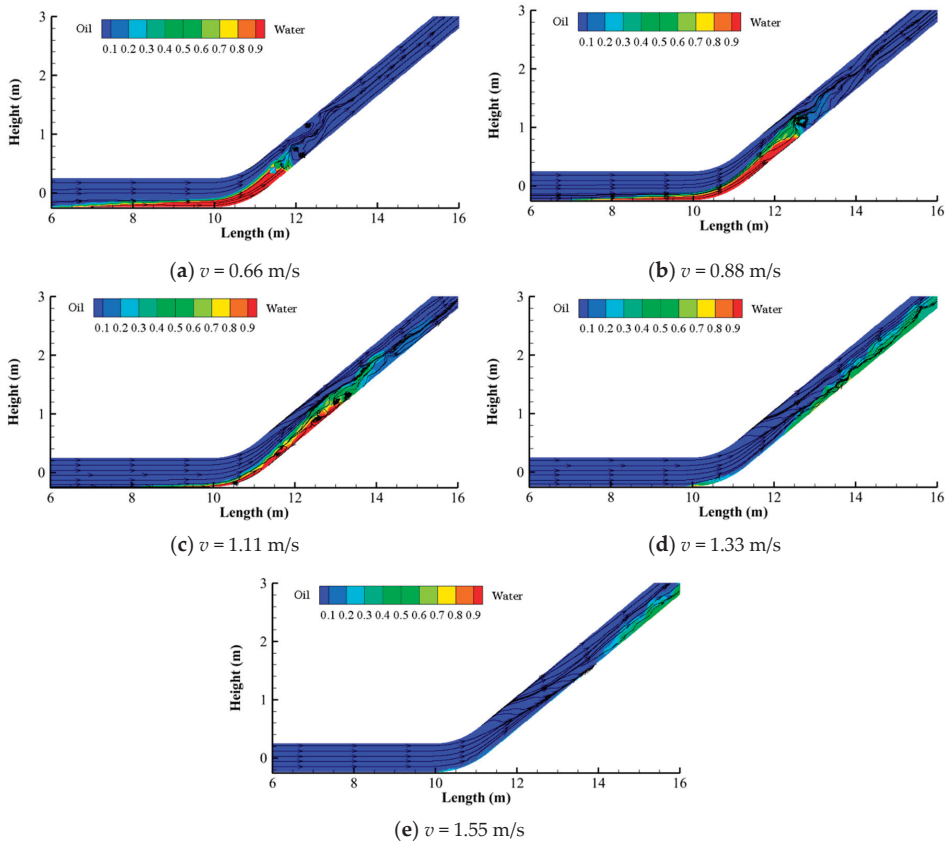


Figure 12. Distribution of oil and water ( $\alpha = 30^\circ$ ,  $t = 11.0$  s).

Figure 13 shows the oil-water distribution and streamline diagram at different oil-phase inlet velocity as the flow time  $t$  is 11 s and the pipe inclination  $\alpha$  is  $40^\circ$ . As the velocity is 0.66 m/s, the oil-water

interface is evenly distributed and the flow pattern is stratified flow. The streamline behind the water phase is greatly affected by disturbance, and vortices exist in every position of the inclined pipe. As the oil inlet velocity is 0.88 m/s, the streamline distortion range increases, the vortex is mainly concentrated on the bottom of the inclined tube, and the flow is wavy stratified flow. As the velocity is 1.11 m/s, the flow pattern is dispersed flow. There is a vortex at the bottom of the inclined pipeline. When the velocity continues to increase, the vortex disappears, the oil carries the water and flows out from the right side of the inclined pipe in a dispersed flow pattern.

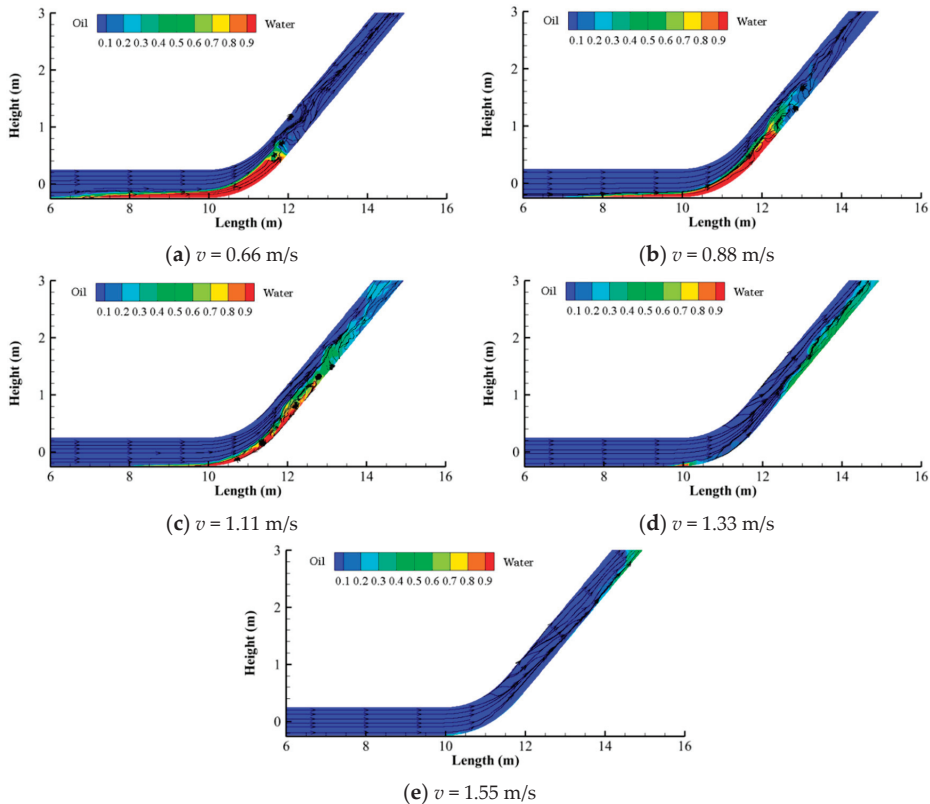


Figure 13. Distribution of oil and water ( $\alpha = 40^\circ$ ,  $t = 11.0$  s).

According to the four inclined angles, the flow patterns in the inclined part change with flow time as the inlet velocity is 0.66~1.55 m/s, shown in Figure 14. There are three main flow patterns in the pipe, such as stratified flow, wavy stratified flow, and dispersed flow. As the pipe inclined angle is fixed and the oil inlet velocity is low, the two phases enter into the inclined pipe at a certain velocity difference due to the carrying effect of oil to the water phase. At this time, the flow pattern is smooth and stratified flow. After a period of time, the kinetic energy of the mixed fluid is gradually transformed into potential energy in the inclined part. The velocity difference between the two phases is further increased on account of the difference of oil-water content and density, which leads to the increase of shear action, the increasingly severe fluctuation of the interface, and the change of flow pattern from stratified flow to wavy stratified flow. When the inlet velocity of the oil phase continues to increase, the shear action is enhanced, the flow state in the pipe is turbulent, the pulsation is very severe, the mixing degree of oil and water is deepened, and the flow pattern tends to a dispersed

flow. In addition, the transition time of flow patterns is gradually advanced with the increase of oil inlet velocity.

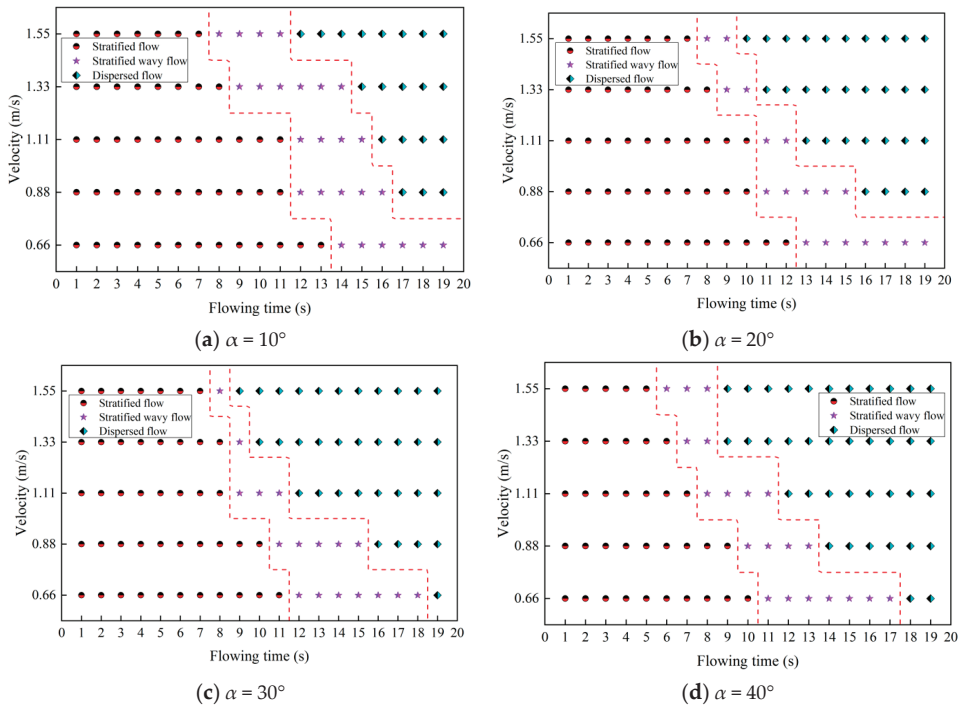


Figure 14. Flow pattern changes under various operating conditions.

As the oil inlet velocity is fixed, the oil flow carries the water phase into the inclined section. With the increase of velocity difference between two phases in the inclined section, the oil-water shearing action increases, and the flow pattern changes from stratified flow to wavy stratified flow. At this time, when the inclined angle of the pipeline gradually increases, the wavy stratified flow becomes a dispersed flow. As the inlet velocity of oil is fixed, the transition time of time for the flow patterns is also accelerated with the increase of pipeline inclination.

#### 4.3.2. Distribution of Oil-Water Velocity

To observe the velocity distribution at different inlet velocities, the velocity distribution in the pipe under the conditions of 20° and 40° inclined angles were studied.

Figure 15 performs the velocity distribution in the pipe at different oil phase inlet flow velocities when the flow time is 11 s and the pipe inclination is 20°. As shown in the figure, the places with higher speed in the pipe are mainly concentrated at the upper part of the inclined pipe, and the velocity at the bottom of the inclined tube is relatively slow. And the area with higher velocity gradually moves to the outlet position of the pipeline with the increase of the oil inlet velocity.

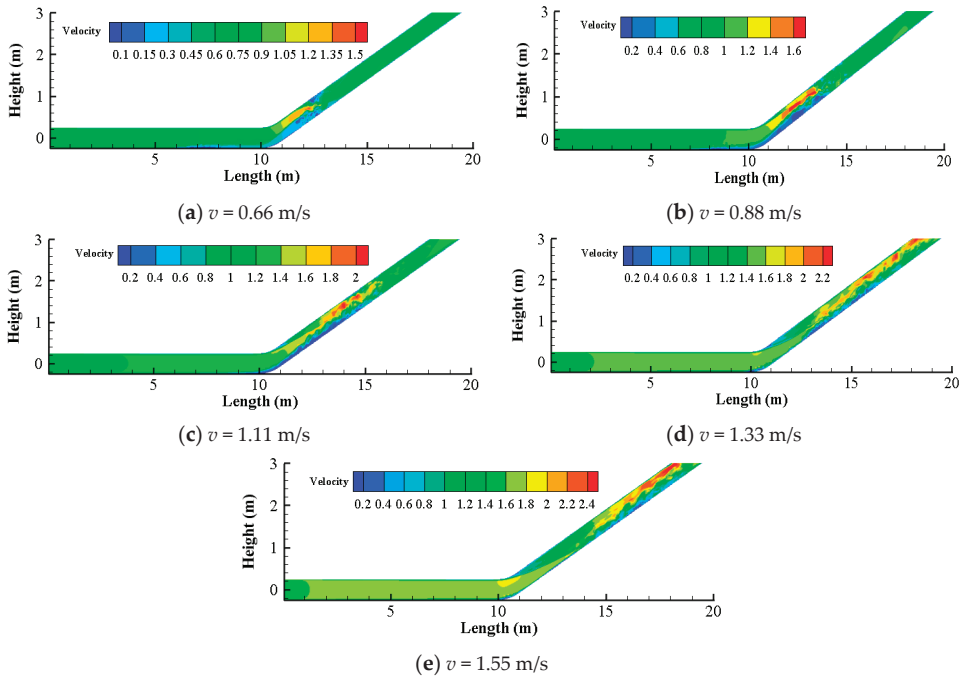


Figure 15. Velocity distribution in pipe at  $\alpha = 20^\circ$  ( $t = 11.0$  s).

As the inclined angle  $\alpha$  is  $20^\circ$  and the flow time is 11.0 s, the velocity distribution, and shear rate distribution at A1 on section A-A in Figure 1 are shown in Figure 16. As shown in Figure 16a, velocities at the bottom and upper section are relatively small, while the velocity in the middle part is relatively large and evenly distributed. With the increase of oil inlet velocity, the velocity in the middle of the pipeline also increases gradually. Among them, the inlet oil phase velocities are 0.66 m/s, 0.88 m/s, 1.11 m/s, 1.33 m/s, and 1.55 m/s, and the corresponding maximum velocities are 0.79 m/s, 1.06 m/s, 1.30 m/s, 1.58 m/s, and 1.82 m/s, respectively.

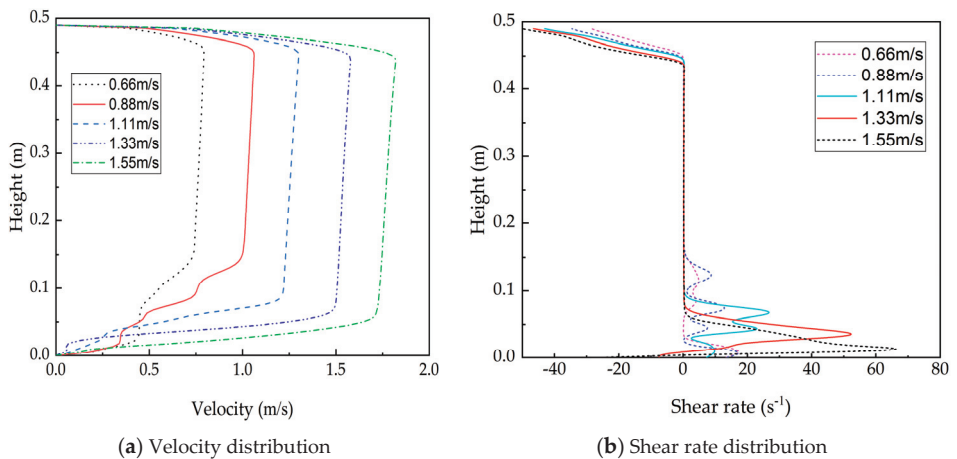


Figure 16. Velocity distribution and shear rate distribution of the A-A section ( $\alpha = 20^\circ$ ).

In Figure 16b, the maximum shear rate  $17.5 \text{ s}^{-1}$  corresponding to  $0.66 \text{ m/s}$  appears at  $y = 9 \text{ mm}$ ; the maximum shear rate  $18.2 \text{ s}^{-1}$  corresponding to  $0.88 \text{ m/s}$  appears at  $y = 7 \text{ mm}$ ; the maximum shear rate  $28.0 \text{ s}^{-1}$  corresponding to  $1.11 \text{ m/s}$  appears at  $y = 68 \text{ mm}$ ; the maximum shear rate of  $54.1 \text{ s}^{-1}$  corresponding to  $1.33 \text{ m/s}$  appears at  $y = 36 \text{ mm}$ ; and the maximum shear rate of  $67.5 \text{ s}^{-1}$  corresponding to  $1.55 \text{ m/s}$  appears at  $y = 14 \text{ mm}$ . In conclusion, as the oil inlet velocity was  $0.66 \text{ m/s}$  and  $0.88 \text{ m/s}$ , the oil-water velocity difference was small and the maximum shear rate was small. As the oil inlet velocity is  $1.11\text{--}1.33 \text{ m/s}$ , the velocity increases, so does the oil-water velocity difference and the shear rate. The region with the maximum positive shear rate gradually moves from the lower part of the pipeline to the bottom of the pipeline with the increase of the velocity.

Figure 17 is a contour of the velocity distribution in the pipe under different oil phase inlet flow rates when the flow time is  $11 \text{ s}$  and the pipe inclination  $\alpha$  is  $40^\circ$ . As shown in the figure, when the velocity is  $0.66 \text{ m/s}$ , the velocity at the bottom and top of the inclined section is smaller while largest in the middle. When the velocity is  $0.88\text{--}1.11 \text{ m/s}$ , the velocity at the top of the pipeline increases with the increase of velocity, and the area with higher velocity flows along the top of the pipeline to the outlet of the pipeline. When the velocity is  $1.33 \text{ m/s}$ , the velocity distribution in the pipeline is relatively uniform except for the high-speed area. When the velocity continues to increase, the velocity distribution in the pipe is uniform, and the oil flow basically carries the water out of the inclined section.

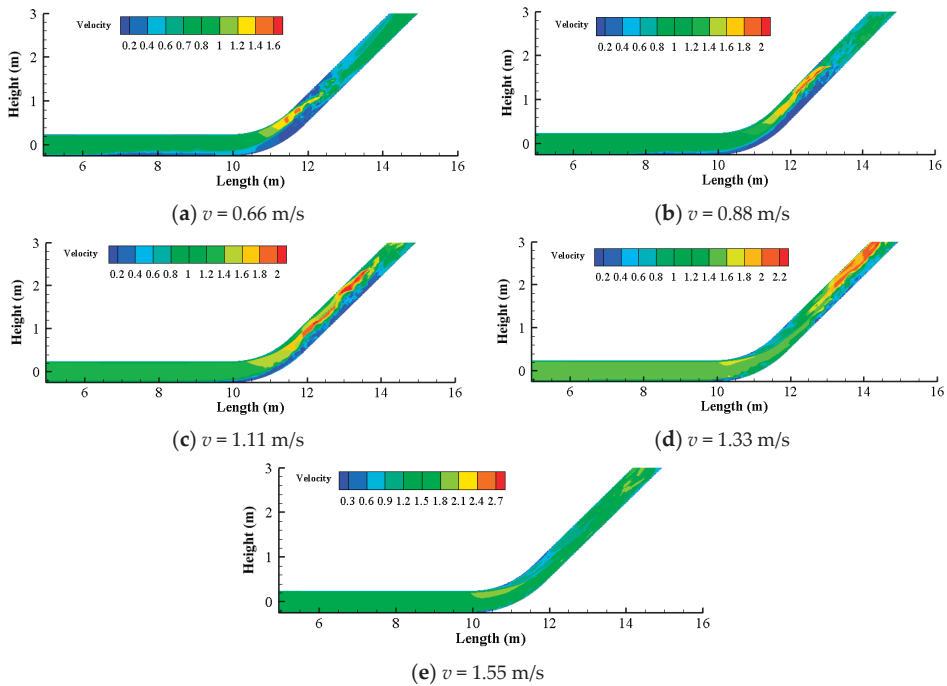
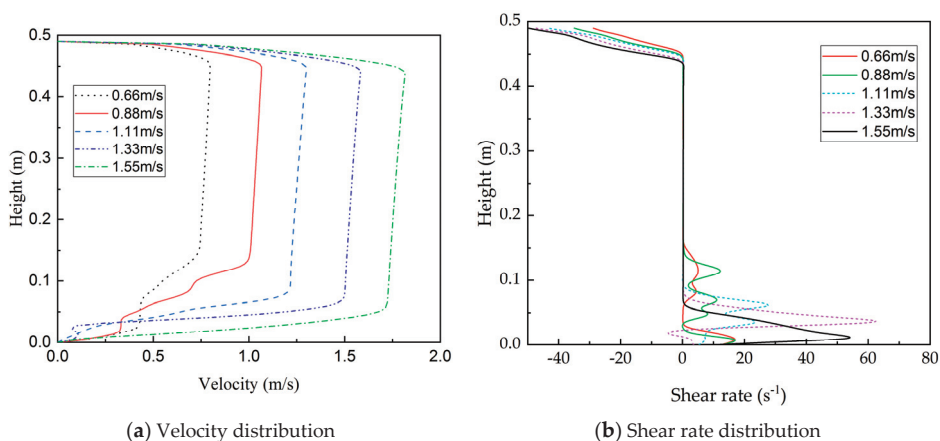


Figure 17. Contour of velocity distribution in pipe at  $\alpha = 40^\circ$  ( $t = 11.0 \text{ s}$ ).

The velocity distribution and shear rate distribution at section A1 of A-A in Figure 1 are shown in Figure 18 at  $\alpha = 40^\circ$  and  $t = 11.0 \text{ s}$ . As the inclined angle  $\alpha$  is  $40^\circ$ , the velocity distribution at section A1 of A-A is basically consistent with that when  $\alpha$  is  $20^\circ$ . The maximum velocities at  $0.66 \text{ m/s}$ ,  $0.88 \text{ m/s}$ ,  $1.11 \text{ m/s}$ ,  $1.33 \text{ m/s}$ , and  $1.55 \text{ m/s}$  are  $0.80 \text{ m/s}$ ,  $1.07 \text{ m/s}$ ,  $1.30 \text{ m/s}$ ,  $1.58 \text{ m/s}$ , and  $1.82 \text{ m/s}$ , respectively. It can be seen that the change of the pipeline inclination has little effect on the velocity distribution and the maximum velocity of the inclined pipe section entrance section.



**Figure 18.** Velocity distribution and shear rate distribution in section A-A ( $\alpha = 40^\circ$ ).

As shown in Figure 18b, when the flow time is 11.0 s and the inclined angle  $\alpha$  is  $40^\circ$ , the maximum shear rate of  $18.6 \text{ s}^{-1}$  corresponding to 0.66 m/s appears at  $y = 9 \text{ mm}$ ; the maximum shear rate of  $18.9 \text{ s}^{-1}$  corresponding to 0.88 m/s appears at  $y = 7 \text{ mm}$ ; the maximum shear rate of  $28.1 \text{ s}^{-1}$  corresponding to 1.11 m/s appears at  $y = 59 \text{ mm}$ ; the maximum shear rate of 1.33 m/s corresponding to  $63.0 \text{ s}^{-1}$  appears at  $y = 36 \text{ mm}$ ; the maximum shear rate of  $54.8 \text{ s}^{-1}$  corresponding to 1.55 m/s appears at  $y = 9 \text{ mm}$ . In conclusion, when the oil inlet velocity is 0.66~0.88 m/s, the oil-water velocity difference is small and the maximum shear rate is small. At this time, the oil flow just begins to carry the water phase, and the shear rate near the pipe wall is the highest; When the oil inlet velocity increases from 1.11 m/s to 1.33 m/s, the oil inlet velocity increases, the oil-water interface fluctuates sharply, the water phase decreases gradually, the oil-water interface moves down, and the maximum positive shear rate also increases and moves down. As the oil velocity is 1.55 m/s, the water in the pipeline basically disappeared. The velocity of water increases after being carried by oil. At this time, the oil-water velocity difference decreases, and the maximum positive shear rate decreases.

#### 4.4. Analysis of Water Carrying Capacity

The process of oil carrying water can determine the changing characteristics of oil-water flow patterns under the influence of different oil inlet velocity and pipeline inclined angle. In addition, the variation law of water accumulation with time is more important to the engineering practice when the oil inlet velocity and pipe inclined angle are different.

Figure 19 shows the variation curve of water accumulation mass with flow time under different velocities at  $\alpha = 10^\circ, 20^\circ, 30^\circ$ , and  $40^\circ$ . The mass of the water in the pipe gradually decreases with the increase of the flow time. In addition, the mass of the water in the pipe decreases with the increase of the oil inlet velocity. As the inclined angle of the pipeline is  $10^\circ$ , the oil inlet velocity is 0.66 m/s, 0.88 m/s, 1.11 m/s, 1.33 m/s, and 1.55 m/s, the corresponding time for the water to be completely output from the pipe is 90 s, 55 s, 36 s, 35 s, and 25 s, respectively. As the inclined angle of the pipeline is  $20^\circ$ , the oil inlet velocity is 0.66 m/s, 0.88 m/s, 1.11 m/s, 1.33 m/s, and 1.55 m/s, the corresponding time for the water to be completely output from the pipe is 85 s, 48 s, 33 s, 23 s, 22 s, respectively. As the inclined angle of the pipeline is  $30^\circ$ , as the oil inlet velocity is 0.66 m/s, 0.88 m/s, 1.11 m/s, 1.33 m/s, 1.55 m/s, the corresponding time for the water to be completely output from the pipe is 92 s, 49 s, 37 s, 24 s, 23 s, respectively. As the inclined angle of the pipeline is  $40^\circ$ , as the oil inlet velocity is 0.66 m/s, 0.88 m/s, 1.11 m/s, 1.33 m/s, 1.55 m/s, the corresponding time for the water to be completely output from the pipe is 95 s, 50 s, 39 s, 26 s, 25 s, respectively.



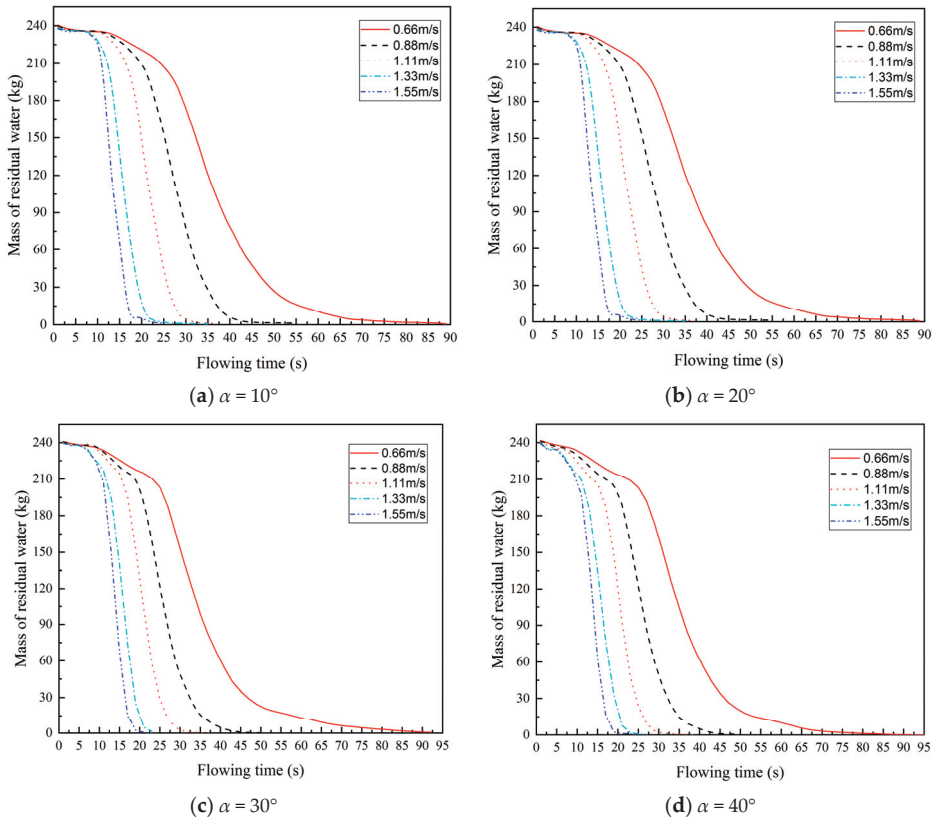


Figure 19. The remaining mass change curve of the water in the pipe.

To sum up, when the inclined angle of the pipeline is the same, the water carrying capacity of oil flow increases with the increase of oil inlet velocity. In addition, when the inclined angle of the pipeline changes, the time required to completely carry the accumulated water in the pipeline out of the pipeline under different inclined angles are shown in Figure 20. As the inclined angle increases from  $10^\circ$  to  $20^\circ$ , the power of part of the water mass moving along the inclined pipe is mainly caused by the shearing action of the high-speed oil and water. At this time, the water-carrying capacity of the oil is gradually increased. The time to completely carry water out of the pipeline is shortened. As the inclined angle of the pipeline increases from  $20^\circ$  to  $40^\circ$ , the increase in the inclined angle of the pipeline gradually converts the kinetic energy of the oil phase into gravitational potential energy, resulting in insufficient water-carrying power of the oil phase and reduced water-carrying capacity, and the oil phase will completely carry out the water. The time required for the pipeline gradually increases. Therefore, as the inclination of the pipeline increases, the water-carrying capacity of oil first increases and then decreases.

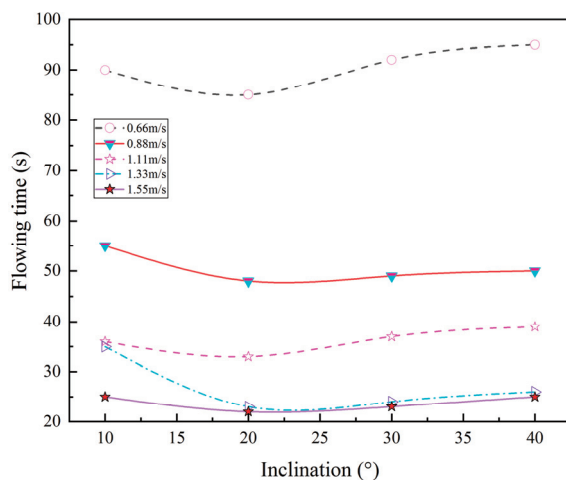


Figure 20. The time required for carrying water by oil with different inclined angles.

## 5. Conclusions

(1) A numerical model based on LES-VOF in the small-diameter pipeline was established. It was applied to study the law of oil carrying water in Lanzhou–Jiangyou section of Lan–Cheng–Yu product oil pipeline. Combined with the research literature on the small pipe diameter and the simulation results of Lan–Cheng–Yu pipeline, it can be seen that the flow patterns in the pipeline of oil carrying water in both large pipe diameter and small pipe diameter mainly include stratified flows, wavy stratified flows, and dispersed flows.

(2) As the pipeline inclined angle is 10~20° and the oil inlet velocity is 0.66 m/s, the flow patterns in the pipeline mainly include stratified flows and wavy stratified flows. As the oil inlet velocity is 0.88~1.55 m/s, the flow patterns in the pipe are mainly stratified flow, wavy stratified flow, and dispersed flow. As the inclined angle of the pipeline is 30~40°, there are three main types of flow in the pipeline: stratified flows, wavy stratified flows, and dispersed flows. The increase of oil inlet velocity accelerates the transition between different flow patterns.

(3) As the maximum positive shear rate is less than or equal to  $17.5 \text{ s}^{-1}$ , the flow pattern in the pipe is a stratified flow. As the maximum positive shear rate is between  $18.2\text{--}28.1 \text{ s}^{-1}$ , the flow pattern in the pipe is a wavy stratified flow. As the maximum positive shear rate is between  $54.1\text{--}67.5 \text{ s}^{-1}$ , the flow pattern in the pipe is a dispersed flow.

(4) The simulation results show that the accumulated water in the pipe can be cleaned from the bottom of the pipe by the oil flow. With the increase of oil phase inlet flow rate, the water carrying capacity of oil also increases. As the pipeline inclined angle increases from 10° to 40°, the water carrying capacity of oil firstly increases and then decreases.

**Author Contributions:** Data analysis, T.Z., B.C.; writing—original draft preparation, T.Z., B.C.; writing—review and editing, T.Z., B.C.; designed the research framework, K.S., W.C. All authors have read and agreed to the published version of the manuscript.

**Funding:** This research received no external funding.

**Conflicts of Interest:** The authors declare no conflict of interest.

## References

- Shi, H.; Wang, L.; Luan, L. Aseismic design of Lanzhou-Chengdu-Chongqing oil product pipeline. *Oil Gas Storage Transp.* **2009**, *28*, 57–93.

2. Zhou, L. Construction experiences of Lanzhou-Chengdu-Chongqing transportation oil pipeline. *Pipeline Tech. Equip.* **2006**, *3*, 1–2. [CrossRef]
3. Wang, R.; Liu, X.; Wang, D. Discussion on formation mechanism of landslide disaster and its prevention. *J. Jiangnan Pet. Univ. Staff Work.* **2015**, *28*, 41–43. [CrossRef]
4. Jin, Z. Corrosion failure analysis of a certain product oil pipeline. *Pet. Tubul. Goods Instrum.* **2015**, *1*, 54–58. [CrossRef]
5. Liu, G.; Hao, J.; Lu, X.; Chen, L.; Sui, B. Development of monitoring system carrying impurity of product oil and corrosion in oil pipeline. *Res. Explor. Lab.* **2017**, *36*, 59–63, 102. [CrossRef]
6. Li, T.; Fan, J.; Liang, Y.; Liu, Y. The numerical simulation of the water's motion states in oil pipeline. *J. Shandong Univ. Technol.* **2015**, *29*, 60–65. [CrossRef]
7. Liu, M.; Jiang, Y.; Han, S.; Lv, X.; Ren, A.; Liu, W.; Yan, B.; Chen, X. Internal corrosion cause analysis of a products pipeline before putting into operation. *Corros. Sci. Prot. Technol.* **2018**, *30*, 496–502. [CrossRef]
8. Xu, G.; Zhang, G.; Zhao, S. An experiment on dewatering for lower location of pipeline. *Oil Gas Storage Transp.* **2011**, *30*, 369–372.
9. Liu, E.; Li, W.; Cai, H.; Peng, S. Formation mechanism of trailing oil in product oil pipeline. *Processes* **2019**, *7*, 7. [CrossRef]
10. Song, X.; Xiong, K.; Zhu, J.; Yu, D. Influence of water carrying capacity of oil products on internal corrosion of pipelines. *Oil Gas Storage Transp.* **2015**, *34*, 834–838. [CrossRef]
11. Peng, S.; Chen, Q.; Zheng, C.; Liu, E. Analysis of particle deposition in a new-type rectifying plate system during shale gas extraction. *Energy Sci. Eng.* **2019**, *8*, 702–717. [CrossRef]
12. Zhang, P.; Zhang, J.; Li, W.; Jiang, H.; Gong, J. Research on oil-water displacement in upward inclined pipes. *Nat. Gas Oil* **2019**, *37*, 8–14. [CrossRef]
13. Su, Z.; Liu, E.; Xu, Y.; Xie, P.; Shang, C.; Zhu, Q. Flow field and noise characteristics of manifold in natural gas transportation station. *Oil Gas Sci. Technol.* **2019**, *74*, 70. [CrossRef]
14. Zhao, S.; Hao, Y. Study on numerical simulation of the wave characteristics at oil-water interface in upward inclined pipeline. *Chem. Equip. Technol.* **2014**, *35*, 10–13. [CrossRef]
15. Song, X.; Li, D.; Sun, X.; Mou, X.; Chen, Y.; Yang, Y. Numerical modeling of the critical pipeline inclination for the elimination of the water accumulation on the pipe floor in oil-water fluid. *Petroleum* **2020**. [CrossRef]
16. Song, X.; Yang, Y.; Zhang, T.; Xiong, K.; Wang, Z. Studies on water carrying of diesel oil in upward inclined pipes with different inclined angle. *J. Pet. Sci. Eng.* **2017**, *157*, 780–792. [CrossRef]
17. Xu, G.; Cai, L.; Ullmann, A.; Brauner, N. Experiments and simulation of water displacement from lower sections of oil pipelines. *J. Pet. Sci. Eng.* **2016**, *147*, 829–842. [CrossRef]
18. Magnini, M.; Ullmann, A.; Brauner, N.; Thome, J. Numerical study of water displacement from the elbow of an inclined oil pipeline. *J. Pet. Sci. Eng.* **2018**, *166*, 1000–1017. [CrossRef]
19. Zhu, S.; Mou, X.; Li, W.; Song, X.; Gu, L. An experimental study on the flow patterns of oil-water two-phase flow in an upwardly inclined pipe. *J. Southwest Pet. Univ.* **2019**, *41*, 144–151. [CrossRef]
20. Wen, S.; Zhang, T.; Zhang, Q. Phase distribution identification method for oil-water two-phase flow in up dip. *Oil Gas Storage Transp.* **2019**, *38*, 1022–1028. [CrossRef]
21. Gao, H.; Gu, H.; Guo, L. Numerical study of stratified oil–water two-phase turbulent flow in a horizontal tube. *Int. J. Heat Mass Transf.* **2003**, *46*, 749–754. [CrossRef]
22. Garmroodi, M.D.; Ahmadpour, A. Numerical simulation of stratified waxy crude oil and water flows across horizontal pipes in the presence of wall heating. *J. Pet. Sci. Eng.* **2020**, *193*, 107458. [CrossRef]
23. Xu, G.; Zhang, G.; Liu, G.; Zhang, X.; Zhang, Y. Distribution Model of Water Phase Interface in Oil Transportation Pipeline with Water. *Oil Gas Storage Transp.* **2010**, *29*, 821–826. [CrossRef]
24. Xu, G.; Zhang, G.; Brauner, N.; Ullmann, A.; Liu, G.; Zhang, X. Interface profile in oil-dragging-water pipeline system. *J. China Univ. Pet.* **2011**, *35*, 124–129. [CrossRef]
25. Zhang, H.; Lan, H.; Lin, N. A numerical simulation of water distribution associated with internal corrosion induced by water wetting in upward inclined oil pipes. *J. Pet. Sci. Eng.* **2019**, *173*, 351–361. [CrossRef]
26. Xu, G.; Zhang, G.; Zhao, S.; Wang, S. Analysis of characteristics of the oil purging water system in horizontal tube. *J. Southwest Pet. Univ.* **2011**, *33*, 173–177, 204. [CrossRef]
27. Wu, J.; Jiang, W.; Liu, Y.; He, Y.; Chen, J.; Qiao, L.; Wang, T. Study on hydrodynamic characteristics of oil-water annular flow in 90° elbow. *Chem. Eng. Res. Des.* **2020**, *153*, 443–451. [CrossRef]

28. Ersoy, G.; Sarica, C.; Al-Safran, E.; Zhang, H. Three-phase gas-oil-water flow in undulating pipeline. *J. Pet. Sci. Eng.* **2017**, *156*, 468–483. [CrossRef]
29. Zhang, T.; Chen, B.; Wen, S.; Song, X.; Zhang, Z. Numerical study on diesel oil carrying water behaviors in inclined pipeline based on large eddy simulation. *IEEE Access* **2019**, *7*, 123219–123230. [CrossRef]
30. Lafmejani, S.S.; Olesen, A.C.; Kær, S.K. VOF modelling of gas–liquid flow in PEM water electrolysis cell micro-channels. *Int. J. Hydrogen Energy* **2017**, *42*, 16333–16344. [CrossRef]
31. Labourasse, E.; Lacanette, D.; Toutant, A.; Lubin, P.; Vincent, S.; Lebaigue, O.; Caltagirone, J.P.; Sagaut, P. Towards large eddy simulation of isothermal two-phase flows: Governing equations and a priori tests. *Int. J. Multiphase Flow* **2007**, *33*, 1–39. [CrossRef]
32. Wang, C.; Zheng, X.; Li, L.; Ai, Z. Influence of  $Y^+$  on the calculation of submarine flow field characteristics of LES. *J. Huazhong Univ. Sci. Technol.* **2015**, *43*, 79–83. [CrossRef]
33. Lodh, B.; Das, A.; Singh, N. Investigation of Turbulence for Wind Flow over a Surface Mounted Cube using Wall  $Y^+$  Approach. *Indian J. Sci. Technol.* **2017**, *10*, 1–11. [CrossRef]



© 2020 by the authors. Licensee MDPI, Basel, Switzerland. This article is an open access article distributed under the terms and conditions of the Creative Commons Attribution (CC BY) license (<http://creativecommons.org/licenses/by/4.0/>).

Article

# Analysis of Influence of Floating-Deck Height on Oil-Vapor Migration and Emission of Internal Floating-Roof Tank Based on Numerical Simulation and Wind-Tunnel Experiment

Gao Zhang <sup>1</sup>, Fengyu Huang <sup>1</sup>, Weiqiu Huang <sup>1,\*</sup>, Zhongquan Zhu <sup>2</sup>, Jie Fang <sup>1</sup>, Hong Ji <sup>1</sup>,  
Lipei Fu <sup>1</sup> and Xianhang Sun <sup>1</sup>

<sup>1</sup> Jiangsu Key Laboratory of Oil & Gas Storage and Transportation Technology, Changzhou University, Changzhou 213164, China; e9940610@gmail.com (G.Z.); hfy524320@163.com (F.H.); fangxyjoyce@sina.com (J.F.); jihong@cczu.edu.cn (H.J.); fulipeiupc@163.com (L.F.); sxh19871124@163.com (X.S.)

<sup>2</sup> Yangzhong Environmental Sanitation Administration Agency, Yangzhong 212200, China; zzq0620@126.com

\* Correspondence: hwq213@cczu.edu.cn

Received: 23 June 2020; Accepted: 19 August 2020; Published: 21 August 2020

**Abstract:** Internal floating-roof tanks (IFRTs) are widely used to store light oil and chemical products. However, if the annular-rim gap around the floating deck becomes wider due to abrasion and aging of the sealing arrangement, the static breathing loss from the rim gap will be correspondingly aggravated. To investigate the oil-vapor migration and emissions from an IFRT, the effects of varying both the floating-deck height and wind speed on the oil-vapor diffusion were analyzed by performing numerical simulations and wind-tunnel experiments. The results demonstrate that the gas space volume and the wind speed of an IFRT greatly influence the vapor-loss rate of the IFRT. The larger the gas space volume, the weaker the airflow exchange between the inside and outside of the tank, thereby facilitating oil-vapor accumulation in the gas space of the tank. Furthermore, the loss rate of the IFRT is positively correlated with wind speed. Meanwhile, negative pressures and the vortices formed on the leeward side of the tank. In addition, the higher concentration areas were mainly on the three vents on the downwind side of the IFRT. The results can provide important theoretical support for the design, management, and improvement of IFRTs.

**Keywords:** internal floating-roof tank; evaporation loss; diffusion; numerical simulation; wind tunnel experiment

## 1. Introduction

Internal floating-roof tanks (IFRTs) are widely used to store light oil, oil products, and chemical products. These tanks can significantly reduce the evaporating area of the stored liquids owing to the arrangement of a floating deck, thereby effectively restraining oil evaporation and reducing oil-vapor discharge from the tank. However, even if an IFRT is equipped with a sealing device on the annular-rim gap between the floating deck and the inner tank wall, the oil surface and the tank gas space cannot be completely isolated for the convenience of the floating deck moving up and down [1]. In addition, when the elasticity of the rim seal gradually decreases, and the gap of the rim seal is widened with long-term usage and abrasion, oil evaporation from the rim gap will gradually increase. Furthermore, oil evaporation from the stored liquid into the tank gas space and vapor emissions from the tank gas space into the atmosphere will cause oil loss, environmental pollution, and potential fire hazards [2]. Therefore, the interior mechanism of oil-vapor migration and emissions in IFRTs must be analyzed to ensure their safe operation.

Scientists have conducted many relevant research works, where the combination of numerical simulations and experimental measurements have been widely used as important tools for studying the oil-evaporation loss mechanism. Pasley et al. [3], and Zhao et al. [4], numerically simulated and experimentally measured the distribution of wind speeds and flow field around an external floating-roof tank and above the floating deck, and they observed that the airflow had two different flow characteristics each for the floating deck at lower positions and higher positions, respectively. Uematsuet et al. [5,6], investigated the wind-force distribution and the buckling behavior for open-topped oil-storage tanks. Wang et al. and Huang et al. [7–9], and Karbasian et al. [10], compared the effects of different oil-collection methods, oil-collection rates, and initial oil-vapor-mass fractions on the oil-vapor-diffusion law in the storage tank during the collection process of oil products. Hou et al. [11], analyzed the evolution of the flow field, temperature field, pressure field, oil-concentration field, and evaporation rate during the refueling process. In addition, many researchers have also studied other factors affecting oil-vapor emissions, such as vehicle and ship loading operations [12,13], the temperature-change characteristics of oil products in a storage tank [14–17], and the characteristics of oil vapors emitted from oil depots [18–20]. Subsequently, the researchers proposed a series of methods for assessing oil-vapor emissions [21,22]. However, these previously conducted studies have paid little attention to oil-vapor migration and emissions from an IFRT. The oil loss in a storage tank under normal operating conditions can be roughly divided into three processes: (1) heat and mass transfer between the liquid phase and the gas phase in the storage tank; (2) oil-vapor migration in the gas phase (i.e., in the gas space) of an IFRT; (3) oil-vapor emission and diffusion from the gas space into the atmosphere. In this study, the oil-evaporation rates were measured using self-made wind-tunnel experimental measurements. Subsequently, the species transfer model and the realizable  $k-\epsilon$  model in the ANSYS Fluent software were used to simulate the oil-vapor diffusion process in an IFRT, following which the effects of floating-deck heights and ambient wind speeds were investigated.

## 2. Methodology

### 2.1. Experimental Protocol

To measure the oil-evaporation rate and the wind speed in the tank under different operating conditions, a model IFRT (1000 m<sup>3</sup>) was built according to the length ratio of 32:1, as depicted in Figure 1. The inner diameter, wall height, roof height, and rim gap of the tank were 360, 375, 39, and 6 mm, respectively. The size of the vents of the model tank was designed according to the selection principle of the prototype tank as follows:

$$B \geq 0.06D \quad (1)$$

where  $B$  denotes the total effective ventilation area of the model-tank vents, m<sup>2</sup>, and  $D$  is the inner diameter of the tank, m. The effective ventilation area of the model-tank vents should be greater than 0.69 m<sup>2</sup>, and the number of vents should not be less than four. Eventually, the model tank was equipped with four vents, each being 19 mm wide and 10 mm high. Further, the vents were evenly placed at the tank wall near the tank roof. In addition, four different floating-deck heights measuring 88, 176, 264, and 312 mm were set for the IFRT.

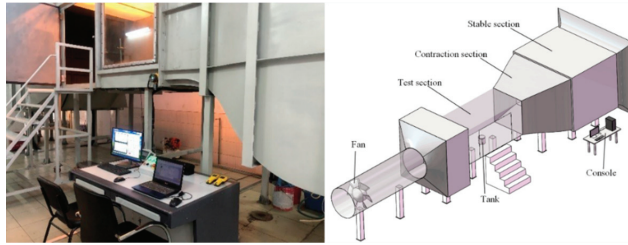


Figure 1. Wind tunnel for the experiment and simulation.

Due to the uncertainty of gasoline composition, the authors used n-hexane as the experimental oil for the convenience of research. The mass-difference method was used to measure the mass change of n-hexane in a certain period of time. The wind fields were generated using a self-made wind tunnel (DFWT-10), the size of the test section is 1.5 (H)  $\times$  1.5 (W)  $\times$  3 m (L), as depicted in Figure 1. The pitot tube anemometer is composed of a static pressure pitot tube (Kimo Instruments Co., Ltd., Bordeaux, France) and a digital micro-manometer (Yokogawa Electric Corporation, Musashino, Japan), which is used for real-time monitoring and feedback of wind speed in the wind tunnel [23]. The wind tunnel could provide wind fields with wind speeds ranging from 0.5 to 20  $\text{m}\cdot\text{s}^{-1}$ . The wind speed, temperature, and humidity were measured using a hot-wire anemometer (TES-1341, TES Co., Ltd., Taiwan, China, having the following specifications: wind-speed range of 0–30  $\text{m}\cdot\text{s}^{-1}$  with a resolution of 0.01  $\text{m}\cdot\text{s}^{-1}$ ; temperature range of  $-10$  to  $-60$   $^{\circ}\text{C}$  with a resolution of 0.01  $^{\circ}\text{C}$ ; humidity range of 10–95% Relative humidity (RH) with a resolution of 0.1% RH). The evaporation loss in the IFRT could be automatically measured using a high-precision electronic balance (WT-30000-1B, Xinheng Electronics Co., Ltd., Shanghai, China, having a range of 0–30 kg with a resolution of 0.01 g). The mass of n-hexane was measured before and after the experiment, and the change in the mass could be calculated as the mass loss of n-hexane during this period. Subsequently, the variation in the mass per unit time can also be calculated as the mass-loss rate of n-hexane. The experiments were arranged under the following conditions: the ambient temperature of 13  $^{\circ}\text{C}$ , and wind speeds of 4.36 and 6.36  $\text{m}\cdot\text{s}^{-1}$ . The wind direction was directly opposite one of the four vents on the tank wall, and the mass-loss rates of n-hexane under different wind speeds were measured respectively.

## 2.2. Theoretical Models for Oil-Vapor Diffusion

### 2.2.1. Basic Governing Equations

The single-phase multicomponent diffusion problem without chemical reaction needs to be solved using the mass- and momentum-conservation equations. The mass-conservation equation can be written as follows:

$$\frac{\partial \rho}{\partial t} + \nabla \cdot (\rho \vec{v}) = S_m \quad (2)$$

where  $S_m$  denotes the mass source term (in  $\text{kg}\cdot\text{m}^{-3}\cdot\text{s}^{-1}$ ), and  $\vec{v}$  the velocity vector ( $\text{m}\cdot\text{s}^{-1}$ ).

The momentum-conservation equation can be written as follows:

$$\frac{\partial}{\partial t}(\rho \vec{v}) + \nabla \cdot (\rho \vec{v} \vec{v}) = -\nabla p + \nabla \cdot [\mu (\nabla \vec{v} + \nabla \vec{v}^T)] + \rho \vec{g} + \vec{F} \quad (3)$$

where  $p$  denotes the static pressure (Pa), and  $\rho \vec{g}$  and  $\vec{F}$  denote the gravitational body force and external body force (both in  $\text{N}\cdot\text{m}^{-3}$ ), respectively. Term  $\mu$  denotes the dynamic viscosity ( $\text{Pa}\cdot\text{s}$ ).

The energy-conservation equation can be written as follows:

$$\frac{\partial}{\partial t}(\rho E) + \nabla \cdot [\vec{v}(\rho E + p)] = \nabla \cdot (k_{eff} \nabla T) + S_h \quad (4)$$

where energy  $E$  ( $\text{J}\cdot\text{kg}^{-1}$ ) and temperature  $T$  (K) are mass average variables,  $k_{eff}$  the effective thermal conductivity ( $\text{W}\cdot\text{m}^{-1}\cdot\text{K}^{-1}$ ), and  $S_i$  the energy source term ( $\text{J}\cdot\text{m}^{-3}\cdot\text{s}^{-1}$ ).

In turbulent flows, the species-conservation equation can be written as follows:

$$\frac{\partial}{\partial t}(\rho Y_i) + \nabla \cdot (\rho \vec{v} Y_i) = -\vec{\nabla} \cdot \vec{J}_i + S_i \quad (5)$$

$$\vec{J}_i = -\left(\rho D_{i,m} + \frac{\mu_t}{S_{ct}}\right) \nabla Y_i - D_{T,i} \frac{\nabla T}{T} \quad (6)$$

where  $Y_i$  denotes the local mass fraction of species  $i$ , and  $\vec{J}_i$  denotes the diffusion flux of species  $i$  ( $\text{kg}\cdot\text{m}^{-2}\cdot\text{s}^{-1}$ ), which arises because of the gradients of concentration and temperature. Furthermore,  $S_i$  denotes the source term ( $\text{kg}\cdot\text{m}^{-3}\cdot\text{s}^{-1}$ ),  $D_{i,m}$  the mass-diffusion coefficient for species  $i$  in the mixture,  $D_{T,i}$  the thermal-diffusion coefficient, and  $S_{ct}$  the turbulent Schmidt number.

### 2.2.2. Turbulence Equation

The oil vapors diffused from the IFRT are greatly affected by the ambient wind, and the oil-diffusion process is a complex unsteady turbulent flow. Therefore, the realizable  $k$ - $\varepsilon$  model with better turbulent accuracy is selected. The following is the modeled transport equation for  $k$  and  $\varepsilon$  in the realizable  $k$ - $\varepsilon$  model:

$$\frac{\partial}{\partial t}(\rho k) + \frac{\partial}{\partial x_j}(\rho k u_j) = \frac{\partial}{\partial x_j} \left[ \left( \mu + \frac{\mu_t}{\sigma_k} \right) \frac{\partial k}{\partial x_j} \right] + G_k + G_b - \rho \varepsilon - Y_M + S_k \quad (7)$$

and

$$\frac{\partial}{\partial t}(\rho \varepsilon) + \frac{\partial}{\partial x_j}(\rho \varepsilon u_j) = \frac{\partial}{\partial x_j} \left[ \left( \mu + \frac{\mu_t}{\sigma_\varepsilon} \right) \frac{\partial \varepsilon}{\partial x_j} \right] + \rho C_1 S_\varepsilon - \rho C_2 \frac{\varepsilon^2}{k + \sqrt{v\varepsilon}} + C_{1\varepsilon} \frac{\varepsilon}{k} C_{3\varepsilon} G_b + S_\varepsilon \quad (8)$$

where

$$C_1 = \max \left[ 0.43, \frac{\eta}{\eta + 5} \right], \quad \eta = S \frac{k}{\varepsilon}, \quad S = \sqrt{2 S_{ij} S_{ij}}$$

In the above-mentioned three equations,  $k$  denotes the turbulence kinetic energy ( $\text{m}^2\cdot\text{s}^{-2}$ ) and  $\varepsilon$  the dissipation rate ( $\text{m}^2\cdot\text{s}^{-3}$ ). Furthermore,  $G_k$  and  $G_b$  denote the generation of the turbulence kinetic energy due to the mean velocity gradients and buoyancy, respectively ( $\text{kg}\cdot\text{m}^{-1}\cdot\text{s}^{-1}$ ).  $Y_M$  denotes the contribution of the fluctuating dilatation in compressible turbulence to the overall dissipation rate ( $\text{kg}\cdot\text{m}^{-1}\cdot\text{s}^{-1}$ ).  $C_2$  and  $C_{1\varepsilon}$  are constants.  $\sigma_k$  and  $\sigma_\varepsilon$  are the turbulent Prandtl numbers for  $k$  and  $\varepsilon$ , respectively.  $S_k$  denotes the source of the turbulence kinetic energy ( $\text{kg}\cdot\text{m}^{-1}\cdot\text{s}^{-3}$ ) and  $S_\varepsilon$  the source of the dissipation rate ( $\text{kg}\cdot\text{m}^{-1}\cdot\text{s}^{-4}$ ).

### 2.3. Physical Model and Methodology

In wind-engineering calculations, the blocking ratio is usually employed as the basis for setting the cross-sectional area of the computational domain. The blocking ratio  $r_b$  is defined as follows:

$$r_b = \frac{A_m}{A_c} \quad (9)$$

where  $A_m$  and  $A_c$  denote the maximum windward area of the model and the cross-sectional area of the computational domain (both in  $\text{m}^2$ ), respectively. If the blocking ratio is less than 5%, the simulation results of the flow field may not be affected by each boundary [24–26]. An experimental model that is too small will increase the difficulty of experimental data measurement and lead to greater errors. We increased the size of the tank in the wind tunnel experiment to make the measurement results more exact. The blockage rate of the wind tunnel experimental model is 6%, calculated by Equation (9). To obtain the numerical-simulation results independent of the computational domain, the computational domain was selected as a cuboid (see Figure 2) of dimensions 2 (H)  $\times$  2 (W)  $\times$  6 (L),



and the size of the model tank (see Figure 3) was consistent with that of the experimental model. A three-dimensional grid-type model of the IFRT was established using ICEM CFD 14.5 software (ANSYS Inc., Pittsburgh, PA, USA).

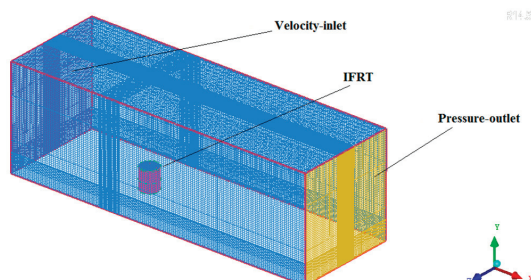


**Figure 2.** Grid model for oil-vapor diffusion of the Internal floating-roof tank (IFRT).

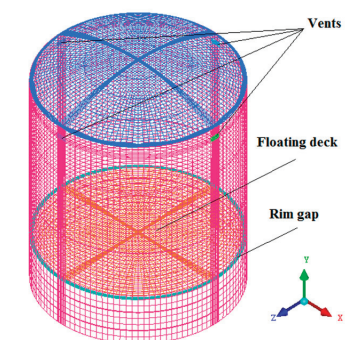


**Figure 3.** Grid model for the IFRT.

In the numerical calculation, the locations where the physical parameters in the flow field change require particular attention. These locations include the annular-rim gap between the floating deck and the inner tank wall of the IFRT, and the four vents on the tank wall. The grid of these regions must be partly encrypted to obtain more accurate numerical solutions. In this study, a structured grid type was designed for the computational domain. The number of cells was approximately 2 million; the quality of the grid was above 0.6, and its independency was also examined. The numerical-calculation procedure was performed using the commercial software package, ANSYS Fluent 14.5. Based on the species-transfer model, the measured oil-vapor-loss rates as the initial values of the mass transfer rate in the annular rim gap. The computational-domain inlet was set as the velocity boundary, and the computational-domain outlet was set as the pressure outlet. The vents on the tank wall were set as the interior boundary. The pressure and velocity were coupled using the SIMPLE scheme, and the spatial discretization of pressure was based on the Standard algorithm. The momentum-conservation equations were discretized using a second-order upwind scheme to reduce the numerical diffusion.

In wind tunnel experiments, we chose the inner floating roof tank as the experimental model.  $Re$  was calculated as 104,495 when the characteristic length is the model diameter, the wind velocity is  $4.36 \text{ m}\cdot\text{s}^{-1}$ , the atmospheric density is  $1.205 \text{ kg}\cdot\text{m}^{-3}$ , and the dynamic viscosity is  $1.81 \times 10^{-5} \text{ Pa}\cdot\text{s}$ . Actually, the model is 1/32 of the actual size, which requires that the inflow speed of the wind tunnel must be 32 times the actual wind speed to achieve  $Re$  equality, it is obviously difficult to achieve. Thus, it is unrealistic to strictly achieve  $Re$  equivalence. Some researchers [27,28] believe that the speed distribution would be independent of  $Re$  if the studied model  $Re$  is over the critical  $Re$ , which is  $Re$ -independence. Based on this, a good agreement was achieved between the CFD simulation and wind-tunnel experiment.

### 3. Results and Analysis

#### 3.1. Verification of the Flow Field

Before using the numerical model, the consistency of the flow field of the numerical simulation must be experimentally verified. This experiment studied the speed boundary layer in the wind tunnel when no tank was placed in the wind tunnel. When the flow speed of the wind tunnel is controlled at  $4 \text{ m}\cdot\text{s}^{-1}$ , the wind speed in the X direction was measured at the center line of the section 500 mm away from the entrance of the wind tunnel test section. The measuring points are 20, 40, 60, 80, 100, 150, 200, 250, 300, 350, 400, 450, 500, 550, and 600 mm from the bottom, respectively. The experimental results are compared with the simulation results, listed in Figure 4. The boundary layer is 60 mm, so the tank is located in a uniform flow. According to Figure 4, the numerical simulation can better simulate the boundary layer conditions of the wind tunnel experiment.

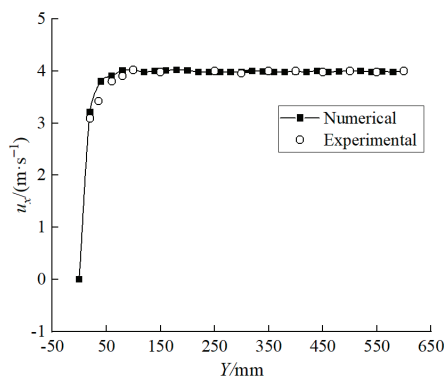


**Figure 4.** Comparison of wind speed in the X direction between the wind-tunnel experiment and numerical simulation on the inlet of 500 mm.

Four points on the tank circumference near the four vents were selected (assuming the center of the tank bottom as the origin). The ambient wind speed was set to  $4.36 \text{ m}\cdot\text{s}^{-1}$ , and the floating-deck height was set to 176 mm. The hot-wire anemometer (TES-1341, TES Co., Ltd., Taiwan, China) was used to measure the wind speeds at these points. Each point was measured five times, and the wind-speed results are presented in Table 1.

**Table 1.** X-axis wind speeds at each measuring point of the tank.

Measuring Point and Its Coordinates, mm	Measured Value, $\text{m}\cdot\text{s}^{-1}$						Simulated Value, $\text{m}\cdot\text{s}^{-1}$	Error, %
	Test 1	Test 2	Test 3	Test 4	Test 5	Average		
Point 1 (190, 360, 0)	0.54	0.53	0.65	0.72	0.61	0.61	0.48	21.3
Point 2 (−190, 360, 0)	2.63	2.71	2.62	2.64	2.68	2.66	2.57	3.4
Point 3 (0, 360, 190)	5.62	4.65	4.70	4.71	4.51	4.84	5.40	11.6
Point 4 (0, 360, −190)	4.76	4.64	4.62	4.51	4.66	4.64	5.39	16.7

It can be seen from Table 1 that the average wind speeds at Points 3 and 4 are approximately equal, both of which are slightly greater than the ambient wind speed of  $4.36 \text{ m}\cdot\text{s}^{-1}$  owing to the effect of the tank body. However, because the airflow was blocked by the tank wall, the average wind speed at Point 2 (which lies in the windward side of the tank) is lower than the ambient wind speed. In addition, the average wind speed at Point 1 (which lies in the back side of the tank) is the smallest. The four measured wind-speed values at Points 1 to 4 basically accord with the distribution law of the flow field around the tank. However, the measured values and the numerically simulated values are slightly different from each other. The reasons for the difference are as follows: (1) although the

flow field is stabilized in general, the uncertainty of turbulence exists partly; the physical parameter (i.e., wind speed) in the flow field fluctuates within a certain range; the measured values are also slightly different at different moments; (2) the error in the measuring instrument itself and the interference of the measuring instrument with the flow field can also cause measurement errors. Therefore, the consistency of the flow field of the numerical simulation was verified using the experiment, and the numerical-simulation model can be considered to be relatively suitable for oil-vapor-diffusion simulation of an oil tank.

### 3.2. Influence of Different Floating-Deck Heights on N-Hexane-Loss Rates

It can be seen from the experimental results in Table 2 that the loss rates of n-hexane can be influenced greatly by varying both floating-deck heights and wind speeds. In general, the floating-deck heights of the IFRT were positively correlated with the evaporation rates of n-hexane. However, the loss rates increased as the floating-deck heights and wind speeds increased. For the ambient wind speeds of 4.36 and 6.36 m·s<sup>-1</sup>, setting the floating-deck height to 312 mm (the highest height), the loss rates of n-hexane reached  $4.139 \times 10^{-6}$  and  $5.960 \times 10^{-6}$  kg·s<sup>-1</sup>, respectively. However, upon setting the floating-deck height to 88 mm (the lowest height), the loss rates were only  $2.189 \times 10^{-6}$  and  $3.773 \times 10^{-6}$  kg·s<sup>-1</sup>, respectively.

**Table 2.** Loss rates of n-hexane measured in model tanks \*.

Floating-Deck Height, mm	Full Coefficient	r1/(10 <sup>-6</sup> kg·s <sup>-1</sup> )	r2/(10 <sup>-6</sup> kg·s <sup>-1</sup> )
88	0.24	2.189	3.773
176	0.48	2.719	4.453
264	0.71	3.560	5.272
312	0.84	4.139	5.960

\*: r1, r2—The loss rates measured for the wind speed of 4.36 and 6.36 m·s<sup>-1</sup>, respectively.

The reasons for this phenomenon are as follows: the evaporation of n-hexane is driven by a diffusion process that is induced by the gradient of n-hexane-vapor concentration at the liquid surface. The larger the gas space inside the tank, the slower the gas flow, and thus the less frequent the gas exchange between the tank and the atmosphere. Therefore, the n-hexane-vapor concentration remains at a relatively stable level, and the driving force for n-hexane evaporation was reduced. Conversely, the smaller the gas space inside the tank, the more frequent the gas exchange between the tank and the atmosphere. As a result, the n-hexane vapor in the tank released into the atmosphere, resulting in fresh air entering the tank from the vents. The n-hexane-vapor concentration in the tank was maintained at a low value, increasing the n-hexane-vapor concentration difference between the gas space and the gas-liquid interface, thereby aggravating the evaporation of n-hexane.

### 3.3. Simulation of the Large IFRT

To investigate the concentration-distribution characteristics of the light oil products in the actual IFRT, the authors continued to simulate the oil-vapor-diffusion process in a large IFRT in the length ratio of 1:1 for a 1000 m<sup>3</sup> IFRT. N-hexane was still chosen as the stored oil product. The inner diameter, wall height, roof height, and rim gap of the tank were 11.5, 12.0, 1.254, and 0.2 m, respectively. The outlet boundary of the flow field was set as the pressure outlet boundary condition while the gap between the floating deck and the tank wall was set as the mass-flow boundary condition. The tank bottom, tank wall, and floating deck were all set as no-slip boundaries and the ambient temperature was set at 13 °C. The mass fraction of the saturated concentration of n-hexane when it diffuses in the gap of the floating disk is 0.30, according to the calculation of the saturated vapor pressure of n-hexane at 13 °C. We took the k-ε turbulence model to describe the diffusion process of the oil vapor.

### 3.3.1. Flow-Field Simulation

The streamtraces inside the tank with different floating-deck heights for the ambient wind speed of  $4.36 \text{ m}\cdot\text{s}^{-1}$  were simulated, as depicted in Figures 5–8. As can be seen from Figure 5, in the larger gas space of the tank, a clockwise vortex was formed, and the streamtraces of the vortex resembled the “0” type. As the gas space became smaller, the streamtraces of the vortex in the tank gradually assumed the shape of a flat ellipse (see Figures 6 and 7). Finally, the gas space became sufficiently small, following which the vortex mentioned above was divided into several small vortices; it means that the airflow in the gas space was faster and more disorderly at this moment. Furthermore, the streamtraces outside the tank were simulated, as depicted in Figure 9. It can be seen from the figure that a part of the airflow from the inlet entered the tank and that the other part of the airflow bypassed the tank. Moreover, the airflow behind the tank did not flow in the original direction, and many vortices were generated there.

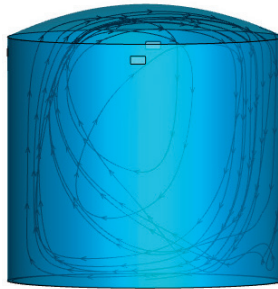


Figure 5. Streamtraces inside the tank for the floating-deck height of 2.82 m.

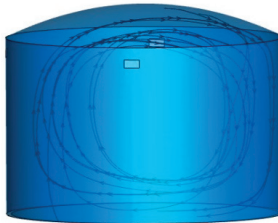


Figure 6. Streamtraces inside the tank for the floating-deck height of 5.63 m.

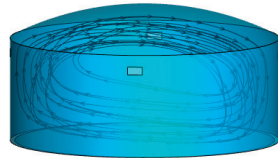


Figure 7. Streamtraces inside the tank for the floating-deck height of 8.45 m.

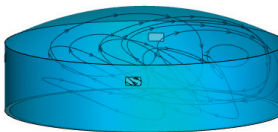


Figure 8. Streamtraces inside the tank for the floating-deck height of 9.98 m.

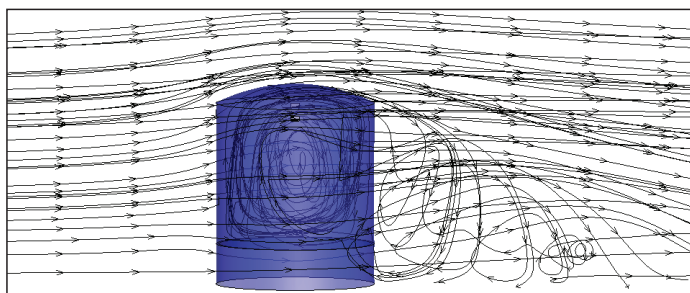


Figure 9. Streamtraces inside and outside the tank.

The diffusion of the n-hexane vapors evaporating from the tank was greatly affected by the ambient wind. In the numerical simulation, the ambient wind was set along the X-axis, and the wind speeds in the inlet were set to 4.36 and 6.36  $\text{m}\cdot\text{s}^{-1}$ , respectively. The velocity-contour distributions both inside and outside the IFRT in the XY plane are depicted in Figures 10 and 11. The results demonstrate that the airflow was obstructed by the tank at the windward side and that the velocity of the airflow was gradually reduced from 4.36 to 0  $\text{m}\cdot\text{s}^{-1}$ . Combined with the pressure-cloud diagram at the windward side of the tank wall in Figure 12, it can be concluded that the pressure on the windward side of the tank body increased because the wind speed translated into stagnation pressure. On the surface of the tank roof, the flow cross-section of the ambient wind shrunk, causing a sudden increase in the wind speed and negative pressure (see Figure 13). The wind speed near the tank roof exceeded the ambient wind speed, and the maximum wind-speed value reached 5.5 and 8.0  $\text{m}\cdot\text{s}^{-1}$ , respectively. On the leeward side of the tank wall, the wind-speed iso-surface continuously shrunk toward the bottom of the tank because of the obstruction of the tank body (see Figures 10 and 11). The minimum value of the wind speed was approximately 0  $\text{m}\cdot\text{s}^{-1}$  at the bottom of the leeward side of the tank wall. Compared to the windward side, the region of lower wind speed was larger in the leeward side. Combined with the wind-flow diagram of the inside and outside of the tank (see Figure 9) and the tank-wall pressure-cloud diagram on the leeward side of the tank (see Figure 13), it can be seen that negative pressure and vortexes appeared near the leeward side of the tank.

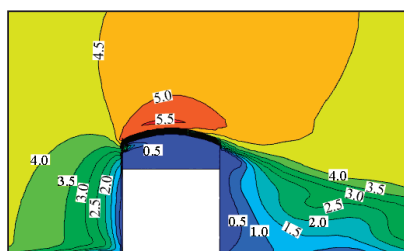


Figure 10. Velocity distribution of the IFRT under the ambient wind speed of 4.36  $\text{m}\cdot\text{s}^{-1}$ .

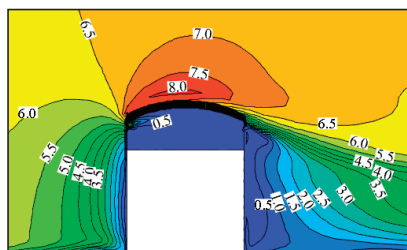


Figure 11. Velocity distribution of the IFRT under the ambient wind speed of 6.36  $\text{m}\cdot\text{s}^{-1}$ .

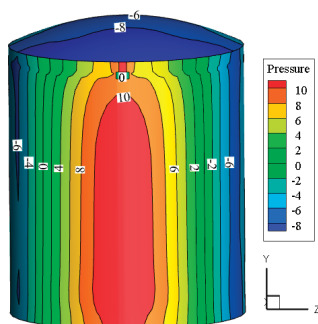


Figure 12. Pressure-cloud diagram for the windward side of the tank wall (Pa).

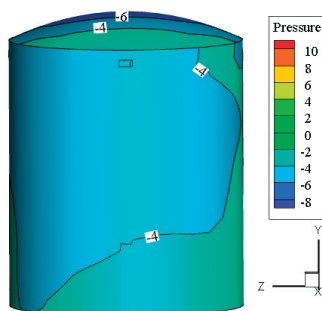


Figure 13. Pressure-cloud diagram for the leeward side of the tank wall (Pa).

Several monitored points were set along the central axis of the tank to obtain the data of wind speed inside the tank, as depicted in Figure 14. The wind speed in the tank was low because the sizes of the vents were too small relative to the size of the gas space. It can be seen from Figure 15 that for the ambient wind speed of  $4.36 \text{ m}\cdot\text{s}^{-1}$ , the velocities of the airflow in the gas space of the tank were less than  $0.6 \text{ m}\cdot\text{s}^{-1}$ . In addition, upon lowering the floating-deck height, the speeds measured from the monitored points changed greatly. The wind speeds at the points near the roof and floating deck were higher than those at other monitored points, while the wind speed at the center of the gas space was low. The minimum wind speed in the gas space was approximately  $0.05 \text{ m}\cdot\text{s}^{-1}$ . Upon increasing the height of the floating deck, the low-velocity region gradually reduced. When the floating-deck height reached a certain height, the velocity distribution became irregular. This irregularity reconfirmed the conclusions drawn previously that upon changing the floating-deck height, the streamtraces of the airflow in the tank also changed.

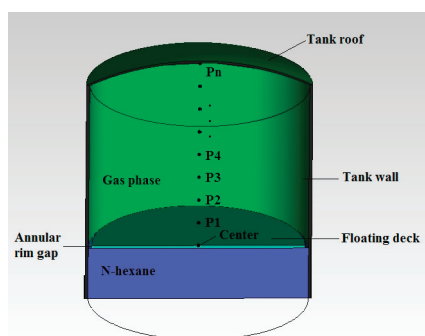


Figure 14. Location of monitored points.

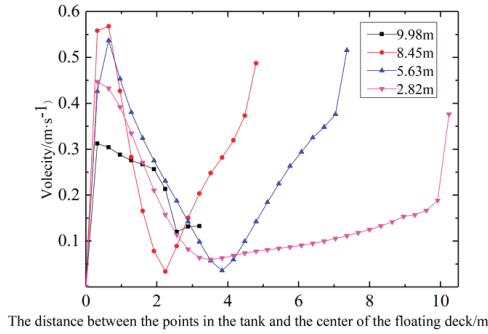


Figure 15. Velocities inside the tank for different floating-deck heights.

### 3.3.2. Concentration Distribution of N-Hexane Vapor in the Tank

The concentration distribution at different floating-deck heights in the tank is depicted in Figure 16. It can be seen that upon increasing the wind speed under a fixed floating-deck height, the concentration of n-hexane in the gas space in the tank becomes low. The higher concentration of n-hexane vapors was mainly distributed near the rim gap, and the concentration distribution of n-hexane vapors in the upper gas space of the tank was relatively uniform. Upon setting the floating-deck height to 2.82 m, because of the resulting large gas space in the tank, the airflow inside and outside the tank is exchanged infrequently, and thus the concentration of n-hexane in the tank becomes evenly distributed. Upon increasing the floating-deck height to 5.63 m, the n-hexane-vapor concentration was affected by the air inflow, which formed a large vortex in the tank. Upon further raising the floating-deck height to 8.45 m, the gas exchange between the inside and outside of the tank was accelerated, and thus the large vortex in the tank was destroyed (wind speed = 6.36 m·s<sup>-1</sup>) or compressed (wind speed = 4.36 m·s<sup>-1</sup>) because of the reduction of the gas space in the tank. Furthermore, upon increasing the floating-deck height to 9.98 m, the n-hexane vapors were mainly concentrated in the area near the gap. In addition, n-hexane vapors at other regions were quickly discharged out of the tank along with the airflow, and it became difficult for the n-hexane vapors to stay in the tank.

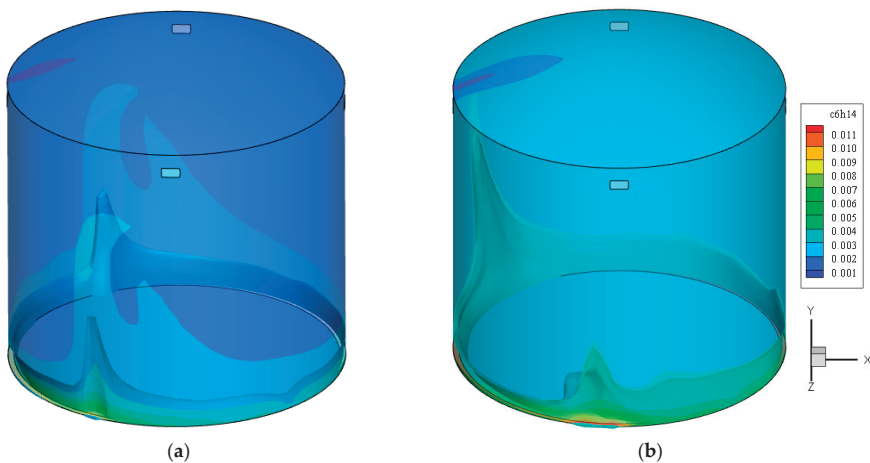
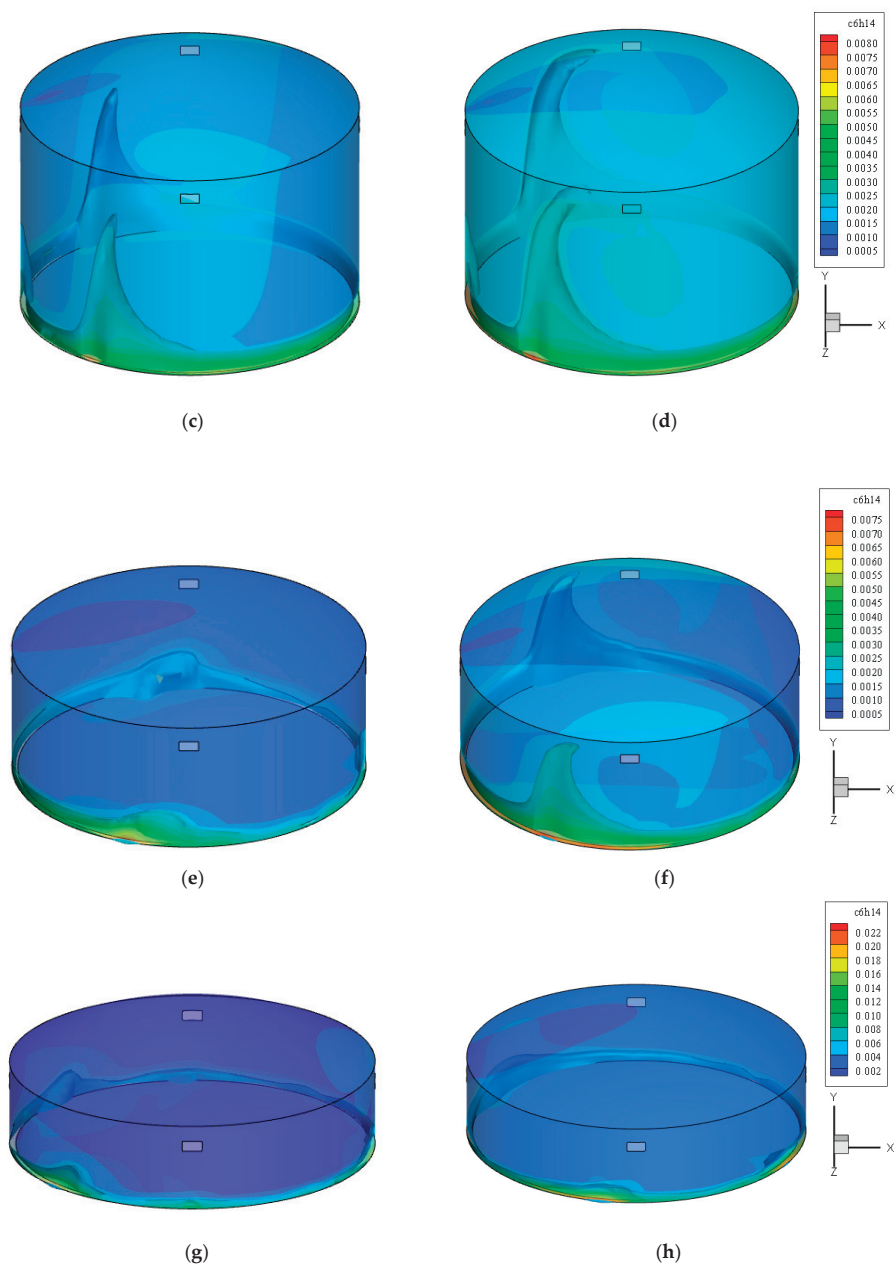


Figure 16. Cont.



**Figure 16.** Distribution of n-hexane vapors (mass fraction) in the IFRT at different floating-deck heights. (a) Wind speed =  $4.36 \text{ m}\cdot\text{s}^{-1}$ , floating-deck height = 2.82 m. (b) Wind speed =  $6.36 \text{ m}\cdot\text{s}^{-1}$ , floating-deck height = 2.82 m. (c) Wind speed =  $6.36 \text{ m}\cdot\text{s}^{-1}$ , floating-deck height = 5.63 m. (d) Wind speed =  $4.36 \text{ m}\cdot\text{s}^{-1}$ , floating-deck height = 5.63 m. (e) Wind speed =  $6.36 \text{ m}\cdot\text{s}^{-1}$ , floating-deck height = 8.45 m. (f) Wind speed =  $4.36 \text{ m}\cdot\text{s}^{-1}$ , floating-deck height = 8.45 m. (g) Wind speed =  $6.36 \text{ m}\cdot\text{s}^{-1}$ , floating-deck height = 9.98 m. (h) Wind speed =  $4.36 \text{ m}\cdot\text{s}^{-1}$ , floating-deck height = 9.98 m.



The n-hexane-vapor emission from the IFRT was also investigated; the floating-deck height was at 9.98 m, wind speed  $4.36 \text{ m}\cdot\text{s}^{-1}$ , and the concentration distribution as depicted in Figure 17. It can be seen that the n-hexane vapors discharged from the vents on the front and rear sides of the tank were diffused along the wind direction and that the vapors discharged from the leeward-side vent spread around the vent. Irrespective of the front and rear sides or the leeward side of the tank (the vent on the windward side is the airflow inlet), the mass fraction of n-hexane vapors near the vents reached 0.002, and such high concentration of vapors discharged into the atmosphere do not meet environmental safety requirements and will cause air pollution. Therefore, if equipping the vents with an oil-vapor-recovery unit is necessary, priority should be given to the above-mentioned three vents.

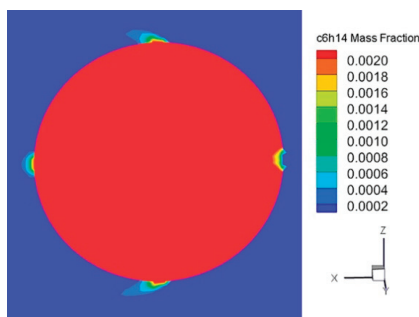


**Figure 17.** Distribution of n-hexane-vapor concentration (mass fraction) near the vents.

#### 4. Conclusions

The evaporative loss rates of n-hexane in the IFRT model and the wind speeds of gas space above the floating deck inside the tank were measured using wind-tunnel experiments and also simulated using ANSYS Fluent software. The conclusions drawn from the research results can be summarized as follows:

- (1) Based on numerical simulation and the wind-tunnel experiments, the oil-vapor diffusion process in the IFRT was simulated and was then verified to be relatively suitable to the oil-vapor-diffusion simulation for different sizes of IFRTs. This further revealed the law of mass transfer between the oil vapors and air for the evaporation and diffusion process in the IFRTs.
- (2) Different floating-deck heights of the IFRT corresponded to different loss rates of n-hexane. The larger the gas space inside the tank, the weaker the airflow exchange between the inside and outside of the tank became. Therefore, the gradient of the n-hexane-vapor in the tank was lower, thereby reducing the driving force for n-hexane evaporation.
- (3) Outside the tank, the direction of the ambient wind would change suddenly while bypassing the tank. In addition, negative pressure and vortices were generated on the leeward side of the tank. Inside the tank, the n-hexane-vapor distribution was relatively uniform at lower floating-deck heights. Upon increasing the floating-deck height, a large vortex formed in the tank, intensifying the airflow disturbance in the tank. Upon further increasing the floating-deck height, the aforementioned large vortex was divided into several small vortices, and the airflow in the gas space became faster and more disorderly than that in the previous floating-height condition.
- (4) The higher vapor-concentration regions near the vents, compared with other regions in the tank, are mainly concentrated on the front and rear sides and the leeward side of the IFRT. Therefore, if it is decided to employ an oil-vapor-recovery unit, more attention should be paid to the regions having higher vapor concentrations.

**Author Contributions:** Conceptualization, G.Z., W.H.; software, F.H.; formal analysis, W.H., G.Z., F.H., L.F. and J.F.; investigation, Z.Z.; data curation, W.H., G.Z., and H.J.; writing—original draft preparation, G.Z., W.H., and X.S.; writing—review and editing, G.Z., W.H., F.H., L.F. and Z.Z.; supervision, W.H.; funding acquisition, W.H. All authors have read and agreed to the published version of the manuscript.

**Funding:** This research was funded by the National Natural Science Foundation of China (No. 51574044 and No. 51804045), the Key Research and Development Program of Jiangsu Province (Industry Foresight and Common Key Technology) (No. BE2018065), the Sci & Tech Program of Changzhou (No. CJ20180053) and Postgraduate Research & Practice Innovation Program of Jiangsu Province (NO. SJCX19\_0668).

**Conflicts of Interest:** The authors declare no conflict of interest.

## References

- Huang, W.Q.; Huang, F.Y.; Fang, J.; Fu, L.P. A calculation method for the numerical simulation of oil products evaporation and vapor diffusion in an internal floating-roof tank under the unsteady operating state. *J. Petrol. Sci. Eng.* **2020**, *188*, 106867. [CrossRef]
- Zhu, Y.; Qian, X.M.; Liu, Z.Y.; Huang, P.; Yuan, M.Q. Analysis and assessment of the Qingdao crude oil vapor explosion accident: Lessons learnt. *J. Loss Prev. Process Ind.* **2015**, *33*, 289–303. [CrossRef]
- Pasley, H.; Clark, C. Computational fluid dynamics study of flow around floating-roof oil storage tanks. *J. Wind Eng. Ind. Aerodyn.* **2000**, *86*, 37–54. [CrossRef]
- Zhao, C.L.; Huang, W.Q.; Zhong, J.; Wang, W.J.; Xu, X.Y.; Wang, Y.X. Numerical simulation of oil vapor leakage from external floating-roof tank. *CIESC J.* **2014**, *65*, 4203–4209.
- Uematsu, Y.; Koo, C.; Yasunaga, J. Design wind force coefficients for open-topped oil storage tanks focusing on the wind-induced buckling. *J. Wind Eng. Ind. Aerodyn.* **2014**, *130*, 16–29. [CrossRef]
- Uematsu, Y.; Yasunaga, J.; Koo, C. Design wind loads for open-topped storage tanks in various arrangements. *J. Wind Eng. Ind. Aerodyn.* **2015**, *138*, 77–86. [CrossRef]
- Wang, Z.L.; Huang, W.Q.; Ji, H. Numerical simulation of vapor diffusion and emission in loading gasoline into dome roof tank. *Acta Petrol. Sin. Petrol. Process. Sect.* **2017**, *33*, 26–33.
- Huang, W.Q.; Wang, Z.L.; Ji, H.; Zhao, C.L.; Lv, A.H.; Xu, X.Y.; Wang, Y.H. Experimental determination and numerical simulation of vapor diffusion and emission in loading gasoline into tank. *CIESC J.* **2016**, *67*, 4994–5005.
- Jing, H.B.; Huang, W.Q.; Ji, H.; Hu, B.G. Study on similarity criteria number of wind tunnel experiment for oil vapor diffusion based on numerical simulation technology. *J. Changzhou Univ.* **2020**, *32*, 83–92.
- Karbasian, H.R.; Kim, D.Y.; Yoon, S.Y.; Ahn, J.H.; Kim, K.C. A new method for reducing VOCs formation during crude oil loading process. *J. Mech. Sci. Technol.* **2017**, *31*, 1701–1710. [CrossRef]
- Hou, Y.; Chen, J.; Zhu, L.; Sun, D.; Li, J.; Jie, P. Numerical simulation of gasoline evaporation in refueling process. *Adv. Mech. Eng.* **2017**, *9*, 1687814017714978. [CrossRef]
- Milazzo, M.F.; Ancione, G.; Lisi, R. Emissions of volatile organic compounds during the ship-loading of petroleum products: Dispersion modelling and environmental concerns. *J. Environ. Manag.* **2017**, *204*, 637–650. [CrossRef] [PubMed]
- Hata, H.; Yamada, H.; Kokuryo, K.; Okada, M.; Funakubo, C.; Tonokura, K. Estimation model for evaporative emissions from gasoline vehicles based on thermodynamics. *Sci. Total Environ.* **2018**, *618*, 1685–1691. [CrossRef]
- Sun, W.; Cheng, Q.; Zheng, A.; Zhang, T.; Liu, Y. Research on coupled characteristics of heat transfer and flow in the oil static storage process under periodic boundary conditions. *Int. J. Heat Mass Transf.* **2018**, *122*, 719–731. [CrossRef]
- Wang, M.; Zhang, X.; Yu, G.; Li, J.; Yu, B.; Sun, D. Numerical study on the temperature drop characteristics of waxy crude oil in a double-plate floating roof oil tank. *Appl. Therm. Eng.* **2017**, *124*, 560–570. [CrossRef]
- Wang, M.; Yu, B.; Zhang, X.; Yu, G.; Li, J. Experimental and numerical study on the heat transfer characteristics of waxy crude oil in a 100,000 m<sup>3</sup> double-plate floating roof oil tank. *Appl. Therm. Eng.* **2018**, *136*, 335–348. [CrossRef]
- Sun, W.; Cheng, Q.; Zheng, A.; Gan, Y.; Gao, W.; Liu, Y. Heat flow coupling characteristics analysis and heating effect evaluation study of crude oil in the storage tank different structure coil heating processes. *Int. J. Heat Mass Transf.* **2018**, *127*, 89–101. [CrossRef]

18. Jovanovic, J.; Jovanovic, M.; Jovanovic, A.; Marinovic, V. Introduction of cleaner production in the tank farm of the Pancevo Oil Refinery, Serbia. *J. Clean. Prod.* **2010**, *18*, 791–798. [CrossRef]
19. Kountouriotis, A.; Aleiferis, P.G.; Charalambides, A.G. Numerical investigation of VOC levels in the area of petrol stations. *Sci. Total Environ.* **2014**, *470*, 1205–1224. [CrossRef]
20. Wei, W.; Lv, Z.; Yang, G.; Cheng, S.; Li, Y.; Wang, L. VOCs emission rate estimate for complicated industrial area source using an inverse-dispersion calculation method: A case study on a petroleum refinery in Northern China. *Environ. Pollut.* **2016**, *218*, 681–688. [CrossRef]
21. Sharma, Y.; Majhi, A.; Kukreti, V.; Garg, M. Stock loss studies on breathing loss of gasoline. *Fuel* **2010**, *89*, 1695–1699. [CrossRef]
22. Tamaddoni, M.; Sotudeh-Gharebagh, R.; Nario, S.; Hajhosseinzadeh, M.; Mostoufi, N. Experimental study of the VOC emitted from crude oil tankers. *Process Saf. Environ. Protect.* **2014**, *92*, 929–937. [CrossRef]
23. Klopfenstein, R., Jr. Air velocity and flow measurement using a Pitot tube. *ISA Trans.* **1998**, *37*, 257–263. [CrossRef]
24. Baetke, F.; Werner, H.; Wengle, H. Numerical simulation of turbulent flow over surface-mounted obstacles with sharp edges and corners. *J. Wind Eng. Ind. Aerodyn.* **1990**, *35*, 129–147. [CrossRef]
25. Saathoff, P.; Melbourne, W. Freestream turbulence and wind tunnel blockage effects on streamwise surface pressures. *J. Wind Eng. Ind. Aerodyn.* **1987**, *26*, 353–370. [CrossRef]
26. Holmes, J.D. *Wind Loading of Structures*; CRC Press: Boca Raton, FL, USA, 2018.
27. Uehara, K.; Wakamatsu, S.; Ooka, R. Studies on critical Reynolds number indices for wind-tunnel experiments on flow within urban areas. *Bound. Layer Meteor.* **2003**, *107*, 353–370. [CrossRef]
28. Cui, P.Y.; Li, Z.; TAO, W.Q. Wind-tunnel experiment and numerical analysis on flow and dispersion in street canyons. *J. Eng. Thermophys.* **2014**, *35*, 2491–2495.



© 2020 by the authors. Licensee MDPI, Basel, Switzerland. This article is an open access article distributed under the terms and conditions of the Creative Commons Attribution (CC BY) license (<http://creativecommons.org/licenses/by/4.0/>).

Article

# Numerical Simulation on Hydraulic Characteristics of Nozzle in Waterjet Propulsion System

Chuan Wang <sup>1</sup>, Xiaoke He <sup>2</sup>, Li Cheng <sup>1,\*</sup>, Can Luo <sup>1</sup>, Jing Xu <sup>3</sup>, Kun Chen <sup>3</sup> and Weixuan Jiao <sup>1,\*</sup>

<sup>1</sup> College of Hydraulic Science and Engineering, Yangzhou University, Yangzhou 214000, China; wangchuan198710@126.com (C.W.); luocan@yzu.edu.cn (C.L.)

<sup>2</sup> School of Electric Power, North China University of Water Resources and Electric Power, Zhengzhou 450045, China; hexiaoke@ncwu.edu.cn

<sup>3</sup> Ningbo Jushen Pumps Industry Co., Ltd., Ningbo 315100, China; xujing1990mail@126.com (J.X.); skyckun2009@163.com (K.C.)

\* Correspondence: chengli@yzu.edu.cn (L.C.); DX120170049@yzu.edu.cn (W.J.)

Received: 17 October 2019; Accepted: 27 November 2019; Published: 3 December 2019

**Abstract:** As an important over-current component of the waterjet propulsion system, the main function of a nozzle is to transform the mechanical energy of the propulsion pump into the kinetic energy of the water and eject the water flow to obtain thrust. In this study, the nozzle with different geometry and parameters was simulated based on computational fluid dynamics simulation and experiment. Numerical results show a good agreement with experimental results. The results show that the nozzle with a circular shape outlet shrinks evenly. Under the designed flow rate condition, the velocity uniformity of the circular nozzle is 0.26% and 0.34% higher than that of the elliptical nozzle and the rounded rectangle nozzle, respectively. The pump efficiency of the circular nozzle is 0.31% and 0.14% higher than that of the others. The pressure recovery and hydraulic loss of the circular nozzle are superior. The hydraulic characteristics of the propulsion pump and waterjet propulsion system are optimal when the nozzle area is 30% times the outlet area of the inlet duct. Thus, the shaft power, head, thrust, and system efficiency of the propulsion pump and waterjet propulsion system are maximized. The system efficiency curve decreases rapidly when the outlet area exceeds 30% times the outlet area of the inlet duct. The transition curve forms greatly affect thrust and system efficiency. The transition of the linear contraction shows improved uniformity, and the hydraulic loss is reduced. Furthermore, the hydraulic performance of the nozzle with a linear contraction transition is better than that of others.

**Keywords:** hydraulic performance; waterjet propulsion; nozzle; energy loss; efficiency; numerical simulation

## 1. Introduction

Waterjet propulsion is a type of special propulsion system that is different from a propeller. This device has been widely used in many high-speed ships because of its high propulsion efficiency, low noise and vibration, and simple transmission structure [1]. Waterjet propulsion systems are gradually developed from small and medium to large-sized, highly efficient, low noise, and high-speed mechanisms to meet the requirements of industrial production and military operations [2–5]. A stern-mounted waterjet propulsion system used in commercial applications can be divided into four components, namely, inlet duct, propulsion pump, nozzle, and steering device. Each component of the waterjet propulsion system should function effectively to achieve higher efficiency and reduce energy loss. The inlet duct transfers the bottom water to the propulsion pump. Its performance directly affects the efficiency of the waterjet propulsion systems. The hydraulic loss of the inlet duct also strongly influences the water jet propulsion system. From the perspective of energy loss, Verbeek et al. [6] found that approximately 7–9% of the total power is lost in the inlet duct due to local flow separation

and non-uniformity. Jiao et al. [7] used the numerical simulation method to simulate cavitation two-phase flow in the waterjet propulsion pump section and waterjet propulsion system. Ding et al. [8] determined the flow loss of the inlet duct through computational fluid dynamics (CFD). Park et al. [9] observed flow separation and predicted the location of the stagnation point on the lip, in accordance with particle image velocimetry measurement. The flow phenomena occurring within the inlet duct are essential to reduce power loss. The pump is the core component of the waterjet propulsion system, and it delivers the head to produce the jet at the nozzle exit. The main function of the pump is turning the circumrotation power energy into the kinetic energy of water. Waterjet propulsion pumps are of two main types: Mixed-flow pump and axial-flow pump. The efficiency of waterjet propulsion depends on the pump and system efficiency. Insufficient understanding of large deviations between theoretical efficiency and measured efficiency is a major problem in waterjet propulsion design and application. Cao et al. [10] found that the low efficiency was primarily due to the non-uniform inflow of the water-jet pump. Cheng et al. [11] observed the rotating stall region, which is an unstable head curve when many mixed-flow and axial-flow pumps are operated. This region should be generally avoided given the risk of instabilities during pump start and operation. Xia et al. [12] analyzed the rotating stall at a low flow rate and suppressed it with separators. Wang et al. [13,14] simulated the self-priming process of a multistage self-priming centrifugal pump by CFD and optimized the design of a typical multistage centrifugal pump based on energy loss model and CFD. Kim et al. [15] and Etter et al. [16] obtained a number of useful results on the performance optimization of waterjet propulsion pumps through model tests. The thrust of the waterjet propulsion system is obtained by the reaction force of the water flow ejected from the propulsion pump. The main function of the nozzle, which is an important part of the waterjet propulsion system, is to transform the mechanical energy of the propulsion pump into the kinetic energy of the water and eject the water flow to obtain thrust. The gross thrust is used as an alternative because measuring the net thrust of a waterjet installation is cumbersome. The relation between net thrust and gross thrust is not fully understood. Eslamdoost et al. [17] used numerical simulations to investigate this relation. Park et al. [18] conducted a numerical simulation to obtain the complicated viscous flow feature of the waterjet and predict the performance of thrust and torque to obtain waterjet propulsion characteristics. In actual operation, the momentum of the water flow cannot be fully converted into the thrust that propels the ship forward due to the existence of energy loss. The hydraulic loss of the nozzle is closely related to the jet velocity loss because the nozzle is installed immediately after the outlet of the pump. Jian et al. [19] used CFD software Fluent 14.0 for the numerical simulation of four different nozzles and analyzed the effects of geometric and dynamic parameters of nozzles on the momentum thrust of the waterjet propulsion system of autonomous underwater vehicles. Abcand et al. [20], Chin [21], and Jiao et al. [22] performed an overall optimization analysis of the waterjet propulsion system with a nozzle. The steering device can deflect the jet to create steering and reversing forces, and its performance is an important characteristic of the waterjet propulsion [23,24].

In previous decades with the rapid development of computer technology, CFD technology has been widely used in many fields, such as pressure fluctuation and vibration [25–27], heat and mass transfer [28,29], flow control [30,31]. At the same time, the test method is still one of the effective research methods [32–34]. In this study, the nozzle with different geometric parameters was simulated based on CFD simulation and experiment. The influences of the nozzles with different geometric parameters on energy loss, efficiency, internal flow characteristics, and hydraulic performance of waterjet propulsion were investigated. The selection of nozzle affects the waterjet propulsion system efficiency. A reasonable nozzle structure is conducive to improving the propulsion system efficiency and reducing energy consumption.

## 2. Numerical Calculation

### 2.1. Numerical Model

Calculations are performed using the commercial code ANSYS CFX 14.5. ANSYS CFX uses the element-based finite volume method. The hull boundary layer, inflow velocity, and pressure affect the water flow. Thus, the water flow into the inlet duct is not uniform. The water around the inlet of the waterjet propulsion system should also be included in the computational domain. As shown in Figures 1 and 2, the entire model includes the water body and waterjet propulsion pump system, composed of the inlet duct, propulsion pump, and nozzle. The propulsion pump consists of an impeller with six blades and a guide vane with seven vanes. The rotating speed of the impeller is 700 rpm.  $D_0$  represents the inlet diameter of the impeller.  $\theta$  represents the dip angle of the inlet duct.

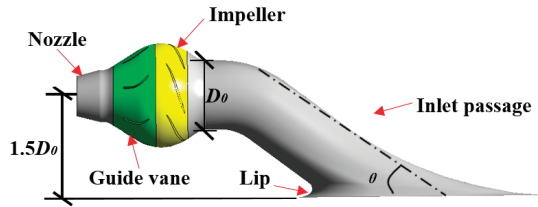


Figure 1. Waterjet propulsion pump system.

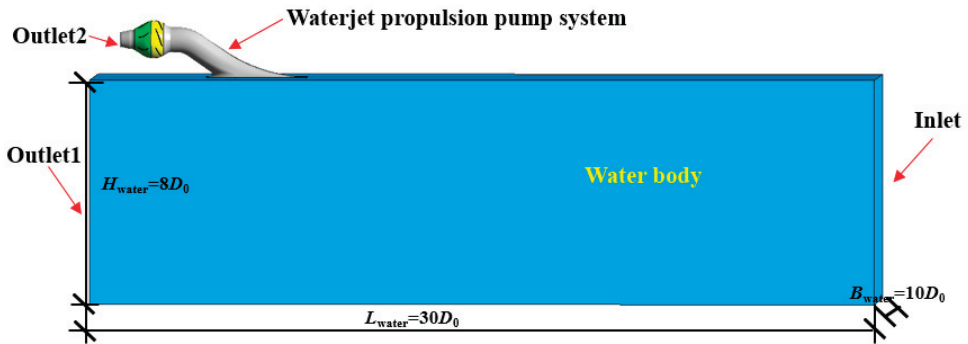


Figure 2. Computational domain.

### 2.2. Governing Equations

Reynolds-averaged  $N$ - $S$  equation and continuity equation were selected to describe the 3D incompressible viscous flow. The continuity equation is as follows:

$$\frac{\partial \rho}{\partial t} + \frac{\partial(\rho u_j)}{\partial x_j} = 0 \tag{1}$$

The momentum conservation equation is as follows:

$$\frac{\partial \rho u_i}{\partial t} + \frac{\partial(\rho u_i u_j)}{\partial x_j} = -\frac{\partial p}{\partial x_i} + \frac{\partial}{\partial x_j} \left[ \mu \left( \frac{\partial u_i}{\partial x_j} + \frac{\partial u_j}{\partial x_i} - \frac{2}{3} \frac{\partial u_i}{\partial x_j} \delta_{ij} \right) \right] + \frac{\partial}{\partial x_j} (-\rho u_i u_j) \tag{2}$$

where  $\rho$  represents water density (in  $\text{m}^3/\text{s}$ ),  $u_i, u_j$  represents velocity component of fluid in the  $i$  and  $j$  directions (in  $\text{m/s}$ ),  $t$  represents time (in  $\text{s}$ ),  $p$  represents pressure (in  $\text{Pa}$ ),  $F_i$  represents volume force component in the  $i$  direction (in  $\text{N}$ ),  $\mu$  represents dynamics viscosity coefficient, and  $x_i, x_j$  represents coordinate component.

### 2.3. Grid Sensitivity Analysis

The computational domain consists of the water body, inlet duct, propulsion pump, and nozzle. The entire computational domain is generated with hexahedral grids and tetrahedral grids by ICEM software. An O-type grid of hexagonal cells was created around the impeller and stator blades by using an extrusion method to ensure good mesh quality in terms of size and skewness. The interior of the impeller and guide vane domain is filled with an unstructured mesh of tetrahedral cells because of the complex topology of the pump. The grid of the calculation domain is shown in Figure 3.

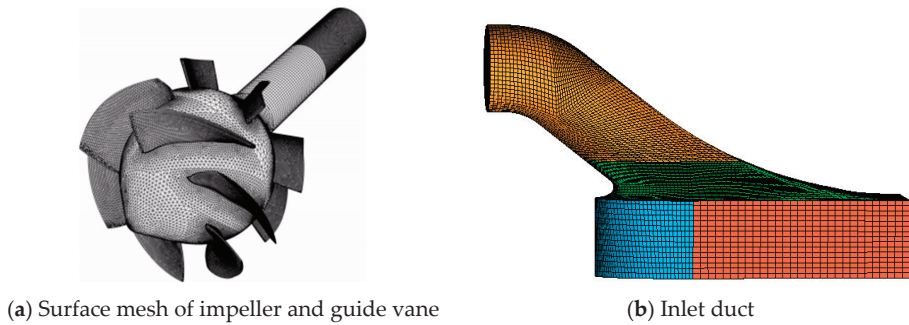


Figure 3. Grid of the computational domain.

A grid sensitivity study was conducted to assess the required grid density. Several grid sizes were considered, ranging from a total number of cells of  $4.3 \times 10^5$  up to  $2.1 \times 10^6$ . The standard  $k-\epsilon$  is selected as the calculation model in this study. Hence, the  $y+$  values are guaranteed to vary between 30 and 100 to satisfy the computational requirements while changing the grid density.

Figure 4 shows the mesh sensitivity analysis of the entire computational domain. The figure reveals that the efficiency and head of the waterjet propulsion pump system increase with the increase in the number of cells. When the number of cells reaches 1.5 million, the head and efficiency remain unchanged with the increase in the number of grids. Theoretically, with the increase in the number and density of grids, the calculation accuracy is generally improved. However, as the number of cells increases, the requirement for computer resources also increases, and the computing speed slows down. Therefore, the final cell number of the entire computational domain is 1,752,299. The  $y+$  value of the propulsion pump is in the range of 30–100 in this study.

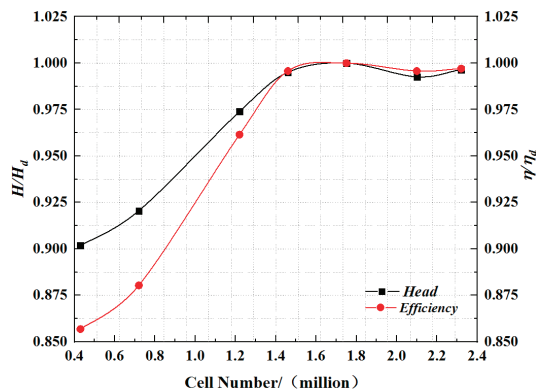


Figure 4. Mesh sensitivity analysis.

## 2.4. Turbulence Model Selecting

The turbulence model was introduced into the numerical calculation to solve the  $N$ - $S$  equations.  $k$ - $\varepsilon$  and  $k$ - $\omega$  are the commonly used turbulence models in calculation [35–37]. To select the most suitable turbulence model for calculation, this study used several different turbulence models, and the numerical results were compared with the experimental results. Table 1 presents the numerical and experimental results of different turbulence models under the operating conditions of 700 rpm. A slight difference was observed between the calculated values. However, under the condition of the standard  $k$ - $\varepsilon$  turbulence model, the calculated values are in good agreement with the experimental values. Therefore, the standard  $k$ - $\varepsilon$  is selected as the calculation model, and the scalable wall-function is used to improve robustness and accuracy.

**Table 1.** Numerical and experimental results with different turbulent models.

Turbulence Model	Standard $k$ - $\varepsilon$	RNG $k$ - $\varepsilon$	Standard $k$ - $\omega$	SST	SSG
$H/H_{td}$	1.0115	1.0263	1.0437	1.0655	1.0271
Efficiency $\eta/\eta_{td}$	1.0237	1.0274	1.1088	1.1098	1.0341

$H_{td}$  represents the test value of head under design flow rate condition.  $\eta_{td}$  represents the test value of pump efficiency under design flow rate condition.

## 2.5. Boundary Conditions

The inlet of the water body was set as the inlet boundary of the entire computational domain, and normal speed 8 m/s was adopted as the inlet boundary condition. The Reynolds number of the water body inlet is  $4.19 \times 10^6$ . The inflow velocity is equal to ship speed, and nominal turbulence intensities (with a value equal to 5%) are used at the inlet boundary. The outlet of the water body and nozzle were set as the outlet boundary. An average static pressure outlet boundary condition is applied with 1 atm at the water body outlet, and the mass-flow rate was adopted as the outlet boundary of the nozzle. No-slip condition was applied at solid boundaries. The interfaces between the rotational impeller and static diffuser were set as the frozen stage condition. The convergence precision is set to  $10^{-5}$ .

## 3. Hydraulic Characteristics Test

### 3.1. Test Rig Set-Up

A test rig is built, as shown in Figure 5, to study the hydraulic performance of the waterjet propulsion pump. The test rig is a closed circulation system that consists of two circulation pipeline systems: Main circulation pipeline and second circulation pipeline. The main circulation pipeline system is designed to ensure the water circulation of the test rig and provide the bottom speed. The second circulation pipeline system is the circulating pipe of the water jet propulsion pump, which is used to test the performance of the waterjet propulsion pump. The propulsion pumping system consists of a propulsion pump, a guide vane, and an inlet duct, as shown in Figure 6.

The propulsion pump with six impeller blades and the guide vane with seven stator vanes are built into the system. The scale model of a waterjet pump is used for ship propulsion. The head, flow rate, torque, and speed were tested to obtain the hydraulic performance of the waterjet propulsion pump. The pump is driven by a DC electromotor at speeds varying from 700 rev/min to 2400 rev/min and equipped with an auxiliary axial pump to regulate the flow rate. The test rig has two electromagnetic flowmeters with an absolute accuracy of  $\pm 0.5\%$ . These flowmeters are used to test the flow rate of the main circulation pipeline system and the second circulation pipeline system. The head of the waterjet propulsion pump is measured by the differential pressure transmitter with an absolute accuracy of  $\pm 0.2\%$ .



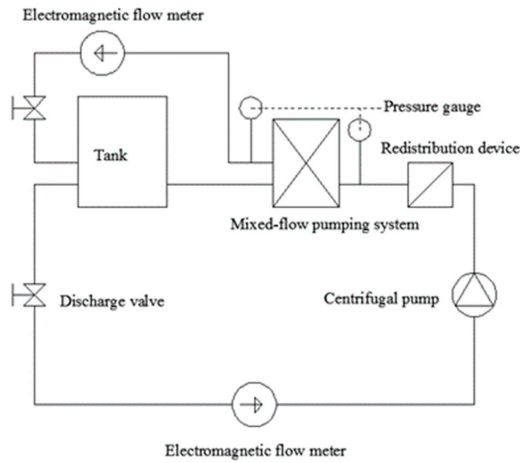


Figure 5. Test rig.

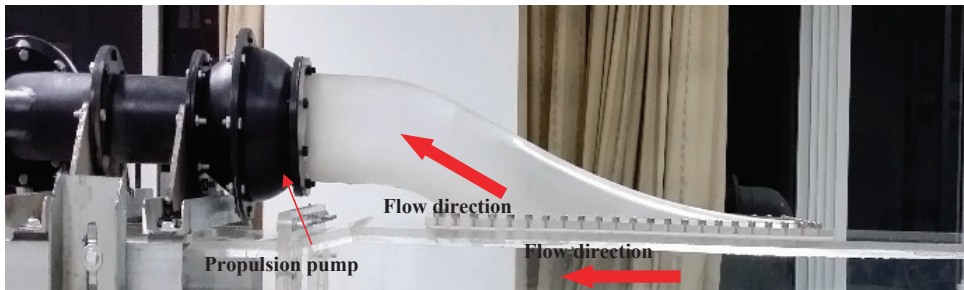


Figure 6. Waterjet propulsion system.

### 3.2. Experimental Verification

As shown in Figure 7, in the numerical calculation, the front section (1—1) of the impeller inlet and the back section of the guide vane outlet (2—2) were considered the pressure measuring sections for the head calculation and analysis.

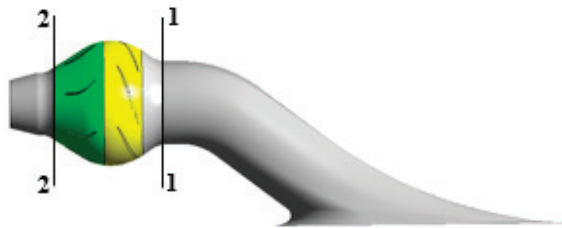


Figure 7. Pressure measuring section.

The pump efficiency  $\eta$ , shaft power  $N$ , and head  $H$  were used to define the hydraulic characteristics of the waterjet propulsion pump system. The calculation formula is as follows:

$$P = P_{2-2} - P_{1-1} \tag{3}$$

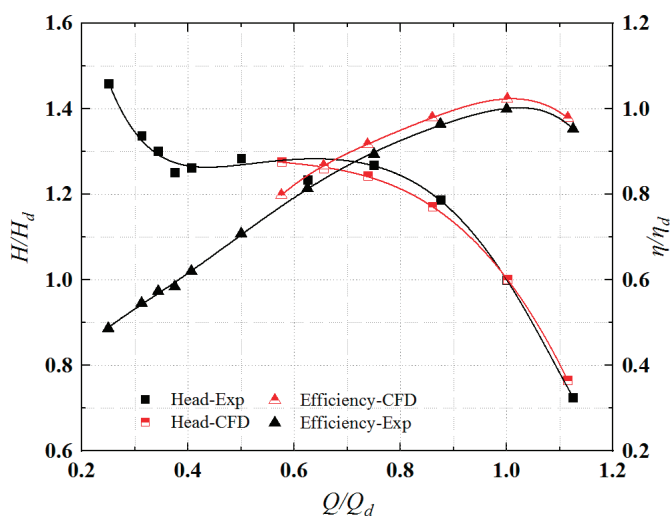
$$H = \frac{P}{\rho g} \tag{4}$$

$$N = \frac{2\pi Tn}{1000 * 60} \quad (5)$$

$$\eta = \frac{\rho g QH}{N} \quad (6)$$

where  $P$  is the pressure of the section (in Pa),  $\rho$  is water density (in  $\text{kg/m}^3$ ),  $g$  is gravitational acceleration (in  $\text{m/s}^2$ ),  $T$  is the torque of blades (in  $\text{N}\cdot\text{m}$ ),  $n$  is the rotating speed of the impeller (in  $\text{r/min}$ ),  $Q$  is the flow rate (in  $\text{m}^3/\text{s}$ ), and  $N$  is the shaft power (in  $\text{kW}$ ).

The comparative finding of the calculation and the experiment results reveals that the overall trend is similar, as shown in Figure 8. In general, the predicted  $H$  and  $\eta$  are in good agreement with the experiment results. Figure 8 shows that the difference between the experiment results and predicted results of  $H$  and  $\eta$  is minimum under the design flow-rate condition. In the numerical results, the performance of the head is better than that in the test results. At the design flow rate, the head difference between the test data and numerical data is 1.2%, and the efficiency difference between them is 2.4%. The findings show that the numerical results are reliable.

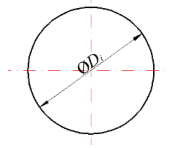
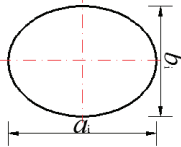
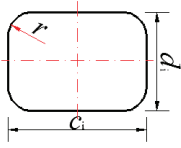
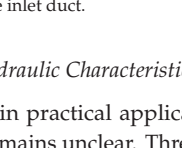


**Figure 8.** Comparison of calculation and experiment results.  $Q_d$  represents the design flow rate.  $H_{BEP}$  and  $\eta_d$  represent the head and efficiency of the waterjet propulsion pump under the designed flow rate condition, respectively.

#### 4. The Influence of Nozzle with Different Geometric Parameters on Hydraulic Characteristics of Waterjet Propulsion System

Conducting an in-depth study on the nozzle is necessary to further improve the hydraulic performance and waterjet propulsion efficiency of the waterjet propulsion system. Nine cases are designed to analyze the influence of nozzles with different geometric parameters on the waterjet propulsion system. As shown in Table 2, Cases 1–3 were selected to further investigate the influence of different nozzle outlet shapes on the hydraulic characteristics of the waterjet propulsion system. Case 1 and Cases 4–7 were selected to further investigate the influence of different nozzle outlet areas on the hydraulic characteristics of the waterjet propulsion system. Case 1 and Cases 8–9 were selected to further investigate the influence of different transition curve forms of the nozzle on the hydraulic characteristics of the waterjet propulsion system.

Table 2. Research cases.

Case	Shape	Area	Transition Curve Form	Note	
				Diagram of Shape	Value
1	Circle	$30\%A_d$	Linear contraction		$D_1 = 0.55 D_0$
2	Elliptical	$30\%A_d$	Linear contraction		$a_2 = 0.33 D_0$ $b_2 = 0.22 D_0$
3	Rounded rectangle	$30\%A_d$	Linear contraction		$c_3 = 0.65 D_0$ $d_3 = 0.43 D_0$ $r = 0.22 D_0$
4	Circle	$10\%A_d$	Linear contraction		$D_1 = 0.32 D_0$
5	Circle	$20\%A_d$	Linear contraction		$D_1 = 0.45 D_0$
6	Circle	$40\%A_d$	Linear contraction		$D_1 = 0.63 D_0$
7	Circle	$50\%A_d$	Linear contraction		$D_1 = 0.71 D_0$
8	Circle	$30\%A_d$	Curve contraction followed by straight line		$D_1 = 0.55 D_0$
9	Circle	$30\%A_d$	Arc contraction	<b>Rounded rectangle</b>	$D_1 = 0.55 D_0$

$A_d$  represents outlet area of the inlet duct.

4.1. The Influence of Different Nozzle Outlet Shapes on the Hydraulic Characteristic

The nozzle with a circular shape was mostly used in practical applications, but whether the hydraulic performance of the circular nozzles is optimal remains unclear. Three different nozzle outlet shapes were set up for comparison, as shown in Figure 9, to explore the influence of different nozzle shapes on the hydraulic characteristics of the waterjet propulsion system. The nozzle outlet section shape is changed under the premise of maintaining a constant outlet area of the nozzle. The outlet section of the nozzle in Case 1 is circular, the outlet section of the nozzle in Case 2 is elliptical, and the outlet section of the nozzle in Case 2 is a rounded rectangle. All three outlet sections of different shapes have an area of  $30\% A_d$ . a and b denote the long axis and short axis of the elliptical outlet section, respectively. Meanwhile, a and b denote the width and height of the rounded rectangle outlet section. The ratio of a and b is 1.5.

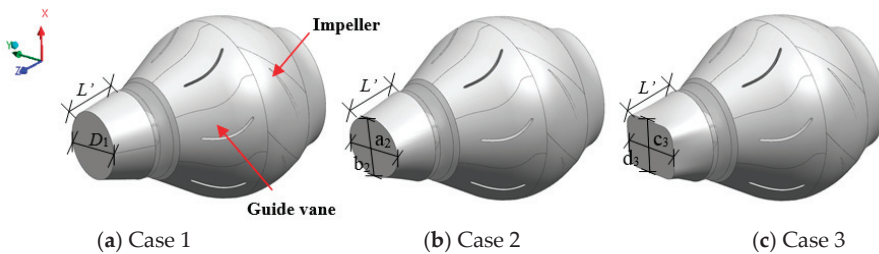


Figure 9. Three-dimensional diagram of nozzles with different shapes.

The pressure coefficient  $C_p$  is used to characterize the change of the nozzle outlet pressure. The pressure coefficient  $C_p$  is a dimensionless value that describes the relative pressure throughout the flow field in fluid dynamics.

$$C_p = \frac{p - \bar{p}}{\frac{1}{2} \rho v_{out}^2} \quad (7)$$

where  $p$  is instantaneous pressure (in Pa),  $\bar{p}$  is average pressure (in Pa), and  $v_{out}$  is averaged outlet velocity at the nozzle (in m/s).

Figure 10 presents the pressure contours and streamlined diagram of the nozzle outlet section with different nozzle shapes. As shown in Figure 10a, the pressure on the outlet of the circular nozzle is distributed uniformly as a ring. The pressure decreases uniformly from the circumference to the center of the circle. The streamline distribution shows that the flow lines on the outlet section intersect at the center of the circle, and the flow direction of the streamlines is consistent with the rotation direction of the impeller mainly because the guide vanes fail to completely recover the velocity loop. As shown in Figure 10b, the pressure distribution of the elliptical nozzle is relatively uneven. The pressure is symmetrically distributed diagonally. The flow direction of the streamlines is consistent with the direction of the rotation of the impeller. The intersection line of the streamlines at the center of the ellipse is curved. Figure 10c shows four high-pressure zones on the outlet section of the rounded rectangle nozzle. The high-pressure zone is mainly distributed at four rounded corners. The area of the high-pressure zones of the upper and lower side walls is larger than that of the left and right side walls. The flow direction of the streamlines is consistent with the direction of the rotation of the impeller. The intersection line of the streamlines at the center of the rounded rectangle is curved.

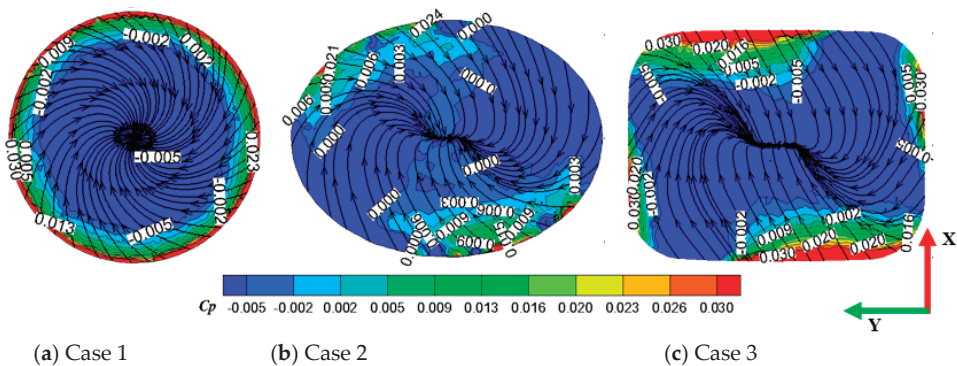


Figure 10. Pressure contours and streamline with different nozzle shapes.

The uniformity of the velocity distribution at the nozzle outlet is represented by the axial velocity distribution coefficient  $\bar{V}$ . The axial velocity distribution is the best when the axial velocity distribution coefficient is close to 100%. The formula for the axial velocity distribution coefficient  $\bar{V}$  is as follows:

$$\bar{V} = \left[ 1 - \frac{1}{u_a} \sqrt{\frac{\sum (u_{ai} - \bar{u}_a)^2}{n}} \right] \times 100\% \quad (8)$$

where  $u_{ai}$  is the axial velocity of each element of the calculated section (in m/s),  $\bar{u}_a$  is the averaged axial velocity of the calculated section (in m/s), and  $n$  is the number of cells of the calculated section.

The velocity uniformity of the three cases is 97.57%, 97.31%, and 97.23%. Different nozzle shapes provide a slight difference in the velocity distribution of the nozzle outlet section. Figure 11 shows the axial velocity distribution curve, and the data point coordinates are normalized. The axial velocity points were uniformly selected for the outlet sections of the three cases along the direction of the vertical

and horizontal centerlines. Figure 11a shows the velocity curve along the vertical direction of the center of the outlet section. The vertical direction is the X-axis direction in Figure 10. The high-velocity zones of the three cases are concentrated in the outlet center. The axial velocity drops rapidly close to the upper and lower walls of the nozzle. The three curves show that the axial velocity curve of Case 1 changes more smoothly and evenly. Among the three cases, Case 3 has the greatest range of velocity variation, and the velocity at the center of the nozzle outlet has the largest difference from the velocity at the side wall. Figure 11b shows the velocity curve along the horizontal direction of the center of the outlet section. The horizontal direction is the Y-axis direction in Figure 10. The high-velocity zones of the three cases are concentrated in the outlet center. However, the velocity of the outlet center fluctuates greatly in the horizontal direction. In particular, because the section shrinkage of Cases 2 and 3 is not as uniform as that of Case 1, the velocity changes of Cases 2 and 3 fluctuate intensely. Among the three cases, Case 1 has the greatest range of velocity variation. However, the velocity curve of Case 1 is the most uniform and has a smooth curve. The velocity drops rapidly at the side wall because the velocity near the nozzle wall is very small. The velocity of the three cases in the Y-axis direction is not as uniform as that in the X-axis direction. In particular, the velocity fluctuates greatly near the center in the Y-axis direction.

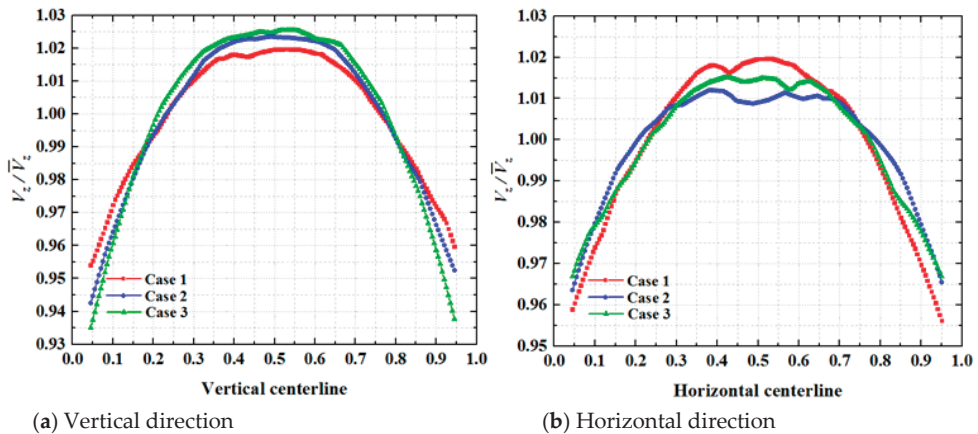


Figure 11. Axial velocity distribution curve.

The hydraulic performance of the nozzle and guide vane is measured by hydraulic loss. The pressure energy recovery coefficient is introduced to reflect the recovery of static pressure on the nozzle and guide vane. The formulas for the hydraulic loss  $\Delta h$  and pressure energy recovery coefficient  $\xi$  are as follows:

$$\Delta h = \frac{P_{in} - P_{out}}{\rho g} \quad (9)$$

$$\xi = \frac{P_{out}}{P_{in}} \times 100\% \quad (10)$$

where  $P_{in}$  is the total pressure of the inlet section of the nozzle or guide vane (in Pa), and  $P_{out}$  is the total pressure of the outlet section of the nozzle or guide vane (in Pa).

Figure 12 shows the relationship between the hydraulic loss and the pressure energy recovery coefficient of the nozzle and guide vane. As shown in Figure 12a, the hydraulic loss of the nozzle is small when the pressure energy recovery coefficient of the nozzle is large. The hydraulic loss and pressure energy recovery coefficients of Cases 1 and 2 are nearly identical when the flow rate is 0.5 to 0.75 times the design flow rate. The hydraulic loss of Case 3 is larger than that of Cases 1 and 2, and the pressure energy recovery coefficient is smaller than that of Cases 1 and 2. The increase in the

hydraulic loss of Case 3 is slower when the flow rate is 0.75 to 1 time the design flow rate, initially larger than that of Cases 1 and 2, and then gradually smaller than that of Cases 1 and 2. The pressure energy recovery coefficient of Case 3 is smaller than that of Cases 1 and 2, and then larger than that of Cases 1 and 2. Under the design flow rate condition, the pressure energy recovery coefficient of Case 3 is the largest, and the hydraulic loss is the smallest. The pressure energy recovery coefficient of Case 2 is minimum. At this time, the pressure recovery coefficients of Cases 1, 2, and 3 are 98.26%, 98.21%, and 98.32%, respectively. When the flow rate is greater than the designed flow rate, the pressure recovery performance of Case 3 is better than that of Cases 1 and 2. Thus, the hydraulic loss of Case 3 is smaller than that of Cases 1 and 2. When the flow rate is greater than 1.25 times the designed flow rate, the hydraulic loss of the three cases decreases more severely with the increase in the flow rate. When the flow rate is 1.5 times the designed flow rate, the pressure energy recovery coefficient of Case 3 is 0.26% and 0.43% higher than that of Cases 1 and 2, respectively. As shown in Figure 12b, the relationship between the pressure energy recovery coefficient and hydraulic loss of the guide vane is opposite to that of the nozzle. In addition, the relationship between the pressure energy recovery coefficient (and the hydraulic loss) and the flow rate of the guide vanes is not a monotonic function. The pressure energy recovery coefficient of the guide vane initially increases and then decreases with the increase in the flow rate. The hydraulic loss of the guide vane initially decreases and then increases with the increase in the flow rate. When the flow rate is 1.25 times the designed flow rate, the hydraulic loss of the guide vanes of the three cases reaches the maximum, and the pressure energy recovery coefficient is the smallest. Figure 12a,b shows that when the pressure recovery of the guide vane is worse, the pressure recovery of the nozzle is better. Under the conditions of small flow rate and designed flow rate, the difference between the pressure recovery coefficient and hydraulic loss of nozzles and guide vanes in the three cases is extremely small. Under large flow rate conditions, the pressure energy recovery coefficient and hydraulic loss of Case 3 are optimal, and those of Case 2 are the worst.

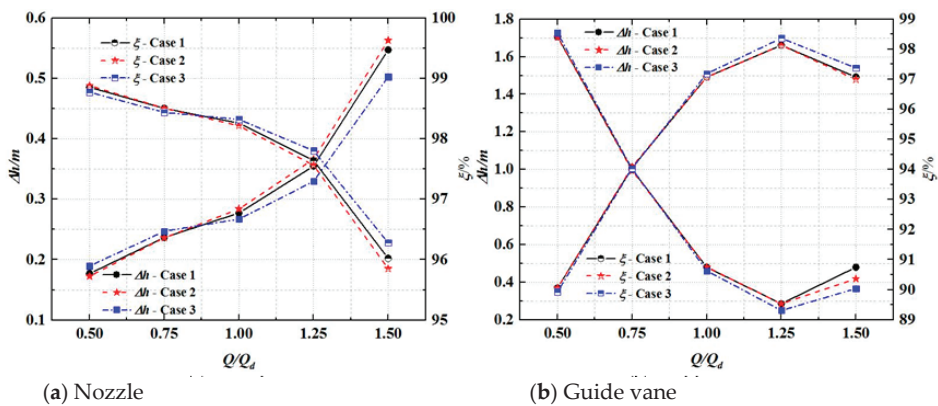


Figure 12. Hydraulic loss and pressure energy recovery coefficient.

Figure 13 shows the distributions of the pressure contours of the longitudinal section of the nozzles. Four longitudinal sections are intercepted equidistantly in the nozzle. As illustrated in the figure, seven high-pressure zones due to the influence of guide vane are shown in Plane 4. Compared with the three results, the change in the shape of the nozzle affects the pressure distribution at the nozzle. In Case 1, as the section approaches the outlet of the nozzle, the pressure distribution in the section becomes increasingly uniform. The pressure distribution in Case 3 is the most uneven. In the three cases, the pressure distribution near the outlet is similar to the shape of the outlet section.

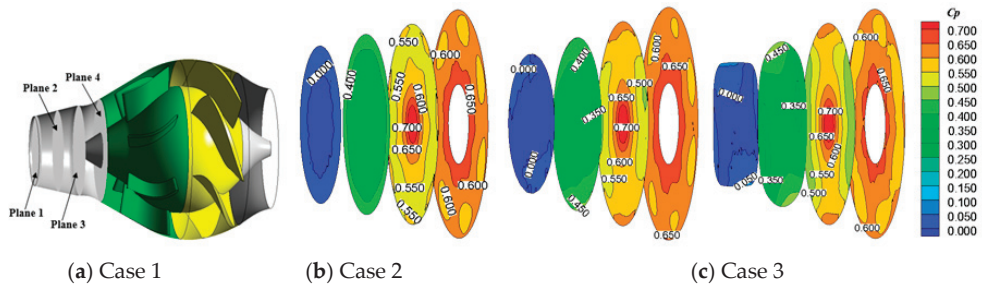


Figure 13. Distributions of pressure contours of the longitudinal section of nozzles.

Figure 14 shows the comparison of the hydraulic performance of different nozzle shapes. The figure shows that the trend of the head and efficiency curves of the three cases is consistent. The head initially decreases and then increases with the increase in the flow rate, and then continues to decrease. The head increases with the flow rate when the flow rate is 0.5 to 0.75 times the designed flow rate. The efficiency initially increases and then decreases with the increase in the flow rate. It has the highest efficiency point. The corresponding flow rate of the high-efficiency area is  $(1.0\text{--}1.2) Q_d$ . When the flow reaches  $(0.42\text{--}1.2) Q_d$ , the flow and head curves of the three cases are almost coincident. Each performance value is higher near the design flow range. The head and efficiency are lower when the flow rate is larger than the designed flow rate. The head and efficiency of Cases 2 and 3 are lower than those of Case 1. When the flow rate is larger than 1.25 times the designed flow rate, the head and efficiency curves of Case 2 drop rapidly because the elliptical nozzle is more irregular and shrinks more sharply than those in the other two cases.

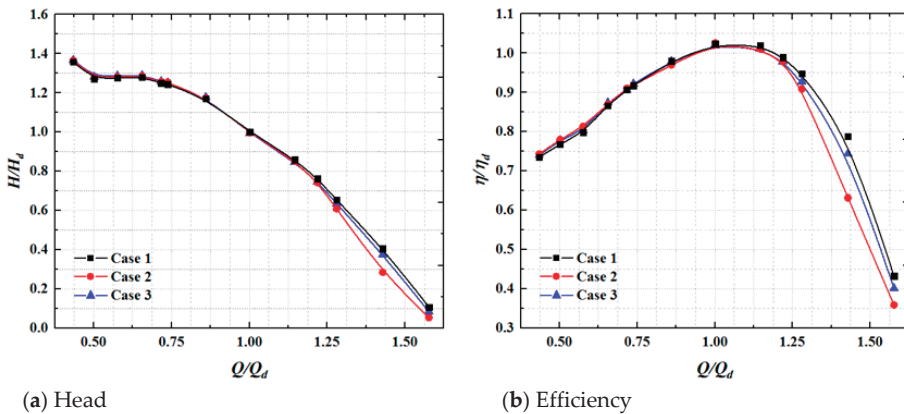


Figure 14. Hydraulic performance curve of pump system with different nozzle shapes.

#### 4.2. The Influence of Different Nozzle Outlet Areas on the Hydraulic Characteristic

Figure 15 shows the 3D diagram of the circular nozzle with different outlet areas. The hydraulic characteristics of the waterjet propulsion pump system are better when the circular nozzle is used. The hydraulic characteristics of different outlet areas of the nozzle were studied under the condition of the circular nozzle. The hydraulic characteristics of the waterjet propulsion systems with five different nozzle areas were studied. The nozzle area varies from 10% to 50% times the outlet area of the inlet duct.

Figure 16 shows the pump efficiency, head, shaft power, and IVR (Inlet Velocity Ratio) curves of the waterjet propulsion pump system with different outlet areas of the nozzle. IVR refers to the ratio of the ship speed to the averaged axial outflow velocity at the duct outlet. The averaged axial

outflow velocity at the duct outlet is an important parameter to describe the flow phenomena in the inlet, where the speed is changed from the ship speed to the pump velocity. IVR is defined as follows:

$$IVR = \frac{v_{duct}}{v_s} \tag{11}$$

where  $v_{duct}$  is the averaged axial outflow velocity at the duct outlet (in m/s), and  $v_s$  is the ship speed (in m/s).

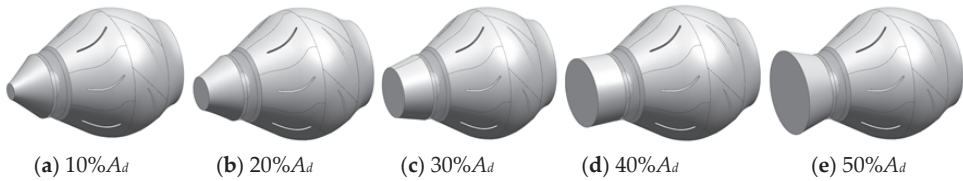


Figure 15. 3D diagram of the circular nozzle with different outlet areas.

Figure 16a presents the relationship between efficiency and head with the nozzle area. The head decreases and efficiency initially increases and then decreases with the increase in the nozzle area. The head decreases slowly when the nozzle outlet area changes from 10%  $A_d$  to 30%  $A_d$ . From the curve, the head drops from 1.14  $H_d$  to 1.0  $H_d$ . Meanwhile, the efficiency curve increases, and the efficiency rises from 0.53  $\eta_d$  to 1.0  $\eta_d$ . When the nozzle area exceeds 30%  $A_d$ , the head curve drops rapidly, and the efficiency curve begins to decline. When the nozzle outlet area changes from 30%  $A_d$  to 50%  $A_d$ , the head drops from 1.0  $H_d$  to 0.36  $H_d$ , and the efficiency is reduced from 1.0  $\eta_d$  to 0.67  $\eta_d$ . The best efficiency point is obtained when the outlet area is near 30%  $A_d$ . Figure 16b shows the relationship between power and IVR with the nozzle area. With the increase in the nozzle outlet area, IVR increases, and the power initially increases and then decreases. When the nozzle outlet area changes from 10%  $A_d$  to 30%  $A_d$ , IVR rises from 0.32  $IVR_d$  to 1.0  $IVR_d$ , and the shaft power rises from 0.69  $N_d$  to 1.0  $N_d$ . When the nozzle outlet area changes from 30%  $A_d$  to 50%  $A_d$ , the IVR curve rises slowly from 1.0  $IVR_d$  to 1.37  $IVR_d$ . When the nozzle outlet area exceeds 30%  $A_d$ , the power curve no longer rises and begins to fall. The maximum power point is obtained when the outlet area is near 30%  $A_d$ . Therefore, the maximum efficiency and shaft power occur when the nozzle outlet area is 30%  $A_d$ , and the hydraulic characteristics of the waterjet propulsion pump system are better.

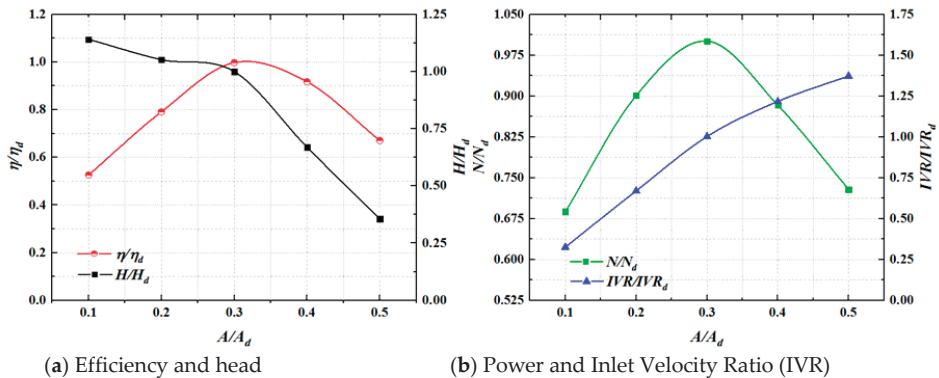


Figure 16. Hydraulic performance curve of waterjet propulsion pump system with different outlet areas. \*  $A_Y$  represents the impeller outlet area.  $\eta_d$ ,  $H_d$ ,  $N_d$ , and  $IVR_d$  represent the pump efficiency, head, shaft power and IVR of the waterjet propulsion pump system under the nozzle outlet area of 30%  $A_d$ , respectively.



The purpose of the waterjet propulsion system is to produce thrust to propel a ship. To study the influence of the nozzle outlet area on the waterjet propulsion system, this study considers two important factors, namely, thrust and system efficiency, in addition to the performance curves.

The thrust of the waterjet propulsion system is defined, considering the influence of the boundary, as follows:

$$T = \rho Q(v_{out} - v_{in}) \tag{12}$$

$$v_{in} = \alpha v_s \tag{13}$$

$$Q = Av_{out} \tag{14}$$

where  $A$  is the outlet area of the nozzle,  $v_{in}$  is the mass-averaged ingested velocity at the duct inlet, and  $\alpha$  is the effect coefficient of the boundary layer, which is 0.95 according to the reference documentation.

The efficiency of the waterjet propulsion system  $\eta_c$  denotes the ratio of the output power of the system to that of the propulsion pump. Considering the pipeline loss coefficient, the formula for the  $\eta_c$  is as follows:

$$\eta_c = \frac{2(k - \alpha)}{kr^2 - \beta + K_1} \tag{15}$$

$$\beta = \alpha^2 \tag{16}$$

where  $K_1$  is the pipeline loss coefficient in the range of 0.40–0.50. In this study,  $K_1$  is 0.45,  $k'$  is the ratio of  $v_{out}$  to  $v_s$  vs, and  $\beta$  is the effect coefficient of the boundary layer.

Figure 17 shows the system efficiency and thrust curves of the waterjet propulsion system with different nozzle outlet areas. The thrust and system efficiency of the waterjet propulsion system initially increase and then decrease with the increase in the outlet area. When the nozzle outlet area changes from 10%  $A_d$  to 30%  $A_d$ , the thrust rises from 0.27  $F_d$  to 1.0  $F_d$ , and the system efficiency rises from 0.89  $\eta_{cd}$  to 1.0  $\eta_{cd}$ . When the nozzle outlet area exceeds 30%  $A_d$ , the thrust and system efficiency curves no longer rise and begin to fall. When the nozzle outlet area changes from 30%  $A_d$  to 50%  $A_d$ , the thrust reduces from 1.0  $F_d$  to 0.51  $F_d$ , and the system efficiency declines from 1.0  $\eta_{cd}$  to 0.19  $\eta_{cd}$ . The maximum system efficiency and thrust are obtained when the outlet area is close to 30%  $A_d$ . The nozzle area greatly influences the thrust. When the outlet area exceeds 30%  $A_d$ , the system efficiency curve decreases rapidly. When the nozzle outlet area is extremely large, the nozzle diffuses the water flow. Thus, the axial velocity of the nozzle outlet  $v_{out}$  is less than the velocity of the inlet section of the inlet duct  $v_{in}$ , and the thrust value is negative.

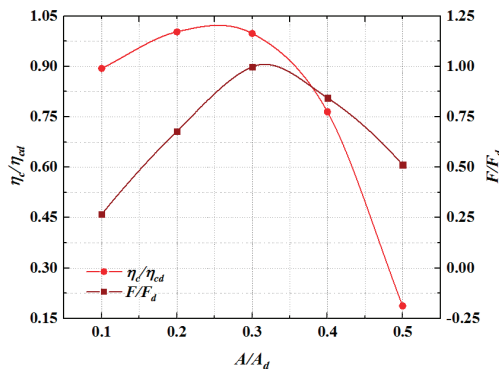


Figure 17. Hydraulic performance curve of waterjet propulsion system with different outlet areas.

#### 4.3. The Effect of Different Transition Curve Forms on the Hydraulic Characteristic

Figure 18 shows the transition curve forms of the nozzle. The first component is the nozzle, and the second component is the guide vane outlet. The total length of the nozzle and outlet section

of the guide vane  $L'$ , guide vane outlet diameter  $D_g$ , nozzle outlet diameter  $D_1$ , and shrinkage arc radius of the guide vane outlet section  $R_1$  are constant. In Cases 1, 8, and 9, the transition curve forms of the nozzle were changed. In Case 1, the linear contraction is selected as the transition curve form. The shrinkage angle  $\theta'$  of the nozzle with linear contraction is  $13^\circ$ . In Case 8, the combined contraction of the curve and the straight line is selected as the transition curve form. The curve segment consists of arc segments with radii  $R_2$  and  $R_3$ . In Case 9, the arc contraction is selected as the transition curve form. The geometric parameters of the nozzle are shown in Table 3.

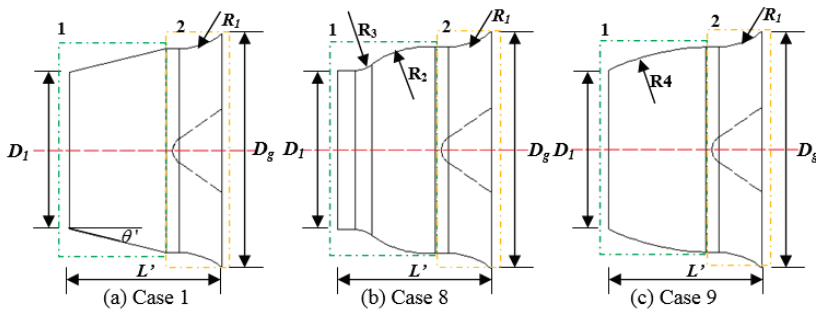


Figure 18. Transition curve forms of the nozzles.

Table 3. Geometric parameters of the nozzles with different contraction curves.

Case	$L'$	$D_1$	$D_g$	$R_1$	$\theta$	$R_2$	$R_3$	$R_4$
1	$0.56D_0$	$0.55D_0$	$0.86D_0$	$0.37D_0$	$13^\circ$	/	/	/
8	$0.56D_0$	$0.55D_0$	$0.86D_0$	$0.37D_0$	/	$0.30D_0$	$0.11D_0$	/
9	$0.56D_0$	$0.55D_0$	$0.86D_0$	$0.37D_0$	/	/	/	$0.87D_0$

Figure 19 shows the ratio of the hydraulic performance of the three types of transition curves to that of Case 1. The thrust value is the axial thrust from the inlet duct to the nozzle section. The figure indicates that the system efficiency and thrust of the system corresponding to Case 1 are the greatest for the three types of nozzles, but their values are similar to those of Case 8. The main reason is that the hydraulic losses of the two types of nozzles are relatively small. The hydraulic losses of Case 9 are larger than those of the others given the excessive contraction at the nozzle.

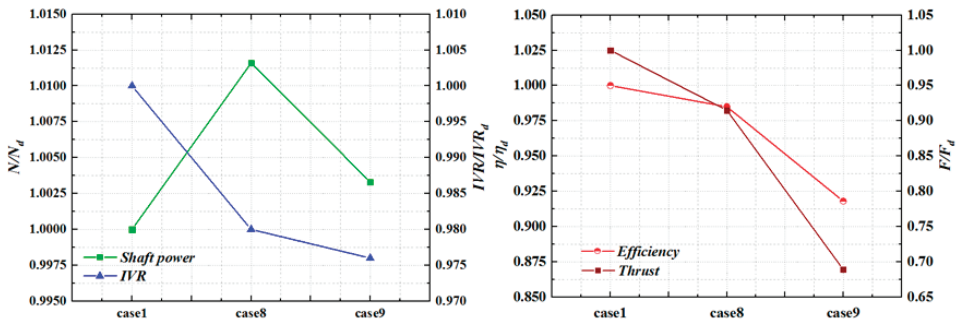


Figure 19. Hydraulic performance curve of waterjet propulsion pump system with different contraction curves.

The ideal nozzle outflow condition is that the outlet water flow angle is perpendicular to the nozzle outlet section. Thus, the mechanical energy of the propulsion pump can be maximally converted into the kinetic energy of the water. The outlet water flow cannot be completely perpendicular to the nozzle outlet section due to the tangential velocity of the nozzle outlet. Thus, the weighted-velocity average swirl angle  $\bar{\theta}$  is used to measure the outflow conditions of the nozzle. The outlet water flow angle perpendicular to the nozzle outlet section is better when  $\bar{\theta}$  is closer to  $90^\circ$ . The formula for velocity-weighted average swirl angle  $\bar{\theta}$  is as follows:

$$\bar{\theta} = \frac{\sum_{i=1}^n \left[ v_{ai} \left( 90 - \arctan \frac{v_{ti}}{v_{ai}} \right) \right]}{\sum_{i=1}^n v_{ai}} \quad (17)$$

where  $u_{ti}$  is the tangential velocity of each element of the calculated section (in m/s), and  $u_{ai}$  is the axial velocity of each element of the calculated section (in m/s).

Table 4 shows the hydraulic performance of the nozzle with different contraction curves.  $v_{\max}$  denotes the maximum axial outlet velocity of the nozzle,  $\bar{v}$  denotes the averaged outlet axial velocity of the nozzle,  $\bar{V}$  denotes the axial velocity distribution coefficient, and  $\bar{\theta}$  denotes the velocity-weighted average swirl angle.

As shown in Table 4, the maximum axial velocity values of the nozzle outlet section of the three cases are basically the same. Therefore, the three cases have good shrinkage effects. The comparative result of the average axial velocity of the three cases shows that the average axial velocity of Case 1 is much larger than that of Cases 2 and 3. The average axial velocity of Case 1 is 1.025 and 1.021 times that of Cases 2 and 3, respectively. The comparative result of the axial velocity distribution coefficient of the three cases shows that the axial velocity distribution coefficient of Case 1 is the best. The axial velocity distribution uniformity of Case 1 is 3.33% and 1.5% more than that of Cases 2 and 3. The velocity-weighted average swirl angle of Case 2 is  $80.1^\circ$ , which is  $1.37^\circ$  and  $5.03^\circ$  higher than that of Cases 1 and 3, respectively. The velocity-weighted average swirl angle of Case 2 is the best mainly due to the rectification effect of the straight section before the outlet of the nozzle in Case 2.

**Table 4.** Hydraulic performance of the nozzle with different contraction curves.

Case	$v_{\max}$ (m/s)	$\bar{v}$ (m/s)	$\bar{V}$	$\bar{\theta}$
1	10.42	10.02	97.57%	$78.73^\circ$
8	10.47	9.78	94.24%	$80.10^\circ$
9	10.44	9.81	96.07%	$75.07^\circ$

Figure 20 shows the axial velocity contours and streamlines of the nozzle outlet section with different contraction curves. The figure shows that the axial velocity of the three cases is distributed in a ring-like manner, and the high-speed zone is concentrated at the center of the circle. The area of the high-speed zone in Cases 2 and 3 is larger, but the axial velocity distribution uniformity of Case 1 is better. The streamline distribution indicates that Case 2 is more affected by the straight section of the outlet of the nozzle, and the flow lines on the outlet section are more deflected.

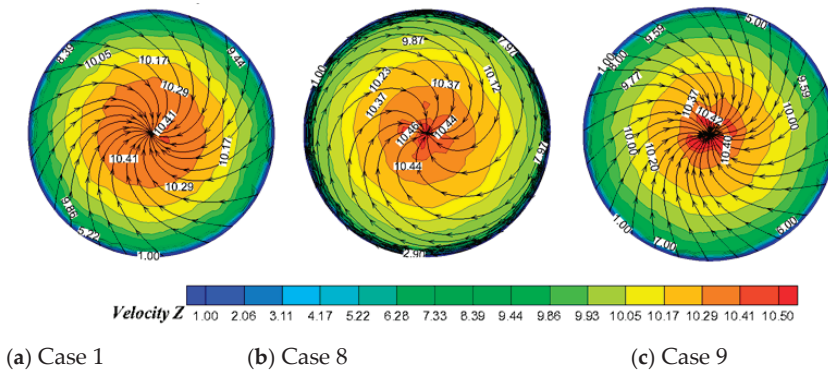


Figure 20. Axial velocity contours and streamlines of the nozzle outlet section with different contraction curves.

## 5. Conclusions

In this study, the hydraulic characteristics of the nozzle of the waterjet propulsion system were studied by a combination of numerical simulation and experimental verification. Different grid values and turbulence models were used for calculation and analysis to determine the appropriate numerical settings and ensure the accuracy of the calculation. The model test was used to verify the external characteristics of the waterjet propulsion pump, and the numerical results are in good agreement with the test results. Therefore, the numerical results are reliable. Nine different cases were established to systematically study the hydraulic characteristics of the nozzle in accordance with the different nozzle outlet shapes, nozzle outlet areas, and nozzle transition curves. The following results are obtained through calculation and analysis:

(1) The pressure coefficient  $C_p$ , axial velocity distribution coefficient  $\bar{V}$ , hydraulic loss  $\Delta h$ , and pressure energy recovery coefficient  $\xi$  were introduced to analyze the hydraulic characteristics of the waterjet propulsion system with different nozzle outlet shapes. The outlet section pressure and streamline the distribution of the circular nozzle case is superior to those in the other two cases. The pressure on the outlet of the circular nozzle is distributed uniformly as a ring, and the flow lines on the outlet section intersect at the center of the circle. Under the design flow-rate condition, the velocity uniformity of the circular nozzle is 0.26% and 0.34% higher than that of the elliptical nozzle and the rounded rectangle nozzle, respectively. The pump efficiency of the circular nozzle is 0.31% and 0.14% higher than that of the others. At this point, the pressure recovery and hydraulic loss of the circular nozzle are superior. Under large flow-rate conditions, the pressure recovery and hydraulic loss of the rounded rectangle nozzle are superior to those in the other two cases. The external characteristic curves show that the circular nozzle case is better. The hydraulic performance of the elliptical nozzle is lower because the elliptical section is more irregular and shrinks more sharply than the other two sections.

(2) The comprehensive hydraulic characteristics are analyzed in accordance with the different nozzle outlet areas, waterjet propulsion pumps, and waterjet propulsion systems. The analysis of the hydraulic performance of the waterjet propulsion pump reveals that when the nozzle outlet area is close to 30%  $A_d$ , the waterjet propulsion system has the highest efficiency and the best hydraulic performance. When the nozzle area exceeds 30%  $A_d$ , the head curve descends faster and the IVR curve ascends slowly. The analysis of the hydraulic performance of the waterjet propulsion system reveals that when the outlet area is close to 30%  $A_d$ , the thrust and system efficiency reach the maximum value. When the outlet area exceeds 30%  $A_d$ , the system efficiency curve decreases rapidly.

(3) The comparison among different transition curve forms of the nozzle shows that the transition curve forms greatly affect the thrust and system efficiency. The linear contraction of Case 1 slightly affects the hydraulic performance of the nozzle mainly because the transition of the linear contraction is more uniform with less hydraulic loss. The average axial velocity and axial velocity distribution

uniformity of Case 1 are better than those of the other cases. The velocity-weighted average swirl angle of Case 2 is optimal, but the hydraulic characteristics of Cases 2 and 3 are not as good as those of Case 1.

**Author Contributions:** Data curation, L.C. and X.H.; Formal analysis, W.J. and C.W.; Methodology, C.L. and J.X.; Writing – original draft, C.W. and W.J.; Writing – review & editing, L.C., C.W. and J.X.; Supervision, K.C.

**Funding:** This research was funded by the National Natural Science Foundation of China (Grant No. 51779214 and No. 51609105), Peak plan six talents in Jiangsu province (Grant No. 2015-JXQC-007), Jiangsu Province 333 high-level talents training project (BRA2018382), and A Project Funded by the Priority Academic Program Development of Jiangsu Higher Education Institutions (PAPD), Jiangsu Province Postdoctoral Science Foundation (Grant No. 1701189B), Jiangsu Province Science Foundation for Youths (Grant No. BK20170507).

**Conflicts of Interest:** The authors declare no conflict of interest.

## Nomenclature

### Symbols

$D_0$	inlet diameter of the impeller, mm
$\theta$	dip angle of inlet duct, °
$u_{i,j}$	velocity component of the direction of $x, y$
$t$	time, s
$P$	pressure, pa
$F_i$	volume force component in the $i$ direction, N
$\mu$	dynamics viscosity coefficient
$x_{i,j}$	coordinate component
$H_d$	head under design flow rate condition, m
$\eta_d$	efficiency under design flow rate condition, %
$Q_d$	design flow rate, m <sup>3</sup> /s
$H_{td}$	test value of head under design flow rate condition, m
$\eta_{td}$	test value of efficiency under design flow rate condition, %
$P_{1-1}$	pressure of section 1-1, Pa
$P_{2-2}$	pressure of section 2-2, Pa
$\rho$	water density, kg/m <sup>3</sup>
$g$	gravitational acceleration, m/s <sup>2</sup>
$T$	torque of blades, N·m
$Q$	flow rate, m <sup>3</sup> /s
$N$	shaft power, kW
$A_d$	outlet area of inlet duct, m <sup>2</sup>
$D_i$	diameter of nozzle with circle shape, m
$a_i$	major axis of nozzle with elliptical shape, m
$b_i$	minor axis of nozzle with elliptical shape, m
$c_i$	length of nozzle with rounded rectangle, m
$\beta$	effect coefficient of boundary layer
$K_I$	pipeline loss coefficient
$k'$	the ratio of $v_{out}$ to $v_s$
$F_d$	thrust under design flow rate condition, N
$D_g$	outlet diameter of guide vane, m
$R_I$	shrinkage arc radius of guide vane outlet section, m
$\theta'$	shrinkage angle of nozzle with linear contraction, °
$L'$	total length of nozzle and outlet section of guide vane, m
$d_i$	width of nozzle with rounded rectangle, m
$r$	radius of nozzle with rounded rectangle, m
$C_p$	pressure coefficient
$\bar{p}$	time-average pressure, Pa
$v_{out}$	averaged outlet velocity at the nozzle, m/s
$\bar{V}$	the axial velocity distribution coefficient, %
$u_{ai}$	axial velocity of each element of the calculated section, m/s

$\bar{u}_a$	averaged axial velocity of the calculated section, m/s
$n$	number of cells of the calculated section
$V_z$	axial velocity of nozzle outlet, m/s
$\bar{V}_z$	averaged axial velocity of nozzle outlet, m/s
$\Delta h$	hydraulic loss, m
$P_{in}$	total pressure of inlet section, Pa
$P_{out}$	total pressure of outlet section, Pa
$\xi$	pressure energy recovery coefficient, %
IVR	inlet velocity ratio
$v_{duct}$	averaged axial outflow velocity at the duct outlet, m/s
$v_s$	ship speed, m/s
$N_d$	shaft power under design flow rate condition, %
IVR <sub>d</sub>	IVR under design flow rate condition
$T$	thrust of the waterjet propulsion system, N
$A$	outlet area of the nozzle, m <sup>2</sup>
$v_{in}$	mass averaged ingested velocity at duct inlet, m/s
$\alpha$	effect coefficient of boundary layer
$\eta_c$	efficiency of waterjet propulsion system, %
$R_2$	first transition arc radius of nozzle in case 8, m
$R_3$	second transition arc radius of nozzle in case 8, m
$R_4$	transition arc radius of nozzle in case 9, m
$\bar{\theta}$	s weighted-velocity average swirl angle, °
$u_{ti}$	tangential velocity of each element of the calculated section, m/s
$v_{max}$	maximum axial outlet velocity of the nozzle, m/s
$\bar{v}$	averaged outlet axial velocity of the nozzle, m/s

## References

- Bulten, N.W.H. Numerical Analysis of a Waterjet Propulsion System. Ph.D. Thesis, Library Eindhoven University of Technology, Eindhoven, Netherlands, 2006.
- Takai, T.; Kandasamy, M.; Stern, F. Verification and validation study of URANS simulations for an axial waterjet propelled large high-speed ship. *J. Mar. Sci. Technol.* **2011**, *16*, 434–447. [CrossRef]
- Lavis, D.R.; Forstell, B.G.; Purnell, J.G. Compact waterjets for high-speed ships. *Ships Offshore Struct.* **2007**, *2*, 11. [CrossRef]
- Hu, B.; Li, X.; Fu, Y.; Zhang, F.; Gu, C.; Ren, X.; Wang, C. Experimental investigation on the flow and flow-rotor heat transfer in a rotor-stator spinning disk reactor. *Appl. Therm. Eng.* **2019**, *162*, 114316. [CrossRef]
- Zhu, Y.; Qian, P.; Tang, S.; Jiang, W.; Li, W.; Zhao, J. Amplitude-frequency characteristics analysis for vertical vibration of hydraulic AGC system under nonlinear action. *AIP Adv.* **2019**, *9*, 035019. [CrossRef]
- Verbeek, R.; Bulten, N.W.H. Recent development in waterjet design. In Proceedings of the International Conference on Waterjet Propulsion, Latest Developments, Amsterdam, The Netherlands, 22–23 October 1998; RINA: Amsterdam, The Netherlands, 1998.
- Jiao, W.X.; Cheng, L.; Xu, J.; Wang, C. Numerical analysis of two-phase flow in the cavitation process of a waterjet propulsion pump system. *Processes* **2019**, *7*, 690. [CrossRef]
- Ding, J.M.; Wang, Y.S. Research on flow loss of inlet duct of marine waterjets. *J. Shanghai Jiaotong Univ. (Sci.)* **2010**, *15*, 158–162. [CrossRef]
- Park, W.G.; Yun, H.S.; Chun, H.H.; Kim, M.C. Numerical flow simulation of flush type intake duct of waterjet. *Ocean Eng.* **2005**, *32*, 2107–2120. [CrossRef]
- Cao, P.; Wang, Y.; Li, G.; Cui, Y.; Yin, G. Numerical hydraulic efficiency analysis of waterjet propulsion. In Proceedings of the International Symposium on Fluid Machinery & Fluid Engineering, Wuhan, China, 22–25 October 2014.
- Cheng, L.; Qi, W. Rotating stall region of water-jet pump. *Trans. Famena* **2014**, *38*, 31–40.
- Xia, C.Z.; Cheng, L.; Luo, C.; Jiao, W.; Zhang, D. Hydraulic characteristics and measurement of rotating stall suppression in a waterjet propulsion system. *Trans. Famena* **2018**, *4*, 85–100. [CrossRef]

13. Wang, C.; He, X.; Zhang, D.; Hu, B.; Shi, W. Numerical and experimental study of the self-priming process of a multistage self-priming centrifugal pump. *Int. J. Energy Res.* **2019**, *43*, 4074–4092. [CrossRef]
14. Wang, C.; Shi, W.; Wang, X.; Jiang, X.; Yang, Y.; Li, W.; Zhou, L. Optimal design of multistage centrifugal pump based on the combined energy loss model and computational fluid dynamics. *Appl. Energy* **2017**, *187*, 10–26. [CrossRef]
15. Kim, M.C.; Chun, H.H. Experimental investigation into the performance of the Axial-Flow-Type Waterjet according to the Variation of Impeller Tip Clearance. *Ocean Eng.* **2007**, *34*, 275–283. [CrossRef]
16. Etter, R.J.; Krishnamoorthy, V.; Sherer, J.O. Model testing of waterjet propelled craft. In Proceedings of the 19th ATTC, Ann Arbor, American, 11–15 August 1980.
17. Eslamdoost, A.; Larsson, L.; Bensow, R. Net and gross thrust in waterjet propulsion. *J. Ship Res.* **2016**, *60*, 1–14. [CrossRef]
18. Park, W.G.; Jang, J.H.; Chun, H.H.; Kim, M.C. Numerical flow and performance analysis of waterjet propulsion system. *Ocean Eng.* **2005**, *32*, 1740–1761. [CrossRef]
19. Liang, J.; Li, X.; Zhang, Z.; Luo, X.; Zhu, Y. Numerical investigation into effects on momentum thrust by nozzle's geometric parameters in water jet propulsion system of autonomous underwater vehicles. *Ocean Eng.* **2016**, *123*, 327–345.
20. Abcand, L.; Cobolli, C.R. Optimization of waterjet propulsion for high-speed ships. *J. Hydronaut.* **1968**, *2*, 2–8. [CrossRef]
21. Chin, P.C. Determination of the main parameters of water-jet propulsion system. *Shipbuild. China* **1978**, *1*, 80–91.
22. Jiao, W.X.; Cheng, L.; Zhang, D.; Zhang, B.; Su, Y.; Wang, C. Optimal design of inlet passage for waterjet propulsion system based on flow and geometric parameters. *Adv. Mater. Sci. Eng.* **2019**, 2320981. [CrossRef]
23. Xin, B.; Luo, X.; Shi, Z.; Zhu, Y. A vectored water jet propulsion method for autonomous underwater vehicles. *Ocean Eng.* **2013**, *74*, 133–140. [CrossRef]
24. Gong, Z.H.; Li, G.Q.; Xiong, W.; Li, J.Z.; Yu, Y.X.; Yuan, J.Q. Modeling and Simulation of the Steering Control System of Marine Water-Jet Propulsion Unit. *J. Shanghai Jiaotong Univ.* **2016**, *50*, 1114–1118.
25. Wang, C.; He, X.; Shi, W.; Wang, X.; Wang, X.; Qiu, N. Numerical study on pressure fluctuation of a multistage centrifugal pump based on whole flow field. *AIP Adv.* **2019**, *9*, 035118. [CrossRef]
26. Zhu, Y.; Tang, S.; Quan, L.; Jiang, W.; Zhou, L. Extraction method for signal effective component based on extreme-point symmetric mode decomposition and Kullback-Leibler divergence. *J. Braz. Soc. Mech. Sci. Eng.* **2019**, *41*, 100. [CrossRef]
27. Wang, C.; Chen, X.; Qiu, N.; Zhu, Y.; Shi, W. Numerical and experimental study on the pressure fluctuation, vibration, and noise of multistage pump with radial diffuser. *J. Braz. Soc. Mech. Sci. Eng.* **2018**, *40*, 481. [CrossRef]
28. Wei, Y.; Yang, H.; Dou, H.S.; Lin, Z.; Wang, Z.; Qian, Y. A novel two-dimensional coupled lattice Boltzmann model for thermal incompressible flows. *Appl. Math. Comput.* **2018**, *339*, 556–567. [CrossRef]
29. Yang, H.; Zhang, W.; Zhu, Z. Unsteady mixed convection in a square enclosure with an inner cylinder rotating in a bi-directional and time-periodic mode. *Int. J. Heat Mass Transf.* **2019**, *136*, 563–580. [CrossRef]
30. Zhu, Y.; Tang, S.N.; Wang, C.; Jiang, W.; Yuan, X.; Lei, Y. Bifurcation characteristic research on the load vertical vibration of a hydraulic automatic gauge control system. *Processes* **2019**, *7*, 718. [CrossRef]
31. Zhu, Y.; Tang, S.; Wang, C.; Jiang, W.; Zhao, J.; Li, G. Absolute stability condition derivation for position closed-loop system in hydraulic automatic gauge control. *Processes* **2019**, *7*, 766. [CrossRef]
32. Li, X.J.; Chen, B.; Luo, X.W.; Zhu, Z. Effects of flow pattern on hydraulic performance and energy conversion characterisation in a centrifugal pump. *Renew. Energy* **2020**, in press. [CrossRef]
33. Wang, X.; Su, B.; Li, Y.; Wang, C. Vortex formation and evolution process in an impulsively starting jet from long pipe. *Ocean Eng.* **2019**, *176*, 134–143. [CrossRef]
34. Chang, H.; Shi, W.; Li, W.; Wang, C.; Zhou, L.; Liu, J.; Yang, Y.; Rameshe, K.A. Experimental optimization of jet self-priming centrifugal pump based on orthogonal design and grey-correlational method. *J. Therm. Sci.* **2019**, *435*, 1–10. [CrossRef]
35. Zhang, S.; Li, X.; Hu, B.; Hu, B.; Liu, Y.; Zhu, Z. Numerical investigation of attached cavitating flow in thermo-sensitive fluid with special emphasis on thermal effect and shedding dynamics. *Int. J. Hydrogen Energy* **2019**, *44*, 3170–3184. [CrossRef]

36. He, X.; Jiao, W.; Wang, C.; Cao, W. Influence of surface roughness on the pump performance based on Computational Fluid Dynamics. *IEEE Access* **2019**, *7*, 105331–105341. [CrossRef]
37. Wang, C.; Hu, B.; Zhu, Y.; Wang, X.; Luo, C.; Cheng, L. Numerical study on the gas-water two-phase flow in the self-priming process of self-priming centrifugal pump. *Processes* **2019**, *7*, 330. [CrossRef]



© 2019 by the authors. Licensee MDPI, Basel, Switzerland. This article is an open access article distributed under the terms and conditions of the Creative Commons Attribution (CC BY) license (<http://creativecommons.org/licenses/by/4.0/>).



Article

# Modeling and Thermal Analysis of a Moving Spacecraft Subject to Solar Radiation Effect

Mohamed Gadalla <sup>1,†</sup>, Mehdi Ghommem <sup>1,\*</sup>, George Bourantas <sup>2,†</sup> and Karol Miller <sup>2</sup>

<sup>1</sup> Department of Mechanical Engineering, American University of Sharjah, Sharjah 26666, UAE; mgadalla@aus.edu

<sup>2</sup> Intelligent Systems for Medicine Laboratory, The University of Western Australia, 35 Stirling Highway, Perth WA 6009, Australia; george.bourantas@uwa.edu.au (G.B.); karol.miller@uwa.edu.au (K.M.)

\* Correspondence: mghommem@aus.edu

† These authors contributed equally to this work.

Received: 8 October 2019; Accepted: 28 October 2019; Published: 4 November 2019

**Abstract:** The impact of solar radiation on spacecraft can increase the cooling load, degrade the material properties of the structure and possibly lead to catastrophic failure of their missions. In this paper, we develop a computational model to investigate the effect of the exposure to solar radiation on the thermal distribution of a spacecraft with a cylindrical shape which is traveling in low earth orbit environment. This is obtained by the energy conservation between the heat conduction among the spacecraft, the heating from the solar radiation, and the radiative heat dissipation into the surroundings while accounting for the dynamics of the space vehicle (rotational motion). The model is solved numerically using the meshless collocation point method to evaluate the temperature variations under different operating conditions. The meshless method is based on approximating the unknown field function and their space derivatives, by using a set of nodes, sprinkled over the spatial domain of the spacecraft wall and functions with compact support. Meshless schemes bypass the use of conventional mesh configurations and require only clouds of points, without any prior knowledge on their connectivity. This would relieve the computational burden associated with mesh generation. The simulation results are found in good agreement with those reported in previously-published research works. The numerical results show that spinning the spacecraft at appropriate rates ensures low and uniform temperature distribution on the spacecraft, treated as thick-walled object of different geometries. Therefore, this would extend its lifetime and protect all on-board electronic equipment needed to accomplish its mission.

**Keywords:** thermal analysis; rotating spacecraft; meshless method; computational model

## 1. Introduction

The space environment during the spacecraft travelling time and mission continues to be a major cause of anomalies in many space missions. The most common factors of such anomalies are surface charging and discharging, solar radiation heating loads, and the existence of orbital debris in space as indicated by several published studies [1–12]. In addition, the solar load, shielding material, onboard equipment location, thermal control and air conditioning systems must be considered during the design stage of spacecraft/satellites [13–19]. The thermal control and vehicle dynamics play a pivotal role during the design stage of the spacecraft [19]. This is mainly due to the exposure of the spacecraft and onboard equipment to high solar loads and the penetration of heat into the spacecraft structure that affect the temperature gradient of the spacecraft body and its cooling load. The design process of any space vehicles such as satellites requires detailed thermal characteristics in addition to the dynamic analysis of the vehicle motion to guarantee no thermal stresses due to high temperature fluctuations on the vehicle structure as well as on the payload. In order to avoid severe thermal stresses that may

damage onboard electronic equipment, the temperature variation of the entire vehicle should be kept within the appropriate range during the entire mission [20]. Since material tensile strength decreases with elevated temperature [13], it is important to study the effect of rotation and solar radiation on temperature distribution around and inside the spacecraft. Thus, thermal control of spacecraft and communication satellites is very important for a successful space mission and safe return [21–24]. Basically, during the spacecraft travel in space at different elevations, it receives heat from the sun and dissipates heat into the surrounding atmosphere. On the other hand, in deep space, the heat received from solar radiation must be dissipated partially by radiation to deep space. As such, the structure of the spacecraft will attain thermal instability with its space environment due to temperature variation along the outer and the inside surfaces of the space vehicle. In general, solar radiation is incident from a fixed direction, one side of the space vehicle body will be shone bright and the other side remains dark and then this will induce temperature variations. The temperature gradients that arise during the heat transfer from the bright side to the dark side lead to temperature variations across the body of the spacecraft in the absence of any rotational dynamics. Consequently, the space astronauts, onboard electronic equipment, and cryogenic-fuel tanks gain severe heat on the bright side and losing heat from the dark side.

As a result of the great interest in space environment, studies concerning the thermal behavior of spacecraft in space during travelling and in deep space during flight mission have become very important in real-time satellite simulators. Controlling the thermal characteristics is mandatory for the safe operation of a spacecraft/satellite [25]. In general, it is considered that the satellite has a pitch angle rotation maneuver due to the severe solar radiation during daytime transition. Modeling of the thermal behavior is then associated with heat radiation effects and thermally-induced vibration may exist at the high temperature gradients [25,26]. Therefore, a coupled-thermal structural analysis for an altitude maneuvering under solar thermal loading and maneuvering dynamics is very important in the analysis. One main aspect of this thermal behavior includes the temperature variation that the spacecraft will attain due to the coupling between the rotational speed, space solar heating, and heat conducted through the spacecraft wall. Not only will the temperature level be of great importance, but also the temperature variation from one point to another point on the spacecraft structure due to the thermal sensitivity of all onboard equipment carried by space vehicle. This variation is associated with the combined effect of conduction, radiation, and spacecraft/satellite spinning speed. During the design stage of any space mission, all hazards should be considered and investigated in a detailed and right manner to avoid any possible damage to the space vehicle and any failure that may happen to the space mission [4,5].

Previous research studies tend to overlook the conductive phase of the heat transfer due to the assumption of a thin-walled spacecraft as indicated by Charnes and Raynor [21] and Nicholes [27]. Roberts [28] derived approximate formulae for the temperature distribution in solid cylinders without considering any spacecraft rotation. Jenness [29] treated the solid cylinder with a uniformly varying surface temperature but also did not consider the effect of rotation. Torres et al. [30] developed a mathematical model that considers spacecraft thermal designs while accounting for the harsh environment on the design temperature of on-board satellite equipment, antenna and subsystems. The authors developed a transient numerical model that is capable to simulate the thermal dynamic behavior of integrating radiators via loop heat pipes and performed thermal control architecture. The mismanagement in thermal control may lead to severe damage to all on-board electronics and subsystems [30].

In this paper, we develop a computational model to obtain the temperature distribution over a rotating spacecraft exposed to solar radiation under different operating conditions. The spacecraft is treated as a thick-walled object of different geometries and it is assumed to be placed or traveling in low Earth orbit environment. The objective is to provide guidance for the design of thermal control systems for space vehicles. The remainder of the paper is organized as follows. In Section 2, we present the mathematical model governing the heat transfer of a rotating spacecraft. Section 3 is concerned

with the description of the numerical procedure based on meshless method. In Section 4, we present and discuss the results of the numerical investigation. In Section 5, we summarize the main findings of the study and conclude with some remarks for the design of spacecraft.

## 2. Heat Transfer Modeling of a Rotating Spacecraft Under Solar Radiation

The performance requirements of a spacecraft’s mission could be assessed at the earliest stages of design through the development of mathematical models and deployment of computational tools. Recent advances in computer hardware and software have enabled to reduce the computational burden associated with the numerical integration of the high-fidelity equations governing the heat transfer of the aforementioned systems [2,9,26]. Software tools can be deployed to assist the design process and provide guidelines to enable enhanced operability of spacecraft.

As a first step towards developing a good understanding of the thermal behavior of a space vehicle, being in exposure to different heat sources while traveling along the atmospheric layers, we represent this system by an infinitely long and hollow cylindrical shape rotating at constant angular speed  $\omega$ . The space vehicle is expected to operate in low Earth orbit environment. The inner boundary of the cylindrical vehicle is assumed fully-insulated and the outer surface is subjected to the solar radiation and the radiative heat dissipation into the surroundings. The axis of the vehicle is placed at an angle  $\psi$  to the direction of the parallel rays of the impinging radiation of intensity  $f_s$  as shown in Figure 1. The objective is to examine the temperature variations within the space vehicle under different operating conditions, including the spinning speed and the altitude.

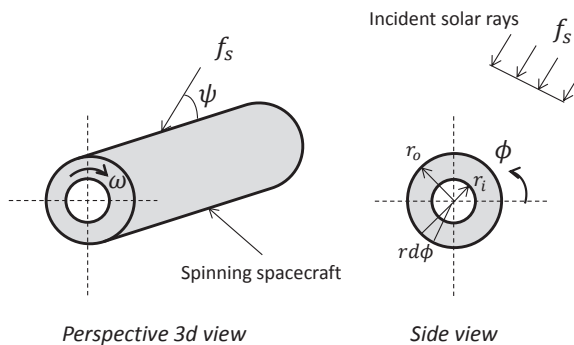


**Figure 1.** Schematic showing the incident solar rays and rotating coordinate system of spacecraft: an infinitely long and hollow cylindrical shape rotating at constant angular speed  $\omega$ .

The governing equation of the temperature field is given by as follows:

$$\frac{1}{\kappa} \frac{\partial T}{\partial t} = \frac{\partial^2 T}{\partial r^2} + \frac{1}{r} \frac{\partial T}{\partial r} + \frac{1}{r^2} \frac{\partial^2 T}{\partial \theta^2} \tag{1}$$

where  $\kappa$  is the thermal diffusivity,  $T$  is the temperature,  $r$  is the radius coordinate,  $t$  is the time, and  $\theta$  is the angular coordinate fixed in the space vehicle. Following [9], we introduce the angular coordinate as

$$\phi = \theta - \omega t \tag{2}$$

and rewrite the governing equation as

$$\frac{\partial^2 T}{\partial r^2} + \frac{\omega}{r} \frac{\partial T}{\partial r} + \frac{\omega}{\kappa} \frac{\partial T}{\partial \phi} + \frac{1}{r^2} \frac{\partial^2 T}{\partial \phi^2} = 0 \tag{3}$$

Accounting for the effect of the solar ray incidence and the radiative heat dissipation, the boundary condition at the outer vehicle surface ( $r = r_o$ ) can be expressed as

$$K \frac{\partial T}{\partial r}(r_o, \phi) = \alpha f_s \sin(\psi) g_s - \sigma \epsilon T^4(r_o, \phi) \tag{4}$$

where  $K$  is the thermal conductivity,  $\alpha$  is the absorptivity of the surface exposed to radiation,  $f_s$  is the intensity of the solar radiation,  $\psi$  is the inclination the vehicle axis to the radiation axis,  $\sigma$  is the Stefan-Boltzman constant,  $\epsilon$  is the emissivity of the vehicle surface, and  $g_s$  is given by

$$g_s = \begin{cases} \cos(\phi), & -\frac{\pi}{2} \leq \phi \leq \frac{\pi}{2} \\ 0, & \frac{\pi}{2} < \phi < \frac{3\pi}{2} \end{cases} \tag{5}$$

The inner vehicle surface ( $r = r_i$ ) is insulated and the corresponding boundary condition is expressed as

$$K \frac{\partial T}{\partial r}(r_i, \phi) = 0 \tag{6}$$

Expanding the nonlinear term of the outer boundary condition while assuming small temperature variation with respect to a characteristic temperature  $T_o$ , introducing the following dimensionless parameters [9]

$$\hat{T} = \frac{T}{T_o} - \frac{3}{4}, \xi = \frac{r}{r_o}, \beta = \sqrt{\frac{\omega}{\kappa}} r_o \tag{7}$$

we obtain the following dimensionless governing equations and boundary conditions

$$\frac{\partial^2 \hat{T}}{\partial \xi^2} + \frac{1}{\xi} \frac{\partial \hat{T}}{\partial \xi} + \beta^2 \frac{\partial \hat{T}}{\partial \phi} + \frac{1}{\xi^2} \frac{\partial^2 \hat{T}}{\partial \phi^2} = 0 \tag{8}$$

$$\frac{\partial \hat{T}}{\partial \xi}(1, \phi) = \frac{\alpha f_s \sin(\psi)}{K T_o} g_s - \frac{4 r_o \sigma \epsilon}{K} T_o^3 \hat{T}(1, \phi) \tag{9}$$

$$\frac{\partial \hat{T}}{\partial \xi}(\xi_i, \phi) = 0, \quad \xi_i = \frac{r_i}{r_o} \tag{10}$$

We note that the characteristic temperature  $T_o$  is given by the following expression as derived in [7]

$$T_o = \left( \frac{\alpha f_s \sin(\psi)}{\sigma \epsilon \pi} \right)^{\frac{1}{4}} \tag{11}$$

The mathematical model presented above will be used to investigate the temperature distribution over a thick-walled cylindrical space vehicle rotating at different angular speeds while exposed to solar radiation.

### 3. Numerical Procedure: Meshless Method

#### 3.1. Theoretical Background

Meshless methods (MMs) have been recently used to solve problems arising in physics and engineering. The motivation behind meshless methods lies in relieving the burden of mesh generation. All traditional mesh-based numerical methods have difficulties on obtaining a suitable mesh. In fact, the problem of generating meshes has become more acute in recent years. Since the application of

computational methods to real world problems appears to be paced by mesh generation, alleviating this bottleneck potentially impacts an enormous field of problems.

Meshless methods are based on approximating the unknown field functions and their derivatives, by using a set of nodes, “sprinkled” over the spatial domain and, functions with compact support. Meshless schemes bypass the use of a conventional mesh. The major fields of computational mechanics, such as finite element methods (FEM), finite difference methods (FDM), and finite volume methods (FVM), rely on the use of elements, interlaced grids, or finite volumes as the underlying structures upon which to discretize governing partial differential equations (PDE). On the other hand, meshless schemes only require clouds of points, without any prior knowledge on their connectivity. On this set of nodes, the spatial domain is represented and PDEs are discretized. Local clouds for each point in a domain are proximity-based subsets of the global set of points. Local clouds of points replace the more traditional forms of connectivity found in FEM, FDM, and FVM. Several formulations of the meshfree method have been formulated such as smoothed particle hydrodynamics (SPH) [31], the diffuse approximation method (DAM) [32], and the element free Galerkin method (EFG). The present study employs the discretization corrected particle strength exchange (DC PSE) [33,34]. DC PSE was formulated as an extension of the particle strength exchange (PSE) method [35]. The latter is used for the evaluation of spatial derivatives of a continuous function, discretized over scattered collocation points. A drawback from the construction procedure of the PSE operators is the introduction of an overlap condition [36], which results in a large number of particles for small kernel sizes. For the DC PSE method, the overlap condition can be relaxed by directly satisfying discrete moment conditions over collocation points. The DC PSE operators ensure that the discretization error at the collocation points does not dominate the overall order of accuracy of the approximation. Next, we introduce the DC PSE operators for strong form formulations (excluding collocation point volumes) in 2D and how to construct them. For higher dimensions and more general analysis and discussion the reader is directed to [36].

We consider the differential operator for a continuous field function  $f(\mathbf{x}) = f(x, y)$  at point  $\mathbf{x}_i = (x_i, y_i)$

$$\mathbf{D}^{(m,n)} f(\mathbf{x}_i) = \frac{\partial^{m+n}}{\partial x^m \partial y^n} f(x, y)|_{x_i, y_i} \quad (12)$$

where  $m$  and  $n$  are integers that determine the order of the differential operator. We define the DC PSE operator for the spatial derivative  $\mathbf{D}^{(m,n)} f(\mathbf{x}_i)$  as follows:

$$\mathbf{Q}^{(m,n)} f(\mathbf{x}_i) = \frac{1}{\epsilon(\mathbf{x}_i)^{m+n}} \sum_{\mathbf{x}_j \in N(\mathbf{x}_i)} \left( f(\mathbf{x}_j \pm f(\mathbf{x}_i)) \right) \frac{1}{\epsilon(\mathbf{x}_i)^2} \eta \left( \frac{\mathbf{x}_i - \mathbf{x}_j}{\epsilon(\mathbf{x}_i)} \right) \quad (13)$$

where  $\epsilon(\mathbf{x})$  is a local scaling parameter,  $\eta(\mathbf{x}, \epsilon(\mathbf{x}))$  is a kernel function normalized by the factor  $\frac{1}{\epsilon(\mathbf{x})^2}$ , and  $N(\mathbf{x})$  is the set of points in the collocation grid within the support of the kernel function. The objective is to construct our DC PSE operators so that as the average spacing between neighbours is decreases,  $h(\mathbf{x}_p)$  tends to zero, around the point  $\mathbf{x}_p$  and then the operator converges to the spatial derivative  $\mathbf{D}^{(m,n)} f(\mathbf{x}_i)$  with an asymptotic rate  $r$ , as expressed below

$$\mathbf{Q}^{(m,n)} f(\mathbf{x}_i) = \mathbf{D}^{(m,n)} f(\mathbf{x}_i) + O\left(h(\mathbf{x}_i)\right) \quad (14)$$

where the average neighbour spacing  $h$  is defined as

$$h(\mathbf{x}_i) = \frac{1}{N} \sum_{\mathbf{x}_j \in N(\mathbf{x}_i)} |x - x_j| + |y - y_j| \quad (15)$$

where  $N$  is the number of points in the support domain of  $\mathbf{x}_i$ . Additionally, we define a kernel function,  $\eta(\mathbf{x})$  and a scaling relation  $\epsilon(\mathbf{x}_p)$  which satisfy Equation (14). To achieve this, we begin by replacing the terms  $f(\mathbf{x}_i)$  in Equation (13) with their Taylor series expansions around the point  $\mathbf{x}_i$ . This gives

$$\begin{aligned} \mathbf{Q}^{(m,n)} f(\mathbf{x}_i) &= \left( \sum_j \sum_k \frac{\epsilon(\mathbf{x}_i)^{j+k-m-n} (-1)^{j+k}}{j!k!} \mathbf{D}^{(j,k)} f(\mathbf{x}_i) Z^{j,k}(\mathbf{x}_i) \right) \\ &\pm Z^{0,0}(\mathbf{x}_i) \epsilon(\mathbf{x}_i)^{-m-n} f(\mathbf{x}_i) \end{aligned} \tag{16}$$

where

$$Z^{j,k}(\mathbf{x}_i) = \sum_{\mathbf{x}_j \in N(\mathbf{x}_i)} \frac{(x_i - x_j)^j (y_i - y_j)^k (-1)^{j+k}}{\epsilon(\mathbf{x}_i)^2} \eta\left(\frac{\mathbf{x}_i - \mathbf{x}_j}{\epsilon(\mathbf{x}_i)}\right) \tag{17}$$

are the discrete moments. The convergence behavior of Equation (16) is determined by the coefficients of the terms  $\epsilon(\mathbf{x}_i)^{j+k-m-n} \mathbf{D}^{(j,k)}$ . We enforce the DC PSE operator to satisfy Equation (16) by setting the coefficients  $m$  and  $n$  of the term  $\mathbf{D}^{(m,n)}$  equal to one, and all other coefficients equal to zero. Finally, using the kernel function we obtain

$$\mathbf{Q}^{(m,n)} f(\mathbf{x}_i) = \frac{1}{\epsilon(\mathbf{x}_i)^{m+n}} \sum_{j \in N(j)} \left( f(\mathbf{x}_j) \pm f(\mathbf{x}_i) \right) p\left(\frac{\mathbf{x}_i - \mathbf{x}_j}{\epsilon(\mathbf{x}_i)}\right) \alpha^T(\mathbf{x}_i) e^{-\frac{(x_i-x_j)^2 - (y_i-y_j)^2}{\epsilon(\mathbf{x}_i)}} \tag{18}$$

The row vector  $p(\mathbf{x})$  contains monomials and vector  $\alpha^T$  is the column vector of unknown coefficients. For example, if we set  $r = 2$  and approximate the first spatial derivative in the  $x$  direction ( $D^{1,0}$ ), we have  $l = 6$  and the monomial basis is  $p(\mathbf{x}) = \{1, x, y, x^2, xy, y^2\}$ . The discrete moment conditions can be expressed as

$$\mathbf{A}(\mathbf{x}) \alpha^T(\mathbf{x}) = \mathbf{b}^T \tag{19}$$

with

$$\mathbf{A}(\mathbf{x}) = \mathbf{B}^T(\mathbf{x}) \mathbf{B}(\mathbf{x}) \tag{20}$$

$$\mathbf{B}(\mathbf{x}) = \mathbf{E}(\mathbf{x}) \mathbf{V}(\mathbf{x}) \tag{21}$$

$$\mathbf{b} = (-1)^{m+n} \mathbf{D}^{(m,n)} p(\mathbf{x})|_{x=0} \tag{22}$$

where  $k$  is the number of points in the support domain of the operator,  $l$  is the number of moment conditions to be satisfied and  $\mathbf{V}(\mathbf{x})$  is the Vandermonde matrix, computed using the set of monomials. The matrix  $\mathbf{E}(\mathbf{x})$  is a diagonal matrix determined by the kernel's window function

$$\mathbf{V}(\mathbf{x}) = \begin{pmatrix} p_1(x_1/\epsilon) & p_2(x_1/\epsilon) & \cdots & p_m(x_1/\epsilon) \\ p_1(x_2/\epsilon) & p_2(x_2/\epsilon) & \cdots & p_m(x_2/\epsilon) \\ \vdots & \vdots & \ddots & \vdots \\ p_1(x_k/\epsilon) & p_2(x_k/\epsilon) & \cdots & p_m(x_k/\epsilon) \end{pmatrix} \tag{23}$$

$$\mathbf{E}(\mathbf{x}) = \text{diag}\left(\left\{e^{-\frac{|x_i|^2}{2\epsilon^2}}\right\}_{i=1}^k\right) \tag{24}$$

The matrix **A**, often referred to as moment matrix, gives information about the spatial distribution of the nodes  $x_i$  around the centre point  $x$ . On the other hand, **b** determines the approximation properties of the kernels. From the mathematical point of view, the invertibility of matrix **A** depends entirely on that of the Vandermode matrix **V**.

### 3.2. Generation of the Point Cloud

In the context of meshless methods, generating point clouds that represent the geometry and computing spatial derivatives is a straightforward procedure. Nodes can be selected randomly or uniformly (following a uniform (Cartesian) or irregular nodal distributions) at the interior domain and on the boundary of the geometry without no prior knowledge on their connectivity. The former is easy to construct while the second requires the use of robust triangular mesh generators.

In this study, we apply an embedded Cartesian grid method to represent the complex geometry (the two cylinders). We start the procedure by setting the boundary nodes from which we will compute the average spacing  $h_c$  for the Cartesian grid (Figure 2b). The Cartesian grid step size  $h_c$ , is defined as the average of the inner and outer boundary nodes spacing, as given by  $h_{ave} = \frac{(h_{in}+h_{out})}{2}$ . From the Cartesian grid, we use only the nodes located in the interior of the domain, while special care is taken for the nodes located close to the boundary nodes. These nodes, often called as degenerated nodes, are the grid nodes with distance less than  $0.2h_c$ , as shown in Figure 2c. The built-in MATLAB function inpolygon has been used to define the Cartesian grid nodes that are located inside the spatial domain. Degenerated nodes are removed and not included in the point cloud, since they give rise to ill-conditioned Vandremode matrices.

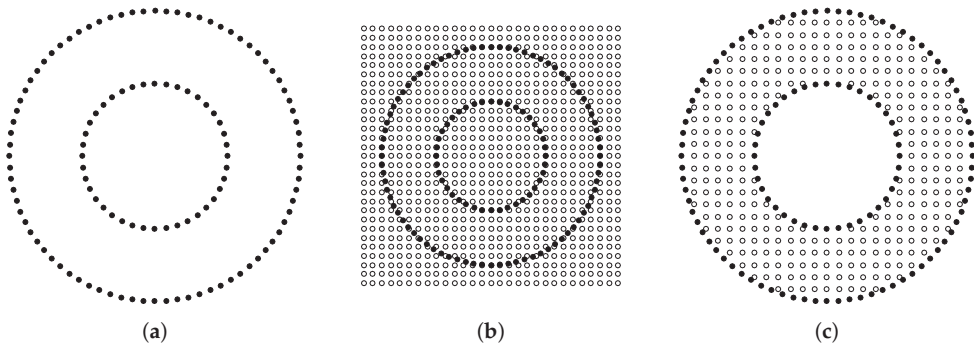


**Figure 2.** Node distribution over the simulated domain: (a) boundary nodes, (b) full set of nodes, (c) interior and boundary nodes.

### 3.3. Explicit Solver

The diffusion–convection problem simulating the temperature variations of the space vehicle is described by Equations (1)–(10). To implement the meshless point collocation method, it is necessary to represent the spatial domain with a set of nodes, distributed over the interior domain and on the boundary. The spatial derivatives of the dependent variable (in our case temperature) are computed by the DC PSE method. As described above, the DC PSE method computes the derivatives of temperature field in a local sense, by using the neighboring nodes. Applying the Euler explicit time integration method, one can rewrite the governing equations in the Cartesian form as follows:

$$\frac{T^{(n+1)} - T^{(n)}}{\delta t} = -u \frac{\partial T^{(n)}}{\partial x} - v \frac{\partial T^{(n)}}{\partial y} + \kappa \left( \frac{\partial^2 T^{(n)}}{\partial x^2} + \frac{\partial^2 T^{(n)}}{\partial y^2} \right) \tag{25}$$

where  $T^{(n+1)}$  and  $T^{(n)}$  are the temperature values at the current and previous time steps, respectively, and  $u = r\omega \cos(\phi)$  and  $v = r\omega \sin(\phi)$  are the velocity components. We note that the time step  $\delta t$  of the explicit solver should be carefully selected to guarantee stable and accurate numerical solutions.

In the present application, Neumann boundary conditions are imposed in the inner and outer surfaces of the cylinder, as given by

$$-K \frac{\partial T}{\partial \mathbf{r}} \Big|_{r=r_i} = -K(\nabla T \cdot \mathbf{n}) = -K \left( \frac{\partial T}{\partial x} n^x + \frac{\partial T}{\partial y} n^y \right) = 0 \tag{26}$$

$$-K \frac{\partial T}{\partial \mathbf{r}} \Big|_{r=r_o} = -K(\nabla T \cdot \mathbf{n}) = -K \left( \frac{\partial T}{\partial x} n^x + \frac{\partial T}{\partial y} n^y \right) = -\alpha f_s \sin(\psi) g_s + \sigma \epsilon T^4 \tag{27}$$

where  $\mathbf{n} = (n^x, n^y)$  is the unit normal vector pointing outward. We compute the values on the boundary nodes with Neumann boundary conditions based on values of interior nodes that belong to the support domain, as shown in Figure 3.

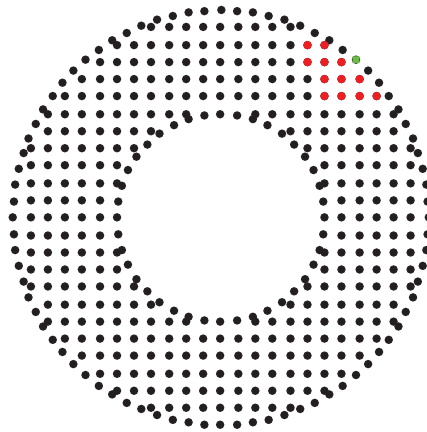


**Figure 3.** A boundary stencil for enforcing no flux boundary conditions. The stencil is based at the one center located on the boundary. Base center marked with a square (green) and supporting centers with a circle (red).

The temperature on the inner and outer surfaces of the cylinder are computed using the Neumann boundary conditions as follows. First, we compute the weights,  $w^x$  and  $w^y$ , for the first spatial derivative with respect to  $x$ - and  $y$ -, respectively, based on the support nodes. The support nodes (stencil) include one boundary point (center number  $i$ ) such as the stencil shown in Figure 3 and the nodes located in the interior of the geometry. The boundary values of the temperature are computed as

$$T_i^{inner} = \frac{1}{(n_i^x w_i^x + n_i^y w_i^y)} \left( -n_i^x (w_2^x T_2 + \dots + w_n^x T_n) - n_i^y (w_2^y T_2 + \dots + w_n^y T_n) \right) \tag{28}$$

$$T_i^{outer} = \frac{1}{(n_i^x w_i^x + n_i^y w_i^y + \frac{4r_o \sigma \epsilon T_o^3}{K} + h)} \left( -n_i^x (w_2^x T_2 + \dots + w_n^x T_n) - n_i^y (w_2^y T_2 + \dots + w_n^y T_n) \right) + \frac{r_o \alpha f_s \sin(\psi) g_s}{K T_o} \tag{29}$$

The computational model described above is implemented on Matlab. We discretize the spatial domain using successively finer uniform Cartesian embedded grids with spacing of  $h = 2.5 \times$



$10^{-3}$ ,  $1.25 \times 10^{-3}$  and  $6.25 \times 10^{-4}$  m to ensure a grid independent solution, resulting in 34,580, 136,972 and 545,416 nodes, respectively. The results on the two finest grids are almost indistinguishable, indicating grid independence. Therefore, in our simulations we use the grid with a spacing of  $h = 1.25 \times 10^{-3}$  m. The time step used in the simulations is set to  $dt = 10^{-3}$  s for all angular velocity values considered while the initial values for all flow variables at the interior points were set to zero. Computations were conducted using an Intel i7 quad core processor with 16 GB RAM.

#### 4. Results and Discussion

The developed model, given by Equations (8)–(10), is obtained by energy conservation between the heat conduction among the space vehicle, the heating from the solar radiation, the radiative heat dissipation into the surroundings while accounting for the dynamics of the space vehicle (rotational motion). This model is solved numerically using the meshless collocation point method (MCP) to evaluate the temperature distribution under different operating conditions. The simulation results are expected to provide baseline and guidance for the design of thermal control systems for space vehicles.

To verify the numerical predictions of the meshless collocation point method, we consider the simulated case of rotating cylinder exposed to solar radiation reported in [9]. The numerical values of the geometry and thermal parameters are presented in Table 1. The vehicle is assumed to be a black body made of natural rubber with a low conductivity. We simulate the thermal response of the space vehicle while varying the spinning speed  $\omega$  from 0 to 1000 rad/h. The current simulation results are compared against those obtained from the finite difference method (FDM) by Gadalla and Wehba [9]. We plot in Figure 4 the variations of the steady-state temperature at the outer surface for different spinning speeds as obtained from the two numerical approaches: MCP (current study) and FDM (as used in [9]). The two sets of data show good agreement. This demonstrates the capability of MCP method to perform thermal analysis of moving space vehicles subjected to heat sources and dissipation. For a fixed space vehicle ( $\omega = 0$  rad/h), we observe a symmetric distribution of the temperature about the location of the radiant heat source. Once the rotational motion is initiated, this symmetry is broken. As the spinning speed increases, the maximum and minimum temperatures shift to lower and higher values, respectively. Clearly, the rotational motion of the space vehicle at higher angular speeds enables further reduction in the temperature gradients. At  $\omega = 1000$  rad/h, the temperature distribution at the outer surface is found almost insensitive to the circumferential position  $\phi$ .

Figure 5 depicts the variations of the temperature with the angular position  $\phi$  at the internal circumferential surface located at  $\zeta = 0.8$ . The current simulation results compare well with those obtained using FDM [9]. The simulations show that the rotational motion tends to reduce more the temperature gradients in the internal circumferential surfaces in comparison to those achieved at the outer surface, directly exposed to the solar radiation. At  $\omega = 2$  rad/h, a slight variation in the temperature distribution is observed.

**Table 1.** Numerical values of the parameters used for the rotating spacecraft [9].

Parameter	Symbol	Numerical Value
Outer radius	$r_o$	0.3048 m
Inner radius	$r_i$	0.1524 m
Inclination of the vehicle	$\psi$	$\frac{\pi}{2}$
Intensity of the solar radiation	$f_s$	1.4 kW/m <sup>2</sup>
Thermal conductivity	$K$	0.173 W/m K
Absorptivity	$\alpha$	1
Emissivity	$\epsilon$	1
Characteristic temperature	$T_o$	297.46 K
Non-dimensional radius	$\zeta$	0.8 and 1
Spinning speed	$\omega$	0–1000 rad/h

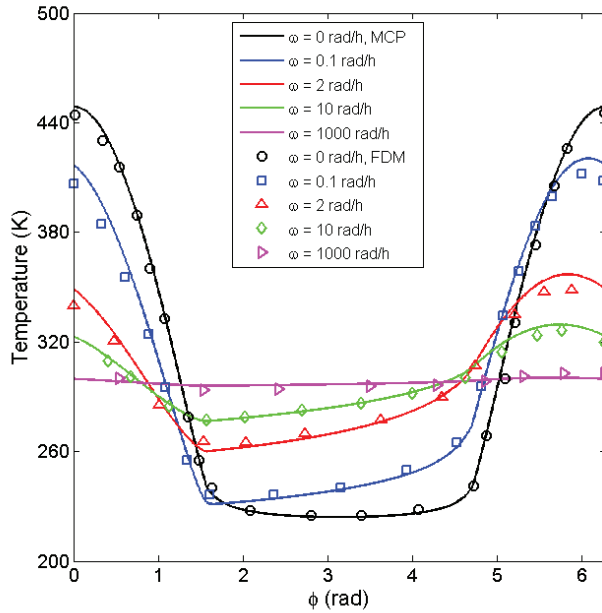


Figure 4. Temperature variations of outer vehicle surface for varying spinning speeds: comparison between current simulations and FDM results [9].

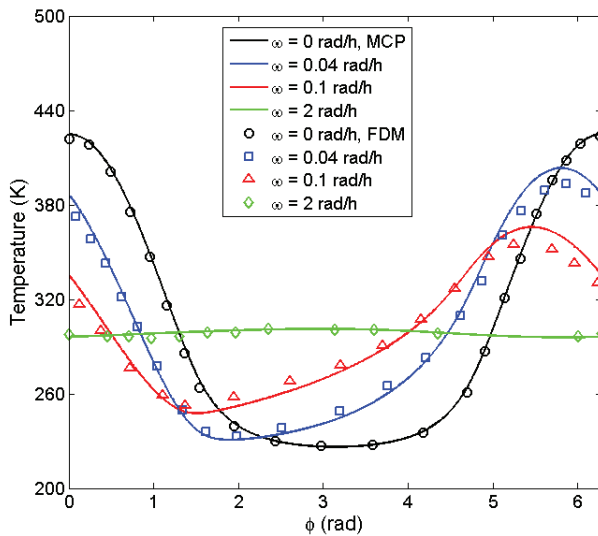
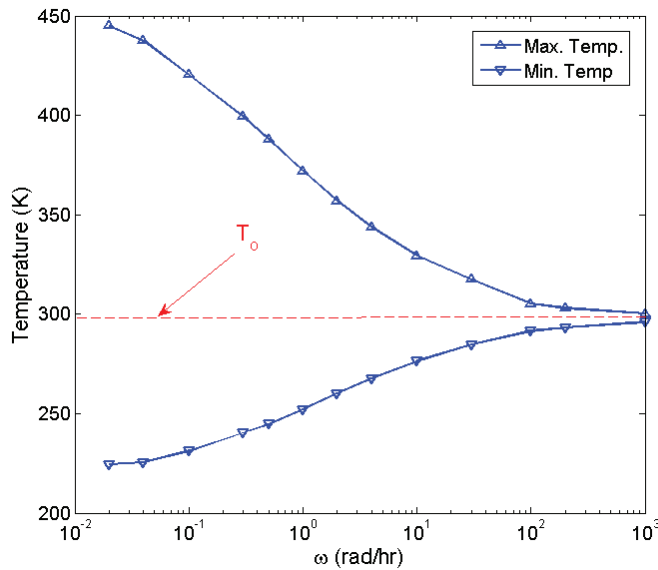


Figure 5. Temperature variations of the internal vehicle surface ( $\frac{r}{r_0} = 0.8$ ) for varying spinning speeds: comparison between current simulations and FDM results.

Figure 6 shows the maximum and minimum temperatures at the outer surface ( $\xi = 1$ ) for different values of the spinning speed  $\omega$ . Rotating the space vehicle at higher speeds results in shrinking the bandwidth between the temperature extrema. At very high rotational speeds ( $\omega \geq 1000$  rad/h),

the maximum and minimum temperatures converge to the reference temperature  $T_o$ , given by Equation (11).



**Figure 6.** Variations of the temperature extrema (maximum and minimum) at the outer surface with the spinning speed: current simulations.

To gain an insight into the impact of the rotational motion on the temperature distribution over the full space vehicle, we plot in Figure 7 the temperature contours for varying spinning speeds. Again, a symmetric temperature field is obtained for a fixed space vehicle. The rotational motion breaks the symmetry and induces reduction in the temperature range. For  $\omega$  higher than 10 rad/h, the temperature is observed to be varying only within a thin layer near the outer surface, otherwise constant over the internal domain. We note that these results are consistent with those obtained in [9]. The simulation results reveal the importance of incorporating the rotational motion of the spacecraft to achieve lower temperature with a uniform distribution over the entire structure. This would enable a safer operability of the spacecraft. The Earth's atmosphere comprises four main layers. Moving upward from ground level, these layers are named the troposphere, stratosphere, mesosphere, and thermosphere, each with its own specific traits. The exposure to different heat and pressure loads within these layers present a major cause of anomalies in many space missions. The present numerical analysis shows that the design of spacecraft can be then significantly enhanced in terms of thermal resistance to the exposure to heat sources by incorporating the rotational motion.

We discretize the spatial domain shown in Figure 8 using successively finer uniform Cartesian embedded grids with a spacing of  $h = 1.875 \times 10^{-3}$ ,  $1.25 \times 10^{-3}$  and  $9.375 \times 10^{-4}$  m to verify the convergence behavior of the numerical solution and obtain a grid independent temperature solutions. We note the aforementioned spacings lead to 114,490, 256,875 and 456,057 nodes, respectively. The results on the two finest grids are almost indistinguishable, indicating grid independence. As such, in the subsequent simulations, we use a grid with spacing of  $h = 1.25 \times 10^{-3}$  m. The time step is set to  $dt = 10^{-6}$  s, while the initial values for all flow variables at the interior points were set to zero. Computations were conducted using an Intel i7 quad core processor with 16 GB RAM.

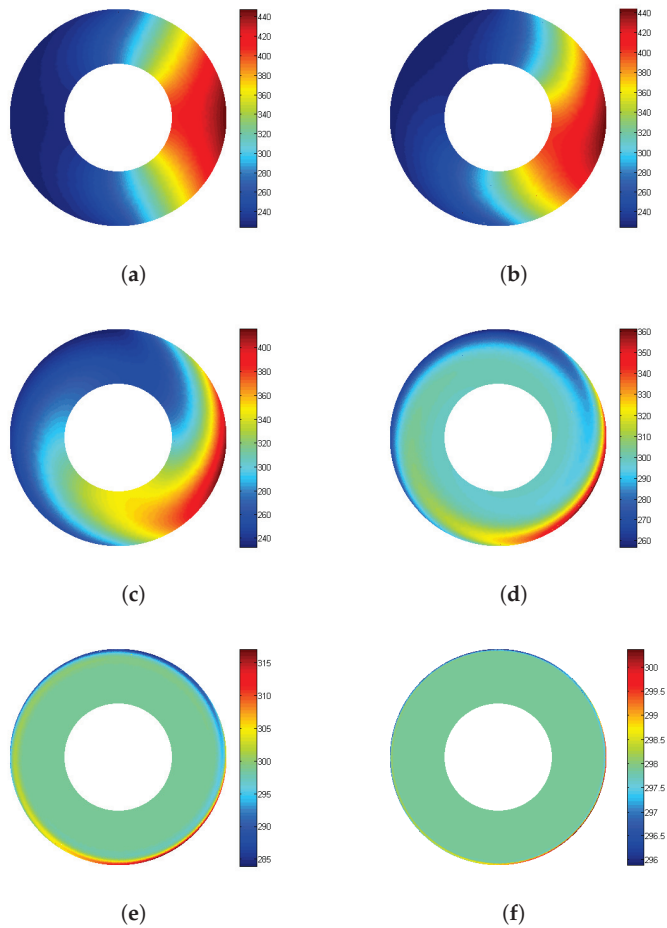


**Figure 7.** Temperature contours obtained for different spinning speeds: current simulations. (a)  $\omega = 0$  rad/h, (b)  $\omega = 0.02$  rad/h, (c)  $\omega = 0.1$  rad/h, (d)  $\omega = 1$  rad/h, (e)  $\omega = 10$  rad/h, (f)  $\omega = 1000$  rad/h.

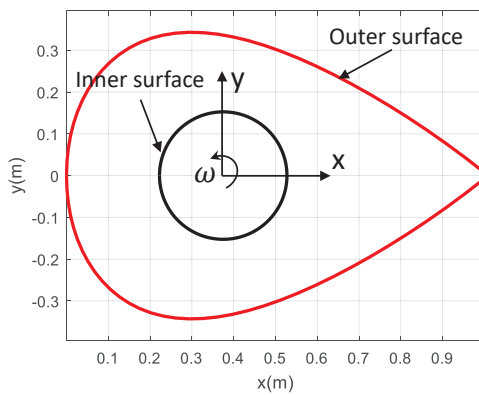


**Figure 8.** Schematic of the cross section of the rotating space vehicle.

We show in Figure 9 the contour plots of the temperature over the thick-walled vehicle for varying angular speeds. Keeping the vehicle at static position leads to a large temperature gradients. Activating the rotational motion results in a significant reduction in temperature variations and enables more uniform temperature distribution on the body of the space vehicle.

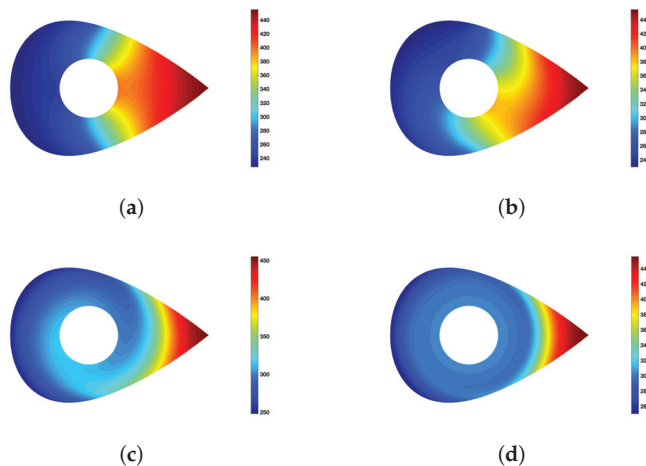


**Figure 9.** Temperature contours obtained for different spinning speeds: current simulations. (a)  $\omega = 0$  rad/h, (b)  $\omega = 0.1$  rad/h, (c)  $\omega = 1$  rad/h, (d)  $\omega = 10$  rad/h.

## 5. Conclusions

In this work, we developed a computational model based on the meshless collocation point method to simulate the temperature distribution over a rotating spacecraft under solar radiation effect. The spacecraft is treated as a thick-walled object of different geometries. The numerical results compared well with those reported in the literature. The simulations revealed that spacecraft may undergo large temperature gradients when traveling over the Earth's atmospheric layers or in low Earth orbit. We showed the usefulness of spinning the spacecraft to avoid large temperature variations that may degrade its performance. Rotating the spacecraft at an angular speed of or higher than 10 rad/h enables a quasi-uniform temperature distribution over its internal domain. The numerical study is expected to provide a baseline for thermal control of space vehicles.

**Author Contributions:** Conceptualization, M.G. (Mohamed Gadalla) and M.G. (Mehdi Ghommem); Methodology, M.G. (Mehdi Ghommem) and G.B.; Software, M.G. (Mehdi Ghommem) and G.B.; Validation, M.G. (Mohamed Gadalla), M.G. (Mehdi Ghommem) and G.B.; Writing-Original Draft Preparation, M.G. (Mohamed Gadalla), M.G. (Mehdi Ghommem) and G.B.; Writing-Review & Editing, M.G. (Mohamed Gadalla), M.G. (Mehdi Ghommem), G.B., and K.M.; Visualization, M.G. (Mehdi Ghommem) and G.B.

**Funding:** This research was supported in part by the Australian Government through the Australian Research Council's Discovery Projects funding scheme (project DP160100714). The views expressed herein are those of the authors and are not necessarily those of the Australian Government or Australian Research Council.

**Conflicts of Interest:** The authors declare no conflict of interest.

## References

1. Schonberg, W.P. Studies of hypervelocity impact phenomena as applied to the protection of spacecraft operating in the MMOD environment. *Procedia Eng.* **2017**, *204*, 4–42.
2. Deim, M.; Suderland, M.; Reiss, P.; Czupalla, M. Development and evaluation of thermal model reduction algorithms for spacecraft. *Acta Astronaut.* **2015**, *110*, 168–179. [CrossRef]

3. Labibian, A.; Alikhani, A.; Pourtakdoust, S.H. Performance of a novel heat based model for spacecraft attitude. *Aerosp. Sci. Technol.* **2017**, *70*, 317–327. [CrossRef]
4. Garmendia, I.; Anglada, E.; Vallejo, H.; Seco, M. Accurate calculation of conductive conductances in complex geometries for spacecraft thermal models. *Adv. Space Res.* **2016**, *57*, 1087–1097. [CrossRef]
5. Fernandez-Rico, G.; Perez-Grande, I.; Sanz-Andres, A.; Torralbo, I.; Woch, J. Quasi-autonomous thermal model reduction for steady-state problems in space systems. *Appl. Therm. Eng.* **2016**, *105*, 456–466. [CrossRef]
6. Perez-Grande, I.; Sanz-Andres, A.; Guerra, C.; Alonso, G. Analytical study of the thermal behaviour and stability of a small satellite. *Appl. Therm. Eng.* **2009**, *29*, 2567–2573. [CrossRef]
7. Gadalla, M.A. Prediction of temperature variation in a rotating spacecraft in space environment. *Appl. Therm. Eng.* **2005**, *25*, 2379–2397. [CrossRef]
8. Gadalla, M.A. Modeling of Thermal Analysis of Rotating Space Vehicles Subjected to Solar Radiation. In Proceedings of the 28th Intersociety Energy Conversion Engineering Conference (IECEC93), ACS, Atlanta, GA, USA, 8–13 August 1993.
9. Gadalla, M.A.; Wahba, E. Computational modeling and analysis of thermal characteristics of a rotating spacecraft subjected to solar radiation. *Heat Transf.-Asian Res.* **2011**, *40*, 655–674. [CrossRef]
10. Poncy, J.; Jubineau, F.; Angelo, F.D.; Perotto, V.; Juillet, J.J. Solar orbiter-heat shield and system technology. *Acta Astronaut.* **2009**, *65*, 1076–1088. [CrossRef]
11. Corpino, S.; Caldera, M.; Nichele, F.; Masoero, M.; Viola, N. Thermal Design and analysis of a nanosatellite in low earth orbit. *Acta Astronaut.* **2015**, *115*, 247–261. [CrossRef]
12. Farrahi, A.; Perez-Grande, I. Simplified analysis of the thermal behavior of a spinning satellite flying over sun-synchronous orbits. *Appl. Therm. Eng.* **2017**, *125*, 1146–1156. [CrossRef]
13. Ross, R.G. Estimation of thermal conduction loads for structural supports of cryogenic spacecraft assemblies. *Cryogenics* **2004**, *44*, 421–424. [CrossRef]
14. Guoliang, M.; Guiqing, J. Comprehensive analysis and estimation system on thermal environment, heat protection and thermal structure of spacecraft. *Acta Astronaut.* **2004**, *54*, 347–356. [CrossRef]
15. Teofilatto, P. Preliminary aircraft design: Lateral handling qualities. *Aircr. Des.* **2001**, *4*, 63–73. [CrossRef]
16. Shen, Z.; Li, H.; Liu, X.; Hu, G. Thermal shock induced dynamics of a spacecraft with a flexible deploying boom. *Acta Astronaut.* **2017**, *141*, 123–131. [CrossRef]
17. Meese, E.A.; Norstrud, H. Simulation of convective heat flux and heat penetration for a spacecraft at re-entry. *Aerosp. Sci. Technol.* **2002**, *6*, 185–194. [CrossRef]
18. Naumann, R.J. An analytical model for transport from quasi-steady and periodic acceleration on spacecraft. *Int. J. Heat Mass Transf.* **2000**, *43*, 2917–2930. [CrossRef]
19. Pippin, G. Space environments and induced damage mechanisms in materials. *Prog. Org. Coatings* **2003**, *47*, 424–431. [CrossRef]
20. Gaité, J.; Andres, A.S.; Grande, I.P. Nonlinear analysis of a simple model of temperature evolution in a satellite. *Appl. Therm. Eng.* **2009**, *29*, 2567–2573. [CrossRef]
21. Charnes, A.; Raynor, S. Solar heating of a rotating cylindrical space vehicle. *ARS* **1960**, *30*, 479–483. [CrossRef]
22. Wu, W.-F.; Liu, N.; Cheng, W.-L.; Liu, Y. Study on the effect of shape-stabilized phase change material on spacecraft thermal control in extreme thermal environment. *Energy Convers. Manag.* **2013**, *69*, 174–180. [CrossRef]
23. Tkachenko, S.I.; Salmin, V.V.; Tkachenko, I.S.; Kaurov, I.V.; Korovin, M.D. Verifying parameters of ground data processing for the thermal control system of small spacecraft AIST based on telemetry data obtained by Samara. *Orocrdia Eng.* **2017**, *185*, 205–211. [CrossRef]
24. Han, J.H.; Kim, C.G. Low earth orbit space environment simulation and its effects. *Compos. Struct.* **2006**, *72*, 218–226. [CrossRef]
25. Azadi, E.; Fazelzadeh, S.A.; Azadi, M. Thermally induced vibrations of smart solar panel in a low-orbit satellite. *Adv. Space Res.* **2017**, *59*, 1502–1513. [CrossRef]
26. Liu, L.; Cao, D.; Huang, H.; Shao, C.; Xu, Y. Thermal-structural analysis for an attitude maneuvering flexible spacecraft under solar radiation. *Int. J. Mech. Sci.* **2017**, *126*, 161–170. [CrossRef]
27. Nicholes, L.D. *Surface Temperature Distribution on Thin-Walled Bodies Subjected to Solar Radiation in Interplanetary Space*; Technical Note D-584; NASA: Washington, DC, USA, 1961.

28. Roberts, A.F. Heating of cylinders by radiation; approximate formulae for the temperature distribution. *ASME* **1964**, *64-HT-39*.
29. Jenness, J.R. Temperature in a cylindrical satellite. *Acta Astronaut.* **1960**, *5*, 241–252.
30. Torres, A.; Mishkinis, D.; Kaya, T. Mathematical modeling of a new satellite thermal architecture system connecting the east and west radiator panels and flight performance. *Appl. Therm. Eng.* **2014**, *65*, 623–632. [CrossRef]
31. Gingold, R.A.; Monaghan, J.J. Smoothed particle hydrodynamics: Theory and application to non-spherical stars. *Mon. Not. R. Astron. Soc.* **1977**, *181*, 275–389. [CrossRef]
32. Nayroles, B.; Touzot, G.; Villon, P. Generalizing the finite element method: Diffuse approximation and diffuse elements. *Comput. Mech.* **1992**, *10*, 307–318. [CrossRef]
33. Schrader, B.; Reboux, S.; Sbalzarini, I.F. Discretization correction of general integral PSE operators for particle methods. *J. Comput. Phys.* **2010**, *229*, 4159–4182. [CrossRef]
34. Bourantas, G.C.; Cheeseman, B.L.; Ramaswamy, R.; Sbalzarini, I.F. Using DC PSE operator discretization in Eulerian meshless collocation methods improves their robustness in complex geometries. *Comput. Fluids* **2016**, *136*, 285–300. [CrossRef]
35. Eldredge, J.D.; Leonard, A.; Colonius, T.A. A General Deterministic Treatment of Derivatives in Particle Methods. *J. Comput. Phys.* **2002**, *180*, 686–709. [CrossRef]
36. Bourantas, G.C.; Ghommem, M.; Kagadis, G.C.; Katsanos, K.; Loukopoulos, V.C.; Burganos, V.N.; Nikiforidis, G.C. Real-time tumor ablation simulation based on the dynamic mode decomposition method. *Med. Phys.* **2014**, *41*, 053301. [CrossRef]



© 2019 by the authors. Licensee MDPI, Basel, Switzerland. This article is an open access article distributed under the terms and conditions of the Creative Commons Attribution (CC BY) license (<http://creativecommons.org/licenses/by/4.0/>).

Article

# Cryogenic Energy for Indirect Freeze Desalination—Numerical and Experimental Investigation

Harith Jayakody \*, Raya Al-Dadah and Saad Mahmoud

School of Mechanical Engineering, University of Birmingham, Birmingham B152TT, UK; r.k.al-dadah@bham.ac.uk (R.A.-D.); s.m.mahmoud@bham.ac.uk (S.M.)

\* Correspondence: harith\_ej@hotmail.com

Received: 24 November 2019; Accepted: 18 December 2019; Published: 21 December 2019

**Abstract:** Renewed interest in freeze desalination has emerged due to its advantages over other desalination technologies. A major advantage of the freeze desalination process over evaporative methods is its lower energy consumption (latent heat of freezing is 333.5 kJ/kg and latent heat of evaporation is 2256.7 kJ/kg). Cryogenic fluids like LN<sub>2</sub>/L<sub>Air</sub> are emerging as an effective energy storage medium to maximise utilisation of intermittent renewable energy sources. The recovery of this stored cold energy has the potential to be used for freeze desalination. Computational Fluid Dynamics (CFD) modelling was developed to simulate the evaporation of liquid nitrogen to simultaneously conduct freeze desalination to investigate the feasibility of using cryogenic energy for freeze desalination. This integrated CFD model was validated using experimental heat exchanger test facility constructed, to evaporate liquid nitrogen to supply the cooling required for freezing. Parametric study on the LN<sub>2</sub> flow rate to observe the volume of ice obtained was also examined using CFD, where increasing the velocity of LN<sub>2</sub> by 6 times, increased the volume of ice obtained by 4.3 times. A number of freezing stages were required in order to reduce the ice salinity from 1.5% down to 0.1% as regarded by the World Health Organisation (WHO) as safe to drink. In the cryogenic desalination test rig, approximately 1.35 L of liquid nitrogen was required to reduce the ice salinity from 1.5% to less than 0.1%. Furthermore, the above results illustrate the potential of using the cold energy of cryogenic fluids such as Liquefied Natural Gas (LNG) and LN<sub>2</sub>/L<sub>Air</sub> for freeze desalination applications as most cold energy during LNG regasification has been unexploited today.

**Keywords:** cryogenic energy; liquid nitrogen; CFD; freeze; desalination

## 1. Introduction

Sustainable resources of water and energy are essential for social, economic and human wellbeing in the modern world [1]. The basic substance for life is water, and it is progressively becoming a scarce resource with half of the population of about 88 developing countries affected by water shortages [2]. In these developing countries, 80% to 90% of all diseases are caused by poor water quality and 30% deaths are also due to poor water quality [2]. The people affected by harsh water shortages are projected to rise in the next 25 years due to the growth in population and the demands of industrialization [3]. At present, the rate of increase of water consumption is twice the rate of population growth, where it doubles every 20 years [4]. There is a vast amount of water available on Earth, about  $1.4 \times 10^9$  km<sup>3</sup> [4]. However, less than 3% of this amount is fresh water, about  $3.5 \times 10^7$  km<sup>3</sup>. A major part of this (about  $2.4 \times 10^7$  km<sup>3</sup>) is not accessible due to it being located in ice caps and glaciers. Approximately,  $1.1 \times 10^7$  km<sup>3</sup> of the Earth's water is retained as groundwater, plants, atmosphere and surface water in rivers, lakes, etc. [5]. The greatest part of this water has slowly accrued over time, and it is not considered to be renewable [2]. Freshwater production by the removal of dissolved minerals from



seawater is known as desalination, and it appears to be an answer to the water shortage issue [6,7]. Cost-effective and possibly climate independent water resources can be produced by desalination technologies for agricultural uses [8]. In order to address the water shortage issue, seawater is the leading feed water in the world for installed desalination techniques, thus making it the most applied solution [8].

Freeze desalination (FD) is an evolving desalination technology due to its low energy usage. In comparison to other desalination techniques, FD has several advantages [9–14]. In freeze desalination, the salts are rejected during ice formation and ice formed is of pure water where the crystal lattice does not allow the inclusion of any salts due to the nature of the ice crystal structure [9,10]. The process of freezing an aqueous salt solution results in ice crystals that are of pure water in the solid phase; this process is the physical principle of freeze desalination [15]. The Low energy usage is achieved in the FD process due to the latent heat of fusion being about 335 kJ/kg while the latent heat of vaporization is about 2256.7 kJ/kg [11,12]. Another key advantage of the freeze desalination process is its low operating cost of 0.34 \$/m<sup>3</sup> compared to 0.75 \$/m<sup>3</sup> for the commonly used Reverse Osmosis (RO) desalination technology. A key advantage of the freeze desalination technology is the ability to utilize the cold energy from the regasification of liquefied natural gas (LNG). This high-quality cold energy source can be used to freeze saltwater in the freeze desalination process, but most cold energy during LNG regasification has been unexploited until today. Approximately 830 kJ/kg of cold energy is released during LNG regasification and this cryogenic exergy can be used for the freeze desalination process [16]. Due to the on-going energy supply-demand disparity, augmenting these technologies can aid in providing solutions for this and in improving the economics of the renewable energy powered desalination systems, as desalination capacity is escalating worldwide [17].

Research has been carried out experimentally and numerically on ice formation on subcooled surfaces for the rate of ice growth and conditions for control [18], temperature distribution [19], heat transfer coefficient [20], unsteady heat transfer [21], and ice growth kinetics for a continuous freezing process [22,23]. Nonetheless, this research did not include the progression of salt separation and the increase of brine salinity in the remaining solution. Abid et al. [24] studied the separation of binary mixture freezing for saltwater desalination, but the effect of saline water ice growth dynamics was not investigated widely. During the FD process, the separation of salt from ice and the rise of brine salinity in the remaining solution were not studied by other researchers.

Energy storage is a vital part of energy production, using renewable energy sources [25]. Cryogenic energy offers better exploitation of renewable energy, due to the fact that liquid nitrogen and liquid air are known to be important energy carriers in the recent past. This is mainly due to the high energy density and the availability of cryogenic energy. Cryogenic energy storage uses surplus electricity to cool air to liquefy it, and then, it is stored in tanks. Liquid air can be stored in a compact manner in small tanks because of the energy density and pressure. In low pressure insulated tanks, these cryogenic fluids can be stored for months with losses as small as 0.005% volume per day [26]. When needed, the liquid air is pressurized and transformed into gaseous state (evaporated), usually using waste heat from another process (higher temperature source). This gas is then expanded to run a turbine to generate electricity [26,27].

The novelty of this research is the study of evaporation of liquid nitrogen for freeze desalination. Many researchers have looked into the use of cryogenics as a source of energy for many applications such as cooling for domestic and industrial processes and driving turbines and engines for power generation, etc. [28–32]. Cryogenic energy has also been utilised in freeze desalination by few researchers [14,16,33]. However, numerical modelling of cryogenic energy for freeze desalination has not yet been studied, and the use of the evaporation of liquid nitrogen for indirect contact freeze desalination has not yet been investigated. Therefore, this paper focuses on the evaporation of liquid nitrogen for indirect contact freeze desalination. Computational fluid dynamics (CFD) analysis of this process was carried out, and an experimental test rig was built to further understand this process and to validate the CFD model.

## 2. CFD Modelling Theory

Literature on CFD modelling of the evaporation of liquid nitrogen process and the freeze desalination process is very limited. Therefore, CFD modelling of the evaporation of liquid nitrogen as a source of cooling for the freeze desalination process was established. In this paper, 3D CFD simulations were developed to simulate the evaporation of liquid nitrogen to simultaneously conduct freeze desalination. The modelling theories of the evaporation of liquid nitrogen process and of the freeze desalination process are discussed in this paper.

### 2.1. Evaporation of Liquid Nitrogen Theory

Liquid nitrogen turns from liquid to nitrogen gas in the evaporation process of LN<sub>2</sub>. Therefore, for modelling the evaporation process where the fluid changes phase (liquid to gas), the multiphase model in ANSYS Fluent (19.1, ANSYS, Canonsburg, Pennsylvania, United States, 2018) is used. Additionally, the energy and the turbulent models were used to determine temperature variation during the turbulent flow of the fluid. In the ANSYS multiphase module, three different Euler–Euler multiphase models are offered: the Eulerian model, the mixture model and the volume of fluid (VOF) model [34]. All of these Euler–Euler multiphase models can be used to model the evaporation of liquid nitrogen. However, only the volume of fluid (VOF) can be used in conjunction with the solidification/melting model that is used to model the freeze desalination process. Therefore, when simulating the evaporation of liquid nitrogen simultaneously with the freeze desalination modelling, only the VOF option in the multiphase model can be used.

By solving a single set of momentum equations and tracking the volume fraction of each of the fluids in the field, the VOF model is able to model two or more immiscible fluids [34]. Key processes that the VOF model is able to model are steady/transient tracking of any liquid–gas interface, motion of bubbles in a liquid, prediction of jet breakup, etc. [34].

In the VOF model, the tracking of the interfaces between the phases is achieved by using the continuity equation for the volume fraction of one or more of the phases. Hence, Equation (1) represents this for the  $q^{\text{th}}$  phase [34].

$$\frac{1}{\rho_q} \left[ \frac{d}{dt} (\alpha_q \rho_q) + \nabla \cdot (\alpha_q \rho_q \vec{v}_q) \right] = S_{\alpha_q} + \sum_{p=1}^n (\dot{m}_{pq} - \dot{m}_{qp}) \quad (1)$$

where the mass transfer from phase  $p$  to phase  $q$  is denoted as  $\dot{m}_{pq}$ , and the mass transfer from phase  $q$  to phase  $p$  is denoted as  $\dot{m}_{qp}$ .  $S_{\alpha_q}$  is a source term which is zero by default, but a user-defined mass source for each phase can be specified.

For the primary phase, the volume fraction equation is not solved; based on the following constraint, the primary-phase volume fraction is calculated as  $\sum_{q=1}^n \alpha_q = 1$ . Through implicit or explicit time discretization, the volume fraction equation is solved [34].

In the VOF model, a single momentum equation is solved, and the subsequent velocity field is shared amid the phases. The momentum equation is dependent on the volume fractions of all phases via the properties  $\mu$  and  $\rho$ , as shown in Equation (2) [34].

$$\frac{d}{dt} (\rho \vec{v}) + \nabla \cdot (\rho \vec{v} \vec{v}) = -\nabla_p + \nabla \cdot [\mu (\nabla \vec{v} + \nabla \vec{v}^T)] + \rho \vec{g} + \vec{F} \quad (2)$$

In the VOF model, the energy Equation (3), is shared among the phases [34].

$$\frac{d}{dt} (\rho E) + \nabla \cdot (\vec{v} (\rho E + p)) = \nabla \cdot (k_{eff} \nabla T) + S_h \quad (3)$$

Energy  $E$  (Equation (4)) and temperature  $T$  are treated as mass-averaged variables in the VOF model.

$$E = \frac{\sum_{q=1}^n \alpha_q \rho_q E_q}{\sum_{q=1}^n \alpha_q \rho_q} \quad (4)$$

where the specific heat of that phase and the shared temperature are what  $E_q$  for each phase is based on [34]. The effective thermal conductivity  $k_{eff}$  and  $\rho$  are shared by the phases. Influences from radiation and any other volumetric heat sources are what the source term  $S_h$  comprises [34].

## 2.2. Freeze Desalination Process Theory

In order to simulate the freeze desalination process, energy (heat transfer), species transport and solidification/melting modules were used. Solidification/melting and species transport modules were utilised in order to separate the pure water (as ice) from the rejected brine solution [17]. Equations (5) to (17) describe the freeze desalination process on ANSYS Fluent and it is detailed by Jayakody et al. [7,17].

The material's enthalpy is calculated from Equation (5).

$$H = h + \Delta H \quad (5)$$

$h$  is the sensible enthalpy calculated by Equation (6).

$$h = h_{ref} + \int_{T_{ref}}^T C_p dT \quad (6)$$

The energy equation for solidification problems with the inclusion of species transport is shown in Equation (7) [17].

$$\frac{d}{dt}(\rho H) + \nabla \cdot (\rho \vec{v} H) = \nabla \cdot (k \nabla T) + \frac{(1-\beta)^2}{(\beta^2 + \epsilon)} A_{mush} \vec{v} \quad (7)$$

The liquid fraction,  $\beta$  is found by Equation (8) [7].

$$\beta = \frac{T - T_{solidus}}{T_{liquidus} - T_{solidus}}, \text{ when } T_{solidus} < T < T_{liquidus} \quad (8)$$

$\beta = 0$ , when  $T < T_{solidus}$

$\beta = 1$ , when  $T > T_{liquidus}$

The latent heat content is determined in terms of the latent heat of the material and the liquid volume fraction  $\beta$  as shown in Equation (9). With values of  $\beta$  ranging from 0 to 1, this latent heat content can differ from 0 (solid) to  $L$  (liquid).

$$\Delta H = \beta L \quad (9)$$

The apparent melting temperature is  $T_{melt}$ , where phase change occurs for solidification of a pure substance. A mushy freeze/melt region happens at a higher liquidus ( $T_{liquidus}$ ) temperature and a lower solidus temperature ( $T_{solidus}$ ) for a multicomponent mixture as shown in Equations (10) and (11) [35].

$$T_{solidus} = T_{melt} + \sum_{solute} m_i Y_i / K_i \quad (10)$$

$$T_{liquidus} = T_{melt} + \sum_{solute} m_i Y_i \quad (11)$$

For species separation, the ‘scheil’ rule has been sourced at the micro-scale as it assumes no diffusion of solute species in the solid, and the species transport Equation (12) is determined as [7,36].

$$\frac{d}{dt}(\rho Y_{i,liq}) + \nabla \cdot (\rho [\beta \vec{v}_{liq} Y_{i,liq} + (1-\beta) Y_{i,sol}]) = \nabla \cdot (\rho \beta D_{i,m,liq} \nabla Y_{i,liq}) - K_i Y_{i,liq} \frac{d}{dt}(\rho(1-\beta)) + \frac{d}{dt}(\rho(1-\beta) Y_{i,liq}) \quad (12)$$

Equation (12) displays the mass fractions of liquid  $Y_{i,liq}$  and solid  $Y_{i,sol}$ , which are related by  $K_i$ , the partition coefficient [7].

$$Y_{i,sol} = K_i Y_{i,liq} \quad (13)$$

For the Scheil rule,  $T^*$ , the temperature at the interface is shown in Equation (14) [7].

$$T^* = T_{melt} + \sum_{i=0}^{N_s-1} m_i Y_i \beta^{K_i-1} \quad (14)$$

Thermal buoyancy occurs due to the variations in density with temperature and is determined by natural convection flows. Solutal buoyancy happens when density varies with species composition, and Equation (15) is used to calculate the solutal buoyancy body forces [17].

$$\vec{F}_s = \rho_{ref} \vec{g} \sum_{i=0}^{N_s} \beta_{s,i} (Y_{l,i} - Y_{ref,i}) \quad (15)$$

ANSYS Fluent uses a conservation equation of mass and momentum to solve for chemical species and the local mass fraction of each species and it is conducted by solving a convection-diffusion Equation (16) [17].

$$\frac{d}{dt}(\rho Y_i) + \nabla \cdot (\rho \vec{v} Y_i) = -\nabla \cdot \vec{J}_i \quad (16)$$

The momentum Equation (17) is solved between the phases and the subsequent velocity is shared [17].

$$\frac{d}{dt}(\rho \vec{v}) + \nabla \cdot (\rho \vec{v} \vec{v}) = -\nabla p + \mu \nabla^2 \vec{v} + \rho \vec{g} \quad (17)$$

### 3. CFD Methodology

Computational fluid dynamics (CFD) was used to model the evaporation of liquid nitrogen to simultaneously conduct freeze desalination of saline water using the software ANSYS Fluent version 19.1 (ANSYS, Canonsburg, Pennsylvania, United States, 2018) [37].

#### 3.1. The Geometry

The geometry has then been modelled using ANSYS geometry modeller of the CFD software, to the exact dimensions of the experimental test rig, which was designed based on results obtained for the cryogenic chill down process studied by Hartwig et al. [38].

Figure 1 shows the 3D geometry modelled using ANSYS geometry modeller consisting of two concentric tubes where the inner one is made of copper with an 8 mm diameter and it is surrounded by a Pyrex glass tube with a 28 mm diameter. The thickness of the copper tube and the glass tube were 0.5 and 3 mm, respectively, with a total length of 1000 mm. Liquid nitrogen flows through the inner tube, while the seawater stays stationary in the glass tube surrounding the copper tube. Only half of the geometry has been modelled due to the symmetrical nature of the pipes as shown in Figure 2, in order to reduce the computational time.

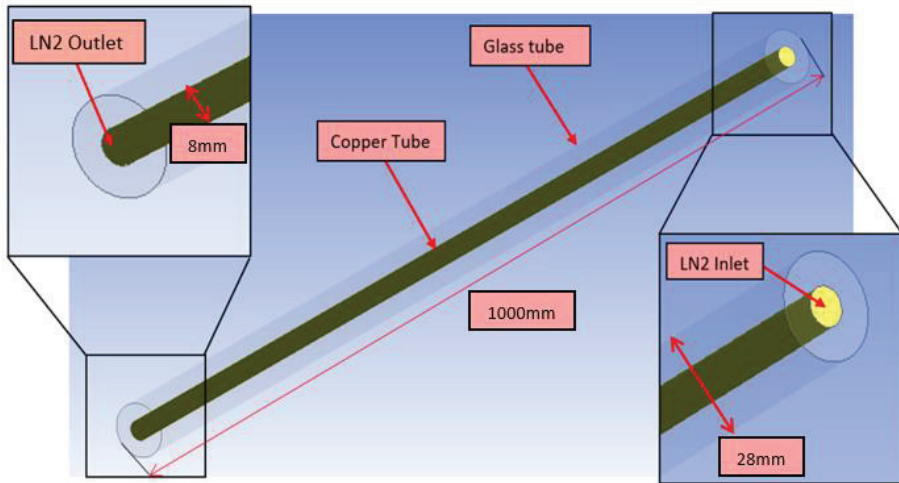


Figure 1. The geometry of the heat exchanger.

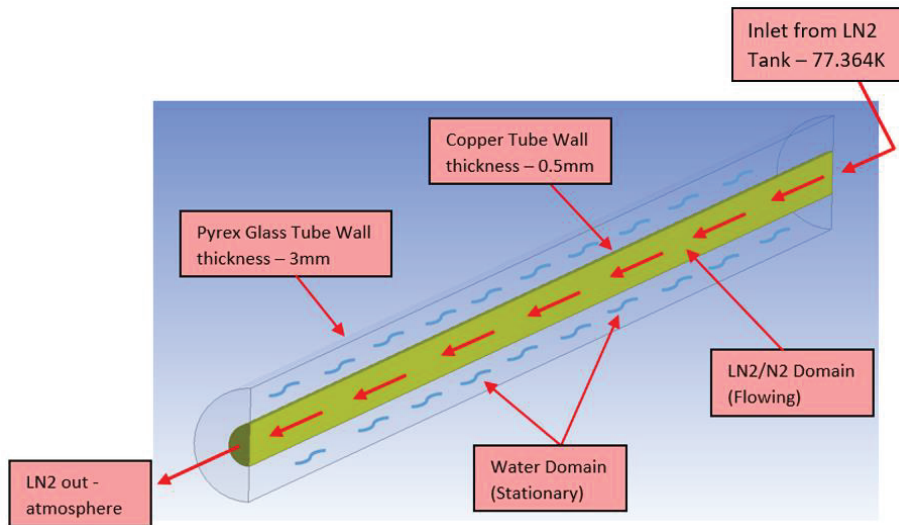
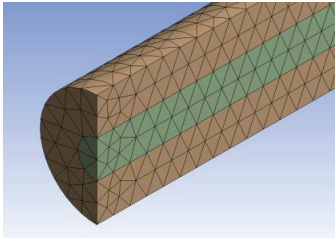
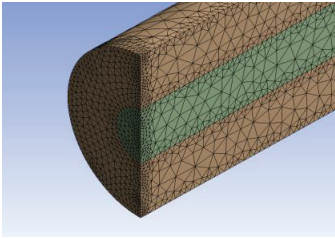
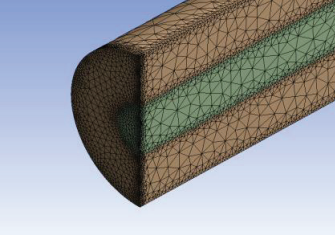


Figure 2. Heat exchanger domains and flow directions—cross-sectional view.

### 3.2. The Mesh

'ANSYS Meshing' (19.1, ANSYS, Canonsburg, Pennsylvania, United States, 2018) was used to create the 3D mesh of the geometry where a tetrahedral mesh has been created with edge sizing in order to optimise the mesh. Mesh independency study was conducted by using finer and coarser meshes with different edge sizing in order to select a suitable mesh as shown in Table 1. The predicted salinity of ice was compared with the measured salinity of ice (0.9%), and the percentage errors are shown in Table 1. The quality of all the three meshes was good; however, increasing the density of the mesh requires longer computational time but produces more accurate results [7]. Further increase in the mesh density did not improve the results a great deal, thus a medium mesh has been chosen.

Table 1. Mesh types used.

Mesh Types	Description
	<ul style="list-style-type: none"> <li>• Coarse mesh without edge sizing.</li> <li>• Nodes: 16750</li> <li>• Elements: 10461</li> <li>• Salinity of ice (%): 0.65</li> <li>• Percentage error (%): 27.8%</li> <li>• Total Running Time: 2 Days</li> </ul>
	<ul style="list-style-type: none"> <li>• Medium mesh with edge sizing.</li> <li>• Nodes: 101081</li> <li>• Elements: 64517</li> <li>• Salinity of ice (%): 0.73</li> <li>• Percentage error (%): 18.9%</li> <li>• Total Running Time: 6 Days</li> </ul>
	<ul style="list-style-type: none"> <li>• Fine mesh with edge sizing.</li> <li>• Nodes: 194542</li> <li>• Elements: 123550</li> <li>• Salinity of ice (%): 0.75</li> <li>• Percentage error (%): 16.7%</li> <li>• Total Running Time: 10 Days</li> </ul>

### 3.3. Set-Up

'ANSYS Fluent-Setup' (19.1, ANSYS, Canonsburg, Pennsylvania, United States, 2018) was used to define the solvers, materials, modules, boundary conditions, solution methods and discretization settings for the imported mesh. A transient solving process was selected due to time variation of the wall temperature during the cryogenic chill down process. A pressure-based solver was used with absolute velocity formulation enabled.

The boundary conditions are set to match the experimental test rig, and Figure 2 displays the labelled cross-sectional view of the CFD model. The system is divided into two sections where, the evaporation of liquid nitrogen domain is inside the copper tube while the surrounding glass tube contains the saltwater mixture domain to be frozen. Initially, the system is at ambient of 293.15 K. Then, liquid nitrogen enters the tube at a temperature of 77.364 K, evaporates inside the tube and leaves as nitrogen gas. The inlet is set as velocity inlet where the velocity of liquid nitrogen entering the system was 0.0006 m/s, and the outlet was set as a pressure outlet at atmospheric pressure. The surrounding salt solution is of 15 g/L concentration (1.5%) with an initial temperature of 293.15 K. This salt solution is present inside the surrounding Pyrex glass tube where the copper tube makes contact with the salt solution to indirectly freeze and desalinate the solution.

In order to obtain the most accurate results in less computational time, a suitable time step must be selected by conducting time step size independency tests. Therefore, it is understood that increasing the time step size, decreased the computational time; however, decreasing the time step size improved the results' accuracy and avoided many errors in the ANSYS Fluent software. After conducting time

step size independency tests by trial and error, a time step of 0.0001 s was used with 20 iterations per time step; thus,  $5.4 \times 10^6$  s of time steps were required to run the simulation for 9 min real time. This was the optimum time step size that could be used, where increasing this time step size produced less accurate results, and decreasing this time step resulted in longer computational time. Increasing this time step also produced many errors such as ‘floating point exception’ to appear in the ‘ANSYS Fluent Solution’, resulting in the system crashing. With this time step size, it took about 6 days to complete one run with the mesh nodes and elements stated above in Table 1.

#### 4. CFD Results

Figures 3–7 display the contours obtained after 9 min of real time. The temperature distribution of the liquid nitrogen in the copper tube in Figure 3 shows that LN<sub>2</sub> travels from left to right, where only the beginning of the tube is at very low temperatures due to the very low velocity of LN<sub>2</sub>. The temperature distribution of the salt water surrounding the copper tube is shown in Figure 4.

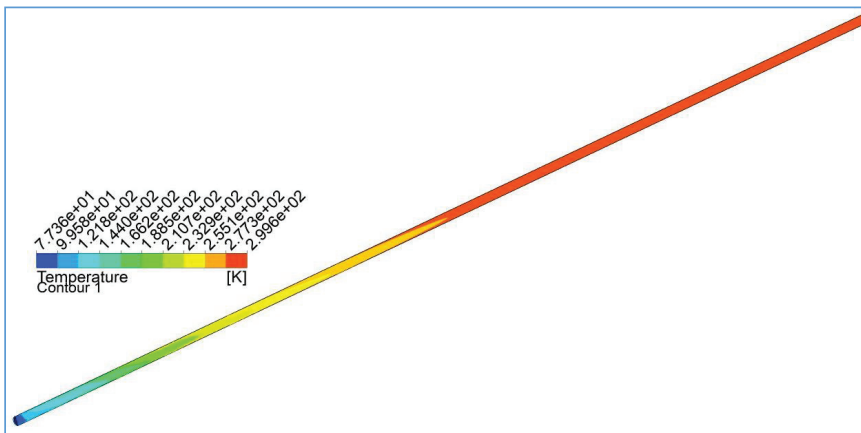


Figure 3. Temperature distribution of the LN<sub>2</sub> copper tube.

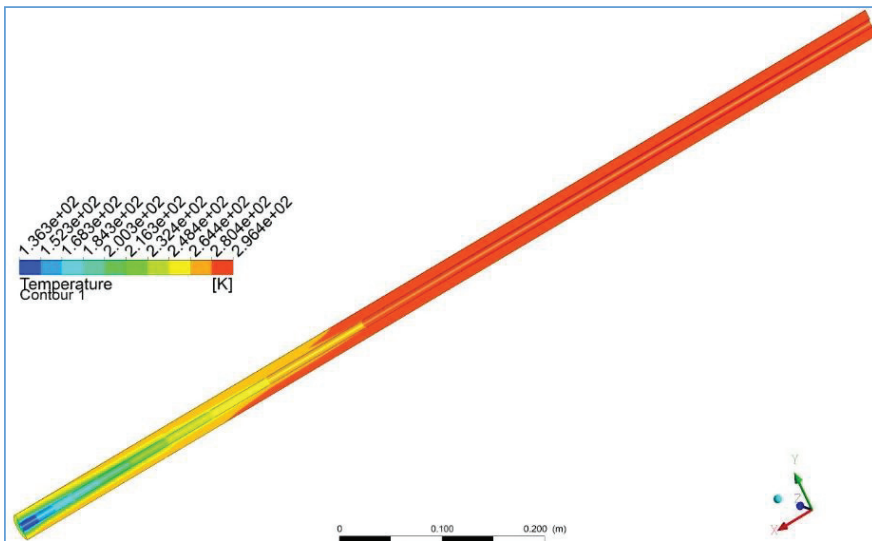


Figure 4. Temperature distribution of the salt water surrounding the copper tube.

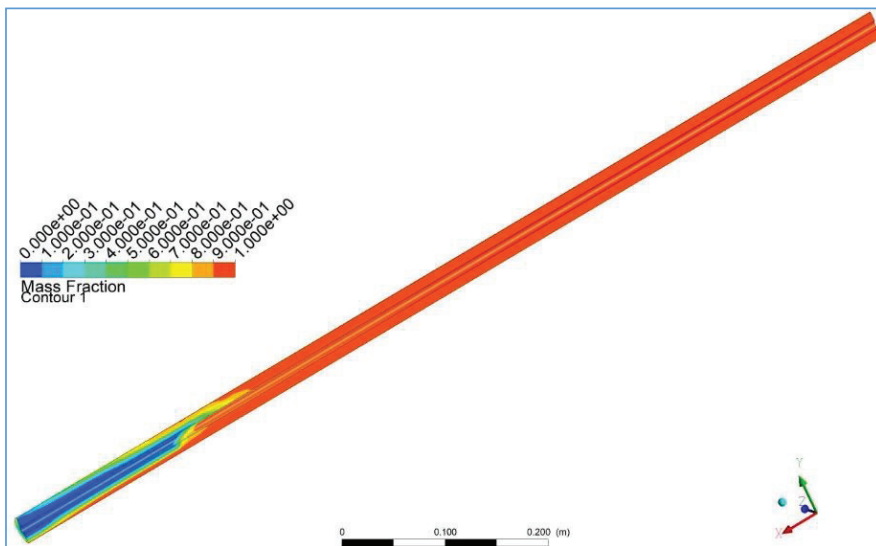


Figure 5. Liquid phase fraction contours.

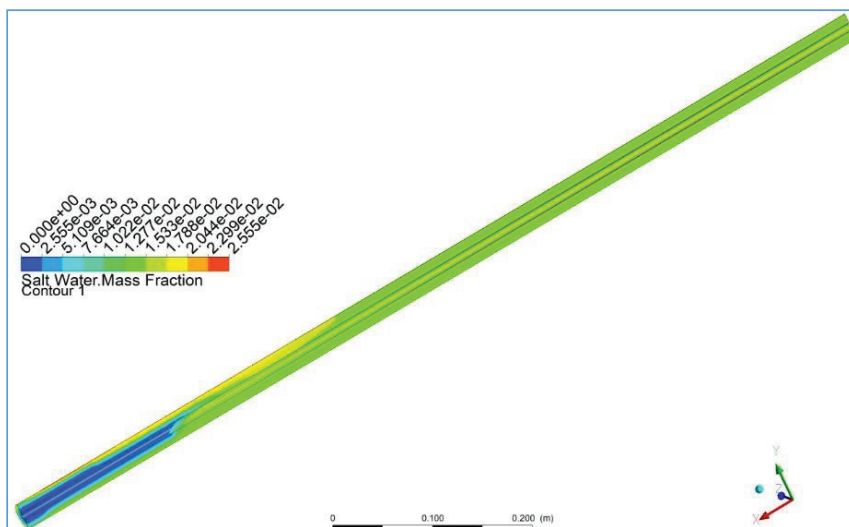


Figure 6. Salt water mass fraction contours.

Figure 5 displays the liquid phase fraction contours, where the formation of ice is shown. The blue region indicates the ice formed; the brine remaining is indicated by the red region, and the intermediate colours denote the liquid/solid mushy zone. Moreover, these contours go from 0 to 1 where 1 means it is pure liquid, 0 means it is pure solid, and the intermediate numbers represent the mushy regions. Liquid phase fraction contours in Figure 5 show that ice was formed only at the beginning of the tube due to the low velocity of LN<sub>2</sub>. The volume of ice formed was calculated by taking the blue region in Figure 5 and generating the volume in the software which is 46.71 mL.



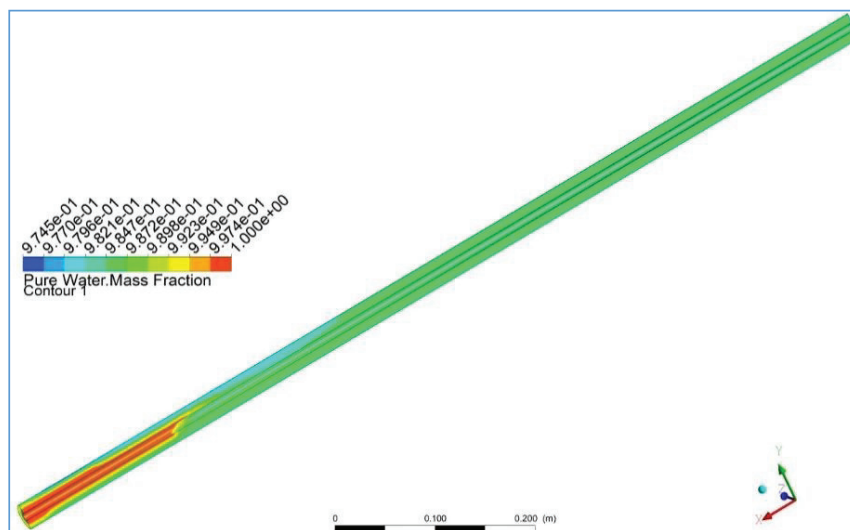


Figure 7. Pure water mass fraction contours.

Figures 6 and 7 show the salt water mass fraction and pure water mass fraction contours respectively. The salt water mass fraction is minimal in the regions where the ice is formed as shown in Figure 6, and the pure water mass fraction is very high in these regions as shown in Figure 7. The ice region generated from Figure 5 was used to calculate the salinity of ice, where the average salinity of the ice volume was calculated by the software. The volume remaining is the brine solution and its average salinity is calculated by the software. Hence, the salinity of ice formed was 0.73%; the salinity of the remaining brine was 1.70%, and it is calculated by taking the volume average over the whole domain.

## 5. Experimental Test Facility

This test rig was constructed to develop a system where the evaporation of liquid nitrogen would simultaneously desalinate seawater. The primary objective of this test rig was to understand the evaporation process of liquid nitrogen to be used for desalinating seawater. The heat transfer process was also examined where a method for enhancement of heat transfer was implemented in order to capitalize on the cold energy stored in liquid nitrogen.

The experimental test facility's schematic diagram is shown in Figure 8. This test rig is divided into two circuits, the evaporation of liquid nitrogen circuit and the freeze desalination one, which are connected by a heat exchanger. The concentric tube heat exchanger consists of a copper tube for the evaporation of  $\text{LN}_2$ , which is surrounded by a glass tube that contains stationary seawater. A glass tube was chosen to store seawater in order to observe the formation of ice, and a copper tube was used for the  $\text{LN}_2$  evaporation process to ensure effective heat transfer between the evaporating nitrogen and the saline water.

In the first circuit, the liquid nitrogen was poured into an insulated  $\text{LN}_2$  tank, and it was circulated through an 8 mm diameter copper tube and into the atmosphere at moderately higher temperature. The  $\text{LN}_2$  flow rate was measured, and cryogenic thermocouples were placed at the inlet and outlet of the heat exchanger and as well as at different locations at the surface of the copper tube to measure the temperatures as shown in Figure 9. The pressure difference between the inlet and outlet was measured using a manometer. Insulation sheets and aluminium foil has been used to insulate the  $\text{LN}_2$  tank and the joining copper tubes.

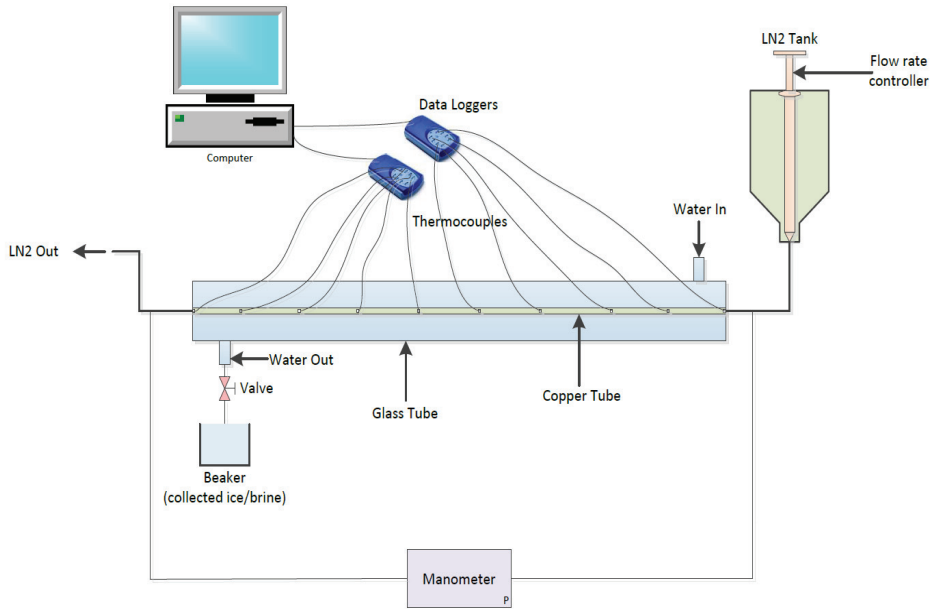


Figure 8. Schematic diagram of the experimental test facility.

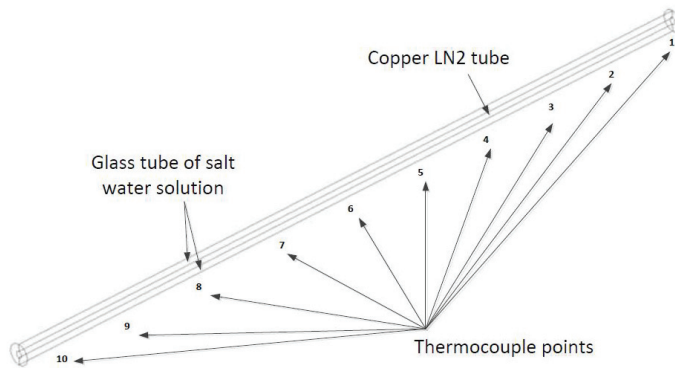


Figure 9. Schematic diagram showing the test rig with the thermocouple points.

In the second circuit, seawater of known salinity is poured into the glass tube which is surrounding the copper tube. This stationary seawater is cooled down by the evaporation of LN<sub>2</sub>. The temperature was measured at different locations at the surface of the copper tube using thermocouples. The temperature sensors were all connected to two data loggers that are connected to a computer to record the data. The complete test rig is shown photographically in Figure 10 with all its main components labelled.

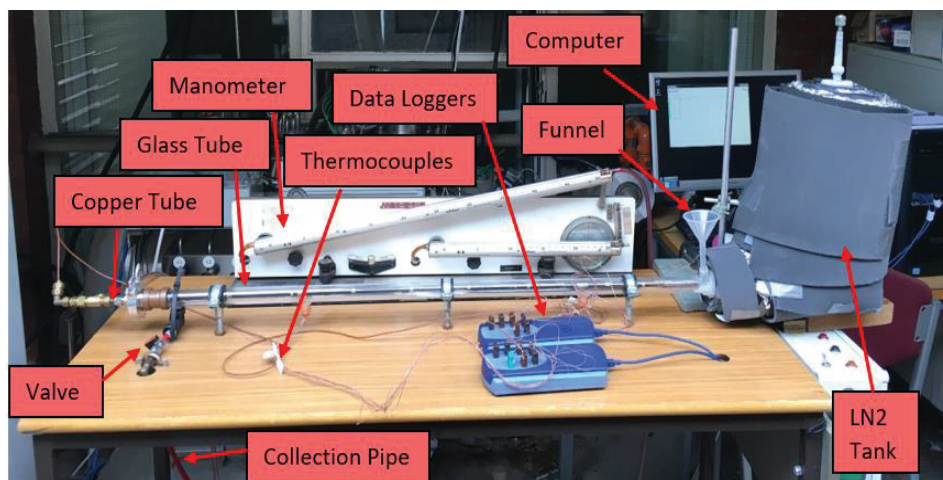


Figure 10. The developed test rig.

The overall length of this heat exchanger is 1000 mm. The copper tube has an inner diameter of 8 mm with a 0.5 mm wall thickness, and the glass tube has an inner 28 mm diameter with a 3 mm wall thickness. The outer tube was made from glass that can handle cryogenic temperatures, and this allows the ice formation to be seen clearly as shown in Figure 10.

This test rig was built to study the evaporation of liquid nitrogen process for freeze desalination. In the first set of tests, the copper tube was kept as it was, and the flow rates were changed. In the second set of tests, a copper mesh was inserted into the copper tube in order to increase the transfer of heat and to improve the freezing rate. The inserted copper mesh had a wire diameter of 0.5 mm and is shown in Figure 11.



Figure 11. Copper Mesh.

The liquid nitrogen cryogenic tank is made of copper which has a total volume of 0.51 L. The 54 mm diameter tank with a 207 mm length is connected to a reducer from 54 to 15 mm by a copper push fitting. This is then welded to another reducer to decrease the diameter to 8 mm. In order to minimize heat transfer from the surrounding to the LN<sub>2</sub> in the tank, 21 insulation sheets were wrapped around it. Moreover, aluminium foil was used between the insulation layers to reduce radiation heat transfer. A total of 21 layers of insulation sheets were selected as the temperature of the last insulation sheet was measured, and it was close to ambient temperature. These insulation sheets have a thermal conductivity of 0.035 W/m.K and of 3 mm thickness. Therefore, the total diameter with the insulation sheets converts to 230 mm. Figure 12 shows the entire tank with its components.

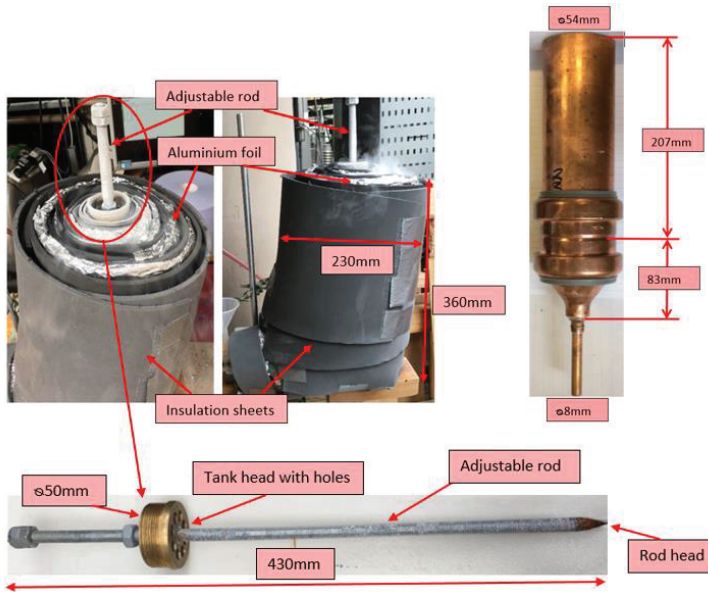


Figure 12. LN<sub>2</sub> tank with its components.

The liquid nitrogen flow rate is controlled using an adjustable rod that is placed inside the tank as shown in Figure 12. The 430 mm rod works similar to a valve, where it is rotated to open and close at the rod head. The adjustable rod has several holes seen in Figure 12, and when it is inserted into the tank and placed at the tank head, it is used to prevent any build-up of pressure due to the evaporation of liquid nitrogen in the tank.

Thermocouples, salinity meter and a manometer were used in this experiment to measure temperatures, salinity and pressure difference respectively. In total, 12 calibrated thermocouples were used to measure the temperature at different locations in the test rig. Out of the 12, two of them were used to measure the temperature at the inlet and outlet of the liquid nitrogen copper tube. These two were thermocouple probes of type-K, which were used to measure the inlet temperature of LN<sub>2</sub> and the outlet temperature of N<sub>2</sub>. The rest of the 10 thermocouples were cement-on surface thermocouples of type-K and were fitted at the outer surface of the copper tube to measure the temperature of the surface. These 10 thermocouples were equidistant from each other as shown in Figure 13, where T1 is closest to the LN<sub>2</sub> inlet and T10 is closest to the N<sub>2</sub> outlet.

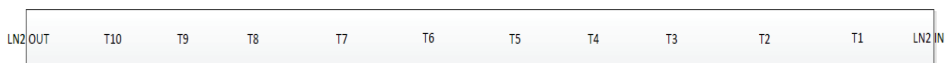


Figure 13. Thermocouple distribution.

The pressure difference between inlet and outlet of the evaporation of liquid nitrogen was measured using an inclined differential manometer. In order to measure the salinity of the saline water, an Omega handheld salinity meter [39] was used. This has a range of 0.1% to 10% salinity and can operate at temperatures from -5 to 60 °C [39]. The salinity meter was used to measure the salinity of ice and brine after the freeze desalination process and also to measure the salinity when making saltwater solutions before the experiment.

## 6. Experimental Results

### 6.1. Effect of Test Conditions on Temperature and Energy

Two tests were conducted, where the first test was conducted by evaporating LN<sub>2</sub> in a smooth copper tube. In the second test, a copper mesh has been inserted in order to increase the heat transfer. The two tests were analysed in terms of the inlet and outlet temperatures of liquid nitrogen; the temperature of ice forming at the surface of the copper tubes and the volume and salinity for the ice and brine. In both tests, the initial saltwater salinity was 1.5%, and three stages were conducted in order to desalinate the salt water to below 0.1%, which is regarded as safe to drink by the WHO (World Health Organisation) [40]. The test matrix for the two tests carried out are shown in Table 2.

**Table 2.** Test matrix for experimental results.

Test Parameters	Test 1—without Mesh	Test 2—with Mesh
LN <sub>2</sub> mass flow rate (kg/s)	0.000869	0.00055
Inlet LN <sub>2</sub> temperature (K)	77.15	79.15
Outlet LN <sub>2</sub> temperature (K)	199.15	276.5
Initial saltwater temperature (K)	291.15	291.15
Final ice temperature (K)	269.74	261.15
Final brine temperature (K)	283.8	278.47
Average surface temperature of copper tube (K)	275.14	273.55
Pressure difference (Pa)	255	950.16
Initial saltwater salinity (%)	1.5	1.5
First stage ice salinity (%)	0.9	0.9
Second stage ice salinity (%)	0.4	0.4
Third stage ice salinity (%)	0.1	0.1
Total energy lost by water (kJ)	31.81	102.65
Total energy in LN <sub>2</sub> (kJ)	149.41	149.41
Percentage of energy lost by water from LN <sub>2</sub> to form ice (%)	21.42	69.61
Heat exchanger effectiveness (%)	21	85

In the first test, liquid nitrogen passed through the copper tube and evaporated at a flow rate of  $8.69 \times 10^{-4}$  kg/s, simultaneously freezing the saline water surrounding the copper tube. Figure 14 shows the temperature distribution of liquid nitrogen at inlet and outlet and the initial and final water temperatures. The inlet temperature of LN<sub>2</sub> was 77.15 K, and the outlet temperature was 199.15 K indicating that energy has been lost by water for ice formation, and a considerable amount of energy has been lost to the surroundings. The initial temperature of salt water was 291.15 K, and the average temperatures for ice formed and brine remaining were 269.74 K and 283.8 K, respectively.

The surface temperatures at the copper tube surface T1 to T10 were monitored and are displayed in Figure 15. It is seen in this figure that the temperature increases from T1, which is closest to the LN<sub>2</sub> inlet to T10, which is closest to the LN<sub>2</sub> outlet. The decrease in temperature causes the water to freeze and to form ice. Hence, it is clear that ice is only formed at locations T1 to T3 where the surface temperature is below 273.15 K. This ice is of low salinity compared to the rest of the remaining brine solution. The mean temperature at the tube surface was calculated to be 275.14 K. The pressure difference was also monitored using the manometer to be 255 Pa.

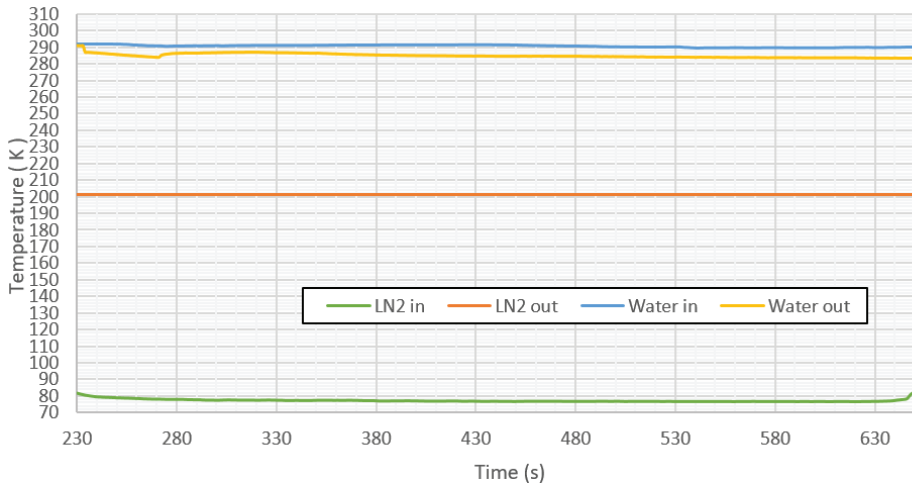


Figure 14. Test 1—LN<sub>2</sub> and water temperature distribution.

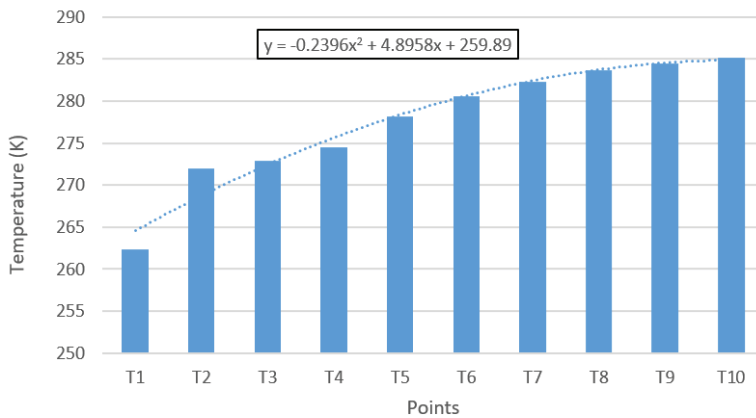


Figure 15. Test 1—Temperature at copper tube surface T1-T10.

The total energy lost by water was calculated using Equation (18), consisting of four terms: firstly, the energy lost from the remaining brine; secondly, the energy lost from water when ice was formed which was calculated from the initial conditions to the freezing point (F.P) of salt water; thirdly, the energy gained by ice which was calculated from the freezing point (F.P) of salt water to the final temperature of ice; and finally, the latent heat of fusion.

$$Q_{total\ water} = Q_{brine} + Q_{water\ to\ F.P} + Q_{F.P\ to\ ice} + mL_f \tag{18}$$

where  $L_f$  is the latent heat of fusion for seawater and  $m$  is the mass. Equation (19) was used to find the energy for ice, water and brine.

$$Q_{ice/water/brine} = m(Cp_2T_2 - Cp_1T_1) \tag{19}$$

where  $Cp_1$  and  $Cp_2$  are the initial and final specific heat capacities of water respectively.  $T_1$  and  $T_2$  are the initial and final temperatures respectively.

The energy balance for the hot stream of saline water and the cold stream of  $LN_2$  passing through the heat exchanger was evaluated. The total energy lost by salt water to form ice was calculated using Equations (18) and (19).

In order to find the percentage of energy lost by water to form ice from liquid nitrogen, first the energy in liquid nitrogen is calculated using Equation (20).

$$E_{LN_2} = \text{Energy Density of } LN_2 \times \text{Volume of } LN_2 \quad (20)$$

The energy density of  $LN_2$  was calculated using  $H_1$  and  $H_2$ , which are the inlet and outlet enthalpies obtained from thermodynamic property tables for nitrogen [41]. The volume of  $LN_2$  used depended on how many freezing stages were carried out.

Then, the percentage of energy lost by water to form ice (overall efficiency) from liquid nitrogen was calculated using Equation (21).

$$\% \text{ of Cold Energy Recovered} = \frac{Q_{total \text{ water}}}{E_{LN_2}} \times 100 \quad (21)$$

where  $Q_{total \text{ water}}$  is the total energy lost by water calculated using Equations (18) and (19).

The energy calculations were calculated using Equations (18) to (21), and they are summarised in Table 3. It can be seen that only 21.42% of energy was absorbed in order to form ice in the first test.

**Table 3.** Test 1—Energy calculations.

Total energy lost by water (kJ)	31.81
Total energy in $LN_2$ (kJ)	149.41
Percentage of energy lost by water from $LN_2$ to form ice (%)	21.42
Heat exchanger effectiveness (%)	21

The heat exchanger effectiveness has been calculated using Equations (22) to (28). When designing a heat exchanger, the two primary approaches are the Log Mean Temperature Difference (LMTD) method and the effectiveness Number of Thermal Units (NTU) method. The heat exchanger effectiveness was calculated as follows. Firstly, the LMTD was calculated using Equation (22).

$$\Delta T_{LMTD} = \frac{\Delta T_2 - \Delta T_1}{\ln \frac{\Delta T_2}{\Delta T_1}} \quad (22)$$

where  $\Delta T_1$  and  $\Delta T_2$  are the difference in temperatures at the ends of the heat exchanger and are calculated by Equations (23) and (24).

$$\Delta T_1 = T_{W1} - T_{N1} \quad (23)$$

$$\Delta T_2 = T_{W2} - T_{N2} \quad (24)$$

$T_{W1}$  and  $T_{W2}$  are the water inlet and outlet temperatures and  $T_{N1}$  and  $T_{N2}$  are the nitrogen inlet and outlet temperatures.

In order to calculate the effectiveness, the NTU, was calculated using Equation (25).

$$NTU = \frac{UA}{C_{\min}} \quad (25)$$

$C_{\min}$  is the smaller heat capacity, and it is calculated by Equation (26).  $A$  is the surface area of the copper tube, and  $U$  is the overall heat transfer coefficient calculated by Equation (27).

$$C_{\min} = \dot{m}C_p \quad (26)$$

$$U = \frac{\dot{Q}}{A\Delta T_{LMTD}} \quad (27)$$

When phase change evaporation occurs in the heat exchanger, then the behaviour of the heat exchanger is independent of flow arrangement. Therefore, the effectiveness of the heat exchanger is calculated using Equation (28).

$$\varepsilon = 1 - e^{-NTU} \quad (28)$$

The heat exchanger effectiveness for the test without the mesh was very low, and it was only 21% as shown in Table 3.

In the second test, a copper mesh (Figure 11) was inserted halfway through the copper tube in order to increase the heat transfer between the fluids, and these two tests varied due to different flow rates of LN<sub>2</sub>. The mesh was only inserted at the halfway point of the tube due to the fact that there is a considerable amount of freezing seen at the beginning of the tube where the liquid nitrogen is entering; therefore, adding a mesh here would mean that there would be an uncontrollable amount of freezing, causing the surrounding glass tube to crack at the beginning of the tube.

In the second test, the LN<sub>2</sub> flow rate was  $5.55 \times 10^{-4}$  kg/s and the water remained stationary. The LN<sub>2</sub> inlet and outlet temperatures were 79.15 and 276.5 K, respectively, as shown in Figure 16. The initial temperature of saline water was 291.15 K, and the produced ice had a temperature of 261.15 K and the remaining brine a temperature of 278.47 K.

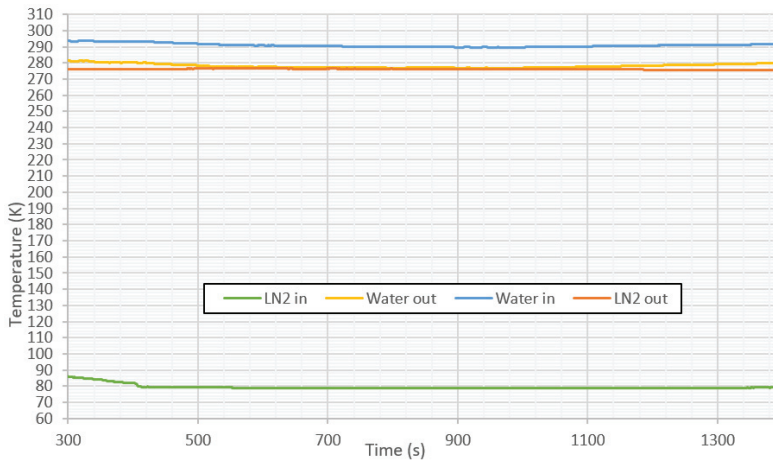


Figure 16. Test 2—LN<sub>2</sub> and water temperature distribution.

The mean temperature at the surface walls was calculated to be 273.55 K. The temperature distribution is very different to the first test as shown in Figure 17. This can be explained as follows; since the copper mesh was inserted up to the halfway point of the tube, a considerable amount of heat transfer is seen at the beginning of the mesh, leading to low temperature, at points T5–T8.

The pressure difference was 950.16 Pa and 69.61% of the cold energy was absorbed by water from LN<sub>2</sub>. The heat exchanger effectiveness was also much higher for the test with the mesh inserted as it is 85%, which is 4 times more than the first test without the mesh as shown in Table 4.



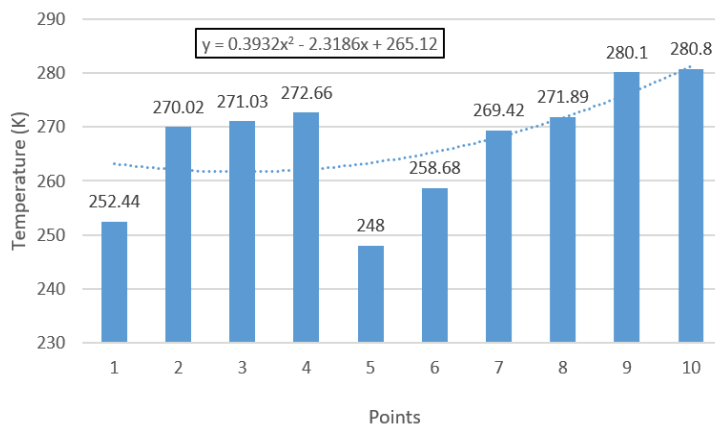


Figure 17. Test 2—Temperature at copper tube surface T1–T10.

Table 4. Test 2—Energy calculations.

Total energy lost by water (kJ)	102.65
Total energy in LN <sub>2</sub> (kJ)	149.41
Percentage of energy lost by water from LN <sub>2</sub> to form ice (%)	69.61
Heat exchanger effectiveness (%)	85

The first test had a higher liquid nitrogen flow rate due to the absence of the copper mesh and resulted in most of the energy being wasted into the atmosphere as the nitrogen leaves at low temperature with trapped liquid droplets. The copper mesh enhanced the heat transfer rate at a great deal resulting in more ice production. The percentage of energy lost by water from LN<sub>2</sub> to form ice is shown in Tables 2 and 3, where it is seen that the mesh improved the percentage of energy lost by water significantly. The heat exchanger effectiveness values for the two tests conducted with and without the mesh are shown in Tables 2 and 3. It is seen that the energy loss is greater in the test conducted without the mesh. The test with a mesh being inserted showed greater effectiveness and less energy loss.

#### 6.2. Effect of Test Conditions on Salinity and Volume of Ice

A salt solution of 1.5% salinity was indirectly freeze desalinated by the evaporation of liquid nitrogen. Three stages of freezing were conducted in order to bring 1.5% salt water salinity to 0.1%, which is recommended as safe to drink by the WHO [40]. In order to obtain accurate results by undergoing repeatability, three experiments were conducted of the same initial conditions, where 1.5% salinity was desalinated in three stages as shown in Figure 18. The salinity dropped to 0.9% in the first stage and then after freezing the 0.9% salinity solution in the second stage, it dropped to 0.4%. The 0.4% solution was then taken to conduct freezing in the final stage and it dropped to 0.1%, which is within the acceptable limits of safe to drink water by the WHO [42].

Figure 19 shows the volume of ice obtained at each freezing stage for the experiment conducted with a mesh being inserted. Therefore, it is seen that in the first stage, the volume of ice obtained is low, and it increases as the salinity of the initial salt solution decreases. Jayakody et al. [7] explained that the ice crystals become less pure at higher initial salt water concentrations. William et al. [43] proved that the initial salt water salinity had a significant effect on salt rejection and water recovery ratios.

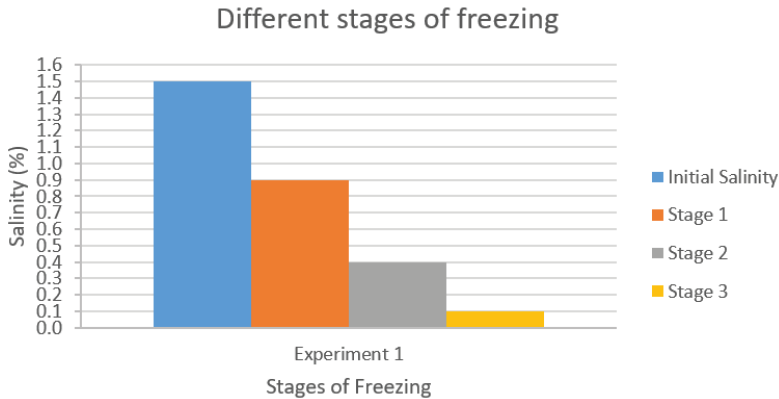


Figure 18. Three experiments conducted in three freezing stages.

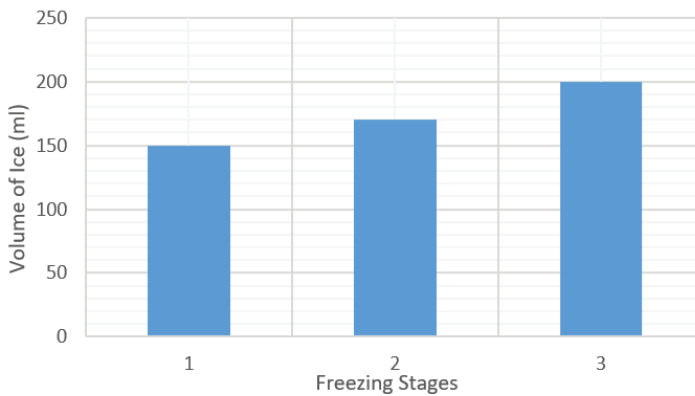
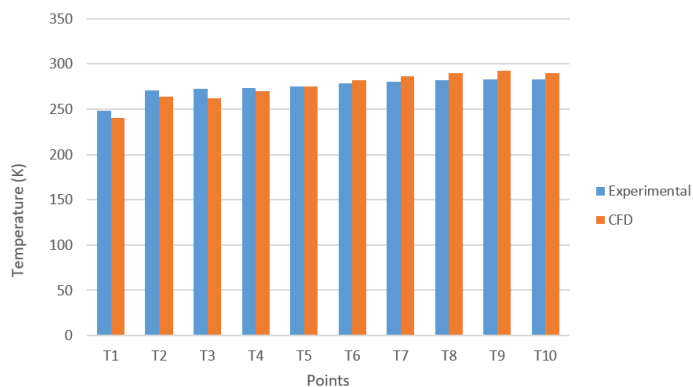


Figure 19. Volume of ice for different freezing stages on average for the 3 experiments conducted for the tests done with the mesh.

### 7. CFD Modelling Validation

The CFD model was validated using experimental work, where the operating conditions of the experiment were inputted in the CFD model as boundary conditions. The validation process was only carried out to a test done without the mesh as including a mesh inside the copper tube would require an excessively large computational time on CFD. The validation process was carried out in terms of the temperatures at the outer surface of the copper tube, volume of ice formed and also the ice and brine salinities.

Figure 20 compared the CFD predicted temperatures to their corresponding measured values at various locations on the copper tube surface at 9 min of real time. In this figure, the experimental (a test carried out with a mass flowrate of  $7.45 \times 10^{-4}$  kg/s) temperature from T1–T10 were compared with those predicted by CFD, showing good agreement. The deviation from the experimental values was minimal with maximum deviations at T3 and T9 of 9.9 and 9.2 K, respectively. Additionally, the average deviation of all the points was 6.3 K. The average wall temperature of the experimental work was 277.75 K and that of the CFD was 275.25 K indicating good agreement.



**Figure 20.** Temperature comparison at different locations of the copper tube.

The CFD predicted volume of ice formed, and the ice and brine salinities were compared to the experimental values for each stage of freezing as shown in Table 5. It is apparent that the ice and brine salinities and the volumes of ice formed at each stage of freezing show good agreement.

**Table 5.** Salinity and volume for each stage of freezing for CFD and experimental without mesh.

Parameters	Initial Salinity of Seawater (%) at Each Stage of Freezing								
	Stage 1—1.5% Salinity			Stage 2—0.9% Salinity			Stage 3—0.4% Salinity		
	Exp.	CFD	% Error	Exp.	CFD	% Error	Exp.	CFD	% Error
Ice Salinity (%)	0.90	0.73	18.78	0.40	0.33	17.75	0.10	0.08	17.00
Brine Salinity (%)	1.50	1.70	13.60	0.90	0.96	6.56	0.40	0.43	6.62
Volume Ice (mL)	55.00	46.71	15.07	70.00	64.29	8.16	75.00	72.73	3.03

It is also seen in Figure 19 and Table 5, for cases done with and without the mesh respectively, that in the third stage of freezing, 2.6 times more volume of ice was produced for the case with the mesh in comparison to the case without the mesh.

## 8. CFD Parametric Analysis—Flow Rate

The validated CFD model was used to carry out parametric analysis to investigate the effect of LN<sub>2</sub> flow rate on the produced volume of ice. Figure 21 shows the volume of ice at various inlet LN<sub>2</sub> velocities ranging from 0.0001 to 0.016 m/s. It can be seen that the volume of ice increased with the increase of LN<sub>2</sub> velocity.

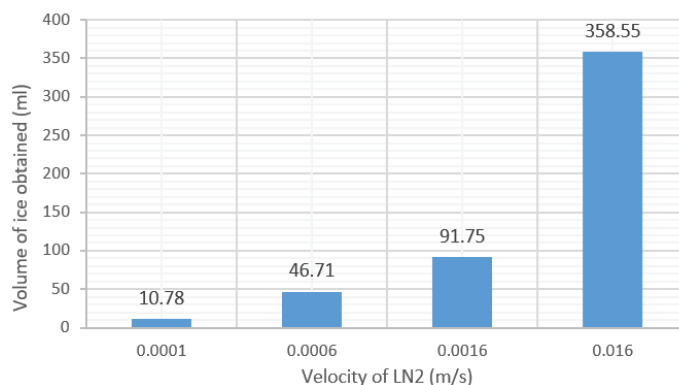


**Figure 21.** Volume of ice obtained at different LN<sub>2</sub> velocities.

Figure 21 shows that for 0.0001 m/s and 0.0006 m/s of LN<sub>2</sub> velocities, a volume of 10.78 mL and 46.71 mL of ice were obtained, respectively. Therefore, increasing the velocity of LN<sub>2</sub> by 6 times, increased the volume of ice by about 4.3 times. For 0.0016 m/s velocity of liquid nitrogen, the volume of ice obtained was 91.75 mL, producing 96.42% more ice in comparison to the 0.0006 m/s velocity of LN<sub>2</sub>. Moreover, for 0.016 m/s velocity of LN<sub>2</sub>, it is seen that a greater volume of ice of about 358.55 mL was obtained, which was about 3.91 times more than the volume obtained at 0.0016 m/s velocity of LN<sub>2</sub>. This is due to the fact that, as the flow rate is increased, LN<sub>2</sub> travels further along the copper tube before being fully evaporated and thus reducing the temperature at a large area of the copper tube. Figures 22 and 23 display the liquid phase fraction contours for 0.0001 and 0.0006 of LN<sub>2</sub> velocity, respectively. It is seen that by increasing the velocity of LN<sub>2</sub>, the LN<sub>2</sub> travels further along the copper tube before being evaporated and thus producing more ice.

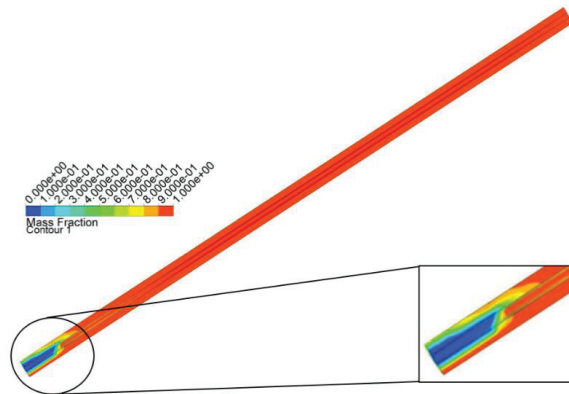


Figure 22. LN<sub>2</sub> velocity of 0.0001 m/s: liquid phase fraction contours.

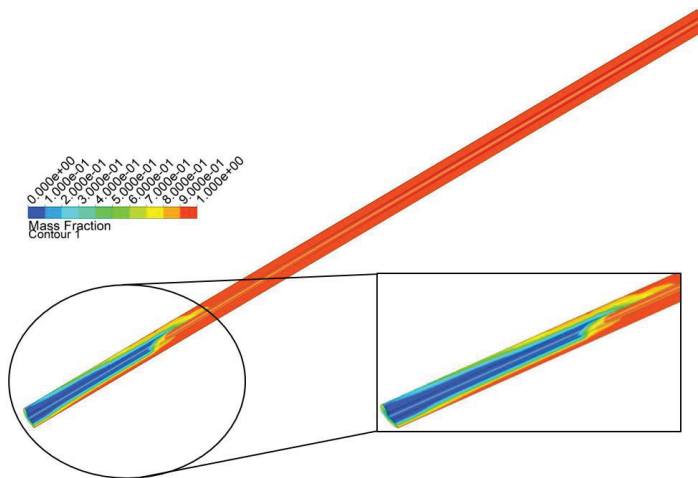


Figure 23. LN<sub>2</sub> velocity of 0.0006 m/s: liquid phase fraction contours.

Therefore, it can be concluded that, by increasing the velocity of LN<sub>2</sub>, more ice would be generated, and thus more water could be desalinated due to the fact that the LN<sub>2</sub> travels further along the copper tube before being evaporated. However, increasing the velocity means that the N<sub>2</sub> outlet conditions will have a higher amount of cold energy.

## 9. Conclusions

This work investigated numerically and experimentally the feasibility of using cryogenic energy by the evaporation of liquid nitrogen for indirect freeze desalination. Computational fluid dynamics have been used to simulate the evaporation of liquid nitrogen to provide the cooling required for freeze desalination. The main physics used in the modelling process were multiphase, solidification/melting, species transport and energy to develop a CFD model for the evaporation of liquid nitrogen to conduct freeze desalination. This CFD model predicted the surface temperatures of the copper tube, the final ice and brine salinities and the volume of ice produced. A heat exchanger test rig was built to evaporate liquid nitrogen while simultaneously freezing seawater in order to validate the CFD model. The CFD results were compared to experimental showing good agreement, where the average surface temperature deviation was 6.3 K, and the percentage errors for ice, brine and volume of ice were 17%, 6.62% and 3.03%, respectively.

Two experiments were conducted with and without a mesh being inserted in order to enhance the heat transfer. Inserting the copper mesh improved the heat transfer to a great deal, producing more ice and more desalinated water. The percentage of energy lost by water (overall efficiency) from liquid nitrogen to form ice increased significantly for the test with the mesh; it was 70% for the test with the mesh and only 21% for the test without the mesh. The heat exchanger effectiveness improved considerably when the mesh was inserted as it increased by about 4 times for the test with the mesh in comparison to the test carried out without using a mesh.

Three stages of freezing were done in order to bring the ice salinity of 1.5% down to 0.1%, which is stated as safe to drink by the WHO [40]. It was also concluded that, the initial salinity of salt water had a significant effect on the volume of ice produced and the rate of freezing. Liquid nitrogen (0.5 L) was evaporated with 104 kJ of energy consumption to freeze 450 mL of salt water in order to obtain a volume of 150, 170 and 200 mL of pure water in the first, second and third freezing stages, respectively, to bring the ice salinity below 0.1%.

Parametric study was then carried out by changing the liquid nitrogen flow rate to observe the volume of ice obtained. When increasing the velocity of LN<sub>2</sub> by 6 times, the volume of ice obtained increased by 4.3 times. It was concluded that by increasing the constant velocity of LN<sub>2</sub>, more volume of ice was generated due to LN<sub>2</sub> travelling further along the copper tube before being evaporated, leading to lower surface temperatures and higher rate of freezing. Hence, the above results illustrate the potential of using the cold energy of cryogenic fluids such as LNG and LN<sub>2</sub>/L<sub>Air</sub> for freeze desalination applications, as most cold energy during LNG regasification has been unexploited today.

**Author Contributions:** Conceptualization, H.J., R.A.-D. and S.M.; Methodology, H.J.; Software, H.J.; Validation, H.J.; Formal Analysis, H.J.; Investigation, H.J.; Resources, R.A.-D. and S.M.; Data Curation, H.J.; Writing—Original Draft Preparation, H.J.; Writing-Review & Editing, H.J.; Visualization, H.J.; Supervision, R.A.-D. and S.M.; Project Administration, R.A.-D. and S.M.; Funding Acquisition, R.A.-D. and S.M. All authors have read and agreed to the published version of the manuscript.

**Funding:** This research received no external funding.

**Acknowledgments:** The author (Harith Jayakody) would like to graciously thank the School of Mechanical Engineering, University of Birmingham, UK; for offering a PhD scholarship to carry out research on the investigation of using cryogenic energy for freeze desalination. The authors appreciatively acknowledge the support of the Engineering and Physical Sciences Research Council (EPSRC) for establishing the Cryogenic Research Facility at UoB (Grant NO. EP/LO17725/1).

**Conflicts of Interest:** The authors declare no conflict of interest.

## Nomenclature

### Symbols

$A$	surface area ( $m^2$ )
$A_{mush}$	mushy zone constant (-)
$C_{min}$	smaller heat capacity (J.kg/K.s)
$Cp_1$	initial specific heat capacity (J/K)
$Cp_2$	final specific heat capacity (J/K)
$D_{i,m}$	mass diffusion coefficient for species ( $m^2/s$ )
$E_{LN2}$	total energy in a known volume of liquid nitrogen (J)
$\vec{F}$	body force (N)
$\vec{F}_s$	solotal buoyancy body forces (N)
$\vec{g}$	gravity ( $m/s^2$ )
$H$	enthalpy [energy/mass (J/kg), energy/mole (J/mol)]
$H_1$	inlet enthalpy (J/kg)
$H_2$	outlet enthalpy (J/kg)
$\vec{J}_i$	diffusion flux of the species ( $kg/m^2\cdot s$ )
$k_{eff}$	effective conductivity (W/m-K)
$K_i$	partition coefficient of the solute (-)
$L$	latent heat (J/kg)
$L_f$	latent heat of fusion (J/kg)
$m$	mass (kg)
$\dot{m}$	mass flow rate (kg/s)
$\dot{m}_{qp}$	rate of mass transfer from phase q to phase p (kg/s)
$\dot{m}_{pq}$	rate of mass transfer from phase p to phase q (kg/s)
$m_i$	slope of the liquidus surface (K)
$n$	number of phases (-)
$N_s$	number of species (-)
$p$	pressure (Pa)
$Q_{brine}$	energy lost by brine remaining (J)
$Q_{ice}$	energy loss by ice (J)
$Q_{water}$	energy loss by water (J)
$S_{\alpha_q}$	source term
$S_h$	influences from radiations and any other volumetric heat sources
$T$	temperature (K)
$T_{W1}$	inlet water temperature (K)
$T_{W2}$	outlet water temperature (K)
$T_{N1}$	inlet nitrogen temperature (K)
$T_{N2}$	inlet nitrogen temperature (K)
$U$	overall heat transfer coefficient ( $W/m^2K$ )
$\vec{v}$	velocity (m/s)
$Y_i$	mass fraction of the solute (-)

### Greek Symbols

$\alpha$	volume fraction (-)
$\beta$	liquid volume fraction (-)
$\beta_{s,i}$	solotal expansion coefficient ( $K^{-1}$ )
$\varepsilon$	small number (0.001) (-)
$\varepsilon$	effectiveness of the heat exchanger (-)
$\mu$	viscosity of the fluid (Pa-s)
$\rho$	density of fluid ( $kg/m^3$ )

### Acronyms

CFD	computational fluid dynamics
FD	freeze desalination
LNG	liquefied natural gas
LMTD	logarithmic mean temperature difference
NTU	number of transfer units
RO	reverse osmosis
F.P	freezing point
VOF	volume of fluid

### Subscripts

<i>Eut</i>	eutectic
<i>i</i>	solute
<i>l</i>	liquid
<i>liq</i>	liquid
<i>liquidus</i>	liquid
<i>m</i>	mixture
<i>melt</i>	melting
<i>N</i>	nitrogen
<i>p</i>	secondary phase p
<i>q</i>	q <sup>th</sup> phase
<i>ref</i>	reference
<i>s</i>	species
<i>sat</i>	saturated
<i>sol</i>	solid
<i>solidus</i>	solid
<i>w</i>	water

### Superscripts

*	interface
<i>T</i>	temperature

### References

1. Mathioulakis, E.; Belessiotis, V.; Delyannis, E. Desalination by using alternative energy: Review and state-of-the-art. *Desalination* **2007**, *203*, 346–365. [CrossRef]
2. Miller, J.E. *Review of Water Resources and Desalination Techniques*; Unlimited Release Report SAND-2003-0800; Sandia National Labs: Livermore, CA, USA, 2003.
3. Engelman, J.W.R.; Cincotta, R.P.; Dye, B.; Gardner-Outlaw, T. *People in the Balance: Population and Natural Resources at the Turn of the Millennium, Population*; Population Action International: Washington, DC, USA, 2000.
4. Clarke, M.B.T. Blue Gold: The Fight to Stop the Corporate Theft of the World’s Water. *Contemp. Hum. Ecol.* **2004**, *11*, 67–71.
5. White, P.H.G.G.F. Water in Crisis: A Guide to the World’s Fresh Water Resources. *Clim. Chang.* **1993**, *31*, 119–122.
6. March, H. The politics, geography, and economics of desalination: A critical review. *Wiley Interdiscip. Rev. Water* **2015**, *2*, 231–243. [CrossRef]
7. Jayakody, H.; Al-Dadah, R.; Mahmoud, S. Numerical investigation of indirect freeze desalination using an ice maker machine. *Energy Convers. Manag.* **2018**, *168*, 407–420. [CrossRef]
8. Burn, S.; Hoang, M.; Zarzo, D.; Olewniak, F.; Campos, E.; Bolto, B.; Barron, O. Desalination techniques-A review of the opportunities for desalination in agriculture. *Desalination* **2015**, *364*, 2–16. [CrossRef]
9. Randall, D.G.J.N. A Succinct Review of the Treatment of Reverse Osmosis Brines Using Freeze Crystallization. *J. Water Process Eng.* **2015**, *8*, 186–194. [CrossRef]
10. Fujioka, R.; Wang, L.P.; Dodbiba, G.; Fujita, T. Application of progressive freeze-concentration for desalination. *Desalination* **2013**, *319*, 33–37. [CrossRef]

11. Attia, A.A.A. New proposed system for freeze water desalination using auto reversed R-22 vapor compression heat pump. *Desalination* **2010**, *254*, 179–184. [CrossRef]
12. Williams, P.M.; Ahmad, M.; Connolly, B.S.; Oatley-Radcliffe, D.L. Technology for freeze concentration in the desalination industry. *Desalination* **2015**, *356*, 314–327. [CrossRef]
13. Lu, Z.; Xu, L. Freezing Desalination Process. *Desalin. Water Resour.* **2014**, *2*, 275–290.
14. Cao, W.; Beggs, C.; Mujtaba, I.M. Theoretical approach of freeze seawater desalination on flake ice maker utilizing LNG cold energy. *Desalination* **2014**, *355*, 22–32. [CrossRef]
15. Curran, H.M. Water desalination by indirect freezing. *Desalination* **1970**, *7*, 273–284. [CrossRef]
16. Lin, W.; Huang, M.; Gu, A. A seawater freeze desalination prototype system utilizing LNG cold energy. *Int. J. Hydrog. Energy* **2017**, *42*, 18691–18698. [CrossRef]
17. Jayakody, H.; Al-Dadah, R.; Mahmoud, S. Computational fluid dynamics investigation on indirect contact freeze desalination. *Desalination* **2017**, *420*, 21–33. [CrossRef]
18. Ratkje, S.K.; Flesland, O. Modelling the freeze concentration process by irreversible thermodynamics. *J. Food Eng.* **1995**, *25*, 553–568. [CrossRef]
19. Qin, F.G.F.; Chen, X.D.; Farid, M.M. Growth kinetics of ice films spreading on a subcooled solid surface. *Sep. Purif. Technol.* **2004**, *39*, 109–121. [CrossRef]
20. Qin, F.G.F.; Chen, X.D.; Free, K. Freezing on subcooled surfaces, phenomena, modeling and applications. *Int. J. Heat Mass Transf.* **2009**, *52*, 1245–1253. [CrossRef]
21. Qin, F.G.F.; Zhao, J.; Russell, A.; Chen, X.; Chen, J.; Robertson, L. Simulation and Experiment of the Unsteady Heat Transport in the Onset Time of Nucleation and Crystallization of Ice from the Subcooled Solution. *Int. J. Heat Mass Transf.* **2003**, *46*, 3221–3231. [CrossRef]
22. Chivavava, J.; Rodriguez-Pascual, M.; Lewis, A.E. Effect of operating conditions on ice characteristics in continuous eutectic freeze crystallization. *Chem. Eng. Technol.* **2014**, *37*, 1314–1320. [CrossRef]
23. Genceli, F.E.; Pascual, M.R.; Kjelstrup, S.; Witkamp, G.-J. Coupled Heat and Mass Transfer during Crystallization of  $\text{MgSO}_4 \cdot 7\text{H}_2\text{O}$  on a Cooled Surface. *Cryst. Growth Des.* **2009**, *9*, 1318–1326. [CrossRef]
24. Abid, A.J.; Safi, M.J. Simulation of Binary Mixture Freezing: Application to Seawater Desalination. *Int. J. Eng. Sci. Innov. Technol.* **2015**, *4*, 158–163.
25. Lim, Y.; Al-Atabi, M.; Williams, R.A. Liquid air as an energy storage: A review. *J. Eng. Sci. Technol.* **2016**, *11*, 496–515.
26. Antonelli, M.; Desideri, U.; Giglioli, R.; Paganucci, F.; Pasini, G. Liquid air energy storage: A potential low emissions and efficient storage system. *Energy Procedia* **2016**, *88*, 693–697. [CrossRef]
27. Morgan, R.; Nemes, S.; Gibson, E.; Brett, G. Liquid air energy storage-Analysis and first results from a pilot scale demonstration plant. *Appl. Energy* **2015**, *137*, 845–853. [CrossRef]
28. Ahmad, A.; Al-Dadah, R.; Mahmoud, S. Liquid nitrogen energy storage for air conditioning and power generation in domestic applications. *Energy Convers. Manag.* **2016**, *128*, 34–43. [CrossRef]
29. Khalil, K.M.; Ahmad, A.; Mahmoud, S.; Al-Dadah, R.K. Liquid air/nitrogen energy storage and power generation system for micro-grid applications. *J. Clean. Prod.* **2017**, *164*, 606–617. [CrossRef]
30. Ahmad, A.; Al-Dadah, R.; Mahmoud, S. Liquid air utilization in air conditioning and power generating in a commercial building. *J. Clean. Prod.* **2017**, *149*, 773–783. [CrossRef]
31. Ahmad, A.; Al-Dadah, R.; Mahmoud, S. Air conditioning and power generation for residential applications using liquid nitrogen. *Appl. Energy* **2016**, *184*, 630–640. [CrossRef]
32. Strahan, D. Dearman. 2017. Available online: [http://dearman.co.uk/wp-content/uploads/2017/11/Dearman\\_Company\\_brochure\\_301017\\_web.pdf](http://dearman.co.uk/wp-content/uploads/2017/11/Dearman_Company_brochure_301017_web.pdf) (accessed on 31 October 2018).
33. Chang, J.; Zuo, J.; Lu, K.J.; Chung, T.S. Freeze desalination of seawater using LNG cold energy. *Water Res.* **2016**, *102*, 282–293. [CrossRef]
34. ANSYS Fluent. *ANSYS Fluent Theory Guide*, 15th ed.; ANSYS: Canonsburg, PA, USA, 2013; Volume 15317, pp. 724–746.
35. Voller, V.R.; Prakash, C. A fixed grid numerical modelling methodology for convection-diffusion mushy region phase-change problems. *Int. J. Heat Mass Transf.* **1987**, *30*, 1709–1719. [CrossRef]
36. Voller, V.R.; Brent, A.D.; Prakash, C. The modelling of heat, mass and solute transport in solidification systems. *Int. J. Heat Mass Transf.* **1989**, *32*, 1719–1731. [CrossRef]
37. ANSYS Fluent. 2018. Available online: <https://www.ansys.com/en-gb/products/fluids/ansys-fluent> (accessed on 23 November 2019).



38. Hartwig, J.; Hu, H.; Styborski, J.; Chung, J.N. Comparison of cryogenic flow boiling in liquid nitrogen and liquid hydrogen chilldown experiments. *Int. J. Heat Mass Transf.* **2015**, *88*, 662–673. [CrossRef]
39. Handheld Meter, O.M.E.G.A. Engineering, Handheld Salinity Meter. 2017. Available online: Omega.co.uk (accessed on 23 November 2019).
40. US Environmental Protection Agency, Water-Quality Criteria, Standards, or Recommended Limits for Selected Properties and Constituents. 1994. Available online: <https://pubs.usgs.gov/wri/wri024094/pdf/mainbodyofreport-3.pdf> (accessed on 14 December 2017).
41. American Society of Heating Refrigerating and Air-Conditioning Engineers. *2009 Ashrae Handbook: Fundamentals, S-I, ed.*; ASHRAE: New York, NY, USA, 2009.
42. Salinity. Available online: [http://www.epa.sa.gov.au/environmental\\_info/water\\_quality/threats/salinity](http://www.epa.sa.gov.au/environmental_info/water_quality/threats/salinity) (accessed on 14 December 2017).
43. Williams, P.M.; Ahmad, M.; Connolly, B.S. Freeze desalination: An assessment of an ice maker machine for desalting brines. *Desalination* **2013**, *308*, 219–224. [CrossRef]



© 2019 by the authors. Licensee MDPI, Basel, Switzerland. This article is an open access article distributed under the terms and conditions of the Creative Commons Attribution (CC BY) license (<http://creativecommons.org/licenses/by/4.0/>).

Article

# A Selection Flowchart for Micromodel Experiments Based on Computational Fluid Dynamic Simulations of Surfactant Flooding in Enhanced Oil Recovery

Santiago Céspedes<sup>1,2</sup>, Alejandro Molina<sup>2</sup>, Betiana Lerner<sup>3,4</sup>, Maximiliano S. Pérez<sup>3,4</sup>, Camilo A. Franco<sup>1</sup> and Farid B. Cortés<sup>1,\*</sup>

- <sup>1</sup> Grupo de Investigación en Fenómenos de Superficie-Michael Polanyi, Department of Processes and Energy, Faculty of Mines, National University of Colombia, Medellín 050034, Colombia; sacespedeszu@unal.edu.co (S.C.); caafrancoar@unal.edu.co (C.A.F.)
- <sup>2</sup> Grupo de Investigación Bioprocesos y Flujos Reactivos, Department of Processes and Energy, Faculty of Mines, National University of Colombia, Medellín 050034, Colombia; amolinao@unal.edu.co
- <sup>3</sup> Facultad Regional Haedo, Universidad Tecnológica Nacional (UTN), Haedo, Buenos Aires 1706, Argentina; betianalerner@gmail.com (B.L.); max@fullgen.com.ar (M.S.P.)
- <sup>4</sup> Department of Electrical and Computer Engineering, Florida International University, Miami, FL 33174, USA
- \* Correspondence: fbcortes@unal.edu.co

**Abstract:** A selection flowchart that assists, through Computational Fluid Dynamics (CFD) simulations, the design of microfluidic experiments used to distinguish the performance in Chemical Enhanced Oil Recovery (CEOR) of two surfactants with very similar values of interfacial tension (IFT) was proposed and its use demonstrated. The selection flowchart first proposes an experimental design for certain modified variables ( $\vec{X}$ : porosity, grain shape, the presence of preferential flowing channels, and injection velocity). Experiments are then performed through CFD simulations to obtain a set of response variables ( $\vec{Y}$ : recovery factor, breakthrough time, the fractal dimension of flow pattern, pressure drop, and entrapment effect). A sensitivity analysis of  $\vec{Y}$  regarding the differences in the interfacial tension (IFT) can indicate the CFD experiments that could have more success when distinguishing between two surfactants with similar IFTs (0.037 mN/m and 0.045 mN/m). In the range of modifiable variables evaluated in this study (porosity values of 0.5 and 0.7, circular and irregular grain shape, with and without preferential flowing channel, injection velocities of 10 ft/day and 30 ft/day), the entrapment effect is the response variable that is most affected by changes in IFT. The response of the recovery factor and the breakthrough time was also significant, while the fractal dimension of the flow and the pressure drop had the lowest sensitivity to different IFTs. The experimental conditions that rendered the highest sensitivity to changes in IFT were a low porosity (0.5) and a high injection flow (30 ft/day). The response to the presence of preferential channels and the pore shape was negligible. The approach developed in this research facilitates, through CFD simulations, the study of CEOR processes with microfluidic devices. It reduces the number of experiments and increases the probability of their success.

**Keywords:** computational fluid dynamic simulations; chemical enhanced oil recovery; surfactant flooding; microfluidics

**Citation:** Céspedes, S.; Molina, A.; Lerner, B.; Pérez, M.S.; Franco, C.A.; Cortés, F.B. A Selection Flowchart for Micromodel Experiments Based on Computational Fluid Dynamic Simulations of Surfactant Flooding in Enhanced Oil Recovery. *Processes* **2021**, *9*, 1887. <https://doi.org/10.3390/pr9111887>

Academic Editor: Alfredo Iranzo

Received: 21 September 2021

Accepted: 8 October 2021

Published: 22 October 2021

**Publisher's Note:** MDPI stays neutral with regard to jurisdictional claims in published maps and institutional affiliations.



**Copyright:** © 2021 by the authors. Licensee MDPI, Basel, Switzerland. This article is an open access article distributed under the terms and conditions of the Creative Commons Attribution (CC BY) license (<https://creativecommons.org/licenses/by/4.0/>).

## 1. Introduction

Oil extraction is becoming more dependent than ever on enhanced oil recovery (EOR) to improve oil production [1]. One of the best-known EOR methods is the injection of surfactants to reduce the IFT between the oil and the displacement fluid, increase the capillary number, separate the crude oil from the reservoir walls, and increase the recovery factor [2].

Surfactant injection has been a widely used technique to increase the recovery factor in hydrocarbon reservoirs. This technique has been extensively studied to optimize its application. One problem present in the surfactant injection is the interaction that it may have with a porous medium, causing adsorption of the fluid on the rock and decreasing the effective concentration of surfactant that will act at the interface between the displacing fluid and the crude. Another point of interest in the surfactant application is the change in wettability that it can cause in the medium, favoring the recovery process.

Regarding the study of surfactants, research focused on optimizing its effect using other substances that decrease adsorption in a porous medium, increasing its effectiveness in reducing IFT, or increasing the displacing fluid's viscosity. The use of ionic liquids as surfactant adsorption inhibitors in porous media have been investigated [3]. In addition, novel technologies such as nanotechnology have also been involved by applying nano-materials of different nature (hydrophilic and hydrophobic) to avoid the adsorption of surfactants in a porous medium [4–10]. On the other hand, surfactants of natural origin that are more effective than synthetic surfactants and are low cost, have high availability, and are biodegradable have been investigated [11–14]. These investigations have demonstrated the great interest of the academy, industry, and the community in general focused on improving EOR processes for evaluating surfactants in search of more efficient processes.

Evaluation of the performance that surfactants may present at reservoir conditions is commonly conducted in core-flooding tests that typically do not allow for flow visualization and are of an extended duration, of the order of 80 h or more [15]. Microfluidic devices can complement, and in some cases even replace, core-flooding tests because they demand shorter evaluation times and allow for the visual characterization of the flow at the pore level [16]. Micromodels of different materials can be fabricated, such as glass [17–21], quartz [22], silicon [19,21], or polymers [23]. The porous media geometry in micromodels can take different forms: perfectly regular [24], partially regular [25–27], fractal [28], and irregular [29]. The geometry of a micromodel device can resemble a reservoir prototype that mimics the texture of scanning electron microscopy (SEM) images from a reservoir rock [30]. The most common fabrication methods for micromodels are optical lithography [31], etching [20,22], stereolithography [31], and soft lithography [32–36]. These fabrication procedures need to guarantee the material's transparency and aim to replicate the flow conditions. The selection of the best combination of microfluidic materials, fabrication methods, and experimental conditions can be overwhelming. There were no guides on selecting all these variables in the refereed literature for a specific microfluidic device application [28]. One way to assist this process is through a selection flowchart that indicates steps to select and classify elements according to defined criteria. Selection flowcharts are part of the decision-making processes in multiple industries such as management [37], waste treatment [38], transportation [39], equipment selection [40], and mining [41]. Moreover, in the oil and gas industry, these selection flowcharts have been used to evaluate methodology for selection of equipment used for the treatment of gas and oil [42], and to evaluate upstream water treatment [43].

This study proposes a selection flowchart that defines key geometric parameters and experimental conditions of a microfluidic test that could make the detection of differences in the performance of surfactants in the low interfacial tension range faster and more reliable. To this aim, it takes advantage of Computational Fluid Dynamics (CFD) [24–27,29,44,45] to represent the flow in microfluidic devices. In this way, this research shows the application of a selection flowchart together with CFD simulations to evaluate a set of variables considered in the experiments carried out in microfluidics to evaluate the performance of surfactants. Additionally, it provides the ability to choose a set of conditions that allows to better compare the effect of surfactants on variables of interest to the oil industry such as the oil recovery factor and other types of variables that are easy to evaluate through micromodels such as the distribution of fluids.

Although this research focuses on applying a selection flowchart, it can be used for a specific oil reservoir. In this case, the variables must be chosen within a range where

they are found, and a multiphase model in CFD that contemplates all the phenomenology around these variables must be used.

CFD has been widely used to study systems that involve fluid flow and heat transfer, among other phenomena, through computer-solved algorithms [46–54]. CFD simulations of microfluidic experiments can address the effect on the micromodel performance on variables such as pore morphology and size-distribution in terms of pore-throat connectivity [29], heterogeneity [25], shape and tortuosity [24,29], viscosity [30], temperature [27], interfacial tension [24,25], wettability [45], and the addition of nanomaterials [26,27,45]. All this research on the CFD analysis of microfluidic devices has led to an enhanced understanding of the process of oil recovery and a reduction in the duration and cost of experimental tests [35,36,55].

To engineer the selection flowchart, typical microfluidic geometries were meshed in CFD. Their performance was analyzed based on characteristic metrics for EOR processes with surfactant injection such as recovery factor, pressure drop, and breakthrough time, as well as with some that are not that frequently used but give more information on the flow and can be easily calculated in CFD, such as the fractal dimension of the flow pattern and the amount of trapped oil. Two surfactants in the low IFT range were evaluated. Sensitivity analysis was carried out to propose a flowchart that can be followed to determine the micromodel experiment that allows for better differentiation of the performance of various surfactants in the low IFT range.

## 2. Towards a Micromodel Experiment Selection Flowchart

Different characteristics of oil exploitation can be explored with microfluidic devices; examples are: porosity [29,56], grain shape [24,29], existence and configuration of preferential channels [57–60], pore size distribution [29,61], shape [24,29], tortuosity [29], pore-throat connectivity [29], and injection velocity [62]. These variables can be modified during the construction of the microfluidic device or the experiment and are inputs ( $\vec{X}$ ) to a model—the microfluidic experiment—that yields several outputs ( $\vec{Y}$ ) that characterize the performance of the flow process. Examples of these outputs are: recovery factor [24–27,29,63–65], pressure drop [65–67], fractal dimension of the flow pattern [68,69], breakthrough time [29], viscosity of the fluid that leaves the microfluid device [27,66], displacement micromechanisms [65,67,70], emulsion formation [71], drop shape [63–65,70,72], and fluid distribution [24–27,29,63,64,67,70].

A flowchart for the design of microfluidic experiments for the evaluation of surfactants, such as the one described in this study, should state the values of the inputs ( $\vec{X}$ ) which would have the most significant effect on the outputs ( $\vec{Y}$ ), so that the performance of surfactants in the low interfacial tension range can be evaluated quickly. Figure 1 summarizes this approach. The start of the flowsheet should be a characterization of the surfactants to be analyzed based on their interfacial tension (IFT). In a second step, the user should define the modified variables of the micromodel ( $\vec{X}$ ) that will be selected in the analysis. Knowledge of ( $\vec{X}$ ) allows for an experimental design step where these variables are combined, for instance, by factorial design. In a third step, the CFD simulations of the microfluidic “experiments” proposed in the previous step are conducted. This process involves multiple CFD simulations that yield the output vector ( $\vec{Y}$ ). A sensitivity analysis of the outputs to the IFT then provides the required information to recommend a microfluidic experiment that can best distinguish the performance of the surfactants. An extensive flowchart is shown in the Figure S10 in Supplementary Material information that includes the steps to follow when CFD simulations are not available and when evaluating one or multiple outputs ( $\vec{Y}$ ).

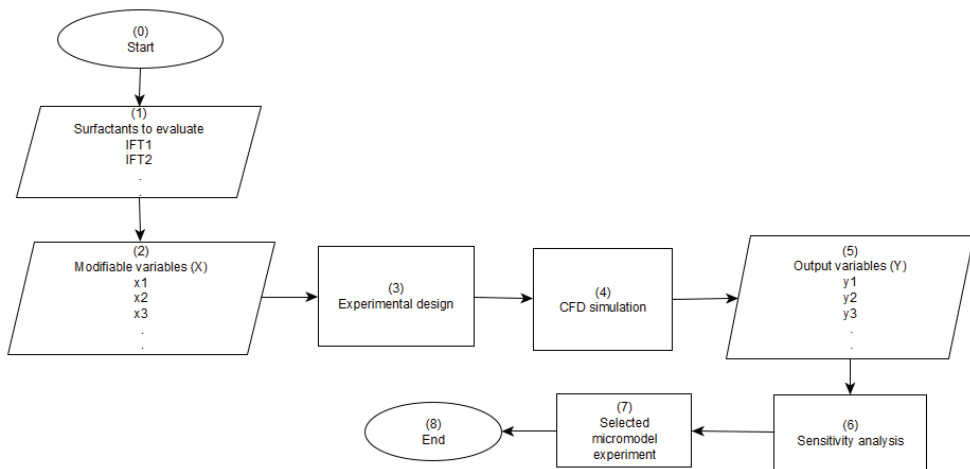


**Figure 1.** Flowchart to select a microfluidic experiment to evaluate the performance of surfactants during EOR through CFD simulations.

### 2.1. Surfactants

The first step in Figure 1 involves knowledge of the IFT of the selected surfactants. The IFTs for the surfactants in the low interfacial range in these studies were: 0.037 mN/m and 0.045 mN/m. While 0.037 mN/m represents the actual IFT of a surfactant [62], a value 20% higher (0.045 mN/m) was arbitrarily selected to test the ability of the flowchart to recommend experimental conditions to differentiate the performance of both surfactants.

### 2.2. Modifiable Variables ( $\vec{X}$ )

If unlimited resources and time were available, all possible input and output variables could be used in the experimental design and sensitivity analysis, respectively. In fact, with the constant improvement in computational capacity and the advances in machine learning and artificial intelligence, it could be a realistic possibility in the following years. Nevertheless, in a more realistic framework, the number of variables in ( $\vec{X}$ ) and ( $\vec{Y}$ ) should be defined based on the number of available resources. To assist in the process of variable selection, Table 1 proposes a scale that grades the relation between ( $\vec{X}$ ) and ( $\vec{Y}$ ). In this way, the total number of possible combinations of ( $\vec{X}$ ) and ( $\vec{Y}$ ) can be reduced. In Table 1 the intensity of the greyscale is indicative of the relationship between variables. An intense gray indicates a strong relationship, while white implies almost no relation between both. For instance, the presence of a preferential flowing channel, the injection velocity, and the pore-throat connectivity have the highest effect on the oil recovery factor. In contrast, the effect of grain and pore shape is lower. The relationships shown between ( $\vec{X}$ ) and ( $\vec{Y}$ ) are obtained from a literature search on the interaction of different variables in EOR processes with surfactant injection [17,25–27,29,30,45,57–60,73]. Table 1 represents a direct relationship between the modifiable variables and the outputs; for a better interpretation, it should be clarified that the combined effects of different modifiable variables must be considered. For this purpose, it is recommended to carry out tests where combinations can be made.

According to Table 1, when a user wants to address the effect of the surfactant on the recovery factor, the input variables that should be analyzed are the presence of preferential flowing channels, injection velocity, and pore-throat connectivity. These are the modifiable variables that significantly impact the recovery factor (strong influence). A similar approach can be used for other outputs.

Implicit in the above analysis is the a priori knowledge of  $(\vec{Y})$ , the vector that involves the results that are going to be measured after the microfluidic experiment.  $(\vec{Y})$  depends, obviously, on the experimental setup and on the objectives of the research. Measurable variables such as recovery factor, breakthrough time, pressure drop, and fluid distribution are standard in most microfluidic experiments. In contrast, other results such as fractal dimension and displacement micromechanisms are more sophisticated and demand more time and resources from the experimentalists. Variables such as emulsion formation and drop shape respond to a particular interest in emulsification processes. While the variables listed for  $(\vec{Y})$  in Table 1 are those of more common use in the microfluidic experiments of the authors, other variables, such as species diffusion, fluid mixing, asphaltene deposition, surfactant adsorption, microemulsion properties, salinity changes, and surfactant solubility, can be readily included in Table 1. However, these have their limitations in the application of CFD models.

From the nine variables in Table 1, five were selected to illustrate the ability of the proposed flowchart to select the microfluidic experiment that distinguishes the effect of the two surfactants. (1) Recovery factor: the amount of crude oil that can be obtained from the displacement of a fluid in a porous medium, usually reported as a percentage of the initial crude oil. The recovery factor is one of the most used variables in microfluidic experiments, given that an increase in the recovery factor is the ultimate goal of any CEOR process. (2) Breakthrough time: the time it takes for the displacement flow to reach the outlet of the porous medium; this variable indicates how easily the displacement fluid can be channeled or can move through the porous medium. It is usually measured as PVI (Pore Volume Injected). (3) Fractal dimension of flow pattern: quantifies the flow pattern of the displacement front within the micromodel. The cases evaluated in this investigation are approximated as occurring in two dimensions, indicating that the fractal dimension takes values between one and two, where two indicates a greater uniformity. (4) Pressure drop: indicates the ease with which a fluid moves within the porous medium. (5) Entrapment effect: quantifies the amount of crude trapped or stuck on the grains of the porous medium due to interfacial forces in areas where the surfactant could enter or contact the crude oil.

### 2.3. Experimental Design

An experimental design should be used to define a proper combination of the variables in  $(\vec{X})$  to assess the applicability of the surfactant. A two-level factorial experimental design with five factors ( $2^5$  factorial designs) was applied [74]. The two limits of each modifiable variable in the CFD simulations were selected from typical values available in the literature. A circular (−) and an irregular (+) grain shape were considered as the former makes the detachment of crude oil easier compared to a quadratic or triangular shape [29], and an irregular pore shape is a better representation of the porous media of the reservoir [30,36]. The minimum and maximum porosities were 0.5 (−) and 0.7 (+), respectively. Although these values are high compared to the typical porosity in the reservoir, much of the research in microfluidics has been conducted within this range [25,28,30,58,59,75–82]. The minimum and maximum injection velocities were 10 ft/day (−) and 30 ft/day (+), respectively. The low-level injection velocity was chosen due to its common use in microfluidics processes [25,62,75,83]. The high level is of interest because it is indicative of the effect of high injection velocities on the flow pattern [75]. The presence (+) or absence (−) of preferential flowing channels assesses the response of other variables, such as pressure drop, recovery factor, and fractal dimension [57,59,60], to disruptions in the grain pattern. Table 2 details the  $2^5$  factorial experimental designs.

**Table 1.** Relation between modifiable  $\vec{X}$  and response variables  $\vec{Y}$  in a micromodel experiment. White, light gray, and dark gray indicate low, medium, and a strong relationship, respectively.

$\vec{Y}$	$\vec{X}$	Porosity	Grain Shape	Presence of Preferential Flowing Channel	Preferential Flowing Channel	Heterogeneity	Tortuosity	Injection Velocity	Pore Shape	Pore-throat Connectivity
Oil recovery factor	Pressure drop									
	Fractal dimension									
	Breakthrough time									
Viscosity										
Displacement micro-mechanisms										
Emulsion formation										
Drops shape										
Fluid distribution										

**Table 2.** The 2<sup>5</sup> factorial experimental design analysis along with the CFD simulation results.

Grain Shape	Porosity	Injection Velocity (ft/day)	Presence of Preferential Flowing Channel	IFT (mN/m)	Capillary Number	Breakthrough Time (PVI)	Recovery Factor	Fractal Dimension	Pressure Drop (Pa)	Entrapment Effect
circular	0.5	10	no	0.037	0.013	0.4351	0.3882	1.5666	9.0840	0.0326
irregular	0.5	10	no	0.037	0.013	0.4069	0.3944	1.6281	42.1359	0.0429
circular	0.7	10	no	0.037	0.013	0.4112	0.3979	1.6610	3.5700	0.0411
irregular	0.7	10	no	0.037	0.013	0.4407	0.4100	1.7155	7.1765	0.0844
circular	0.5	30	no	0.037	0.039	0.4274	0.3800	1.5743	25.2136	0.0367
irregular	0.5	30	no	0.037	0.039	0.3829	0.3797	1.6428	117.325	0.0439
circular	0.7	30	no	0.037	0.039	0.3954	0.3832	1.6394	9.5758	0.0345
irregular	0.7	30	no	0.037	0.039	0.4476	0.4135	1.7102	19.2405	0.0974
circular	0.5	10	yes	0.037	0.013	0.4227	0.3855	1.5880	9.4705	0.0579
irregular	0.5	10	yes	0.037	0.013	0.3992	0.3785	1.6251	41.8144	0.0517
circular	0.7	10	yes	0.037	0.013	0.4127	0.4027	1.6871	3.1050	0.0394
irregular	0.7	10	yes	0.037	0.013	0.4426	0.4069	1.6933	6.7786	0.0788
circular	0.5	30	yes	0.037	0.039	0.4031	0.3662	1.5834	26.1504	0.0151
irregular	0.5	30	yes	0.037	0.039	0.3563	0.3390	1.6192	127.808	0.0708
circular	0.7	30	yes	0.037	0.039	0.4245	0.4135	1.6763	8.6735	0.0554
irregular	0.7	30	yes	0.037	0.039	0.4484	0.4093	1.7125	19.1542	0.1001
circular	0.5	10	no	0.045	0.011	0.4322	0.3861	1.5767	8.9602	0.0368
irregular	0.5	10	no	0.045	0.011	0.4392	0.4054	1.6229	42.6613	0.0491
circular	0.7	10	no	0.045	0.011	0.4045	0.3927	1.6627	3.5694	0.0408

Table 2. Cont.

Grain Shape	Porosity	Injection Velocity (ft/day)	Presence of Preferential Flowing Channel	IFT (mN/m)	Capillary Number	Breakthrough Time (PVI)	Recovery Factor	Fractal Dimension	Pressure Drop (Pa)	Entrapment Effect
irregular	0.7	10	no	0.045	0.011	0.4470	0.4178	1.7228	7.2455	0.0652
circular	0.5	30	no	0.045	0.032	0.4393	0.3906	1.5623	24.8362	0.0355
irregular	0.5	30	no	0.045	0.032	0.3705	0.3608	1.6484	119.187	0.0725
circular	0.7	30	no	0.045	0.032	0.4501	0.4325	1.6664	9.5706	0.0433
irregular	0.7	30	no	0.045	0.032	0.4257	0.3946	1.7056	20.9500	0.0935
circular	0.5	10	yes	0.045	0.011	0.4306	0.3938	1.5859	9.3153	0.0640
irregular	0.5	10	yes	0.045	0.011	0.3882	0.3702	1.6110	43.8324	0.0621
circular	0.7	10	yes	0.045	0.011	0.4183	0.4079	1.6742	3.1890	0.0398
irregular	0.7	10	yes	0.045	0.011	0.4468	0.4106	1.7297	7.0466	0.0766
circular	0.5	30	yes	0.045	0.032	0.4075	0.3758	1.5831	26.0617	0.0757
irregular	0.5	30	yes	0.045	0.032	0.3623	0.3457	1.6378	124.657	0.0558
circular	0.7	30	yes	0.045	0.032	0.4303	0.4182	1.6680	8.7053	0.0528
irregular	0.7	30	yes	0.045	0.032	0.4386	0.4031	1.7209	20.4482	0.0944



#### 2.4. Sensitivity Analysis

The response in an output variable ( $Y_i$ ) to changes in IFT was used as indicative of the capacity of the micromodel to differentiate the properties of the surfactant. This response was measured as a normalized sensitivity coefficient ( $\chi_{i,IFT}$ ) such as that described in Equation (1):

$$\chi_{i,IFT} = \left( \frac{1}{Y_{i,max}} \right) \frac{\partial Y_i}{\partial IFT} \approx \left( \frac{1}{Y_{i,max}} \right) \frac{Y_{i1} - Y_{i2}}{IFT_1 - IFT_2} \quad (1)$$

where,  $\frac{\partial Y_i}{\partial IFT}$  is the change of the variable  $Y_i$ ,  $Y_{i,max}$  is the maximum value of the output variable in the CFD experiment  $i$ ,  $Y_{i1}$  is the value of the output variable in the CFD experiment  $i$  when using surfactant one,  $Y_{i2}$  is the response variable in the CFD experiment  $i$  when using surfactant two, and  $IFT_1$  and  $IFT_2$  are the interfacial tensions between each surfactant and the crude oil.

### 3. Numerical Implementation

The center in the selection flowchart in Figure 1 is the experiment based on CFD simulations (CFD experiments). In the case of this research, those CFD experiments are simulations that typically include a geometry or representation of the physical space where simulations take place, i.e., a mesh that discretizes the geometry so that the balance equations can be solved, and the actual CFD solution.

#### 3.1. Geometry

The micromodels were considered in a two-dimensional space given their negligible depth (0.099 mm) when compared to their other dimensions ( $12.7a \times 26.5 \text{ mm}^2$ ). The experimental design in Table 2 results in eight different micromodels, given the possible combinations between grain shape, porosity, and the presence of preferential flowing channels.

The geometries with circular pore shapes were generated using Matlab to randomly distribute non-overlapping circles with a radius between 0.4 mm and 0.6 mm for porosities of 0.7, and a radius between 0.5 mm and 0.7 mm for porosities of 0.5. Micromodels with irregular pore shapes were based on a micromodel template obtained from the literature [62]. A micromodel without the presence of a preferential flowing channel with an irregular pore shape is the same as that used to validate the CFD results below [62]. Preferential flowing channels were placed in the center of the porous medium with an average width of 1.8 mm positioned at an angle of  $45^\circ$  with respect to the direction of the fluid. Figure 2 and Table 3 show the geometries and the main characteristics of all the micromodels used in the simulations.

**Table 3.** Characteristics of the micromodels.

Micromodel	Grain Shape	Porosity	Presence of Preferential Flowing Channel
a	Circular	0.5	no
b	Circular	0.7	no
c	Irregular	0.5	no
d	Irregular	0.7	no
e	Circular	0.5	yes
f	Circular	0.7	yes
g	Irregular	0.5	yes
h	Irregular	0.7	yes

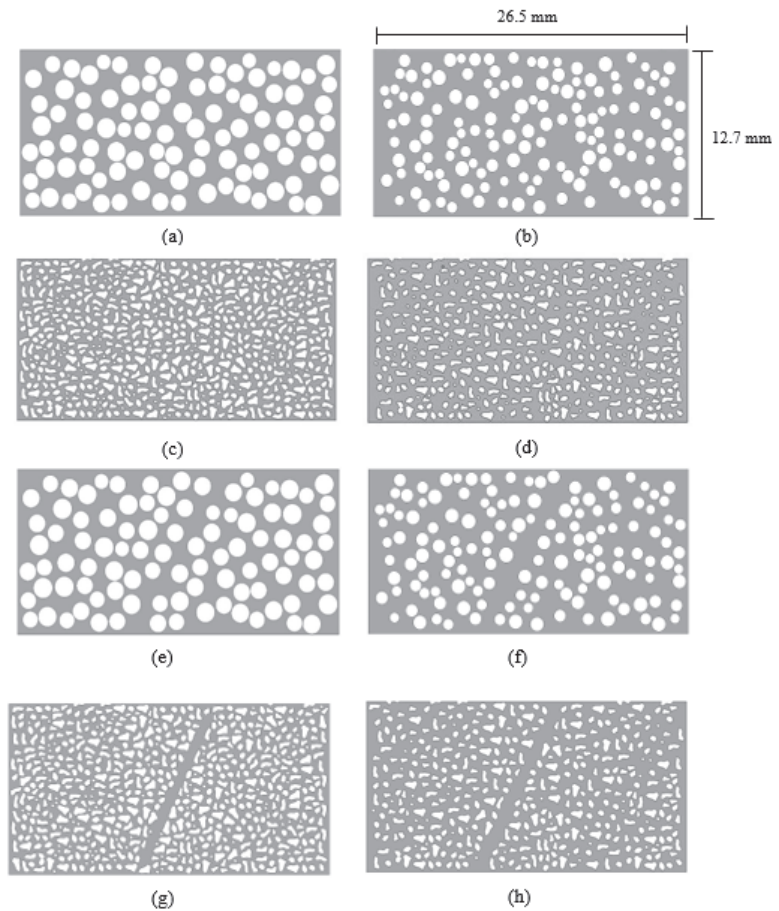


**Figure 2.** Geometries of the micromodels in Table 3. (a) Micromodel with circular grain shape and porosity 0.5. (b) Micromodel with circular grain shape and porosity 0.7. (c) Micromodel with irregular grain shape and porosity 0.5. (d) Micromodel with irregular grain shape and porosity 0.7. (e) Micromodel with circular grain shape, presence of preferential flowing channel, and porosity 0.5. (f) Micromodel with circular grain shape, presence of preferential flowing channel, and porosity 0.7. (g) Micromodel with irregular grain shape, presence of preferential flowing channel, and porosity 0.5. (h) Micromodel with irregular grain shape, presence of preferential flowing channel, and porosity 0.7.

### 3.2. Mesh

The geometry was discretized in two-dimensional, unstructured meshes with triangular elements. The evaluation of grid independence was carried out for water injection with a velocity inlet of 10 ft/day. The relative difference ( $\delta_{mesh}$ ) between the pressure drops, expressed as described by Equation (2), within micromodels with a different number of elements was considered when comparing the grids

$$\delta_{mesh} = \frac{|\Delta P_{Finer} - \Delta P_{Coarser}|}{\Delta P_{Finer}} \quad (2)$$

where  $\Delta P_{Finer}$  and  $\Delta P_{Coarser}$  are the pressure drops between the inlet and outlet of the microfluidic device in the finer and coarser meshes, respectively. Table 4 shows the number of cells and nodes, the pressure drop, and  $\delta_{mesh}$  for all grids. The ratio between the number

of elements in the mesh  $i$  ( $n_i$ ) and those in the mesh with the lowest number of elements ( $n_0$ ) varied between 1.6 and 2.4 for an initial refinement and between 3.5 and 6.4 for final refinement. Grid independence was carried out for all eight micromodel geometries. When  $\delta_{mesh}$  was lower than 0.060, the grid with the lower number of cells was selected as the grid for simulating the surfactant injection process. Figure 3 shows the grid of micromodel (d) as an example. Figures S1–S8 in the Supplementary Material information depict the mesh for all the geometries. The geometry of the cell was adjusted to guarantee that the skewness had average values below 0.28 and maxima below 0.98 for all the micromodels.

**Table 4.** Analysis of mesh independence.

Micromodel	Number of Grid	Number of Cells	Number of Nodes	$n_i/n_0$	$\Delta P$ (Pa.)	$\delta_{mesh}$
a	1	106232	82422	1.0	0.0175	
	2	178656 *	118890	1.7	0.0166	0.051
	3	683801	372377	6.4	0.0161	0.034
b	1	83248	51722	1.0	0.0068	
	2	146637 *	83689	1.7	0.0064	0.059
	3	379198	200661	4.5	0.0063	0.022
c	1	253863	143892	1.0	0.0954	
	2	411068 *	227317	1.7	0.0777	0.229
	3	1163110	617919	4.5	0.0761	0.020
d	1	134200	74919	1.0	0.0137	
	2	324776 *	175961	2.4	0.0128	0.073
	3	701344	36823	5.2	0.0127	0.005
e	1	94784	76642	1.0	0.0218	
	2	155622 *	107304	1.6	0.0186	0.171
	3	335658	197753	3.5	0.0179	0.042
f	1	106986	63755	1.0	0.0083	
	2	218876 *	120112	2.1	0.0074	0.122
	3	378635	200444	3.6	0.0070	0.058
g	1	252252	143061	1.0	0.0941	
	2	408536 *	226044	1.7	0.0807	0.166
	3	1169517	620897	4.7	0.0777	0.039
h	1	133312	74410	1.0	0.0150	
	2	320726 *	173874	2.4	0.0134	0.125
	3	694060	364896	5.2	0.0129	0.039

\* Number of elements selected for the simulations.

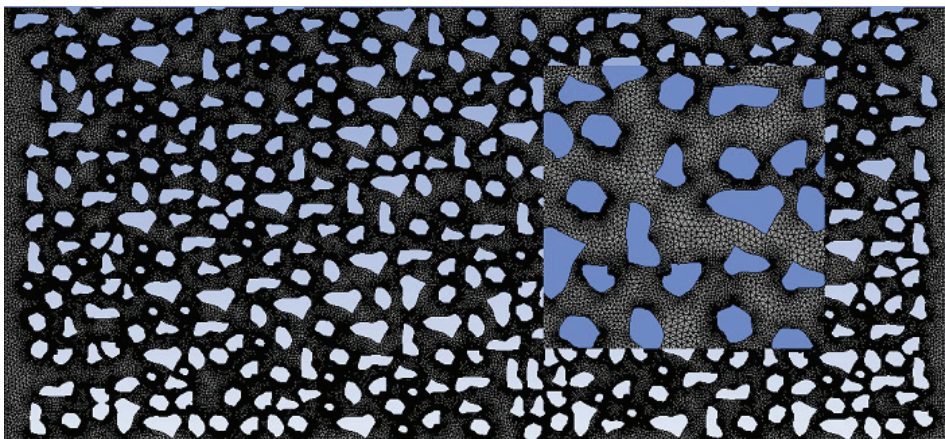


**Figure 3.** Detail of the mesh for the micromodel (d).

### 3.3. CFD Implementation

The commercial software Ansys Fluent 19.1 was used to model the flow in the micro-models [84].

The characteristics of the machine used for the simulations are as follows:

- Intel® Xeon® CPU E5-1620 v2 3.70 GHz
- 4 Cores
- 8 Logic processors
- 16.0 GB RAM

#### 3.3.1. Governing Equations

CFD solves the continuity (Equation (3)), momentum conservation (Equation (4)), and Volume of Fluid (VOF) (Equations (5) and (6)) to represent the flow in the porous medium. The multiphase VoF approach tracks the interface between the oil and the displacing fluid. VoF calculates the volumetric fraction of each of the phases within each cell in the domain [84], taking into account the IFT between phases and the contact angle of each phase to describe the wettability of the medium:

$$\frac{\partial \rho}{\partial t} + \nabla \cdot (\rho \vec{u}) = 0 \quad (3)$$

where  $\vec{u} = (u, v)$  is the velocity vector and  $\rho$  is the fluid volume-averaged density, which is considered constant due to the low compressibility of the fluids.

$$\frac{\partial (\rho \vec{u})}{\partial t} + \nabla \cdot (\rho \vec{u} \vec{u}) = -\nabla p + \nabla \cdot \left[ \mu \left( \nabla \vec{u} + \nabla \vec{u}^T \right) \right] + \vec{F} \quad (4)$$

where  $p$  is the pressure,  $\mu$  the dynamic viscosity coefficient, and  $\vec{F}$  is the vector representing external forces, which for this research is the surface tension force.

$$\frac{1}{\rho_i} \left[ \frac{\partial (\alpha_i \rho_i)}{\partial t} + \nabla \cdot (\alpha_i \rho_i \vec{u}_i) \right] = S_{\alpha_i} \quad (5)$$

where  $S_{\alpha_i}$  is the source term of phase  $i$ ,  $\rho_i$  is the density of phase  $i$ ,  $\vec{u}_i$  is the velocity vector for phase  $i$ , and  $\alpha_i$  is the volume fraction of phase  $i$ . The phases within the micromodel are considered immiscible. The volume fraction,  $\alpha_i$ , is 0 if the cell is empty, varies between 0 and 1 if the interface is located in the cell, and is 1 if the cell is filled with phase  $i$ . The sum of the volumetric fractions of each phase in the domain must be one.

$$\sum_{i=1}^n \alpha_i = 1 \quad (6)$$

The density ( $\rho$ ) and viscosity ( $\mu$ ) of the fluid in a cell where the interface is located are calculated as the volume-weighted average of each of the phases (Equations (7) and (8)).

$$\rho = \alpha_i \rho_i + (1 - \alpha_i) \rho_j \quad (7)$$

$$\mu = \alpha_i \mu_i + (1 - \alpha_i) \mu_j \quad (8)$$

To calculate the surface tension force ( $\vec{F}$ ), the continuum surface force model (Equation (9)) is used [85]:

$$\vec{F} = \sigma_{ij} \frac{\rho \kappa_i \nabla \alpha_i}{\frac{1}{2}(\rho_i + \rho_j)} \quad (9)$$

where  $\sigma_{ij}$  is the coefficient of surface tension, which represents the effect of each surfactant through the IFT, and it is considered constant and  $\kappa_i$  is the curvature of the interface taken

from inside phase  $i$ .  $\kappa_i$  is defined in terms of the divergence of the unit vector ( $\hat{n}$ ) of the gradient of the volume fraction of phase  $i$  as Equations (10) and (11) describe:

$$n = \nabla \alpha_i \quad (10)$$

$$\kappa_i = \nabla \hat{n} \quad (11)$$

where  $n$  is the vector normal to the interface surface, and the phase wettability and the contact angle are used to adjust the interface curvature in areas close to the grains of the micromodel.

$$\hat{n} = \hat{n}_w \cos \theta_i + \hat{t}_w \sin \theta_i \quad (12)$$

where  $\hat{n}_w$  and  $\hat{t}_w$  are unit vectors that are normal and tangential to the grains, respectively, and  $\theta_i$  is the contact angle of phase  $i$  with the grains.

From the equations presented in this section, the effect of IFT (Equation (9)), wettability of the medium (Equation (12)), phase distribution (Equation (5)), viscosity, and velocity are related, allowing the analysis of the process through solving equations in different scenarios.

### 3.3.2. Solver and Boundary Conditions

The CFD simulation used the Pressure Implicit with Splitting of Operators (PISO) approach, a convergence criterion of 0.001 for all the parameters (continuity and velocities), under-relaxation factors of 0.7, 1.0, 1.0, and 0.3 for pressure, density, body forces, and momentum, respectively, and a second-order upwind scheme.

The boundary conditions applied to the simulations were a uniform velocity inlet (left side of the geometry in Figure 2) that was varied according to the CFD experiments defined in Table 2 and a constant pressure outlet (right side in Figure 2) that was set equal to the atmospheric pressure. All grain surfaces were considered walls with total wettability to oil ( $\theta_{oil} = 0$ ). The gravitational forces were supposed to have a negligible effect on the flow through the porous media. The micromodels were initially saturated with crude oil. A variable time-step approach was used with a global Courant number of two. The Supplementary Material information (Section S2) presents additional parameters of the variable time-step algorithm.

### 3.3.3. CFD Model Limitations

The chemistry of the EOR processes is fundamental because it allows the description of the processes and phenomena to understand the interaction between the phases better. Processes such as adsorption of surfactant in the porous medium, microemulsion properties, surfactant solubility, distribution of surfactant between phases, among other processes, were not considered in the development of this research. However, these are of great importance in EOR processes with surfactants, as can be seen in additional research [3–7,11–14,86].

This model was specified with a constant IFT (Equation (9)), and the adsorption process would modify the IFT, making it sensitive to changes in adsorption rate and fluid distribution inside the micromodel. In the model developed in this research, only the IFT effect was considered; for this reason, a constant IFT and a simple relationship with wettability were proposed.

The model developed focuses on the displacement of fluids and their interaction through interfacial tension. Parameters such as retaining surfactants in the walls can be modeled through boundary conditions and dynamic changes in IFT. For this purpose, it is essential to consider the experimental adsorption kinetics and the adsorption isotherms of the different components of the system in the medium and their effect on the effective concentration of surfactant in the displacement front [87]. Moreover, asphaltene deposition can be modeled through reaction models, where equilibrium constants are necessary [88]. Furthermore, emulsions can be modeled with an Eulerian type multiphase model for each phase present in the system [89]. However, these were not considered for

the simplicity of the model and the practicality of micromodel evaluation, as done in other research [26,27,29,45].

Supplementary Material information (Section S4) gives more information about the phase behavior and the modeling carried out in this research.

### 3.4. Evaluation of Output Variables

The oil recovery factor was obtained through an area-weighted average of the mass of oil inside the micromodel at the end of the CFD experiment. This number was compared with the amount of crude oil at the beginning of the displacement process to compute the recovery factor. The breakthrough time was determined as when the concentration of displacing fluid at the exit of the micromodel changed from 0 to 0.03 and was reported as injected pore volume. The pressure drop was determined as the difference from line averages of the pressure at the exit and the entrance of the simulation domain. The calculation of the fractal dimension of the flow pattern at the breakthrough time involved image analysis and the fractal box-counting method [90]. With the box-counting method, the fractal dimension is obtained as the slope of the line of the logarithm of the number of boxes occupied by the pattern ( $N$ ) and the logarithm of the inverse of the box size ( $r$ ). Supplementary Material information (Section S3) gives more details on the procedure to compute the fractal dimension of the flow pattern. High values of the fractal dimension (close to two) indicate a more uniform displacement front, where the flow pattern looks like a square. In contrast, low values (close to one) suggest a line-like displacement front, where the fluid is not distributed throughout the available space in the micromodel. For the entrapment effect, the proportion of area enclosed by the displacing fluid was calculated. As an example, Figure 4 illustrates the entrapment effect as the oil, in red color along with the grains where the crude is stuck, is enclosed by the displacing fluid (black) on the porous media (white). The flow direction is from left to right. The fraction of oil entrapped was calculated by a custom-made subroutine that, through color differentiation, identifies areas of the micromodel where the oil is surrounded by displacing fluid and/or around a pore through which the displacing fluid has passed, the subroutine calculates the area of this section and compares it with the total area available in the micromodel, subtracting the area of the grains only to consider the amount of crude stuck to them. Thus, the areas in red color presented in Figure 4 are subtracted from the grains located in those red zones to calculate the total amount of crude oil stuck in the micromodel. The entrapment effect in Figure 4 is 0.041.



**Figure 4.** The entrapment effect in the micromodel. The flow direction is from left to right. White represents the porous medium, black is the displacing fluid, and red is the entrapped oil.

### 3.5. Fluid Properties

The properties of the displacing fluid (surfactant solution) and the oil used in the analysis were taken from reference [62]. Table 5 presents the values of density and rheological parameters for both fluids. Equation (13) shows the power-law used to estimate the non-Newtonian viscosity:

$$\eta = k \dot{\gamma}^{n-1} \quad (13)$$

where  $\eta$  is the apparent viscosity of the fluid,  $k$  is the consistency index that is a measure of the average viscosity of the fluid,  $\dot{\gamma}$  is the shear rate, and  $n$  is a measure of the deviation of the fluid from Newtonian. The properties of the oil phase were the same as those reported in [62].

**Table 5.** Density and rheological parameters of the fluids used in the simulations.

Fluid	Density (kg/m <sup>3</sup> )	k	n	Maximum Viscosity (Pa·s)	Minimum Viscosity (Pa·s)
Surfactant solution	1084.3	0.028	0.638	0.017	0.005
Oil	926.5	0.103	0.977	0.099	0.092

The modeling of properties such as viscosity allows for obtaining a better detail of the flow characteristics within the micromodel, considering that the analyzed medium presents geometric characteristics that dispose the fluid at different stresses.

## 4. Results

### 4.1. Validation of Numerical Results

The oil recovery factor, the breakthrough time, the fractal dimension of the flow pattern, and the entrapment effect at the breakthrough time were compared with experimental data reported in reference [62], and these variables were also analyzed in different scenarios in order to evaluate the expected trend with the results of the numerical simulation. As the mentioned study [62] does not report the pressure drop, the CFD predictions were compared to Darcy's law.

The experimental data were carried out in previous research [62] which described the detailed experimental setup that consisted of the following elements: a digital camera, microfluidic device, light source, computer, OEM (Original Equipment Manufacturers) syringe pump, and waste storage.

The fluids used in the experimental test consisted of synthetic brines formulated based on saltwater of a Colombian field. The brine composition consisted of 6.46 g L<sup>-1</sup> of NaCl, 0.136 g L<sup>-1</sup> of CaCl<sub>2</sub>·2H<sub>2</sub>O, and 0.20 g L<sup>-1</sup> of MgCl<sub>2</sub>·2H<sub>2</sub>O. The surfactant used in the experimental test consisted of a mixture of hydrophilic and hydrophobic surfactant in a ratio of 80:20. In preparing the surfactant mixture, the hydrophilic surfactant was first added to the synthetic brine and then the hydrophobic surfactant was added.

Displacement tests were carried out at atmospheric pressure at a temperature of 25 °C in a micromodel made of polydimethylsiloxane (PMDS). Details of the process of fabrication can be found in [91]. The tests were evaluated through image analysis taken in a high-resolution digital camera, where the high contrast between the phases is taken advantage of, and by pixel analysis, it is possible to calculate the recovery factor and the distribution of phases within the micromodel. Other details can be consulted in [62].

To validate the predictions for the recovery factor and breakthrough time, the surfactant injection process was simulated in the oil-saturated micromodel (d) with an injection velocity of 10 ft/day, the interfacial tension between the fluid and crude oil was 0.03 mN/m; these conditions were the same as those in the experimental test in [62], as well as those of the oil and surfactant already reported in Table 5. Figure 5 shows that the numerical results present the same trend as that of the experimental data and that the change in slope

around 0.55 PVI was captured. The relative errors were 10% (experiments: 0.50, simulation: 0.45) for the oil recovery factors at the breakthrough time and 12.7% (experiments: 0.47, simulation: 0.41) for the breakthrough time. These errors are within the uncertainty of the experiments.

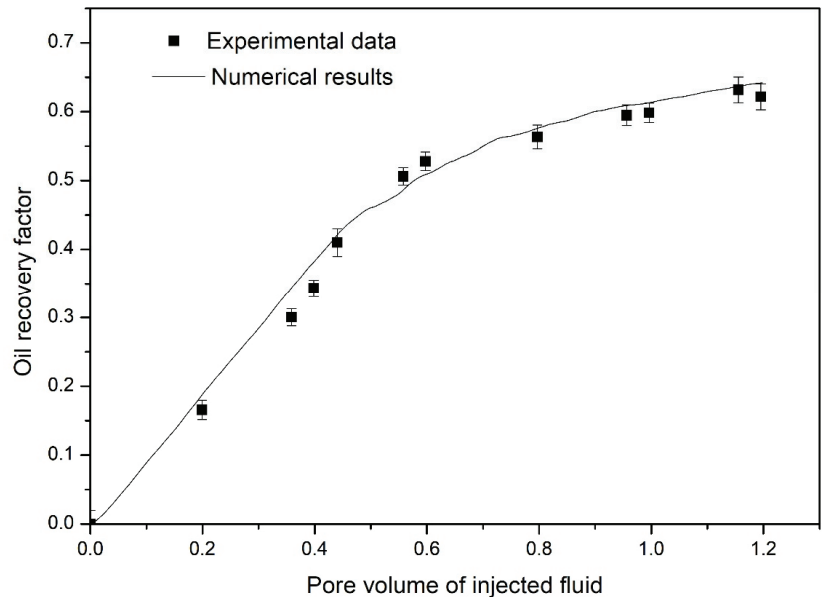
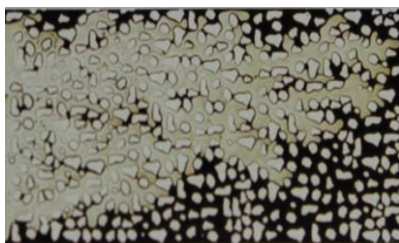
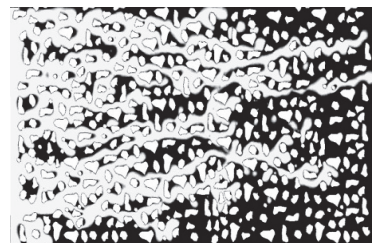


**Figure 5.** Comparison of numerical results with experimental data from Betancur et al. [62]. Reproduced with permission from Céspedes-Zuluaga S, Computational fluid dynamics as a tool for the design of micromodels for the evaluation of surfactant injection in enhanced oil recovery processes; published by Universidad Nacional de Colombia, 2020.

Figure 6 shows the distribution of fluids at the breakthrough time in the CFD experiments (Figure 6a) and as predicted by the CFD simulation (Figure 6b). While the pattern is not the same, both images present a certain resemblance. The images in Figure 6 were analyzed to calculate the fractal dimension of the flow pattern as explained above. The fractal dimension for the experimental test was 1.85, while this value for the numerical simulation was 1.83 as in the experimental test, the fluid maintains a more defined front of advance with less interdigitation, while in the numerical simulation, interdigitation is more evident.



(a)



(b)

**Figure 6.** Flow distribution within the micromodel at rupture time. Injection velocity: 10 ft/day and IFT 0.03 mN/m. (a) Experimental and (b) simulation.



The simulation response to changes in IFT, an essential part of the selection flowchart given the presence of the derivative in the sensitivity analysis, was validated with experimental data. The predicted recovery factor, breakthrough time, fractal dimension of the flow pattern, and entrapment effect were compared in a surfactant injection process in the oil-saturated micromodel (d) with an injection velocity of 10 ft/day and a value of IFT between the fluid and crude oil of 2.7 mN/m. Figure 7 compares the distribution of fluids at the breakthrough time predicted by CFD with the one reported in the experiments in [62]. Interdigitation is evident, in the upper part of the figure, for both images. The model predicts a second preferential path at the lower part of the image, although this one is more advanced in the simulation.

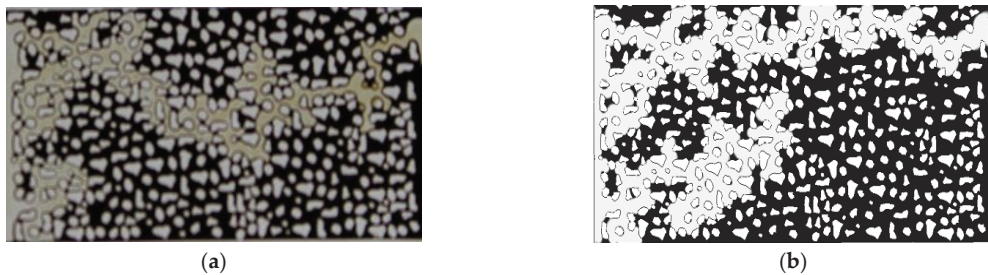


**Figure 7.** Flow distribution within the micromodel at rupture time. Injection velocity: 10 ft/day and IFT 2.7 mN/m. (a) Experimental and (b) simulation.

The simulation finely predicts the breakthrough time (0.26 PVI both for simulation and experiment) as well as the recovery factor (experiment: 0.375, simulation: 0.362), the fractal dimension of the flow pattern (experiment: 1.72, simulation: 1.76), and entrapment effect (experiment: 0.0397, simulation: 0.0417). These results give confidence in the model's performance to exhibit the effect of changes in IFT on the characteristics of the porous flow.

A final validation involved comparing the pressure drop predicted by CFD and that predicted by Darcy's law [92] for the medium's permeability (5.71 D) and the length of the porous media (26.5 mm). Both values (Darcy's law: 11.76 Pa, simulation: 11.96 Pa) are in good agreement.

On the other hand, Table 2 shows the capillary number for each system evaluated. This number indicates the relationship between viscous and surface forces and was calculated as shown in Equation (14) [93]:

$$C_N = \frac{\mu U}{\sigma \cos(\theta)} \quad (14)$$

where  $C_N$  is the capillary number,  $\mu$  (N/m) and  $U$  (m/s) are the viscosity and velocity of displacement phase,  $\sigma$  (N/m) is the IFT between the phases inside the micromodel, and  $\theta$  is the oil phase contact angle. The numerator involved in Equation (14) refers to viscous forces, while the denominator to surface forces or those related to the interface between the fluids.

Due to the conditions proposed for the simulations, the capillary number takes four values: 0.013, 0.039, 0.011, and 0.032. All these values indicate the superiority of the interfacial forces ( $C_N < 1$ ) [65], giving importance to the interfacial tension value between the crude oil and the displacing phase. In this way, in each case evaluated, it is guaranteed that the surfactant solution is of great importance.

Considering that the decrease in IFT between the phases is one of the main mechanisms used in EOR processes with surfactant injection, as shown [2,86], this research considers this effect as the main one for the development of the selection flowchart.

4.2. Application of the Micromodel Experiment Selection Flowchart

Table 2 presents the values of  $(\vec{Y})$  for the 32 simulations proposed in the factorial experimental design. The 32 CFD experiments in Table 2 can be grouped in four cases based on the characteristics of the micromodel (grain shape and the presence of a preferential flowing channel): case 1, micromodels without the presence of a preferential flowing channel with circular grain shape; case 2, micromodels without the presence of a preferential flowing channel with irregular grain shape; case 3, micromodels with a preferential flowing channel with circular grain shape; and case 4, micromodels with a preferential flowing channel with irregular grain shape. Table 6 presents the values of the normalized sensitivity coefficient  $\chi_{i,IFT}$  (Equation (1)) obtained from the CFD results in Table 2. The last column in Table 6 presents  $\chi_{Total,IFT}$  that sums up the contribution of all the individual values of  $\chi_{i,IFT}$ . A high value for  $\chi_{i,IFT}$  indicates those CFD experiments where the difference in IFT has a higher effect on the output variable or the CFD experiments that would more easily predict a difference in the behavior of both surfactants. For instance, for case 1, the highest  $\chi_{Total,IFT}$  (42.4) was calculated for the CFD experiment with the largest porosity, 0.7, and the highest injection velocity (30 ft/day) as the CFD model indicated a significant effect of changes in IFT in the recovery factor ( $\chi_{recovery\ factor, IFT} = 14.2$ ) and breakthrough time ( $\chi_{breakthrough\ time, IFT} = 15.2$ ). As a comparison, for the same case 1, an injection velocity of 10 ft/day decreased  $\chi_{Total,IFT}$  to only 3.88. Table 6 allows for identifying for each displacement condition and micromodel, the output most affected by the difference in interfacial tension presented for each surfactant. In addition, it can be identified in each micromodel which is the output where the IFT change has the most impact. This type of analysis, the result of the application of a selection flowchart, together with CFD simulations and a statistical treatment, allows for having a clearer idea regarding the necessary parameters in a micromodel for the evaluation of surfactants.

Table 6. Normalized sensitivity coefficients  $\chi_{i,IFT}$  obtained from the CFD simulations.

Case	Grain Shape	Presence of Preferential Flowing Channel	Porosity	Injection Velocity (ft/day)	$\chi_{RF,IFT}$ <sup>a</sup>	$\chi_{BT T,IFT}$ <sup>b</sup>	$\chi_{FD,IFT}$ <sup>c</sup>	$\chi_{P,IFT}$	$\chi_{Ent,IFT}$ <sup>d</sup>	$\chi_{TOTAL,IFT}$
1	circular	no	0.5	10	0.59	0.80	0.73	0.12	5.17	7.41
	circular	no	0.7	10	1.49	1.85	0.12	0.00	0.42	3.88
	circular	no	0.5	30	3.05	3.31	0.87	0.37	1.51	9.12
	circular	no	0.7	30	14.24	15.18	1.95	0.01	11.01	42.38
2	irregular	no	0.5	10	3.18	8.97	0.38	0.51	7.72	20.75
	irregular	no	0.7	10	2.23	1.74	0.53	0.07	23.94	28.51
	irregular	no	0.5	30	5.40	3.43	0.41	1.82	35.76	46.85
	irregular	no	0.7	30	5.48	6.10	0.33	1.67	4.83	18.42
3	circular	yes	0.5	10	2.40	2.19	0.15	0.15	7.67	12.56
	circular	yes	0.7	10	1.50	1.57	0.93	0.08	0.44	4.53
	circular	yes	0.5	30	2.76	1.22	0.02	0.09	75.58	79.68
	circular	yes	0.7	30	1.36	1.62	0.60	0.03	3.23	6.84
4	irregular	yes	0.5	10	2.41	3.06	1.02	1.97	13.04	21.50
	irregular	yes	0.7	10	1.07	1.16	2.63	0.26	2.75	7.87
	irregular	yes	0.5	30	1.93	1.67	1.34	3.08	18.72	26.74
	irregular	yes	0.7	30	1.79	2.72	0.61	1.27	7.12	13.50

<sup>a</sup> RF: Recovery factor, <sup>b</sup> BT T: Breakthrough time, <sup>c</sup> FD: Fractal dimension of the flow, <sup>d</sup> Ent: entrapment factor.

A similar analysis for all the other cases can be conducted to yield Table 7, which summarizes what experimental conditions have the most significant change based on differences in IFT. This table considers the conditions where the performance of the evaluated surfactants can be better differentiated, grouped according to the grain shape and the presence of preferential flow paths. In this way, it is possible to identify parameters that can be used in microfluidic experiments for the evaluation of surfactants, highlighting some of the outputs (recovery factor, breakthrough time, fractal dimension, pressure drop, entrapment effect).

**Table 7.** Conditions of injection velocity and porosity that yield the highest values of  $\chi_{i,IFT}$ .

Case	Recovery Factor		Breakthrough Time		Fractal Dimension		Pressure Drop Change		Entrapment Effect	
	Major Change	Minor Change	Major Change	Minor Change	Major Change	Minor Change	Major Change	Minor Change	Major Change	Minor Change
1: Circular grain shape and non-preferential channel micromodel	High injection velocity— High porosity	Low injection velocity— Low porosity	High injection velocity— High porosity	Low injection velocity— Low porosity	High injection velocity— High porosity	Low injection velocity— High porosity	High injection velocity— Low porosity	High injection velocity— High porosity	High injection velocity— High porosity	Low injection velocity— High porosity
2: Irregular grain shape and non-preferential channel micromodel	High injection velocity	Low injection velocity	Low injection velocity— Low porosity	Low injection velocity— High porosity	Low injection velocity— High porosity	High injection velocity— High porosity	High injection velocity— Low porosity	Low injection velocity— High porosity	High injection velocity— Low porosity	High injection velocity— High porosity
3: Circular grain shape and preferential channel micromodel	Low injection velocity— Low porosity	High injection velocity— High porosity	Low injection velocity— Low porosity	High injection velocity— Low porosity	Low injection velocity— High porosity	High injection velocity— Low porosity	Low injection velocity— Low porosity	High injection velocity— High porosity	High injection velocity— Low porosity	Low injection velocity— High porosity
4: Irregular grain shape and preferential channel micromodel	Low injection velocity— Low porosity	Low injection velocity— High porosity	Low injection velocity— Low porosity	Low injection velocity— High porosity	Low injection velocity— High porosity	High injection velocity— High porosity	High injection velocity— Low porosity	Low injection velocity— High porosity	High injection velocity— Low porosity	Low injection velocity— High porosity

For case 4 (irregular grain shape with the presence of preferential flowing channel), low injection velocity and low porosity are preferred to distinguish the effect of IFT on the recovery factor. At the same time, changes in the pressure drop become more evident for a high injection velocity and low porosity. The data in Table 7 can readily be used to determine experimental conditions that can favor the evaluation of the effect of IFT on any of the output variables ( $\vec{Y}$ ) considered in this study.

Table 8 presents a global summary of the results in Table 7 that provide a comprehensive response to the question of what experimental configuration would best differentiate between two IFTs. While Table 7 responds to the question of what conditions are preferred to have a more noticeable effect on an individual output variable ( $Y_i$ ), Table 8 considers the set of experimental conditions that would indicate the largest change in ( $\vec{Y}$ ) for smallest differences in IFT. Table 8 indicates that for case 3, for instance, a high injection velocity and low porosity, in the range of the simulations used in this paper, should be preferred when evaluating two different surfactants.

Finally, from the values of  $\chi_{TOTAL,IFT}$  in Table 6, it is possible to choose the micromodel among the eight evaluated in this research. The conditions where a higher value of  $\chi_{TOTAL,IFT}$  (76.98) was obtained were those of the micromodel with circular grain shape, with the presence of a preferential flowing channel, a porosity of 0.5, and an injection velocity of 30 ft/day. This means that this micromodel with the evaluated conditions is the one that allows the best differentiation of the performance between the surfactants analyzed in this research. This was obtained from the application of the selection flowchart. The example outlined above illustrates how the flowchart proposed in Figure 1, which uses CFD simulations to represent the flow in a microfluidic device, can assist in selecting the

microfluidic experiment that would have more success in distinguishing the performance of two surfactants with very similar IFTs.

**Table 8.** Conditions of injection velocity and porosity that yield the highest values of  $\chi_{Total,IFT}$ .

Case	Changes Considering the Effect of All Response Variables (Y)	
	Major Change	Minor Change
1: Circular grain shape and non-preferential flowing channel micromodel	High injection velocity—High porosity	Low injection velocity—High porosity
2: Irregular grain shape and non-preferential flowing channel micromodel	High injection velocity—Low porosity	High injection velocity—High porosity
3: Circular grain shape and preferential flowing channel micromodel	High injection velocity—Low porosity	Low injection velocity – High porosity
4: Irregular grain shape and preferential flowing channel micromodel	High injection velocity—Low porosity	Low injection velocity—High porosity

Also, the conditions where the micromodel best differentiates the performance of surfactants is found for the highest capillary numbers, with values of 0.039 and 0.032, corresponding to an IFT of 0.037 mN/m and 0.045 mN/m, respectively. However, this indicates a significant influence of viscous forces, specifically the injection velocity, other parameters must also be considered as will be discussed later depending on the output variables evaluated.

Further information can be obtained from the analysis of Table 6, particularly on the importance of the output variables on the evaluation of surfactants. The sum of all  $\chi_{i,IFT}$  over all the CFD experiments indicates that the entrapment effect ( $\sum \chi_{Ent,IFT} = 218.9$ ) is the variable that can more easily differentiate the performance of both surfactants. The recovery factor and breakthrough time ( $\sum \chi_{RF,IFT} = 50.9$ ,  $\sum \chi_{BT T,IFT} = 56.6$ ) can also be used to distinguish the performance of surfactants with very similar IFTs. The fractal dimension ( $\sum \chi_{FD,IFT} = 12.6$ ) and pressure drop ( $\sum \chi_{P,IFT} = 11.5$ ) have the smallest sensitivities to changes in IFT. The strong influence of the surfactant on the entrapment effect, the recovery factor, and the breakthrough time is probably because surfactants have a substantial effect on entrapment as they modify the surface interaction between the oil and the porous media, and increase the amount of crude oil displaced through the micromodel to increase the recovery factor and reduce the breakthrough time. The low effect on the fractal dimension of flow indicates that in the small length scale of a microfluidic device, such as those used in this study, the fractal dimension of flow differences are slight for surfactants of very similar IFTs, such as those used in this study. The same is true for the pressure drop.

A similar attempt at correlating the microfluidic grain shape (circular vs. irregular) or the presence or absence of preferential flowing channel does not allow a definitive conclusion as similar values of  $\sum \chi_{i,IFT}$  were obtained for these variables

$$\left( \overbrace{\sum \chi_{TOTAL,IFT} = 177.3}^{\text{no preferential channel}}, \overbrace{\sum \chi_{TOTAL,IFT} = 173.2}^{\text{preferential channel}}, \overbrace{\sum \chi_{TOTAL,IFT} = 166.4}^{\text{circular}}, \overbrace{\sum \chi_{TOTAL,IFT} = 184.1}^{\text{irregular}} \right)$$

A lower porosity  $\left( \overbrace{\sum \chi_{TOTAL,IFT} = 224.6}^{\text{porosity}=0.5}, \overbrace{\sum \chi_{TOTAL,IFT} = 125.9}^{\text{porosity}=0.7} \right)$  and a higher injection

flow  $\left( \overbrace{\sum \chi_{TOTAL,IFT} = 107.0}^{10\text{ft/day}}, \overbrace{\sum \chi_{TOTAL,IFT} = 243.5}^{30\text{ft/day}} \right)$  increase the ability of the microflu-

idic experiment to distinguish between two surfactants. This indicates that more extreme conditions, lower porosity, and a higher velocity make the effect of the surfactant in the oil recovery process more evident.

## 5. Conclusions

This research proposed and demonstrated a flowchart for selecting microfluidic experiments to evaluate the performance of surfactants in the low interfacial tension range. The flowchart guides the user through comprehensive CFD simulations, experimental design, and sensitivity analysis with the ultimate goal of defining the microfluidic characteristics and the experimental conditions that can make the difference between two surfactants either in one specific output variable, e.g., recovery factor, or in a set of performance variables more evident.

For the output variables that can be measured in microfluidic experiments and that were considered in the analysis, i.e., recovery factor, breakthrough time, fractal dimension, pressure drop, and entrapment effect, the latter is the one that makes the differences between the surfactants used in the study more evident; however, the recovery factor and the breakthrough time can also be used to distinguish between surfactants.

For the microfluidic design characteristics and experimental conditions evaluated in this study, a high injection velocity and a low porosity have the most significant effect on the ability of the CFD experiments to differentiate the performance of the surfactant. The presence of preferential flowing channels on whether circular or irregular grains form the microfluidic does not have a significant effect when the objective is to analyze the performance of a surfactant.

Although this type of process facilitates the evaluation of EOR technologies with surfactant injection, it is recommended to carry out experimental tests to complement the results obtained from this type of research. The objective of this research is not the design of EOR processes, but of micromodels that help to select surfactants and other variables before the application of the technologies in the field.

Phenomena such as adsorption of surfactant in the porous medium, microemulsion properties, surfactant solubility, distribution of surfactant between phases, among other processes, were not considered in the model proposed. However, they are essential for evaluating surfactants and should be included in future studies.

The results obtained in this research facilitate the design of micromodels to evaluate surfactants in EOR processes. The application of surfactants in the field involves different types of phenomena and interactions between surfactant-porous media that were not considered in the modeling present in this investigation. For this reason, the results and conclusions obtained in this investigation are limited to the design of micromodels in the evaluation of surfactants.

**Supplementary Materials:** The following are available online at <https://www.mdpi.com/article/10.3390/pr9111887/s1>, Figure S1: Detail of the mesh for micromodel (a), Figure S2: Detail of the mesh for micromodel (b), Figure S3: Detail of the mesh for micromodel (c), Figure S4: Detail of the mesh for micromodel (d), Figure S5: Detail of the mesh for micromodel (e), Figure S6: Detail of the mesh for micromodel (f), Figure S7: Detail of the mesh for micromodel (g), Figure S8: Detail of the mesh for micromodel (h), Figure S10: Extensive Selection Flowchart for micromodel experiments. Table S1: Parameters for the variable time-step algorithm used in the simulations, Section S3: Fractal dimension of the flow pattern, Section S4: Phase behavior.

**Author Contributions:** Conceptualization, S.C., A.M. and F.B.C.; methodology, S.C.; software, S.C.; validation, S.C., A.M., F.B.C., B.L. and M.S.P.; formal analysis, S.C. and C.A.F.; investigation, S.C.; resources, B.L. and M.S.P.; writing—original draft preparation, S.C., A.M. and F.B.C.; writing—review and editing, A.M., C.A.F. and F.B.C.; visualization, S.C., A.M. and F.B.C.; supervision, A.M. and F.B.C.; project administration, F.B.C.; funding acquisition, F.B.C. All authors have read and agreed to the published version of the manuscript.

**Funding:** This research was funded by MINCIENCIAS AND Agencia Nacional de Hidrocarburos (ANH) through the Agreement 064-2018.

**Institutional Review Board Statement:** Not applicable.

**Informed Consent Statement:** Not applicable.

**Data Availability Statement:** Not applicable.

**Acknowledgments:** The authors acknowledge MINCIENCIAS, ANH, and Universidad Nacional de Colombia for their financial and logistic support.

**Conflicts of Interest:** The authors declare no conflict of interest.

## References

- Liu, Z.-x.; Liang, Y.; Wang, Q.; Guo, Y.-j.; Gao, M.; Wang, Z.-b.; Liu, W.-l. Status and progress of worldwide EOR field applications. *J. Pet. Sci. Eng.* **2020**, *193*, 107449. [CrossRef]
- Sheng, J.J. Status of surfactant EOR technology. *Petroleum* **2015**, *1*, 97–105. [CrossRef]
- Hanamertani, A.S.; Pilus, R.M.; Idris, A.K.; Irawan, S.; Tan, I.M. Ionic liquids as a potential additive for reducing surfactant adsorption onto crushed Berea sandstone. *J. Pet. Sci. Eng.* **2018**, *162*, 480–490. [CrossRef]
- Ahmadi, M.A.; Shadizadeh, S.R. Induced effect of adding nano silica on adsorption of a natural surfactant onto sandstone rock: Experimental and theoretical study. *J. Pet. Sci. Eng.* **2013**, *112*, 239–247. [CrossRef]
- Ahmadi, M.-A.; Ahmad, Z.; Phung, L.T.K.; Kashiwao, T.; Bahadori, A. Experimental investigation the effect of nanoparticles on micellization behavior of a surfactant: Application to EOR. *Pet. Sci. Technol.* **2016**, *34*, 1055–1061. [CrossRef]
- Amedi, H.; Ahmadi, M.-A. Experimental investigation the effect of nanoparticles on the oil-water relative permeability. *Eur. Phys. J. Plus* **2016**, *131*, 1–8. [CrossRef]
- Ahmadi, M.-A.; Shadizadeh, S.R. Nanofluid in hydrophilic state for EOR implication through carbonate reservoir. *J. Dispers. Sci. Technol.* **2014**, *35*, 1537–1542. [CrossRef]
- Ahmadi, M.A.; Sheng, J. Performance improvement of ionic surfactant flooding in carbonate rock samples by use of nanoparticles. *Pet. Sci.* **2016**, *13*, 725–736. [CrossRef]
- Ahmadi, M.A.; Shadizadeh, S.R. Nano-surfactant flooding in carbonate reservoirs: A mechanistic study. *Eur. Phys. J. Plus* **2017**, *132*, 1–13. [CrossRef]
- Ahmadi, M.A. Use of nanoparticles to improve the performance of sodium dodecyl sulfate flooding in a sandstone reservoir. *Eur. Phys. J. Plus* **2016**, *131*, 1–9. [CrossRef]
- Ahmadi, M.A.; Shadizadeh, S.R. Spotlight on the new natural surfactant flooding in carbonate rock samples in low salinity condition. *Sci. Rep.* **2018**, *8*, 1–15. [CrossRef]
- Ahmadi, M.A.; Shadizadeh, S.R. Adsorption of a nonionic surfactant onto a silica surface. *Energy Sources Part A* **2016**, *38*, 1455–1460. [CrossRef]
- Ahmadi, M.A.; Shadizadeh, S. Experimental and theoretical study of a new plant derived surfactant adsorption on quartz surface: Kinetic and isotherm methods. *J. Dispers. Sci. Technol.* **2015**, *36*, 441–452. [CrossRef]
- Ahmadi, M.A.; Galedarzadeh, M.; Shadizadeh, S.R. Wettability alteration in carbonate rocks by implementing new derived natural surfactant: Enhanced oil recovery applications. *Transp. Porous Media* **2015**, *106*, 645–667. [CrossRef]
- Keelan, D.; Koepf, E. The role of cores and core analysis in evaluation of formation damage. *J. Pet. Technol.* **1977**, *29*, 482–490. [CrossRef]
- Chapman, E.M. Microfluidic Visualisation and Analysis of Multiphase Flow Phenomena at the Pore Scale. Ph.D. Thesis, Imperial College London, London, UK, 2014.
- Cheraghian, G. An experimental study of surfactant polymer for enhanced heavy oil recovery using a glass micromodel by adding nanoclay. *Pet. Sci. Technol.* **2015**, *33*, 1410–1417. [CrossRef]
- Hematpour, H.; Arabjamloei, R.; Nematzadeh, M.; Esmaili, H.; Mardi, M. An experimental investigation of surfactant flooding efficiency in low viscosity oil using a glass micromodel. *Energy Sources Part A* **2012**, *34*, 1745–1758. [CrossRef]
- Hug, T.; Parrat, D.; Kunzi, P.-A.; Staufer, U.; Verpoorte, E.; de Rooij, N.F. Fabrication of nanochannels with PDMS, silicon and glass walls and spontaneous filling by capillary forces. In Proceedings of the 7th International Conference on Miniaturized Chemical and Biochemical Analysts Systems, Squaw Valley, CA, USA, 5–9 October 2003.
- Kolari, K.; Saarela, V.; Franssila, S. Deep plasma etching of glass for fluidic devices with different mask materials. *J. Micromech. Microeng.* **2008**, *18*, 064010. [CrossRef]
- Rock, A.; Hincapie, R.; Wegner, J.; Ganzer, L. Advanced Flow Behavior Characterization of Enhanced Oil Recovery Polymers using Glass-Silicon-Glass Micromodels that Resemble Porous Media. In Proceedings of the SPE Europec Featured at 79th EAGE Conference and Exhibition, Paris, France, 12–15 June 2017.
- Wegner, M.; Christie, J. Chemical etching of deformation sub-structures in quartz. *Phys. Chem. Miner. Vol.* **1983**, *9*, 67–78. [CrossRef]
- Park, D.; Bou-Mikael, S.; King, S.; Thompson, K.; Willson, C.; Nikitopoulos, D. Design and fabrication of rock-based polymer micromodel. In Proceedings of the ASME 2012 International Mechanical Engineering Congress & Exposition, Houston, TX, USA, 9–15 November 2012; pp. 709–716.
- Mohammadi, F.; Haghtalab, A.; Jafari, A.; Gharibshahi, R. CFD study of surfactant flooding in a micromodel with quadratic pore shape. In Proceedings of the 1st National Conference on Oil and Gas Fields Development (OGFD), Tehran, Iran, 28–29 January 2015.

25. Jafari, A.; Pour, S.E.F.; Gharibshahi, R. CFD Simulation of Biosurfactant Flooding into a Micromodel for Enhancing the Oil Recovery. *Int. J. Chem. Eng. Appl.* **2016**, *7*, 353–358. [CrossRef]
26. Ghanad Dezfally, M.; Jafari, A.; Gharibshahi, R. CFD simulation of enhanced oil recovery using nanosilica/supercritical CO<sub>2</sub>. *Adv. Mater. Res.* **2015**, *1104*, 81–86. [CrossRef]
27. Gharibshahi, R.; Jafari, A.; Ahmadi, H. CFD investigation of enhanced extra-heavy oil recovery using metallic nanoparticles/steam injection in a micromodel with random pore distribution. *J. Pet. Sci. Eng.* **2019**, *174*, 374–383. [CrossRef]
28. Karadimitriou, N.; Hassanizadeh, S. A review of micromodels and their use in two-phase flow studies. *Vadose Zone J.* **2012**, *11*, vzj2011.0072. [CrossRef]
29. Gharibshahi, R.; Jafari, A.; Haghtalab, A.; Karambeigi, M.S. Application of CFD to evaluate the pore morphology effect on nanofluid flooding for enhanced oil recovery. *RSC Adv.* **2015**, *5*, 28938–28949. [CrossRef]
30. Clemens, T.; Tsikouris, K.; Buchgraber, M.; Castanier, L.M.; Kovscek, A. Pore-Scale Evaluation of Polymers Displacing Viscous Oil—Computational-Fluid-Dynamics Simulation of Micromodel Experiments. *SPE Reserv. Eval. Eng.* **2013**, *16*, 144–154. [CrossRef]
31. Melchels, F.P.; Feijen, J.; Grijpma, D.W. A review on stereolithography and its applications in biomedical engineering. *Biomaterials* **2010**, *31*, 6121–6130. [CrossRef] [PubMed]
32. Anbari, A.; Chien, H.T.; Datta, S.S.; Deng, W.; Weitz, D.A.; Fan, J. Microfluidic model porous media: Fabrication and applications. *Small* **2018**, *14*, 1703575. [CrossRef] [PubMed]
33. Gerami, A.; Alzahid, Y.; Mostaghimi, P.; Kashaninejad, N.; Kazemifar, F.; Amirian, T.; Mosavat, N.; Warkiani, M.E.; Armstrong, R.T. Microfluidics for porous systems: Fabrication, microscopy and applications. *Transp. Porous Media* **2018**, *130*, 277–304. [CrossRef]
34. Gerold, C.T.; Krummel, A.T.; Henry, C.S. Microfluidic devices containing thin rock sections for oil recovery studies. *Microfluid. Nanofluid.* **2018**, *22*, 76. [CrossRef]
35. Gogoi, S.; Gogoi, S.B. Review on microfluidic studies for EOR application. *J. Pet. Explor. Prod. Technol.* **2019**, *9*, 2263–2277. [CrossRef]
36. Lifton, V.A. Microfluidics: An enabling screening technology for enhanced oil recovery (EOR). *Lab. Chip* **2016**, *16*, 1777–1796. [CrossRef]
37. Bergman, D.; Cire, A.A.; van Hoes, W.-J.; Hooker, J. *Decision Diagrams for Optimization*; Springer: Berlin/Heidelberg, Germany, 2016; Volume 1.
38. Shamma, A.; Evanson, I.E.J.; Stuetz, R.M. Selection framework for the treatment of sewer network emissions. *J. Environ. Manag.* **2019**, *249*, 109305. [CrossRef]
39. Salman, B.; Salem, O.; He, S. Project-Level Sustainable Asphalt Roadway Treatment Selection Framework Featuring a Flowchart and Analytic Network Process. *J. Transp. Eng. Part B* **2020**, *146*, 04020041. [CrossRef]
40. Gupta, A.; Kamat, D.; Shahrum, Z.; Firmansyah, A.; Salleh, N.; Tan, B.; Madon, B. Unique & practical approach in selection and classification of hydrocyclone desander technology: Utilizing a decade of experience. In Proceedings of the SPE/IATMI Asia Pacific Oil & Gas Conference and Exhibition, Jakarta, Indonesia, 17–19 October 2017.
41. Trumm, D. Selection of passive AMD treatment systems-flow charts for New Zealand conditions. In Proceedings of the Australasian Institute of Mining and Metallurgy New Zealand Branch 40th Annual Conference, Christchurch, New Zealand, 13–15 August 2007.
42. Priyanta, D.; Zaman, M. The development of a risk-based maintenance flowchart to select the correct methodology to develop maintenance strategies of oil and gas equipment. In Proceedings of the IOP Conference Series: Materials Science and Engineering, Suzhou, China, 17–19 March 2021; p. 012042.
43. Bagheri, M.; Roshandel, R.; Shayegan, J. Optimal selection of an integrated produced water treatment system in the upstream of oil industry. *Process Saf. Environ. Prot.* **2018**, *117*, 67–81. [CrossRef]
44. Gharibshahia, R.; Jafaria, A.; Haghtalaba, A.; Karambeigib, M.S. Simulation of nanofluid flooding in a micromodel with quadratic pore shape using CFD. In Proceedings of the 5th International Congress on Nanoscience & Nanotechnology, Tehran, Iran, 11 June 2014.
45. Rostami, P.; Sharifi, M.; Aminshahidy, B.; Fahimpour, J. The effect of nanoparticles on wettability alteration for enhanced oil recovery: Micromodel experimental studies and CFD simulation. *Pet. Sci.* **2019**, *16*, 859–873. [CrossRef]
46. Versteeg, H.K.; Malalasekera, W. *An Introduction to Computational Fluid Dynamics: The Finite Volume Method*; Pearson Education: London, UK, 2007.
47. Pires, J.C.; Alvim-Ferraz, M.C.; Martins, F.G. Photobioreactor design for microalgae production through computational fluid dynamics: A review. *Renew. Sustain. Energy Rev.* **2017**, *79*, 248–254. [CrossRef]
48. Windt, C.; Davidson, J.; Ringwood, J.V. High-fidelity numerical modelling of ocean wave energy systems: A review of computational fluid dynamics-based numerical wave tanks. *Renew. Sustain. Energy Rev.* **2018**, *93*, 610–630. [CrossRef]
49. Yu, H.; Engel, S.; Janiga, G.; Thévenin, D. A review of hemolysis prediction models for computational fluid dynamics. *Artificial Organs* **2017**, *41*, 603–621. [CrossRef]
50. Park, H.W.; Yoon, W.B. Computational fluid dynamics (CFD) modelling and application for sterilization of foods: A review. *Processes* **2018**, *6*, 62. [CrossRef]
51. Faizal, W.; Ghazali, N.; Khor, C.; Badruddin, I.A.; Zainon, M.; Yazid, A.A.; Ibrahim, N.B.; Razi, R.M. Computational fluid dynamics modelling of human upper airway: A review. *Comput. Methods Programs Biomed.* **2020**, *196*, 105627. [CrossRef] [PubMed]

52. Toja-Silva, F.; Kono, T.; Peralta, C.; Lopez-Garcia, O.; Chen, J. A review of computational fluid dynamics (CFD) simulations of the wind flow around buildings for urban wind energy exploitation. *J. Wind Eng. Ind. Aerodyn.* **2018**, *180*, 66–87. [CrossRef]
53. Tey, W.Y.; Asako, Y.; Sidik, N.A.C.; Goh, R.Z. Governing equations in computational fluid dynamics: Derivations and a recent review. *Progress Energy Environ.* **2017**, *1*, 1–19.
54. Xu, G.; Luxbacher, K.D.; Ragab, S.; Xu, J.; Ding, X. Computational fluid dynamics applied to mining engineering: A review. *Int. J. Min. Reclam. Environ.* **2017**, *31*, 251–275. [CrossRef]
55. Vavra, E.D.; Zeng, Y.; Xiao, S.; Hirasaki, G.J.; Biswal, S.L. Microfluidic Devices for Characterizing Pore-scale Event Processes in Porous Media for Oil Recovery Applications. *J. Vis. Exp.* **2018**, *131*, e56592. [CrossRef]
56. Owete, O.S.; Brigham, W.E. Flow behavior of foam: A porous micromodel study. *SPE Reserv. Eng.* **1987**, *2*, 315–323. [CrossRef]
57. Farzaneh, S.; Ghazanfari, M.; Kharrat, R.; Vossoughi, S. An experimental and numerical investigation of solvent injection to heavy oil in fractured five-spot micromodels. *Pet. Sci. Technol.* **2010**, *28*, 1567–1585. [CrossRef]
58. Mohajeri, M.; Hemmati, M.; Shekarabi, A.S. An experimental study on using a nanosurfactant in an EOR process of heavy oil in a fractured micromodel. *J. Pet. Sci. Eng.* **2015**, *126*, 162–173. [CrossRef]
59. Sedaghat, M.; Mohammadzadeh, O.; Kord, S.; Chatzis, I. Heavy oil recovery using ASP flooding: A pore-level experimental study in fractured five-spot micromodels. *Can. J. Chem. Eng.* **2016**, *94*, 779–791. [CrossRef]
60. Wan, J.; Tokunaga, T.K.; Tsang, C.F.; Bodvarsson, G.S. Improved glass micromodel methods for studies of flow and transport in fractured porous media. *Water Resour. Res.* **1996**, *32*, 1955–1964. [CrossRef]
61. Willingham, T.W.; Werth, C.J.; Valocchi, A.J. Evaluation of the effects of porous media structure on mixing-controlled reactions using pore-scale modeling and micromodel experiments. *Environ. Sci. Technol.* **2008**, *42*, 3185–3193. [CrossRef] [PubMed]
62. Betancur, S.; Olmos, C.M.; Pérez, M.; Lerner, B.; Franco, C.A.; Riaz, M.; Gallego, J.; Carrasco-Marín, F.; Cortés, F.B. A microfluidic study to investigate the effect of magnetic iron core-carbon shell nanoparticles on displacement mechanisms of crude oil for chemical enhanced oil recovery. *J. Pet. Sci. Eng.* **2020**, *184*, 106589. [CrossRef]
63. Lv, M.; Wang, S. Pore-scale modeling of a water/oil two-phase flow in hot water flooding for enhanced oil recovery. *RSC Adv.* **2015**, *5*, 85373–85382. [CrossRef]
64. Zhao, J.; Wen, D. Pore-scale simulation of wettability and interfacial tension effects on flooding process for enhanced oil recovery. *RSC Adv.* **2017**, *7*, 41391–41398. [CrossRef]
65. Goudarzi, B.; Mohammadmoradi, P.; Kantzas, A. Pore-level simulation of heavy oil reservoirs; competition of capillary, viscous, and gravity forces. In Proceedings of the SPE Latin America and Caribbean Heavy and Extra Heavy Oil Conference, Lima, Cyprus, 19–20 October 2016.
66. Timgren, A.; Trägårdh, G.; Trägårdh, C. Effects of cross-flow velocity, capillary pressure and oil viscosity on oil-in-water drop formation from a capillary. *Chem. Eng. Sci.* **2009**, *64*, 1111–1118. [CrossRef]
67. Zhao, J.; Yao, G.; Wen, D. Pore-scale simulation of water/oil displacement in a water-wet channel. *Front. Chem. Sci. Eng.* **2019**, *13*, 803–814. [CrossRef]
68. Ferer, M.; Sams, W.N.; Geisbrecht, R.; Smith, D.H. Fractal nature of viscous fingering in two-dimensional pore level models. *AIChE J.* **1995**, *41*, 749–763. [CrossRef]
69. Nittmann, J.; Daccord, G.; Stanley, H.E. Fractal growth viscous fingers: Quantitative characterization of a fluid instability phenomenon. *Nature* **1985**, *314*, 141–144. [CrossRef]
70. Nabizadeh, A.; Adibifard, M.; Hassanzadeh, H.; Fahimpour, J.; Moraveji, M.K. Computational fluid dynamics to analyze the effects of initial wetting film and triple contact line on the efficiency of immiscible two-phase flow in a pore doublet model. *J. Mol. Liq.* **2019**, *273*, 248–258. [CrossRef]
71. XU, K.; Zhu, P.; Tatiana, C.; Huh, C.; Balhoff, M. A microfluidic investigation of the synergistic effect of nanoparticles and surfactants in macro-emulsion based EOR. In Proceedings of the SPE Improved Oil Recovery Conference, Tulsa, OK, USA, 11–13 April 2016.
72. Afsharpoor, A.; Balhoff, M.T.; Bonnecaze, R.; Huh, C. CFD modeling of the effect of polymer elasticity on residual oil saturation at the pore-scale. *J. Pet. Sci. Eng.* **2012**, *94*, 79–88. [CrossRef]
73. Dong, M.; Liu, Q.; Li, A. Displacement mechanisms of enhanced heavy oil recovery by alkaline flooding in a micromodel. *Particulology* **2012**, *10*, 298–305. [CrossRef]
74. Gutiérrez Pulido, H.; Vara Salazar, R.D.L. *Análisis y Diseño de Experimentos*; McGraw-Hill: New York, NY, USA, 2012.
75. Ferrari, A.; Jimenez-Martinez, J.; Borgne, T.L.; Méheust, Y.; Lunati, I. Challenges in modeling unstable two-phase flow experiments in porous micromodels. *Water Resour. Res.* **2015**, *51*, 1381–1400. [CrossRef]
76. Rosero, G.; Peñaherrera, A.; Olmos, C.; Boschan, A.; Granel, P.; Golmar, F.; Lasorsa, C.; Lerner, B.; Perez, M. Design and analysis of different models of microfluidic devices evaluated in Enhanced Oil Recovery (EOR) assays. *Matéria* **2018**, *23*, e12129. [CrossRef]
77. Nilsson, M.A.; Kulkarni, R.; Gerberich, L.; Hammond, R.; Singh, R.; Baumhoff, E.; Rothstein, J.P. Effect of fluid rheology on enhanced oil recovery in a microfluidic sandstone device. *J. Non-Newton. Fluid Mech.* **2013**, *202*, 112–119. [CrossRef]
78. Karambeigi, M.; Schaffie, M.; Fazaelpoor, M. Improvement of water flooding efficiency using mixed culture of microorganisms in heterogeneous micro-models. *Pet. Sci. Technol.* **2013**, *31*, 923–931. [CrossRef]
79. Maaref, S.; Rokhfrouz, M.R.; Ayatollahi, S. Numerical investigation of two phase flow in micromodel porous media: Effects of wettability, heterogeneity, and viscosity. *Can. J. Chem. Eng.* **2017**, *95*, 1213–1223. [CrossRef]



80. Borji, M. Alkali-based Displacement Processes in Microfluidic Experiments: Application to the Matzen Oil Field. Ph.D. Thesis, University of Leoben, Leoben, Austria, 2017.
81. Karadimitriou, N.K. Two-phase flow experimental studies in micro-models. Ph.D. Thesis, Faculty of Geosciences—UU Department of Earth Sciences, Utrecht, The Netherlands, 2013.
82. Cui, J.; Babadagli, T. Use of new generation chemicals and nano materials in heavy-oil recovery: Visual analysis through microfluidics experiments. *Colloids Surf. A* **2017**, *529*, 346–355. [CrossRef]
83. Yarveicy, H.; Javaheri, A. Application of Lauryl Betaine in enhanced oil recovery: A comparative study in micromodel. *Petroleum* **2019**, *5*, 123–127. [CrossRef]
84. ANSYS. *ANSYS Fluent Theory Guide*; ANSYS: Canonsburg, PA, USA, 2013.
85. Brackbill, J.U.; Kothe, D.B.; Zemach, C. A continuum method for modeling surface tension. *J. Comput. Phys.* **1992**, *100*, 335–354. [CrossRef]
86. Levitt, D.; Jackson, A.; Heinson, C.; Britton, L.N.; Malik, T.; Dwarakanath, V.; Pope, G.A. Identification and evaluation of high-performance EOR surfactants. In Proceedings of the SPE/DOE Symposium on Improved Oil Recovery, Tulsa, OK, USA, 22–26 April 2006.
87. Belhaj, A.F.; Elraies, K.A.; Mahmood, S.M.; Zulkifli, N.N.; Akbari, S.; Hussien, O.S. The effect of surfactant concentration, salinity, temperature, and pH on surfactant adsorption for chemical enhanced oil recovery: A review. *J. Pet. Explor. Prod. Technol.* **2020**, *10*, 125–137. [CrossRef]
88. Haghshenasfard, M.; Hooman, K. CFD modeling of asphaltene deposition rate from crude oil. *J. Pet. Sci. Eng.* **2015**, *128*, 24–32. [CrossRef]
89. Roudsari, S.F.; Turcotte, G.; Dhib, R.; Ein-Mozaffari, F. CFD modeling of the mixing of water in oil emulsions. *Comput. Chem. Eng.* **2012**, *45*, 124–136. [CrossRef]
90. Falconer, K. *Fractal Geometry: Mathematical Foundations and Applications*; John Wiley & Sons: Hoboken, NJ, USA, 2004.
91. Olmos, C.M.; Vaca, A.; Rosero, G.; Peñaherrera, A.; Perez, C.; de Sá Carneiro, I.; Vizueté, K.; Arroyo, C.R.; Debut, A.; Pérez, M.S. Epoxy resin mold and PDMS microfluidic devices through photopolymer flexographic printing plate. *Sens. Actuators B* **2019**, *288*, 742–748. [CrossRef]
92. Neuman, S.P. Theoretical derivation of Darcy's law. *Acta Mech.* **1977**, *25*, 153–170. [CrossRef]
93. Moore, T.; Slobod, R. Displacement of oil by water—effect of wettability, rate, and viscosity on recovery. In Proceedings of the Fall Meeting of the Petroleum Branch of AIME, New Orleans, LA, USA, 2–5 October 1955.

Article

# Swirled Jet Flame Simulation and Flow Visualization Inside Rotary Kiln—CFD with PDF Approach

Hassan F. Elattar <sup>1,2,\*</sup>, Eckehard Specht <sup>3</sup>, Ali Fouda <sup>1,4</sup>, Saeed Rubaiee <sup>1,5</sup>, Ahmed Al-Zahrani <sup>1</sup> and Sameh A. Nada <sup>2,6</sup>

<sup>1</sup> Department of Mechanical and Materials Engineering, Faculty of Engineering, University of Jeddah, Jeddah 21589, Saudi Arabia; aafoudah@uj.edu.sa (A.F.); salrubaiee@uj.edu.sa (S.R.); aalzahrani@uj.edu.sa (A.A.-Z.)

<sup>2</sup> Department of Mechanical Engineering, Benha Faculty of Engineering, Benha University, Benha, Qalyubia 13511, Egypt; samehnadar@yahoo.com

<sup>3</sup> Institute of Fluid Dynamics and Thermodynamics, Otto-von-Guericke-University of Magdeburg, Universitätsplatz 2, 39106 Magdeburg, Germany; eckehard.specht@vst.uni-magdeburg.de

<sup>4</sup> Department of Mechanical Power Engineering, Faculty of Engineering, Mansoura University, El-Mansoura 35516, Egypt

<sup>5</sup> Department of Industrial and Systems Engineering, Faculty of Engineering, University of Jeddah, Jeddah 21589, Saudi Arabia

<sup>6</sup> Egypt-Japan University of Science and Technology, New Borg El-Arab City, Alexandria 21934, Egypt

\* Correspondence: hassan.alattar@bhit.bu.edu.eg; Tel.: +966-501-531-215

Received: 29 December 2019; Accepted: 22 January 2020; Published: 29 January 2020

**Abstract:** CFD (computational fluid dynamics) simulation using a commercial package (Fluent-ANSYS) on industrial rotary kilns using annulus-type burners and methane gas was carried out to examine the characteristics of the flame length and flow visualization. New influencing design and operating parameters—primary air swirl number, primary air inlet annulus diameter, and secondary air temperature—were investigated and discussed. The influence of these parameters on axial temperature distribution, axial mean mixture fractions, velocity vectors, mixture fractions, and temperature contours were investigated. The current numerical findings were compared with existing experimental results to validate the simulation approach. The results showed that the primary air swirl number had a remarkable influence on the flame length at a lower primary air inlet annulus diameter ratio of 2.3. Moreover, the flame length increased by 20% and 6% with increasing the swirl number from zero to one for primary air inlet annulus diameter ratios of 2.3 and 5, respectively, and it also increased by 19% with increasing primary air inlet annulus diameter ratio from 2.3 to 5.

**Keywords:** numerical simulation; rotary kiln; annulus burner; flame length; swirled flow

## 1. Introduction

Rotary kiln is a rotated cylinder lined with refractory material and is slightly axially inclined for the production of cement or other materials. Basically, rotary kilns can be considered as heat exchangers in which heat is liberated from combustion gases through the solid material and produces cement [1]. Rotary kilns are used in several industrial applications comprising lime and cement firing [2], petroleum coke calcination [3], and aluminum oxide calcination [4,5]. Cement production is considered to be dominated by the use of rotary kilns. Moreover, rotary kilns are widely utilized in waste incineration, as it can provide different kinds of waste solids and it can incinerate them effectively [6].

Over the last several years, the CFD (computational fluid dynamics) technique as a useful tool was implemented strongly for problems concerned with the effects of operating conditions and geometric parameters on rotary kiln performance. In the design stage, the flame heat transfer rate to materials has

a vital influence on the kiln performance. The flame characteristics (i.e., length, maximum temperature, and shape) play significant role in the kiln performance, which influence significantly the heat transfer rate, the product quality, the lining material life time, and the emissions. The flame instability may lead to a large deviation in combustion gas temperatures, where the short flame can destroy the lining material and the long flame may not be capable of liberating sufficient heat to complete the chemical reaction. The operating variables such as kind and flow rate of fuel have a remarkable influence on the flame characteristics [7]. Because of the variation in the kiln operating variables, the research on the flame behavior is challenging to study [8–11]. Elattar et al. [8] presented a two-dimensional simulation to explain the influence of rotary kiln main operating and construction parameters on the flame characteristics, including heat and fluid flow using gaseous fuels ( $\text{CH}_4$ , CO, and Biogas). Elattar [9] developed flame length numerical correlations for rotary kilns as a function of excess-air factor, diameter of air inlet, and kind of fuel, which have considerable influence on the flame behavior.

The impacts of primary air ratio, geometry of the burner (annulus type), and burner powers (i.e., several jet momentums of the fuel) on the flow field and kiln wall peak temperature were numerically investigated by Elattar et al. [10] using methane fuel. Nada et al. [11] studied the flow field and mixing characteristics of outwardly injected jets into a cross flow in a cylindrical chamber simulating the flow field in Kiln burner. Khoei et al. [12] presented a mathematical simulation including heat transfer and fluid flow to find and enhance the temperature distributions inside the rotary kiln using the ELFEN finite element package. Mastorakos et al. [13] presented CFD modeling for rotary kilns used in cement production including heat transfer, flame shape, and clinker chemistry simulations using CFD commercial code and the Monte Carlo technique for radiation modelling. It was observed that radiation is the dominant heat-transfer mode from combustion gases to kiln walls, and heat losses across kiln walls is about 10%. Marias [14] presented a study using CFD simulation for the kiln gaseous phase and the postcombustion chamber including turbulence, combustion, and radiation, using natural gas fuel. The model was capable of expecting the radiation received by kiln walls and the volatile matter combustion.

Most of the industrial kilns use annulus burners for flame stability. Moreover, the secondary air is used in the kiln to reduce the overall kiln energy consumption by recuperating the heat from the charge to the kiln again, in addition to supplying the oxygen required in the combustion process. Furthermore, the swirl of primary air plays an important role in kiln flame stability and service life time of burner tips, as well as the refractory wall. Khalil et al. [15] studied experimentally the flow field of swirl confined/unconfined flames. It was found that confinement improves recirculation for both reacting and nonreacting flow. Moreover, the turbulence intensity and recirculation strength improved by flame confinement cause the increase of the Reynolds number. Elbaz and Roberts [16] examined experimentally the influence of quarl geometry on the flame shape of swirling  $\text{CH}_4$  for un-pre-mixed combustion, which represents a significant parameter in industrial burners and gas turbine applications. It was found that air swirling and quarl geometry considerably affects flame structure and flow shape, flame stability, and emissions. Elbaz and Roberts [17] experimentally studied flow field of non-pre-mixed swirled  $\text{CH}_4$  flames settled in quartz quarl by measuring the flow field instantaneously. Two different flames (i.e., two different fuel-jet velocities) were tested. The results showed a couple of vortex regions appeared at quarl exit corners at low fuel-jet velocity, while in the high fuel-jet velocity, additional downstream vortex collapsing varies the flame sheet path close to the central flame region.

The above literature review showed that investigations on flame geometry (shape and length), gas temperature, and flow field in rotary kilns are not completely covered. Several operating/design parameters relating to rotary kilns are still under study like primary air swirl number ( $S_n$ ), primary air inlet annulus diameter ratio ( $d_p/d_o$ ), and secondary air temperature ( $T_{sa}$ ) on the flame length characteristic. Therefore, the current work is conducted in order to examine and discuss the influence of swirl number and annulus diameter of the primary inlet air and temperature of the secondary air on the flame length characteristic, which directly affects the thermal processes and consequently the product's quality throughout the rotary kiln.

## 2. Physical Model, Grid Generation, and Boundary Conditions

For studying the effects of kiln operating conditions and geometric parameters of the burner on flame length, the physical model of the simulated kiln was developed as schematically shown in Figure 1. The kiln diameter and length was 2.6 and 20 m, respectively, and it was fully opened for secondary air (i.e., secondary air inlet diameter ratio,  $d_{a,i}/D = 1$ ). The kiln was operated by a pilot annulus tube burner using methane fuel having uniform axial velocity of 30 m/s with 20 °C and 1.975 MW burner thermal powers. The fuel nozzle diameter, primary air ratio, and excess air number were assumed  $d_o = 50$  mm,  $\alpha = 0.1$ , and  $\lambda = 1.3$ , respectively. The studied parameters are—swirl number of primary air ( $S_n = 0, 0.3, 0.5, 0.7, \text{ and } 1$ ), primary air inlet annulus diameter ratio ( $d_p/d_o = 2.3 \text{ and } 5$ ) and secondary air temperature ( $T_{sa} = 20, 200, 400, 600, 800, \text{ and } 1000$  °C). A comparison between 2-D and 3-D simulation studies was carried out by Elattar [9] as an earliest step to present the maximum errors. The maximum error refers to the maximum deviation between the calculated variables obtained from 2-D and 3-D simulations throughout the computational domain. The results showed that the maximum error in axial velocity, axial temperature, and centerline mixture-fraction profiles were 5%, 2%, and 6%, respectively. So, for time and cost savings, 2-D axisymmetric simulation was preferred to fulfill the current work within acceptable errors.

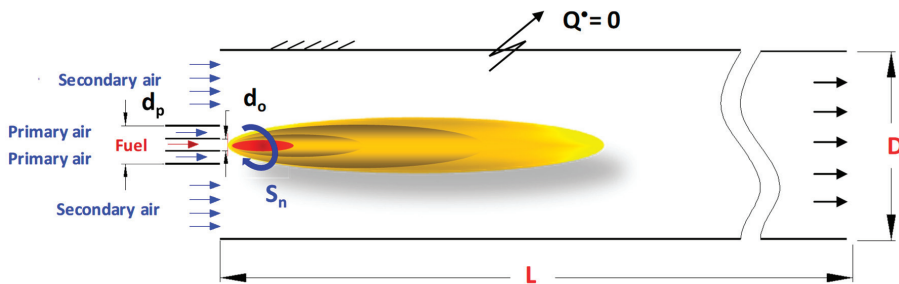
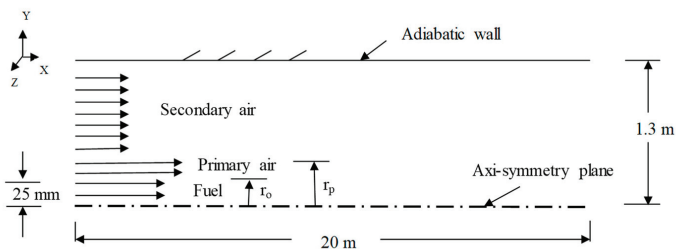


Figure 1. Physical model layout.

2-D computational domain geometry and grids with boundary types are illustrated in Figure 2, as presented by Elattar [18]. A hemikiln was used for computational cost saving and an ANSYS package preprocessing tool was used for mesh generation (structured and quadrilateral cells). In the flame region, the grid generated was dense. The boundary conditions of the computational domain were inlet velocities of fuel, primary air and secondary air, pressure of outlet flue gases, and the kiln walls were considered adiabatic. All temperatures and velocities at the kiln inlet were specified as uniform. The grid independence study was carried out using several 2-D meshes with various resolutions. The cells numbers varied from  $3 \times 10^3$  to  $100 \times 10^3$  for illustrating the flame length convergence as depicted in Figure 3. The study shows that cells greater than  $30 \times 10^3$  had diversity in flame length prediction smaller than 0.2%. Accordingly, the mesh of  $30 \times 10^3$  cells was used to accomplish the present study.



(a)

Figure 2. Cont.

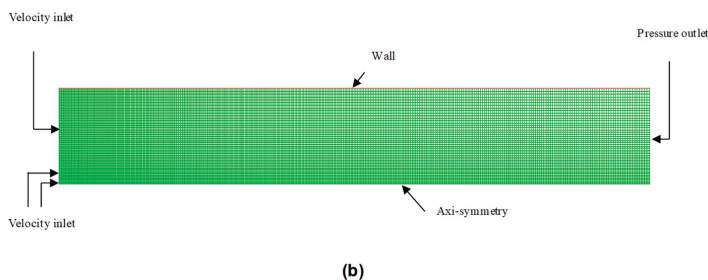


Figure 2. Computational domain: (a) Geometry, (b) grid and boundary types.

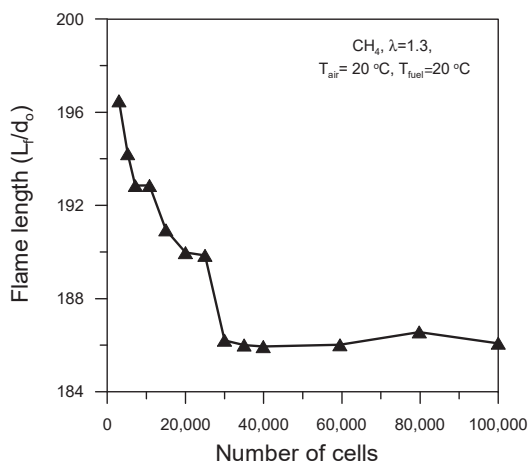


Figure 3. Grid independence study.

### 3. Computational Methodology

#### 3.1. Mathematical Procedure and Assumptions

A CFD approach using ANSYS-Fluent (finite volume technique) was engaged in the current simulation to resolve the Reynolds-Averaged Navier-Stokes equations (RANS) in addition to energy, radiation, and the species transport equations. Steady, incompressible, and axi-symmetry flow were assumed. Moreover, the walls were considered adiabatic (i.e., heat flux = 0) with zero thickness and internal wall emissivity = 1. These assumptions result in relatively approximated and acceptable results if compared with real conditions [19,20]. Kiln rotational speed, bed percent filling, and buoyancy have remarkable impacts on the characteristics and aerodynamics of the flame [21].

Continuity and momentum equations for steady-state flow gas are presented in Equations (1) and (2), respectively, as follows [22]:

$$\frac{\partial}{\partial x_i}(\rho u_i) = S_m \quad (1)$$

$$\frac{\partial}{\partial x_j}(\rho u_i u_j) = -\frac{\partial p}{\partial x_i} + \frac{\partial \tau_{ij}}{\partial c_j} + \rho g_i + F_i + S_m \quad (2)$$

where  $S_m$  is the source term produced from fuel injection.

The turbulence model (realizable  $k$ - $\epsilon$ ) is distinct from other  $k$ - $\epsilon$  models in its constant terms, and  $k$  and  $\epsilon$  are transport formulations which are given by Equations (3) and (4).

$$\frac{\partial}{\partial x_j}(\rho k u_j) = \frac{\partial}{\partial x_j} \left[ \left( \mu + \frac{\mu_t}{\sigma_k} \right) \frac{\partial k}{\partial x_j} \right] + G_k + G_b - \rho \epsilon \quad (3)$$

$$\frac{\partial}{\partial x_j}(\rho \epsilon u_j) = \frac{\partial}{\partial x_j} \left[ \left( \mu + \frac{\mu_t}{\sigma_\epsilon} \right) \frac{\partial \epsilon}{\partial x_j} \right] + \rho C_1 S \epsilon - \rho C_2 \frac{\epsilon^2}{k + \sqrt{\nu \epsilon}} + C_{1\epsilon} \frac{\epsilon}{k} C_{3\epsilon} G_b \quad (4)$$

where  $G_k$  and  $G_b$  denote turbulence kinetic energy generation of mean velocity gradients and buoyancy. While  $\sigma_k$  and  $\sigma_\epsilon$  are turbulent Prandtl numbers of  $k$  and  $\epsilon$ ,  $C_{1\epsilon}$  and  $C_2$  are constants. For the current simulations, the turbulent intensity at inlet ( $I$ ) was specified 10% for air and 5% for fuel according to Equation (5) [23]:

$$I = 0.16(\text{Re}_{DH})^{-0.125} \quad (5)$$

The chemical reaction was simulated based on PDF and non-pre-mixed combustion models which are effective computational models because of using fewer formulations for resolving. In addition, the chemical reaction kinetics state is fast and the flow can fulfill close to the state of chemical equilibrium [23]. The PDF is a favored method in the case of turbulent combustion flow because of variation in turbulent mixing properties. The current simulation utilizes the  $\beta$ -PDF model for turbulent non-pre-mixed combustion flow simulation because of its distinct results compared to other PDF models [24]. The  $\beta$ -PDF is stated based on the two parameters—mean scalar quantity and variance. Therefore, for simplicity in solution of the species formulations, the mixture fraction in a  $\beta$ -PDF ( $f$ ) was calculated based on species mass fraction ( $Z_i$ ) as follows:

$$f = \frac{Z_i - Z_{i,ox}}{Z_{i,fuel} - Z_{i,ox}} \quad (6)$$

where  $ox$  and  $fuel$  refer to oxidizer and fuel inlets,  $f$  equals 1 and 0 for fuel and oxidizer streams, respectively, and it varies from 0 to 1 in the flow domain.

The formulations of  $\bar{f}$  and  $\overline{f'^2}$  (mean mixture fraction and variance) are given by Equations (7) and (8), respectively.

$$\frac{\partial}{\partial t}(\rho \bar{f}) + \frac{\partial}{\partial x_j}(\rho u_j \bar{f}) = \frac{\partial}{\partial x_j} \left( \frac{\mu_t}{\sigma_t} \frac{\partial \bar{f}}{\partial x_j} \right) \quad (7)$$

$$\frac{\partial}{\partial t}(\rho \overline{f'^2}) + \frac{\partial}{\partial x_j}(\rho u_j \overline{f'^2}) = \frac{\partial}{\partial x_j} \left( \frac{\mu_t}{\sigma_t} \frac{\partial \overline{f'^2}}{\partial x_j} \right) + C_g \mu_t \left( \frac{\partial \bar{f}}{\partial x_j} \right)^2 - C_d \rho \frac{\epsilon}{k} \overline{f'^2} \quad (8)$$

where  $f' = f - \bar{f}$ ,  $\sigma_t = 0.850$ ,  $C_g = 2.860$ , and  $C_d = 2$ . Thus, the chemical reaction was simplified in one variable ( $f$ ) which features the mixture fraction modeling. Moreover, species mass fractions, density, and temperature and other thermochemical properties were completely associated with  $f$  and the instant scalars depend on  $f$  as follows:

$$\phi_i = \phi_i(f) \quad (9)$$

$$\phi_i = \phi_i(f, H) \quad (10)$$

where  $\phi_i$  represents instant thermochemical scalar quantities and  $H$  is the instant enthalpy. Species and temperature average mass fraction,  $\bar{\phi}_i$ , can be given by Equation (11) for adiabatic systems and Equation (12) for nonadiabatic systems, where the PDF model is expressed as  $p(f)$ .

$$\bar{\phi}_i = \int_0^1 p(f) \phi_i(f) df \quad (11)$$

$$\bar{\phi}_i = \int_0^1 p(f) \phi_i(f, \bar{H}) df \quad (12)$$

Accordingly, the mean time-averaged fluid density,  $\bar{\rho}$ , is given by Equation (13).

$$\frac{1}{\bar{\rho}} = \int_0^1 \frac{p(f)}{\rho(f)} df \quad (13)$$

where  $p(f) = \frac{f^{\alpha-1}(1-f)^{\beta-1}}{\int f^{\alpha-1}(1-f)^{\beta-1} df}$ ;  $\alpha$  and  $\beta$  are  $\alpha = \bar{f} \left[ \frac{\bar{f}(1-\bar{f})}{f'^2} - 1 \right]$ ,  $\beta = (1-\bar{f}) \left[ \frac{\bar{f}(1-\bar{f})}{f'^2} - 1 \right]$ .

For solving the formulation of mean enthalpy,  $\bar{H}$ , Equation (14) is used:

$$\frac{\partial}{\partial t} (\rho \bar{H}) + \nabla \cdot (\rho \vec{v} \bar{H}) = \nabla \cdot \left( \frac{k_t}{c_p} \nabla \bar{H} \right) \quad (14)$$

For pressure interpolation the PRESTO algorithm was used, while SIMPLE algorithm was engaged for coupling pressure and velocity. Species thermal properties were calculated based on the temperature and at a pressure of  $1.013 \times 10^5$  Pa (standard atmospheric pressure). For solving the enthalpy, the following energy equation was utilized.

$$\frac{\partial}{\partial x_i} (\rho v_i h) = \frac{\partial}{\partial x_i} \left( \Gamma_h \frac{\partial h}{\partial x_i} \right) + S_h \quad (15)$$

where  $S_h$  is the source term including radiation and combustion heat transfer rate.

For calculating kiln-radiation heat flux, the P-1 radiation model was used, which is the simplest model amongst the other P-N radiation models [25,26]. It is appropriate for use at higher optical thickness ( $\kappa L$ ), where  $\kappa$  and  $L$  are the absorption coefficient and domain length scale, respectively. The  $\kappa$  is determined based on the local concentrations of  $H_2O$  and  $CO_2$ , total pressure, and path length according to a Weighted-Sum-of-Gray-Gases model which was used in the current simulation and given by Equation (16),

$$-\nabla q_r = \kappa G - 4\kappa \sigma T^4 \quad (16)$$

where the  $-\nabla q_r$  term is utilized in energy equation for radiation heat source.

To describe burner swirl, a swirl number (defined as ratio of angular to axial momentum) was used as given by Beer [27]:

$$S_n = \frac{\int_0^{r_p} (wr) \rho u_p 2\pi r dr}{r_p \int_0^{r_p} u_p \rho u_p 2\pi r dr} \quad (17)$$

For constant parameters:  $S_n = \frac{2}{3} \frac{w}{u_p}$ .

### 3.2. Model Validation

The present model was validated by comparing its results with the experimental results of TECFLAM [19,20]. TECFLAM is a German corporation that presented a series of experimental measurements to provide a database for various flames to improve and validate various numerical model for combustions. Among their work, a database for swirled confined flames generated by natural-gas standard burners is available. The results of the current model are compared with the data in Figure 4. The goals of TECFLAM research programs are to establish a wide experimental database from selective flames and to validate and improve the mathematical combustion models. From this point, the comparisons between experimental measurements of TECFLAM [19,20] and current numerical results are presented in Figure 4.

For the validation work, the model was run based on methane fuel at the conditions— $T_{\text{air}} = 300$  K,  $T_o = 300$  K,  $S_n = 0.9$ , and  $\lambda = 1.2$ . Figure 4 compares axial, radial, and tangential velocity components of the radial profiles at 30 and 60 mm away from the burner tips. The radial distribution of mixture fraction, mean temperature,  $CO_2$  mass fraction, and  $CH_4$  mass fraction at different distances from the burner tips are also compared. A reasonable agreement between the results of the current model using (realizable  $k-\epsilon$ ) the turbulence model and TECFLAM [19,20] experimental data was obtained as shown in Figure 4.

The small deviation between the two results can be attributed to the simplifying assumptions used in combustion and turbulence models and to the uncertainty in experimental measurements. Thus, the turbulence model (realizable  $k-\varepsilon$ ) was capable of accomplishing this simulation work.

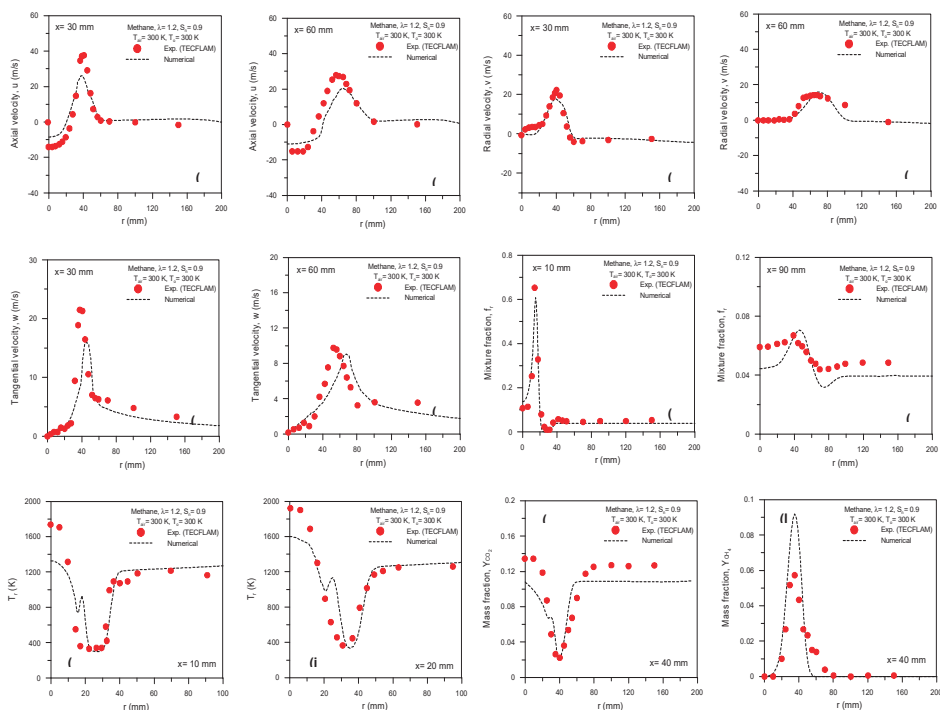


**Figure 4.** Model validation—comparisons between present numerical and experimental data of TECFLAM [19,20].

## 4. Results and Discussion

### 4.1. Influence of Primary air Swirl Number ( $S_n$ )

The influences of swirl number ( $S_n$ ) of the primary air at  $T_{pa} = 20^\circ\text{C}$ ,  $T_{sa} = 20^\circ\text{C}$ ,  $T_o = 20^\circ\text{C}$ ,  $\lambda = 1.3$ , and  $\alpha = 0.10$  on temperature profiles and inverted mixture fraction profiles, velocity vectors, flame length, and mixture fraction contours are shown in Figures 5–9 for  $dp/do = 2.3$  and 5.

Figure 5a,b illustrates centerline temperature profiles over flame at various swirl numbers ( $S_n$ ) for two different dimensionless annulus burner diameters of 2.3 and 5. The figures show that the location of the highest flame temperature was moved to right by 20% and 6% with increasing swirl number from 0 to 1 for  $dp/do = 2.3$  and 5, respectively. Moreover, the peak flame temperature magnitudes were unchanged. Furthermore, the impact of swirl number of primary air on the maximum temperature location in the flame vanished with the increase of the annulus diameter for specific excess air and primary air ratio. This is due to the decrease of the size of the recirculation zone and less air diffusion in the fuel with the increase of the swirl number (see Figure 6). The decreased penetration of air into the fuel leads to the increase of the flame length, which causes a shift in highest flame temperature location.



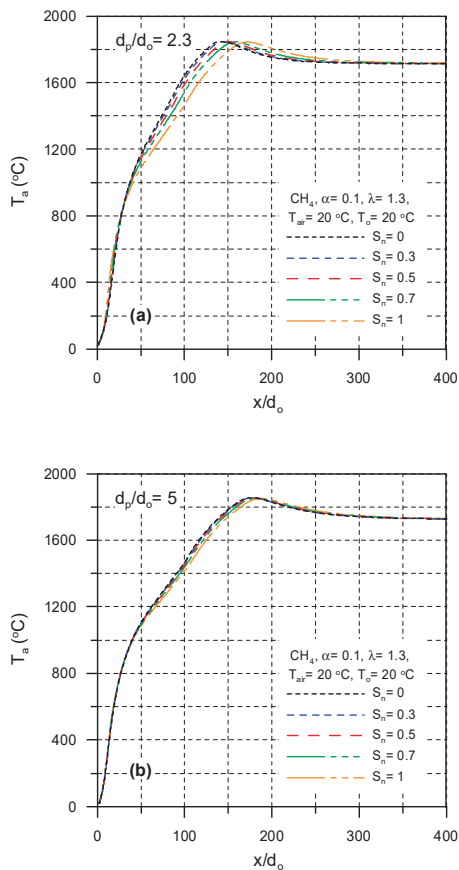


Figure 5. Effect of swirl number of primary air on centerline temperature profiles: (a)  $d_p/d_o = 2.3$  and (b)  $d_p/d_o = 5$ .

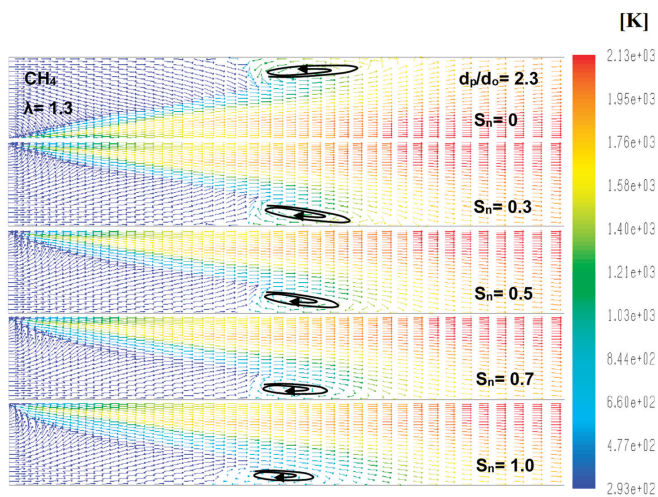


Figure 6. Effect of swirl number of primary air velocity vectors at  $T_{air} = 20\text{ }^\circ\text{C}$ ,  $T_o = 20\text{ }^\circ\text{C}$ ,  $u_o = 30\text{ m/s}$ , and  $\alpha = 0.1$ .

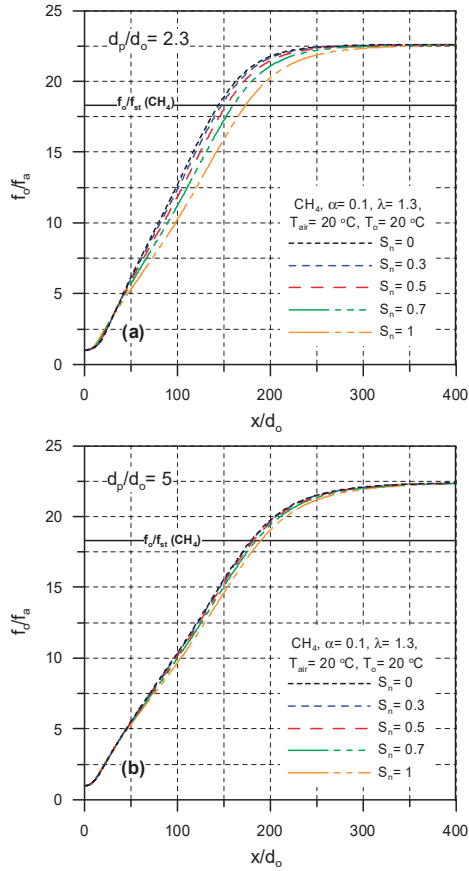


Figure 7. Centerline mixture fraction profiles for different primary air swirl numbers at  $u_0 = 30$  m/s: (a)  $d_p/d_0 = 2.3$  and (b)  $d_p/d_0 = 5$ .

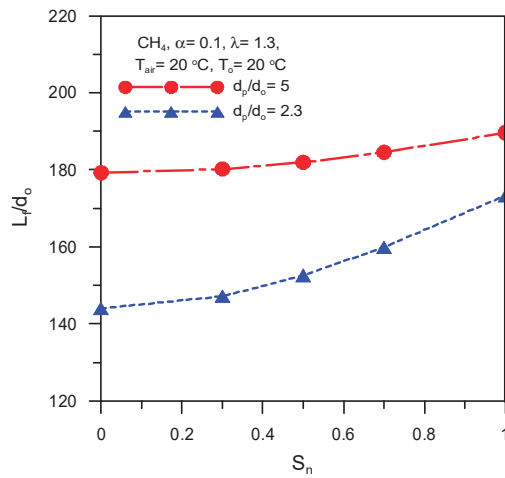
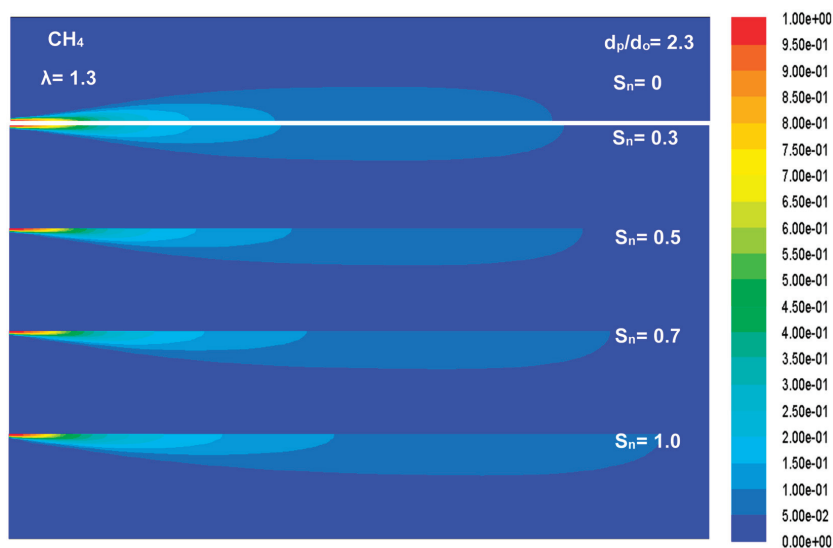


Figure 8. Effects of swirl number on flame length at  $d_p/d_0 = 2.3$  and 5 and  $u_0 = 30$  m/s.



**Figure 9.** Mixture fraction contours for different primary air swirl numbers at  $T_{\text{air}} = 20\text{ }^{\circ}\text{C}$ ,  $T_o = 20\text{ }^{\circ}\text{C}$ ,  $u_o = 30\text{ m/s}$ , and  $\alpha = 0.1$ .

Effect of swirl number of primary air on centerline mixture fraction profiles for two different annulus diameters ( $d_p/d_o = 2.3$  and  $5$ ) is explained in Figure 7a,b, respectively. The figure shows that the swirl number of the primary air has a remarkable influence on the profile of the mixture fraction and the flame length. Accordingly, the flame length increases with the increase of the swirl number due to the less diffusion and penetration of air in the fuel, which lead to incomplete reaction in a small distance and the spread of the flame for complete oxidation. The effect of the swirl number of primary air on the flame lengthening is strong at a small annulus diameter and weak at a large annulus diameter. The figures show that the flame lengthens by 20% and 6% with increasing the swirl number of the primary air in the range 0–1 at  $d_p/d_o = 2.3$  and  $5$ , respectively. The predicted flame lengths in the entire range of the swirl number are shown in Figure 8 for annulus diameters  $d_p/d_o = 2.3$  and  $5$ . The figure shows that the swirl number has a remarkable and slight impact on the flame length at  $d_p/d_o = 2.3$  and  $d_p/d_o = 5$ , respectively. Figure 9 shows the effect of the swirl number on the mean mixture fraction contours at  $d_p/d_o = 2.3$  for illustrating the influence of  $S_n$  on the flame length.

#### 4.2. Influence of Primary air Inlet Annulus Diameter Ratio ( $d_p/d_o$ )

Concentric/annulus burners are commonly used in industrial applications with a confined flame for flame stability. The flame characteristics are mainly dependent on the annulus diameter as shown in Figures 10 and 11, which show the effects of the dimensionless annulus diameter on temperature and mixture-fraction profiles, temperature and mixture fraction contours, and velocity vectors.

Figure 10a gives centerline axial temperature profiles for  $d_p/d_o = 2.3$  and  $5$  and  $T_{pa} = 20\text{ }^{\circ}\text{C}$ ,  $T_{sa} = 20\text{ }^{\circ}\text{C}$ , and  $S_n = 0.5$ . The figure shows that the location of the maximum flame temperature point transferred to the right keeping its value with increasing  $d_p/d_o$  from  $2.3$  and  $5$ . This can be attributed to the increase of the velocity of the primary air velocity with the decrease of annulus diameter. The increase of the velocity enhances the mixing process of the fuel and oxidizer leading to a complete reaction in a short distance close to the burner tip. Accordingly, the location of the maximum flame temperature point moved to left with the decrease of annulus diameter leading to a shortening in the flame length (see Figure 10b). Figure 10a,b shows that the location of the maximum flame temperature point moved to the right, i.e., the flame lengthened by 19% due to the increase of  $d_p/d_o$  from  $2.3$  to  $5$ .

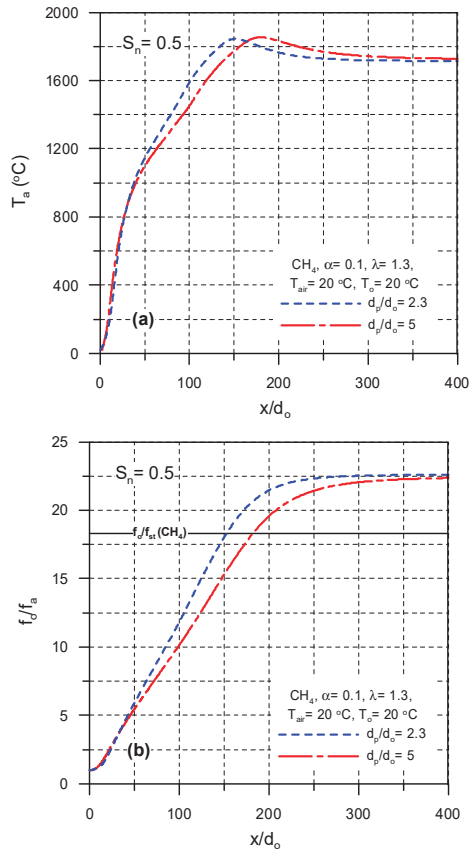


Figure 10. Effects of annulus diameters on: (a) centerline temperature profiles, (b) centerline mixture fraction profiles at  $u_0 = 30$  (m/s).

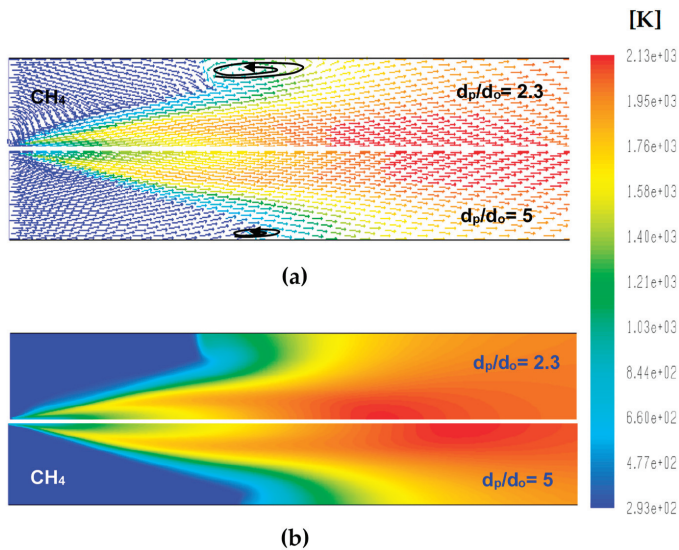
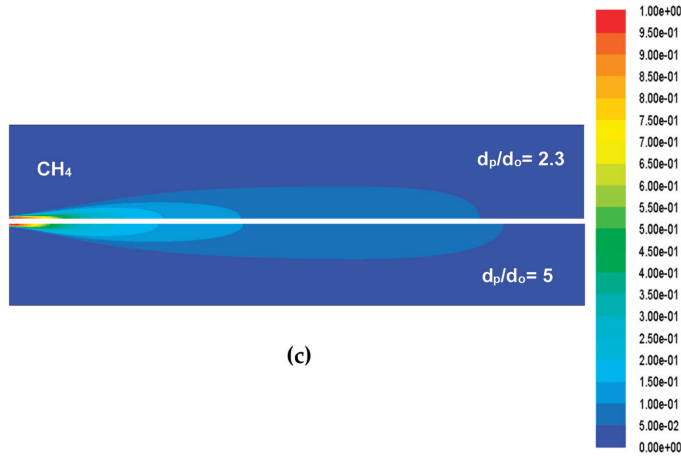


Figure 11. Cont.



**Figure 11.** Effect of annulus diameters on (a) velocity vectors, (b) temperature contours, and (c) mixture fraction contours at  $T_{air} = 20\text{ }^{\circ}\text{C}$ ,  $T_o = 20\text{ }^{\circ}\text{C}$ ,  $u_o = 30\text{ m/s}$ ,  $\alpha = 0.1$ ,  $\lambda = 1.3$ , and  $S_n = 0.5$ .

The vectors of the velocity for two annulus diameters,  $d_p/d_o = 2.3$  and  $5$ , are shown in Figure 11a. The figure shows that the recirculation region size decreases with increasing annulus diameter and the location of the maximum flame temperature point moved to the right, causing the increase of the flame length as shown in Figure 11b,c.

#### 4.3. Influence of Temperature of Secondary Air ( $T_{sa}$ )

To increase efficiencies of furnaces, heat recovery by preheating the air before combustion is commonly used in the practice of industrial furnaces. The effects of the temperature of the secondary air on air temperature profiles, wall temperature profiles, temperature contours, and velocity vectors are shown in Figures 12 and 13. The variation of the centerline temperature profiles with the temperature of the secondary air in the range  $20\text{--}1000\text{ }^{\circ}\text{C}$  is illustrated in Figure 12a for  $d_p/d_o = 2.3$ ,  $T_{pa} = 20\text{ }^{\circ}\text{C}$ ,  $T_o = 20\text{ }^{\circ}\text{C}$  and  $S_n = 0$ . The figure shows the increase of the centerline temperature with the increase of the temperature of the secondary from  $20$  to  $200\text{ }^{\circ}\text{C}$ , then the centerline temperature decreases with the increase of the temperature of the secondary air up to  $600\text{ }^{\circ}\text{C}$ . Increasing the temperature of the secondary air above  $600\text{ }^{\circ}\text{C}$  does not affect the centerline axial temperature profile.

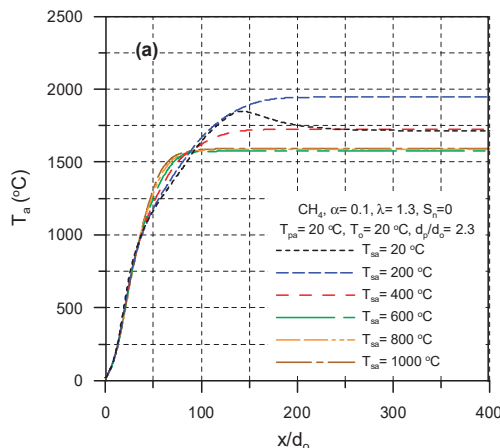


**Figure 12.** Cont.

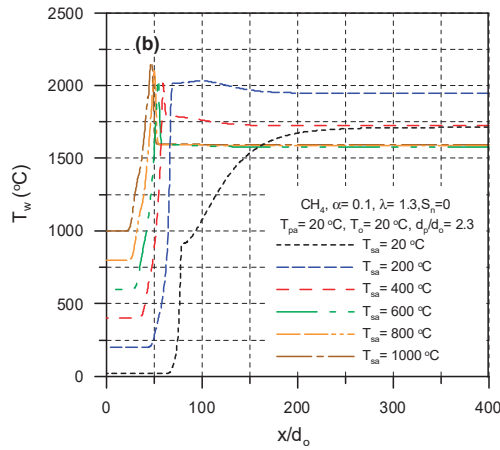


**Figure 12.** Effect of temperature of secondary air temperature on: (a) temperature profiles and (b) mixture fraction profiles at  $u_0 = 30$  (m/s).

Figure 12b shows the increase of the maximum wall temperature with the increase of the temperature of the secondary air and the shifting of the location of the maximum wall temperature point to the left. This can be attributed to the decrease of the air density with the increase of the temperature of the secondary air, which leads to weak diffusion and mixing of the combustion air with the fuel. This causes the existence of a hot zone close to the air entrance at a high temperature of the secondary air. Figure 13a,b shows the growth of the recirculation region with the increase of the temperature of the secondary air due to the reduction of the momentum of the secondary air causing entrainment and recirculation.

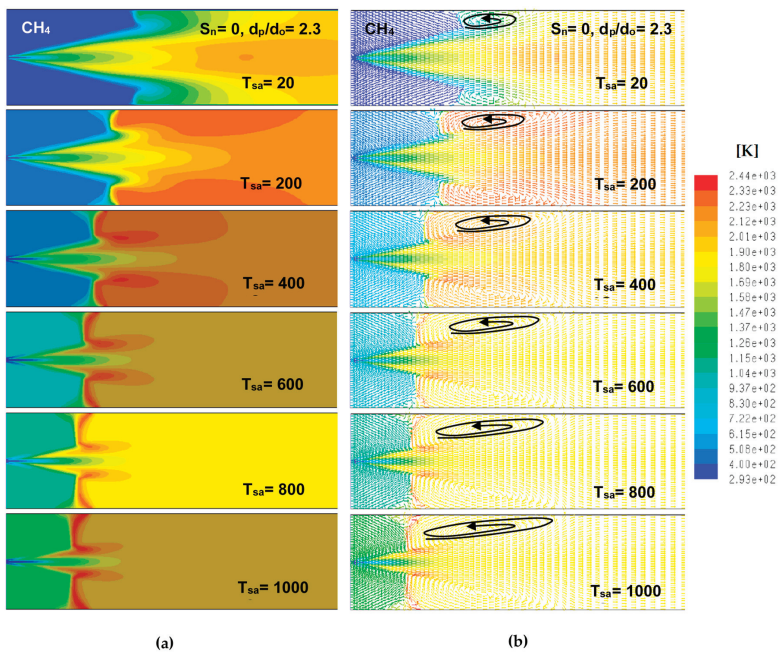


**Figure 13.** Effect of temperature of secondary air on: (a) temperature contours and (b) velocity vectors at  $T_{pa} = 20$  °C,  $T_0 = 20$  °C,  $u_0 = 30$  m/s,  $\alpha = 0.1$ , and  $\lambda = 1.3$ .

## 5. Conclusions

Numerical simulation using the CFD method is implemented to predict and discuss the influences of primary air swirl number, primary air inlet annulus diameter, and temperature of secondary air on the length of the rotary kiln flame and its flow field. The main findings obtained from this study are as follows:

- The swirl number of the primary has a remarkable influence on flame length at lower primary air inlet annulus diameter ratio ( $d_p/d_o = 2.3$ );
- The flame lengthens with increasing primary air swirl number—the length increases by 20% and 6% with increasing the swirl number from 0 to 1 for  $d_p/d_o = 2.3$  and 5, respectively;
- The flame lengthens with the increase of the annulus diameter of the inlet primary air—the flame lengthens by ~19% with rising of  $d_p/d_o$  from 2.3 to 5;
- The peak wall temperature rises and moves close to the burner tip and the recirculation region size growths with the increase of the temperature of the secondary air.

**Author Contributions:** H.F.E. performed the simulations and drew the figures; E.S. provided the simulation tools and supervision; A.F. and S.R. performed review and wrote computational methodology; A.A.-Z. and S.A.N. wrote and edited the paper. All authors have read and agreed to the published version of the manuscript.

**Funding:** This research received no external funding.

**Conflicts of Interest:** The authors declare no conflict of interest.

## Nomenclatures

$D$	kiln diameter (m)
$d_{a,i}$	diameter of secondary air inlet (m)
$d_o$	fuel-nozzle diameter (m)
$d_p$	annulus diameter of primary air inlet (m)
$f$	mean mixture-fraction
$L$	air-fuel ratio, mass basis ( $\text{kg}_{\text{air}}/\text{kg}_{\text{fuel}}$ )
$L_f$	length of flame (m)
$R$	rotary kiln-radius (m)
$r_p$	radius of primary air (m)
$S_n$	swirl number
$T$	local temperature ( $^{\circ}\text{C}$ )
$u$	axial velocity (m/s)
$v$	velocity in radial direction (m/s)
$w$	velocity in tangential direction (m/s)
$x$	longitudinal distance measured from burner (m)
$\varepsilon$	turbulent dissipation rate ( $\text{m}^2/\text{s}^3$ )
$\lambda$	excess-air factor
$\phi$	equivalence ratio, $\Phi = (A/F)_{st}/(A/F)_{actual}$ .
$\rho$	density ( $\text{kg}/\text{m}^3$ )
<i>Subscript</i>	
$a$	axial
$air$	air
$o$	fuel
$pa$	primary air
$sa$	secondary air
$st$	stoichiometric

## References

1. Boateng, A.A. *Rotary Kilns Transport Phenomena and Transport Processes*; Elsevier Inc.: Oxford, UK, 2008.

2. Georgallis, M. *Mathematical Modeling of Lime Kilns*. Ph.D. Thesis, The University of British Columbia, Vancouver, BC, USA, 2004.
3. Peray, K.E. *The Rotary Cement Kiln*; Chemical Publishing Co.: New York, NY, USA, 1972.
4. Maniatus, A.; Kureyuz, E.; Kawecki, W. Mathematical Model of the Aluminum Oxide Rotary Kiln. *Ind. Eng. Chem. Process Des. Dev.* **1974**, *13*, 132–142. [CrossRef]
5. Bui, R.T.; Simard, G.; Charette, A.; Kocafe, Y.; Perron, J. Mathematical Modeling of the Rotary Coke Calcining Kiln. *Can. J. Chem. Eng.* **1995**, *73*, 534–545. [CrossRef]
6. Rovaglio, M.; Manca, D.; Biardi, G. Dynamic Modeling of Waste Incineration Plants with Rotary Kilns: Comparisons between Experimental and Simulation Data. *Chem. Eng. Sci.* **1998**, *53*, 2727–2742. [CrossRef]
7. Kolev, D.; Stefanov, B.; Borisov, D.; Choshnova, D. Method for numerical simulation and graphical presentation of the rate field in a physical model of flash smelting furnaces. *J. UCTM* **2003**, *38*, 1147–1154.
8. Elattar, H.F.; Stanev, R.; Specht, E.; Fouda, A. CFD simulation of confined non-premixed jet flames in rotary kilns for gaseous fuels. *Comput. Fluids* **2014**, *102*, 62–73. [CrossRef]
9. Elattar, H.F.; Specht, E.; Fouda, A.; Bin-Mahfouz, A.S. CFD modeling using PDF approach for investigating the flame length in rotary kilns. *Heat Mass Transf.* **2016**, *52*, 2635–2648. [CrossRef]
10. Elattar, H.F.; Specht, E.; Fouda, A.; Bin-Mahfouz, A.S. Study of Parameters Influencing Fluid Flow and Wall Hot Spots in Rotary Kilns using CFD. *Can. J. Chem. Eng.* **2016**, *94*, 355–367. [CrossRef]
11. Nada, S.A.; Fouda, A.; Elattar, H.F. Parametric study of flow field and mixing characteristics of outwardly injected jets into a crossflow in a cylindrical chamber. *Int. J. Therm. Sci.* **2016**, *102*, 185–201. [CrossRef]
12. Khoei, A.R.; Masters, I.; Gethin, D.T. Numerical modelling of the rotary furnace in aluminum recycling processes. *J. Mater. Process. Technol.* **2003**, *139*, 567–572. [CrossRef]
13. Mastorakos, E.; Massias, A.; Tsakiroglou, C.D.; Goussis, D.A.; Burganos, V.N.; Payatakes, A.C. CFD predictions for cement kilns including flame modelling, heat transfer and clinker chemistry. *Appl. Math. Model.* **1999**, *23*, 55–76. [CrossRef]
14. Marias, F. A model of a rotary kiln incinerator including processes occurring within the solid and the gaseous phases. *Comput. Chem. Eng.* **2003**, *27*, 813–825. [CrossRef]
15. Khalil, A.E.; Brooks, J.M.; Gupta, A.K.; Hasan, A.K. Impact of confinement on flowfield of swirl flow burners. *Fuel* **2016**, *184*, 1–9. [CrossRef]
16. Elbaz, A.M.; Roberts, W.L. Investigation of the effects of quarl and initial conditions on swirling non-premixed methane flames: Flow field, temperature, and species distributions. *Fuel* **2016**, *169*, 120–134. [CrossRef]
17. Elbaz, A.M.; Roberts, W.L. Conical quarl swirl stabilized non-premixed flames: Flame and flow field interaction. *Energy Procedia* **2017**, *120*, 206–213. [CrossRef]
18. Elattar, H.F. *Flame Simulation in Rotary Kilns Using Computational Fluid Dynamics*. Ph.D Thesis, Magdeburg University, Magdeburg, Germany, 2011.
19. TECFLAM Cooperation. Available online: [www.tu-darmstadt.de/fb/mb/ekt/tecflam](http://www.tu-darmstadt.de/fb/mb/ekt/tecflam) (accessed on 26 November 2014).
20. Repp, S.; Sadiki, A.; Schneider, C.; Hinz, A.; Landenfeld, T.; Janicka, J. Prediction of swirling confined diffusion flame with a Monte Carlo and a presumed-PDF-model. *Int. J. Heat Mass Transf.* **2002**, *45*, 1271–1285. [CrossRef]
21. Moles, P.B.L.F.D.; Watson, D. The aerodynamics of the rotary cement kiln. *J. Inst. Fuel* **1973**, *46*, 353–362.
22. Shih, T.H.; Liou, W.W.; Shabbir, A.; Yang, Z.; Zhu, J. A new  $k-\epsilon$  eddy viscosity model for high Reynolds number turbulent flows. *Comput. Fluids* **1995**, *24*, 227–238. [CrossRef]
23. ANSYS, Inc. *ANSYS FLUENT User's Guide*; Ansys Inc.: Canonsburg, PA, USA, 2011.
24. Poinot, T.; Veynante, D. *Theoretical and Numerical Combustion*; R.T. Edwards, Inc.: Philadelphia, PA, USA, 2001.
25. Cheng, P. Two-dimensional radiating gas flow by a moment method. *AIAA J.* **1964**, *2*, 1662–1664. [CrossRef]
26. Siegel, R.; Howell, J.R. *Thermal Radiation Heat Transfer*; Hemisphere Publishing Corporation: Washington, DC, USA, 1992.
27. Beer, J.M.; Chigier, N.A. *Combustion Aerodynamics*; Krieger Publishing: Malabar, FL, USA, 1983.





Article

# Modeling the Effect of Channel Tapering on the Pressure Drop and Flow Distribution Characteristics of Interdigitated Flow Fields in Redox Flow Batteries

Pablo A. García-Salaberri <sup>1,\*</sup>, Tugba Ceren Gokoglan <sup>2</sup>, Santiago E. Ibáñez <sup>1,3</sup>, Ertan Agar <sup>2</sup> and Marcos Vera <sup>1</sup>

<sup>1</sup> Departamento de Ingeniería Térmica y de Fluidos, Universidad Carlos III de Madrid, 28911 Leganés, Spain; santiago.ibanez@imdea.org (S.E.I.); mvcoello@ing.uc3m.es (M.V.)

<sup>2</sup> Department of Mechanical Engineering, Energy Engineering Graduate Program, University of Massachusetts Lowell, Lowell, MA 01854, USA; TugbaCeren\_Gokoglan@student.uml.edu (T.C.G.); Ertan\_Agar@uml.edu (E.A.)

<sup>3</sup> Unidad de Procesos Electroquímicos, Instituto IMDEA Energía, Avda. Ramón de La Sagra 3, 28935 Móstoles, Spain

\* Correspondence: pagsalab@ing.uc3m.es; Tel.: +34-916249407

Received: 4 June 2020; Accepted: 26 June 2020; Published: 1 July 2020

**Abstract:** Optimization of flow fields in redox flow batteries can increase performance and efficiency, while reducing cost. Therefore, there is a need to establish a fundamental understanding on the connection between flow fields, electrolyte flow management and electrode properties. In this work, the flow distribution and pressure drop characteristics of interdigitated flow fields with constant and tapered cross-sections are examined numerically and experimentally. Two simplified 2D along-the-channel models are used: (1) a CFD model, which includes the channels and the porous electrode, with Darcy's viscous resistance as a momentum sink term in the latter; and (2) a semi-analytical model, which uses Darcy's law to describe the 2D flow in the electrode and lubrication theory to describe the 1D Poiseuille flow in the channels, with the 2D and 1D sub-models coupled at the channel/electrode interfaces. The predictions of the models are compared between them and with experimental data. The results show that the most influential parameter is  $\gamma$ , defined as the ratio between the pressure drop along the channel due to viscous stresses and the pressure drop across the electrode due to Darcy's viscous resistance. The effect of  $Re$  in the channel depends on the order of magnitude of  $\gamma$ , being negligible in conventional cells with slender channels that use electrodes with permeabilities in the order of  $10^{-12}$  m<sup>2</sup> and that are operated with moderate flow rates. Under these conditions, tapered channels can enhance mass transport and facilitate the removal of bubbles (from secondary reactions) because of the higher velocities achieved in the channel, while being pumping losses similar to those of constant cross-section flow fields. This agrees with experimental data measured in a single cell operated with aqueous vanadium-based electrolytes.

**Keywords:** modeling; interdigitated flow field; channel tapering; pressure drop; flow distribution; lubrication theory; redox flow battery

## 1. Introduction

The extensive use of fossil fuels in today's lifestyle has led to climate change from greenhouse gas emissions and has increased the need for use of renewable energy [1]. The major issue limiting the wide-spread usage of intermittent renewable energy sources is the availability of efficient and cost-effective energy storage systems [2]. Recently, redox flow batteries (RFBs) have attracted significant attention due to their flexible design and ability to efficiently store large amounts of energy [3–5]. RFBs

are composed of two differently charged electrolyte systems that convert electrical energy directly into chemical energy by means of reversible electrochemical reactions [6–9]. The electrolytes are stored in external tanks and pumped through an electrochemical redox cell, where the redox reactions take place, storing or producing electricity [9–12]. In the redox cell, a membrane separates the electrode and electrolyte of each half-cell. The role of the electrode is to allow for electrolyte transport and enable the reactions in each half-cell, while the membrane serves to prevent the mixing of the electrolytes and allow for the proton transfer between the two half-cells, to maintain electro-neutrality [13,14]. Once the charged electrolytes have participated in the reaction, they are circulated back to the electrolyte tanks for recharging. Unlike traditional batteries, the key advantage of RFBs is that power generation and energy storage are decoupled, such that the energy storage capacity is determined by the volume of electrolytes, whereas the power rating is dictated by the size of redox cells [3–9]. This makes them ideally suited for a wide range of applications, especially grid-scale energy storage. RFBs are typically categorized based on the redox active species that are used. Among various types of flow batteries, all-vanadium flow batteries (VRFBs), which employ the  $V_2^+/V_3^+$  and  $V_4^+/V_5^+$  redox couples in an aqueous solution as the negative and positive electrolytes, offer unique advantages [15,16]. The use of the same but differently charged species in both half-cells of VRFBs eliminates cross-contamination of electrolytes, which is considered to be one of the major problems that affect the life and durability of other RFBs [17]. Therefore, significant emphasis has been placed on all-vanadium systems since the invention of the flow battery technology [4,18].

The flow-assisted nature of RFBs presents many challenging issues, including but not limited to significant transport losses due to poor electrode and cell design and the related low power density [19–26]. It can be hypothesized that many of these challenges are primarily related to the concept of electrolyte utilization [27–32]. Electrolyte utilization is described as the most effective use of electrolyte circulation for the optimum charge and discharge of the RFB. The primary issues of concern regarding electrolyte utilization are gathered around (i) electrode design and (ii) electrolyte flow mechanisms in the cell. The primary role of the electrode is to enable transport of electrolytes, facilitate charge transfer and provide reaction sites for electrochemical reactions [21,33]. Therefore, the nature of the electrode is critically important as it directly governs the transport related losses [23,34,35], cell resistance [36,37], performance degradation [20,38] and many other issues. For instance, proper engineering of electrolyte circulation within the electrode can potentially increase the amount of electrode surface area used for reactions and charge transfer [39–41]. Failure to do so will increase the mass transport losses and the concentration overpotential, reducing overall battery performance.

Proper selection of electrolyte flow configuration is critical for the effective use of electrolyte. Two different flow configurations have been widely used in the field, namely flow-through and flow-by flow fields, which are defined based on how the electrolyte flows with respect to the electrode [19,29,42]. In a flow-through design, the electrolyte is forced to permeate through the porous electrodes, whereas in a flow-by design, the electrolyte is directed along the surface of the electrode (i.e., flows parallel to the electrode surface) in two ways: (i) through a flow frame placed between the electrode and the membrane, or (ii) through the flow channels in the current collector (similar to a fuel cell) [27,28,43]. Understanding the unique aspects of each flow scheme is critical for selecting the flow cell architecture that leads to minimum losses. While one flow configuration can minimize certain types of losses, it may inadvertently increase others. For instance, the flow-through design maximizes the contact between the electrolyte and the electrode; however, it increases the pressure drop and induces accelerated electrode degradation due to the high viscous forces. While the flow-by configuration eliminates the pressure drop losses, it suffers from poor electrolyte utilization.

Existing studies show the possibility of achieving higher performance ratings through the use of different flow-field geometries [23,27,28,42,43]. Among these studies, one promising solution is to use flow fields with non-uniform depth by adding channel obstructions and ramps. According to a recent study [28], integration of ramps (i.e., with tapered channels) into flow fields results in improvements in peak power densities for both open-ended (e.g., parallel flow field) and close-ended (e.g., interdigitated

flow field) geometries. A reduction in the pressure drop has also been observed in interdigitated flow fields with tapered flow fields [28]. In this work, the pressure drop and flow characteristics of constant cross-section and tapered interdigitated flow fields used in RFBs (and related electrochemical devices) are investigated theoretically, numerically and experimentally. The organization of the paper is as follows. In Section 2, the formulation of the 2D CFD model used to analyze the problem is presented, along with a simplified 2D+1D model based on lubrication theory (Appendix A). In Section 3, the pressure drop experiments conducted in a single cell VRFB are described. The results are discussed in Section 4, including a comparison between both numerical models and the experimental data. Finally, the concluding remarks are given in Section 5.

## 2. Mathematical Model

Figure 1 shows schematically the repeating unit cell of an interdigitated flow field typically used in electrochemical devices, such as RFBs or fuel cells. The liquid electrolyte enters the system with uniform velocity,  $U$ , continues through the inlet channel,  $\Omega_i$ , permeates through the porous electrode,  $\Omega_e$ , and is finally collected at the outlet channel,  $\Omega_o$ , before leaving the system. In typical cell designs, the height and width of the channels,  $H \sim w_{ch} \sim 1$  mm, are comparable to the characteristic, effective channel-to-channel distance,  $w_e^{eff}$ , and also to the electrode thickness,  $\delta_e$ , to provide a good balance between charge and mass transport. Note that the effective channel-to-channel distance includes the out-of-plane movement of the fluid as it travels around the rib, through the porous electrode. The characteristic, effective channel-to-channel distance is of the same order as the rib width and electrode thickness ( $w_e^{eff} \sim w_{rib} \sim \delta_e$ ). By contrast, the channel length,  $L$ , is much larger than the characteristic cross-sectional size,  $L \gg H \sim w_{ch} \sim w_e^{eff} \sim \delta_e$ , which results in slender channel geometries. Hence, the flow in the channels is slender, or quasi-one-dimensional, with  $v/u \sim H/L \ll 1$ , as implied by mass conservation. Here,  $u$  and  $v$  are the axial and transverse velocity components in the  $x$  and  $y$  directions, respectively.

Considering the above hierarchy of scales, a 2D CFD model is used here to facilitate the analysis and reduce computational cost, while still retaining the main physics of the problem. A detailed study would require the use of 3D geometries to account for the effective channel-to-channel distance, but this is out of the scope of this work, which seeks to understand the role of the main parameters governing the fluid-dynamic problem. The 2D geometry is shown in the bottom panel of Figure 1, where  $x = (x, y)$ , being  $x$  and  $y$  the Cartesian coordinates in the axial and transverse direction, respectively. The fluid enters the system through the inlet channel,  $\Omega_i$ , which runs in the  $x$ -direction parallel to the porous electrode. In the domain of interest,  $0 \leq x \leq L$ , hereafter referred to as the flow-through section, the height of the inlet channel decreases gradually from its initial value,  $h_i(0)$ , to the dead-end height,  $h_i(L)$ . Similarly, the height of the outlet channel,  $\Omega_o$ , located at the opposite side of the electrode, grows gradually from the dead-end height,  $h_o(0)$ , to its final value,  $h_o(L)$ . To facilitate the analytical treatment, the analysis is restricted to cases where the height of the inlet and outlet channels are equal,  $h_i(0) = h_o(L) = H$ , so that the pressure gradients in the channels upstream and downstream the flow-through section are equal. The inlet and outlet channels have a trapezoidal (i.e., tapered) geometry given by the following expressions

$$h_i(x) = H \left[ 1 - (1 - \phi) \frac{x}{L} \right] \quad \text{and} \quad h_o(x) = H \left[ \phi + (1 - \phi) \frac{x}{L} \right] \quad \text{for} \quad 0 \leq x \leq L, \quad (1)$$

with constant cross-section channels corresponding to  $\phi = 1$ , and tapered channels to  $0 \leq \phi < 1$ . The geometrical parameters and fluid properties used in the analysis are listed in Table 1. To remove the singularity that emerges at the closed end of ramped channels with  $\phi = 0$ , ramped profiles are truncated to a trapezoidal shape assuming a fixed taper ratio  $\phi = 0.1$ , which results in an end-wall height of 10% of the initial height  $H$ . In Section 4.3, a nearly triangular along-the-channel shape ( $\phi = 10^{-2}$ ) is also considered for comparison with a semi-analytical lubrication model that will help with the interpretation of the pressure drop results. The formulation of the lubrication model is

presented in Appendix A. To ensure that the flow is fully developed in the electrode region, the inlet and outlet channels are provided with upstream and downstream extensions of constant height  $H$  to allow for the complete development of the flow and avoid any effect of the inlet and outlet boundary conditions. The length of these extensions,  $20H$ , is of the order of the flow development length for the highest Reynolds numbers considered in this study.

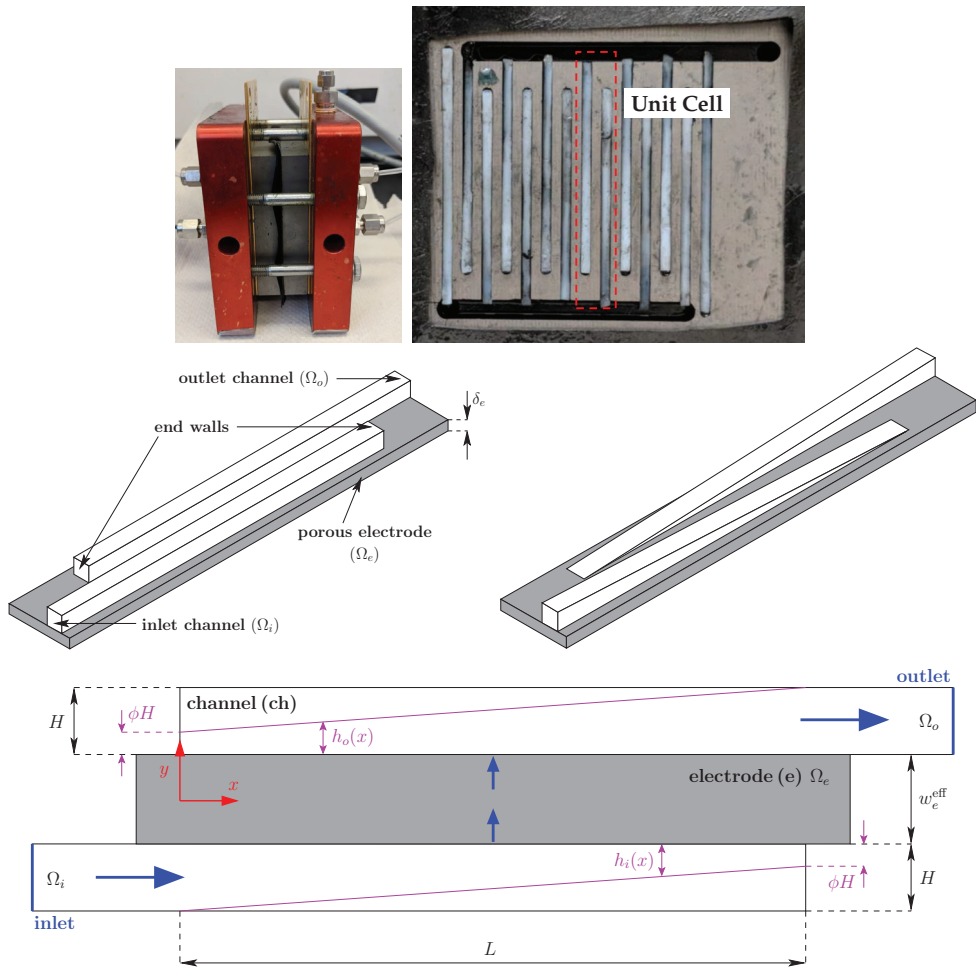


**Figure 1.** (top) Cell fixture and constant cross-section interdigitated flow field used in the experiments, indicating the repeating unit cell, (middle) schematic representation of the 3D geometry of a unit cell of an interdigitated flow field with constant cross-section and tapered channels, and (down) the simplified 2D along-the-channel geometry used in the CFD model. The flow direction (blue arrows), the notation used for the geometrical parameters and the coordinate system are indicated.

The density and viscosity of the fluid,  $\rho$  and  $\mu$ , depend strongly on the type of electrolyte, state of charge and temperature [7,44,45]. Whereas the feed flow rate,  $Q$ , used in a cell with, e.g., 10 inlet and outlet channel segments and an active area of roughly  $16 \text{ cm}^2$  does not usually exceed  $200 \text{ ml/min}$ , corresponding to  $20 \text{ ml/min}$  per channel segment [27,28,46,47]. This leads to a characteristic inlet velocity below  $U \approx 0.33 \text{ m/s}$  and a Reynolds number in the channel lower than  $Re = \rho UH/\mu \approx 300$ , considering an inlet area of  $1 \times 1 \text{ mm}^2$  and the properties of liquid water at room temperature. However, aqueous and non-aqueous electrolytes often exhibit higher viscosities [48], so that  $Re < 100$

is expected in most practical applications. In this exploratory work, liquid water is taken as working fluid, and the inlet velocity is conveniently varied (see Table 1) to investigate the role of inertia in an extended range of Reynolds numbers,  $Re = 1 - 800$ .

**Table 1.** Geometrical parameters, fluid properties and operating conditions used in the 2D CFD model.

Parameter	Symbol	Value
Characteristic channel length	$L$	4 cm, 10 cm †
Reference inlet/outlet channel height	$H$	1 mm
Effective channel-to-channel distance	$w_e^{eff}$	1.5 mm
Electrode permeability	$K_e$	$10^{-13}$ – $10^{-10}$ m <sup>2</sup> †
Density	$\rho$	$10^3$ kg m <sup>-3</sup>
Dynamic viscosity	$\mu$	$10^{-3}$ kg m <sup>-1</sup> s <sup>-1</sup>
Inlet velocity (volume flow rate)	$U (Q')$	1–800 mm s <sup>-1</sup> (1–800 mm <sup>2</sup> s <sup>-1</sup> )

† An additional channel length of  $L = 10$  cm and various electrode permeabilities  $K_e$  are explored in Section 4.3.

The equations determining the flow and pressure drop are the steady-state Navier–Stokes equations for an incompressible fluid of uniform density and viscosity, written here in their generalized form for flow in porous media

$$\nabla \cdot \mathbf{u} = 0 \tag{2a}$$

$$\frac{\rho}{\varepsilon^2} (\mathbf{u} \cdot \nabla) \mathbf{u} = -\nabla p + \frac{\mu}{\varepsilon} \nabla^2 \mathbf{u} + S_u \tag{2b}$$

where  $\mathbf{u} = (u, v)$  is the superficial velocity (equal to the fluid velocity in the channels),  $\varepsilon$  is the porosity (equal to unity in the channels), and  $S_u$  is the momentum sink term due to Darcy’s viscous resistance

$$S_u = \begin{cases} -\frac{\mu}{K_e} \mathbf{u}, & \text{in } \Omega_e \\ 0, & \text{in } \Omega_i \text{ and } \Omega_o, \end{cases} \tag{3}$$

where  $K_e$  is the (isotropic) electrode permeability.

Inertial effects (i.e., Forchheimer drag [46,49,50]) can be neglected in the porous electrode because the characteristic Reynolds number,  $Re_e$ , based on the fiber diameter,  $d_f$ , and the interstitial velocity,  $u_e/\varepsilon$ , is usually of order unity or smaller. From mass conservation, the superficial velocity in the electrode can be estimated as  $u_e \sim [H^2/(\delta_e L)]U \sim (H/L)U$ , given that  $\delta_e \sim H$ , which for the representative geometry considered here,  $H/L = 0.025$ , with  $U \approx 800$  mm/s, results in  $u_e \sim 20$  mm/s for the highest flow rates under study. Using the properties of liquid water, a characteristic fiber diameter  $d_f \approx 10$  μm, and a porosity  $\varepsilon \approx 0.7$  typical of carbon papers and felts [33,51–54], leads to

$$Re_e = \frac{\rho u_e d_f}{\varepsilon \mu} = \frac{10^3 \cdot 2 \times 10^{-2} \cdot 10^{-5}}{0.7 \cdot 10^{-3}} \approx 0.3 \tag{4}$$

$Re_e$  would be even lower for electrolytes more viscous than water.

Equations (2a) and (2b) can alternatively be written in the form

$$\tilde{\nabla} \cdot \tilde{\mathbf{u}} = 0 \tag{5a}$$

$$\frac{1}{\varepsilon^2} \frac{Re \beta}{\Lambda} (\tilde{\mathbf{u}} \cdot \tilde{\nabla}) \tilde{\mathbf{u}} = -\frac{12}{\gamma} \tilde{\nabla} \tilde{p} + \frac{\beta}{\Lambda \varepsilon} \tilde{\nabla}^2 \tilde{\mathbf{u}} - \begin{cases} \frac{12\Lambda}{\gamma} \tilde{\mathbf{u}} & \text{in } \Omega_e \\ 0 & \text{in } \Omega_i \text{ and } \Omega_o, \end{cases} \tag{5b}$$

where  $\tilde{\nabla}(\cdot) = H\nabla(\cdot)$  is the dimensionless nabla operator, associated with the dimensionless spatial variable

$$\tilde{x} = \frac{x}{H}, \quad (6)$$

while

$$\tilde{\mathbf{u}} = (\tilde{u}, \tilde{v}) = \frac{\mathbf{u}}{U} \quad \text{and} \quad \tilde{p} = \frac{(p - p_{\text{ref}})K_e L}{\mu H U w_e^{\text{eff}}} \quad (7)$$

are the dimensionless velocity and pressure, the latter referred to a conveniently defined reference pressure,  $p_{\text{ref}}$ . These are made non-dimensional using the average inlet velocity,  $U = Q'/H$ , based on the volume flow rate  $Q'$  per unit length in the spanwise direction (i.e., the out-of-plane direction), and the characteristic pressure drop across the porous electrode,  $\Delta p_e = (\mu/K_e)(H/L)Uw_e^{\text{eff}}$ .

The dimensionless parameters that emerge in the problem are

$$Re = \frac{\rho U H}{\mu}, \quad \Lambda = \frac{L}{w_e^{\text{eff}}}, \quad \beta = \frac{H}{w_e^{\text{eff}}}, \quad \gamma = \frac{12K_e L^2}{w_e^{\text{eff}} H^3}, \quad (8)$$

which represent the characteristic Reynolds number of the flow in the channels,  $Re$ , the slenderness parameter,  $\Lambda \sim 10\text{--}10^2$ , the ratio between the channel height and the effective channel-to-channel distance,  $\beta \sim 1$ , and the ratio between the characteristic pressure drop along the channel due to viscous stresses,  $\Delta p_{\text{ch}}^v = (12\mu/H^2)UL$ , and the pressure drop across the porous electrode due to Darcy's viscous resistance,  $\Delta p_e = (\mu/K_e)(H/L)Uw_e^{\text{eff}}$ ,  $\gamma \sim 10^{-2}\text{--}1$ . The former is estimated as the pressure drop of a planar Poiseuille flow in a flat channel of length  $L$  and uniform cross-section  $H$  (i.e., with an equivalent permeability  $K_{\text{ch}} = H^2/12$ ), while the latter is determined from Darcy's law using the characteristic velocity in the porous electrode,  $u_e \sim (H/L)U$ .

No-slip boundary conditions are imposed at solid walls, while a prescribed uniform velocity is imposed at the inlet and a zero dimensionless pressure at the outlet

$$\tilde{\mathbf{u}} \cdot \mathbf{n} = -1 \quad \text{at the inlet} \quad (9)$$

$$\tilde{p} = \tilde{p}_{\text{ref}} = 0 \quad \text{at the outlet} \quad (10)$$

where  $\mathbf{n}$  denotes the outward unit normal vector.

The above equations were integrated in ANSYS Fluent using the viscous solver with the SIMPLE algorithm to handle the pressure-velocity coupling, least square cell-based discretization for gradients, the standard pressure interpolation scheme, and second-order upwind discretization for the momentum conservation equation. Structured quadrilateral meshes with 0.5–2 million cells were used in the simulations, including a refinement near the channel-electrode interfaces to capture velocity gradients adequately. The grid independency study performed in the simulation campaign can be found in Appendix B. The convergence criterion of the residuals was set to  $10^{-8}$ .

### 3. Experimental

Pressure drop measurements were performed in a 5 cm<sup>2</sup> flow cell with Nafion 212 membrane and impervious graphite bipolar plates with constant cross-section and ramped ( $\phi \rightarrow 0$ ) interdigitated flow fields. The inlet and outlet channels had an inlet area of  $0.8 \times 0.8$  mm<sup>2</sup> and a length  $L = 1.7$  cm, and were separated by ribs with a width  $w_{\text{rib}} = 0.8$  mm. The feed flow rate was distributed among  $N_{\text{ch}} = 7$  channel segments. Two layers of AvCarb F250C (200 and 250  $\mu\text{m}$ ) carbon paper were used as electrodes. 25 mL of electrolyte (1.6 M vanadium dissolved in 2.5 M sulfuric acid) was placed in each external tank, and pumped through the cell with a peristaltic pump (Masterflex L/S, Cole-Parmer, Vernon Hills, IL, USA) at various flow rates ranging from 16 mL/min to 80 mL/min. Pressure drop measurements were performed when the cell was switched off using Honeywell board mount pressure sensors inserted into a T-junction tube between the peristaltic pump and the inlet of the flow cell.

Pressure drop measurements were repeated 3 times and data recorded every 0.2 s for 10 min. Each dataset was averaged over time for analysis, observing a deviation lower than 1% in averaged pressure.

#### 4. Discussion of Results

As previously discussed, the geometrical parameters  $\beta = H/w_e^{\text{eff}} \sim 1$  and  $\Lambda = L/w_e^{\text{eff}} \sim 10\text{--}10^2$  take reasonably uniform values in electrochemical cells, so they will be kept fixed in the study with the values presented in Table 1,  $\beta = 1/1.5 = 0.67$  and  $\Lambda = 40/1.5 = 26.67$ . Additionally,  $\Lambda = 100/1.5 = 66.67$  is examined in Section 4.3. Larger variations are found in the Reynolds number in the channels,  $Re = \rho UH/\mu$ , which changes with the feed flow rate and electrolyte properties, as well as the pressure drop ratio,  $\gamma = 12K_e L^2/(w_e^{\text{eff}} H^3)$ , which increases linearly with the electrode permeability. Here, the Reynolds number is varied in the range 1–800 to study the full range of variation of  $Re$  expected in practice ( $Re \sim 1\text{--}100$ ), along with the effect of inertia at higher Reynolds numbers ( $Re \sim 100\text{--}800$ ) that may appear in the operation of large cell designs, not accounted for in the lubrication model (see Appendix A). In addition, two different electrode permeabilities are examined,  $K_e = 10^{-10} \text{ m}^2$  and  $K_e = 10^{-12} \text{ m}^2$ , corresponding to  $\gamma = 1.28$  and  $\gamma = 1.28 \times 10^{-2}$ . The former is close to the upper limit of permeabilities found in uncompressed fibrous electrodes, while the latter is of the order of the permeability of compressed samples during operation [51,52,55–58]. Some extra permeabilities are analyzed in Section 4.3 to study the combined effect of  $\gamma$  and  $\Lambda$  on the pressure drop predicted by the CFD and the lubrication models.

Before proceeding further, it is convenient to examine the relative importance of the different terms in the along-the-channel momentum equation. Considering Equation (5b), we have that

$$\rho(\mathbf{u} \cdot \nabla) \mathbf{u} = -\nabla p + \mu \nabla^2 \mathbf{u} \quad (11a)$$

$$\sim \frac{\rho U^2}{L} \quad \sim \frac{\Delta p_{\text{ch}}}{L} \quad \sim \mu \frac{12U}{H^2} \quad (11b)$$

where the numerical factor that appears in the estimate of the viscous term is due to the use of the exact solution for a planar Poiseuille flow and is included here to increase the accuracy of the estimates. When convective effects are negligible, the pressure drop along the channel can be estimated by imposing that the longitudinal pressure gradient must be of the same order as the viscous term, leading to  $\Delta p_{\text{ch}}^v = (12\mu/H^2)UL$ . Convective effects in the channel start to play a role when they become of the order of the viscous term,  $\rho U^2/L \sim 12\mu U/H^2$ , or

$$Re \sim 12 \frac{L}{H} = 12 \frac{\Lambda}{\beta}, \quad (12)$$

which for  $H = 1 \text{ mm}$  and  $L = 4 \text{ cm}$  ( $\beta = 0.67$ ,  $\Lambda = 26.67$ ) yields  $Re \sim 480$ .

In addition, the relative importance of the terms in the across-the-electrode momentum equation is

$$\nabla p = -\frac{\mu}{K_e} \mathbf{u} \quad (13a)$$

$$\sim \frac{\Delta p_e}{w_e^{\text{eff}}} \quad \sim \frac{\mu}{K_e} \frac{UH}{L} \quad (13b)$$

Therefore, the pressure drop along the channel due to convective effects,  $\Delta p_{\text{ch}}^c$ , becomes comparable to the pressure drop across the electrode due to Darcy's viscous resistance,  $\Delta p_e$ , when  $\rho U^2 \sim (\mu UH/K_e)(w_e^{\text{eff}}/L)$ , or

$$Re \sim \frac{H^2 w_e^{\text{eff}}}{K_e L} = 12 \frac{\Lambda}{\beta} \gamma^{-1} \quad (14)$$

which for  $H = 1 \text{ mm}$ ,  $w_e^{\text{eff}} = 1.5 \text{ mm}$ ,  $L = 4 \text{ cm}$  and  $K_e = 10^{-12} \text{ m}^2$ ,  $10^{-10} \text{ m}^2$  ( $\beta = 0.67$ ,  $\Lambda = 26.67$ ) yields  $Re = 375$  and  $Re = 3.75 \times 10^4$  for  $\gamma = 1.28$  and  $\gamma = 1.28 \times 10^{-2}$ , respectively.

In the discussion below, the analysis is focused on along-the-channel  $x$ -variations, so distributions are locally averaged in the transverse  $y$ -direction. The averaged axial velocity is only presented for the inlet channel, since the local crossflow across the porous electrode is almost 1D (see Appendix B). The 1D character of the flow in the electrode is explained by the higher local permeability of both the constant and tapered cross-section channels ( $K_{ch}(x) = h_i^2(x)/12 = 10^{-9}\text{--}10^{-7} \text{ m}^2$ ), which is at least one order of magnitude higher than the maximum electrode permeability considered in this study ( $K_e = 10^{-10} \text{ m}^2$ ). Therefore, the longitudinal velocity profile in the outlet channel is virtually the complementary of that in the inlet channel. The expressions of the  $y$ -averaged variables used in the analysis, i.e., dimensionless axial velocity in the channel, dimensionless transverse velocity in the electrode, and dimensionless pressure in the inlet and outlet channels, are as follows

$$\begin{aligned} \langle \tilde{u}_i \rangle(x) &= \frac{Q'_i(x)/h_i(x)}{U}; \quad \langle \tilde{v}_e \rangle(x) = \frac{1}{w_e^{\text{eff}}} \int_{-w_e^{\text{eff}}/2}^{w_e^{\text{eff}}/2} \frac{L}{UH} v_e(x, y) dy; \\ \langle \tilde{p}_i \rangle(x) &= \frac{1}{h_i(x)} \int_{-w_e^{\text{eff}}/2-h_i(x)}^{-w_e^{\text{eff}}/2} \frac{K_e L}{\mu H U w_e^{\text{eff}}} p_i(x, y) dy; \\ \langle \tilde{p}_o \rangle(x) &= \frac{1}{h_o(x)} \int_{w_e^{\text{eff}}/2}^{w_e^{\text{eff}}/2+h_o(x)} \frac{K_e L}{\mu H U w_e^{\text{eff}}} p_o(x, y) dy \end{aligned} \tag{15}$$

Additionally, three overall variables are considered, i.e., overall pressure drop, overall average velocity in the inlet channel, and homogeneity factor of the flow across the electrode, which are defined as

$$\begin{aligned} \langle \tilde{\Delta p} \rangle &= \int_{-w_e^{\text{eff}}/2}^{-w_e^{\text{eff}}/2-H} \langle \tilde{p}_i \rangle(0) dy - \int_{w_e^{\text{eff}}/2}^{w_e^{\text{eff}}/2+H} \langle \tilde{p}_o \rangle(L) dy; \\ \langle \tilde{u}_i \rangle &= \frac{1}{L} \int_0^L \langle \tilde{u}_i \rangle(x) dx; \quad \text{HF}_e = 1 - \frac{\sigma[\langle \tilde{v}_e \rangle(x)]}{\frac{1}{L} \int_0^L \langle \tilde{v}_e \rangle(x) dx} \end{aligned} \tag{16}$$

where  $\sigma$  is the standard deviation of the transverse velocity distribution in the electrode  $\langle \tilde{v}_e \rangle(x)$ .

#### 4.1. Case of High Electrode Permeability, $K_e = 10^{-10} \text{ m}^2$ ( $\gamma = 1.28 \sim 1$ )

When  $\gamma \sim 1$ , the pressure drop along the channel due to viscous stresses is comparable to the pressure drop across the electrode ( $\Delta p_{ch}^v \sim \Delta p_e$ ), while convection in the channels becomes important for  $Re \sim 100$ . Please note that Equations (12) and (14) lead to the same order of magnitude estimation since  $\gamma \sim 1$ . This result can be seen in Figure 2, which shows the along-the-channel variation of the dimensionless axial velocity,  $\langle \tilde{u}_i \rangle(x)$ , and the dimensionless transverse velocity in the electrode,  $\langle \tilde{v}_e \rangle(x)$ , of the constant cross-section (left panel) and the tapered (right panel) flow fields.

In constant cross-section channels, the axial velocity decreases monotonously with  $x$  due to the gradual loss of mass caused by the crossflow towards the porous electrode [59,60]. For  $Re \ll 12H/L$ , the role of inertia is negligible, resulting in roughly uniform crossflow distributions and nearly linear longitudinal velocity profiles. However, for larger Reynolds numbers,  $Re \sim 12H/L$ , inertia becomes important and forces the fluid to continue straight towards the end of the channel. The axial velocity exhibits now a clearly non-linear behavior, decreasing more slowly at the inlet but falling more rapidly at the end. Therefore, higher pressure drops arise near the end of the channel, as required to sustain the larger crossflow velocities present there, which result in a reduction of the streamline spacing in this region (see Appendix B). Summarizing, inertia keeps the fluid moving in the streamwise direction, increases the axial and crossflow velocities near the end of the channel, and results in less uniform crossflow distributions and higher overall pressure drops.



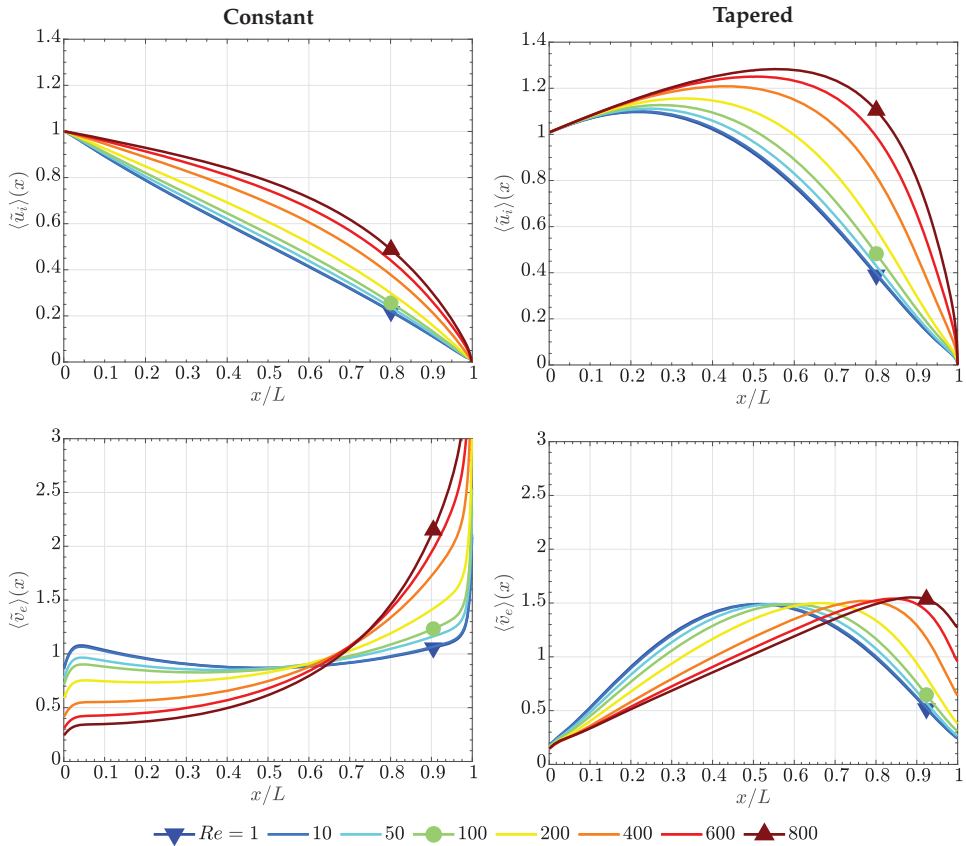


**Figure 2.** Variation of (top) the  $y$ -averaged axial velocity in the inlet channel,  $\langle \tilde{u}_i \rangle(x)$ , and (down) the  $y$ -averaged transverse velocity in the electrode,  $\langle \tilde{v}_e \rangle(x)$ , as a function of the along-the-channel tapered coordinate,  $x/L$ , for  $Re = 1$ –800, corresponding to (left) the constant cross-section and (right) the tapered flow fields. Electrode permeability,  $K_e = 10^{-10} \text{ m}^2$  ( $\gamma \sim 1$ ), and  $\Lambda = 26.67$ .

Tapered channels exhibit higher axial velocities as a result of the gradual reduction of the cross-section, which tends to accelerate the flow and partially compensates for the deceleration caused by the crossflow. Consequently, as shown in Figure 3, higher pressure drops are found in the tapered flow field. For instance, Figure 2 shows that the axial velocity experiences significant overshoots with respect to the inlet velocity in a significant fraction of the channel close to the inlet. This result agrees with previous studies analyzing the effect of channel tapering on fuel cell performance [61–64]. The initial growth rate of the axial velocity can be estimated from the condition that the volume flow rate in the inlet channel must remain approximately constant,  $u(x)h_i(x) \approx UH = Q'$ , at the beginning of the channel, namely

$$\tilde{u} = \frac{u(x)}{U} \approx \frac{H}{h_i(x)} = \frac{1}{1 - (1 - \phi)(x/L)} \approx 1 + (1 - \phi)(x/L) \quad \text{for } \frac{x}{L} \ll 1 \quad (17)$$

This condition stems from the fact that the equivalent permeability of a flat channel is  $K_{ch} = h^2(x)/12$ , so that the ratio of the equivalent permeabilities of the inlet and outlet channels for  $x/L \ll 1$  is of order  $K_{ch,i}/K_{ch,o} \approx h_i^2(0)/h_o^2(0) \approx 1/\phi^2 = 100$  for  $\phi = 0.1$ . As a result, a negligible volume flow rate is expected to cross the porous electrode at the beginning of the inlet channel, which motivates the assumption of roughly constant volume flow rate in this region leading to (17). Similar considerations

apply for the dead-ended region of the inlet channel, where the small equivalent permeability strongly reduces the volume flow rate until it eventually vanishes at the end, thus resulting in a parabolic-like crossflow distribution along the channel. The location of the peak transverse velocity shifts towards the dead-ended region when  $Re$  is increased due to inertia, although the additional inhomogeneity introduced in the crossflow distribution is lower than that observed for the constant cross-section flow field.

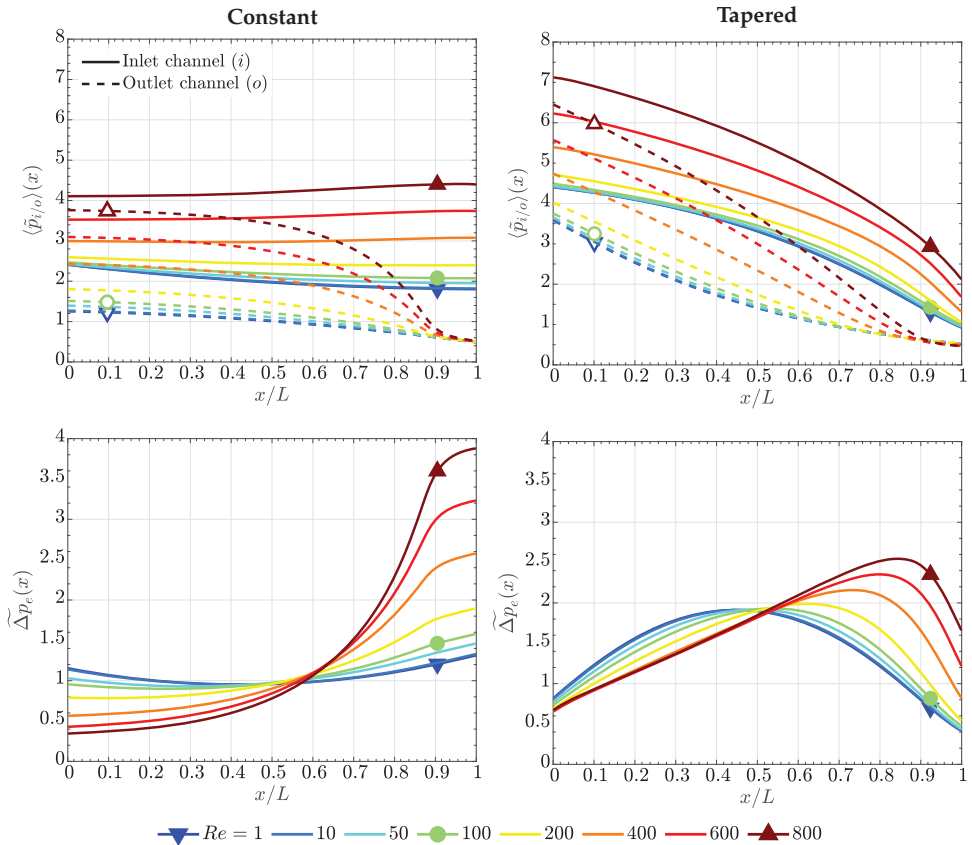


**Figure 3.** Variation of (top) the  $y$ -averaged pressure in the inlet and outlet channels,  $\langle \bar{p}_{i/o} \rangle(x)$ , and (down) the pressure drop across the electrode,  $\Delta \bar{p}_e$ , as a function of the along-the-channel coordinate,  $x/L$ , for  $Re = 1\text{--}800$ , corresponding to (left) the constant cross-section and (right) the tapered flow fields. Electrode permeability,  $K_e = 10^{-10} \text{ m}^2$  ( $\gamma \sim 1$ ), and  $\Lambda = 26.67$ .

The main global differences between both flow fields are shown in Figure 4. The left panel shows the variation of the average channel velocity and the homogeneity factor of the flow across the electrode as a function of  $Re$ , while the right panel shows the variation of the overall pressure drop as a function of  $Re$ . As can be seen, the dimensionless channel velocity and pressure drop in both flow fields remain approximately constant for  $Re \sim 1\text{--}100$ , and increase quadratically for  $Re \sim 100\text{--}800$ . The channel velocity and pressure drop are about 1.5 and 2 times higher in the tapered flow field in the full  $Re$  range. Two regimes are also differentiated for the homogeneity factor depending on  $Re$ . For  $Re \sim 1\text{--}100$ , the homogeneity factor remains almost constant, being significantly higher in the constant cross-section flow field ((constant)  $HF_e = 0.9$  vs. (tapered)  $HF_e = 0.6$ ). As discussed before, this is caused by the preferential crossflow accumulation towards the middle of the channel in the tapered flow field. However, for  $Re \gtrsim 100$ , the homogeneity factor in the constant cross-section

flow field drops strongly due to the effect of inertia, while it only varies slightly in the tapered flow field ( $HF_e \approx 0.55$  at  $Re = 800$ ). As a result, the homogeneity factor of the constant cross-section flow field becomes lower than that of the tapered flow field for  $Re > 300$ , reaching values as low as  $HF_e \approx 0.15$  at  $Re \approx 800$ .

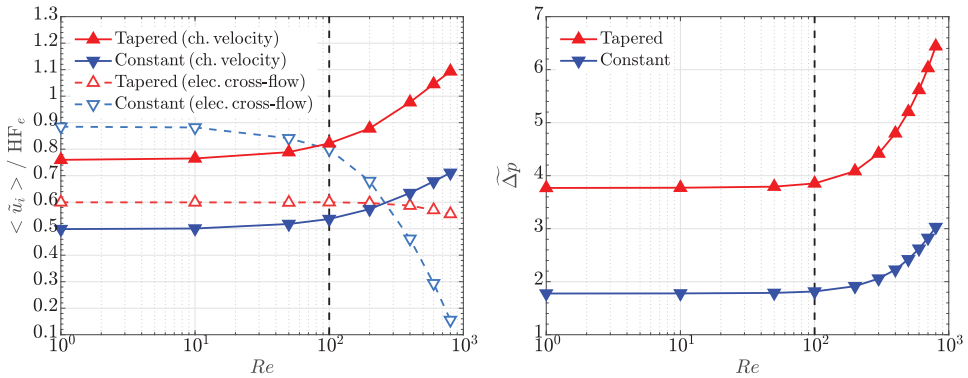


**Figure 4.** Variation of (left) the average axial velocity in the inlet channel,  $\langle \tilde{u}_i \rangle$ , and the homogeneity factor of the transverse velocity in the electrode,  $HF_e$ , and (right) the overall pressure drop,  $\Delta p$ , as a function of the Reynolds number,  $Re$ , corresponding to the constant cross-section and tapered flow fields. Electrode permeability,  $K_e = 10^{-10} \text{ m}^2$  ( $\gamma \sim 1$ ), and  $\Lambda = 26.67$ .

4.2. Case of Low Electrode Permeability,  $K_e = 10^{-12} \text{ m}^2$  ( $\gamma = 1.28 \times 10^{-2} \sim 10^{-2}$ )

When  $\gamma \sim 10^2$ , the pressure drop along the channel due to viscous stresses is negligible compared to the pressure drop across the electrode ( $\Delta p_{ch}^v \ll \Delta p_e$ ). In addition, according to Equation (14), convection in the channels introduce variations in the order of the pressure drop across the electrode ( $\Delta p_{ch}^c \sim \Delta p_e$ ) when  $Re \sim 10^4$ , which exceeds the critical Reynolds number of the laminar regime. Hence, the high pressure drop across the electrode dominates the solution. This can be clearly seen in Figures 5 and 6, where the pressure in the channels is virtually constant, so the overall pressure drop is concentrated in the electrode. The constant pressure difference across the electrode in turn leads to an even crossflow distribution, which is accompanied by a strong 1D local flow across the electrode (see streamlines in Appendix B).

The corresponding along-the-channel variations of the axial velocity can be obtained from Equations (A2) and (A3a)–(A3b) considering a constant transverse velocity across the electrode,  $v_e(x) = v = \text{cte}$ . The analytical results for the constant cross-section and tapered flow fields are included in Figure 5.

Mass conservation for the inlet and outlet channels gives, respectively

$$\frac{dQ'_i(x)}{dx} = -v \Rightarrow Q'_i(x) = C_i - vx \tag{18}$$

$$\frac{dQ'_o(x)}{dx} = v \Rightarrow Q'_o(x) = C_o + vx \tag{19}$$

where the unknown constants  $C_i$ ,  $C_o$ , and  $v$  must be determined so as to satisfy the boundary conditions  $Q'_i(0) = Q'_o(L) = UH$  and  $Q'_i(L) = Q'_o(0) = 0$ . This leads to  $C_i = UH$ ,  $C_o = 0$ , and  $v = UH/L$ , which results in the average axial velocity profiles

$$\langle \tilde{u}_i \rangle(x) = \frac{Q'_i(x)/h_i(x)}{U} = \frac{1 - (x/L)}{h_i(x)/H} \quad \text{and} \quad \langle \tilde{u}_o \rangle(x) = \frac{Q'_o(x)/h_o(x)}{U} = \frac{x/L}{h_o(x)/H} \tag{20}$$

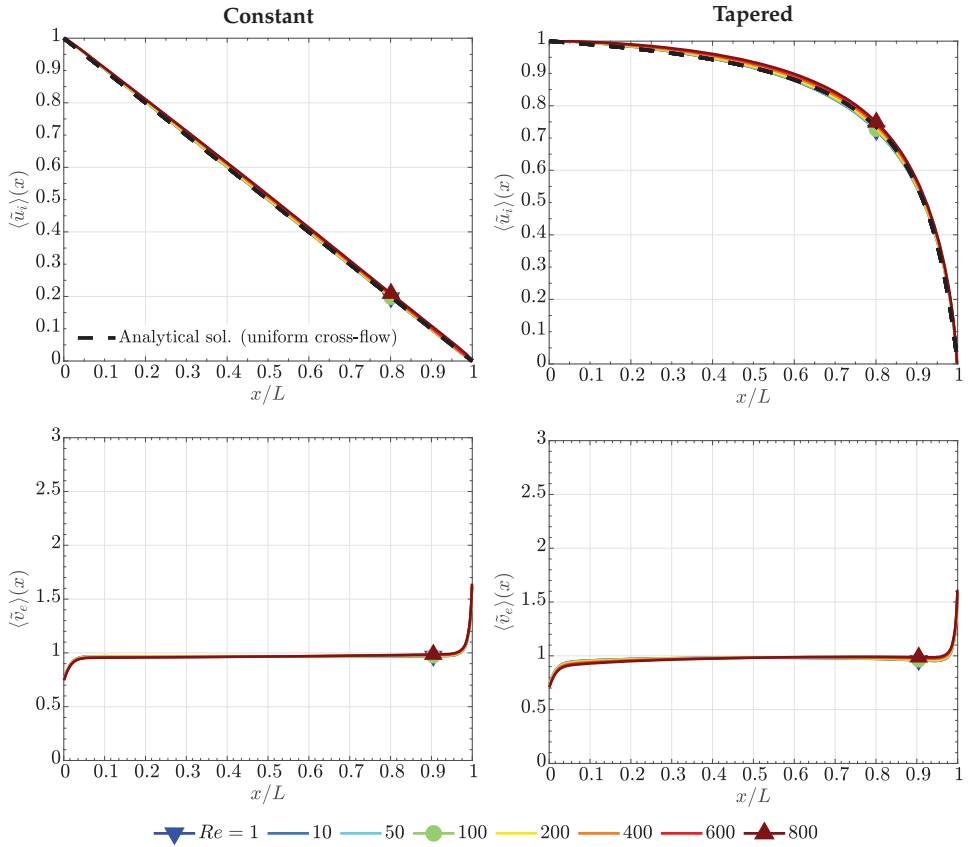


**Figure 5.** Variation of (top) the  $y$ -averaged axial velocity in the inlet channel,  $\langle \tilde{u}_i \rangle(x)$ , and (down) the  $y$ -averaged transverse velocity in the electrode,  $\langle \tilde{v}_e \rangle(x)$ , as a function of the along-the-channel coordinate,  $x/L$ , for  $Re = 1$ –800, corresponding to (left) the constant cross-section and (right) the tapered flow fields. Electrode permeability,  $K_e = 10^{-12} \text{ m}^2$  ( $\gamma \sim 10^{-2}$ ), and  $\Lambda = 26.67$ .

For constant cross-section channels,  $h_i(x) = h_o(x) = H$ , this leads trivially to

$$\langle \tilde{u}_i \rangle(x) = 1 - \frac{x}{L} \quad \text{and} \quad \langle \tilde{u}_o \rangle(x) = \frac{x}{L} \tag{21}$$

showing a linear decrease of the average axial velocity along the inlet channel, and a linear increase along the outlet channel. For tapered channels, use of the expressions for  $h_i(x)$  and  $h_o(x)$  given in Equation (1) leads to the nontrivial results

$$\langle \tilde{u}_i \rangle(x) = \frac{1 - (x/L)}{1 - (1 - \phi)(x/L)} \quad \text{and} \quad \langle \tilde{u}_o \rangle(x) = \frac{x/L}{\phi + (1 - \phi)x/L} \tag{22}$$

The analytical solution shows that, as  $\phi \rightarrow 0$ , the inlet channel velocity tends to  $\langle \tilde{u}_i \rangle = 1$  almost everywhere along the channel length, except at distances of order  $\phi$  from the dead-end wall, where the velocity drops suddenly to zero. The limit of uniform axial velocity thus corresponds to ramped channels with sharp corners, in which the linear acceleration created by the ramped geometry fully compensates for the deceleration caused by the uniform crossflow distribution along the channel. However, for  $\phi = 0.1$ , as considered here, the linear acceleration introduced by the tapered geometry is

lower, leading to a parabolic-like variation of the axial velocity along the channel. The channel velocity varies smoothly in most of the channel, and drops strongly in a region of size  $\Delta x \sim \phi L$  close to the dead-ended wall. Similar considerations apply for the outlet channel, but in that case the crossflow coming from the electrode accelerates the flow in the channel and the tapered geometry tends to decelerate it.

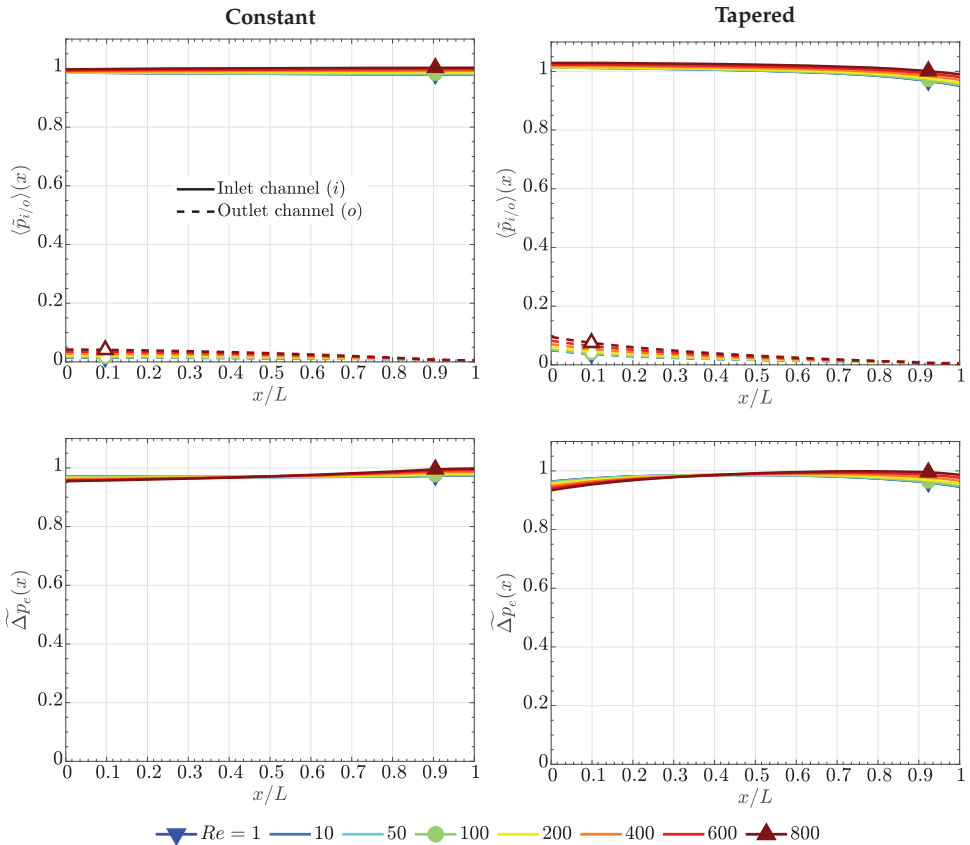


**Figure 6.** Variation of (top) the  $y$ -averaged pressure in the inlet and outlet channels,  $\langle \bar{p}_{i/o} \rangle(x)$ , and (down) the pressure drop across the electrode,  $\Delta \bar{p}_e$ , as a function of the along-the-channel coordinate,  $x/L$ , for  $Re = 1 - 800$ , corresponding to (left) the constant cross-section and (right) the tapered flow fields. Electrode permeability,  $K_e = 10^{-12} \text{ m}^2$  ( $\gamma \sim 10^{-2}$ ), and  $\Lambda = 26.67$ .

Figure 7 shows a comparison between both flow fields, using a similar representation to that in Figure 4. As discussed earlier, all the variables of interest are independent of  $Re$ , except the channel velocity. The pressure drop and the crossflow distribution are dominated by the viscous resistance of the electrode, and the impact of the channel geometry is negligible [46,65,66]. As shown in Figure 8, the results for  $\gamma \sim 10^{-2}$  are in agreement with the experimental data measured in a single cell VRFB with commercial AvCarb carbon-paper electrodes, whose permeability is in the order of  $10^{-12} \text{ m}^2$  for mid-compressed samples (similar to Toray carbon paper) [52,67]. Minor variations are observed in the pressure drop of both channel types, which increases almost linearly with the feed flow rate because of the higher velocities reached in the electrode (i.e.,  $\Delta \bar{p}_{ch} \approx 1$ ). Indeed, the pressure drop across the electrode can be estimated as

$$\Delta p = \frac{\mu w_e^{\text{eff}}}{K_e} \frac{(Q/2N_{\text{ch}})}{\delta_e L} \tag{23}$$

where  $L = 1.7$  cm,  $\delta_e \approx 0.45$  mm,  $w_e^{\text{eff}} \approx 2$  mm (approximated as the rib width plus two times the channel half-width and the electrode half-thickness,  $w_e^{\text{eff}} \approx w_{\text{rib}} + w_{\text{ch}} + \delta_e$ ), and  $\mu = 3 \times 10^{-3}$  Pa s (a typical viscosity found in vanadium electrolytes [45]). The factor of 2 takes into account that the flow rate in each inlet channel is collected by two neighboring outlet channels. A good fit to the experimental data can be obtained with  $K_e \approx 6.5 \times 10^{-12}$  m<sup>2</sup>, corresponding to  $\gamma \approx 10^{-2}$ , which confirms the dominant role of the porous electrode on the overall pressure drop.

The properties of the electrode are further examined in Figure 9, which shows the variation of the electrode permeability and overall pressure drop (see Equation (23)) with porosity and fiber diameter as predicated by the Carman–Kozeny equation. This correlation has previously been successfully used to describe the permeability of fibrous porous layers by Gostick et al. [52]

$$K_e = \frac{d_f^2 \epsilon^3}{16k_{ck}(1 - \epsilon)^2} \tag{24}$$

In the calculations, the Carman–Kozeny constant was taken equal to  $k_{ck} = 5$ , while the variables in Equation (23) were kept the same as those used before, together with a flow rate  $Q = 30$  mL/min.

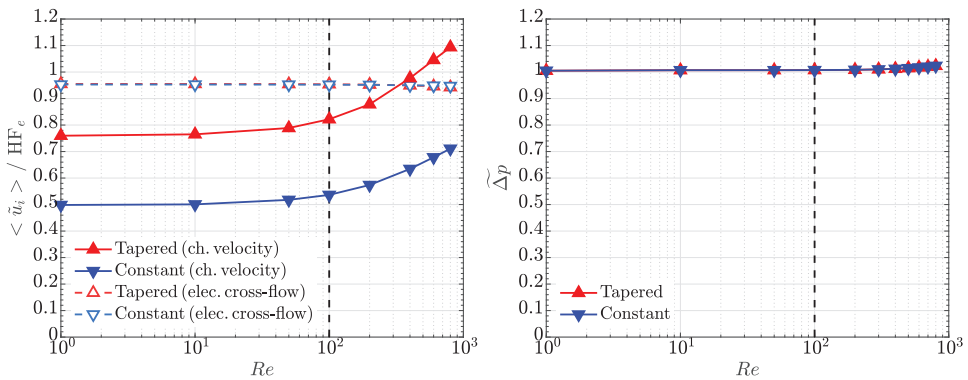


**Figure 7.** Variation of (left) the average axial velocity in the inlet channel,  $\langle \bar{u}_i \rangle$ , and the homogeneity factor of the transverse velocity in the electrode,  $HF_e$ , and (right) the overall pressure drop,  $\Delta p$ , as a function of the Reynolds number,  $Re$ , corresponding to the constant cross-section and tapered flow fields. Electrode permeability,  $K_e = 10^{-12}$  m<sup>2</sup> ( $\gamma \sim 10^{-2}$ ), and  $\Lambda = 26.67$ .

As can be seen, the permeability and the pressure drop change around two orders of magnitude when the porosity and the fiber diameter are varied between  $\epsilon = 0.5\text{--}0.9$  and  $d_f \approx 1\text{--}20$   $\mu\text{m}$ , respectively. This result emphasizes the strong importance of porous media microstructure on the pressure drop and internal flow distribution across the electrode. As a matter of fact, strong channeling effects has been previously reported in RFB operation that can lead to significant distributed ohmic and mass transport losses, as well as reduced durability [50,68–70].

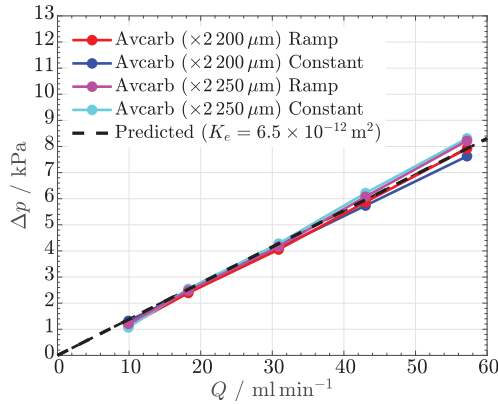


**Figure 8.** Pressure drop,  $\Delta p$ , as a function of the feed flow rate,  $Q$ , measured in a VRFB with constant cross-section and ramped interdigitated flow fields, including different AvCarb carbon-paper electrodes. The black dashed line shows the predicted pressure drop across the electrode for  $K_e = 6.5 \times 10^{-12} \text{ m}^2$  ( $\gamma \sim 10^{-2}$ ).

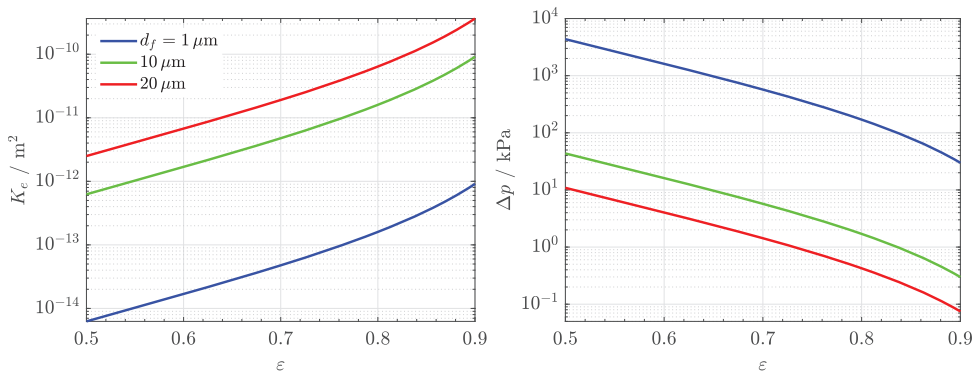


**Figure 9.** Variation of (left) the permeability of the electrode,  $K_e$ , and (right) the overall pressure drop,  $\Delta p$ , as a function of the porosity of the electrode,  $\epsilon$ , for various fiber diameters,  $d_f$ . The permeability is estimated according to the Carman–Kozeny equation (Equation (24)).

#### 4.3. Comparison with the Lubrication Model

In this section, the results of the 2D CFD model and the semi-analytical lubrication model are compared. Non-linear channel shapes were considered in the lubrication model according to the expressions

$$h_i = H [1 - (x/L)^\alpha]; \quad h_o = H [1 - [1 - (x/L)]^\alpha], \quad (25)$$

so that  $\alpha = 1$  corresponds to a ramped geometry;  $\alpha = 0.99$  was used in practice to avoid the singularity introduced by a sharp corner. The constant cross-section geometry was reproduced by setting  $\alpha = 100$ , which led to virtually the same results as higher values of this parameter.  $N = 50$  terms were used in Equation (A10), which resulted in negligible variations compared to  $N = 100$ .

In the CFD model,  $\phi = 10^{-2}$  was considered instead of  $\phi = 10^{-1}$  to introduce a sharp dead-ended region. In addition, three values of  $\gamma$  were simulated,  $\gamma = 1.28 \times 10^{-2}$ ,  $\gamma = 1.28 \times 10^{-1}$  and  $\gamma = 1.28$ , for two different values of  $\Lambda$ ,  $\Lambda = 26.67$  and  $\Lambda = 66.67$ . This corresponds to  $K_e = 10^{-12} \text{ m}^2$ ,  $K_e = 10^{-11} \text{ m}^2$  and  $K_e = 10^{-10} \text{ m}^2$  for  $L = 4 \text{ cm}$ , and  $K_e = 1.6 \times 10^{-13} \text{ m}^2$ ,  $K_e = 1.6 \times 10^{-12} \text{ m}^2$  and  $K_e = 1.6 \times 10^{-11} \text{ m}^2$  for  $L = 10 \text{ cm}$ , which are in the expected range of variation of  $K_e$  and  $L$ . The results computed with the CFD model as a function of  $Re/(12\Lambda\beta^{-1}\gamma^{-1})$  are shown in Figure 10. In addition, a

quantitative comparison between the CFD model and the lubrication model for  $Re/(12\Lambda\beta^{-1}\gamma^{-1}) \ll 1$  (i.e.,  $Re = 1$ ) is listed in Table 2.

As can be seen in Figure 10, the pressure drop of both flow fields depends on  $\gamma$  and  $Re/(12\Lambda\beta^{-1}\gamma^{-1})$ , with an exceedingly small contribution of  $\Lambda$  (and  $\beta$ , which is fixed to  $\beta \sim 1$ ). The predictions of both models are in good agreement when convective effects in the channel are unimportant compared to Darcy's viscous resistance (i.e.,  $Re/(12\Lambda\beta^{-1}\gamma^{-1}) \ll 1$ ), being the relative error below 5%. Convective effects in the CFD model become significant when  $12\Lambda\beta^{-1}\gamma^{-1} \sim 1$ , introducing variations of order unity in the overall pressure drop  $\Delta p$ . These results show that the lubrication model can be used as a preliminary tool to examine the flow in interdigitated flow fields for small values of  $Re/(12\Lambda\beta^{-1}\gamma^{-1})$ , as usually found in RFBs and other electrochemical devices.

**Table 2.** Overall pressure drop,  $\widetilde{\Delta p}$ , predicted by the CFD model and the lubrication model for the constant cross-section and the tapered flow fields corresponding to different values of  $\gamma$  and  $\Lambda$ . Nearly ramped channels were considered for the tapered geometry in the CFD model ( $\phi = 10^{-2}$ ) and the lubrication model ( $\alpha = 0.99$ ).

$\gamma$	$\Lambda$	CFD Model Constant/Tapered	Lubrication Model Constant/Tapered	Relative Variation/%
1.28	26.67	1.80/4.64	1.84/4.69	2.22/1.08
	66.67	1.78/4.62	1.84/4.69	3.37/1.51
$1.28 \times 10^{-1}$	26.67	1.05/1.51	1.08/1.55	2.86/2.65
	66.67	1.03/1.49	1.08/1.55	4.85/4.00
$1.28 \times 10^{-2}$	26.67	1.01/1.03	1.01/1.05	0/1.94
	66.67	1.00/1.00	1.01/1.05	1.00/5.00

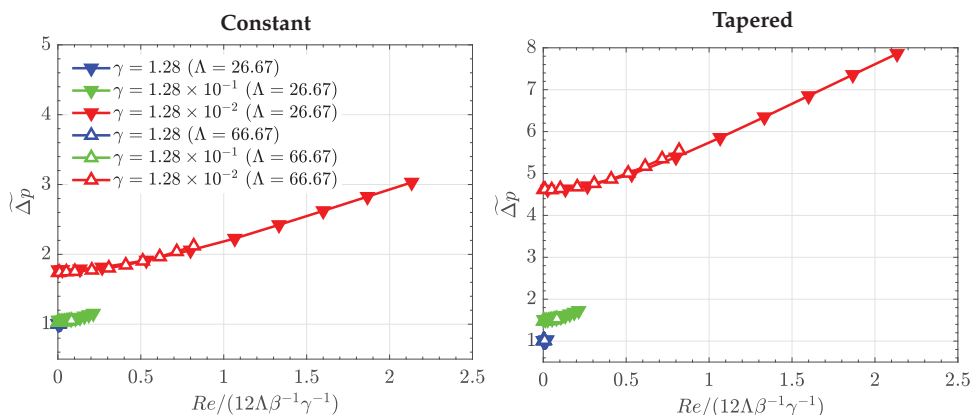


**Figure 10.** Variation of the overall pressure drop,  $\widetilde{\Delta p}$ , as a function of  $Re/(12\Lambda\beta^{-1}\gamma^{-1})$  computed with the CFD model for different values of  $\gamma$  and  $\Lambda$ , corresponding to the constant cross-section and tapered flow fields. Tapered channels with  $\phi = 10^{-2}$  were considered to introduce a sharp corner similar to that used in the lubrication model.

## 5. Conclusions

In this work, the effect of channel tapering on the flow distribution and pressure drop characteristics of interdigitated flow fields used in vanadium redox flow batteries (VRFBs) and related electrochemical devices was examined. The description was simplified using two 2D along-the-channel models: (1) a laminar CFD model, which considers the flow in the channels and the porous electrode, including Darcy's viscous resistance in the latter; and (2) a semi-analytical model, which considers



lubrication theory to describe the 1D Poiseuille flow in the channels and Darcy's law to describe the 2D flow in the electrode. The 2D and 1D sub-models are coupled at the channel/electrode interfaces.

The physical parameters that govern the problem are: (1) the slenderness parameter,  $\Lambda = L/w_e^{\text{eff}}$ , (2) the ratio between the characteristic channel height (or width) and the characteristic, effective channel-to-channel distance,  $\beta = H/w_e^{\text{eff}}$ , (3) the ratio between the pressure drop along the channel due to viscous stresses and the pressure drop across the electrode,  $\gamma = \Delta p_{\text{ch}}^v / \Delta p_e$ , and (4) the Reynolds number in the channel,  $Re = \rho UH/\mu$ . In conventional cells,  $\beta \sim 1$  and  $\Lambda \sim 10\text{--}10^2$ , so in the study  $\beta$  was fixed to 0.67, while two values of  $\Lambda$  were considered, 26.67 and 66.67.  $Re$  was varied in the range 1–800 to examine the effect of inertia in the laminar regime. The analysis has shown that the most influential parameters are  $\gamma$  and  $Re/(12\Lambda\beta^{-1}\gamma^{-1})$ , where the latter measures the relative importance of the pressure drop along the channel due to convection compared to the pressure drop across the electrode due to Darcy's viscous resistance. Therefore, convective effects in the channel are negligible when  $Re/(12\Lambda\beta^{-1}\gamma^{-1}) \ll 1$  and introduce variations in the order of the pressure drop across the electrode when  $Re/(12\Lambda\beta^{-1}\gamma^{-1}) \sim 1$ . For high permeability electrodes ( $\gamma \sim 1$ ), tapered flow fields lead to higher pressure drops compared to constant cross-section flow fields owing to the higher channel velocities reached in the channel. Hence, the beneficial effect of channel tapering on the overall cell efficiency would depend on the relative importance of the enhancement of species transport versus the increase of pumping losses. In contrast, for low permeability electrodes ( $\gamma \sim 10^{-2}$ ), the influence of  $Re$  is negligible (i.e.,  $Re/(12\Lambda\beta^{-1}\gamma^{-1}) \ll 1$ ), so that the overall pressure drop is dominated by the electrode permeability. Consequently, the tapered and the constant cross-section flow fields show similar pressure drops. This result agrees with experiments performed in a single cell VRFB with commercial carbon-paper electrodes. Hence, tapered channels can lead to a higher overall cell efficiency due to the larger velocities achieved in the channel and the similar pumping losses. The improvement of species mass transport and removal of bubbles from side reactions or surrounding air should explain the better performance previously reported in VRFBs with ramped channels.

The results of the semi-analytical lubrication model were similar to those of the CFD model for  $Re/(12\Lambda\beta^{-1}\gamma^{-1}) \ll 1$ , so this model provides a computationally efficient tool to perform preliminary estimations of the flow characteristics in interdigitated flow fields. Future work should consider the effects of assembly compression and electrode anisotropy using a 3D multiphysics CFD model to analyze cell performance and efficiency, and conduct a one-to-one comparison with experimental data.

**Author Contributions:** Conceptualization, P.A.G.-S., E.A. and M.V.; methodology, P.A.G.-S., T.C.G. and E.A.; software, P.A.G.-S. and M.V.; validation, P.A.G.-S. and T.C.G.; formal analysis, P.A.G.-S. and E.A.; investigation, P.A.G.-S., E.A. and M.V.; resources, P.A.G.-S., T.C.G. and E.A.; data curation, P.A.G.-S.; writing—original draft preparation, P.A.G.-S., E.A. and M.V.; writing—review and editing, P.A.G.-S., S.E.I. and E.A.; visualization, P.A.G.-S., T.C.G., S.E.I., E.A. and M.V.; supervision, P.A.G.-S. and E.A.; project administration, P.A.G.-S.; funding acquisition, P.A.G.-S. and E.A. All authors have read and agreed to the published version of the manuscript.

**Funding:** This work was supported by the research project PID2019-106740RB-I00 of the Spanish Ministry of Science, Innovation and Universities, the project PEM4ENERGY-CM-UC3M funded by the call "Programa de apoyo a la realización de proyectos interdisciplinares de I+D para jóvenes investigadores de la Universidad Carlos III de Madrid 2019-2020" under the frame of the "Convenio Plurianual Comunidad de Madrid-Universidad Carlos III de Madrid", and the Energy and Environment Research Grant of the Spanish Iberdrola Foundation.

**Conflicts of Interest:** The authors declare no conflict of interest.

## Nomenclature

$C$	dimensionless coefficient in Equation (A10)
$D$	dimensionless coefficient in Equation (A10)
$h$	local channel height/m
$H$	initial height/m
HF	homogeneity factor defined in Equation (16)
$I_{i/o}$	integral defined in Equation (A13)
$J_{i/o}$	integral defined in Equation (A13)
$K$	absolute permeability/m <sup>2</sup>
$K_{i/o}$	integral defined in Equation (A13)
$L$	length/m
$N_{ch}$	number of channel segments
$p$	pressure/kg m <sup>-1</sup> s <sup>-2</sup>
$Q$	feed flow rate/m <sup>3</sup> s <sup>-1</sup>
$Q'$	flow rate per unit length in the spanwise direction/m <sup>2</sup> s <sup>-1</sup>
$Re$	Reynolds number of the flow in the channels
$S_u$	momentum source term/kg m <sup>-2</sup> s <sup>-2</sup>
$u$	axial velocity in $x$ -direction/m s <sup>-1</sup>
$\mathbf{u}$	superficial velocity vector/m s <sup>-1</sup>
$U$	inlet velocity/m s <sup>-1</sup>
$v$	transverse velocity in $y$ -direction/m s <sup>-1</sup>
$w$	width/m
$x$	$x$ -coordinate/m
$y$	$y$ -coordinate/m

### Greek letters

$\alpha$	exponent in Equation (25)
$\beta$	dimensionless governing parameter in Equation (8)
$\gamma$	dimensionless governing parameter in Equation (8)
$\delta$	thickness/m
$\Delta$	variation
$\Delta_e$	dimensionless parameter in Equation (A9)
$\varepsilon$	porosity
$\Lambda$	dimensionless governing parameter in Equation (8)
$\mu$	dynamic viscosity/kg m <sup>-1</sup> s <sup>-1</sup>
$\tilde{\pi}_0$	dimensionless parameter defined in Equation (A14)
$\rho$	density/kg m <sup>-3</sup>
$\phi$	tapering parameter in Equation (1)
$\Omega$	spatial region

### Subscripts

ch	channel
$e$	electrode
$f$	fiber
$i$	inlet
$n$	index
$o$	outlet
ref	reference
rib	flow-field rib

### Superscripts

$c$	convective
eff	effective
$v$	viscous

## Appendix A. Lubrication Model

As discussed in Section 2, conventional cell designs involve slender channels,  $H/L = \beta\Lambda^{-1} \ll 1$ , with effective channel-to-channel distances that are also small compared to the channel length,  $w_e^{\text{eff}}/L \sim \Lambda^{-1} \ll 1$ . As a result, the flow in the channels is slender and quasi-one-dimensional, i.e., the transverse velocities are much smaller than the axial velocities,  $u \sim (w_e^{\text{eff}}/L)U = \Lambda^{-1}U \ll U$ . If in addition the reduced Reynolds number that pre-multiplies the convective term in Equation (5b) is sufficiently small,  $ReH/L = Re\beta\Lambda^{-1} \ll 1$ , then all the hypotheses of Reynolds' lubrication theory are fulfilled, which enables an approximated semi-analytical treatment of the problem.

The momentum equation in the porous electrode reduces to Darcy's law,  $\mathbf{u} = -(K_e/\mu)\nabla p$ , which introduced in the continuity equation,  $\nabla \cdot \mathbf{u} = 0$ , yields Laplace's equation for pressure

$$\frac{\partial^2 p}{\partial x^2} + \frac{\partial^2 p}{\partial y^2} = 0 \quad \text{in } \Omega_e \quad (\text{A1})$$

The flow in the electrode is coupled with the flow in the channels through the continuity of pressures  $p$  and transverse velocities  $v$  at the channel-electrode interfaces. According to lubrication theory, the local velocity profile in the channels is given by a planar Poiseuille flow with volume flow rates per unit length in the spanwise direction

$$Q'_{i/o}(x) = \frac{h_{i/o}^3}{12\mu} \left( -\frac{dp_{i/o}}{dx} \right), \quad (\text{A2})$$

circulating through the inlet and outlet channels.

Integrating the continuity equation across the inlet and outlet channels leads to Reynolds' lubrication equations

$$\frac{d}{dx} \left[ \frac{h_i^3}{12\mu} \left( -\frac{dp_i}{dx} \right) \right] = -v(x, -w_e^{\text{eff}}/2) \quad \text{in } \Omega_i \quad (\text{A3a})$$

$$\frac{d}{dx} \left[ \frac{h_o^3}{12\mu} \left( -\frac{dp_o}{dx} \right) \right] = v(x, w_e^{\text{eff}}/2) \quad \text{in } \Omega_o \quad (\text{A3b})$$

which upon substitution of the transverse velocities appearing on the right-hand-side in terms of the transverse pressure gradients in the porous electrode, yields the boundary conditions to Equation (A1) at the channel-electrode interfaces

$$-\frac{K_e}{\mu} \frac{\partial p}{\partial y} = \frac{d}{dx} \left[ \frac{h_i^3}{12\mu} \left( \frac{dp}{dx} \right) \right] \quad \text{at } 0 < x < L, \quad y = -w_e^{\text{eff}}/2 \quad (\text{A4a})$$

$$\frac{K_e}{\mu} \frac{\partial p}{\partial y} = \frac{d}{dx} \left[ \frac{h_o^3}{12\mu} \left( \frac{dp}{dx} \right) \right] \quad \text{at } 0 < x < L, \quad y = w_e^{\text{eff}}/2 \quad (\text{A4b})$$

The longitudinal pressure gradient at the inlet and outlet sections of the flow-through region,  $x = 0$  and  $x = L$ , must be compatible with the linear pressure drop imposed by the planar Poiseuille flows that emerge upstream and downstream the inlet and outlet channels (see, e.g., Equation (A2))

$$-\frac{\partial p}{\partial x} = \frac{12\mu Q'}{H^3} \quad \text{at } x = 0 \quad \text{and} \quad x = L, \quad -w_e^{\text{eff}}/2 < y < w_e^{\text{eff}}/2 \quad (\text{A5})$$

This pressure gradient induces an axial velocity in the porous electrode that results in an additional volume flow rate

$$Q'_e = \frac{K_e}{\mu} \left( \frac{12\mu Q'}{H^3} \right) w_e^{\text{eff}} = \frac{12K_e w_e^{\text{eff}}}{H^3} Q' \quad (\text{A6})$$

flowing through the system. However, this volume flow rate is small compared to the one flowing through the channels and crossing the electrode

$$\frac{Q'_e}{Q'} = \frac{12K_e L^2}{w_e^{\text{eff}} H^3} \left( \frac{w_e^{\text{eff}}}{L} \right)^2 = \frac{\gamma}{\Lambda^2} \ll 1 \quad (\text{A7})$$

Hence, the flow in the inlet and outlet regions of the porous electrode, along with the additional flow rate  $Q'_e$ , are anticipated to have a negligible influence on the results.

To write the problem in dimensionless form, it is convenient to introduce the modified dimensionless coordinates  $\hat{x} = x/L = \beta\bar{x}/\Lambda$  and  $\hat{y} = y/w_e^{\text{eff}} = \beta\bar{y}$ , measured with the characteristic scales of the porous electrode, while keeping the same definition for the dimensionless pressure given in Equation (7). With these definitions, the problem reduces to

$$\frac{1}{\Lambda^2} \frac{\partial^2 \tilde{p}}{\partial \hat{x}^2} + \frac{\partial^2 \tilde{p}}{\partial \hat{y}^2} = 0 \quad \text{in} \quad 0 < \hat{x} < 1, \quad 0 < \hat{y} < 1 \quad (\text{A8})$$

subject to the boundary conditions

$$-\frac{\partial \tilde{p}}{\partial \hat{x}} = \gamma \quad \text{at} \quad \hat{x} = 0, \quad \hat{x} = 1, \quad 0 < \hat{y} < 1 \quad (\text{A9a})$$

$$-\frac{\partial \tilde{p}}{\partial \hat{y}} = \Delta_e \frac{d}{d\hat{x}} \left[ \frac{\hat{h}_i^3}{12} \left( \frac{d\tilde{p}}{d\hat{x}} \right) \right] \quad \text{at} \quad 0 < \hat{x} < 1, \quad \hat{y} = -1/2 \quad (\text{A9b})$$

$$\frac{\partial \tilde{p}}{\partial \hat{y}} = \Delta_e \frac{d}{d\hat{x}} \left[ \frac{\hat{h}_o^3}{12} \left( \frac{d\tilde{p}}{d\hat{x}} \right) \right] \quad \text{at} \quad 0 < \hat{x} < 1, \quad \hat{y} = 1/2 \quad (\text{A9c})$$

where  $\hat{h}_i = h_i/w_e^{\text{eff}}$ ,  $\hat{h}_o = h_o/w_e^{\text{eff}}$ ,  $\Delta_e = 12/(\gamma\beta^3)$ , and the dimensionless pressure gradient  $\gamma$  is given by the pressure drop ratio defined in Equation (8).

The solution of the problem stated above involves the integration of Laplace's equation (A8) in a square domain with linear boundary conditions. It is then possible to use separation of variables and express the solution as an infinite series of eigenfunctions of the form

$$\tilde{p}(\hat{x}, \hat{y}) = \tilde{\pi}_0 - \hat{y} - \gamma\hat{x} + \sum_{n=1}^{\infty} \left( C_n e^{n\pi\hat{y}/\Lambda} + D_n e^{-n\pi\hat{y}/\Lambda} \right) \cos(n\pi\hat{x}), \quad (\text{A10})$$

with the associated dimensionless pressure gradient

$$\begin{aligned} \frac{\partial \tilde{p}}{\partial \hat{x}}(\hat{x}, \hat{y}) &= -\gamma - \sum_{n=1}^{\infty} n\pi \left( C_n e^{n\pi\hat{y}/\Lambda} + D_n e^{-n\pi\hat{y}/\Lambda} \right) \sin(n\pi\hat{x}), \\ \frac{\partial \tilde{p}}{\partial \hat{y}}(\hat{x}, \hat{y}) &= -1 + \sum_{n=1}^{\infty} \frac{n\pi}{\Lambda} \left( C_n e^{n\pi\hat{y}/\Lambda} - D_n e^{-n\pi\hat{y}/\Lambda} \right) \cos(n\pi\hat{x}), \end{aligned} \quad (\text{A11})$$

where the coefficients  $C_n$  and  $D_n$  must be chosen to satisfy the boundary conditions (A9b) and (A9c). The boundary condition (A9a) is automatically enforced by the choice of longitudinal eigenfunctions and the inclusion of the linear term  $-\gamma\hat{x}$  in Equation (A10).

An approximated solution can be obtained by truncating the summation in (A10) to  $N$  terms and taking the inner product of Equations (A9b) and (A9c) with respect to the longitudinal eigenfunction  $\cos(m\pi\hat{x})$ . To this end, one must substitute the truncated series from (A10) into (A9b) and (A9c),

multiply the resulting expressions by  $\cos(m\pi\hat{x})$ , and integrate from  $\hat{x} = 0$  to  $\hat{x} = 1$ . Repeating the operation for  $m = 1, 2, \dots, N$  yields  $2N$  equations for the  $2N$  coefficients  $C_n$  and  $D_n$  with the form

$$-\frac{1}{\Delta_e} \left( \frac{m\pi}{2\Lambda} \right) \left( C_m e^{-\frac{m\pi}{2\Lambda}} - D_m e^{\frac{m\pi}{2\Lambda}} \right) + \sum_{n=1}^N n\pi \left( C_n e^{-\frac{n\pi}{2\Lambda}} + D_n e^{\frac{n\pi}{2\Lambda}} \right) [n\pi I_i(m, n) + J_i(m, n)] = \frac{K_i(m)}{\Delta_e} \quad m = 1, \dots, N \quad (A12a)$$

$$\frac{1}{\Delta_e} \left( \frac{m\pi}{2\Lambda} \right) \left( C_m e^{\frac{m\pi}{2\Lambda}} - D_m e^{-\frac{m\pi}{2\Lambda}} \right) + \sum_{n=1}^N n\pi \left( C_n e^{\frac{n\pi}{2\Lambda}} + D_n e^{-\frac{n\pi}{2\Lambda}} \right) [n\pi I_o(m, n) + J_o(m, n)] = \frac{K_o(m)}{\Delta_e} \quad m = 1, \dots, N \quad (A12b)$$

in terms of the integrals

$$\begin{aligned} I_{i/o}(m, n) &= \int_0^1 \frac{\hat{h}_{i/o}^3}{12} \cos(m\pi\hat{x}) \cos(n\pi\hat{x}) d\hat{x} \\ J_{i/o}(m, n) &= \int_0^1 \frac{\hat{h}_{i/o}^2}{4} \frac{d\hat{h}_{i/o}}{d\hat{x}} \cos(m\pi\hat{x}) \sin(n\pi\hat{x}) d\hat{x} \\ K_{i/o}(m) &= \int_0^1 \frac{\hat{h}_{i/o}^2}{4} \frac{d\hat{h}_{i/o}}{d\hat{x}} \cos(m\pi\hat{x}) d\hat{x} \end{aligned} \quad (A13)$$

These integrals can be evaluated a priori with any robust quadrature integration method, such as the adaptive Cash–Karp Runge–Kutta method with variable step size used here based on embedded Runge–Kutta formulas of fourth and fifth order. The use of an accurate integrator is particularly convenient if the functions  $\hat{h}_i(\hat{x})$  and  $\hat{h}_o(\hat{x})$  present discontinuities in their first derivatives, as may be the case in piecewise linear tapering geometries. The above linear system (A12) can be solved using any standard linear algebra package to yield the values of  $C_n$  and  $D_n$ . Finally, the value of  $\tilde{\pi}_0$  is determined by the condition that the dimensionless pressure is zero at the outlet section

$$\tilde{p}(1, 1/2) = 0 \quad \rightarrow \quad \tilde{\pi}_0 = \frac{1}{2} + \gamma - \sum_{n=1}^{\infty} \left[ C_n e^{n\pi/(2\Lambda)} + D_n e^{-n\pi/(2\Lambda)} \right] \cos(n\pi) \quad (A14)$$

The overall pressure drop between the inlet and outlet sections of the flow-through region is given by the dimensionless pressure at the inlet

$$\tilde{p}(0, -1/2) = \tilde{\pi}_0 + \frac{1}{2} - \sum_{n=1}^{\infty} \left[ C_n e^{-n\pi/(2\Lambda)} + D_n e^{n\pi/(2\Lambda)} \right]. \quad (A15)$$

### Appendix B. Mesh Independency Study and Streamlines

The results of the mesh independency study are shown in Figure A1. Structured meshes were used for the simulations with a spacing in  $x$  and  $y$  directions equal to  $\Delta x = 50 \mu\text{m}$  and  $\Delta y = 5 \mu\text{m}$ . For the tapered flow field,  $\Delta y$  indicates the  $y$  spacing at the inlet section, so that the  $y$  spacing at the dead-ended wall is ten times smaller for a taper ratio  $\phi = 0.1$  ( $\Delta y = 0.5 \mu\text{m}$ ). The study was performed at the highest Reynolds number ( $Re = 800$ ) and  $\gamma \sim 1$ , since this case requires capturing larger gradients; the same mesh resolution was used for other cases. The channel length was set to  $L = 4 \text{ cm}$  ( $\Lambda = 26.67$ ), so that the number of cells increased proportionally in the simulations with  $L = 10 \text{ cm}$  (66.67). The meshes used in the study led to a relative variation in the overall pressure drop lower than 1% compared to meshes with 4 times more cells ( $\Delta x = 25 \mu\text{m}$  and  $\Delta y = 2.5 \mu\text{m}$ ), so this degree of precision was considered high enough.

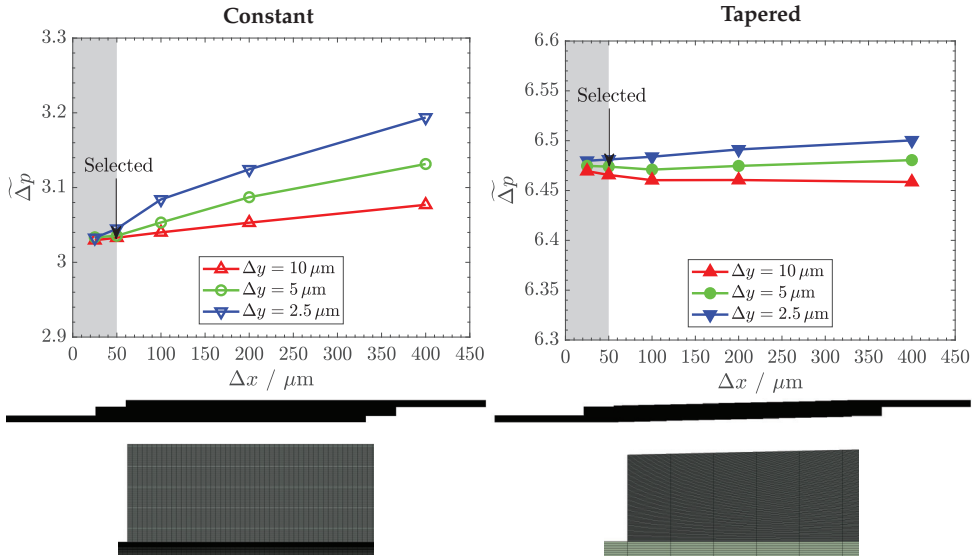


**Figure A1.** Variation of the overall pressure drop,  $\widetilde{\Delta p}$ , as a function of the spacing in the  $x$  and  $y$  directions,  $\Delta x$  and  $\Delta y$ , of the structured meshes used in the simulations of the constant cross-section and tapered flow fields. The selected meshes ( $\Delta x = 50 \mu\text{m}$  and  $\Delta y = 5 \mu\text{m}$ ) are shown at the bottom, together with a close-up view of the dead-ended region. Electrode permeability,  $K_e = 10^{-10} \text{ m}^2$  ( $\gamma \sim 1$ ),  $\Lambda = 26.67$  and  $Re = 800$ .

Figures A2 and A3 show the streamlines for the cases  $\gamma \sim 1$  and  $\gamma \sim 10^{-2}$  ( $\Lambda = 26.67$ ), corresponding to the constant cross-section (left panel) and tapered (right panel) flow fields at different Reynolds numbers,  $Re$ .

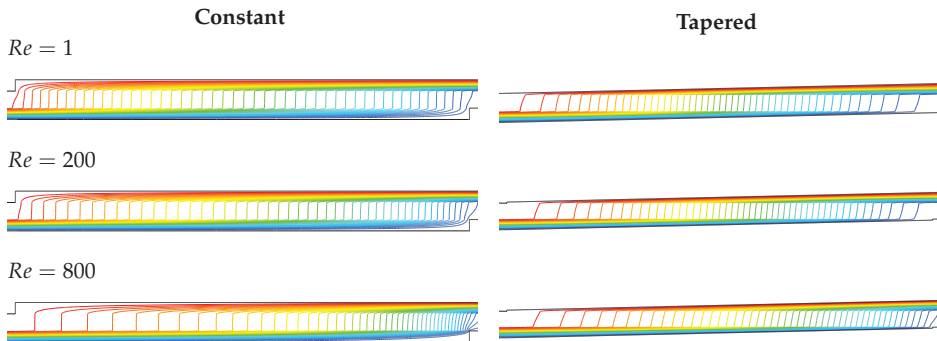


**Figure A2.** Streamlines in (left) the constant cross-section and (right) the tapered flow fields at different Reynolds numbers,  $Re$ , corresponding to an electrode permeability,  $K_e = 10^{-10} \text{ m}^2$  ( $\gamma \sim 1$ ), and  $\Lambda = 26.67$ .

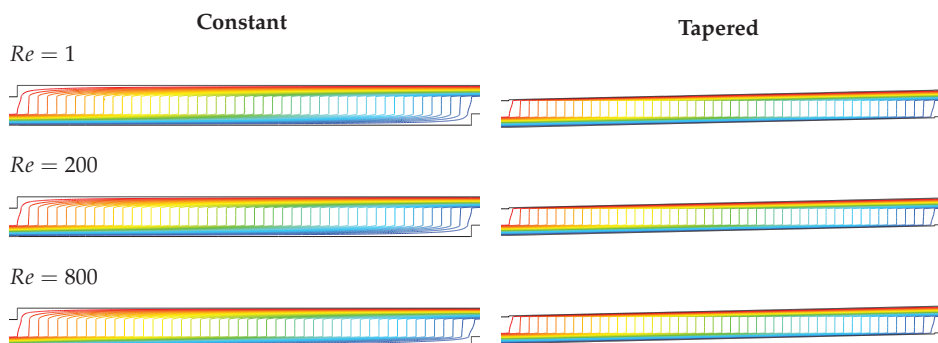


**Figure A3.** Streamlines in (left) the constant cross-section and (right) the tapered flow fields at different Reynolds numbers,  $Re$ , corresponding to an electrode permeability,  $K_e = 10^{-12} \text{ m}^2$  ( $\gamma \sim 10^{-2}$ ), and  $\Lambda = 26.67$ .

## References

- Williams, J.H.; DeBenedictis, A.; Ghanadan, R.; Mahone, A.; Moore, J.; Morrow III, W.R.; Price, S.; Torn, M.S. The Technology Path to Deep Greenhouse Gas Emissions Cuts by 2050: The Pivotal Role of Electricity. *Science* **2012**, *335*, 53–59. [CrossRef] [PubMed]
- Rugolo, J.; Aziz, M.J. Electricity Storage for Intermittent Renewable Sources. *Energy Environ. Sci.* **2012**, *5*, 7151–7160. [CrossRef]
- Dennison, C.R.; Vrubel, H.; Amstutz, V.; Peljo, P.; Toghiani, K.E.; Girault, H.H. Redox Flow Batteries, Hydrogen and Distributed Storage. *Chimia* **2015**, *69*, 753–758. [CrossRef] [PubMed]
- Soloveichik, G.L. Flow Batteries: Current Status and Trends. *Chem. Rev.* **2015**, *115*, 11533–11558. [CrossRef] [PubMed]
- Li, B.; Liu, J. Progress and Directions in Low-Cost Redox-Flow Batteries for Large-Scale Energy Storage. *Natl. Sci. Rev.* **2017**, *4*, 91–105. [CrossRef]
- Perry, M.L.; Weber, A.Z. Advanced Redox-Flow Batteries: A Perspective. *J. Electrochem. Soc.* **2016**, *163*, A5064–A5067. [CrossRef]
- Knehr, K.W.; Agar, E.; Dennison, C.R.; Kalidindi, A.R.; Kumbur, E.C. A Transient Vanadium Flow Battery Model Incorporating Vanadium Crossover and Water Transport through the Membrane. *J. Electrochem. Soc.* **2012**, *159*, A1446–A1459. [CrossRef]
- Chen, D.; Hickner, M.A.; Agar, E.; Kumbur, E.C. Optimized Anion Exchange Membranes for Vanadium Redox Flow Batteries. *ACS Appl. Mater. Interfaces* **2013**, *5*, 7559–7566. [CrossRef]
- Weber, A.Z.; Mench, M.M.; Meyers, J.P.; Ross, P.N.; Gostick, J.T.; Liu, Q. Redox Flow Batteries: A Review. *J. Appl. Electrochem.* **2011**, *41*, 1137–1164. [CrossRef]
- Boettcher, P.A.; Agar, E.; Dennison, C.R.; Kumbur, E.C. Modeling of Ion Crossover in Vanadium Redox Flow Batteries: A Computationally-Efficient Lumped Parameter Approach for Extended Cycling. *J. Electrochem. Soc.* **2016**, *163*, A5244–A5252. [CrossRef]
- Gokoglan, T.C.; Pahari, S.K.; Hamel, A.; Howland, R.; Cappillino, P.J.; Agar, E. Operando Spectroelectrochemical Characterization of a Highly Stable Bioinspired Redox Flow Battery Active Material. *J. Electrochem. Soc.* **2019**, *166*, A1745–A1751. [CrossRef]
- Nourani, M.; Dennison, C.R.; Jin, X.; Liu, F.; Agar, E. Elucidating Effects of Faradaic Imbalance on Vanadium Redox Flow Battery Performance: Experimental Characterization. *J. Electrochem. Soc.* **2019**, *166*, A3844–A3851. [CrossRef]
- Benjamin, A.; Agar, E.; Dennison, C.R.; Kumbur, E.C. On the Quantification of Coulombic Efficiency for Vanadium Redox Flow Batteries: Cutoff Voltages vs. State-of-charge Limits. *Electrochem. Commun.* **2013**, *35*, 42–44. [CrossRef]
- Gandomi, Y.A.; Aaron, D.S.; Mench, M.M. Coupled Membrane Transport Parameters for Ionic Species in All-Vanadium Redox Flow Batteries. *Electrochim. Acta* **2016**, *218*, 174–190. [CrossRef]

15. Sum, E.; Rychcik, M.; Skyllas-Kazacos, M. Investigation of the V(V)/V(IV) System for Use in the Positive Half-Cell of a Redox Battery. *J. Power Sources* **1985**, *16*, 85–95. [CrossRef]
16. Sun, B.; Skyllas-Kazacos, M. Modification of Graphite Electrode Materials for Vanadium Redox Flow Battery Application-I. Thermal Treatment. *Electrochim. Acta* **1992**, *37*, 1253–1260. [CrossRef]
17. Agar, E.; Benjamin, A.; Dennison, C.R.; Chen, D.; Hickner, M.A.; Kumbur, E.C. Reducing Capacity Fade in Vanadium Redox Flow Batteries by Altering Charging and Discharging Currents. *J. Power Sources* **2014**, *246*, 767–774. [CrossRef]
18. Gentil, S.; Reynard, D.; Girault, H.H. Aqueous Organic and Redox-Mediated Redox Flow Batteries: A Review. *Curr. Opin. Electrochem.* **2020**, *21*, 7–13. [CrossRef]
19. Darling, R.M.; Perry, M.L. The Influence of Electrode and Channel Configurations on Flow Battery Performance. *J. Electrochem. Soc.* **2014**, *161*, A1381–A1387. [CrossRef]
20. Nourani, M.; Zackin, B.I.; Sabarirajan, D.C.; Taspinar, R.; Artyushkova, K.; Liu, F.; Zenyuk, I.V.; Agar, E. Impact of Corrosion Conditions on Carbon Paper Electrode Morphology and the Performance of a Vanadium Redox Flow Battery. *J. Electrochem. Soc.* **2019**, *166*, A353–A363. [CrossRef]
21. Forner-Cuenca, A.; Penn, E.E.; Oliveira, A.M.; Brushett, F.R. Exploring the Role of Electrode Microstructure on the Performance of Non-Aqueous Redox Flow Batteries. *J. Electrochem. Soc.* **2019**, *166*, A2230–A2241. [CrossRef]
22. Pezeshki, A.M.; Clement, J.T.; Veith, G.M.; Zawodzinski, T.A.; Mench, M.M. High Performance Electrodes in Vanadium Redox Flow Batteries through Oxygen-Enriched Thermal Activation. *J. Power Sources* **2015**, *294*, 33–338. [CrossRef]
23. Houser, J.; Pezeshki, A.; Clement, J.T.; Aaron, D.; Mench, M.M. Architecture for Improved Mass Transport and System Performance in Redox Flow Batteries. *J. Power Sources* **2017**, *351*, 96–105. [CrossRef]
24. Wei, L.; Zhao, T.S.; Xu, Q.; Zhou, X.L.; Zhang, Z.H. In-situ investigation of hydrogen evolution behavior in vanadium redox flow batteries. *Appl. Energy* **2017**, *190*, 1112–1118. [CrossRef]
25. Ma, K.; Zhang, Y.; Liu, L.; Xi, J.; Qiu, X.; Guan, T.; He, Y. In situ mapping of activity distribution and oxygen evolution reaction in vanadium flow batteries. *Nat. Commun.* **2019**, *10*, 5286. [CrossRef] [PubMed]
26. Bevilacqua, N.; Eifert, L.; Banerjee, R.; Köble, K.; Faragó, T.; Zuber, M.; Bazylak, A.; Zeis, R. Visualization of electrolyte flow in vanadium redox flow batteries using synchrotron X-ray radiography and tomography – Impact of electrolyte species and electrode compression. *J. Power Sources* **2019**, *439*, 227071. [CrossRef]
27. Dennison, C.R.; Agar, E.; Akuzum, B.; Kumbur, E.C. Enhancing Mass Transport in Redox Flow Batteries by Tailoring Flow Field and Electrode Design. *J. Electrochem. Soc.* **2016**, *163*, A5163–A5169. [CrossRef]
28. Akuzum, B.; Alparslan, Y.C.; Robinson, N.C.; Agar, E.; Kumbur, E.C. Obstructed Flow Field Designs for Improved Performance in Vanadium Redox Flow Batteries. *J. Appl. Electrochem.* **2019**, *49*, 551–561. [CrossRef]
29. Ke, X.; Prah, J.M.; Alexander, J.I.D.; Savinell, R.F. Redox Flow Batteries with Serpentine Flow Fields: Distributions of Electrolyte Flow Reactant Penetration into the Porous Carbon Electrodes and Effects on Performance. *J. Power Sources* **2018**, *384*, 295–302. [CrossRef]
30. Zeng, Y.; Li, F.; Lu, F.; Zhou, X.; Yuan, Y.; Cao, X.; Xiang, B. A Hierarchical Interdigitated Flow Field Design for Scale-up of High-Performance Redox Flow Batteries. *Appl. Energy* **2019**, *238*, 435–441. [CrossRef]
31. MacDonald, M.; Darling, R.M. Modeling Flow Distribution and Pressure Drop in Redox Flow Batteries. *AIChE J.* **2018**, *64*, 3746–3755. [CrossRef]
32. Barton, J.L.; Milshtein, J.D.; Hinricher, J.J.; Brushett, F.R. Quantifying the Impact of Viscosity on Mass-Transfer Coefficients in Redox Flow Batteries. *J. Power Sources* **2018**, *399*, 133–143. [CrossRef]
33. Greco, K.V.; Forner-Cuenca, A.; Mularczyk, A.; Eller, J.; Brushett, F.R. Elucidating the Nuanced Effects of Thermal Pretreatment on Carbon Paper Electrodes for Vanadium Redox Flow Batteries. *ACS Appl. Mater. Interfaces* **2018**, *10*, 44430–44442. [CrossRef] [PubMed]
34. Lisboa, K.M.; Marschewski, J.; Ebejer, N.; Ruch, P.; Cotta, R.M.; Michel, B.; Poulikakos, D. Mass Transport Enhancement in Redox Flow Batteries with Corrugated Fluidic Networks. *J. Power Sources* **2017**, *15*, 322–331. [CrossRef]
35. Zhou, X.L.; Zhao, T.S.; An, L.; Zeng, Y.K.; Wei, L. Critical Transport Issues for Improving the Performance of Aqueous Redox Flow Batteries. *J. Power Sources* **2017**, *339*, 1–12. [CrossRef]
36. Milshtein, J.D.; Barton, J.L.; Carney, T.J.; Kowalski, J.A.; Darling, R.M.; Brushett, F.R. Towards Low Resistance Nonaqueous Redox Flow Batteries. *J. Electrochem. Soc.* **2017**, *164*, A2487–A2499. [CrossRef]



37. Aaron, D.S.; Liu, Q.; Tang, Z.; Grim, G.M.; Papandrew, A.B.; Turhan, A.; Zawodzinski, T.A.; Mench, M.M. Dramatic Performance Gains in Vanadium Redox Flow Batteries through Modified Cell Architecture. *J. Power Sources* **2012**, *206*, 450–453. [CrossRef]
38. Derr, I.; Przyrembel, D.; Schweer, J.; Fetyan, A.; Langner, J.; Melke, J.; Weinelt, M.; Roth, C. Electroless Chemical Aging of Carbon Felt Electrodes for the All-Vanadium Redox Flow Battery (VRFB) Investigated by Electrochemical Impedance and X-ray Photoelectron Spectroscopy. *Electrochim. Acta* **2017**, *246*, 783–793. [CrossRef]
39. García-Salaberri, P.A.; Gostick, J.T.; Zenyuk, I.V.; Hwang, G.; Vera, M.; Weber, A.Z. On the limitations of volume-averaged descriptions of gas diffusion layers in the modeling of polymer electrolyte fuel cells. *ECS Trans.* **2017**, *80*, 133–143. [CrossRef]
40. Liu, J.; García-Salaberri, P.A.; Zenyuk, I.V. The impact of reaction on the effective properties of multiscale catalytic porous media: A case of polymer electrolyte fuel cells. *Transport Porous Med.* **2019**, *128*, 363–384. [CrossRef]
41. Liu, J.; García-Salaberri, P.A.; Zenyuk, I.V. Bridging Scales to Model Reactive Diffusive Transport in Porous Media. *J. Electrochem. Soc.* **2020**, *167*, 013524. [CrossRef]
42. Xu, Q.; Zhao, T.S.; Leung, P.K. Numerical Investigations of Flow Field Designs for Vanadium Redox Flow Batteries. *Appl. Energy* **2013**, *105*, 47–56. [CrossRef]
43. Jyothi, L.T.; Jayanti, S. Hydrodynamic Analysis of Flow Fields for Redox Flow Battery Applications. *J. Appl. Electrochem.* **2014**, *44*, 995–1006. [CrossRef]
44. Qi, Z.; Koenig, G.M., Jr. A carbon-free lithium-ion solid dispersion redox couple with low viscosity for redox flow batteries. *J. Power Sources* **2016**, *323*, 97–106. [CrossRef]
45. Xiao, S.; Yu, L.; Wu, L.; Liu, L.; Qiu, X.; Xi, J. Broad temperature adaptability of vanadium redox flow battery—Part 1: Electrolyte research. *Electrochim. Acta* **2016**, *187*, 525–534. [CrossRef]
46. Gerhardt, M.R.; Wong, A.A.; Aziz, M.J. The Effect of Interdigitated Channel and Land Dimensions on Flow Cell Performance. *J. Electrochem. Soc.* **2018**, *165*, A2625–A2643. [CrossRef]
47. Davies, T.J.; Tummino, J.J. High-Performance Vanadium Redox Flow Batteries with Graphite Felt Electrodes. *J. Carbon Res.* **2018**, *4*, 8. [CrossRef]
48. Gong, K.; Fang, Q.; Gu, S.; Li, S.F.Y.; Yan, Y. Nonaqueous redox-flow batteries: organic solvents, supporting electrolytes, and redox pairs. *Energy Environ. Sci.* **2015**, *8*, 3515–3530. [CrossRef]
49. Xu, A.; Zhao, T.S.; Shi, L.; Shu, J.B. Lattice Boltzmann Simulation of Mass Transfer Coefficients for Chemically Reactive Flows in Porous Media. *J. Heat Transf.* **2018**, *140*, 052601. [CrossRef]
50. Kok, M.D.R.; Jervis, R.; Tranter, T.G.; Sadeghi, M.A.; Brett, D.J.L.; Shearing, P.R.; Gostick, J.T. Mass transfer in fibrous media with varying anisotropy for flow battery electrodes: Direct numerical simulations with 3D X-ray computed tomography. *Chem Eng. Sci.* **2019**, *196*, 104–115. [CrossRef]
51. García-Salaberri, P.A.; Zenyuk, I.V.; Shum, A.D.; Hwang, G.; Vera, M.; Weber, A.Z.; Gostick, J.T. Analysis of representative elementary volume and through-plane regional characteristics of carbon-fiber papers: diffusivity, permeability and electrical/thermal conductivity. *Int. J. Heat Mass Tran.* **2018**, *127*, 687–703. [CrossRef]
52. Gostick, J.T.; Fowler, M.W.; Pritzker, M.D.; Ioannidis, M.A.; Behra, L.M. In-plane and through-plane gas permeability of carbon fiber electrode backing layers. *J. Power Sources* **2006**, *162*, 228–238. [CrossRef]
53. Wang, Q.; Qu, Z.G.; Jiang, Z.Y.; Yang, W.W. Experimental study on the performance of a vanadium redox flow battery with non-uniformly compressed carbon felt electrode. *Appl. Energy* **2018**, *213*, 293–305. [CrossRef]
54. Hack, J.; García-Salaberri, P.A.; Kok, M.D.R.; Jervis, R.; Shearing, P.R.; Brandon, N.; Brett, D.J.L. X-ray Micro-Computed Tomography of Polymer Electrolyte Fuel Cells: What is the Representative Elementary Area? *J. Electrochem. Soc.* **2020**, *167*, 013545. [CrossRef]
55. García-Salaberri, P.A.; Vera, M.; Iglesias, I. Modeling of the anode of a liquid-feed DMFC: Inhomogeneous compression effects and two-phase transport phenomena. *J. Power Sources* **2014**, *246*, 239–252. [CrossRef]
56. Goshtasbi, A.; García-Salaberri, P.A.; Chen, J.; Talukdar, K.; Sanchez, D.G.; Ersal, T. Through-the-membrane transient phenomena in PEM fuel cells: A modeling study. *J. Electrochem. Soc.* **2019**, *166*, F3154–F3179. [CrossRef]
57. Zhou, X.L.; Zhao, T.S.; Zeng, Y.K.; An, L.; Wei, L. A highly permeable and enhanced surface area carbon-cloth electrode for vanadium redox flow batteries. *J. Power Sources* **2016**, *329*, 247–254. [CrossRef]

58. Chen, L.; He, Y.; Tao, W.Q.; Zelenay, P.; Mukundan, R.; Kang, Q. Pore-scale study of multiphase reactive transport in fibrous electrodes of vanadium redox flow batteries. *Electrochim. Acta* **2017**, *248*, 425–439. [CrossRef]
59. Marschewski, J.; Brenner, L.; Ebejer, N.; Ruch, P.; Michel, B.; Poulikakos, D. 3D-printed fluidic networks for high-power-density heat-managing miniaturized redox flow batteries. *Energy Environ. Sci.* **2017**, *10*, 780–787. [CrossRef]
60. Reed, D.; Thomsen, E.; Li, B.; Wang, W.; Nie, Z.; Koepfel, B.; Sprenkle, V. Performance of a low cost interdigitated flow design on a 1 kW class all vanadium mixed acid redox flow battery. *J. Power Sources* **2016**, *306*, 24–31. [CrossRef]
61. Wang, C.; Zhang, Q.; Lu, J.; Shen, S.; Yan, X.; Zhu, F.; Cheng, X.; Zhang, J. Effect of height/width-tapered flow fields on the cell performance of polymer electrolyte membrane fuel cells. *Int. J. Hydrogen Energy* **2017**, *42*, 23107–23117. [CrossRef]
62. Mancusi, E.; Fontana, É.; Augusto Ulson de Souza, A.; Guelli Ulson de Souza, S.M.A. Numerical study of two-phase flow patterns in the gas channel of PEM fuel cells with tapered flow field design. *Int. J. Hydrog. Energy* **2014**, *39*, 2261–2273. [CrossRef]
63. Liu, H.C.; Yan, W.M.; Soong, C.Y.; Chen, F.; Chu, H.S. Reactant gas transport and cell performance of proton exchange membrane fuel cells with tapered flow field design. *J. Power Sources* **2006**, *158*, 78–87. [CrossRef]
64. Akhtar, N.; Kerkhof, P.J.A.M. Dynamic behavior of liquid water transport in a tapered channel of a proton exchange membrane fuel cell cathode. *Int. J. Hydrog. Energy* **2011**, *36*, 3076–3086. [CrossRef]
65. Kok, M.D.R.; Khalifa, A.; Gostick, J.T. Multiphysics Simulation of the Flow Battery Cathode: Cell Architecture and Electrode Optimization. *J. Electrochem. Soc.* **2016**, *163*, A1408–A1419. [CrossRef]
66. Tsushima, S.; Suzuki, T. Modeling and Simulation of Vanadium Redox Flow Battery with Interdigitated Flow Field for Optimizing Electrode Architecture. *J. Electrochem. Soc.* **2020**, *167*, 020553. [CrossRef]
67. Zhao, J.; Shahgaldi, S.; Alaefour, I.; Xu, Q.; Li, X. Gas permeability of catalyzed electrodes in polymer electrolyte membrane fuel cells. *Appl. Energy* **2018**, *209*, 203–210. [CrossRef]
68. Pezeshki, A.M.; Sacci, R.L.; Delnick, F.M.; Aaron, D.S.; Mench, M.M. Elucidating effects of cell architecture, electrode material, and solution composition on overpotentials in redox flow batteries. *Electrochim. Acta* **2017**, *229*, 261–270. [CrossRef]
69. Wong, A.A.; Aziz, M.J.; Rubinstein, S. Direct Visualization of Electrochemical Reactions and Comparison of Commercial Carbon Papers in operando by Fluorescence Microscopy Using a Quinone-Based Flow Cell. *ECS Trans.* **2017**, *77*, 153–161. [CrossRef]
70. Zhang D.; Forner-Cuenca, A.; Oluwadamilola, O.T.; Vladimir, Y.; Brushett, F.R.; Brandon, N.P.; Gu, S.; Cai, Q. Elucidating effects of cell architecture, electrode material, and solution composition on overpotentials in redox flow batteries. *J. Power Sources* **2020**, *447*, 227249. [CrossRef]



© 2020 by the authors. Licensee MDPI, Basel, Switzerland. This article is an open access article distributed under the terms and conditions of the Creative Commons Attribution (CC BY) license (<http://creativecommons.org/licenses/by/4.0/>).

Article

# CFD Modeling and Experimental Validation of an Alkaline Water Electrolysis Cell for Hydrogen Production

Jesús Rodríguez and Ernesto Amores \*

Centro Nacional del Hidrógeno (CNH2), Prolongación Fernando El Santo s/n,  
13500 Puertollano, Ciudad Real, Spain; [jesus.rodriguez@cnh2.es](mailto:jesus.rodriguez@cnh2.es)

\* Correspondence: [ernesto.amores@cnh2.es](mailto:ernesto.amores@cnh2.es); Tel.: +34-926-420-682

Received: 19 November 2020; Accepted: 9 December 2020; Published: 11 December 2020

**Abstract:** Although alkaline water electrolysis (AWE) is the most widespread technology for hydrogen production by electrolysis, its electrochemical and fluid dynamic optimization has rarely been addressed simultaneously using Computational Fluid Dynamics (CFD) simulation. In this regard, a two-dimensional (2D) CFD model of an AWE cell has been developed using COMSOL® software and then experimentally validated. The model involves transport equations for both liquid and gas phases as well as equations for the electric current conservation. This multiphysics approach allows the model to simultaneously analyze the fluid dynamic and electrochemical phenomena involved in an electrolysis cell. The electrical response was evaluated in terms of polarization curve (voltage vs. current density) at different operating conditions: temperature, electrolyte conductivity, and electrode-diaphragm distance. For all cases, the model fits very well with the experimental data with an error of less than 1% for the polarization curves. Moreover, the model successfully simulates the changes on gas profiles along the cell, according to current density, electrolyte flow rate, and electrode-diaphragm distance. The combination of electrochemical and fluid dynamics studies provides comprehensive information and makes the model a promising tool for electrolysis cell design.

**Keywords:** energy storage; green hydrogen; alkaline water electrolysis; polarization curve; void fraction; CFD analysis; numerical simulation; renewable energy

## 1. Introduction

The current fossil fuel-based energy system has to face the most important challenge of our time: climate change. The energy transition to a zero-carbon model requires an ambitious growth plan for renewable energies [1]. However, renewable energy sources (mainly wind and solar power) involve a critical issue that needs to be addressed [2]; their dependence on weather conditions makes them very intermittent, causing a mismatch between supply and demand. Furthermore, in the medium-long term, it is expected that these discrepancies can produce failures in the electricity grid. So, to prevent these problems, adequate energy storage systems are required.

Regarding long-term storage of renewable energies, only chemical energy carriers can be considered nowadays as real solution. Among them, hydrogen has been identified as the best candidate because it can be more efficiently produced from renewable energy surplus in combination with water electrolysis [3]. Furthermore, hydrogen can be transported by its own hydrogen distribution grid as admixture in the natural gas grid, or it can be also stored in appropriate facilities. When required, hydrogen can be efficiently transformed into electricity by fuel cells and returned to the electricity grid or used as fuel for the transport sector or even for new industrial processes [4,5]. In this way, electrolysis enables large scale production of green hydrogen and electrical energy storage.

With respect to water electrolysis, different technologies are commercially available: alkaline, proton exchange membrane (PEM) and solid oxide (SO) electrolysis cells, according to the electrolyte used. Among them, alkaline water electrolysis (AWE) stands out as being a highly developed technology in the industry and the main way to obtain “green hydrogen”. Compared to other technologies, the key advantages of alkaline electrolysis are its proven durability, maturity, and low specific costs. Nowadays, electrolyzers are commercially available in the MW range, offering high hydrogen production capacities. The cost of alkaline electrolysis systems is currently in the range of 600–1000 €/kW at the MW level. Regarding the disadvantages, these are mainly the low current densities and the problems derived from working in dynamic conditions. In practice, hydrogen production is limited to an operating range of 20% to 100% of the nominal power in order to prevent the formation of flammable mixtures due to gas diffusion (crossover) through the diaphragm at very low current densities ( $<0.1 \text{ A/cm}^2$ ) [2,6–8].

For these reasons, the research and development efforts in this technology are mainly focused on increasing the current density and solving the problems derived from working in dynamic conditions. The fluctuations in power supplies to the electrolyzer could cause problems such as the generation of explosive mixtures, corrosion of materials, lower efficiency, pressure drops, and temperature changes, etc. Therefore, the design of alkaline electrolyzers powered by renewable energy is a critical issue [9]. In this sense, the optimization of the cell design and the space between electrodes is a fundamental step to reduce ohmic overpotentials and increase the nominal current density of the electrolyzer [6,10,11].

Therefore, in the last few decades, a significant effort has been made to model, characterize, and analyze the operation of alkaline electrolyzers [2]. In this sense, Olivier et al. [12] conducted an exhaustive and comprehensive analysis of the existing modelling works concerning low temperature electrolysis systems. Therefore, numerous empirical and semi-empirical models have been proposed. One of the most widely used models was proposed by Ulleberg [13], which provides a mathematical description of the polarization curve with parameters fitted empirically. However, these models usually do not include geometric aspects, nor are they capable of modelling those effects that depend on the complete design of the cell.

In this context, Computational Fluid Dynamics (CFD) simulation is a critical and powerful design tool that can be used to improve flow distribution and minimize energy consumption, allowing efficient electrolyte inlet and gas removal from the cell as soon as possible [9]. CFD models allow for the description of thermal, electrochemical, and fluid dynamic phenomena that occur at the same time, from a multiphysics perspective, according to the considered cell geometry. In this way, the voltage required to carry out electrolysis, the generation of  $\text{H}_2/\text{O}_2$  bubbles at the electrodes, the flow distribution within each electrolysis cell, and the heat generation according to current density are some of the processes that happen simultaneously in an electrolyzer during its operation.

However, few analytical models based on CFD simulation that describe the behavior of alkaline electrolysis cells have been reported and validated. With this in mind, Aldas [14] applied a two-phase mathematical model to the numerical investigation of gas evolution in a vertical electrochemical cell using the PHOENICS computer code. In other work, Mat et al. [15] investigated the hydrogen evolution, flow field, and current density distribution in an electrochemical cell using a two-phase flow model. The predicted results satisfactorily agreed with data available in the literature. Later, Hawkes et al. [16] used a three-dimensional (3D) CFD electrochemical model to study a high-temperature electrolysis stack using the commercial code FLUENT. Alternatively, Hreiz et al. [17] simulated bubble hydrodynamics on vertical plane electrodes using an Euler–Lagrange CFD approach, and the results were compared with gas velocity fields obtained by a Particles Image Velocimetry (PIV) algorithm, which were in good agreement. Later, El-Askary et al. [18] modeled the hydrodynamics characteristics of the hydrogen evolution process to predict the flow characteristics, gas release rate, and void fraction distribution in electrolysis cells; subsequently, an experimental study was also carried out to verify the calculations made. Zarghami et al. [19] used an Euler–Euler model in FLUENT to simulate the multiphase flow in an alkaline water electrolyzer and compared the results to existing experimental data. Recently,

Le Bideau et al. [20] developed a two-phase hydrodynamics model and validated the results with the experimental velocity profiles measured using the Laser Doppler Velocimetry (LDV) method.

Considering the increasing industrial development of water electrolysis that is expected in the coming years [21], it is crucial to consider the effect of renewable energies on the performance of electrolyzers. For these reasons, in the present paper, a two-dimensional (2D) CFD model of an alkaline electrolysis cell implemented in COMSOL is reported based on a work previously published by the authors [9]. The aim of the work is to show the capacity of the model to predict the behavior of the electrolysis cell under different operational conditions and also show how it can influence its performance. Thus, a novel CFD model that simultaneously simulates the electrochemical and fluid dynamic behavior is described, taking a real alkaline water electrolysis cell as a reference. In this way, the response of an AWE cell is simulated under different temperatures and electrolyte concentrations. Polarization curve and gas-liquid fraction can be analyzed at the same time using the presented model. Furthermore, the model shows a wide versatility regarding geometrical parameters, being able to consider the effect of modifying the electrode-diaphragm distance. In order to evaluate the accuracy of the model, simulated results were validated against the real response of the AWE cell at different operating conditions, reporting a very good agreement with a mean relative absolute difference error lower than 1%. In addition, fluid dynamics phenomena such as gas-liquid distribution, turbulence, or formed gas profile were predicted. Therefore, the capacity to simulate both phenomena (electrochemistry and fluid dynamics) in the same model make it a complete design tool.

## 2. Methodology: Modeling and Experimental

### 2.1. Alkaline Water Electrolysis

Water electrolysis deals with decomposition of water into hydrogen and oxygen by passing an electric current (DC) between two electrodes separated by an aqueous electrolyte with high ionic conductivity [22]. The overall reaction for water splitting is:



Figure 1 shows a scheme of an alkaline electrolysis cell. The two electrodes (anode and cathode) are immersed in a KOH aqueous solution (electrolyte), and they are separated by a porous diaphragm that allows the ionic transport ( $OH^-$ ) but is impermeable to gases. In a typical operation, electrolyte enters into the anodic and cathodic compartments by the bottom inlets. At the anode, oxygen bubbles are produced and, at the cathode, hydrogen is generated. These bubbles grow until they detach from the electrode surface. The mixture of generated gases and electrolyte then leaves each compartment through the upper outlets [9].

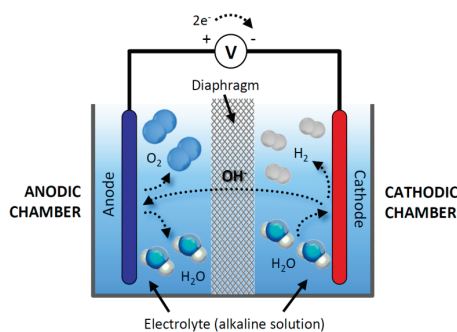
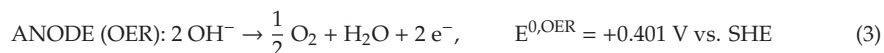


Figure 1. General scheme and operation of an alkaline electrolysis cell [6].

In this way, in an alkaline electrolysis cell, when the required potential between the electrodes is applied, the following semi-reactions take place simultaneously in the cathode (hydrogen evolution reaction (HER)) and anode (oxygen evolution reaction (OER)) [6]:



Thus, for alkaline water electrolysis to occur, a minimum voltage is required (reversible voltage,  $U_{rev}$ ), which, according to the semi-reactions potential ( $E^0$ ) from Equations (2) and (3), is equal to 1.23 V ( $E^{0,\text{OER}} - E^{0,\text{HER}}$ ) at standard conditions (1 bar and 25 °C). This value, in agreement with the second law of thermodynamics, corresponds to  $\Delta g^\circ = 273.2 \text{ kJ/mol}$ .

However, the real cell voltage ( $U$ ) is always higher than the latter because of irreversibilities or overpotentials. Therefore, the real cell voltage can be defined as the sum of reversible voltage ( $U_{rev}$ ) and the overpotentials ( $\eta$ ), as shown in Equation (4):

$$U = U_{rev} + \sum \eta \quad (4)$$

The term  $\sum \eta$  is the sum of activation, ohmic, and concentration overpotentials. These overpotentials are defined as follows [23]:

- (1) Activation overpotentials: related to activation energies of hydrogen and oxygen formation reactions on the surface of electrodes;
- (2) Ohmic overpotentials: sum of the electrical resistance of several components such as electrodes, current collectors, etc., and the transport resistance related to gas bubbles, ionic transfer in the electrolyte, and resistivity of the diaphragm;
- (3) Concentration overpotentials: due to mass-transport limitations occurring on the surface of the electrodes at high currents.

The total contribution of these overpotentials to the cell voltage ( $U$ ) can be analyzed through the polarization curve of an electrolysis cell, as represented in Figure 2.

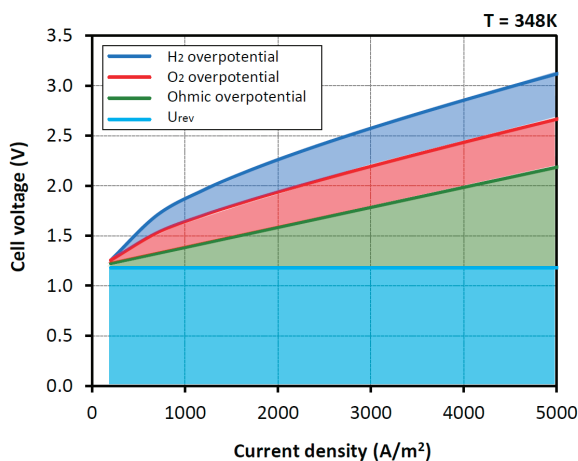


Figure 2. Graphical representation of a polarization curve with the contribution of each overpotential.

## 2.2. CFD Modeling of an Alkaline Electrolysis Cell

### 2.2.1. Model Geometry and Mesh

As mentioned previously in Figure 1, a conventional alkaline water electrolysis cell is divided into two compartments separated by a diaphragm. In the cathodic chamber, the reduction of water to produce  $H_2$  takes place, and the oxygen evolution reaction occurs at the anode. The function of the diaphragm is to avoid the mixture of the two gases while maintaining a low resistivity.

Taking as reference a rectangular laboratory electrolysis cell (Figure 3a), the geometry of the model was built following fluid dynamic requirements. In this way, simplifications were made in order to reduce the model complexity (Figure 3b). As result, a good approximation can be made just by 2D geometry, which allows an optimal study of the main involved variables (Figure 3c). The electrode surfaces (33 mm height) were considered by two simple boundary conditions (1 and 5 in Figure 3c) on both sides of the cell. These domains work as current collectors where potential was applied. Regarding the separator (3 in Figure 3c), it was introduced in the geometry as a thin rectangle (0.5 mm) that separates both compartments. In this case, only ionic conductivity is allowed in this component. Concerning the anodic and cathodic compartments (2 and 4 in Figure 3c), they were defined as two thick rectangles (1.5, 4, or 10 mm depending on the model considered) between the separator and the corresponding electrode with the electrolyte inlet at the bottom and the biphasic mixture (electrolyte and gases) outlet at the top.

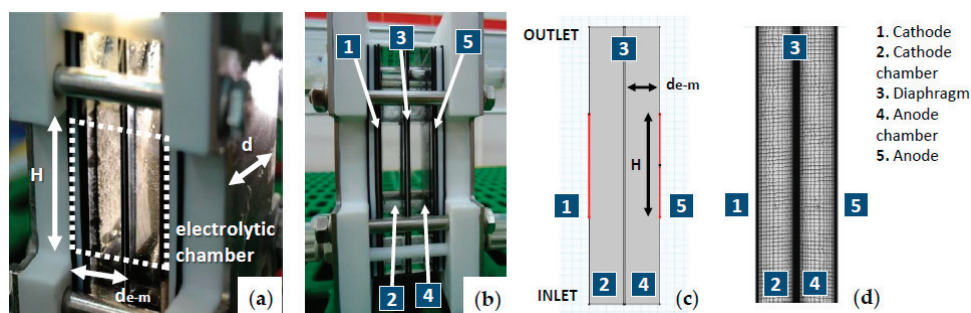


**Figure 3.** Alkaline electrolysis cell used in the model: (a) Detail image of the electrolysis cell; (b) Main components; (c) Simplified geometry and control domain; (d) Mesh applied in the model.

Regarding the meshing of the control domain, a rectangular mesh was generated, taking advantage of the regular geometry of the cell, with a total of 7200 elements (when the electrode-diaphragm distance was 10 mm). Previously, a mesh independence study was carried out in order to determine the number of nodes and elements that should be used. In the anode and cathode chamber, a maximum element size of 0.8 mm was established, reducing this value to 0.1 mm in the diaphragm domain (these values in the mesh were scaled when the electrode-diaphragm distance decreased from 10 mm to 1.5 mm). Furthermore, at the boundary of the electrodes and on the surfaces between the diaphragm and the electrolytic chambers, inflation layers were incorporated to correctly model the effects that take place in these contours (Figure 3d).

### 2.2.2. Mathematical Procedure and Governing Equations

As previously mentioned, the proposed model is based on previous work carried out by the authors [9] using the CFD simulation program COMSOL Multiphysics v4.3a. In this way, the model has been built using the “electric currents” module to calculate both the current distribution and the polarization curve, and the “two-phase turbulent bubbly flow” module was used to study the generation and distribution of gas, one for each electrolytic chamber. An implicit backward differentiation formula

(BDF) method was used for the numerical integration of the differential equations. The tolerance was fixed at 0.001 in the solver to control the absolute error.

The coupling between the electrochemical and fluid dynamic results was linked by the current density. The intensity supplied to the electrolysis cell allows the electric field to be resolved and at the same time determines the generation of hydrogen and oxygen. The gas formation in the cell is studied by means of the conservation equations for the biphasic mixture (hydrogen/electrolyte in cathode and oxygen/electrolyte in anode) that solves, among other variables, the fraction of gas ( $\Phi_g$ ) in each electrolytic chamber. This fraction of gas is used in each instance to determine how the conductivity of the electrolyte varies and again to resolve the electric field inside the cell.

### Electrical Current Conservation

The electric charge transport was studied using the “electric currents” module of COMSOL, which solves the current conservation problem ( $J$  in  $A/m^2$ ) for the scalar electric potential ( $U$  in V). For time dependent studies, the equation takes the following form [24]:

$$\nabla \cdot \vec{J} = Q_j \Rightarrow -\nabla \cdot \left[ \sigma (\nabla U) - \frac{\partial \vec{D}}{\partial t} - \vec{J}_e \right] \cdot d = Q_j \cdot d \quad (5)$$

where  $\sigma$  (S/m) is the equivalent electrical conductivity,  $Q$  ( $A/m^3$  in a 3D approximation) is the current source and  $J_e$  ( $A/m^2$ ) is the externally generated current density. Regarding the electric displacement ( $\vec{D}/\partial t$ ), it is a constitutive relation that describes the macroscopic properties of the medium. Otherwise, in planar 2D, it is assumed that the model has symmetry and the electric potential varies only in the “x” and “y” directions and is constant in the “z” direction. This implies that the electric field is tangential to the “xy” plane. To solve it, the thickness in the “z” direction (electrode depth) is introduced in the equation by the parameter  $d$  (m) [24], as shown in Figure 3a.

On the other hand, to define the equivalent electrical conductivity ( $\sigma$ ), the following three equations were incorporated to define the conductivity of the medium (electrolyte) and the diaphragm (see parameters in Table 1):

**Table 1.** Constants, initial, and boundary conditions for the two-dimensional (2D) model [25–28].

Symbol	Value	Unit	Description
$d_{e-m}$	1.5 to 10	mm	Electrode-diaphragm distance
$F$	96485	C	Faraday constant
$i$	250 to 4000	$A \cdot m^{-2}$	Current density (polarization curve)
$i_{0,c}$	21.1 to 93.5	$A \cdot m^{-2}$	Exchange current density (cathode) [25]
$i_{0,a}$	1.1 to 9.3	$A \cdot m^{-2}$	Exchange current density (anode) [26]
$M_{H_2}$	2	$g \cdot mol^{-1}$	Hydrogen molecular weight
$M_{O_2}$	32	$g \cdot mol^{-1}$	Oxygen molecular weight
$p$	1	bar	Pressure operation
$R$	8.314	$J \cdot K^{-1} \cdot mol^{-1}$	Ideal gas constant
$T$	303 to 343	K	Temperature operation
$v_0$	700	$ml \cdot min^{-1}$	Electrolyte flow rate (inlet velocity)
$w$	5 to 10	M	Electrolyte concentration (22–42 wt% KOH)
$\alpha_a$	0.60	-	Charge transfer coefficient (anode)
$\alpha_c$	0.77	-	Charge transfer coefficient (cathode)
$\varepsilon_m$	0.55	-	Diaphragm porosity [27]
$\tau_m$	1.89	-	Diaphragm tortuosity [28]



1. An empirical relationship for specific conductivity of electrolyte ( $\sigma_0$  in S/m) with respect to temperature ( $T$ ) and KOH concentration ( $w$ ) was used [29]:

$$\sigma_0 = -204.1 \cdot w - 0.28 \cdot w^2 + 0.5332 \cdot (w \cdot T) + 20720 \cdot \frac{w}{T} + 0.1043 \cdot w^3 - 0.00003 \cdot (w^2 \cdot T^2) \quad (6)$$

2. The conductivity of the diaphragm ( $\sigma_m$  in S/m) was defined as a function of the conductivity of electrolyte ( $\sigma_0$ ) and geometric parameters such as porosity ( $\varepsilon_m$ ) and tortuosity ( $\tau_m$ ), according to [28]:

$$\sigma_m = \sigma_0 \cdot \frac{\varepsilon_m}{\tau_m} \quad (7)$$

3. The Bruggeman equation ( $\sigma_e$  in S/m) relates the variation of conductivity of electrolyte ( $\sigma_0$ ) with the volume fraction of gas ( $\Phi_g$ ) inside the cell [30]. The gas fraction for both electrolytic chambers at each current density value was calculated according to the equations described in the “liquid-gas flow distribution” section:

$$\sigma_e = \sigma_0 \cdot (1 - \Phi_g)^{1.5} \quad (8)$$

Finally, according to Equation (5), the electric transport charges on the electrodes were not considered (only ionic transport was studied inside the electrolysis cell). In order to incorporate the activation overpotentials and the reversible voltage at different temperatures in the polarization curve, the following two auxiliary equations, whose parameters are defined in Table 1, were introduced into the model (as boundary conditions in the electrode):

1. The reversible potential ( $U_{rev}$  in V) was defined according to the LeRoy et al. [31] equation as a function of temperature ( $T$ ):

$$U_{rev} = 1.5184 - 1.5421 \cdot 10^{-3} \cdot T + 9.523 \cdot 10^{-5} \cdot T \cdot \ln(T) + 9.84 \cdot 10^{-8} \cdot T^2 \quad (9)$$

2. Activation overpotentials ( $\eta_{act}$  in V) were defined for the cathode and the anode by the Butler–Volmer equation (Tafel equation form) for each current density ( $i$ ), according to:

$$\eta_{act} = 2.3 \cdot \frac{R \cdot T}{\alpha \cdot F} \cdot \log\left(\frac{i}{i_0}\right) \quad (10)$$

### Liquid-Gas Flow Distribution

The gas and liquid flow distribution was modeled, applying the “two-phase turbulent bubbly flow” module of COMSOL. This mathematical approach describes the two-phase flow using an Euler-Euler model. The module solves the volume fraction occupied by each of the two phases, without defining each bubble in detail. This mathematical approach is suitable for modeling the macroscopic behavior of many gas bubbles rising through a liquid. It treats the two phases as interpenetrating media, tracking the averaged concentration of the phases. One velocity field is associated with each phase, and the dynamics of each of the phases are described by a momentum balance equation and a continuity equation [9,32].

Based on these assumptions, the sum of the momentum equations for the two phases gives a momentum equation for the liquid velocity, a continuity equation, and a transport equation for the volume fraction of the gas phase. The momentum equation is [32]:

$$\begin{aligned} \Phi_l \cdot \rho_l \cdot \frac{\partial \vec{u}_l}{\partial t} + \Phi_l \cdot \rho_l \cdot (\vec{u}_l \cdot \nabla) \vec{u}_l \\ = -\nabla p + \nabla \cdot \left[ \Phi_l \cdot (\psi_l + \psi_T) \cdot \left( \nabla \vec{u}_l + \nabla \vec{u}_l^T - \frac{2}{3} \cdot (\nabla \vec{u}_l) \cdot \vec{I} \right) \right] + \Phi_l \cdot \rho_l \cdot \vec{g} + \vec{F} \end{aligned} \quad (11)$$

where  $u$  is velocity (m/s),  $p$  is the pressure (Pa),  $\Phi$  is the phase volume fraction,  $\rho$  is the density (kg/m<sup>3</sup>),  $g$  is the gravity vector (m/s<sup>2</sup>),  $F$  is any additional volume force (N/m<sup>3</sup>),  $\psi_l$  is the dynamic viscosity of the liquid (Pa·s), and  $\psi_T$  is the turbulent viscosity (Pa·s). The subscripts “l” and “g” denote quantities related to the liquid phase and the gas phase, respectively [32].

The continuity equation is:

$$\frac{\partial}{\partial t}(\Phi_l \rho_l + \Phi_g \rho_g) + \nabla \cdot (\Phi_l \rho_l \vec{u}_l + \Phi_g \rho_g \vec{u}_g) = 0 \quad (12)$$

And the transport of the volume fraction of gas is given by Equation (13):

$$\frac{\partial \Phi_g \rho_g}{\partial t} + \nabla \cdot (\Phi_g \rho_g \vec{u}_g) = -\dot{m}_{gl} \quad (13)$$

where  $\dot{m}_{gl}$  is the mass transfer rate from gas to liquid (g·m<sup>-3</sup>·s<sup>-1</sup>). In the simplified 2D geometry considered in this study, the gas flows generated (g·m<sup>-2</sup>·s<sup>-1</sup>) on the active surfaces of the electrodes (H<sub>2</sub> and O<sub>2</sub>) were defined by the Faraday equation for each current density ( $i$ ):

$$\dot{m}_{H_2} = \frac{M_{H_2}}{2 \cdot F} \cdot i \quad (14)$$

$$\dot{m}_{O_2} = \frac{M_{O_2}}{4 \cdot F} \cdot i \quad (15)$$

Table 1 summarizes the parameters corresponding to Equation (14) for hydrogen production (boundary condition at cathode) and to Equation (15) for oxygen production (boundary condition at the anode).

Regarding the turbulence, a  $k - \varepsilon$  model was used. This model solves two extra transport equations for two additional variables: the turbulent kinetic energy,  $k$  (m<sup>2</sup>/s<sup>2</sup>), and the dissipation rate of turbulent energy,  $\varepsilon$  (m/s<sup>3</sup>). The turbulent viscosity ( $\psi_T$ ), the transport equations for the turbulent kinetic energy ( $k$ ), and the evolution of the turbulent energy's dissipation ( $\varepsilon$ ) are defined as [32]:

$$\psi_T = \rho_l C_\mu \frac{k^2}{\varepsilon} \quad (16)$$

$$\rho_l \frac{\partial k}{\partial t} - \nabla \cdot \left[ \left( \psi + \frac{\psi_T}{\Phi_k} \right) \nabla k \right] + \rho_l \vec{u}_l \cdot \nabla k = \frac{1}{2} \psi_T \left( \nabla \vec{u}_l + (\nabla \vec{u}_l)^T \right)^2 - \rho_l \varepsilon + S_k \quad (17)$$

$$\begin{aligned} \rho_l \frac{\partial \varepsilon}{\partial t} - \nabla \cdot \left[ \left( \psi + \frac{\psi_T}{\Phi_\varepsilon} \right) \nabla \varepsilon \right] + \rho_l \vec{u}_l \cdot \nabla \varepsilon \\ = \frac{1}{2} C_{\varepsilon 1} \frac{\varepsilon}{k} \psi_T \left( \nabla \vec{u}_l + (\nabla \vec{u}_l)^T \right)^2 - \rho_l C_{\varepsilon 2} \frac{\varepsilon^2}{k} + \frac{\varepsilon}{k} C_\varepsilon S_k \end{aligned} \quad (18)$$

where  $C_\varepsilon$ ,  $C_\mu$ ,  $\Phi_k$ , and  $\Phi_\varepsilon$  are constants of the turbulent model. The term  $S_k$  is related to the bubble-induced turbulence. Finally, the gas velocity ( $\vec{u}_g$  in m/s) is calculated according to:

$$\vec{u}_g = \vec{u}_l + \vec{u}_{slip} + \vec{u}_{drift} \quad (19)$$

where  $\vec{u}_{slip}$  is the relative velocity between the phases and  $\vec{u}_{drift}$  is an additional contribution from the turbulence model used [32].

### 2.2.3. Initial and Boundary Conditions

To solve the different equations described above, the following simplifications were considered in order to improve convergence and reduce the computational cost of the model [5,9,32]:

- (1) The gas density is negligible compared to the liquid density;
- (2) The movement of gas bubbles in relation to the liquid phase is determined by a balance between viscous drag and pressure forces;
- (3) The two phases share the same pressure field;
- (4) Hydrogen and oxygen crossover through the diaphragm is negligible;
- (5) The electrolysis cell works with a high enough flow rate of electrolyte to avoid the accumulation of gas bubbles in the cell;
- (6) The bubbles have a diameter of less than 1 mm, so the Hadamard–Rybczynski drag law for spherical gas bubbles in liquid is used for the gas velocity;
- (7) The electrical resistance of the electrodes (Ni) is negligible with respect to the rest of the elements of the electrolysis cell.

Figure 4 shows the boundary conditions implemented in this study. Regarding the different materials used in the model, the COMSOL material library was used to define hydrogen, oxygen, and water. In the latter case, the density and dynamic viscosity were also corrected to take into account the KOH dissolution (electrolyte). Table 1 summarizes, the different parameters and constants considered in the model.

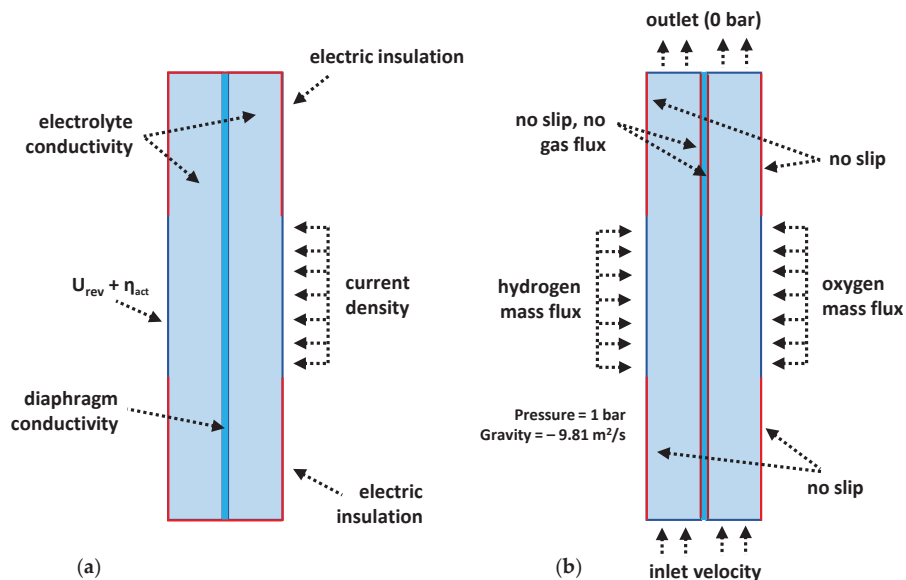


**Figure 4.** Initial and boundary conditions for the 2D Computational Fluid Dynamics (CFD) model of the alkaline electrolysis cell: (a) Electrochemical model; (b) Fluid dynamic model.

Regarding the charge transfer coefficient ( $\alpha$ ), it is worth noting that 0.5 is the value usually reported in most of the models in which electrochemical kinetics are considered. According to the literature [33], this value is usually used in the absence of actual measurements. However,  $\alpha$ , in most systems, turns out to be between 0.3 and 0.7 [33]. In this work, as can be seen from Table 1, 0.60 and 0.77 were used for anodic and cathodic reactions, respectively. These values were chosen because they reported the best fit with the experimental values. In the case of the anode,  $\alpha_a$  is in the common experimental range. On the other hand, the cathodic charge transfer coefficient ( $\alpha_c = 0.77$ ) is slightly higher than the upper limit of the usually experimental range. However, this value well agrees with experimental values reported by authors working on alkaline water electrolysis [34]. In fact, some authors [35] working with real electrolysis stacks have noted that  $\alpha$  cannot be considered as a constant, because it

varies with temperature, electrode materials, etc., and, thus, it is expected to change even with the experimental system. Furthermore, differences are expected when  $\alpha$  is determined in an electrochemical laboratory cell than when it is done in a real water electrolysis cell or even a commercial stack.

### 2.3. Experimental Test Facility and Methodology

#### 2.3.1. Alkaline Water Electrolysis Test-Bench

Figure 5 shows the alkaline water electrolysis test bench used in this study, located in the *Centro Nacional del Hidrógeno* ([www.cnh2.es](http://www.cnh2.es)). The system is constituted by all the elements of a typical electrolyzer, but on a laboratory scale, which allows for the study of a wide range of parameters. Therefore, the system is suitable for analyzing electrochemical and fluid dynamic processes.

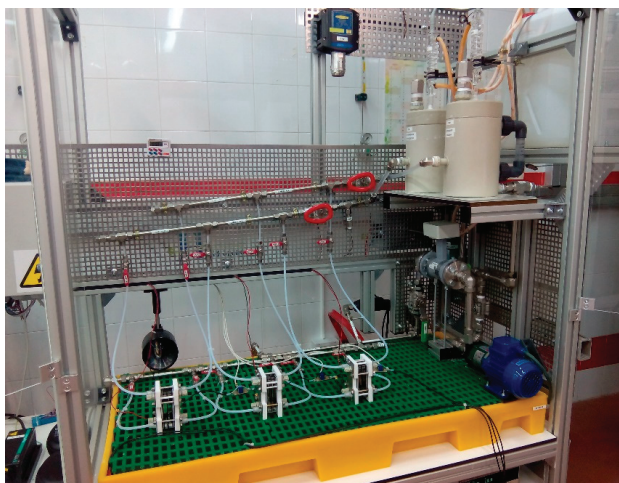


**Figure 5.** Alkaline water electrolysis cell test bench of the *Centro Nacional del Hidrógeno*.

As can be seen in Figure 5, the test bench has three electrolysis cells (ELECTROCELL, Micro Flow Cell) that are electrically connected in series, a DC power supply (Elektro-Automatik, EA-PSI 6000), a centrifugal magnetic drive pump (IWAKI, MD-30RVM-220N), two gas-liquid separators to separate the oxygen and hydrogen produced from the electrolyte and a heating system (Hillesheim, H300 DN12). Additionally, the facility has different measurement and control devices that are monitored by a Supervisory Control and Data Acquisition (SCADA) system [10].

#### 2.3.2. Experimental Protocol

The polarization curves were obtained according to a previously established experimental procedure [5,10]. These curves describe the electrochemical behavior of an electrolysis cell and allow determination of the values of voltage and current in which it works. For this purpose, several temperatures (from 30 to 70 °C) were tested. The electrolyte used in the test bench was a concentrated KOH solution in water (from 22 to 42 wt% KOH), and the overall flow rate was fixed at 1.4 l/min per cell. Regarding the electrodes, Ni > 99% was used for the anodes and cathodes. In all cases, the active area was 10 cm<sup>2</sup>. The diaphragms used were Zirfon® Perl 500 UTP (AGFA) with a pore size of 0.15 μm and a thickness of 500 μm [10]. The electrode-diaphragm distance was fixed from 1.5 to 10 mm according to the case considered (see Figure 3b).

For each of the tests, the following protocol was used: Once the cell was assembled, both the electrolyte pump and the heating system were turned on. Once the flow rate and temperature were stable, the power supply was switched on and a gradual current sweep from 50 to 400 mA/cm<sup>2</sup> was

performed. For each current intensity value, different operating parameters, such as the cell voltage to obtain the different polarization curves, were monitored and recorded [5,10].

### 3. Results and Discussion

#### 3.1. Polarization Curve

The electrochemical response of the model was validated by comparing simulated polarization curves ( $U_{cell}^{model}$ ) against those experimentally obtained for the electrolysis cell ( $U_{cell}^{test}$ ). The accuracy of the CFD model was also studied by varying some of the most critical operating parameters in an alkaline water electrolysis system. Additionally, the mean relative absolute difference error ( $MRAD_{error}$ ) was calculated according to Equation (20) in order to ensure the accuracy and validity of the proposed model [5]:

$$MRAD_{error} = \frac{1}{N} \cdot \sum_{j=1}^N \left( \frac{U_{cell}^{model} - U_{cell}^{test}}{U_{cell}^{test}} \right) \quad (20)$$

The error calculated was lower than 0.51%, which indicates an excellent correlation between the experimental and modeled results. Figure 6 shows a parity chart between the model and the experimental voltage results. From this figure, it is confirmed that the main discrepancy between the model and real data occurs at low current densities (corresponding to the lowest voltages in the polarization curve). In this zone, activation overpotentials represent the major contribution to the energy required for the electrolysis process. In other words, at these potentials the cathodic and anodic reactions are the limiting steps and, thus, it can be considered that the differences are related to electro-kinetics. In the model, the main electrochemical kinetics parameters involved are  $i_0$  and  $\alpha$ . It is well known [35] that both concepts strongly depend on operating conditions (temperature, pressure, reaction, electrode material, etc.). While the influence of  $i_0$  has been widely studied on electrolysis [25,26,35], the charge transfer coefficient has not been treated in much detail. In fact, as described above, in the literature, typically a constant value of 0.5 is given to  $\alpha$  for both reactions. In the present work, different values of  $i_0$ , depending on temperature and reaction, have been used (see Table 1). In the case of  $\alpha$ , although in the model different values were used for oxidation and reduction, these chosen values were constant for all the operating conditions. The use of these approximations, instead of the real value for each temperature, can be the cause of the discussed deviations at low current densities. Nevertheless, it is worth noting that, despite these differences, the error reported value is very low and the model works satisfactory, as shown in the following sections.

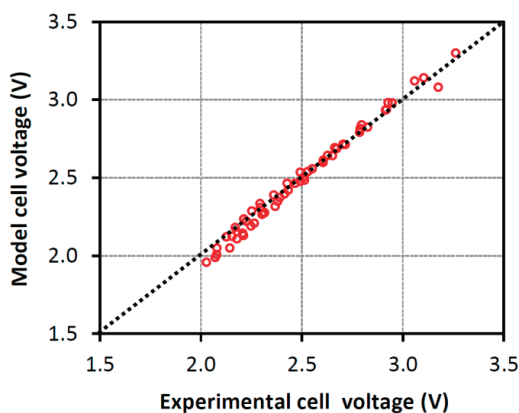


**Figure 6.** Parity chart between the model and experimental voltage results for all the conditions of temperature, electrolyte conductivity, and electrode-diaphragm distance analyzed.

### 3.1.1. Influence of Temperature

Polarization curves simulated by the model were compared with experimental ones in Figure 7, at different temperatures. As expected, the cell potential at a certain current density value decreases as temperature increases within the analyzed range (Figure 7a). This trend is due to the fact that an increase in temperature favors the reaction kinetics, decreasing the reversible voltage and therefore the required energy. This behavior was previously reported by other authors for AWE systems [2,5,10,13,22,23]. From Figure 7b, it is evidenced that the best correlation between experimental and calculated results can be seen at 30 °C, 50 °C, and 70 °C.

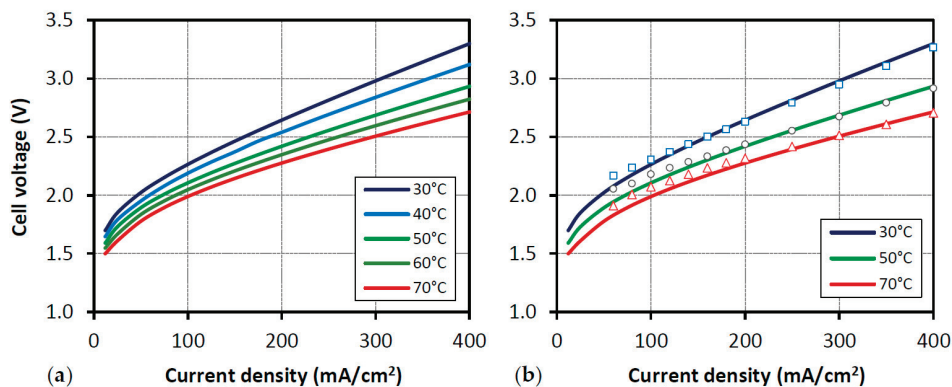


**Figure 7.** Polarization curve at different temperatures (30–70 °C) at 32 wt% KOH, 10 mm, and 1.4 l/min: (a) model; (b) model vs. experimental electrolysis cell voltage. Experimental data are indicated with dots.

### 3.1.2. Influence of Electrolyte Conductivity

Electrolyte conductivity is a parameter that has a significant effect on the ohmic overpotential. As described from Equation (6) to Equation (8), it is a critical aspect to determine not only the electrolyte ohmic losses, but also those related to diaphragm and generated gas bubbles in both cathodic and anodic compartments. In the case of the diaphragm, it must be taken into account that it is just a physical barrier, without ionic or electronic conductivity, so its conductivity is determined by the conductivity of the electrolyte inside the diaphragm channels. Regarding the gas bubbles, when H<sub>2</sub> and O<sub>2</sub> are generated, a biphasic mixture gas-electrolyte is formed, in which the gas fraction is a non-conductor. The greater the number of gas bubbles in this biphasic mixture, the greater the fraction of gas ( $\Phi_g$ ). As a result, the electrolyte conductivity will be lower according to Equation (8), especially in the close electrode region.

In Figure 8, the polarization curves for different electrolyte concentration values calculated with the model are compared with those experimentally obtained. From this figure, the following points are discussed:

- (1) As previously reported [10], increasing the electrolyte conductivity implies a better electrolysis performance due to a reduction of ohmic losses, which turns out in a lower required energy.
- (2) An optimum value of electrolyte concentration is identified at 32 wt% KOH, which corresponds to 94.54 S/m at 50 °C [29]. Above this value, mass transfer limitations can occur, but below it, the ohmic losses are too high because the electrolyte conductivity is very low [29].
- (3) The model shows an accurate agreement with the experimental polarization curves for the different electrolyte conductivity values considered (Figure 8b).

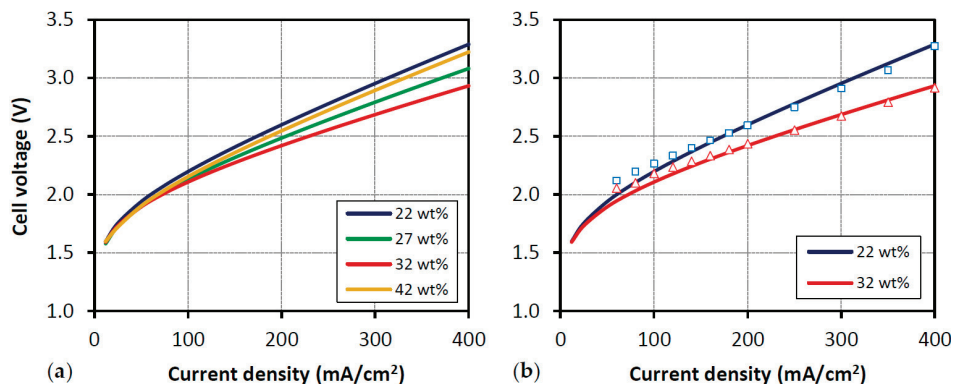


**Figure 8.** Polarization curve at different electrolyte concentrations (22–42 wt% KOH) at 50 °C, 10 mm, and 1.4 l/min: (a) model; (b) model vs. experimental electrolysis cell voltage. Experimental data are indicated with dots.

### 3.1.3. Influence of Electrode-Diaphragm Distance

In AWE cells, the ohmic overpotential is strongly affected by the proximity of the electrode to the diaphragm. The reason for this is that a reduction of this distance means a lower quantity of electrolyte between both components, and thus the ohmic contribution of this compartment decreases. However, very narrow cells can favor high gas fraction during the electrolysis, which can result in a significant increasing of ohmic overpotential. Hence, it seems reasonable that there is an optimal electrode-diaphragm distance to achieve the best AWE cell performance. In fact, several works have calculated this optimum distance [11,36].

Figure 9 shows the simulated and experimental polarization curves when different electrode-diaphragm distances were used, for an electrolyte flow rate of 1.4 l/min. The tendency of the modeled curves well coincide with the real ones; the decrease of the distance between electrode and diaphragm leads to a lower electrolysis potential.

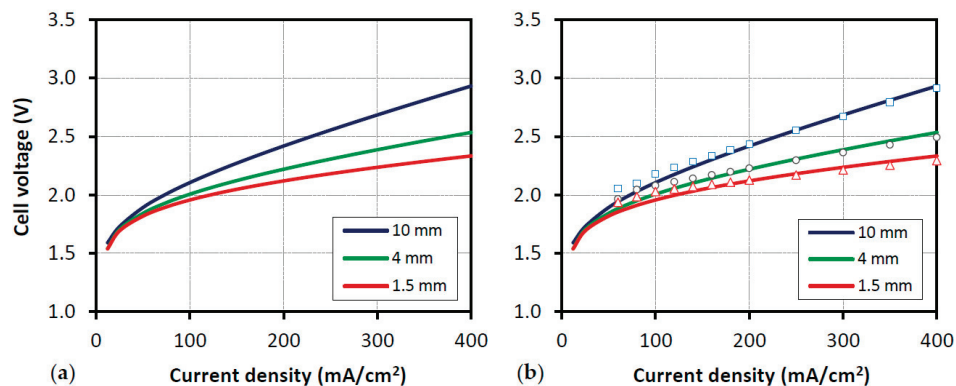


**Figure 9.** Polarization curve at different electrode-diaphragm distances (1.5–10 mm) at 50 °C, 32 wt% KOH, and 1.4 l/min: (a) model; (b) model vs. experimental electrolysis cell voltage. Experimental data are indicated with dots.

### 3.2. Gas Generation Profile

Evolution of gas profile with current density is shown in Figure 10. Hydrogen and oxygen void fractions (space occupied by gas bubbles in each electrolytic chamber) draw a typical profile next to the electrode surface [17,18,37,38]: void fraction progressively increases from the bottom to the top of the electrode due to the accumulation of generated gas and the effect of the flow rate [15].

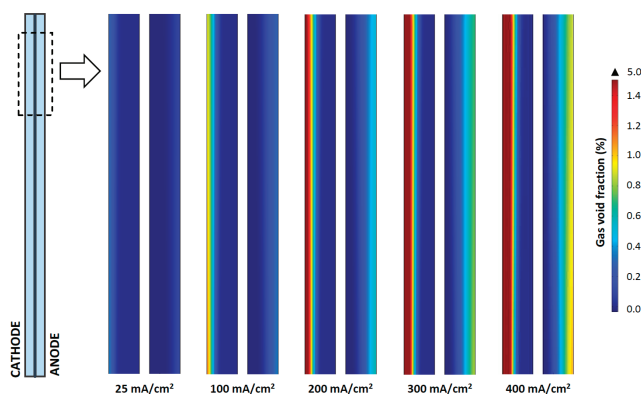


**Figure 10.** Void fraction distribution in cathodic and anodic compartments at different current density values (model conditions: 50 °C, 32 wt% KOH, 1.5 mm, and 1.4 l/min).

Hydrodynamic characteristics of the biphasic flow (generated gas/electrolyte) in the AWE cell strongly influence the performance of the system. In these systems the generated gas bubbles have a multiple and critical role. On one hand, when they are produced, bubbles form a curtain of increasing thickness along the surface of the electrode in a vertical direction, causing a turbulence phenomenon that contributes to the mixing and distribution of present species and so too to mass transfer. On the other hand, when bubbles are produced, they can adhere to some sections of the electrode surface, making them inactive for electrochemical reaction. This causes an increase in the ohmic overpotential, a higher required energy and, as a result, a worse cell performance [19].

According to the previous discussion, the model results show that gas fraction reaches the highest value next to the electrode surface ( $x = 0$  cm) and it decreases towards the diaphragm ( $x = 0.15$  cm) for all studied current densities (Figure 11). In addition to the expected increase in the fraction of gas with the current, from this graph it can also be deduced that the higher the current density, the greater the penetration of gas in the lateral direction, due to the increase in the lateral gas velocity [14].

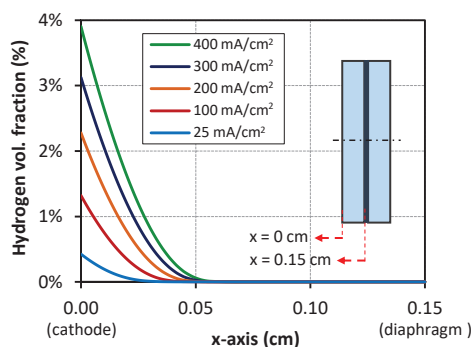


**Figure 11.** Hydrogen fraction distribution at different current densities in the  $x$ -axis at the middle of the electrode height (model conditions: 50 °C, 32 wt% KOH, 1.5 mm, and 1.4 l/min).



#### 4. Conclusions and Future Work

In the present work, the development and experimental validation of an alkaline water electrolysis cell 2D CFD model was reported. The strong points of the model are its versatility to simulate different operating conditions as well as the simultaneous analysis of fluid dynamic and electrochemical phenomena. These aspects make it a powerful and cheap design tool, particularly suitable for the study of new cell configurations.

Regarding the variation of electrolysis parameters, the response of the model was evaluated in terms of polarization curves at different values of temperature, electrode-diaphragm distance, and electrolyte concentration. Performance of the electrolysis cell was improved for high temperatures, small electrode-diaphragm distances, and high electrolyte conductivity, as observed from both experimental and simulated data. In this regard, the mean relative absolute difference error was calculated in order to ensure the accuracy and validity of the proposed model. The error calculated was lower than 0.51% for the polarization curve, which indicates an excellent correlation between the experimental and modeled results. Therefore, the proposed model is suitable for predicting the behavior of the AWE cell under a wide range of operating conditions.

In addition to electrochemical studies, the proposed model also offers a fluid dynamic analysis. From simulation results, it was concluded that produced gases generate a “curtain profile” in the electrode, increasing the void fraction in a vertical direction due to the accumulation of gas. Furthermore, the model simulates the gas profile along the  $x$ -axis of the electrolytic chamber (from the electrode to the diaphragm), proving that the higher the current, the greater the gas distribution in the electrolytic chamber space. These results provide very useful information for cell design purposes.

On the other hand, although the results confirm that the model well fits the experimental results, various points still need to be studied:

- (1) Charge transfer coefficient ( $\alpha$ ): the influence of this term over the performance of real electrolysis systems has hardly been studied. Even though it is possible to find different values in the literature, some authors have claimed significant differences when working with a laboratory electrochemical cell and with an electrolysis stack. Experimental values up to 1.035 [35] have been reported, which contrast with that which is considered to be the common range (0.3–0.7). In fact, it greatly depends on operating conditions: electrode materials, electrolyte, etc. For these reasons, it would be very interesting to experimentally determine this parameter in the test bench shown in Figure 5 in order to improve the accuracy of the model, especially in the activation overpotentials zone where the model fits worse with real data. This is extensible to exchange current density, which is another critical kinetic parameter.
- (2) Zero-gap cell design: this is one of the most extended alkaline water electrolysis cell designs in commercial systems. This configuration allows us to “ideally” eliminate bubbles between the electrodes because cathode and anode are placed directly over the diaphragm. For this to happen, the electrodes have to be porous. Therefore, in order to improve the model applicability to real systems, this geometry should be implemented in the model, making it a more useful design tool.

**Author Contributions:** Conceptualization, J.R. and E.A.; methodology, E.A. and J.R.; software, J.R. and E.A.; Validation, E.A.; formal analysis, J.R.; data curation, E.A. and J.R.; writing—original draft preparation, J.R. and E.A.; writing—review and editing, E.A. and J.R. All authors have read and agreed to the published version of the manuscript.

**Funding:** This research was funded by *Ministerio de Ciencia e Innovación* (MICINN, Spain), *Junta de Comunidades de Castilla-La Mancha* (JCCM, Spain) and *European Regional Development Fund* (ERDF), in the framework of the project entitled “Singular and Strategic Project of Renewable Hydrogen” (PSEH2RENOV, n° 120000-2009-3).

**Conflicts of Interest:** The authors declare no conflict of interest. The funders had no role in the design of the study; in the collection, analyses, or interpretation of data; in the writing of the manuscript, and in the decision to publish the results.

## References

1. Armaroli, N.; Balzani, V. Solar electricity and solar fuels: Status and perspectives in the context of the energy transition. *Chem. Eur. J.* **2016**, *22*, 32–57. [CrossRef]
2. Sánchez, M.; Amores, E.; Rodríguez, L.; Clemente-Jul, C. Semi-empirical model and experimental validation for the performance evaluation of a 15 kW alkaline water electrolyzer. *Int. J. Hydrog. Energy* **2018**, *43*, 20332–20345. [CrossRef]
3. Mais, L.; Palmas, S.; Mascia, M.; Sechi, E.; Casula, M.F.; Rodriguez, J.; Vacca, A. Porous Ni photocathodes obtained by selective corrosion of Ni-Cu films: Synthesis and photoelectrochemical characterization. *Catalysts* **2019**, *9*, 453. [CrossRef]
4. Rodríguez, J.; Rojas, N.; Sánchez-Molina, M.; Rodríguez, L.G.; Campana, R.; Rodríguez, L. Hybrid membranes based in Nafion-metallic oxides: Performance evaluations. *Chem. Eng. Trans.* **2016**, *47*, 415–420. [CrossRef]
5. Amores, E.; Rodríguez, J.; Oviedo, J.; de Lucas-Consuegra, A. Development of an operation strategy for hydrogen production using solar PV energy based on fluid dynamic aspects. *Open Eng.* **2017**, *7*, 141–152. [CrossRef]
6. Amores, E.; Sánchez, M.; Rojas, N.; Sánchez-Molina, M. Renewable hydrogen production by water electrolysis. In *Sustainable Fuel Technologies Handbook*, 1st ed.; Dutta, S., Hussain, C.M., Eds.; Academic Press: London, UK, 2021; pp. 271–313. [CrossRef]
7. Lehner, M.; Tichler, R.; Steinmüller, H.; Koppe, M. *Power-To-Gas: Technology and Business Models*, 1st ed.; Springer: Cham, Switzerland, 2014. [CrossRef]
8. Bertuccioli, L.; Chan, A.; Hart, D.; Lehner, F.; Madden, B.; Standen, E. *Development of Water Electrolysis in the European Union*. FCH-JU Funded Studies 2014: Element Energy, E4tech Sarl. Available online: [https://www.fch.europa.eu/sites/default/files/FCHJUElectrolysisStudy\\_FullReport%20\(ID%20199214\).pdf](https://www.fch.europa.eu/sites/default/files/FCHJUElectrolysisStudy_FullReport%20(ID%20199214).pdf) (accessed on 10 November 2020).
9. Amores, E.; Rodríguez, J.; Merino, C.; García, P. Study of an alkaline electrolyzer powered by renewable energy. In Proceedings of the COMSOL Conference, Stuttgart, Germany, 26–28 October 2011; COMSOL AB: Burlington, VT, USA, 2011.
10. Amores, E.; Rodríguez, J.; Carreras, C. Influence of operation parameters in the modeling of alkaline water electrolyzers for hydrogen production. *Int. J. Hydrog. Energy* **2014**, *39*, 13063–13078. [CrossRef]
11. Nagai, N.; Takeuchi, M.; Nakao, M. Influences of bubbles between electrodes onto efficiency of alkaline water electrolysis. In Proceedings of the PSFVIP-4, Chamonix, France, 3–5 June 2003.
12. Olivier, P.; Bourasseau, C.; Bouamama, B. Low-temperature electrolysis system modelling: A review. *Renew. Sustain. Energy Rev.* **2017**, *78*, 280–300. [CrossRef]
13. Ulleberg, Ø. Modeling of advanced alkaline electrolyzers: A system simulation approach. *Int. J. Hydrog. Energy* **2003**, *28*, 21–33. [CrossRef]
14. Aldas, K. Application of a two-phase flow model for hydrogen evolution in an electrochemical cell. *Appl. Math. Comput.* **2004**, *154*, 507–519. [CrossRef]
15. Mat, M.D.; Aldas, K.; Ilegbusi, O.J. A two-phase flow model for hydrogen evolution in an electrochemical cell. *Int. J. Hydrog. Energy* **2004**, *29*, 1015–1023. [CrossRef]
16. Hawkes, G.; O'Brien, J.; Stoots, C.; Hawkes, B. 3D CFD model of a multi-cell high-temperature electrolysis stack. *Int. J. Hydrog. Energy* **2009**, *34*, 4189–4197. [CrossRef]
17. Hreiz, R.; Abdelouahed, L.; Fünfschilling, D.; Lopicque, F. Electrogenerated bubbles induced convection in narrow vertical cells: PIV measurements and Euler–Lagrange CFD simulation. *Chem. Eng. Sci.* **2015**, *134*, 138–152. [CrossRef]
18. El-Askary, W.A.; Sakr, I.M.; Ibrahim, K.A.; Balabel, A. Hydrodynamics characteristics of hydrogen evolution process through electrolysis: Numerical and experimental studies. *Energy* **2015**, *90*, 722–737. [CrossRef]
19. Zarghami, A.; Deen, N.G.; Vreman, A.W. CFD modeling of multiphase flow in an alkaline water electrolyzer. *Chem. Eng. Sci.* **2020**, *227*, 115926–115935. [CrossRef]
20. Le Bideau, D.; Mandin, P.; Benbouzid, M.; Kim, M.; Sellier, M.; Ganci, F.; Inguanta, R. Eulerian two-fluid model of alkaline water electrolysis for hydrogen production. *Energies* **2020**, *13*, 3394. [CrossRef]
21. Hydrogen Roadmap Europe, FCH-JU 2019. Available online: [https://www.fch.europa.eu/sites/default/files/Hydrogen%20Roadmap%20Europe\\_Report.pdf](https://www.fch.europa.eu/sites/default/files/Hydrogen%20Roadmap%20Europe_Report.pdf) (accessed on 10 November 2020).

22. Divisek, J. Water electrolysis in a low- and medium-temperature regime. In *Electrochemical Hydrogen Technologies: Electrochemical Production and Combustion of Hydrogen*; Wendt, H., Ed.; Elsevier: Oxford, UK, 1990; pp. 137–212.
23. Zeng, K.; Zhang, D. Recent progress in alkaline water electrolysis for hydrogen production and applications. *Prog. Energy Combust. Sci.* **2010**, *36*, 307–326. [CrossRef]
24. *AC/DC Module User's Guide v4.3. Part n° CM020101*; COMSOL AB: Stockholm, Sweden, 2012.
25. Kibria, M.F.; Mridha, M.S.; Khan, A.H. Electrochemical studies of a nickel electrode for the hydrogen evolution reaction. *Int. J. Hydrog. Energy* **1995**, *20*, 435–440. [CrossRef]
26. Kibria, M.F.; Mridha, M.S. Electrochemical studies of the nickel electrode for the oxygen evolution reaction. *Int. J. Hydrog. Energy* **1996**, *21*, 179–182. [CrossRef]
27. AGFA: Zirfon H2 Advanced. Available online: <https://www.agfa.com/specialty-products/solutions/membranes/zirfon/> (accessed on 30 October 2020).
28. Rodríguez, J.; Palmas, S.; Sánchez-Molina, M.; Amores, E.; Mais, L.; Campana, R. Simple and precise approach for determination of ohmic contribution of diaphragms in alkaline water electrolysis. *Membranes* **2019**, *9*, 129. [CrossRef]
29. Gilliam, R.J.; Graydon, J.W.; Kirk, D.W.; Thorpe, S.J. A review of specific conductivities of potassium hydroxide solutions for various concentrations and temperatures. *Int. J. Hydrog. Energy* **2007**, *32*, 359–364. [CrossRef]
30. Weijs, M.P.M.G.; Janssen, L.J.J.; Visser, G.J. Ohmic resistance of solution in a vertical gas-evolving cell. *J. Appl. Electrochem.* **1997**, *27*, 371–378. [CrossRef]
31. LeRoy, R.L.; Bowen, C.T.; LeRoy, D.J. The thermodynamics of aqueous water electrolysis. *J. Electrochem. Soc.* **1980**, *127*, 1954–1962. [CrossRef]
32. *Chemical Engineering Module User's Guide v3.5a. Part n° CM020501*; COMSOLAB: Stockholm, Sweden, 2008.
33. Bard, A.J.; Faulkner, L.R. *Electrochemical Methods: Fundamentals and Applications*, 2nd ed.; John Wiley & Sons: New York, NY, USA, 2001.
34. Santos, D.M.F.; Sequeira, C.A.C.; Macciò, D.; Saccone, A.; Figuereido, J.L. Platinum–rare earth electrodes for hydrogen evolution in alkaline water electrolysis. *Int. J. Hydrog. Energy* **2013**, *38*, 3137–3145. [CrossRef]
35. Tijani, A.S.; Kamarudin, N.A.B.; Mazlan, F.A.B. Investigation of the effect of charge transfer coefficient (CTC) on the operating voltage of polymer electrolyte membrane (PEM) electrolyzer. *Int. J. Hydrog. Energy* **2018**, *43*, 9119–9132. [CrossRef]
36. Nagai, N.; Takeuchi, M.; Oka, T. Existence of optimum space between electrodes on hydrogen production by water electrolysis. *Int. J. Hydrog. Energy* **2003**, *28*, 35–41. [CrossRef]
37. Sasaki, T.; Nagai, N.; Murai, Y.; Yamamoto, F. Particle image velocimetry measurement of bubbly flow induced by alkaline water electrolysis. In Proceedings of the PSFVIP-4, Chamonix, France, 3–5 June 2003.
38. Aldas, K.; Pehlivanoglu, N.; Mat, M.D. Numerical and experimental investigation of two-phase flow in an electrochemical cell. *Int. J. Hydrog. Energy* **2008**, *33*, 3668–3675. [CrossRef]

**Publisher's Note:** MDPI stays neutral with regard to jurisdictional claims in published maps and institutional affiliations.



© 2020 by the authors. Licensee MDPI, Basel, Switzerland. This article is an open access article distributed under the terms and conditions of the Creative Commons Attribution (CC BY) license (<http://creativecommons.org/licenses/by/4.0/>).

## Article

# Research on High-Pressure Hydrogen Pre-Cooling Based on CFD Technology in Fast Filling Process

Sen Li <sup>1,2,3</sup>, Jinxing Guo <sup>4</sup>, Xin Lv <sup>1,2,3</sup>, Teng Deng <sup>1,2,3</sup>, Bo Cao <sup>1,2,3</sup> and Juan Wang <sup>1,2,3,\*</sup>

<sup>1</sup> School of Mechanical & Electrical Engineering, Xi'an University of Architecture and Technology, Xi'an 710055, China; xauatsenli@163.com (S.L.); lvxinALZN123@163.com (X.L.); dengteng2021@126.com (T.D.); xauatbocao@163.com (B.C.)

<sup>2</sup> Shaanxi Key Laboratory of Nanomaterials and Nanotechnology, Xi'an University of Architecture and Technology, Xi'an 710055, China

<sup>3</sup> Xi'an Key Laboratory of Clean Energy, Xi'an University of Architecture and Technology, Xi'an 710055, China

<sup>4</sup> Xi'an Aerospace Propulsion Institute, Xi'an 710100, China; guomalevenus@163.com

\* Correspondence: juanwang@xauat.edu.cn

**Abstract:** In the fast filling process, in order to control the temperature of the vehicle-mounted storage tank not to exceed the upper limit of 85 °C, it is an effective method to add a hydrogen pre-cooling system upstream of the hydrogenation machine. In this paper, Fluent is used to simulate the heat transfer process of high-pressure hydrogen in a shell-and-tube heat exchanger and the phase change process of refrigerant R23. The accuracy of the model is proven by a comparison with the data in the references. Using this model, the temperature field and gas volume fraction in the heat transfer process are obtained, which is helpful to analyze the heat transfer mechanism. At the same time, the influence of hydrogen inlet temperature, hydrogen inlet pressure, and refrigerant flow rate on the refrigeration performance was studied. The current work shows that the model can be used to determine the best working parameters in the pre-cooling process and reduce the operating cost of the hydrogen refueling station.

**Keywords:** hydrogen refueling station; hydrogen pre-cooling system; computational fluid dynamics (CFD); shell and tube heat exchanger

**Citation:** Li, S.; Guo, J.; Lv, X.; Deng, T.; Cao, B.; Wang, J. Research on High-Pressure Hydrogen Pre-Cooling Based on CFD Technology in Fast Filling Process. *Processes* **2021**, *9*, 2208. <https://doi.org/10.3390/pr9122208>

Academic Editor: Alfredo Iranzo

Received: 30 October 2021

Accepted: 26 November 2021

Published: 8 December 2021

**Publisher's Note:** MDPI stays neutral with regard to jurisdictional claims in published maps and institutional affiliations.



**Copyright:** © 2021 by the authors. Licensee MDPI, Basel, Switzerland. This article is an open access article distributed under the terms and conditions of the Creative Commons Attribution (CC BY) license (<https://creativecommons.org/licenses/by/4.0/>).

## 1. Introduction

Hydrogen energy is a potentially clean energy with high energy density and is pollution-free [1–3]. As a secondary energy source, hydrogen can be obtained directly from fossil raw materials, or it can be produced by electrolyzing water from renewable energy sources (such as solar energy, wind energy, etc.) [2,3]. The development of a hydrogen energy economy can reduce the emission of greenhouse gases and small particle pollutants, and at the same time achieve energy diversification. It is a potential substitute for ordinary fossil energy carriers [4]. Therefore, various countries around the world have regarded hydrogen energy as the strategic development direction of new energy source in the future.

In the field of transportation, hydrogen fuel cell vehicles have received widespread attention in recent years. Due to the high cost of acquiring and using liquid hydrogen, the current hydrogen storage methods used in hydrogen fuel cell vehicles utilize gaseous hydrogen storage. Hydrogen is the smallest known gas in the world, as the density of hydrogen is only 1/14 that of air, namely at one standard atmospheric pressure and 0 °C, hydrogen density is 0.089 g/L. To improve the cruising range of fuel cell vehicles, it is necessary to increase the storage pressure in the onboard storage tank [5,6]. At the same time, more than 80% of hydrogen refueling stations use high-pressure gaseous hydrogen storage [7]. To improve the competitiveness of hydrogen fuel cell vehicles, the filling process needs to be completed within 3–5 min [8,9]. However, in the process of rapid filling, the temperature of the storage tank rises rapidly as the pressure of the onboard

storage tank rises. The increase in tank temperature is mainly caused by the following three main thermodynamic phenomena [10]. First of all, the kinetic energy of the fast-flowing hydrogen converted into internal energy gas generates a lot of heat during the filling process. Secondly, the hydrogen expanded through the throttle valve causes the temperature to rise, which is called the Joule–Thomson effect. Third, the compression of hydrogen during the filling process of the storage tank will also cause the temperature to rise, and the increase in temperature not only reduces the storage capacity of the hydrogen tank, but may also bring potential safety hazards. Therefore, it is necessary to adopt appropriate means to control the temperature not to exceed the limit.

To ensure safety during the rapid filling process, the SAE J2601 filling agreement stipulates that the temperature of hydrogen in the onboard storage tank during the rapid filling process cannot exceed 85 °C [11,12]. There are two main reasons for setting the upper-temperature limit of 85 °C: The first is to protect the tank material from thermal degradation, and the second is to be able to fill the storage tank to the maximum without exceeding the maximum working pressure (125% of the nominal working pressure). In the research of Ortiz et al. [13], it is shown that the inlet temperature of hydrogen plays a vital role in the increase of the temperature of the vehicle-mounted storage tank during the rapid filling process. The hydrogen pre-cooling system is the most effective way to control the temperature of hydrogen [14].

Among various heat exchangers, the shell-and-tube heat exchanger (STHX) has the advantages of a reliable structure, mature technology, and wide application range, and it has been widely used in various industries [15–18]. The shell and tube heat exchanger is a very important part of the pre-cooling system, and its working parameters directly affect the effect of hydrogen pre-cooling. At the same time, in the heat exchange process of the shell-and-tube heat exchanger, the refrigerant R23 has phase change heat transfer and two-phase flow problems, which has a vital impact on the heat transfer efficiency and service life of the heat exchanger itself. With the development of computer technology, more and more numerical simulation techniques are applied to the heat transfer research of heat exchangers. Compared with experimental research methods, numerical simulation methods better facilitate the simulation of more complex or ideal working conditions. The software can obtain the fluid flow distribution field, temperature field, and velocity vector field, etc., which makes the research on the heat exchanger and its heat transfer clearer, more convenient, and faster [19]. Therefore, the effective and reasonable use of numerical simulation research will help promote the further development of heat exchanger flow and heat transfer research.

In the past, research on heat exchangers mainly focused on the study of single-phase flow, while there are few studies on the two-phase flow and heat transfer of the fluid medium in the presence of phase change heat transfer. This paper aims at analyzing the phase change heat transfer and two-phase flow through numerical simulation in the heat exchange process of high-pressure hydrogen in the shell-and-tube heat exchanger. The phase change process of refrigerant R23 was simulated using the evaporation and condensation model of the commercial fluid mechanics software Fluent 19.0 [20].

In this study, a simplified two-dimensional model of a shell-and-tube heat exchanger was simulated using CFD technology. After the grid is divided, the appropriate turbulence model and discretization scheme are selected, before the simulation is carried out by changing the hydrogen inlet temperature, the hydrogen inlet pressure, and the flow rate of the refrigerant. Through the cloud diagram and numerical curve obtained by simulation, the influence of working parameters on the pre-cooling effect is explained in detail. This provides a certain reference for selecting suitable working parameters when the pre-cooling system of the hydrogen refueling station is running and reducing the operating cost of the hydrogen refueling station.

## 2. Modeling Details

For large-scale hydrogen refueling stations that require high refueling capacity, the heat exchanger in the hydrogen pre-cooling system is a shell-and-tube heat exchanger. The diagram of the pre-cooling system of the hydrogen refueling station is shown in Figure 1. Because the cascade refrigeration system can meet the cooling requirements of  $-30\text{ }^{\circ}\text{C}\sim-55\text{ }^{\circ}\text{C}$  [21], combined with the research of Sun et al. [22], R404 a is selected as the high-temperature refrigerant, and R23 is selected as the low-temperature refrigerant in the low-temperature cycle. The shell-and-tube heat exchanger in the low-temperature system is a heat exchange device for high-pressure hydrogen and refrigerant R23. Therefore, the main content of this paper addresses the heat exchange process of the shell-and-tube heat exchanger during operation.

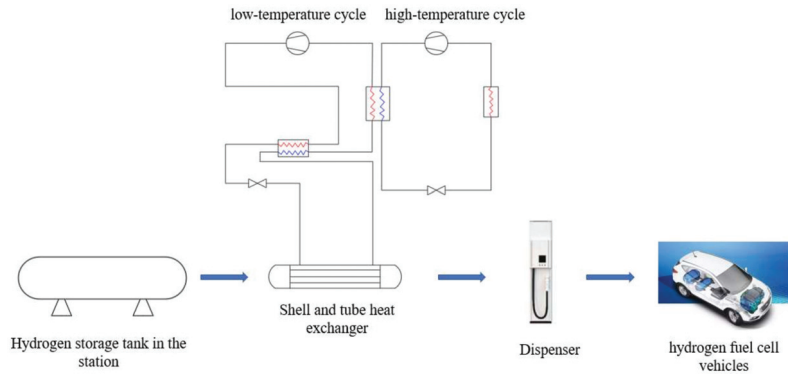


**Figure 1.** Schematic diagram of hydrogen pre-cooling system in hydrogen refueling station.

The basic principle of the shell and tube heat exchanger is that two fluids flow at different temperatures, separated by the heat exchange tube wall. According to the second law of thermodynamics, there is a temperature difference between the two fluids. Heat is transferred from the fluid with a higher temperature to the fluid with a lower temperature. The heat transfer is achieved through heat conduction and convection heat transfer mechanisms. The heat transfer principle is shown in Figure 2. Figure 2 shows the temperature change of the hot and cold fluid during the heat exchange process.  $t'_1$  and  $t''_1$  represent the inlet and outlet temperature of the hot fluid, and  $t'_2$  and  $t''_2$  represent the inlet and outlet temperature of the cold fluid.

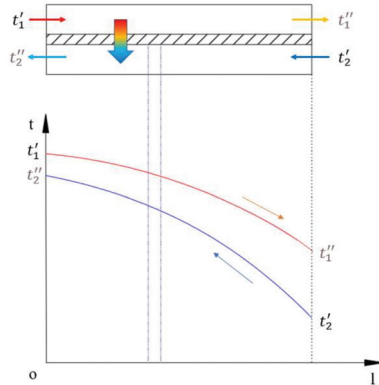


**Figure 2.** Heat transfer principle of shell and tube heat exchanger.

Due to the large difference between the outlet temperature and the inlet temperature of high-pressure hydrogen, if a multi-process shell and tube heat exchanger is used, the high-temperature gas at the inlet will exchange heat with the cooled gas, causing unnecessary cold energy loss. Therefore, this model uses a single-process shell-and-tube heat exchanger in which high-pressure hydrogen flows on the tube side and the refrigerant R23 flows on the shell side. In the heat exchange process, the shell side flow, that is, the flow of refrigerant R23 has a transition from the liquid phase to the gas phase. The commonly used single-curved baffle is shown in Figure 3a. The refrigerant R23 undergoes a phase change when heated, and the gas phase will gather in the area indicated by the arrow in the figure, which reduces the heat transfer performance of the heat exchanger. This article uses the flower (mentioned in [23,24]) type baffle to improve the heat exchange performance in the heat exchange process, as shown in Figure 3b. The material of the heat exchange tube and the shell is 316 L stainless steel. According to the actual working conditions in the heat exchange process, the average temperature difference method is used to design the heat exchanger. The geometric parameters are shown in Table 1. The three-dimensional model of the shell and tube heat exchanger is shown in Figure 4.



**Figure 3.** Single-curved baffle and flower baffle in shell and tube heat exchanger. (a) Single-curved baffle, (b) flower baffle.

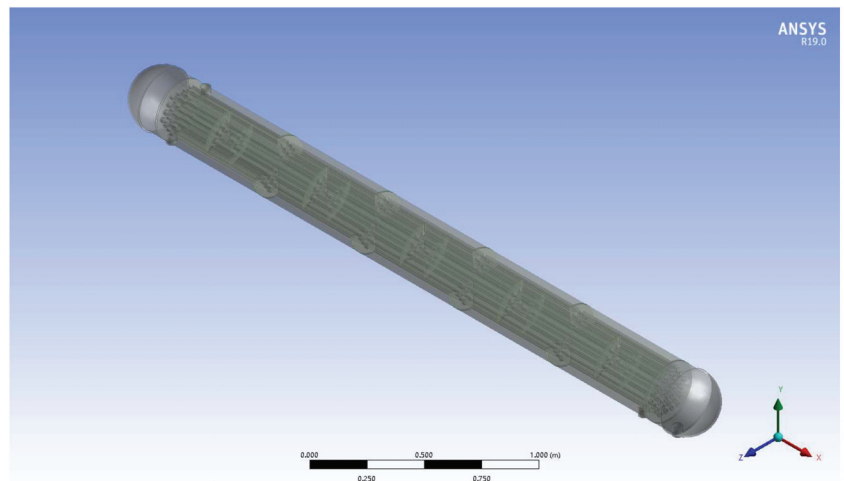


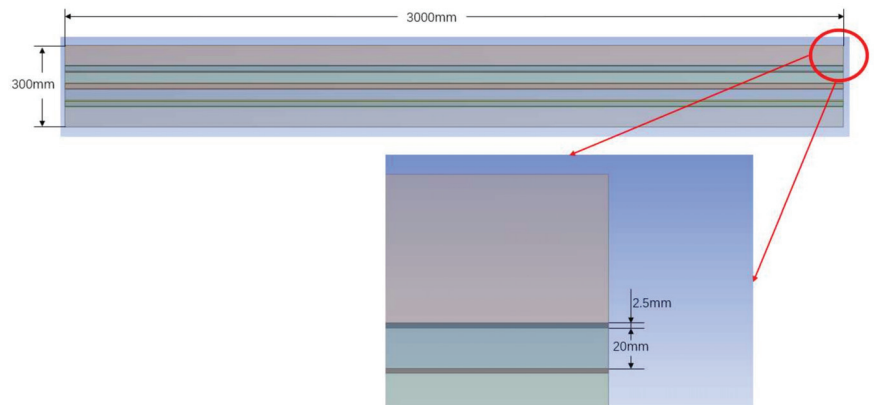
**Figure 4.** Three-dimensional model of shell-and-tube heat exchanger.

**Table 1.** Geometric parameters of the heat exchanger.

Parameter	Value
Length (m)	3.000
Shell inside diameter (m)	0.300
Number of tubes	31
Tube outside diameter (mm)	25
Tube pitch (mm)	37
Tube thickness (mm)	2.500
Tube layout	Triangular arrangement
Baffle form	Flower shape
Number of baffles	9
Spacing of baffles (mm)	300
Number of holes on baffle	14
Shell and tube type	BEM

### 2.1. Two-Dimensional Axisymmetric Model Establishment and Meshing

The physical model is directly established according to the designed heat exchanger parameters, the number of elements reaches tens of millions, the calculation cycle is long, and the requirements for the computer are relatively high. In the hydrogen pre-cooling process, high-pressure hydrogen flows in the heat exchange tube, R23 flows outside the tube, and the cold and hot fluids exchange heat through the tube wall. The two-dimensional axisymmetric model can well simulate the flow of hot and cold fluids and the heat transfer process during flow. Therefore, to facilitate the calculation, the physical model of the heat exchanger is simplified to a two-dimensional axisymmetric model, as shown in Figure 5. In addition, the reason for removing the baffle is that the addition of the baffle to the two-dimensional axisymmetric model will block the flow of refrigerants.

**Figure 5.** Two-dimensional axisymmetric model of the heat exchanger.

The two-dimensional axisymmetric model of the shell-and-tube heat exchanger consists of three regions. The pipeline flow area is a high-pressure hydrogen flow area. The shell side basin is the basin of refrigerant R23. The tube wall is located between the two to exchange heat between hot and cold fluids.

Due to the regular geometric shape and good symmetry of the research object, the mesh function is used to divide the two-dimensional axisymmetric structure grid, and at the same time, the grid is refined near the wall of the heat exchange tube, so that it is enough to capture the evaporation near the wall [25]. To calculate the accuracy, the grid size of the area near the heat exchange tube is set to 0.1 mm, and the grid size of the other areas is set to 2.5 mm. The total number of grids is 282,036. The details of the grid are shown in Figure 6.



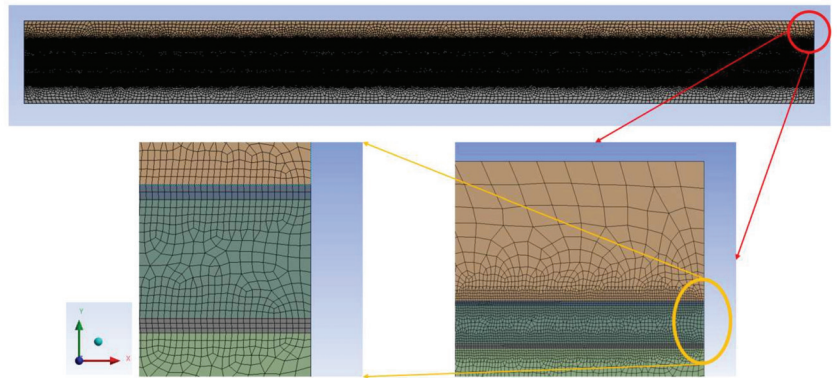


**Figure 6.** Meshing of 2D axisymmetric models.

## 2.2. Basic Assumptions

By solving a series of control equations applied to the micro-control unit, the computational fluid dynamics method can obtain the detailed distribution of the temperature field and various volume fractions, which is helpful to analyze the heat and mass transfer behavior.

According to the heat transfer principle, a theoretical model is established. In the fluid dynamics simulation calculation, the following assumptions are made to simplify the analysis.

- Working fluid is continuous.
- Radiation heat transfer is negligible.
- The density satisfies Boussinesq approximation [26].
- Phase change materials meet the assumptions of homogeneity and isotropy.
- The liquid phase change material is a Newtonian fluid.

## 2.3. Governing Equation

The physical model of the heat exchanger was developed in the commercial computational fluid dynamics software Ansys Fluent 19.0. Together with the control equations described below, it forms the mathematical model of the shell-and-tube heat exchanger.

Mass conservation equation:

$$\frac{\partial \rho}{\partial t} + \nabla \cdot (\rho u) = 0 \quad (1)$$

Momentum conservation equation:

$$\frac{\partial}{\partial t}(\rho u) + \nabla \cdot (\rho u) = -\nabla \cdot p + \nabla \left[ \mu \left( \nabla u + \nabla u^T - \frac{2}{3} \mu \nabla \cdot u \right) \right] + \rho g + F_s \quad (2)$$

where:  $\rho = \varphi_l \rho_l + \varphi_v \rho_v$ ,  $\mu = \varphi_l \mu_l + \varphi_v \mu_v$ ,  $F_S = 2\sigma_{l,v} \times \frac{\varphi_l \rho_l c_v \nabla \varphi_v + \varphi_v \rho_v c_l \nabla \varphi_l}{\rho_l + \rho_v}$ .

Energy conservation equation:

$$\frac{\partial}{\partial t}(\rho E) + \nabla \cdot \left[ u \frac{\partial}{\partial t}(\rho E) + \nabla \cdot [u(\rho E + p)] \right] = \nabla \cdot (k_{eff} \nabla T) + S_E \quad (3)$$

where:  $k_{eff} = \varphi_l k_l + \varphi_v k_v$ ,  $E = \frac{\varphi_l \rho_l E_l + \varphi_v \rho_v E_v}{\varphi_l \rho_l + \varphi_v \rho_v}$ ,  $E_v = c_{Pv} \times (T - T_{sat})$ ,  $E_l = c_{Pl} \times (T - T_{sat})$ .

The heat conduction equation in the solid of the heat pipe wall:

$$\rho_{sol} c_{P_{sol}} \frac{\partial T_{sol}}{\partial t} = k_{sol} \left( \frac{\partial^2 T_{sol}}{\partial x^2} + \frac{\partial^2 T_{sol}}{\partial y^2} \right) \quad (4)$$

where  $\rho$  and  $\rho_{sol}$  are the two-phase mixing density and solid density,  $\text{kg}/\text{m}^3$ ;  $u$  is the speed,  $\text{m}/\text{s}$ ;  $\mu$  is the dynamic viscosity,  $\text{Pa}/\text{s}$ ;  $F_s$  is the surface tension,  $\text{N}$ ;  $\sigma_{l,v}$  is the surface tension coefficient,  $\text{N}/\text{m}$ ;  $c_v$  and  $c_l$  are the surface curvatures;  $k_{eff}$  and  $k_{sol}$  are the two-phase mixed thermal conductivity and solid thermal conductivity, respectively,  $\text{W}/(\text{m}\cdot\text{K})$ ;  $E$  is the mass average internal energy,  $E_v$  and  $E_l$  is the internal energy of the gas and liquid phases,  $\text{J}$ ;  $T$ ,  $T_{sat}$  and  $T_{sol}$  are the two-phase mixing temperature, saturation temperature, and solid wall temperature, respectively,  $\text{K}$ ;  $c_{p_g}$  and  $c_{p_l}$  are the specific constant pressure heat capacities of the gas and liquid phases, respectively,  $\text{J}/(\text{kg}\cdot\text{K})$ ;  $c_{p_{sol}}$  is the specific heat capacity of solid at constant pressure,  $\text{J}/(\text{kg}\cdot\text{K})$ .

#### 2.4. Heat and Mass Transfer Phase Change Model

To reproduce the gas-liquid two-phase flow, the heat exchange of high-pressure hydrogen and refrigerant R23, and the phase change process of refrigerant R23 in heat exchange, the Mixture model and Lee model are used to quantitatively calculate the vapor-liquid phase change heat transfer during evaporation and condensation. The saturation temperature of R23 will change with changes in pressure, but for the stability of the calculation and the rapid convergence of the calculation results, the saturation temperature of R23 is set to 191 K. When the temperature is higher than this value, the calculation unit where the liquid phase is located will perform Evaporate. On the contrary, proceed with the condensation process.

#### 2.5. Initial Conditions and Boundary Conditions

To observe the evaporation and condensation phenomenon faster, the initial temperature of R23 is set to 190.00 K, the flow rate is 0.5 m/s, the initial temperature of high-pressure hydrogen is 298.00 K, and the flow rate is 0.1 m/s. At the initial moment, the shell side fluid is all R23 liquid phase, and the tube side fluid is high-pressure hydrogen. Both the hydrogen inlet and the R23 inlet adopt the velocity inlet boundary, and the hydrogen outlet and the R23 outlet both adopt the pressure outlet boundary. Because in the actual heat exchange process, the outer layer of the heat exchanger is provided with an insulation layer to prevent the heat exchanger from exchanging heat with the external environment and reduce the loss of cooling capacity, the outer wall surface other than the inlet and outlet of the heat exchanger is set as an adiabatic boundary. The impermeable, non-slip adiabatic wall boundary conditions are used for the heat exchange tube wall. The physical parameters of the cold and hot fluid and heat exchanger materials are shown in Table 2. This paper mainly studies the phase transition and two-phase flow process of the shell side of the heat exchanger and the cooling process of the high-pressure hydrogen in the tube side. For the accuracy of the calculation, the heat exchange tube wall is treated as a constant temperature wall surface.

**Table 2.** Physical parameters of heat exchange fluid and heat exchanger materials.

Materials	Density $\text{kg}/\text{m}^3$	Thermal Conductivity $\text{W}/(\text{m}\cdot\text{K})$	Molar Mass $\text{g}/\text{mol}$
42 MPa hydrogen	26.9598	0.22	2.0159
47 MPa hydrogen	29.4032	0.2249	2.0159
77 MPa hydrogen	41.828	0.2563	2.0159
R23(Liquid)	1456	0.1377	70.01432
R23(Gas)	3.9554	0.00772787	70.01432
316 L Stainless steel	8030	16.27	/

#### 2.6. Solve Settings

The commercial code FLUENT 19.0 is adopted to simulate the flow and heat transfer in the computational model. The numerical simulation is performed with a two-dimensional transient-state turbulent flow system. The simulation time is 0–30 s, among which: the time step is 0.01 s and the number of steps is 3000 steps. The separation implicit solver is selected,

the SIMPLE algorithm based on the staggered grid is used to process the pressure-velocity coupling equation, and the first-order upwind difference format is selected to discretize the physical quantity of the control volume interface. The Mixture model is selected as the calculation model of the two-phase flow, and considered Velocity slip between phases, while the Lee model is used to simulate the transformation process of R23 from liquid phase to gas phase. The Realizable  $k-\varepsilon$  model is selected, the performance of the model is improved with mathematical constraints, the medium-strength swirling flow is predicted, and the wall-enhanced function is used to process the flow near the wall. The residual convergence standard of the continuity equation and momentum equation is  $10^{-4}$ , and the residual convergence standard of the energy equation is  $10^{-6}$ .

### 3. Model Verification

The mesh check is performed for the model. For ensuring the grid independence, the temperature of the hot fluid at the output is determined and evaluated for various meshes. Figure 7 illustrates the results of the mesh sensitivity analysis in this work. It can be seen that the output temperature of the hot liquid varies negligibly between the grid containing  $2.82 \times 10^5$  and  $3.24 \times 10^5$  cells. Thus, the grid with  $2.82 \times 10^5$  cells is used for the simulations.

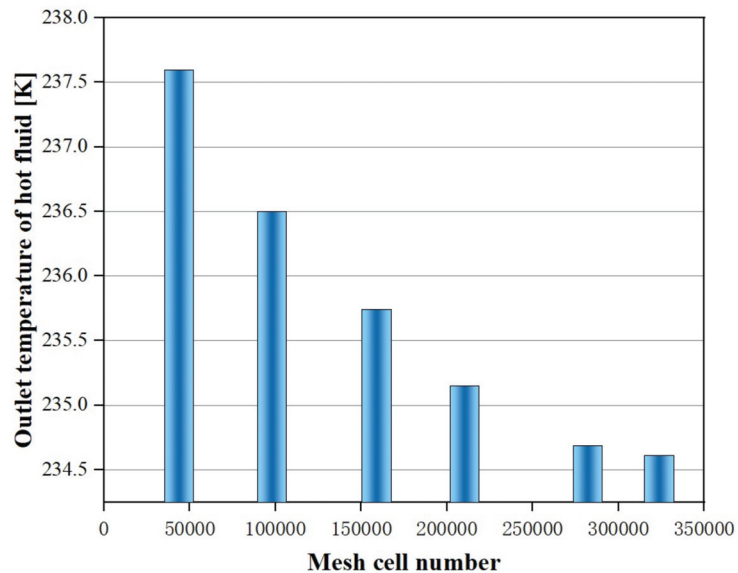


Figure 7. Results of the grid test for the exit temperature of the hot fluid versus the grid cell number.

To verify the feasibility of the model, the average temperature at the outlet of the shell-and-tube heat exchanger during the 77 MPa high-pressure hydrogen pre-cooling was compared with the inlet temperature of the vehicle-mounted storage tank in the fast-charging stage in the literature [27].

The hydrogen inlet temperature during the rapid filling process needs to be cooled to within  $-33\sim-40\text{ }^{\circ}\text{C}$  within the 30 s [8], so this simulation selects the data from the previous 30 s of the simulation and references. As shown in Figure 8, the trend of the simulated temperature in this study is consistent with the data in the literature. The temperature in [27] is the inlet temperature of the vehicle-mounted storage tank during fast charging. In the refueling system of the hydrogen refueling station, the high-pressure hydrogen outlet of the shell-and-tube heat exchanger is at a distance from the hydrogen refueling machine. There is a loss of cold capacity, so the inlet temperature of the hydrogen on the vehicle storage tank is slightly higher than the outlet temperature of the hydrogen when

the simulation is completed. During the first 15 s of filling, the two temperature differences increased first and then decreased. The reason for this is that the temperature of the pipeline was still high at the beginning of the filling process. As the filling process continued, the temperature of the pipeline continued to decrease. After 15 s, the temperature difference between the two stabilized at about 5 °C. Therefore, it is appropriate to use Fluent to simulate the heat exchange process in the hydrogen pre-cooling system.

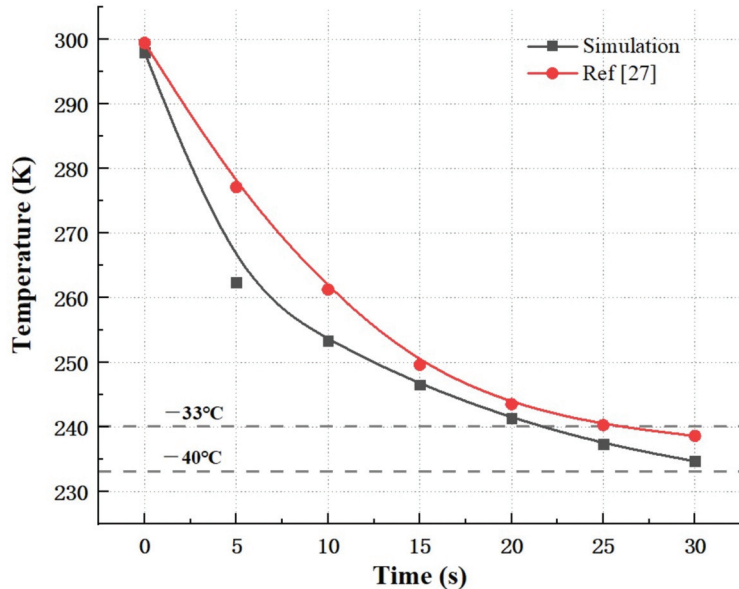


Figure 8. Comparison of simulation data and literature data.

#### 4. Calculation Results and Discussion

After verifying the feasibility of the simulation, CFD-POST was used to visually analyze the calculation results. The influence of working parameters, such as hydrogen inlet temperature and pressure, on the pre-cooling performance is also studied.

##### 4.1. Analysis of Temperature Distribution and Flow Pattern in the Heat Exchanger

###### 4.1.1. Temperature Distribution

The hydrogen enters the heat exchange tube and exchanges heat with the refrigerant. Figure 9 shows that the temperature at the hydrogen outlet gradually decreases over time. At  $t = 0$  s, the hydrogen temperature is the initial temperature of 298 K, and the pipe wall begins to cool the hydrogen. At  $t = 5$  s, it can be seen that the temperature of hydrogen in the heat exchange tube has a significant drop. As time goes by, the temperature of hydrogen slowly decreases. As can be seen from Figure 6, the temperature drops to  $-33$  °C at 22 s and the temperature drops at 30 s. There is a downward trend around  $-38$  °C, which can meet the requirement that the temperature falls within the range of  $-33$ ~ $-40$  °C within the 30 s [8]. It can be seen from the 30 s cloud chart that the temperature in the vicinity of the high-pressure hydrogen inlet is higher, and the temperature gradient in the inlet section is larger, so the hydrogen inlet section is the area with the highest heat exchange degree of the heat exchanger.

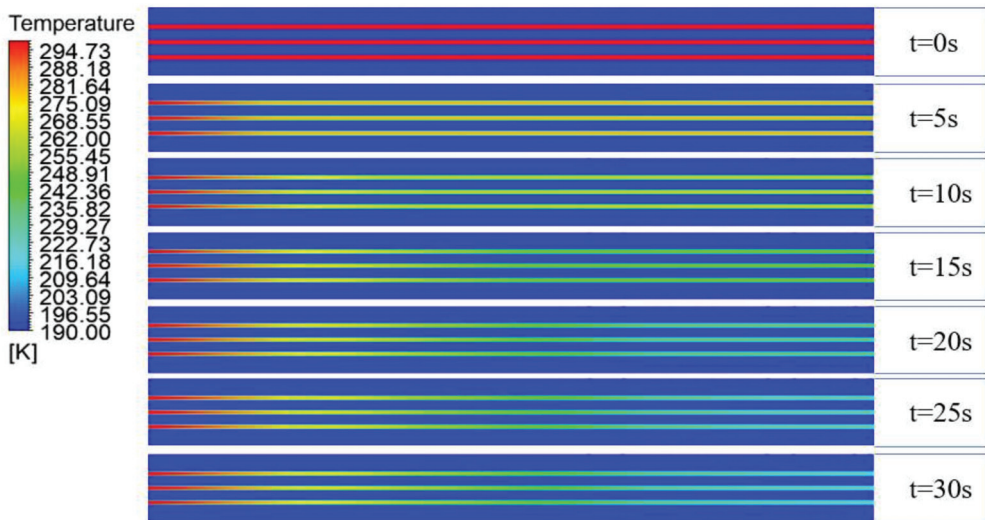
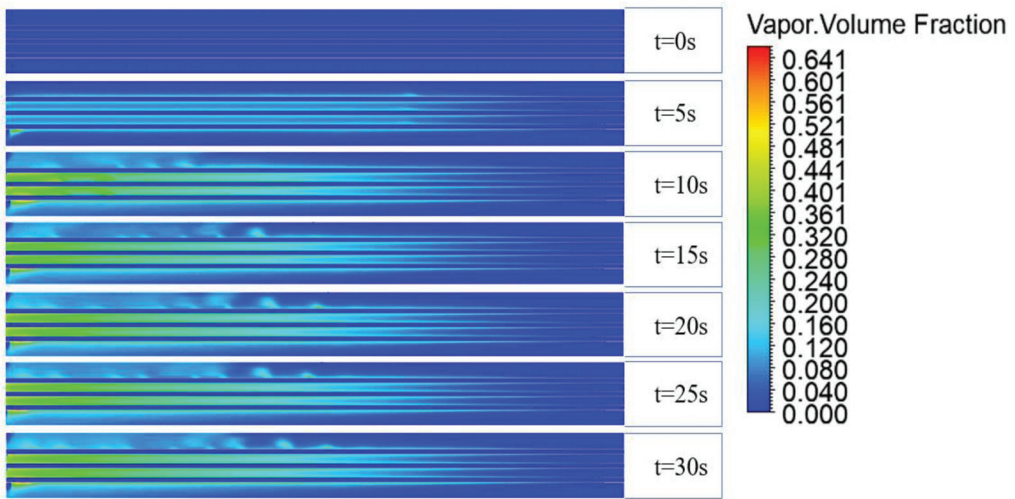


Figure 9. CFD simulation results in temperature cloud map.

#### 4.1.2. Flow Pattern Analysis

In the simulation, the evaporation-condensation model was used to simulate the phase change process of the refrigerant R23, and the gas phase volume fraction cloud diagram during the simulation process and the gas phase volume fraction of the shell-side basin with time change were obtained. The value of the gas phase volume fraction in 4.2–4.4 summary is the overall gas phase volume fraction in the refrigerant flow domain. The gas-phase volume fractions of four parts of the shell-side watershed were extracted and the average value obtained was used as the gas-phase volume fraction at a certain moment. Figure 10 is the R23 vapor fraction cloud map. At  $t = 0$  s, the shell side drainage area is dark blue, and the liquid phase occupies 100% of the shell side drainage area. It is heated by the shell side heat exchange tube wall, and the liquid phase is heated at the beginning near the wall. In the gas phase transition, as the heat exchange time increases, the proportion of the gas phase volume fraction gradually increases. From the gas phase distribution at different moments in Figure 10, it can be seen that R23 undergoes the heating phase transition of the tube wall and flows with the shell side fluid to the outlet. When  $t = 30$  s, the gas fraction near the right side is smaller. The decrease in the dryness of R23 vapor in the final cooling phase may be due to the decrease in the temperature difference between hydrogen and R23 and the resulting decrease in flux of transferred heat and the heat transfer coefficient on the R23 side. In summary 2.5, we set the R23 outlet boundary to the pressure outlet boundary, and considering that the outlet area of the refrigerant R23 has a certain heat exchange with the outside world, the appropriate return temperature is set, which is obvious in the cold flow outlet area.



**Figure 10.** CFD simulation results in R23 gas-phase fraction cloud map.

#### 4.2. The Influence of Hydrogen Inlet Pressure

To meet different refueling requirements, hydrogen refueling stations are generally equipped with several in-station storage tanks with different pressures. The physical parameters of high-pressure hydrogen at different pressures will be different, as shown in Table 2, which will have different effects on the pre-cooling process. This study mainly analyzed the influence of pressure on the hydrogen outlet temperature during the filling process of 42 MPa, 47 MPa, and 77 MPa [2,3]. Figure 11 depicts that under different hydrogen pressures, the hydrogen outlet temperature decreases with the increase of time, and the gas volume fraction of the shell side refrigerant increases with the increase of time. It can be seen from Figure 11 that the higher the hydrogen inlet pressure, the higher the final hydrogen outlet temperature.

The maximum temperature difference between the three pressures of hydrogen during the pre-cooling process is 5.686 °C. Since the pressure of the vehicle-mounted storage tank is lower than the pressure of the storage tank in the hydrogen refueling station, in the pre-cooling system, the outlet pressure of the heat exchanger tube of the shell and tube heat exchanger is lower than the inlet pressure, and there is a certain degree of pressure drop. the pressure drop during hydrogen flow is accompanied by a temperature increase, which increases together with hydrogen pressure (Joule-Thomson effect for hydrogen). However, according to Table 2, the thermal conductivity of 77 MPa hydrogen is higher than that of 42 MPa and 47 MPa hydrogen, and the heat transfer coefficient of the entire system in the heat exchange process is higher. In summary, during the heat exchange process of 77 MPa hydrogen, the temperature is slightly higher than that of the other two pressures of hydrogen. Since the temperature difference between 42 MPa and 47 MPa hydrogen in the pre-cooling process is not very obvious, the change in the volume fraction of the gas phase reflected in the refrigerant is not very obvious.

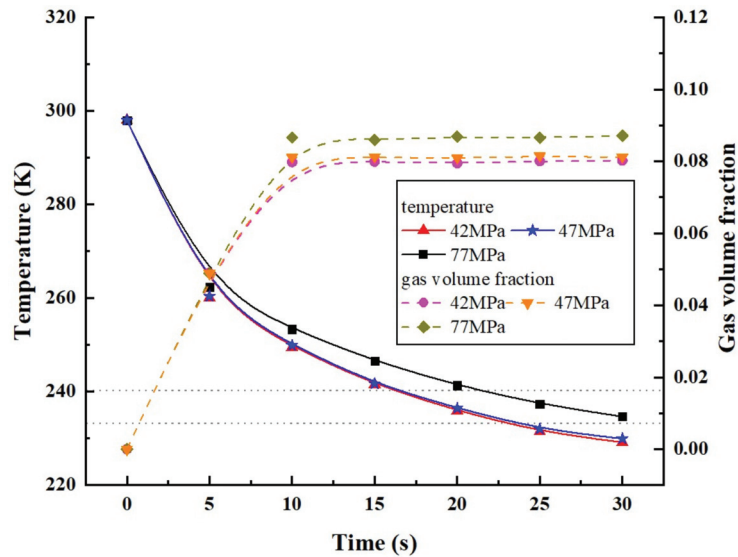


**Figure 11.** Influence of different hydrogen inlet pressures on precooling temperature and R23 gas volume fraction.

#### 4.3. The Influence of Hydrogen Inlet Temperature

The inlet temperature of hydrogen is a key factor, which largely determines the temperature of hydrogen after pre-cooling. In order to obtain the relationship between the two, the simulated pressure is 77 MPa, the hydrogen flow rate is 0.1 m/s, the refrigerant flow rate is 0.5 m/s, and the hydrogen inlet temperature is 288 K, 298 K, and 308 K, respectively. The details of the pre-cooling of different hydrogen inlet temperatures are shown in Figure 12. It can be seen that the simulation results are the same as the research results of [28], and the hydrogen outlet temperature increases with the increase of the inlet temperature. When the hydrogen inlet temperature is 288 K, the hydrogen outlet temperature will drop below  $-40\text{ }^{\circ}\text{C}$  after the 20 s. At this time, other operating parameters need to be controlled so that the temperature is not too low to avoid unnecessary cooling loss. For the inlet temperature of 308 K, at the 30 s, the hydrogen outlet temperature is  $-33.11\text{ }^{\circ}\text{C}$ , which barely meets the pre-cooling temperature requirements. For higher hydrogen inlet temperatures, other operating parameters need to be changed to meet the refueling requirements. In addition, in the first 15 s, the changing trend of the outlet temperature corresponding to the three different hydrogen inlet temperatures is the same. After 15 s, it can be clearly seen that the outlet temperature corresponding to the inlet temperature of 288 K hydrogen drops a little bit more. At the same time, it can be seen that a higher inlet temperature will cause a greater increase in the vapor fraction. In the first 10 s, during the pre-cooling process where the hydrogen inlet temperature is 308 K, the R23 vapor volume fraction rises the fastest. Therefore, as the temperature of high-pressure hydrogen increases, the average temperature on both sides of the cold and hot increases, the viscosity of the gas increases with the increase in temperature, and the viscosity of the refrigerant R23 decreases with the increase in temperature [28]. In the actual filling process, if the hydrogen inlet temperature is too high, the outlet temperature of the hydrogen can be reduced by increasing the flow rate of the refrigerant or reducing the flow rate of the high-pressure hydrogen to meet the filling requirements.

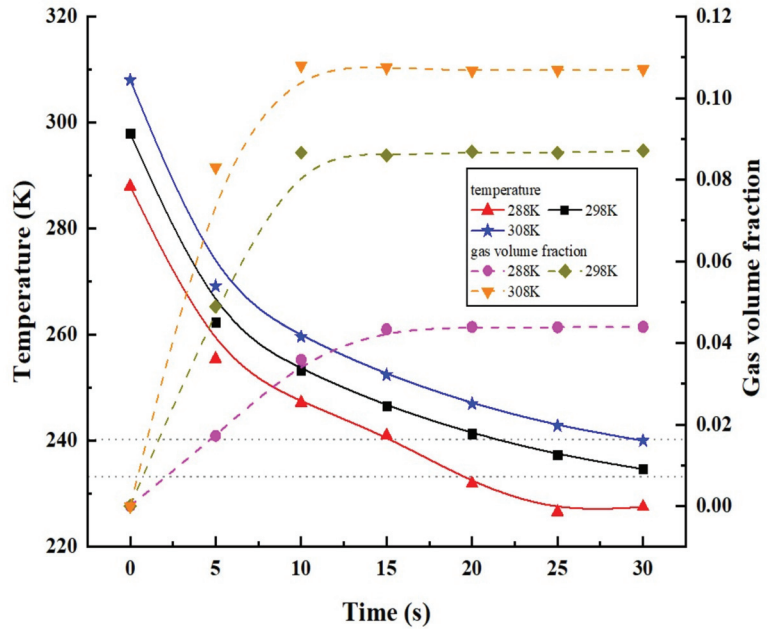


**Figure 12.** The influence of different hydrogen inlet temperatures on the pre-cooling temperature and R23 gas volume fraction.

#### 4.4. Influence of Refrigerant Flow Rate

Figure 13 shows the changes of hydrogen outlet temperature and refrigerant gas volume fraction under three different refrigerant flow rates of 0.3 m/s, 0.5 m/s, and 0.7 m/s. It can be seen from the figure that the faster the refrigerant flow rate, the better the refrigeration performance, and the greater the temperature change of the thermal fluid. The simulation results are the same as those in the literature [29]. When the refrigerant flows, the fluid is affected by the generation, floating, and flow of bubbles during the phase change of the refrigerant, causing the fluid to vortex and increase the degree of turbulence. The turbulence intensity at the inlet of the refrigerant is relatively small, and as the fluid flows along the shell side, the turbulence intensity gradually increases. When the refrigerant flow rate increases, the turbulence intensity on the shell side is significantly enhanced, which is beneficial to enhance the heat transfer effect. Since the heat transfer coefficient on the shell side is smaller than that on the tube side, the increase in the heat transfer coefficient on the shell side improves the overall heat transfer effect [30,31]. In addition, the flow rate of the refrigerant increases, the shell side fluid contacts the heat exchange tube wall more fully, the effective heat transfer area of the heat exchanger becomes larger, and the heat exchange amount of the heat exchanger also becomes larger.

It can be seen from Figure 13 that the larger the refrigerant flow rate, the smaller the volume fraction of the gas phase on the shell side. On the one hand, because the flow rate of the refrigerant increases, the gas phase is attached to the sidewall of the heat exchange tube shell and the shell side is taken out of the heat exchanger. On the other hand, the higher the refrigerant flow rate, the higher the heat transfer efficiency of the heat exchanger [28], and the lower the temperature of the shell-side tube wall, the smaller the amount of R23 that changes from liquid phase to gas phase.



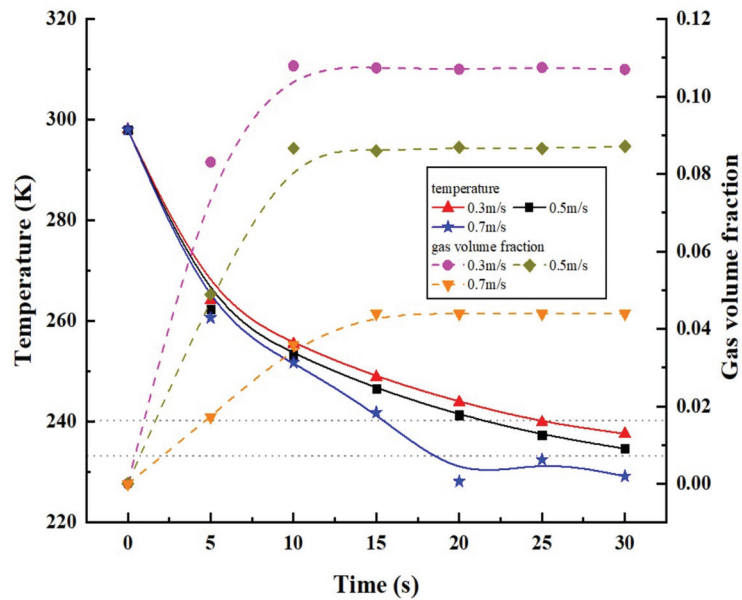


**Figure 13.** The influence of different refrigerant flow rates on pre-cooling temperature and R23 gas volume fraction.

## 5. Conclusions

In this paper, the method of computational fluid dynamics is used to simulate the heat exchange process of the shell-and-tube heat exchanger in the hydrogen pre-cooling system. Fluent software was used to simulate the cooling process of high-pressure hydrogen, the phase change heat transfer, and the two-phase flow process of R23, and the verification was carried out based on the filling data in the references. The hydrogen outlet temperature of the heat exchanger is in good agreement with the literature data. It reveals the change law of temperature field, gas volume fraction, and local heat flow in the process of liquid-phase transforming into gas-phase. According to the simulation results, the main conclusions are as follows:

- The use of CFD simulation technology can well reflect the heated phase change process, two-phase flow, and high-pressure hydrogen cooling process of R23 in the heat exchange process.
- The shell-and-tube heat exchanger for the hydrogen pre-cooling system is designed using the average temperature difference method, and the inlet temperature of the hydrogen gas during the rapid filling process is controlled to be kept within the range of  $-33\text{ }^{\circ}\text{C}\sim-40\text{ }^{\circ}\text{C}$ .
- CFD is used to simulate the heat transfer process of the shell-and-tube heat exchanger and compare it with the data in the reference. The simulation results and the experimental results have high consistency, so the simulation method is suitable for simulating the heat transfer of high-pressure hydrogen in the shell-and-tube heat exchanger.
- In the heat exchange process, the working parameters have a certain influence on the result of hydrogen pre-cooling to varying degrees. Among them, the hydrogen inlet temperature and the flow rate of the refrigerant have more obvious effects than other parameters. In the actual pre-cooling process, it is necessary to select appropriate working parameters according to the actual situation, and under the premise of ensuring safety, make the filling cost the lowest.

The results help to understand the internal flow of the tube shell heat exchanger under phase transformation heat conditions and provide appropriate working parameters for

hydrogen station in the face of different filling requirements, to reduce the operating cost of the hydrogen refueling station and promote the development of hydrogen energy.

**Author Contributions:** Conceptualization, S.L., J.G., J.W.; methodology, S.L., J.G.; software, S.L., X.L., B.C.; validation, S.L., T.D.; investigation, S.L., X.L.; writing—original draft preparation, S.L.; writing—review and editing, J.W., J.G.; funding acquisition, J.W., J.G. All authors have read and agreed to the published version of the manuscript.

**Funding:** This work was partially supported by Xi’an Key Laboratory of Clean Energy (2019219914SY S014CG036), The Yulin Industry-University-Research Cooperation Project (2019-173), and Key Research and Development Program of Shaanxi (2021ZDLGY13-02).

**Conflicts of Interest:** The authors declare no conflict of interest.

## References

- Alazemi, J.; Andrews, J. Automotive hydrogen fuelling stations: An international review. *Renew. Sustain. Energy Rev.* **2015**, *48*, 483–499. [CrossRef]
- Apostolou, D.; Xydias, G. A literature review on hydrogen refuelling stations and infrastructure. Current status and future prospects. *Renew. Sustain. Energy Rev.* **2019**, *113*, 109292. [CrossRef]
- Abdalla, A.M.; Hossain, S.; Nisfindy, O.B.; Azad, A.T.; Dawood, M.; Azad, A.K. Hydrogen production, storage, transportation and key challenges with applications: A review. *Energy Convers. Manag.* **2018**, *165*, 602–627. [CrossRef]
- Talpacci, E.; Reuß, M.; Grube, T.; Cilibrizzi, P.; Gunnella, R.; Robinius, M.; Stolten, D. Effect of cascade storage system topology on the cooling energy consumption in fueling stations for hydrogen vehicles. *Int. J. Hydrogen Energy* **2018**, *43*, 6256–6265. [CrossRef]
- Ahluwalia, R.K.; Hua, T.; Peng, J.K. On-board and Off-board performance of hydrogen storage options for light-duty vehicles. *Int. J. Hydrogen Energy* **2012**, *37*, 2891–2910. [CrossRef]
- Zheng, J.; Liu, X.; Xu, P.; Liu, P.; Zhao, Y.; Yang, J. Development of high pressure gaseous hydrogen storage technologies. *Int. J. Hydrogen Energy* **2012**, *37*, 1048–1057. [CrossRef]
- Maus, S.; Hapke, J.; Na Ranong, C.; Wüchner, E.; Friedlmeier, G.; Wenger, D. Filling procedure for vehicles with compressed hydrogen tanks. *Int. J. Hydrogen Energy* **2008**, *33*, 4612–4621. [CrossRef]
- Elgowainy, A.; Reddi, K.; Lee, D.-Y.; Rustagi, N.; Gupta, E. Techno-economic and thermodynamic analysis of pre-cooling systems at gaseous hydrogen refueling stations. *Int. J. Hydrogen Energy* **2017**, *42*, 29067–29079. [CrossRef]
- DOE (U.S. Department of Energy). Fuel Cell Electric Vehicles. 2016. Available online: [http://www.afdc.energy.gov/vehicles/fuel\\_cell.html](http://www.afdc.energy.gov/vehicles/fuel_cell.html) (accessed on 1 November 2021).
- Liu, Y.-L.; Zhao, Y.-Z.; Zhao, L.; Li, X.; Chen, H.-G.; Zhang, L.-F.; Zhao, H.; Sheng, R.-H.; Xie, T.; Hu, D.-H. Experimental studies on temperature rise within a hydrogen cylinder during refueling. *Int. J. Hydrogen Energy* **2010**, *35*, 2627–2632. [CrossRef]
- SAE. Fueling Protocols for Light Duty and Medium Duty Gaseous Hydrogen Surface Vehicles (Standard J2601-201407). 2014. Available online: [http://standards.sae.org/j2601\\_201612/](http://standards.sae.org/j2601_201612/) (accessed on 3 June 2021).
- European Commission. ‘2020 Climate & Energy Package’ 23-Nov- Climate Action-European Commission. 2016. Available online: [https://ec.europa.eu/clima/policies/strategies/2020\\_en](https://ec.europa.eu/clima/policies/strategies/2020_en) (accessed on 3 March 2021).
- Cebolla, R.O.; Acosta, B.; de Miguel, N.; Moretto, P. Effect of precooled inlet gas temperature and mass flow rate on final state of charge during hydrogen vehicle refueling. *Int. J. Hydrogen Energy* **2015**, *40*, 4698–4706. [CrossRef]
- Li, M.; Bai, Y.; Zhang, C.; Song, Y.; Jiang, S.; Grouset, D.; Zhang, M. Review on the research of hydrogen storage system fast refueling in fuel cell vehicle. *Int. J. Hydrogen Energy* **2019**, *44*, 10677–10693. [CrossRef]
- Wang, Y.; Liu, Z.; Huang, S.; Liu, W.; Li, W. Experimental investigation of shell-and-tube heat exchanger with a new type of baffles. *Heat Mass Transf.* **2011**, *47*, 833–839. [CrossRef]
- Lei, Y.; Li, Y.; Jing, S.; Song, C.; Lyu, Y.; Wang, F. Design and performance analysis of the novel shell-and-tube heat exchangers with louver baffles. *Appl. Therm. Eng.* **2017**, *125*, 870–879. [CrossRef]
- Chen, J.; Lu, X.; Wang, Q.; Zeng, M. Experimental investigation on thermal-hydraulic performance of a novel shell-and-tube heat exchanger with unilateral ladder type helical baffles. *Appl. Therm. Eng.* **2019**, *161*, 114099. [CrossRef]
- Darbandi, M.; Abdollahpour, M.-S.; Hasanpour-Matkolaei, M. A new developed semi-full-scale approach to facilitate the CFD simulation of shell and tube heat exchangers. *Chem. Eng. Sci.* **2021**, *245*, 116836. [CrossRef]
- Ozden, E.; Tari, I. Shell side CFD analysis of a small shell-and-tube heat exchanger. *Energy Convers. Manag.* **2010**, *51*, 1004–1014. [CrossRef]
- ANSYS Fluent Version 19.0. Fluent 2019 User’s Guide. Available online: [https://ansyshelp.ansys.com/account/secured?returnurl=/Views/Secured/corp/v195/flu\\_ug/flu\\_ug.html](https://ansyshelp.ansys.com/account/secured?returnurl=/Views/Secured/corp/v195/flu_ug/flu_ug.html) (accessed on 10 January 2020).
- Rezayan, O.; Behbahaninia, A. Thermoeconomic optimization and exergy analysis of CO<sub>2</sub>/NH<sub>3</sub> cascade refrigeration systems. *Energy* **2011**, *36*, 888–895. [CrossRef]
- Sun, Z.; Liang, Y.; Liu, S.; Ji, W.; Zang, R.; Liang, R.; Guo, Z. Comparative analysis of thermodynamic performance of a cascade refrigeration system for refrigerant couples R41/R404A and R23/R404A. *Appl. Energy* **2016**, *184*, 19–25. [CrossRef]

23. He, L.; Li, P. Numerical investigation on double tube-pass shell-and-tube heat exchangers with different baffle configurations. *Appl. Therm. Eng.* **2018**, *143*, 561–569. [CrossRef]
24. You, Y.; Fan, A.; Huang, S.; Liu, W. Numerical modeling and experimental validation of heat transfer and flow resistance on the shell side of a shell-and-tube heat exchanger with flower baffles. *Int. J. Heat Mass Transf.* **2012**, *55*, 7561–7569. [CrossRef]
25. Gu, X.; Zheng, Z.; Xiong, X.; Wang, T.; Luo, Y.; Wang, K. Characteristics of Fluid Flow and Heat Transfer in the Shell Side of the Trapezoidal-like Tilted Baffles Heat Exchanger. *J. Therm. Sci.* **2018**, *27*, 602–610. [CrossRef]
26. Gray, D.D.; Giorgini, A. The validity of the boussinesq approximation for liquids and gases. *Int. J. Heat Mass Transf.* **1976**, *19*, 545–551. [CrossRef]
27. The Hydrogen Data E Sharing Site. Available online: <http://www.h2protocol.com/h2-fueling-data> (accessed on 18 May 2020).
28. Dang, T.; Teng, J.-T. The effects of configurations on the performance of microchannel counter-flow heat exchangers—An experimental study. *Appl. Therm. Eng.* **2011**, *31*, 3946–3955. [CrossRef]
29. Dang, T.; Teng, J.-T.; Chu, J.-C. A study on the simulation and experiment of a microchannel counter-flow heat exchanger. *Appl. Therm. Eng.* **2010**, *30*, 2163–2172. [CrossRef]
30. Bahiraei, M.; Naseri, M.; Monavari, A. A CFD study on thermohydraulic characteristics of a nanofluid in a shell-and-tube heat exchanger fitted with new unilateral ladder type helical baffles. *Int. Commun. Heat Mass Transf.* **2021**, *124*, 105248. [CrossRef]
31. Zhang, J.-F.; Guo, S.-L.; Li, Z.-Z.; Wang, J.-P.; He, Y.-L.; Tao, W.-Q. Experimental performance comparison of shell-and-tube oil coolers with overlapped helical baffles and segmental baffles. *Appl. Therm. Eng.* **2013**, *58*, 336–343. [CrossRef]

## Article

# Valuation of Climate Performance of a Low-Tech Greenhouse in Costa Rica

Adriana Rojas-Rishor <sup>1</sup>, Jorge Flores-Velazquez <sup>2,\*</sup>, Edwin Villagran <sup>3</sup> and Cruz Ernesto Aguilar-Rodríguez <sup>4,\*</sup>

<sup>1</sup> Facultad de Ingeniería de Biosistemas, Universidad de Costa Rica, Montes de Oca, San José 11501-2060, Costa Rica; adri.rojas.rishor@gmail.com

<sup>2</sup> Posgrado en Hidrociencias, Colegio de Postgraduados Campus Montecillos, Carretera Mexico Texcoco, Km. 36.52, Texcoco 56230, Mexico

<sup>3</sup> Department of Biological and Environmental Sciences, Faculty of Natural Sciences and Engineering, Universidad Jorge Tadeo Lozano, Bogotá 111321, Colombia; edwina.villagranm@utadeo.edu.co

<sup>4</sup> Tecnológico Nacional de México/ITS de los Reyes, Carretera Los Reyes-Jacona, Col. Libertad, Los Reyes de Salgado Michoacán 60300, Mexico

\* Correspondence: jorgelv@colpos.mx (J.F.-V.); ernesto.ar@losreyes.tecnm.mx (C.E.A.-R.)

**Abstract:** The expansion of protected agriculture has technological, climatic, and topographic limitations. The agricultural regions of Costa Rica use the greenhouse concept and adapt it to its conditions. The objective of this work was to describe the variation in temperature and humidity in a greenhouse ventilated passively and on land with a more than 45% slope. To evaluate the environment inside the greenhouse, temperature and humidity variations were measured with a weather station installed outside of the greenhouse to measure the external environment. Inside the greenhouse, 17 sensors were placed to measure the temperature (T) and relative humidity (RH). During data recording inside the greenhouse, tomato crops were in the fruit formation stage, and pepper was less than one week old. Six scenarios were tested to determine the air temperature and humidity dynamic under different climatic conditions. An evaluation of the greenhouse environment was carried out employing an analysis of variance of temperature and RH to establish if there are significant differences in the direction of the slope of the cross-section. The uniformity of temperature and RH do not present stratifications derived from wind currents that can affect the effective production of these crops.

**Keywords:** landsloping greenhouse; relative humidity; thermal difference; tomato and pepper crop

**Citation:** Rojas-Rishor, A.; Flores-Velazquez, J.; Villagran, E.; Aguilar-Rodríguez, C.E. Valuation of Climate Performance of a Low-Tech Greenhouse in Costa Rica. *Processes* **2022**, *10*, 693. <https://doi.org/10.3390/pr10040693>

Academic Editor: Alfredo Iranzo

Received: 17 February 2022

Accepted: 28 March 2022

Published: 2 April 2022

**Publisher's Note:** MDPI stays neutral with regard to jurisdictional claims in published maps and institutional affiliations.



**Copyright:** © 2022 by the authors. Licensee MDPI, Basel, Switzerland. This article is an open access article distributed under the terms and conditions of the Creative Commons Attribution (CC BY) license (<https://creativecommons.org/licenses/by/4.0/>).

## 1. Introduction

Advances in technology have brought solutions in regions with adverse climatic conditions. The objective is to produce crops with the efficient use of natural resources to avoid fossil energy to improve the quality and yield of crops all year long. These structures have had to evolve to answer each condition and necessity. Tropical conditions imply high humidity, and topographic restrictions mean that greenhouses must be built on a non-plane surface, in which there are hardly any management systems for climate control.

Passive ventilation is used in greenhouses to evacuate heat excess, which occurs at specific times due to insolation, which is characterized as a function of geographic localization (latitude) and topographic condition (high over sea level). In a greenhouse, windows in different positions (roof, lateral or frontal) are used to maintain an adequate environment for crops. The density of crops and the design of the greenhouse also contribute to air renovation and, consequently, better climatic conditions [1–3].

Greenhouses in Costa Rica have slowly increased functional crop production: in 2010, 681 greenhouses covered an area of 688.23 hectares. Most of the existing greenhouses are artisanal; therefore, there are problems regarding climate control of the variables used to obtain better environmental conditions for crops in greenhouses, affecting the production quality [4–6]. For this reason, natural ventilation has become one of the most important

phenomena for managing the environmental conditions inside the structure. Through the airflows generated by the difference in pressures, it is possible to regulate temperature ( $T^{\circ}$ ) and relative humidity (RH) surplus into the greenhouse [7,8].

Greenhouse evolution and the prospect of achieving better environmental conditions are central to knowledge concerning climate condition [9,10]. The condition of crops within a greenhouse depends a combination of climate factors such as radiation, and, consequently, temperature ( $T^{\circ}\text{C}$ ), relative humidity (RH %), carbon dioxide ( $\text{CO}_2$ , ppm), vapor pressure deficit (VPD, Pa), etc. each of which determine the condition of crops along their lifecycle [11,12]. In addition to agronomic conditions, auxiliary climatic systems are also defined as a function of energy variables such as temperature and relative humidity [13].

Climatic restrictions for the establishment and operation of greenhouses were normally exposed and fixed with natural or mechanical ventilation systems [9]. Even though other restrictions exist for the expansion of protected agriculture, such as those with topographic land characteristics, these have not been documented. In specific regions of Costa Rica, they are typically used for agricultural production in an irregular topographic land as an optional crop production system under controlled environments; however, if the optimum conditions have not existed, the adaptation can be expensive and prevent the benefits of its use. Such an aspect can become one of the most delimited factors when a project to build such a greenhouse is undertaken.

Throughout the world it is common to build greenhouses on a plane surface to facilitate agronomic labour. The idea of the use of a sloping greenhouse, in general, was to avoid, per se, problems such as the concentration of water and nutritive solution in the irrigation systems and non-uniformity concentration of heat and moisture. However, there are few studies concerning the environmental performance of greenhouses in hillside regions and the subject is relatively unknown [6,14].

Natural ventilation is a prominent phenomenon responsible for managing the environmental conditions inside greenhouses. The airflows generated by the difference in thermal or wind pressure regulate the thermal and humidity excesses inside a greenhouse [7,15]. Moreover, these same airflows are responsible for exchanging air between the interior and exterior, improving thermal and  $\text{CO}_2$  conditions [16].

The study of natural ventilation in agricultural structures is not a simple activity to perform experimentally. Although the development of climate monitoring equipment allows the study of air flows through sonic anemometry and temperature sensors, anemometers only allow estimating the velocity and direction of airflow at a spatial point for a given time [17–19].

The objective of this work was to describe the variation in temperature and humidity in a greenhouse ventilated passively and with a land slope of more than 45%. In addition to this analysis, with the climatic information and analysis, in future investigations, the use of CFD simulation will be possible to contribute to achieving the design and climate management of this kind of greenhouse.

## 2. Materials and Methods

### 2.1. Study Area Localization Zone

The greenhouse used in this study is located at Zarcero, in the province of Alajuela ( $10^{\circ}14'19.2''$  N,  $84^{\circ}22'58.8''$  W) with an altitude of 1875 masl built on land with a more than 45% slope, which represents the local characteristics in the Alajuela region under tropical conditions for cultivation [20,21]. According to the Köppen–Geiger climate classification, the predominant climate in the region is classified as Aw. The average annual temperature ranges from  $22.3^{\circ}\text{C}$ , and an average rainfall of 2069 mm has been recorded. The greenhouse used was built by hand and has an area of  $891\text{ m}^2$ , covered with a low-density polyethylene and insect-proof screen on the side and roof opening (Figure 1a).

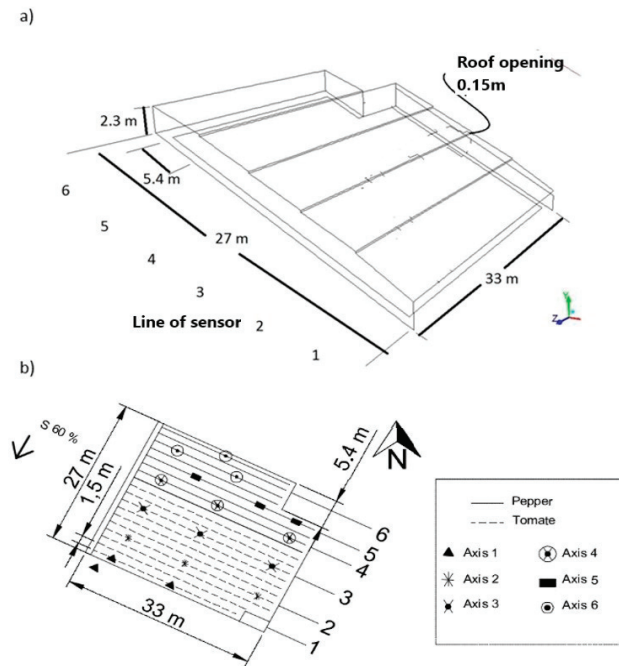


**Figure 1.** (a) Dimensions of the experimental greenhouse and (b) Installation of the sensors.

For data acquisition of climatic variables, a weather station (Vantage Pro2 Plus, Davis Instruments, Hayward, CA, USA) was installed 50 m northwest of the greenhouse location and 1.5 m high to record the environmental variables of solar radiation, RH, and temperature every 15 min (Table 1). In the greenhouse, 17 Temperature ( $^{\circ}\text{C}$ ) and RH (%) sensors (HOBO U10/003, Onset Computer Corporation, Bourne, MA, USA) were installed 1.65 m from the floor, divided into three perpendicular blocks and six lines parallel to the slope to analyse the differences in the slope and cross-section every 5 min (Figure 1b).

**Table 1.** Range of measured and precision of climate sensors.

Sensor	Range of Work	Precision
Temperature	$-40$ to $65$ $^{\circ}\text{C}$	$\pm 0.5$ $^{\circ}\text{C}$
Relative Humidity	1 to 100%	$\pm 3\%$ y $\pm 4\%$ over 90%
Radiation	0 to $1800$ $\text{W m}^{-2}$	$\pm 5\%$
Wind velocity	1 to $80$ $\text{ms}^{-1}$	$\pm 5$ $\text{ms}^{-1}$
Wind directions	16 points of compass	$\pm 5$

The monitoring period was from 2 October 2014 to 8 December 2014, using the WeatherLink<sup>©</sup> for Vantage Pro2TM (Davis Instrument, CA, USA) and HOBO(HOBO Inc., Bourne, MA, USA) version 3.7.3 computer package.

The outdoor weather station was 1.5 m above the ground. The sensors in the indoor greenhouse were placed at 1.65 m to allow them to record the air temperature data without the influence of the crops. The shield of the sensors was appropriate to the climate station.

Data recording and storage were recorded every 15 min for the weather station and every 5 min on the OOBSet HOBO sensors. The monitoring period was from 2 October 2014 to 8 December 2014, using the WeatherLink<sup>©</sup> computing package for Vantage Pro2TM and HOBO W version 3.7.3. The six lines of the sensor (axes) were separated, each 5.6 m, in the other directions (33 m); the separation was 10 m from the centre of the greenhouse (Figure 1).

## 2.2. Sampling and Data Acquisition

For the analysis of temperature and RH behaviour, the information from the sensors was grouped by axes and blocks, shown in Figure 1 in two intervals: daytime from 6:00 a.m. to 5:45 p.m., and night-time from 6:00 p.m. to 5:45 a.m. from 2 October to 8 December 2014, to allow a comparison between axes and to analyze the differences in the slope and between blocks in the cross-section to the slope.

In the first case, the frequency of hours with higher temperatures in the time interval during the sensor monitoring period was considered (Figure 2a). The chosen time was 12:30 p.m. instead of 5:45 p.m., as the maximum temperatures at 5:45 p.m. were during December, the month where the daily temperatures are the lowest of the year. The results showed that the highest temperature (20.3 °C) was at 12:30 p.m. on 23 October (Figure 2b).

To broaden the view of the environmental behaviour of the greenhouse, two random dates were selected so that the analysis included at least one day of each month registered. The days selected were 6 October and 6 December 2014. Each day was evaluated considering the two hours evaluated in cases I and II. Table 2 shows the weather conditions recorded by the weather station of the six case studies (half-hourly average values used as an initial boundary condition of the computational model for each evaluated case).

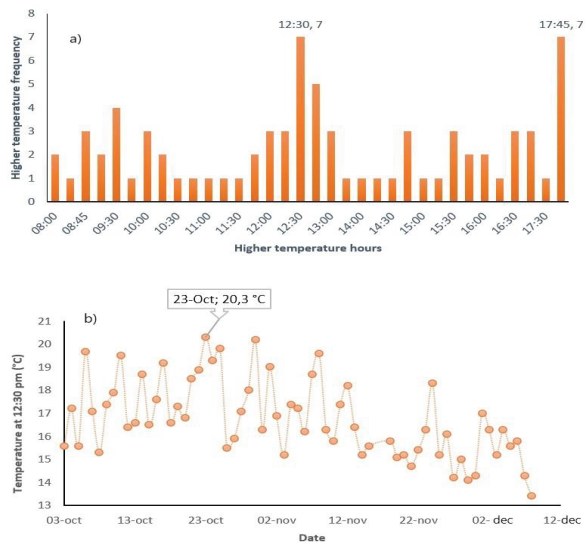


**Figure 2.** (a) Frequency analysis of the hours with higher temperatures in the daytime period. (b) Temperature values at 12:30 p.m. of the daytime period.

The frequency of hours with the lowest temperature in the night interval during the sensor monitoring period was considered for the second case. The highest frequency of minimum recorded data was at 4:45 h. The date with the lowest temperature occurred on 7 November at 4:45 a.m. (12.0 °C) (Figure 3).

To determine whether there are spatial variations in temperature and relative humidity in the greenhouse, an analysis of variance was performed using Tukey's method and orthogonal contrasts, as well as the values of temperature and RH during the study days analysed in the direction of the slope (between axes) and the transverse direction (between blocks).

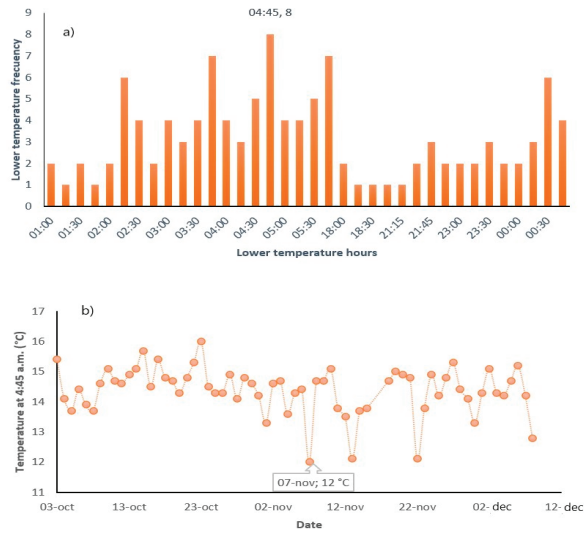


**Figure 3.** (a) Frequency analysis of the hours with lower temperatures in the daytime period. (b) Temperature values at 04:45 am of the daytime period.

**Table 2.** Values of climatic variables considered in the case studies.

Case	Date	Time (h)	Temperature (°C)	RH (%)	Wind	
					Velocity (m/s)	Predominant Direction
I	23 October	12:30	20.3	85	2.2	SW
II	07 November	04:45	12.0	97	0.4	SW
IIIA	06 October	12:30	19.7	87	1.8	SE
IIIB	06 October	04:45	14.4	95	0.9	W
IVA	06 December	12:30	15.8	95	0.9	SE
IVB	06 December	04:45	15.2	96	0.9	NW

### 3. Results and Discussion

#### 3.1. Statistical Analysis of Experimental Data

The analysis of variance for temperature and RH of the scenario is presented in Table 3. It is observed that there is no significant difference for both temperature and RH in the axes or blocks. The same happened for cases II, IIIA, IIIB, and IVB.

**Table 3.** Tukey’s method for the case I analyses the temperature and relative humidity variance between axes and blocks.

Temperature (°C)					RH (%)			
Axis	Average	n	E.E.		Axis	Average	n	E.E.
1	30.59	2	1.01	a	1	50.06	1	5.74
2	30.71	3	0.82	a	2	49.55	3	3.31
3	31.53	3	0.82	a	3	49.72	2	4.06
4	32.48	3	0.82	a	4	42.13	2	4.06
5	32.55	3	0.82	a	5	43.53	3	3.31
6	31.8	3	0.82	a	6	47.36	3	3.31

Temperature (°C)					RH (%)			
Block	Average	n	E.E.		Block	Average	n	E.E.
A	31.69	5	0.67	a	A	44.97	4	2.89
B	31.68	7	0.57	a	B	47.02	6	2.36
C	31.64	5	0.67	a	C	48.27	4	2.89

Means with a joint letter are not significantly different ( $p > 0.05$ ).



Table 4 shows the results of the analysis of variance for the IVA case. It is highlighted that only for this case, there are significant differences between axis 1 and axis 5, and axis 1 with axis 6. On the other hand, the values of the RH mean between axes and blocks did not present statistically significant differences [20].

**Table 4.** Tukey's method for the case IVA analyses the temperature and relative humidity variance between axes and blocks.

Temperature (°C)				RH (%)			
Axis	Average	n	E.E.	Axis	Average	n	E.E.
1	22.04	2	0.55	1	68.56	1	4.41
2	23.11	3	0.45	2	66.88	3	3.6
3	23.72	3	0.45	3	65.85	2	4.41
4	24.12	3	0.45	4	59.74	2	3.6
5	25.18	3	0.45	5	58.98	3	3.6
6	24.88	3	0.45	6	60.07	3	3.6

Temperature (°C)				RH (%)			
Block	Average	n	E.E.	Block	Average	n	E.E.
A	23.88	5	0.58	A	59.35	4	3.24
B	24.01	7	0.49	B	63.37	6	2.45
C	23.92	5	0.58	C	64.97	4	2.9

Means with a joint letter are not significantly different ( $p > 0.05$ ).

From the above results, it can be concluded that there is not always a statistically representative thermal difference in the direction of the slope in the greenhouse built on a hillside. In none of the cases analysed were statistically representative differences of RH obtained in the direction of the slope. Furthermore, in the transverse direction of the slope, a statistically representative difference was obtained for temperature or RH in no case.

### 3.2. Temperature and RH Variation between Axes and between Blocks (Day Time)

Temperature and RH recorded by sensors in an experimental greenhouse during the scenarios presented in Table 1 show that for the day, the temperature distribution in axes for case I, IIIA, and IVA (Figure 4) showed that in all cases, there was a tendency of temperature increase in the direction of the slope, thermal difference prevailing in consecutive axes between the 3, 4 and 5 with a value of 1 °C to 2 °C. In case I, the thermal difference was 1.96 °C between axis 1 and axis 5; for case IIIA, it was 2.92 °C between axis 3 and axis 6, and in the case, IVA was 3.14 °C between axis 1 and 5. The RH distribution (Figure 3) shows that in case I, the RH difference was 7.93% between axis 1 and axis 4; for case IIIA, it was 6.55% between axis 2 and axis 5, and in the case, IVA was 9.58% between axis 1 and axis 5. However, for cases I and IIIA, temperatures were above 30 °C, outside the maximum recommended threshold for tomato development [20,21].

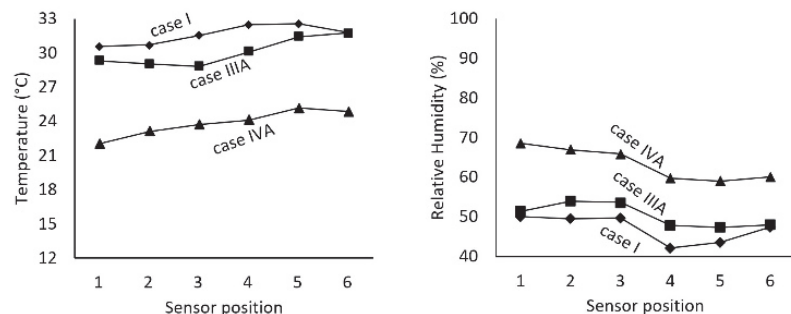


**Figure 4.** Variation of temperature (°C) and RH (%) for daytime period.

The IVA case (December) presents a uniform temperature within the recommended range. Regarding RH, the IVA case increases 20% compared to the other cases, an increase caused by the appearance of cold fronts during the winter season.

### 3.3. Night-Time Period

In case II, the thermal difference was 0.11 °C between axis 2 and 1. In case IIIB, it was 0.61 °C concerning axis 4, and in case IVB, the difference was 0.18 °C between axis 1 and 5. There is a higher temperature homogeneity than in the described cases of the diurnal interval (Figure 4). For RH (Figure 5), there is a tendency of an appreciable decrease in case II and IVB, of an appreciable decrease in axis 3, so in both cases, the moisture difference was lost from axis 2 to 3 with 11.25% 8.45%, respectively. For IIIB, a difference between axis 2 and axis 6 of 3.36% was obtained. However, the RH for all three cases exceeds the recommended maximum (50–70%), making it necessary to look for alternatives to reduce RH, avoid condensation inside the greenhouse and improve crop quality and yield.

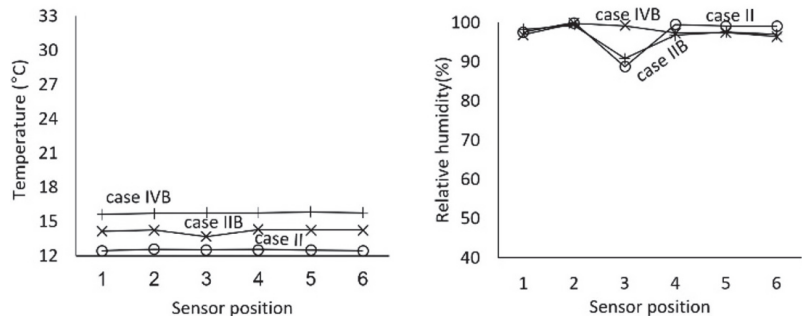


**Figure 5.** Variation of temperature (°C) and RH (%) for night-time period.

The analysis by RH blocks in cases I, II, IIIA, IIIB, IVA, and IVB. There was an upward trend from block A to block C for cases I, IIIA, and IVA, with a difference between blocks of 3.3% for the case I, 3.79% for case IIIA, and 5.62% for IVA. While for cases II, IIIB and IVB, there was an increase from block A to B (Case I, 1.08 °C; Case IIIB, 0.99 °C; Case IVB, 1.41 °C) followed by a decrease in block C (Case I, 6.04%; Case IIIB, 0.92%; Case IVB, 4.02%).

Regarding the analysis by temperature blocks in case I, the most significant thermal difference was from block A to C (0.05 °C); in case II, it was from block A to B (0.15 °C); for case IIIA, it was from B to C (0.63 °C); in case of IIIB it was from A to C (0.37 °C); in case of IVA, it was from A to B (0.013 °C), and for case IVB it was from A to C (0.04).

### 3.4. Orthogonal Contrasts in the Slope Direction for Temperature and Relative Humidity

Orthogonal contrasts were performed to determine the effect of slope on temperature and RH, utilizing a statistical analysis grouping axes. If the contrasts are not orthogonal ( $p < 0.05$ ), it implies covariance between them and is related to a certain degree. The results of the orthogonal contrasts are shown in Table 5 for temperature, which reflects that the IIIA and IVA cases obtained a significance greater than 0.05, so that for the IIIA case, contrast 1 (grouping axes 1, 2, and 3, and comparing them with axes 4, 5 and 6) obtained the most significant difference between groups, followed by contrast 2 (grouping axes 1, 2 and comparing them with axes 5 and 6) and finally contrast 3 (comparing axis 1 with axis 6). A higher significance value was obtained for the IVA case than in contrast 2, followed by contrast 1 and 3.

**Table 5.** Significance of orthogonal contrasts of temperature values.

Axis Grouping Contrast	1–2–3/4–5–6 (1)	1–2/5–6 (2)	1/6 (3)
Case I	0.0824	0.1076	0.3704
Case II	0.7833	0.6896	0.9441
Case IIIA	0.0067 ( $p < 0.05$ )	0.007 ( $p < 0.05$ )	0.045 ( $p < 0.05$ )
Case IIIB	0.2476	0.7794	0.7708
Case IVA	0.0007 ( $p < 0.05$ )	0.0003 ( $p < 0.05$ )	0.0021 ( $p < 0.05$ )
Case IVB	0.2864	0.1777	0.3585

For RH, Table 6 shows covariance in the case IVA in contrast 1, but not in contrast 2 and 3.

**Table 6.** Significance of orthogonal contrasts of RH values.

Axis Grouping Contrast	1–2–3/4–5–6 (1)	1–2/5–6 (2)	1/6 (3)
Case I	0.1395	0.3141	0.694
Case II	0.2859	0.9424	0.8291
Case IIIA	0.1199	0.2156	0.5903
Case IIIB	0.0890	0.1552	0.7830
Case IVA	<b>0.04 (<math>p &lt; 0.05</math>)</b>	0.0576	0.1672
CasoeIVB	0.5855	0.4823	0.6848

According to the orthogonal analysis between axes, it is observed that most of the cases present independence between the mean temperature values of the groupings. The cases that are not orthogonal present a higher covariance between a more significant number of grouped axes, as in contrast 1, and not for individually related axes, as in contrast 3. This tendency is also reflected in the temperature and RH distribution results, where there is a more significant temperature difference between axes 3, 4, and 5 during the day, especially in the daytime interval.

Likewise, there are more significant differences in the slope direction for both variables, not in the cross-section. There is a tendency for the temperature to rise as the altitude increases due to differences in densities and difference in altitude between axes and, in turn, a decrease in RH. In blocks, there is a slight upward trend in relative humidity in the daytime interval and a drop in block C in the night-time interval. In the case of temperature for both intervals, spatial uniformity is observed.

According to Lopez [22], the most significant differences in a flat greenhouse were 2.3 °C temperature and 5.3% relative humidity. The most significant differences were 3.14 °C and 11.25% between greenhouse extremes concerning the results obtained.

### 3.5. Behavior of Temperature and RH in the Days of Study in Relation to the Needs of the Crop

According to Tesi [23], the optimal intervals of RH are between 65% and 70% for pepper and between 55% and 60% for tomato. In the case of pepper, the suggested temperature range is between 22 °C to 28 °C during the day, and 16 °C to 18 °C at night. For tomatoes, it is between 22 °C to 26 °C during the day and between 13 °C to 16 °C during the night.

The temperature and RH distribution on October 6 and 23, November 7, and December 6 are shown in Table 7. During the day, the crops were not inside the optimum temperature range for approximately four hours, which could cause a higher incidence of pests and a decrease in crop yield. In the night period, the temperature conditions remained in the optimum range for the tomato. However, the RH remained in the optimum range for two hours before noon and between one and two hours in the afternoon. On December 6, the RH was outside the optimal range for the tomato, and at night the humidity increased to values above the maximum recommended for both crops, derived from the temperature drop.

**Table 7.** Temperature and RH recorded inside the greenhouse during the case studies.

Axis	Date	Day Time Period		Night-Time Period	
		Tmax (°C)	RH (%)	Tmin (°C)	RH (%)
1	6 October	31.04	45.60	14.04	97.42
	23 October	30.81	46.24	13.08	96.13
	7 November	31.59	44.59	11.71	97.73
	6 December	22.06	69.01	14.94	98.27
2	6 October	30.63	48.40	14.16	99.87
	3 October	31.22	44.68	13.65	98.25
	7 November	33.01	39.18	12.18	100.00
	6 December	23.11	67.46	15.04	99.28
3	6 October	30.24	48.71	14.16	98.78
	23 October	31.84	40.16	13.89	96.15
	7 November	33.89	39.44	12.23	88.75
	6 December	23.75	66.14	15.09	90.86
4	6 October	31.74	48.82	14.24	97.22
	23 October	33.19	40.62	13.95	94.34
	7 November	35.40	31.20	12.22	99.94
	6 December	24.13	59.64	15.06	96.72
5	6 October	33.26	41.92	14.23	97.49
	23 October	33.39	39.71	13.87	95.10
	7 November	36.29	32.13	12.16	99.22
	06 December	25.17	59.37	15.10	97.64
6	6 October	33.48	43.07	14.19	96.47
	23 October	32.77	43.07	13.88	94.34
	7 November	37.44	32.59	12.12	99.40
	6 December	24.89	60.39	15.00	96.89

According to the distribution of temperature and RH over the days analysed, it was observed that the times out of range are very high, and these affect crop yields, with the direct consequence of a decrease in the profitability of agricultural activity.

According to Leal and Costa [5], essential processes such as photosynthesis, respiration, and other plant processes depend on temperature, affecting plant growth and reproduction.

During high temperatures, the cells collapse due to the drought they suffer, so the stomata close automatically, limiting the loss of more water. By closing the stomata, CO<sub>2</sub> capture is reduced, causing a limitation of the photosynthesis process. Before a high temperature occurs, the plant stops its vegetative development. At low temperatures, proteins in plant cells precipitate and dehydrate.

In the case of RH, vapor pressure differences between leaf and air can increase evaporation losses, leading to wilting. Lack of humidity decreases pressure differences, and transpiration is intense. Low RH associated with high temperatures can cause leaf tip burn, and high RH stimulates the development of most germs and pathogenic organisms.

These aspects justify the need to generate tools that allow the correct design of protected environments according to the climate and define if it is necessary to resort to mechanical systems to correct the deficiencies that cannot be controlled utilizing the design with natural systems [24–28].

The presence of slopes in the soil influences the airflow; these conditions generate a loss of wind speed once the air enters the greenhouse causing it to be directed towards the roof windows in the opposite direction to the slope, with areas of low speed in the leeward side, as reported by Taloub et al. [29]; this effect is due to that during the day inside the greenhouse, there is a difference in temperature between the windward and leeward areas.

The behaviour of the greenhouse shows a temperature gain (areas with higher altitudes) for each of the scenarios studied during the day (12:30), where the air inside the

greenhouse is heated by solar radiation, as demonstrated by [30]. This temperature increase is typical of structures on flat surfaces, where the thermal gradient is a function of the prevailing wind direction [31]. For this reason, it is necessary to study the thermal homogeneity of the greenhouses to reduce the effects caused when the maximum temperatures are higher than those recommended [32–34]. During the night (04:45), the thermal difference in the greenhouse was lower, given that the environmental heterogeneity depends on the level of solar radiation; these results are consistent with those reported by [31,34,35].

#### 4. Future Analysis

One way to simulate the environment of a greenhouse to predict its thermal behaviour under natural ventilation conditions is by using the Computational Dynamic Fluid Computing (CFD) tool. Using computational models has allowed us to characterize and modify the variables that analytically affect greenhouse production [14]. In recent years, computational models have been used to simulate the thermal difference in different types of greenhouses [15,25,36,37], evaluating the effect of orientation [38], roofing material [20], airflow obstruction by vegetation, anti-insect proof mesh, and greenhouse length [26,38,39], looking for the increase in the renewal rate of air inside the greenhouse [27,28] and environmental comfort for the present crop.

#### 5. Conclusions

The environmental analysis in the experimental greenhouse showed that there was not a stable stratification of the temperature, and RH in the direction of the slope was not found during the analysis period. The highest thermal difference within the greenhouse was presented in 3.14 °C in the slope direction and 0.63 °C in the cross-section direction. In the case of higher RH, it is 11.25% in the slope direction and 6.04% in the direction of the presented cross-section. Using the Tukey method and orthogonal contrasts, it was possible to demonstrate that 60.0% slope has no inference on the thermal difference in the greenhouse. For this reason, it is established that greenhouses on hillsides have a distribution very similar to that of greenhouses on a flat terrain. The design, height, length, and management are factors to be considered for the environmental comfort of the crops.

Most of the days analysed during the day were three consecutive hours outside the optimum temperature range for chili and tomato. In addition, during the entire night interval, they were outside the optimum RH for both crops, which could cause damage to the development and growth of the crops and increase the probability of growth of some pathogens. For this reason, it is established that greenhouses on hillsides have a distribution very similar to greenhouses on flat terrain, where the thermal gradient is a function of the prevailing wind direction. Therefore, it is necessary to study the thermal homogeneity of greenhouses to reduce the effects caused when maximum temperatures are higher than recommended, in order to seek future strategies to improve the design, height, length, and management, factors to be taken into account for the environmental comfort of the crops.

**Author Contributions:** A.R.-R. (Methodology, software, data curation, writing); J.F.-V. (Conceptualization, formal analysis, supervision); C.E.A.-R. (Methodology, review and editing, validation); E.V. (Conceptualization, review and editing). All authors have read and agreed to the published version of the manuscript.

**Funding:** This research received no external funding.

**Institutional Review Board Statement:** Not applicable.

**Informed Consent Statement:** Not applicable.

**Data Availability Statement:** Not applicable.

**Acknowledgments:** The authors want to thank everyone at Mexican Institute of Water Technology on the project RD1701.1. 2017. Caracterización agroclimática de la agricultura protegida para la seguridad alimentaria y su adaptación ante el cambio climático. This work is a part of the Bachelor thesis of Adriana Rojas Rishor in the University of Costa Rica. Authors want to thank you at Colegio de Postgraduados and Tecnológico de los Reyes, by the payment of APC.

**Conflicts of Interest:** The authors declare no conflict of interest. The funders had no role in the design of the study; in the collection, analyses, or interpretation of data; in the writing of the manuscript, or in the decision to publish the results.

## References

1. Flores, J. Estudio Del Clima en Los Principales Modelos de Invernaderos en México (Malla Sombra, Multitunel y Baticenital), Mediante la Técnica Del CFD (Computational Fluid Dynamics). Ph.D. Thesis, University of Almería, Almería, Spain, 2010.
2. McCartney, L.; Orsat, V.; Lefsrud, M.G. An experimental study of the cooling performance and airflow patterns in a model Natural Ventilation Augmented Cooling (NVAC) greenhouse. *Biosyst. Eng.* **2018**, *174*, 173–189. [CrossRef]
3. Akrami, M.; Javadi, A.A.; Hassanein, M.J.; Farmani, R.; Dibaj, M.; Tabor, G.R.; Negm, A. Study of the effects of vent configuration on mono-span greenhouse ventilation using computational fluid dynamics. *Sustainability* **2020**, *12*, 986. [CrossRef]
4. Rico-García, E.; Soto-Zarazua, G.M.; Alatorre-Jacome, O.; De La Torre-Gea, G.A.; Gomez-Melendez, D.G. Aerodynamic study of greenhouses using computational fluid dynamics. *Int. J. Phys. Sci.* **2011**, *6*, 6541–6547. [CrossRef]
5. Leal, P.M.; Costa, E. *Apostilla de Ingeniería de Confort en Cultivos Protegidos*, 1st ed.; University of Campinas: São Paulo, Brasil, 2011.
6. Villagran, E.; Leon, R.; Rodriguez, A.; Jaramillo, J. 3D numerical analysis of the natural ventilation behavior in a Colombian greenhouse established in warm climate conditions. *Sustainability* **2020**, *12*, 8101. [CrossRef]
7. Bournet, P.E.; Boulard, T. Effect of ventilator configuration on the distributed climate of greenhouses: A review of experimental and CFD studies. *Comput. Electron. Agric.* **2010**, *74*, 195–217. [CrossRef]
8. Aguilar-Rodríguez, C.E.; Flores-Velázquez, J.; Rojano, F.; Flores-Magdaleno, H.; Panta, E.R. Simulation of Water Vapor and Near Infrared Radiation to Predict Vapor Pressure Deficit in a Greenhouse Using CFD. *Processes* **2021**, *9*, 1587. [CrossRef]
9. Soussi, M.; Chaibi, M.T.; Buchholz, M.; Saghrouni, Z. Comprehensive Review on Climate Control and Cooling Systems in Greenhouses under Hot and Arid Conditions. *Agronomy* **2022**, *12*, 626. [CrossRef]
10. Sedat, B.; Adil, A. Effect of greenhouse cooling methods on the growth and yield of tomato in a Mediterranean climate. *Int. J. Hortic. Agric. Food Sci. (IJHAF)* **2018**, *2*, 199–207.
11. Adams, S.R.; Cockshull, K.E.; Cave, C.R.J. Effects of temperature on the growth and development of tomato fruits. *Ann. Bot.* **2001**, *88*, 869–877. [CrossRef]
12. Morales, D.; Rodriguez, P.; Dell'Amico, J.; Nicolas, J.; Torrecillas, A.; Sanchez-Blanco, M.J. High temperature preconditioning and thermal shock imposition affects water relations, gas exchange and root hydraulic conductivity in Tomato. *Biol. Plant.* **2003**, *47*, 6–12. [CrossRef]
13. Peet, M.; Sato, S.; Clemente, C.; Pressman, E. Heat stress increases sensitivity of pollen, fruit and seed production in tomatoes (*Lycopersicon esculentum* Mill.) to non-optimal vapor pressure deficits. *Acta Hortic.* **2003**, *618*, 209–215. [CrossRef]
14. Liu, X.; Li, H.; Li, Y.; Yue, X.; Tian, S.; Li, T. Effect of internal surface structure of the north wall on Chinese solar greenhouse thermal microclimate based on computational fluid dynamics. *PLoS ONE* **2020**, *15*, e0231316. [CrossRef] [PubMed]
15. Bartzanas, T.; Boulard, T.; Kittas, C. Numerical simulation of the airflow and temperature distribution in a tunnel greenhouse equipped with insect-proof screen in the openings. *Comput. Electron. Agric.* **2002**, *34*, 207–221. [CrossRef]
16. Benni, S.; Tassinari, P.; Bonora, F.; Barbaresi, A.; Torreggiani, D. Efficacy of greenhouse natural ventilation: Environmental monitoring and CFD simulations of a study case. *Energy Build.* **2016**, *125*, 276–286. [CrossRef]
17. Reynafarje, X.; Villagrán, E.A.; Bojacá, C.R.; Gil, R.; Schrevens, E. Simulation and validation of the airflow inside a naturally ventilated greenhouse designed for tropical conditions. *Acta Hortic.* **2020**, *1271*, 55–62. [CrossRef]
18. Villagrán, E.A.; Romero, E.J.B.; Bojacá, C.R. Transient CFD analysis of the natural ventilation of three types of greenhouses used for agricultural production in a tropical mountain climate. *Biosyst. Eng.* **2019**, *188*, 288–304. [CrossRef]
19. Molina-Aiz, F.D.; Valera, D.L.; López, A. Airflow at the openings of a naturally ventilated Almería-type greenhouse with insect-proof screens. *Acta Hortic.* **2011**, *893*, 545–552. [CrossRef]
20. Villagrán, E.; Bojacá, C.; Akrami, M. Contribution to the Sustainability of Agricultural Production in Greenhouses Built on Slope Soils: A Numerical Study of the Microclimatic Behavior of a Typical Colombian Structure. *Sustainability* **2021**, *13*, 4748. [CrossRef]
21. Kobayashi, K.; Salam, M.U. Comparing Simulated and Measured Values Using Mean Squared Deviation and its Components. *Agron. J.* **2000**, *92*, 345. [CrossRef]
22. Lopez, A. Validación de un Modelo Matemático Para Predecir Las Condiciones Climáticas Interna en un Invernadero Localizado en la Zona Norte de Cartago, Costa Rica. Bachelor Thesis, Universidad de Costa Rica, San Jose de Costa Rica, Costa Rica, 2012.
23. Tesi, R. *Medios de Protección Para la Horto Florofruticultura y el Viverismo*, 3rd ed.; Mundiprensa: Madrid, Spain, 2001.
24. Subin, M.C.; Lourence, J.S.; Karthikeyan, R.; Periasamy, C. Analysis of materials used for Greenhouse roof covering-structure using CFD. *IOP Conf. Ser. Mater. Sci. Eng.* **2018**, *334*, 012068. [CrossRef]

25. Aguilar-Rodríguez, C.E.; Flores-Velázquez, J.; Rojano, F.; Ojeda-Bustamante, W.; Iñiguez-Covarrubias, M. Tomato (*Solanum lycopersicum* L.) crop cycle estimation in greenhouse, based on degree day heat (GDC) simulated in CFD. *Tecnol. Cienc. Agua* **2020**, *11*, 27–57. [CrossRef]
26. Mesmoudi, K.; Meguallati, K.; Bournet, P.E. Effect of the greenhouse design on the thermal behavior and microclimate distribution in greenhouses installed under semi-arid climate. *Heat Transfer–Asian Res.* **2017**, *46*, 1294–1311. [CrossRef]
27. Chu, C.R.; Lan, T.W.; Tasi, R.K.; Wu, T.R.; Yang, C.K. Wind-driven natural ventilation of greenhouses with vegetation. *Biosyst. Eng.* **2017**, *164*, 221–234. [CrossRef]
28. Cemek, B.; Atiş, A.; Küçüktopçu, E. Evaluation of temperature distribution in different greenhouse models using computational fluid dynamics (CFD). *Anadolu J. Agric. Sci.* **2017**, *32*, 54. [CrossRef]
29. Taloub, D.; Bouras, A.; Driss, Z. Effect of the Soil Inclination on Natural Convection in Half-Elliptical Greenhouses. *J. Eng. Res. Afr.* **2020**, *50*, 70–78. [CrossRef]
30. Villagran, E.; Bojacá, C. Three-dimensional numerical simulation of the thermal and aerodynamic behavior of a roof structure built on a slope and used for horticultural production. *Comun. Sci.* **2021**, *12*, e3593.
31. Villagran, E.; Bojacá, C. Analysis of the microclimatic behavior of a greenhouse used to produce carnation (*Dianthus caryophyllus* L.). *Ornam. Hortic.* **2020**, *26*, 109–204. [CrossRef]
32. Ma, D.; Carpenter, N.; Maki, H.; Rehman, T.U.; Tuinstra, M.R.; Jin, J. Greenhouse environment modeling and simulation for microclimate control. *Comput. Electron. Agric.* **2019**, *162*, 134–142. [CrossRef]
33. Saberian, A.; Sajadiye, S.M. The effect of dynamic solar heat load on the greenhouse microclimate using CFD simulation. *Renew. Energy* **2019**, *138*, 722–737. [CrossRef]
34. Villagran, E.; Bojacá, C. Experimental evaluation of the thermal and hygrometric behavior of a Colombian greenhouse used for the production of roses (*Rosa* spp.). *Ornam. Hortic.* **2020**, *26*, 205–219. [CrossRef]
35. Bojacá, C.R.; Gil, R.; Gómez, S.; Cooman, A.; Schrevens, E. Analysis of greenhouse air temperature distribution using geostatistical methods. *Trans. ASABE* **2009**, *52*, 957–968. [CrossRef]
36. Villagrán, E.A.; Bojacá, C.R. CFD simulation of the increase of the roof ventilation area in a traditional Colombian greenhouse: Effect on air flow patterns and thermal behavior. *Int. J. Heat Technol.* **2019**, *37*, 881–892.
37. Akrami, M.; Mutlum, C.D.; Javadi, A.A.; Salah, A.H.; Fath, H.; Dibaj, M.; Farmani, R.; Mohammed, R.H.; Negm, A. Analysis of inlet configurations on the microclimate conditions of a novel standalone agricultural greenhouse for Egypt using computational fluid dynamics. *Sustainability* **2021**, *13*, 1446. [CrossRef]
38. Kuroyanagi, T. Investigating air leakage and wind pressure coefficients of single-span plastic greenhouses using computational fluid dynamics. *Biosyst. Eng.* **2017**, *163*, 15–27. [CrossRef]
39. Jiao, W.; Liu, Q.; Gao, L.; Liu, K.; Shi, R.; Ta, N. Computational Fluid Dynamics-Based Simulation of Crop Canopy Temperature and Humidity in Double-Film Solar Greenhouse. *J. Sens.* **2020**, *2020*, 8874468. [CrossRef]

Article

# Simulation of Water Vapor and Near Infrared Radiation to Predict Vapor Pressure Deficit in a Greenhouse Using CFD

Cruz Ernesto Aguilar-Rodríguez <sup>1</sup>, Jorge Flores-Velázquez <sup>2,\*</sup>, Fernando Rojano <sup>3</sup>, Hector Flores-Magdaleno <sup>2</sup> and Enrique Rubiños Panta <sup>2</sup>

<sup>1</sup> Tecnológico Nacional de México/ITS de los Reyes, Carretera Los Reyes-Jacona, Col. Libertad, Los Reyes de Salgado 60300, Michoacán, México; ernesto.ar@losreyes.tecnm.mx

<sup>2</sup> Posgrado en Hidrociencias, Colegio de Postgraduados, Campus Montecillo, Carretera México-Tezcoco Km 36.5, Tezcoco 56230, Estado de México, México; mhector@colpos.mx (H.F.-M.); jerp@colpos.mx (E.R.P.)

<sup>3</sup> Gus R. Douglass Institute, West Virginia State University, Institute, WV 25112, USA; fernando.rojano@wvstateu.edu

\* Correspondence: jorgelv@colpos.mx; Tel.: +52-59595-20200

**Abstract:** Vapor pressure deficit (VPD) can be used as an indicator to schedule greenhouse irrigation. VPD can be estimated as a function of relative humidity (RH) and temperature (T). The objective of this work was to analyze spatial variation in VPD as an indicator of water stress influenced by concentration of water vapor and intensity of near infrared (NIR). The study was carried out in an empty three-span sawtooth greenhouse with natural ventilation under the local climate in Montecillo, México; these findings established a base value to analyze greenhouse field conditions prior to the influence from a crop. The experimental phase consisted of recording data (3 February 2019–24 February 2019) on temperature, humidity, solar radiation, and wind speed, which were used for developing a model in computational fluid dynamics (CFD). Then, this model was used to estimate VPD, considering changes in mass fraction of water vapor and the intensity of NIR. Scenarios with 50, 70, and 90% external RH were evaluated. It was found that without a crop, temperature was not affected by the variation in the mass fraction of water vapor and the intensity of NIR in the simulated scenarios, each of which generated a thermal gradient within the range of 4 °C. When considering the scenario of 90% external RH, we found the best VPD range along the greenhouse (2–3 kPa) that would be a favorable field condition for crops. Differences between VPD with and without a crop can be used to estimate the water quantity needs for crop growth based on the climate variables examined in this study, where higher VPD values require more water for irrigation.

**Keywords:** greenhouse irrigation; environmental comfort; naturally ventilated greenhouse

**Citation:** Aguilar-Rodríguez, C.E.; Flores-Velázquez, J.; Rojano, F.; Flores-Magdaleno, H.; Panta, E.R. Simulation of Water Vapor and Near Infrared Radiation to Predict Vapor Pressure Deficit in a Greenhouse Using CFD. *Processes* **2021**, *9*, 1587. <https://doi.org/10.3390/pr9091587>

Academic Editor: Alfredo Iranzo

Received: 28 July 2021

Accepted: 31 August 2021

Published: 4 September 2021

**Publisher's Note:** MDPI stays neutral with regard to jurisdictional claims in published maps and institutional affiliations.



**Copyright:** © 2021 by the authors. Licensee MDPI, Basel, Switzerland. This article is an open access article distributed under the terms and conditions of the Creative Commons Attribution (CC BY) license (<https://creativecommons.org/licenses/by/4.0/>).

## 1. Introduction

In greenhouses, the ventilation system favors the distribution of temperature inside. With natural ventilation, air exchange sometimes becomes insufficient due to outside wind speeds equal to or less than 1 m s<sup>-1</sup>, causing an increase in temperature and reducing the concentration of CO<sub>2</sub> and relative humidity [% (RH)] [1–3]. In 2017, Cemek et al. [4] concluded that ventilation efficiency should be further analyzed with the aim of establishing the best environmental conditions favoring plant growth parameters. Wind speed and direction are factors impacting the environmental comfort of the internal climate of a greenhouse, specifically in terms of the exchange of heat and mass between the inside and outside [5–7]. The ventilation system of a greenhouse may eliminate excess heat and maintain acceptable CO<sub>2</sub> and water vapor levels for crops [8,9]. Strategies of natural ventilation are diversified according to the season of the year; for instance, during winter, natural ventilation allows the elimination of excess humidity, while in summer it sometimes provides insufficient cooling, requiring the use of auxiliary mechanical ventilation systems [10].



One of the parameters for greenhouse climate management that integrates temperature and relative humidity in a single value, used as an indicator of water vapor environment, is the vapor pressure deficit (VPD). Fernández et al., Prenger and Ling, and Dik and Wubben [11–13] mention that VPD is a tool that can be used for climate, water, and disease management within the greenhouse. López and Shtienberg [14,15] point out that a VPD greater than 1.25 kPa in a greenhouse generates a high transpiration rate of plants, so it is important to maintain VPD levels. VPD can be used as an indicator to infer the time to apply irrigation because it measures the amount of water that the surrounding atmosphere can receive. Veluzan [16] mentions that the loss of water by a plant depends on the VPD; when the VPD increases, the plant begins to perspire, and when it reaches 2 kPa, stomatal closure may be observed, reducing plant growth. The planning and management of VPD values in a greenhouse imply a knowledge of the levels of humidity (RH) and radiation (NIR) that prevail during different seasons.

Similarly, the distribution of solar radiation in a greenhouse is important because it is an input and the driving force of the physiological functions of plants. Solar radiation is the main factor for crop growth inside greenhouses, having an indirect impact on air temperature and regulating two physiological phenomena in plants: (i) transpiration and (ii) photosynthesis [17]. The energy consumption of a greenhouse depends on the incoming solar radiation [18], which is influenced by the greenhouse design (orientation and shape of the roof), the thermo-physical and optical properties of the cladding, and the climate [19]. Therefore, the orientation and shape of the roof become the most important physical elements in the distribution of solar radiation [20–22].

Solar radiation is a factor used to determine the energy balance of greenhouses. A numerical model makes it possible to estimate transmission of solar radiation, emphasizing the properties of cladding materials [23]. In the 1980s, dynamic models of the greenhouse climate were developed with the aim of calculating effects of solar radiation on the quality and production of crops [24,25]. Solar radiation modeling was initially approached indirectly using analytical models to calculate the surface temperatures that developed due to short- and long-wave radiation [26]. Likewise, the radioactive effect as a heat source was estimated in the energy equation attributed to short-wave and thermal solar radiation emitted by heated surfaces [27].

Water vapor absorbs and emits more infrared radiation in the atmosphere; its concentration increases as global warming increases [28,29], inducing an increase in environmental evaporation because the saturated water vapor margin widens due to the increase in temperature. Water vapor participates as a greenhouse gas, having an impact on atmospheric structure and the precipitation regime [30]. Water vapor is characterized by absorbing at wavelengths centered at 940, 1100, 1380, and 1870 nm, between 80 and 99.5% of solar energy at these lengths. Water vapor absorbs more near-infrared (NIR) radiation than any other component in the atmosphere. Under atmospheric conditions and a clear sky (no clouds), the water vapor absorbs approximately  $43 \text{ W m}^{-2}$  of the annual average of incident solar radiation [31]. Of this absorbed solar radiation, 98% belongs to the near infrared (NIR) zone, that is to say, wavelengths greater than  $0.7 \mu\text{m}$  [32].

In more recent years, computational models have been used to solve radiation transport, the most popular being the discrete ordinate (DO) model used by ANSYS FLUENT [8,33–36]. The DO model bases its calculations on solving the short-wave and long-wave radioactive transfer equations (RTE) [33,37–40]. It is useful for calculating surface-to-surface radiation exchanges, but not for transfers within the canopy [41].

Full-scale simulations with 2D and 3D CFD models have been used to study the microclimate distribution in greenhouses through the incorporation of solar radiation models and sensible and latent heat exchange sub-models [42]. Likewise, these models were used to evaluate the environmental effect in the greenhouse caused by its design [43], cladding material [44], time of day, season of the year [45,46], the type of ventilation, and its configuration [47]. However, scarce or no information is available to analyze the effect of the intensity of NIR and the concentration of water vapor on the air temperature of a

greenhouse [48–50]. VPD is the difference between the amount of water in air as vapor and the amount of moisture the air can retain when it is saturated with water, so it can be considered a useful way to measure the microclimate of a greenhouse; the value of VPD can be estimated through the equation of Rosenberg et al. [51],  $VPD = 0.61078 \exp \left[ \frac{(17.269 \cdot T)}{(T + 237.3)} \right] \cdot [1 + RH/100]$ , where T is the air temperature.

The objective of this work was to develop and evaluate a computational model to estimate VPD values as an indicator of water stress, due to the relationship between water quantity or vapor concentration (RH) and NIR in the greenhouse environment. The idea of simulating an empty greenhouse assumed that the exchange of mass and energy between the exterior and interior of the greenhouse only occurs through natural ventilation, and there is no generation of water vapor inside the greenhouse. Predicting VPD values without cultivation facilitates an easier understanding of the requirements to achieve recommended ranges.

## 2. Materials and Methods

### 2.1. Description of Experimental Site

The greenhouse used in this study is located at Campus Montecillo, Colegio de Postgraduados in the State of Mexico ( $19^{\circ}27'45.5''$  N,  $98^{\circ}54'12.2''$  W) with an altitude of 2239 masl, oriented from north to south on a plain where monthly mean temperatures range from 5 to 25 °C. It has an area of 1050 m<sup>2</sup>; it is a three-span sawtooth type covered with translucent polyethylene on the floor and sides, polycarbonate on the roof, and anti-insect mesh on three side windows and three roof windows. The greenhouse relies on a natural ventilation system with the roof and side windows fully open.

For data acquisition, an eddy covariance system was installed at a distance of 2.4 m, windward, equipped with a sonic anemometer (3D, Campbell Scientific Ltd., Antony, France), an EC150 gas analyzer (Campbell Scientific Inc., Logan, UT, USA), a net radiometer (NR-LITE2 Kipp and Zone BV, Delft, The Netherlands), an LI-200 pyranometer (LI-COR Inc., Lincoln, NE, USA), an LI-190R Quantum sensor (Li-Cor Inc., Lincoln, NE, USA), a temperature and humidity sensor (HMP155A, Campbell Scientific, Logan, UT, USA), and four sensors for recording soil temperature (TCAV thermocouple, Campbell Scientific Inc., Logan, UT, USA). Seven temperature sensors (DS18B20, Maxim Integrated, San Jose, CA, USA) and three humidity sensors (DHT22, Zhengxinyuan Electronics Co., Ltd., Shenzhen, China) were installed in distributed locations in the three spans at a height of 3 m (Figure 1).

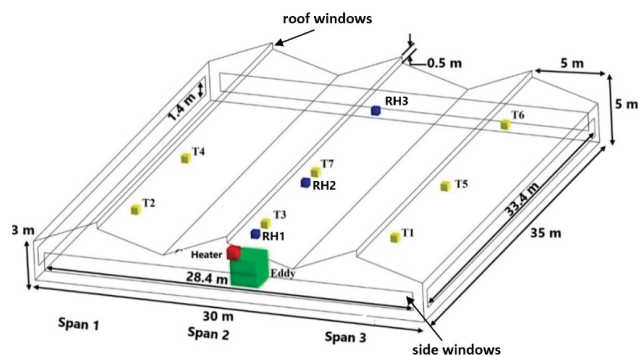


**Figure 1.** Dimensions and distribution of the heater (■) and the temperature (■), humidity (■), and eddy covariance system (■) sensors in the three spans of the experimental greenhouse.

Data logging and storage were performed every 5 s for temperature and humidity, 100 ms for the anemometer, and 20 s for the net radiometer. The monitoring period was during the month of February 2019, the month when there commonly is a RH gradient that oscillates between 30–100% inside the greenhouse between the day and night periods, respectively. During data collection, there was no crop, thus the humidity inside the

greenhouse came from outside. Information storage was carried out with a data logger system (CR3000 Micrologger, Campbell Scientific, Inc., Logan, UT, USA) for the eddy covariance system, and an Arduino Data Logger Shield for the DS18B20 and DHT22 sensors. Outside the greenhouse there was a meteorological station (Vantage Pro2 Plus, Davis Instruments, Hayward, CA, USA) used to collect data on temperature, humidity, solar radiation, and wind direction and speed—measurements that were used as the initial boundary conditions of the computational model. The stored information was downloaded and processed in Microsoft Excel to determine the input environmental conditions of the computational model.

## 2.2. Computational Model

The computational model was developed and simulated in ANSYS® *Fluent*®. The geometry was developed in ANSYS® *Workbench* using the SpaceClaim tool. The mesh of the model domain was built in *Meshing*. The properties of the greenhouse materials were incorporated into the model following Tables 1 and 2 [8,19,44,52]. Mesh sensitivity analysis of the model was performed to obtain reliable predictions in the same way as in [53]. Mesh was built with structured elements, using an orthogonal quality of 0.98 and distortion of  $1.935 \times 10^{-0.02}$ .

**Table 1.** Properties of cladding materials.

Material	Density ( $\rho$ ) ( $\text{kg m}^{-3}$ )	Specific Heat ( $CP$ ) ( $\text{J kg}^{-3} \text{ }^\circ\text{C}^{-1}$ )	Thermal Conductivity ( $k$ ) ( $\text{W m}^{-1} \text{ }^\circ\text{C}^{-1}$ )	Thickness (mm)
Soil	1300	800	1	
Wall and mulch (Polyethylene PE)	925.5	1900	0.3	0.18
Roof (Polycarbonate PC)	1200	1200	0.19	6

**Table 2.** Optical properties of materials to thermal radiation.

Materials	Emissivity ( $\mathcal{E}$ )	Transmissivity ( $\tau$ )	Reflectivity ( $\delta$ )
Polycarbonate	0.935	0.25	0.09
Polyethylene	0.8	0.1	0.03
Soil	0.95		1.92
Air	0.0015		1.009

The conditions of the model and of the variables applied to the air flow to solve the transport equations discretized in algebraic equations and calculated by numerical methods are defined in Table 3. For the species model, the mass fraction of water vapor was used to calculate the relative humidity distribution.

**Table 3.** Settings of the computational model.

Condition	Method
Solver	Pressure-based
Analysis Type	Steady
Viscosity Model	Sstandard k-ε (2 equations)
Energy model	Turn on
Radiation model	Discrete ordinate (DO)
Grey longwave	NIR 0.76–1.1 μm
Species	Mass fraction constant
Boundary conditions	
Air Temperature	Constant (22 °C)
Air Flow Rate	Constant (3136 kg s <sup>-1</sup> )
Porous jump	Permeability face, thin porous media and drag coefficient
Heat source	Constant from soil (44.1 °C)

### 2.3. Fundamental Equations of Modeled Flow

The general transport equation that can be solved numerically by CFD to explicitly calculate the velocity and temperature field associated with a flow in three dimensions at steady state can be described in the following terms [19,51,54]:

$$\frac{\partial \Phi}{\partial t} + \frac{\partial(U\Phi)}{\partial x} + \frac{\partial(V\Phi)}{\partial y} + \frac{\partial(W\Phi)}{\partial z} = -\Gamma \Delta \Phi^2 + S_{\Phi} \quad (1)$$

where,  $\Phi$  represents the concentration of the dimensionless term, that is, momentum, mass (air and water vapor mass fraction), and energy.  $U$ ,  $V$ , and  $W$  are the velocity vector components in the three dimensions (m s<sup>-1</sup>),  $\Gamma$  is the diffusive coefficient (kg m<sup>-1</sup> s<sup>-1</sup>), and  $S_{\Phi}$  is the source term.

Turbulence inside the greenhouse was considered using the  $k$ - $\epsilon$  model [18,55] that gave rise to two supplementary equations and species. The choice of the model resulted from the comparison of different turbulence models in greenhouses [38].

For energy, the source term is a function of NIR absorption. Therefore, the equation can be described in general terms as follows [38,41]:

$$c_p \left( \frac{\partial(\bar{\rho}\bar{T})}{\partial t} + \frac{\partial}{\partial x_j} (\bar{\rho}(\bar{u}_j\bar{T})) \right) = \frac{\partial}{\partial x_i} \left( \lambda_f + \frac{\mu_t c_p}{Pr_t} \right) \frac{\partial \bar{T}}{\partial x_i} + S_r \quad (2)$$

where,  $c_p$  is the specific heat of air (J kg<sup>-1</sup> K<sup>-1</sup>),  $\rho$  is the air density (kg m<sup>-3</sup>),  $\bar{T}$  is the air temperature (K or °C),  $u_i$  is the velocity component (m s<sup>-1</sup>),  $\lambda_f$  is the thermal conductivity of air (W m<sup>-1</sup> K<sup>-1</sup>),  $\mu_t$  is the turbulent viscosity of air (kg m<sup>-1</sup> s<sup>-1</sup>),  $Pr_t$  is the turbulent Prandtl number, and  $S_r$  is the source term.

### 2.4. Radiative Modeling Equation

The discrete ordinate model (DO) solves the radiative transfer equation (RTE) for a finite number of angles, each associated with a  $\vec{s}$  vector direction in the global Cartesian system [17,19,33,38,56]. The luminance distribution  $I_{\lambda}(\vec{r}, \vec{s})$  was obtained through the solution of the RTE; the activation of the RTE submodel was used to couple the DO model and divide the near infrared NIR spectral region (0.76–1.1 μm) [33,37,57].

$$\frac{dI_{\lambda}(\vec{r}, \vec{s})}{ds} + (a_{\lambda} + \sigma_s)I_{\lambda}(\vec{r}, \vec{s}) = a_{\lambda}n^2I_{b\lambda} + \frac{\sigma_s}{4\pi} \int_0^{4\pi} I_{\lambda}(\vec{r}, \vec{s}^I) \phi\left(\frac{\vec{s}}{\vec{s}^I}\right) d\Omega' \quad (3)$$

where,  $I_{\lambda}$  is the radiation intensity for the wavelength (W m<sup>-2</sup> sr<sup>-1</sup>),  $\phi$  is the scattering phase function,  $\Omega'$  is the solid angle,  $\vec{r}$  is the position vector (m),  $\vec{s}$  is the unitary vector

along the radiation propagation direction,  $\vec{s}^{-1}$  is the direction of the scattering vector,  $\sigma_s$  is the scattering coefficient ( $\text{m}^{-1}$ ),  $a_\lambda$  is the spectral absorption coefficient ( $\text{m}^{-1}$ ),  $I_{b\lambda}$  is the monochromatic luminance of a black body ( $\text{W m}^{-3} \text{sr}^{-1}$ ), and  $n$  is the refractive index.

The radiation parameter was considered as constant in the band length. The net radiation flux absorbed by a control volume was then defined by the expression described by Nebbali et al. [38]:

$$S_r = -\text{div} \left[ \int_0^\infty \left( \int_0^{4\pi} I_\lambda(\vec{r}, \vec{s}) \vec{s} \, d\Omega \right) d\lambda \right] \quad (4)$$

where  $S_r$  is the source term of the energy Equation (1), allowing a coupling between the energy and radiation transfer equations.

### 2.5. Evaluation of the Computational Model

The computational model was evaluated by means of a statistical analysis of the average of the temperature data, RH inside the greenhouse, and the point data of wind speed and NIR, simulated, and experimental. An analysis of variance (ANOVA) with a significance level of 0.05 was used to parametrically contrast the difference of the variables. The data of the experimental models used for the evaluation were obtained between 01:30 p.m. and 03:30 p.m. (3 February 2019); this time was considered to be the solar middle day, where a change of position occurs at the zenith.

### 2.6. Simulation Scenarios

The simulated scenarios were based on a hypothesis regarding variation in the mass fraction of water vapor concentration in the air derived from temporal climatic variations. The change in concentration of the water vapor mass fraction in the computational model was performed on the basis of the RH range recorded in the air from February 3 to 24. The computational model was focused on the highest NIR intensity during the day, which was used for the simulation scenarios. In the computational model, only the exterior RH concentration was artificially changed to three scenarios for simulating: (a) 50, (b) 70, and (c) 90%, which were equivalent to a water vapor mass fraction of 0.013, 0.018, and 0.023 (g/g), respectively. The change in percent of RH to grams of water vapor per grams of air allowed estimating the effect of moisture concentration on the thermal gradient, assuming that water vapor is a greenhouse gas and impacts the temperature and VPD variables of a greenhouse. Subsequently, two more simulations were performed to modify the NIR intensity ( $b1 = 50 \text{ W m}^{-2}$  and  $b2 = 100 \text{ W m}^{-2}$ ), for which scenario b was considered because it represents the RH of a typical day in February for the site of study. The simulation of the scenario incorporating cultivation was performed using only the porous medium approach, where there is an effect on pressure drop, which the Forchheimer equation can express. The environmental analysis of the simulations inside the greenhouse was carried out at a height between 1.5 and 2 m, a height considered representative for growing tomatoes, and at which environmental changes affect the quality of the crop.

## 3. Results and Discussion

### 3.1. Validation of the Computational Model

To evaluate the feasibility of using the computational model, we used a statistical indicator that measures the correlation between the simulated temperature, humidity, wind speed, and NIR values and those recorded by the sensors on 9 February 2019. The variation of the experimental temperature data from 2:00 p.m. to 2:30 p.m. shows that the values were concentrated, indicating that the average value of the temperature recorded by the sensors was very probable, and the recorded data were reliable (Figure 2).

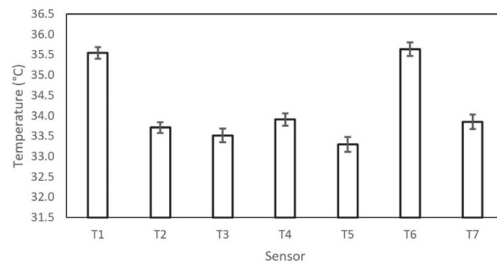


**Figure 2.** Spatial variation in temperature from 2:00 p.m. to 2:30 p.m.

Table 4 shows that the mean measurements of temperature, wind speed, RH, and NIR, registered and simulated, are values close to each other. To measure this correlation, an ANOVA statistical analysis was performed with a significance level of 0.05, considering that if the significance level was less than the probability value  $p$  (level of significance  $< p$  value) there was no significant difference between the registered and simulated variables. (Table 5). Therefore, the evaluated model could be used in the simulations.

**Table 4.** Mean measurements of temperature, relative humidity, NIR, and wind speed data in the models were evaluated after midday.

Hour	Temperature (°C)		Hour	Relativity Humidity (%)	
	Model	Experimental		Model	Experimental
1:30	31.587	32.716	1:30	36.082	37.184
2:00	31.905	32.849	2:00	36.222	36.631
2:30	31.931	33.795	2:30	36.896	35.978
3:00	32.017	32.688	3:00	36.66	35.81
3:30	32.458	30.812	3:30	34.206	35.747

Hour	NIR ( $W m^{-2}$ )		Hour	Wind Velocity ( $m s^{-1}$ )	
	Model	Experimental		Model	Experimental
1:30	120.885	127.62	1:30	0.03	0.033
2:00	174.962	161.78	2:00	0.031	0.03
2:30	189.99	176.42	2:30	0.03	0.037
3:00	162.082	153	3:00	0.032	0.027
3:30	118.073	120.22	3:30	0.023	0.023

**Table 5.** Comparison between the level of significance and the  $p$ -value.

Variable	Level of Significance and the $p$ -Value
Temperature	0.05 < 0.27
Relative humidity	0.05 < 0.65
Wind speed	0.05 < 0.85
NIR	0.05 < 0.85

### 3.2. Analysis of the Results of Simulated Scenarios

The environmental analysis of the simulated scenarios was performed on the basis of the concentration of water vapor in the air, temperature, NIR, and vapor pressure deficit (VPD)—indicators used to manage the greenhouse environment and maintain suitable conditions for growing tomatoes within it. The analysis of the influence of concentration of the water vapor on the temperature was limited to measurements at the center of each span; in contrast, simulated data were computed as averages along the greenhouse, away from the predominant air inlet in the greenhouse. In each simulated scenario, a dataset of 100 data points was obtained longitudinally at a height of 1.5 m and was used for the environmental analysis shown in Figure 3. These distances were selected for the analysis

because the central span was characterized by greater thermal and humidity gradients in the air between the windward and leeward zones. The results in Figure 3 show a decrease in temperature in relation to the increase in water vapor concentration in the simulated scenarios. The thermal gradient range in the greenhouse (length) was around 2 °C in the crop zone (1.5 m height), being remarkable in the first half of the greenhouse. In the area near the outlet, the thermal gradient range was negligible (0.15 °C) between scenarios a, b, and c.

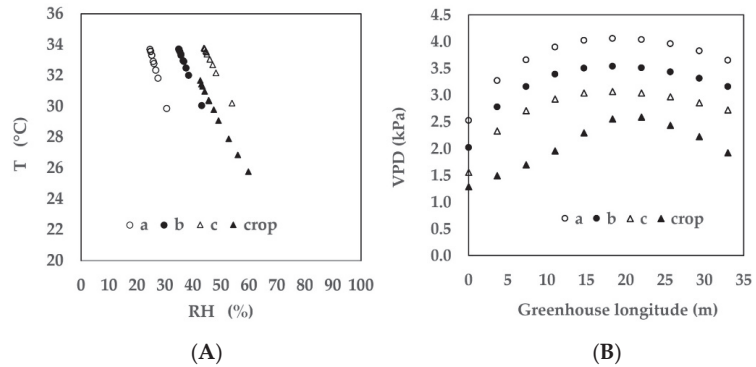


**Figure 3.** (A) Temperature distribution (°C) and (B) VPD (kPa) for the simulated scenarios along the length of greenhouse at 1.5 m height. The three scenarios a, b and c, and simulating the incorporation of a tomato crop to develop LAI 3.5.

On the other hand, for the VPD along the greenhouse length, there was a 2 kPa difference between scenarios, and this remained constant. This finding was derived from the influence on temperature (T) and relative humidity (RH) from external local climate conditions. In addition, for crop simulations, enhanced environmental conditions favoring crop growth were observed inside the greenhouse. We concluded that the most significant change occurred in the first half of the greenhouse. In the area near the outlet, the increase in water vapor concentration did not influence the increase in temperature.

To calculate the VPD in the greenhouse, the equation was programmed with a user-defined function (UDF) in CFD. The VPD value was estimated as the difference between the saturation vapor pressure value and the actual vapor pressure of the air ( $VPD = PV_{sat} - P_{vair}$ ), a method recommended by Howell and Dusek, and FAO [58,59]. The greenhouse analysis was performed in all the simulated scenarios as an average of 10 data points uniformly distributed within a height range of 1.9–2 m at the inlet, center, and outlet of the central span. The results in Table 6 show the spatial variation in the water vapor concentration and thermal gradient at three points of observation along the length of the greenhouse.

**Table 6.** Average of ten data of the variables: T, RH, and VPD simulated at a height from 1.9 to 2 m at the inlet, center, and outlet area of the central span of the greenhouse.

Position	Scenario	T (°C)	RH (%)	VPD (kPa)
Inlet	a	32.94	25.68	3.73
	b	33.10	36.15	3.23
	c	33.23	45.49	2.78
Center	a	34.83	23.11	4.28
	b	34.92	32.67	3.77
	c	34.99	41.24	3.30
Outlet	a	34.70	23.29	4.24
	b	34.77	32.93	3.72
	c	34.85	41.56	3.26

The temperature increase was generated from the absorption of NIR by water vapor; however, when the mass fraction of water vapor remains constant in the air at the center and outlet areas of the greenhouse, the RH gradient is minimal equal to 0.78%. Therefore, the thermal effect generated by the energy exchange between water vapor and NIR is negligible. In all scenarios, there is a reduction between the outside RH and that of the greenhouse with a gradient that ranges between 45 and 50% caused by the low speed of the outside wind ( $0.64 \text{ m s}^{-1}$ ) and the anti-insect mesh in the windows.

The increase in temperature inside the greenhouse, given the increase in water vapor concentration in the air, was not significant, ranging from  $0.15$  to  $0.28 \text{ }^\circ\text{C}$  (Table 6). For this reason, it was inferred that the temperature remained constant under the simulated conditions and was not influenced by the variation in the mass fraction of water vapor.

The simulation of scenario b was carried out with a change in the intensity emitted by the NIR ( $50$  and  $100 \text{ W m}^{-2}$ ) to analyze the effect it had on temperature. The results of the simulations (Table 7) show that when there was a change in the intensity of NIR, the highest thermal gradient ( $0.23 \text{ }^\circ\text{C}$ ) occurred at the inlet and outlet areas of span 2 of the greenhouse, where the wind speeds were below  $0.01 \text{ m s}^{-1}$  and air movement was generated by the convective effect caused by temperature differences. This was also demonstrated by Sun et al., and Zeroual et al. [3,7], where outside wind speeds close to  $1 \text{ m s}^{-1}$  were insufficient to renew the air inside the greenhouse, affecting the exchange of heat and mass between the outside and the inside.

**Table 7.** Climate variation with a change in NIR intensity for scenario b.

Position	Scenario	T ( $^\circ\text{C}$ )	RH (%)	VPD (kPa)	NIR ( $\text{W m}^{-2}$ )
Inlet	b1	32.97	36.42	3.19	60.46
	b	33.02	36.31	3.21	120.91
	b2	33.10	36.15	3.23	189.98
Center	b1	34.75	32.97	3.72	66.33
	b	34.82	32.85	3.74	132.67
	b2	34.92	32.67	3.77	195.94
Outlet	b1	34.59	33.26	3.67	68.45
	b	34.66	33.13	3.69	136.91
	b2	34.77	32.93	3.72	198.69

Derived from the change in the concentration of the mass fraction of water vapor and the NIR intensity in the simulated scenarios, the highest thermal gradient occurred in the inlet area ( $0.29 \text{ }^\circ\text{C}$ ), where the RH of the greenhouse was higher due to the air exchange between outside and inside. Therefore, it could be assumed that the generated temperature gradient was negligible, as in most of the greenhouse it oscillated between  $0.08$ – $0.16 \text{ }^\circ\text{C}$ .

Figure 4 shows the distribution of RH and VPD inside the greenhouse in the simulated scenarios at a height of  $1.5 \text{ m}$ . The results indicate that scenario c presented better environmental conditions for tomato cultivation with lower VPD (kPa), temperature T ( $^\circ\text{C}$ ), and higher RH (%) inside the greenhouse. Nevertheless, there was a 53% reduction in RH between the outside and inside of the greenhouse, causing this scenario to be outside the desirable optimum for tomato (50–60%) [60]. The RH deficit inside the greenhouse caused an increase in the VPD, with values over  $1.3 \text{ kPa}$  for all simulated scenarios, values outside the range for tomato ( $0.3$ – $1.25 \text{ kPa}$ ) according to Grange et al., Körner et al. and Shtienberg [15,61,62]. The VPD values in Figure 4 show that under the conditions of the simulated scenarios, the crop inside the greenhouse would undergo a high rate of transpiration, causing the closure of its stomata and impeding its growth [14].



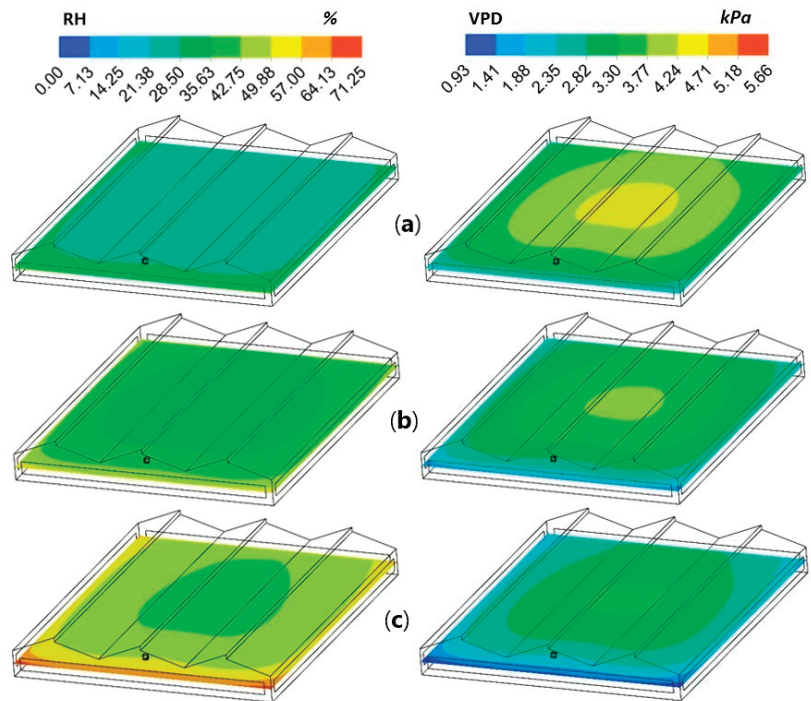


**Figure 4.** Distribution of RH (%) and VPD (kPa) in the greenhouse at 1.5 m height in the simulations for the three scenarios (a–c) specified in Table 6.

Scenario b was simulated with the mean monthly wind speed ( $1.59 \text{ m s}^{-1}$ ) during the month of February in Montecillo, Mexico according to data from the National Meteorological Service (SMN). The purpose of the simulation under these conditions was to predict the effects on environmental conditions that can occur when wind speed increases. These changes were simulated, and the results in Figure 5 show enhanced environmental conditions for tomato crop cultivation compared to the scenario b of Figure 4 with decreases in temperature and VPD that oscillated between  $4\text{--}6 \text{ }^{\circ}\text{C}$  and  $0.9\text{--}1.63 \text{ kPa}$ , respectively. Likewise, it presents an increase in RH of between  $8.3\text{--}15.4\%$  throughout the greenhouse. However, these generated changes were not enough to maintain a RH between  $50\text{--}60\%$ , a temperature below  $30 \text{ }^{\circ}\text{C}$ , and a VPD between  $0.3\text{--}1.25 \text{ kPa}$  throughout the greenhouse.

The results of the simulations carried out in this work also confirm what was described by Chu, Lan, Tasi, Wu, and Yang; and Tong et al. [46,63], where lengths greater than six times the height of the greenhouse present problems in the ventilation rate due to the obstruction generated by the anti-insect mesh and the length of the greenhouse. Therefore, the use of fans and extractors is recommended to avoid stagnant areas in the center of greenhouse buildings when natural ventilation is insufficient to improve the ventilation rate [9,10,64].

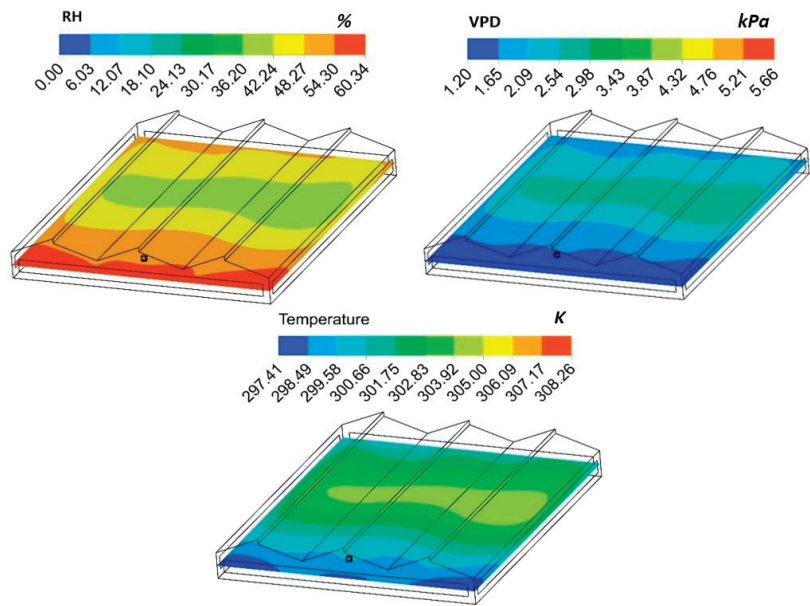


**Figure 5.** Distribution of RH (%), temperature (K), and VPD (kPa) in the greenhouse at 1.5 m height in scenario b, considering the mean monthly wind speed ( $1.59 \text{ m s}^{-1}$ ) during February.

#### 4. Conclusions

The greenhouse air inlet area was the location with the highest energy exchange in all of the simulated scenarios, with a temperature increase of  $0.29 \text{ }^{\circ}\text{C}$  generated by the absorption of NIR and by the exchange of air between the outside and inside. The greenhouse scenarios did not present favorable environmental conditions for tomato cultivation. The temperature exceeded  $30 \text{ }^{\circ}\text{C}$  with an average thermal gradient between the outside and inside of up to  $12 \text{ }^{\circ}\text{C}$ , causing an RH deficit and an increase in VPD to values higher than  $2 \text{ kPa}$ , which consequently would cause excess perspiration in tomato and an expected stomatal closure. The temperature gradient between the outside and inside of the greenhouse was the result of the low wind speed ( $0.64 \text{ m s}^{-1}$ ) and the anti-insect mesh, causing air movement within the greenhouse to be generated by the difference between soil and air temperatures. Environmental conditions improved when the scenario was simulated with the monthly mean wind speed for the month of February ( $1.59 \text{ m s}^{-1}$ ) in Texcoco; however, this was not enough to maintain favorable environmental conditions. From this, it is inferred that natural ventilation is insufficient to reduce the thermal gradient and increase the RH to acceptable values for tomato. Therefore, the use of fans and extractors is recommended to increase the exchange of heat and mass between the outside and inside and help to distribute the RH and temperature evenly in the stagnant area of the greenhouse (in the center of the spans).

**Author Contributions:** C.E.A.-R., conceptualization, investigation, writing—review and editing and data curation. J.F.-V., conceptualization, methodology and supervision. F.R., methodology, review and editing and formal analysis. H.F.-M., validation and visualization. E.R.P., resources and funding acquisition. All authors have read and agreed to the published version of the manuscript.

**Funding:** This research received no external funding.

**Acknowledgments:** The authors want to thank everyone at Mexican Institute of Water Technology. This work is a part of the PhD thesis of C. Ernesto Aguilar in the Graduate Studies of Water Technology and Science. Also, we thank to Migdalia E. Rodriguez Rosales (Professor at the UNISON Mexico) for taking care of the English grammar and style.

**Conflicts of Interest:** The authors declare no conflict of interest.

## References

- Liu, J.Q.; Yin, C.; Zhao, H.D. Ventilation management of solar greenhouse. *Vegetables* **2003**, *2*, 33–34.
- Molina-Aiz, F.D.; Valera, D.L.; Peña, A.A.; Gil, J.A.; López, A. A study of natural ventilation in an Almería-type greenhouse with insect screens by means of tri sonic anemometry. *Biosyst. Eng.* **2009**, *104*, 224–242. [CrossRef]
- Sun, M.; Luo, W.H.; Feng, W.L.; Xiang, L.; Fu, X.G. A web-based expert system for diagnosis and control management of diseases in vegetable crops cultivated under protected conditions. *J. Nanjing Agric. Univ.* **2014**, *37*, 7–14.
- Cemek, B.; Atiş, A.; Küçüktopçu, E. Evaluation of temperature distribution in different greenhouse models using computational fluid dynamics (CFD). *Anadolu J. Agric. Sci.* **2017**, *32*, 54–63. [CrossRef]
- Teitel, M.; Liran, O.; Tanny, J.; Barak, M. Wind driven ventilation of a mono-span greenhouse with a rose crop and continuous screened side vents and its effect on flow patterns and microclimate. *Biosyst. Eng.* **2008**, *101*, 111–122. [CrossRef]
- Rico-Garcia, E.; Soto-Zarazua, G.; Alatorre-Jacome, O.; De la Torre-Gea, G.A.; Gomez-Melendez, D.J. Aerodynamic study of greenhouses using computational fluid dynamics. *Int. J. Phys. Sci.* **2011**, *6*, 6541–6547. [CrossRef]
- Zeroual, S.; Bougoul, S.; Benmoussa, H. Effect of radiative heat transfer and boundary conditions on the airflow and temperature distribution inside a heated tunnel greenhouse. *J. Appl. Mech. Tech. Phys.* **2018**, *59*, 1008–1014. [CrossRef]
- Fidaros, D.; Baxevanou, C.A.; Bartzanas, T.; Kittas, C. Numerical simulation of thermal behavior of a ventilated arc greenhouse during a solar day. *Renew. Energy* **2010**, *35*, 1380–1386. [CrossRef]
- Teitel, M.; Wenger, E. Air exchange and ventilation efficiencies of a monospan greenhouse with one inflow and one outflow through longitudinal side openings. *Biosyst. Eng.* **2014**, *119*, 98–107. [CrossRef]
- Bournet, P.; Boulard, T. Effect of ventilator configuration on the distributed climate of greenhouses: A review of experimental and CFD studies. *Comput. Electron. Agric.* **2010**, *74*, 195–217. [CrossRef]
- Fernandez, M.; Orgaz, F.; Fereres, E.; Lopez, J.; Cespedes, A.; Perez, J.; Bonachela, S.; Gallardo, M. *Programación del Riego de Cultivos Hortícolas Bajo Invernadero en el Sudeste Español*; Fundación CAJAMAR. Caja Rural de Almería y Málaga: Barcelona, Spain, 2001; p. 71.
- Prenger, J.; Ling, P. *Greenhouse condensation control, understanding and using vapor pressure deficit (VPD)*. Extension FactSheet; Ohio State University Extension Fact Sheet: Columbus, OH, USA, 2001; p. 4.
- Dik, A.; Wubben, J. Epidemiology of Botrytis cinerea diseases in greenhouses. In *Biology, Pathology and Control*, 2nd ed.; Elad, Y., Williamson, B., Tudzynsky, P., Delen, N., Eds.; Springer: Dordrecht, The Netherlands, 2001; pp. 319–331.
- Lopez, J. *Control Climático en Invernaderos*, 1st ed.; Novedades agrícolas: Murcia, Spain, 2005; p. 4.
- Shtienberg, D. Rational management of Botrytis-incited diseases: Integration of control measures and use of warning systems. In *Biology, Pathology and Control*, 2nd ed.; Elad, Y., Williamson, B., Tudzynsky, P., Delen, N., Eds.; Springer: Dordrecht, The Netherlands, 2007; pp. 335–346.
- Beluzán, J. Déficit de presión de vapor (DPV) y factores microclimáticos como herramientas de pronóstico de *Botrytis cinerea* Pers. ex Fr., en *Lactuca sativa* L. bajo invernadero. Master Thesis, Universidad Austral de Chile Facultad de Ciencias Agrarias, Valdivia, Chile, 2013.
- Baxevanou, C.; Fidaros, D.; Bartzanas, T.; Kittas, C. Numerical simulation of solar radiation, air flow and temperature distribution in a naturally ventilated tunnel greenhouse. *Agric. Eng. Int. CIGR J.* **2010**, *12*, 48–67.
- Sethi, V.P.; Sharma, S.K. Thermal modeling of a greenhouse integrated to an aquifer coupled cavity flow heat exchanger system. *Sol. Energy* **2007**, *81*, 723–741. [CrossRef]
- Mesmoudi, K.; Meguallati, K.H.; Bournet, P.E. Effect of the greenhouse design on the thermal behavior and microclimate distribution in greenhouses installed under semi-arid climate. *Heat Transf. Asian Res.* **2017**, *46*, 1294–1311. [CrossRef]
- Kendirli, B. Structural analysis of greenhouses: A case study in Turkey. *Build. Environ.* **2006**, *41*, 864–871. [CrossRef]
- Stanciu, C.; Stanciu, D.; Dobrovicescu, A. Effect of greenhouse orientation with respect to E-W axis on its required heating and cooling loads. *Energy Procedia* **2016**, *85*, 498–504. [CrossRef]
- Mobtaker, H.G.; Ajabshirchi, Y.; Ranjbar, S.F.; Matloobi, M. Simulation of thermal performance of solar greenhouse in north-west of Iran: An experimental validation. *Renew. Energy* **2018**, *135*, 88–97. [CrossRef]
- Geoola, F.; Kashti, Y.; Peiper, U.M. A model greenhouse for testing the role of condensation, dust and dirt on the solar radiation. *J. Agric. Eng. Res.* **1998**, *71*, 339–346. [CrossRef]
- Kindelan, M. Dynamic modelling of greenhouse environment. *Trans. ASAE* **1980**, *23*, 1232–1239. [CrossRef]
- Bot, G.P.A. Greenhouse Climate: From Physical Processes to a Dynamic Model. Ph.D. Thesis, Agricultural University of Wageningen, Wageningen, The Netherlands, 1983.
- Molina-Aiz, F.D.; Valera, D.L.; Álvarez, A.J. Measurement and simulation of climate inside Almería-type greenhouses using computational fluid dynamics. *Agric. For. Meteorol.* **2004**, *125*, 33–51. [CrossRef]
- Campan, J.B.; Bot, G.P.A. Determination of greenhouse-specific aspects of ventilation using three-dimensional computational fluid dynamics. *Biosyst. Eng.* **2003**, *84*, 69–77. [CrossRef]
- Miller, G.T. *Ciencia Ambiental: Preservemos la Tierra*, 5th ed.; Thomson: Belmont, Australia, 2002; p. 456.
- Nebel, B.J.; Wright, R.T. *Ciencias ambientales: Ecología y desarrollo sostenible*, 6th ed.; Pearson Educación: London, UK, 1999; p. 69.

30. Collins, W.D.; Lee-Taylor, J.M.; Edwards, D.P.; Francis, G.L. Effects of increased near-infrared absorption by water vapor on climate system. *J. Geophys. Res.* **2006**, *111*. [CrossRef]
31. Kiehl, J.T.; Trenberth, K.E. Earth's annual global mean energy budget. *Bull. Am. Meteorol. Soc.* **1997**, *78*, 197–208. [CrossRef]
32. Ramaswamy, V.; Freidenreich, S.M. Solar radiative line-by-line determination of water vapor absorption and water cloud extinction in inhomogeneous atmospheres. *J. Geophys. Res.* **1991**, *96*, 9133–9157. [CrossRef]
33. Bournet, P.E.; Ould-Khaoua, S.A.; Boulard, T. Numerical prediction of the effect of vents arrangement on the ventilation and energy transfer in a multispans glasshouse using a bi-band radiation model. *Biosyst. Eng.* **2007**, *98*, 224–234. [CrossRef]
34. Kim, K.; Yoon, J.; Kwon, H.; Han, J.; Son, J.E.; Nam, S.; Giacomelli, G.; Lee, I. 3-D CFD analysis of relative humidity distribution in greenhouse with a fog cooling system and refrigerative dehumidifiers. *Biosyst. Eng.* **2008**, *100*, 245–255. [CrossRef]
35. Wang, X.W.; Luo, J.Y.; Li, X.P. CFD based study of heterogeneous microclimate in a typical chinese greenhouse in central China. *J. Integr. Agric.* **2013**, *12*, 914–923. [CrossRef]
36. Chen, J.; Xu, F.; Tan, D.; Shen, Z.; Zhang, L.; Ai, Q. A control method for agricultural greenhouses heating based on computational fluid dynamics and energy prediction model. *Appl. Energy* **2015**, *141*, 106–118. [CrossRef]
37. Kichah, A.; Bournet, P.E.; Migeon, C.; Boulard, T. Measurements and CFD simulations of microclimate characteristics and transpiration of an Impatiens pot plant crop in a greenhouse. *Biosyst. Eng.* **2012**, *112*, 22–34. [CrossRef]
38. Nebbali, R.; Roy, J.C.; Boulard, T. Dynamic simulation of the distributed radiative and convective climate within a cropped greenhouse. *Renew. Energy* **2012**, *43*, 111–129. [CrossRef]
39. Morille, B.; Migeon, C.; Bournet, P.E. Is the Penman-Monteith model adapted to predict crop transpiration under greenhouse conditions? Application to a New Guinea Impatiens crop. *Sci. Hortic.* **2013**, *152*, 80–91. [CrossRef]
40. Roy, J.C.; Pouillard, J.B.; Boulard, T.; Fatnassi, H.; Grisey, A. Experimental and CFD results on the CO<sub>2</sub> distribution in a semi-closed greenhouse. *Acta Hortic.* **2014**, *1037*, 993–1000. [CrossRef]
41. Boulard, T.; Roy, J.C.; Pouillard, J.B.; Fatnassi, H.; Grisey, A. Modelling of micrometeorology, canopy transpiration and photosynthesis in a closed greenhouse using computational fluid dynamics. *Biosyst. Eng.* **2017**, *158*, 110–133. [CrossRef]
42. Majdoubi, H.; Boulard, T.; Fatnassi, H.; Bouirden, L. Airflow and microclimate patterns in a one-hectare Canary type greenhouse: An experimental and CFD assisted study. *Agric. For. Meteorol.* **2009**, *149*, 1050–1062. [CrossRef]
43. Sethi, V.P. On the selection of shape and orientation of a greenhouse: Thermal modeling and experimental validation. *Sol. Energy* **2009**, *83*, 21–38. [CrossRef]
44. Baxevanou, C.; Fidaros, D.; Bartzanas, T.; Kittas, C. Yearly numerical evaluation of greenhouse cover materials. *Comput. Electron. Agric.* **2018**, *149*, 54–70. [CrossRef]
45. Muñoz, P.; Montero, J.; Anton, A.; Iglesias, N. Computational fluid dynamic modelling of night-time energy fluxes in unheated greenhouses. *Acta Hortic.* **2004**, *691*, 403–410.
46. Tong, G.; Christopher, D.; Li, T.; Wang, T. Passive solar energy utilization: A review of cross-section building parameter selection for Chinese solar greenhouses. *Renew. Sustain. Energy Rev.* **2013**, *26*, 540–548. [CrossRef]
47. Bartzanas, T.; Boulard, T.; Kittas, C. Effect of vent arrangement on windward ventilation of a tunnel greenhouse. *Biosyst. Eng.* **2004**, *88*, 479–490. [CrossRef]
48. Lamnatou, C.; Chemisana, D. Solar radiation manipulations and their role in greenhouse claddings: Fresnel lenses, NIR- and UV-blocking materials. *Renew. Sustain. Energy Rev.* **2013**, *18*, 271–287. [CrossRef]
49. Stanghellini, C.; Dai, J.; Kempkes, F. Effect of near-infrared-radiation reflective screen materials on ventilation requirement, crop transpiration and water use efficiency of a greenhouse rose crop. *Biosyst. Eng.* **2011**, *110*, 261–271. [CrossRef]
50. Murakami, K.; Fukuoka, N.; Noto, S. Improvement of greenhouse microenvironment and sweetness of melon (*Cucumis melo* L.) fruits by greenhouse shading with a new kind of near-infrared ray-cutting net in mid-summer. *Sci. Hortic.* **2017**, *218*, 1–7. [CrossRef]
51. Rosenberg, N.J.; Blad, B.L.; Verma, S.B. *Microclimate: The Biological Environment*, 2nd ed.; John Wiley and Sons: Hoboken, NJ, USA, 1983; p. 495.
52. Senhaji, A.; Majdoubi, H.; Mouqalid, M.; De, E.; Meknès, E. Solar distribution in a greenhouse at different crops orientation during production season. In Proceedings of the 13ème Congrès Mécanique, Meknes, Morocco, 11–14 April 2017; pp. 13–15.
53. Aguilar-Rodriguez, C.E.; Flores-Velazquez, J.; Ojeda-Bustamante, W.; Rojano, F.; Iñiguez-Covarrubias, M. Valuation of the energy performance of a greenhouse with an electric heater using numerical simulations. *Processes* **2020**, *8*, 600. [CrossRef]
54. Bouhoun-Ali, H.; Bournet, P.E.; Cannavo, P.; Chantoiseau, E. Development of a CFD crop submodel for simulating microclimate and transpiration of ornamental plants grown in a greenhouse under water restriction. *Comput. Electron. Agric.* **2017**, *149*, 26–40. [CrossRef]
55. Launder, B.E.; Spalding, D.B. *Lectures in Mathematical Models of Turbulence*; Academic Press: London, UK, 1972.
56. Launder, B.E.; Spalding, D.B. The numerical computation of turbulent flows. *Comput. Methods Appl. Mech. Eng.* **1974**, *3*, 269–289. [CrossRef]
57. Bouhoun-Ali, H.; Bournet, P.E.; Danjou, V.; Morille, B.; Migeon, C. CFD simulations of the night-time condensation inside a closed glasshouse: Sensitivity analysis to outside external conditions, heating and glass properties. *Biosyst. Eng.* **2014**, *127*, 159–175. [CrossRef]
58. Howell, T.; Dusek, D. Comparison of vapor pressure deficit calculation methods, southern high plains. *J. Irrig. Drain. Eng.* **1995**, *121*, 191–198. [CrossRef]

59. Food Agricultural Organization (FAO). *Evapotranspiración del Cultivo*; FAO: Rome, Italy, 2006; p. 298.
60. Huerres, P.C.; Caraballo, N. *Horticultura*; Editorial Pueblo y Educación: La Habana, Cuba, 1988; p. 193.
61. Grange, R.; Hand, D. A review of the effects of atmospheric humidity on the growth of horticultural crops. *J. Hortic. Sci.* **1987**, *62*, 125–134. [CrossRef]
62. Körner, O.; Challa, H. Process-based humidity control regime for greenhouse crops. *Comp. Electr. Agric.* **2003**, *39*, 173–192. [CrossRef]
63. Chu, C.R.; Lan, T.W.; Tasi, R.K.; Wu, T.R.; Yang, C.K. Wind-driven natural ventilation of greenhouses with vegetation. *Biosyst. Eng.* **2017**, *164*, 221–234. [CrossRef]
64. Flores-Velázquez, J.; Villarreal-Guerrero, F. Design of a forced ventilation system for a Zenithal greenhouse using CFD. *Rev. Mex. De Cienc. Agrícolas* **2015**, *6*, 303–316.

Article

# Indoor Environmental Quality (IEQ) Analysis of a Two-Sided Windcatcher Integrated with Anti-Short-Circuit Device for Low Wind Conditions

Payam Nejat <sup>1,2</sup>, Hasanen Mohammed Hussien <sup>3</sup>, Fodil Fadli <sup>4,\*</sup>, Hassam Nasarullah Chaudhry <sup>5,\*</sup>, John Calautit <sup>6,\*</sup> and Fatemeh Jomehzadeh <sup>1</sup>

<sup>1</sup> Department of of Civil Engineering, Faculty of Engineering, University Technology of Malaysia (UTM), Skudai 81310, Malaysia; payam.nejaat@gmail.com (P.N.); jomehzadehfatemeh2@graduate.utm.my (F.J.)

<sup>2</sup> Advanced Building and Environment Research (ABER) Group, Johor Bahru 81300, Malaysia

<sup>3</sup> Department of Mechanical Engineering, University of Technology (UOT), Baghdad 10066, Iraq; 20046@uotechnology.edu.iq

<sup>4</sup> Department of Architecture and Urban Planning, College of Engineering, Qatar University, Doha 2713, Qatar

<sup>5</sup> School of Energy, Geoscience, Infrastructure and Society, Heriot-Watt University, Edinburgh EH14 4AS, UK

<sup>6</sup> Department of Architecture and Built Environment, The University of Nottingham, Nottingham NG7 2RD, UK

\* Correspondence: f.fadli@qu.edu.qa (F.F.); H.N.Chaudhry@hw.ac.uk (H.N.C.);

john.calautit1@nottingham.ac.uk (J.C.)

Received: 15 June 2020; Accepted: 6 July 2020; Published: 15 July 2020

**Abstract:** Windcatchers are considered as promising passive ventilation and cooling strategy, but the ventilation performance of this system is still of concern in areas with low speed and unpredictable winds. The air short circuiting in windcatchers can reduce its ventilation performance and ability to introduce clean air and remove stale air. The current work aimed to evaluate the indoor environmental quality (IEQ) performance of a two-sided windcatcher fitted with an anti-short-circuit device (ASCD) for improving its performance in low wind speed conditions. Computational Fluid Dynamics (CFD) simulations were performed for different ASCD configurations. The CFD method was verified using grid-sensitivity analysis and validated by comparing the simulation results with wind tunnel data. The results indicated that the average difference between CFD results and previous experimentation was below 10%, therefore indicating good agreement. Building on the findings of the previous research, the study focused on evaluating the impact of the length of ASCD on the achieved fresh air supply rates and air change rate. The length of the ASCD was varied between 5 cm to 50 cm, while the angle was maintained at 80°. The shorter ASCD was still able to minimize the fresh supply airflow short-circuiting to the exhaust stream, and at the same time, it would also require a smaller ceiling space for installation and lower material cost. Hence, the 15 cm ASCD with 80° angle was selected for further analysis in this study. Then, consideration of low wind speed and various directions were studied to evaluate the ventilation performance of windcatcher with ASCD. The study simulated wind speeds between 0.5–2 m/s and two wind directions. Based on the assessment of IEQ factors, including mean age of air and percentage of dead zone, a 0° incident angle demonstrated slightly better results. The achieved fresh air supply rates ranged between 180 L/s to 890 L/s in 45° wind angle, while, for 0°, these values were from 160 L/s to 642 L/s. Likewise, the range of air change rates (ACH) was from 8 ACH to 32 ACH in 0° wind angle and increased to 9 ACH and then to 45 ACH in 45° wind angle.

**Keywords:** passive cooling; natural ventilation; indoor air quality; windcatcher; badgir

## 1. Introduction and Literature Review

The built environment sector accounts for 30–40% of world energy consumption [1]. This Figure is expected to increase by up to 50% by 2050. Buildings account for more than a third of the total emissions released to the atmosphere, which gives rise to climate change and global warming [2]. Cooling and ventilation are significant contributors to the high building energy demand, in particular in tropical and hot climates. Hence, researchers are looking for solutions to eliminate or minimize the cooling energy requirement of buildings. Many are focused on exploring how passive techniques, such as natural ventilation strategies, can be effectively incorporated into the building design [3]. Many works [4–6] have shown that natural ventilation and passive cooling strategies can reduce energy consumption during the cooling season and, at the same time, improve the indoor air quality and, in some cases, the comfort level of occupants.

An excellent example of a passive cooling strategy is a windcatcher, which is recently gaining lots of attention due to its capability to provide high fresh air rates and, at the same time, extract stale air out of the building [4–6]. The windcatcher utilizes two driving forces to ventilate building spaces: buoyancy forces, which are due to the temperature differential between indoor and outdoor; and wind forces which are due to the pressure differential between the openings [7]. The windcatcher concept is not exactly new and has been effectively utilized in traditional buildings for centuries in the Middle East [8]. Recently, a modern version of the windcatcher was employed in buildings in the UK, such as in schools and open-plan offices [9–11].

Another advantage of using a windcatcher is that it incorporates no moving parts, which leads to low maintenance cost. It can be an attractive option for large spaces, such as gyms and storage facilities, which are typically ventilated by mechanical ventilation systems. Moreover, unlike simple natural ventilation methods, such as windows, a windcatcher can capture the wind at higher elevations [12,13]. This can lead to higher ventilation rates, especially in urban or built-up areas where neighboring structures can obstruct the flow. A windcatcher can also have several openings which allow it to capture wind from different directions [14]. Windcatchers located in areas with variable wind directions can have two or four openings. A problem for both the commercial and traditional windcatcher, which outweigh its advantages, is the air short circuit phenomena which were observed and discussed by previous researches [8,15–17]. It occurs when the fresh supply airflow immediately leaves the outlet/exhaust channel, instead of circulating inside the space to be ventilated. Hence, effectively reducing the ventilation performance of multi-opening windcatchers [18,19].

Several works have investigated the ventilation performance of two-sided windcatchers. Montazeri et al. [14] employed wind tunnel testing and Computational Fluid Dynamics (CFD) modeling to evaluate the impact of the wind direction on the ventilation efficiency of a two-sided rectangular windcatcher. The study observed that air short-circuiting was present at higher wind angles, reaching a maximum value at 60°. Ghadiri et al. [20] also used CFD to assess the wind-induced cross ventilation for a room with a two-sided windcatcher at different wind directions (0–90°). The results focused on comparing different types of turbulence models and showed that the SSG Reynolds Stress Model provided the most accurate results as compared to experimental data. Furthermore, Afshin et al. [21] evaluated the ventilation performance of a two-sided windcatcher at different wind conditions using wind tunnel testing and smoke flow visualization. The highest rate of ventilation was seen at a wind angle of 90°, and the windcatcher was observed to be functioning as a chimney for wind angles larger than 55° (windward transition angle).

In one previous study [22], it was found that the use of a new windcatcher component, called an anti-short-circuit device (ASCD), resulted in a significant reduction of air short-circuiting in two-sided windcatchers. It was observed that the supply airflow could be effectively directed toward the occupied zone instead of leaving the exhaust immediately. Different angles of ASCD (10° to 90°) were studied by evaluating the windcatcher ventilation performance. The results showed that the ASCD (with different angles) could significantly reduce the short circuit, but the maximum reduction was seen between 80° to 90°. The present work builds on the previous study to assess the influence of the ASCD on

the indoor environmental quality (IEQ) of the ventilated space, by assessing parameters, such as air change rate (ACE) and mean age of air (MAA).

Furthermore, the effect of the ASCD length (5 cm to 50 cm) on the induced supply airflow and IEQ in low wind speed conditions was evaluated. Different wind conditions were simulated for a small room integrated with windcatcher and ASCD. The computational model that was employed was validated using experimental data.

## 2. Method

In this study, CFD was used to model and assess the performance of a two-sided windcatcher. The initial computational model of a two-sided windcatcher with ACD was validated by comparing the results with wind tunnel experiment data. For the validation, identical boundary conditions were utilized, simulating similar conditions as in the experiment. Then, the performance of the windcatcher integrated with ASCD was investigated in terms of the airflow patterns and IEQ parameters.

### 2.1. Solver Settings

The 3D steady Reynolds-Averaged Navier-Stokes (RANS) simulations were performed using the commercial CFD software, ANSYS Fluent. The RANS approach is the most commonly used method for the simulation of natural ventilation and windcatchers. The numerical model utilized the SIMPLEC pressure-velocity coupling algorithm with second-order pressure interpolation. For the convection and viscous terms, the second-order upwind discretization was used. The verification of the turbulence model is necessary to assess the reliability of CFD modeling. The turbulence model analysis of a similar geometry was conducted in previous research [23,24], which found that the standard k-epsilon model provided accurate predictions and therefore, this study also utilized same turbulence mode. The standard k-epsilon model was also employed in other natural ventilation studies, such as Reference [25–28], and was concluded to be accurate and reliable. The momentum, mass, and energy equations, along with the turbulence kinetic energy and energy dissipation rate equations, were solved. These governing equations were not modified in this study and are fully detailed in the Fluent theory guide [29].

### 2.2. Geometry and Computational Domain

In this work, Computational Fluid Dynamics (CFD) modeling was employed for evaluating the ventilation performance of the proposed windcatcher design [23]. As shown in Figure 1, the physical domain included a rectangular shaped room with a floor area of 4 m × 6 m and a height of 3 m. A two-sided windcatcher was mounted on top of the room. The windcatcher was separated by an internal wall forming two air channels; one for supplying the airflow and another for exhausting the stale air out of the space. In some cases, both channels will function as exhaust channels, depending on the direction of the wind [30]. The windcatcher cross-sectional area and opening were 1 m × 1 m and height of 1.5 m. The form and size of the windcatcher were based on the study of Reference [22,23]. As detailed previously, the anti-short-circuit device (ASCD) was incorporated below the windcatcher channel to eliminate or minimize the air short-circuiting between the two channels (Figure 1). The ASCD had an angle of 80°, based on previous research [22].

To select the size of the numerical domain, COST Action 732 [31] guidelines were used to simulate the wind flow around the windcatcher and building model (Figure 2). As per the guidelines, the lateral domain boundaries were 5 H from the room sidewalls (H is the height of the room). The inlet of the domain was 5 H from the windward wall of the building. However, further extension (15 H) is recommended for outlet boundary to permit the redevelopment of flow in the back of the wake region because the fully developed flow is one of underlying assumption in steady RANS computations. Extension between 4 H and 10 H is advised for the vertical direction (while considering the blockage effect). 5 H was selected to ensure that the blockage was below 5%.



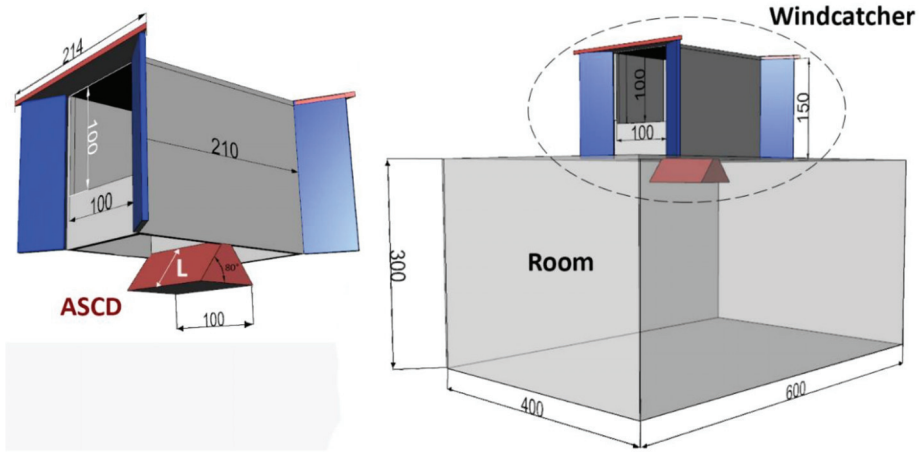


**Figure 1.** Dimensions of the test room and windcatcher model integrated with the anti-short-circuit device (ASCD) in centimeter.

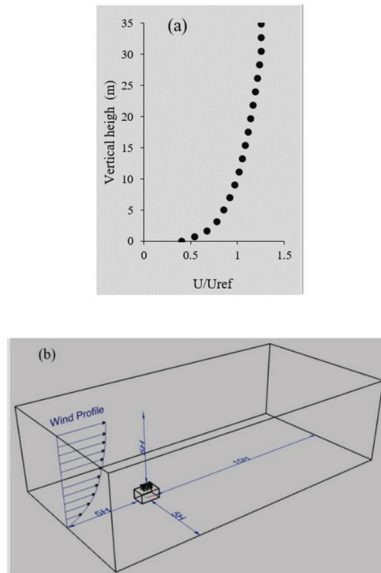


**Figure 2.** (a) Atmospheric boundary layer (ABL) profile of the approach flow and (b) schematic of the Computational Fluid Dynamics (CFD) domain.

### 2.3. Mesh Generation

The computational model, which consisted of the outdoor domain, windcatcher with ASCD, and test room, was meshed using tetrahedral type elements, with a finer resolution near the regions of interest, such as the windcatcher and indoor space (Figure 3). The mesh was generated using the preprocessing tool ANSYS Mesh which resulted in an unstructured mesh with 1.5 million nodes and 8.5 million elements. The mesh resolution was selected based on a grid sensitivity analysis and comparison with experimental data, which will be explained in Section 3.1.

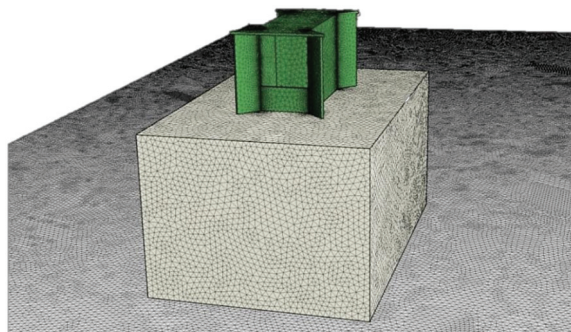


**Figure 3.** Mesh at the surface of the windcatcher and building model, showing the key areas refined in the Mesh tool.

#### 2.4. Solution Convergence and Flux Balance

For assessing the CFD solution convergence, the residual values were monitored, and, at the same time, variables of interest were also monitored to judge if convergence was reached [29]. In order to monitor the variable or quantity of interest (airflow velocity), point surfaces (supply air and indoor points) were defined in the model, and each one was monitored during the numerical calculations. The solution was run until the monitored flow variables no longer changed with more iterations. In addition, the flux report tool in Fluent was used to examine the overall mass balance when the solution converged. This was conducted by checking the mass flow rate flux for the inlet and outlet and ensuring that the net imbalance through the domain was lower than 1%.

#### 2.5. Boundary Conditions

The recommendations of COST Action 732 [31] and AIJ guidelines for urban wind simulations [32] were followed when defining the boundary conditions in this study. Wind profile (Figure 2) and turbulence kinetic energy profiles were set as inflow boundary conditions [33]. As detailed previously, the focus of the research is to enhance the ventilation performance of windcatchers in areas with low wind speed conditions; hence, the wind velocity at H was varied between 0.5–2 m/s. For the wall boundaries, the standard wall function was employed [34]. However, for the ground surface, the sand-grain wall function was adjusted based on Reference [35]. This provides an accurate description of the flow near the ground. The roughness of the wall was specified by an equivalent sand grain roughness  $k_s$  in the wall functions. For the top and sides of the computational domain, the symmetry wall boundary conditions were defined, i.e., zero gradients for all the variables at the walls. The pressure outlet was set to zero static pressure. Table 1 summarizes the computational modeling setup and boundary conditions.

**Table 1.** A summary of the computational setup and specified boundary conditions.

Parameters	Setting
Simulation	Steady-state, 3D with coupled indoor-outdoor
Solver type	Pressure-based
Indoor domain (volume)	Fluid domain
Outdoor domain (volume)	Fluid domain
Wall surfaces (domain)	Top and side: Symmetry walls Ground: Wall
Wall surfaces (model)	Building: Wall Windcatcher: Wall ASCD: Wall
Velocity inlet	Atmospheric boundary layer profile, $U_H = 0.5\text{--}2$ m/s
Pressure outlet	Atmospheric 0 Pa
Turbulence model	k-epsilon (standard)
Near-Wall treatment	Standard wall functions

### 3. Results and Discussion

The following sections will discuss the validation of the numerical modeling of the two-sided windcatcher against the experimental data. Then, the influence of the addition of ASCD on ventilation performance and IEQ will be discussed. Furthermore, the impact of the ASCD length will also be covered.

#### 3.1. Validation and Grid Adoption of CFD Simulation

Before carrying out further simulations and analysis, the numerical modeling accuracy was evaluated by validating against wind tunnel measurements. The simulation results were compared against the supply and exhaust airflow velocity measurements from the wind tunnel testing of the windcatcher with ASCD, as detailed in previous work [22]. A total of 12 measurement points inside the windcatcher channels were used for the comparison of the two methods, as shown in Figure 4. A hot-wire anemometer was used to carry out the airflow velocity measurements at different points. Figure 5 compares the simulation results of the airflow velocity against the experimental data [22]. Overall, a good agreement between the numerical and measurements values was observed. It was found that the average difference in the values was 9%. This is in line with the findings of Reference [36,37], which showed the capabilities of the turbulence model for the prediction of natural ventilation airflows.

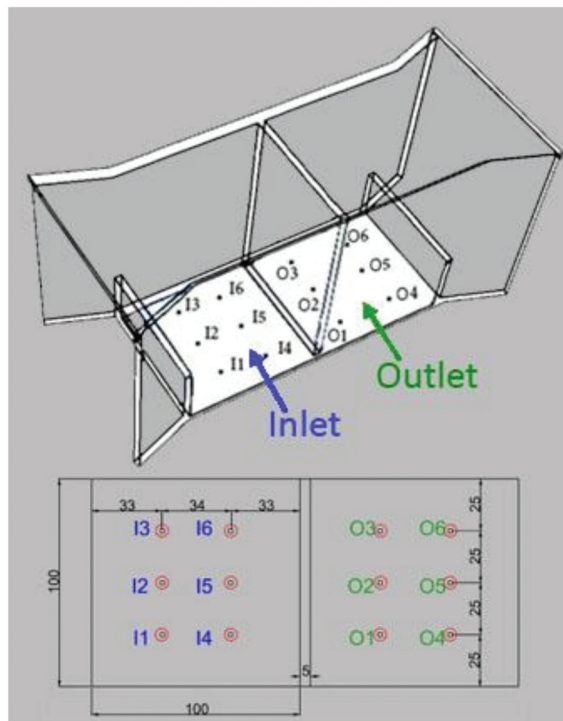


**Figure 4.** The inlet and outlet channel measurement points for the air velocity values; dimensions are in millimeters.

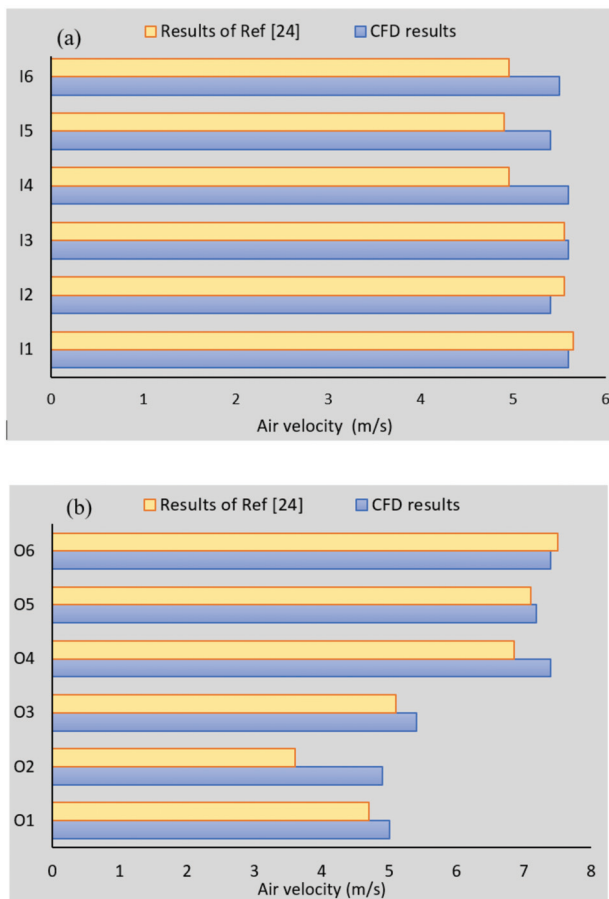


**Figure 5.** Comparison of airflow velocity between CFD results and the wind tunnel measurements of Reference [22] in the (a) inlet points (I1 to I6) and (b) outlet points (O1 to O6).

The selected mesh resolution was based on a sensitivity analysis which was accomplished by carrying out simulations with two additional mesh sizes: coarser (4 million elements) and finer mesh (12 million elements). The analysis is conducted for the reference windcatcher model with ASCD using the same computational domain and boundary conditions. The airflow velocity values across a vertical line in the supply airstream was compared for the three mesh sizes, as shown in Figure 6. It was observed that the velocity values variation between the three mesh sizes was negligible and mostly independent from the mesh sizes. The largest deviation was observed for the points near the supply channel. At the height of 2.8 m, the deviation between the medium (reference with 8 million mesh) and the finer mesh (12 million) was 2.1%. While taking into account the negligible dependence on the mesh resolution and, at the same time, to minimize the computational time, the medium mesh was utilized for further analysis.

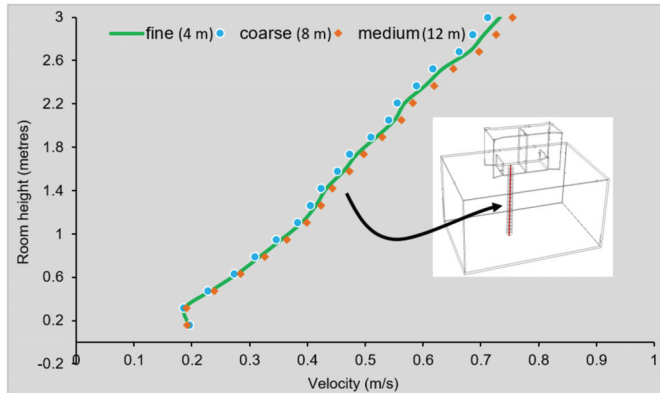


**Figure 6.** Mesh verification: sensitivity analysis of different mesh sizes (4 million, 8 million, and 12 million).

### 3.2. Impact of the Length of ASCD on the Ventilation Performance

Building on the findings of Reference [24], which evaluated the impact of ASCD angle, this section will evaluate the influence of the length of the ASCD on the ventilation performance based on simulation analysis. Ideally, a shorter and compact ASCD design which requires smaller space for integration and lower cost is preferred. However, it should still be able to prevent the air short-circuiting of the fresh air into the exhaust region. Hence, a detailed evaluation of ventilation performance is required before progressing on to the IEQ analysis. The length of the ASCD was varied between 5 cm to 50 cm, while the angle was maintained at 80°.

The mean airflow velocity was compared at two heights using a planar surface created at 1.1 m, which represents the breathing height at sitting position; and 1.7 m, which represents the standing height [38]. As shown in Figure 7, although the effect was minimal, the mean airflow speed in the 1.7 m plane increased as the length of the ASCD increased. An opposite trend was observed for the mean airflow speed in the 1.1 m plane. This can be better explained by the velocity contour and vector diagram in Figure 8, which shows how the increased in ASCD length redirected the airflow towards one corner of the room, which influenced the mean airflow speed at the upper and lower regions of the room.

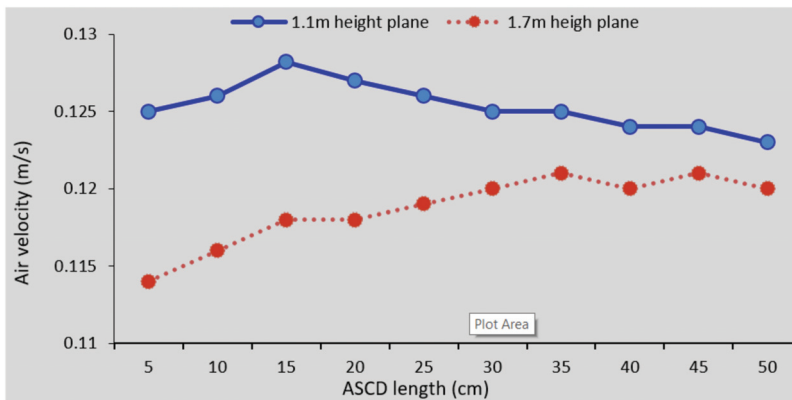


**Figure 7.** The average of air velocity in 1.1 m and 1.7 m horizontal plane of windcatcher with different ASCD lengths.

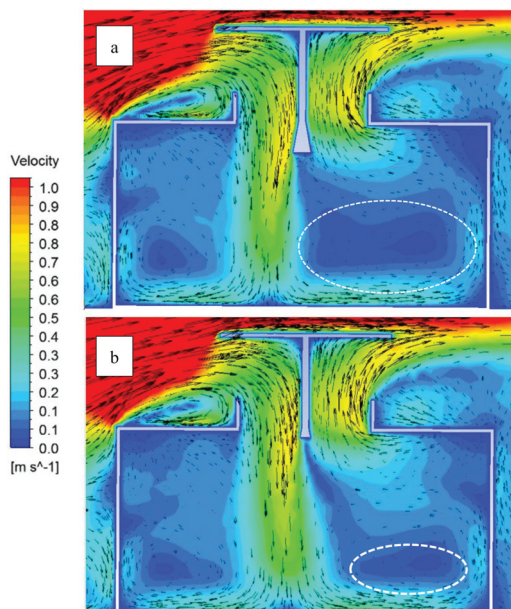


**Figure 8.** Contour plot of the airflow velocity magnitude in the vertical cross-sectional plane of (a) 50 cm ASCD and (b) 15 cm ASCD ( $U_H = 1$  m/s).

Figure 8 shows a comparison between the airflow distribution of the windcatcher with 15 cm ASCD and 50 cm ASCD. As observed, the indoor space with the 15 cm ASCD had less stagnant air spots (dark blue color in Figure 8). The shorter ASCD was still able to minimize the fresh supply airflow short-circuiting to the exhaust stream, and, at the same time, it would also require a smaller ceiling space for installation and lower material cost. Hence, the 15 cm ASCD was selected for further analysis in this study. The influence of the ASCD length on the achieved airflow supply rate (L/s) and air change rate (1/h) are shown in Figure 9. Similarly, the effect was minimal, and the device was capable of providing the recommended fresh air rates (15 L/s), even at low wind speed conditions, assuming there are 15 occupants in the space.

### 3.3. IEQ evaluation of Windcatcher with ASCD under Low Wind Speed Conditions

In this section, the natural ventilation performance of the windcatcher integrated with the ASCD (15 cm length,  $80^\circ$  angle) was assessed under low wind speed conditions, such as the ones experienced in Malaysia. The study will simulate wind speeds between 0.5–2 m/s and two predominant wind directions. In Malaysia, the North and South wind directions are the most predominant wind directions followed by the North-East and South-West wind directions [39,40]. Since the two-sided windcatcher design is symmetrical, both  $0^\circ$  and  $45^\circ$  wind incident angles can characterize the predominant wind directions and simplify the analysis. The ventilation performance criteria are the airflow velocity, supply rate, air change rate, distribution, and mean age of air. The overall aim is to evaluate the capabilities of the windcatcher in providing the required fresh air rates and enhancing the IEQ in low wind speed areas.

Figure 10 displays the airflow velocity contours in the vertical cross-sectional plane in the computational domain at different wind speed conditions, showing the airflow distribution within and around the test room and windcatcher channels. As observed, air recirculation was observed on the top edge of the roof of the test room (windward side), which affected the wind flow approaching the windcatcher. Large vortices were observed at the leeward side of the building and windcatcher. For the indoor space, a similar airflow pattern can be observed regardless of the wind speed. It can

be seen that the ASCD device could redirect the supply airstream away from the exhaust airstream, minimizing or eliminating the airflow short-circuiting. At lower outdoor wind speeds, uneven airflow distribution was observed inside the space with very low air movement in the bottom region of the space. However, significant improvement was observed as the wind speed increased. In general, higher airflow speeds were observed in the windward side of the space where the supply or inflow jet was redirected by the ASCD device.

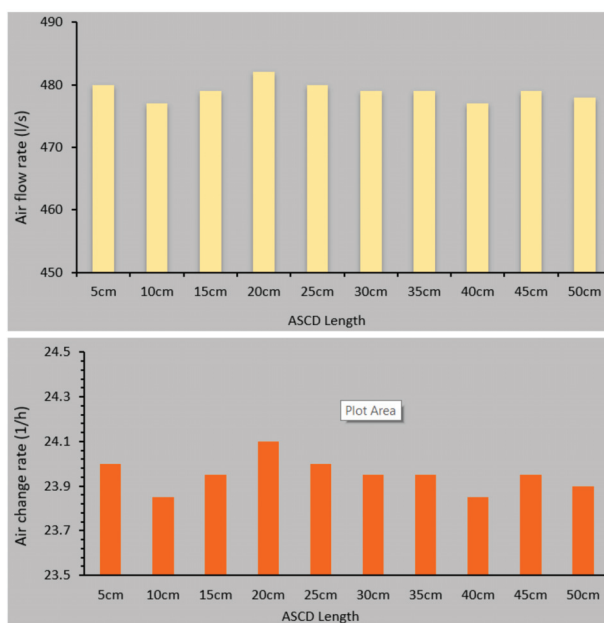


**Figure 9.** Impact of different ASCD lengths on the achieved airflow supply rate (L/s) and air change rate (1/h).

In Figure 11, air velocity in the windcatcher horizontal planes (1.1 m and 1.7 m height) is compared in various outdoor wind speeds ranging from 0.5 m/s to 2 m/s at  $0^\circ$  wind incident angle. As observed, good airflow distribution can be observed inside the space at 0.5 m/s outdoor wind; however, as the wind speed increased to 1–1.5 m/s, it was clear that the ASCD device redirected the supply airflow towards one corner of the space, which could potentially cause draft issues, particularly if the occupant is sitting directly below this area. Although the airspeeds observed in the space were still within acceptable levels, several design considerations should be considered in areas with higher outdoor wind speeds. A potential solution for high wind speeds locations could be to use ASCDs with lower angles, which could redirect the airflow towards the sidewall and reduce the supply speed. It should be noted that the same issue is faced by windcatchers without ASCD, but the high-speed airflow jet is directed towards the floor directly below the windcatcher. Volume control dampers are typically used to address this issue but are not suitable in areas with low wind speeds. An improved airflow distribution was observed at higher wind speeds (2 m/s and higher), which was due to the increased extraction of airflow from the exhaust side of the windcatcher. Figure 12 shows a comparison between the average airflow speed at 1.1 m and 1.7 m height.

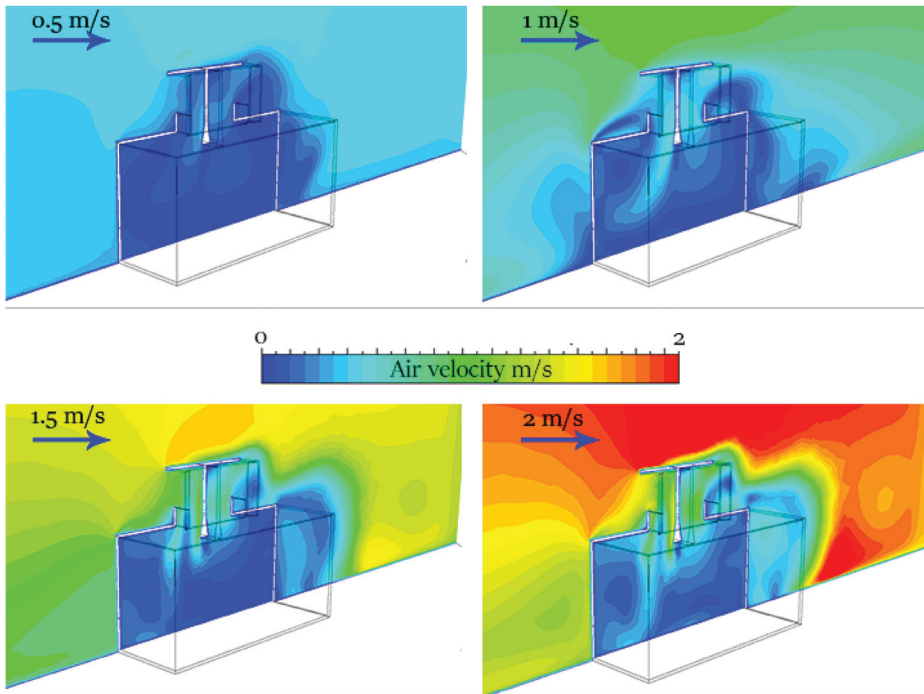


**Figure 10.** Air velocity contours of the vertical cross-sectional plane (outdoor wind speed  $U_H = 0.5$  m/s to 2 m/,  $0^\circ$  wind angle).

The influence of the wind conditions (outdoor wind speed  $U_H = 0.5$  m/s to 2 m/,  $0^\circ$  wind angle) on the achieved airflow supply rate (L/s) and air change rate (1/h) are shown in Figure 13. Similarly, the effect was minimal, and the device was capable of providing the recommended fresh air rates (10 L/s), even at low wind speed conditions, assuming there are 15 occupants in the space. The mean supply air velocity was 0.16 m/s at  $U_H = 0.5$  m/s and increased to 0.64 m/s at  $U_H = 2$  m/s. With regard to the fresh air supply rates, the device was capable of providing the recommended fresh air rates (15 L/s per person) even at the low wind speed conditions (higher than  $U_H = 1$  m/s), assuming there are 15 occupants in the space. Specific air change rates (ACH) are necessary for building spaces to manage the internal air temperatures and bring in clean air while removing stale, humid air. The ACH was 8 at  $U_H = 0.5$  m/s and reached up to 32 at  $U_H = 2$  m/s. As compared to Haw et al.'s [41] field study, which used a similar windcatcher, the average ACH was 57 at 3 m/s wind speed, which was 40% more than maximum of the windcatcher in the present work but with larger size openings and higher wind speed.



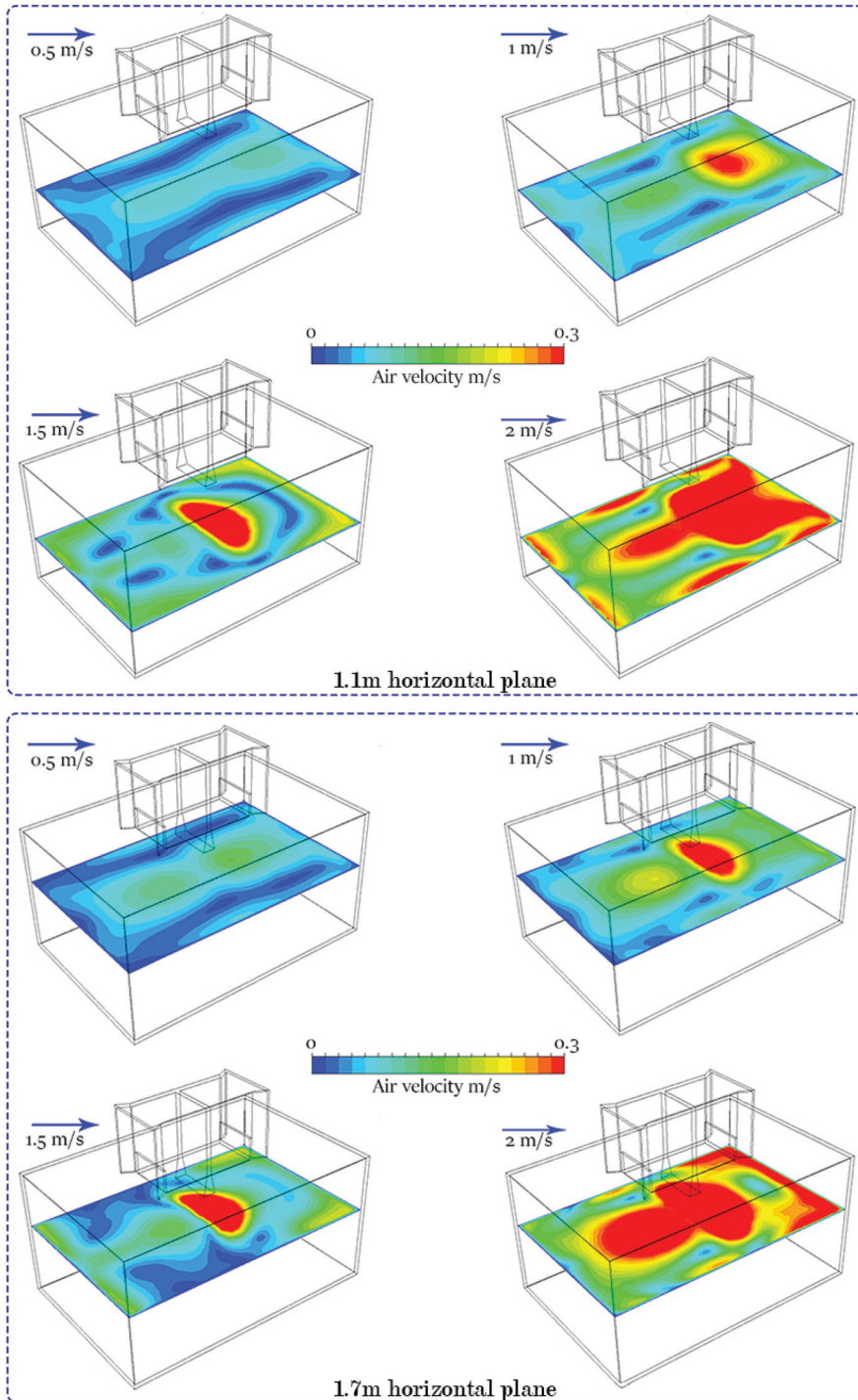


**Figure 11.** Air velocity contours of the indoor horizontal cross-sectional plane (outdoor wind speed  $U_H = 0.5\text{ m/s}$  to  $2\text{ m/s}$ ,  $0^\circ$  wind angle).

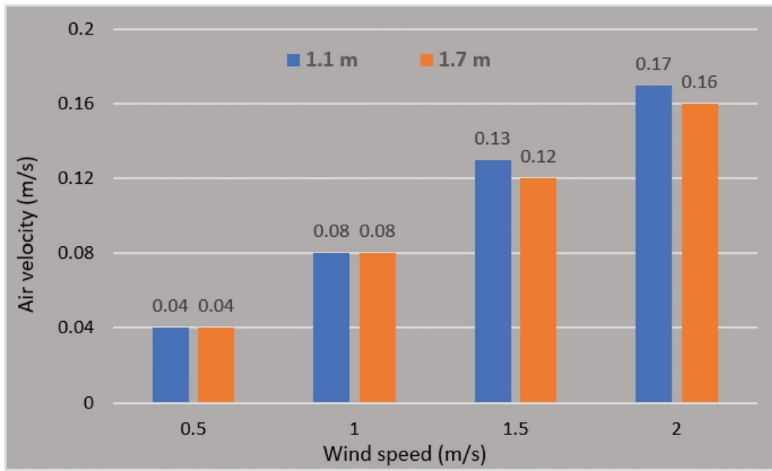


**Figure 12.** Comparison of the mean airflow velocity in 1.1 m and 1.7 m horizontal planes (outdoor wind speed  $U_H = 0.5$  m/s to 2 m/,  $0^\circ$  wind angle).

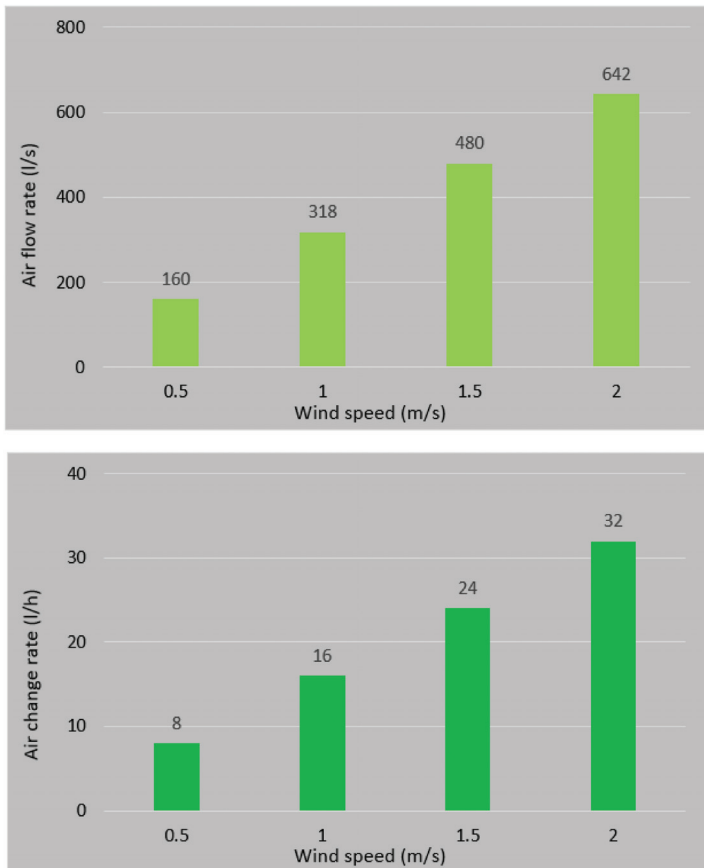


**Figure 13.** Impact of wind conditions (outdoor wind speed  $U_H = 0.5$  m/s to 2 m/,  $0^\circ$  wind angle) on the achieved airflow supply rate (L/s) and air change rate (1/h).

Next, the windcatcher with ASCD was simulated at  $45^\circ$  wind incident angle. Figure 14 displays the airflow velocity contours in the vertical cross-sectional plane in the computational domain at different wind speeds, showing the airflow distribution within and around the test room and windcatcher channels. A slightly different outdoor airflow pattern was observed the air recirculation, particularly at the top of the roof (windward side), which was more prominent at  $0^\circ$  wind angle. Large vortices were still observed at the leeward side of the building and windcatcher, which generated negative pressure in this area. For the indoor space, the airflow pattern was observed to be variable depending on the wind speed. However, the ASCD device was able to redirect the supply airstream away from the exhaust airstream irrespective of the wind speed and direction. For the  $0^\circ$  wind angle, higher airflow speeds were observed in the windward side of the space, where the supply or inflow jet was redirected by the ASCD device.

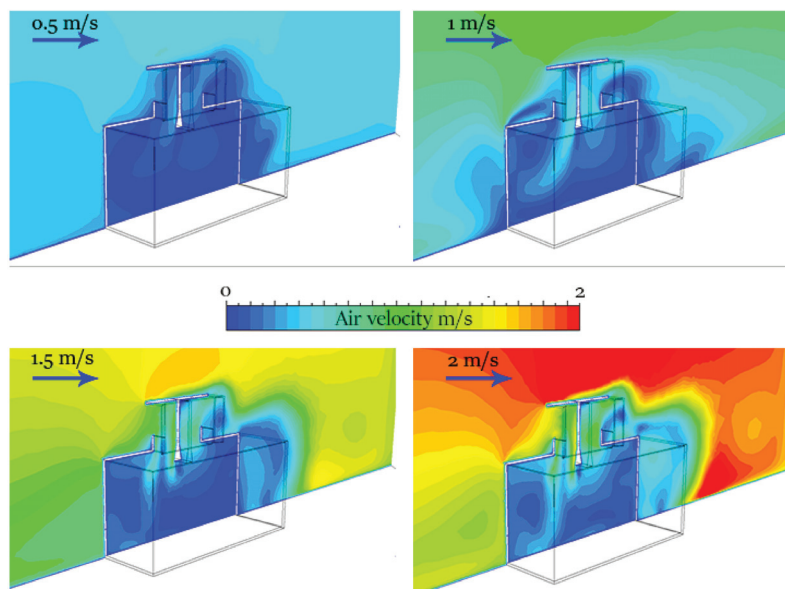


**Figure 14.** Air velocity contours of the vertical cross-sectional plane (outdoor wind speed  $U_H = 0.5$  m/s to 2 m/,  $45^\circ$  wind angle).

In Figure 15, airflow velocity in the windcatcher horizontal planes (1.1 m and 1.7 m height) is compared in various outdoor wind speeds ranging from 0.5 m/s to 2 m/s at  $45^\circ$  wind incident angle. Similar to the result of  $0^\circ$  wind angle, good airflow distribution can be observed inside the space at 0.5 m/s outdoor wind, however as the wind speed increased to 1–2 m/s, it was clear that the ASCD redirected the high-speed supply airflow towards one corner of the space. As shown in Figure 16, both the horizontal plane heights showed nearly similar mean wind speed values; hence, an improved overall airflow distribution was observed when the wind direction was at  $45^\circ$ .

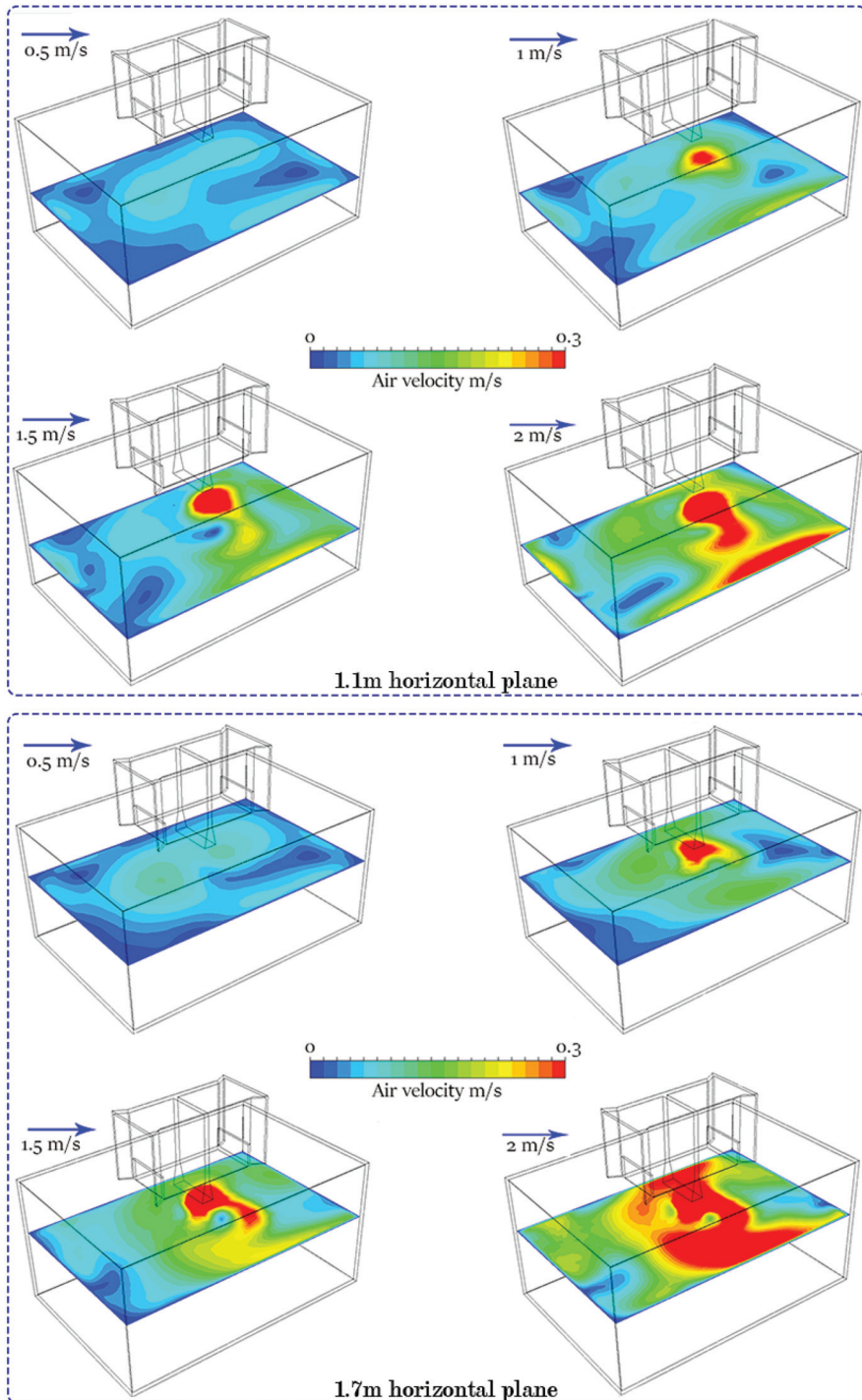


**Figure 15.** Air velocity contours of the indoor horizontal cross-sectional plane (outdoor wind speed  $U_H = 0.5 \text{ m/s}$  to  $2 \text{ m/s}$ ,  $45^\circ$  wind angle).

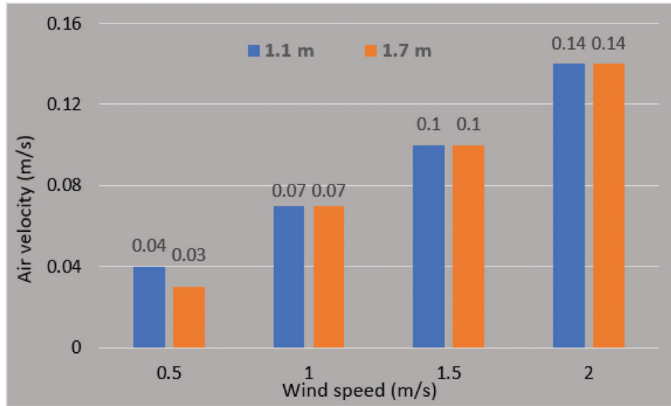


**Figure 16.** Comparison of the mean airflow velocity in 1.1 m and 1.7 m horizontal planes (outdoor wind speed  $U_H = 0.5$  m/s to 2 m/,  $45^\circ$  wind angle).

The influence of the wind conditions (outdoor wind speed  $U_H = 0.5$  m/s to 2 m/,  $45^\circ$  wind angle) on the achieved airflow supply rate (L/s) and air change rate (1/h) are shown in Figure 17. The overall trend of Figure 17 is comparable to the results of  $0^\circ$  wind direction (refer to Figure 13); nonetheless, the overall ventilation performance increased in  $45^\circ$  wind incident angle. These results are consistent with the findings of previous studies [42,43].

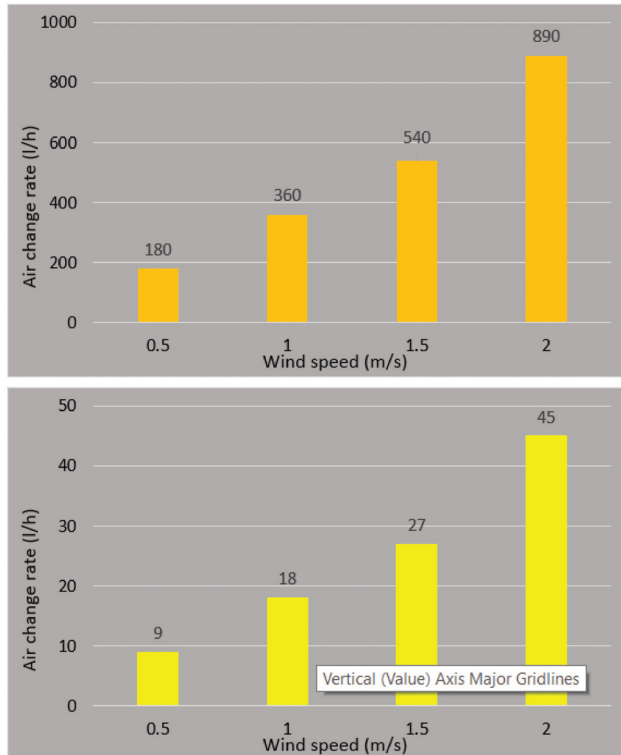


**Figure 17.** Impact of wind conditions (outdoor wind speed  $U_H = 0.5$  m/s to 2 m/,  $0^\circ$  wind angle) on the achieved airflow supply rate (L/s) and air change rate (1/h).

With respect to the American Society of Heating, Refrigerating and Air-Conditioning Engineers (ASHRAE) standard 62 [44], 15 L/s is suggested as the minimum ventilation rate for this room. The device was capable of providing the minimum requirements even at the low wind speed conditions (higher than  $U_H = 1$  m/s), assuming there are 15 occupants in the space. Comparing the performance of the windcatcher in the present work with other types of windcatcher can better show its merits. For example, Calautit and Hughes [17] found that a 1 m × 1 m commercial windcatcher at a wind speed of 2 m/s was able to provide 275 L/s fresh air supply rate. However, at the same wind speed, the windcatcher design proposed in the current study could supply more than 890 L/s.

Moreover, another study conducted by Hughes and Ghani [45] indicated that their commercial four-sided windcatcher could deliver airflow rate in the range of 90 L/s to 650 L/s at 1 m/s to 5 m/s wind speed, which was in the same range as in this study. Wing Jetter is a new natural ventilation device, which was invented in Japan. The device had a 1.5 m height and 1.5 m width and can provide 110 L/s airflow rate in a wind speed of 6 m/s which was much lower than in this study [46]. Hence, the proposed windcatcher can be operational in regions with low outdoor wind speed and can compete with other typical ventilation systems.

### 3.4. Mean Age of Air (MAA)

Another IEQ indicator which was evaluated in this research was the mean age of air (MAA) which is the average time of air displacing from supply point to any position in the ventilated space [47]. This parameter can help to evaluate the ventilation quality and recognize area with poor ventilation. To calculate MAA in Fluent, the method expressed in Reference [48] was utilized. MAA values of 1.1 horizontal plane were plotted in the line graph in Figure 18, with respect to different wind speeds.

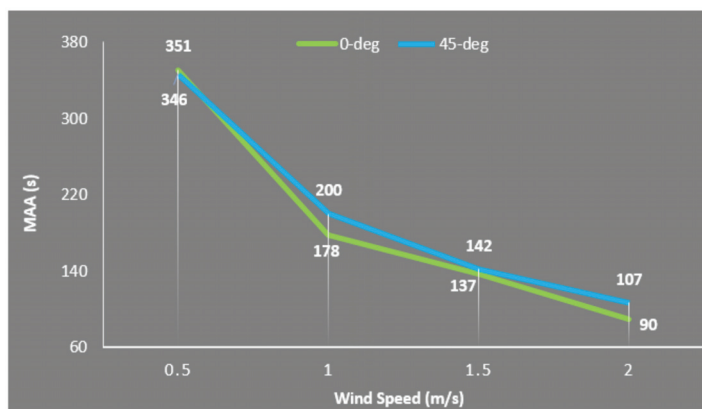


**Figure 18.** Mean age of air (MAA) values in different wind speeds and angles.

It is noticeable that the increase in wind speed can reduce the MAA significantly because the MAA was influenced directly by the supply airflow. The MAA at 0.5 m/s wind speed was within the unacceptable range, as the MAA peaked at nearly 350 s. In other words, at wind speed below 1 m/s, the risk of stale air and related IEQ problems can significantly increase in the occupant space. Nevertheless, for a wind speed of 2 m/s the MAA was below 107 s, which can provide a safety margin of related risk.

### 3.5. Dead Zone

Apart from MAA, the dead zone concept can assist to have better understanding of poor ventilations spots in living area, which can potentially augment the risk of low indoor air quality (IAQ). As Dehghan [43] defined, dead zones are points in the room where air is steady or having near zero velocity (less than 0.1 m/s). Thus, identifying these positions in the room can complete the role of MAA

results. In this regard, ISO clip contours were plotted in CFD post environment, with condition of air velocity less than 0.1 m/s to illustrate the dead zone areas. Figure 19a displays a detailed view of dead zones, colored in dark in the 1.1 m horizontal plane, which is drawn in blue, and size of dead zone area falls as wind speed climbs.

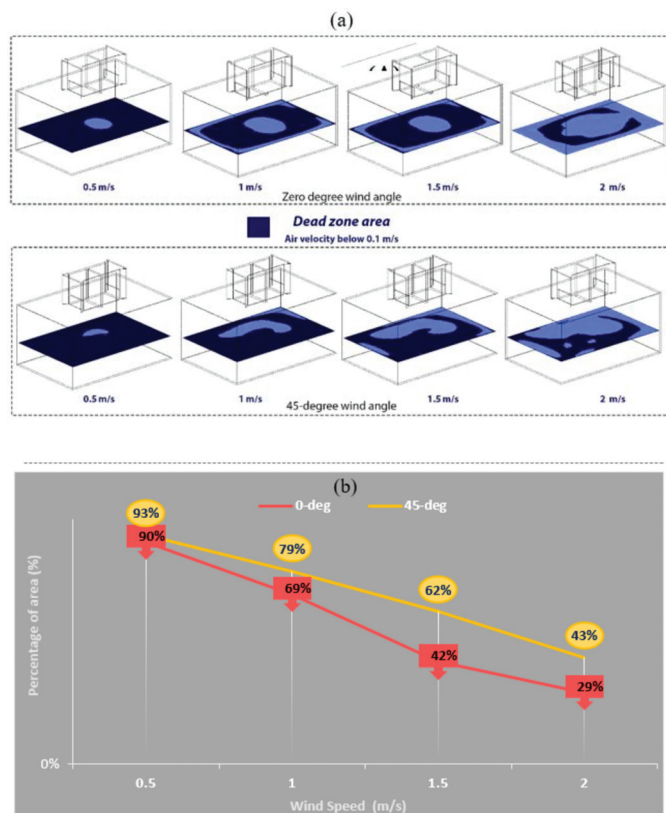


**Figure 19.** (a) The ISO plane contours which demonstrate the dead zone area in dark color (air velocity below 0.1 m/s) in different wind speeds and (b) the percentage of in 1.1 m horizontal plane with dead zone in different outdoor wind speeds.

To specify the area percentage of dead zone in 1.1 horizontal plane, the FLUENT function calculation was utilized, the finding of which are shown in Figure 19b. The results suggest that dead zone formed 90% to 70% in wind speed between 0.5 m/s and 1 m/s, which indicates a serious IAQ challenge in this range. However, wind speed rise can improve the conditions considerably when it reaches to 2 m/s, which leads to a steep fall in dead zone percentage from 29% in 0° wind direction.

#### 4. Conclusions and Future Works

This study carried out extensive CFD simulations and evaluation of the ventilation performance of a two-sided windcatcher fitted with ASCD. The CFD method was validated, and the results indicated that the average difference between CFD results and experimental data was below 10%, therefore indicating good agreement. It should be noted that detailed validation of the model was carried out in our previous works [22–24] and was not included in the present work.

Building upon the findings of the previous research, the study focused on the length of ASCD to observe its impact on the achieved fresh air supply rates and air change rate. Ideally, a shorter

and compact ASCD design, which requires smaller space for integration and lower cost, is preferred. However, it should still be able to prevent the air short-circuiting of the fresh air into the exhaust region. Hence, a detailed evaluation of ventilation performance is required before progressing on to the IEQ analysis. The length of the ASCD was varied between 5 cm to 50 cm, while the angle was maintained at 80°. The shorter ASCD was still able to minimize the fresh supply airflow short-circuiting to the exhaust stream, and, at the same time, it would also require a smaller ceiling space for installation and lower material cost. Hence, the 15 cm ASCD with 80° angle was selected for further analysis in this study.

Then, consideration of low wind speed and various directions were studied to evaluate the ventilation performance of windcatcher with ASCD. The study simulated wind speeds between 0.5–2 m/s and two predominant wind directions. The ventilation performance criteria are the airflow velocity, supply rate, air change rate, distribution, and mean age of air. The overall aim was to evaluate the capabilities of the windcatcher in providing the required fresh air rates and enhancing the IEQ in low wind speed areas, such as in Malaysia. It was revealed that the ventilation performance of the windcatcher in 45° wind incident angle was improved as compared to the 0° wind incident angle. The achieved fresh air supply rates ranged between 180 L/s to 890 L/s in 45° wind angle, while, for 0°, these values were from 160 L/s to 642 L/s. Likewise, the range of ACH was from 8 ACH to 32 ACH in the 0° wind angle and increased to 9 ACH and then to 45 ACH in the 45° wind angle. Consequently, it was concluded that the windcatcher could be effective in low wind speed conditions of Malaysia and other countries with similar wind conditions. Future works can focus on improving the thermal performance of the windcatcher and evaluation of the impact on the thermal comfort of occupants. Further wind tunnel and field testing are also necessary to further validate the numerical modeling.

**Author Contributions:** The contribution of each author is as below: Conceptualization, P.N.; Methodology, P.N.; Software, P.N., J.C.; Validation, P.N.; Investigation F.J.; Data Curation, P.N.; Writing-Original Draft Preparation, P.N. and F.J.; Writing-Review & Editing, J.C., F.J., H.M.H., F.F. and H.N.C.; Supervision, H.M.H. All authors have read and agreed to the published version of the manuscript.

**Funding:** This research received no external funding.

**Acknowledgments:** The authors would like to thank the Advanced Building and Environment Research (ABER) group to support to conduct this research, as well as the Academic Research Center (ARC).

**Conflicts of Interest:** The authors declare no conflict of interest.

## References

1. Izadyar, N.; Miller, W.; Rismanchi, B.; Garcia-Hansen, V. Impacts of façade openings' geometry on natural ventilation and occupants' perception: A review. *Build. Environ.* **2020**, *170*, 106613. [CrossRef]
2. Boukhanouf, R.; Amer, O.; Ibrahim, H.; Calautit, J. Design and performance analysis of a regenerative evaporative cooler for cooling of buildings in arid climates. *Build. Environ.* **2018**, *142*, 1–10. [CrossRef]
3. Calautit, J.K.; Chaudhry, H.N.; Hughes, B.R.; Ghani, S.A. Comparison between evaporative cooling and a heat pipe assisted thermal loop for a commercial wind tower in hot and dry climatic conditions. *Appl. Energy* **2013**, *101*, 740–755. [CrossRef]
4. Moosavi, L.; Zandi, M.; Bidi, M.; Behroozzade, E.; Kazemi, I. New design for solar chimney with integrated windcatcher for space cooling and ventilation. *Build. Environ.* **2020**. [CrossRef]
5. Hosseini, S.H.; Shokry, E.; Ahmadian Hosseini, A.J.; Ahmadi, G.; Calautit, J.K. Evaluation of airflow and thermal comfort in buildings ventilated with wind catchers: Simulation of conditions in Yazd City, Iran. *Energy Sustain. Dev.* **2016**, *35*, 7–24. [CrossRef]
6. Sheikhshahrokhdehordi, M.; Khalesi, J.; Goudarzi, N. High-performance building: Sensitivity analysis for simulating different combinations of components of a two-sided windcatcher. *J. Build. Eng.* **2020**, *28*, 101079. [CrossRef]
7. Farouk, M. Comparative study of hexagon & square windcatchers using CFD simulations. *J. Build. Eng.* **2020**, *31*, 101366. [CrossRef]



8. Sadeghi, M.; Wood, G.; Samali, B.; de Dear, R. Effects of urban context on the indoor thermal comfort performance of windcatchers in a residential setting. *Energy Build.* **2020**, *219*, 110010. [CrossRef]
9. Varela-Boydo, C.A.; Moya, S.L. Inlet extensions for wind towers to improve natural ventilation in buildings. *Sustain. Cities Soc.* **2020**, *53*, 101933. [CrossRef]
10. Sadeghi, M.; Samali, B.; Wood, G.; de Dear, R. Comfort cooling by wind towers in the Australian residential context—Experimental wind tunnel study of comfort. *J. Wind Eng. Ind. Aerodyn.* **2020**, *196*, 104014. [CrossRef]
11. Nejat, P.; Jomehzadeh, F.; Hussien, H.; Calautit, J.; Abd Majid, M. Application of Wind as a Renewable Energy Source for Passive Cooling through Windcatchers Integrated with Wing Walls. *Energies* **2018**, *11*, 2536. [CrossRef]
12. Zaki, A.; Richards, P.; Sharma, R. Analysis of airflow inside a two-sided wind catcher building. *J. Wind Eng. Ind. Aerodyn.* **2019**, *190*, 71–82. [CrossRef]
13. Nejat, P.; Jomehzadeh, F.; Majid, M.Z.A.; Yusof, M.B.M.; Zeynali, I. Windcatcher as sustainable passive cooling solution for natural ventilation in hot humid climate of Malaysia. In Proceedings of the IOP Conference Series: Materials Science and Engineering, Palembang, Indonesia, 15–16 October 2018; Volume 620.
14. Montazeri, H.; Montazeri, F.; Azizian, R.; Mostafavi, S. Two-sided wind catcher performance evaluation using experimental, numerical and analytical modeling. *Renew. Energy* **2010**, *35*, 1424–1435. [CrossRef]
15. Calautit, J.K.; Wenbin Tien, P.; Wei, S.; Calautit, K.; Hughes, B.R. Numerical and experimental investigation of the indoor air quality and thermal comfort performance of a low energy cooling windcatcher with heat pipes and extended surfaces. *Renew. Energy* **2020**, *145*, 744–756. [CrossRef]
16. Calautit, J.K.; O'Connor, D.; Hughes, B.R. Determining the optimum spacing and arrangement for commercial wind towers for ventilation performance. *Build. Environ.* **2014**, *82*, 274–287. [CrossRef]
17. Calautit, J.K.; Hughes, B.R. Measurement and prediction of the indoor airflow in a room ventilated with a commercial wind tower. *Energy Build.* **2014**, *84*, 367–377. [CrossRef]
18. Chaudhry, H.N.; Calautit, J.K.; Hughes, B.R. Computational analysis of a wind tower assisted passive cooling technology for the built environment. *J. Build. Eng.* **2015**, *1*, 63–71. [CrossRef]
19. Montazeri, H. Experimental and numerical study on natural ventilation performance of various multi-opening wind catchers. *Build. Environ.* **2011**, *46*, 370–378. [CrossRef]
20. Ghadiri, M.H.; Lukman, N.; Ibrahim, N.; Mohamad, M.F. Computational Analysis of Wind-Driven Natural Ventilation in a Two Sided Rectangular Wind Catcher. *Int. J. Vent.* **2013**, *12*, 51–61. [CrossRef]
21. Afshin, M.; Sohankar, A.; Manshadi, M.D.; Esfeh, M.K. An experimental study on the evaluation of natural ventilation performance of a two-sided wind-catcher for various wind angles. *Renew. Energy* **2016**, *85*, 1068–1078. [CrossRef]
22. Nejat, P.; Calautit, J.K.; Majid, M.Z.A.; Hughes, B.R.; Jomehzadeh, F. Anti-short-circuit device: A new solution for short-circuiting in windcatcher and improvement of natural ventilation performance. *Build. Environ.* **2016**, *105*, 24–39. [CrossRef]
23. Nejat, P.; Calautit, J.K.; Majid, M.Z.A.; Hughes, B.R.; Jomehzadeh, F. Data on the natural ventilation performance of windcatcher with anti-short-circuit device (ASCD). *Data Brief* **2016**, *9*, 252–256. [CrossRef] [PubMed]
24. Nejat, P.; Calautit, J.K.; Majid, M.Z.A.; Hughes, B.R.; Zeynali, I.; Jomehzadeh, F. Wind tunnel and numerical data on the ventilation performance of windcatcher with wing wall. *Data Brief* **2016**, *9*, 448–452. [CrossRef] [PubMed]
25. Jomehzadeh, F.; Nejat, P.; Calautit, J.K.; Yusof, M.B.M.; Zaki, S.A. A review on windcatcher for passive cooling and natural ventilation in buildings, Part 1: Indoor air quality and thermal comfort assessment. *Renew. Sustain. Energy Rev.* **2017**, *70*, 736–756. [CrossRef]
26. Ghoulem, M.; El Moueddeb, K.; Nehdi, E.; Zhong, F.; Calautit, J. Design of a Passive Draught Evaporative Cooling Windcatcher (PDEC-WC) System for Greenhouses in Hot Climates. *Energies* **2020**, *13*, 2934. [CrossRef]
27. Calautit, J.; O'Connor, D.; Tien, T.; Wei, S.; Pantua, C.; Hughes, H. Development of a natural ventilation windcatcher with passive heat recovery wheel for mild-cold climates: CFD and experimental analysis. *Renew. Energy* **2020**. [CrossRef]
28. Hughes, B.R.; Calautit, J.K.; Ghani, S.A. The development of commercial wind towers for natural ventilation: A review. *Appl. Energy* **2012**, *92*, 606–627. [CrossRef]

29. ANSYS Incorporated ANSYS 14.5 FLUENT Theory Guide. Available online: <http://www.ansys.com> (accessed on 13 July 2020).
30. Calautit, J.K.; Hughes, B.R.; Chaudhry, H.N.; Ghani, S.A. CFD analysis of a heat transfer device integrated wind tower system for hot and dry climate. *Appl. Energy* **2013**, *112*, 576–591. [CrossRef]
31. Franke, J.; Hellsten, A.; Schlünzen, H.; Carissimo, B. *COST Action 732, Best Practice Guideline for the CFD Simulation of Flows in The Urban Environment*; University of Hamburg: Brussels, Belgium, 2007.
32. Tominaga, Y.; Mochida, A.; Yoshie, R.; Kataoka, H.; Nozu, T.; Yoshikawa, M.; Shirasawa, T. AIJ guidelines for practical applications of CFD to pedestrian wind environment around buildings. *J. Wind Eng. Ind. Aerodyn.* **2008**, *96*, 1749–1761. [CrossRef]
33. Tominaga, Y.; Akabayashi, S.; Kitahara, T.; Arinami, Y. Air flow around isolated gable-roof buildings with different roof pitches: Wind tunnel experiments and CFD simulations. *Build. Environ.* **2015**, *84*, 204–213. [CrossRef]
34. Launder, B.E.; Spalding, D.B. The numerical computation of turbulent flows. *Comput. Methods Appl. Mech. Eng.* **1974**, *3*, 269–289. [CrossRef]
35. Cebeci, T.; Bradshaw, P. *Momentum Transfer in Boundary Layers*; Hemisphere Publishing Corp: New York, NY, USA, 1977.
36. Zhang, Z.; Zhang, W.; Zhai, Z.J.; Chen, Q.Y. Evaluation of Various Turbulence Models in Predicting Airflow and Turbulence in Enclosed Environments by CFD: Part 2—Comparison with Experimental Data from Literature. *Hvac R Res.* **2011**, *13*, 871–886. [CrossRef]
37. Calautit, J.K.; Hughes, B.R. Wind tunnel and CFD study of the natural ventilation performance of a commercial multi-directional wind tower. *Build. Environ.* **2014**, *80*, 71–83. [CrossRef]
38. ASHRAE. *ASHRAE Standard 55 Thermal Environmental Conditions for Human Occupancy*; American Society of Heating, Refrigerating and Air-Conditioning Engineers: Atlanta, GA, USA, 2013.
39. Kubota, T.; Supian, A. Wind Environment Evaluation of Neighborhood Areas in Major Towns of Malaysia. *J. Asian Archit. Build. Eng.* **2006**, *5*, 199–206. [CrossRef]
40. Mozaffari, F. *Indoor Natural Ventilation with Wing Wall in Balcony in Medium-Rise Building in Hot and Humid Climate*; Universiti Teknologi Malaysia: Skudai, Malaysia, 2015.
41. Haw, L.C.; Saadatian, O.; Sulaiman, M.Y.; Mat, S.; Sopian, K. Empirical study of a wind-induced 561 natural ventilation tower under hot and humid climatic conditions. *Energy Build.* **2012**, *52*, 28–562. [CrossRef]
42. Mozaffari Ghadikolaei, F.; Remaz Ossen, D.; Farid Mohamed, M. Effects of wing wall at the balcony on the natural ventilation performance in medium-rise residential buildings. *J. Build. Eng.* **2020**, *31*, 101316. [CrossRef]
43. Dehghani Mohamadabadi, H.; Dehghan, A.A.; Ghanbaran, A.H.; Movahedi, A.; Mohamadabadi, A.D. Numerical and experimental performance analysis of a four-sided wind tower adjoining parlor and courtyard at different wind incident angles. *Energy Build.* **2018**, *172*, 525–536. [CrossRef]
44. ASHRAE. *ASHRAE Standard 62.1: Ventilation for Acceptable Indoor Air Quality*; American Society of Heating, Refrigerating and Air-Conditioning Engineers, Inc.: Atlanta, GA, USA, 2019.
45. Hughes, B.R.; Ghani, S.A.A.A. Investigation of a windvent passive ventilation device against current fresh air supply recommendations. *Energy Build.* **2008**, *40*, 1651–1659. [CrossRef]
46. Khan, N.; Su, Y.; Riffat, S.B. A review on wind driven ventilation techniques. *Energy Build.* **2008**, *40*, 1586–1604. [CrossRef]
47. Shi, Z.; Lu, Z.; Chen, Q. Indoor airflow and contaminant transport in a room with coupled displacement ventilation and passive-chilled-beam systems. *Build. Environ.* **2019**, *161*, 106244. [CrossRef]
48. Montazeri, H.; Montazeri, F. CFD simulation of cross-ventilation in buildings using rooftop wind-catchers: Impact of outlet openings. *Renew. Energy* **2018**, *118*, 502–520. [CrossRef]



Article

# Valuation of the Energy Performance of a Greenhouse with an Electric Heater Using Numerical Simulations

Cruz Ernesto Aguilar-Rodriguez <sup>1,\*</sup>, Jorge Flores-Velazquez <sup>1</sup>, Waldo Ojeda-Bustamante <sup>1</sup>,  
Fernando Rojano <sup>2</sup> and Mauro Iñiguez-Covarrubias <sup>1</sup>

<sup>1</sup> Mexican Institute of Water Technology, Jiutepec, Morelos 62550, Mexico; jorgelv@colpos.mx (J.F.-V.); w.ojeda@riego.mx (W.O.-B.); mic@tlaloc.imta.mx (M.I.-C.)

<sup>2</sup> Gus R. Douglass Institute, West Virginia State University, Institute, WV 25112, USA; fernando.rojano@wvstateu.edu

\* Correspondence: cruz.aguilar@posgrado.imta.edu.mx

Received: 16 April 2020; Accepted: 14 May 2020; Published: 18 May 2020

**Abstract:** In Mexico, there are regions where the temperature drops below the minimum threshold for tomato cultivation (10 °C), requiring the implementation of auxiliary equipment to heat greenhouse air. The objective of this work was to estimate the energy consumption necessary to maintain climate requirements of a greenhouse located in Texcoco, State of Mexico, by using a model of energy balance implemented on Computational Fluid Dynamics (CFD) simulations. The temperature prediction relied on a numerical model based on CFD, proposing a benchmarking on the position and direction of the heater to estimate its effect on the thermal distribution. Results indicated that heater operation on January 2019, a power of 85.56 kW was needed to keep the greenhouse at 12 °C. Also, simulations indicated that electric heater used was not enough to get a homogeneous temperature inside the greenhouse. To achieve well-distributed thermal conditions, it was necessary to consider both the direction and position of heaters. Consequently, airflow direction became more important than height of the heater in order to homogenize the greenhouse area, given that the thermal gradient was reduced due to reverse heat flows.

**Keywords:** energy engineering; thermal stratification; crop requirements; Computational Fluid Dynamics (CFD)

---

## 1. Introduction

Plant growth greatly depends on the temperature and humidity. For winter production in Central Mexico, greenhouses provide better environmental conditions for plant growth compared to most agricultural production systems. Given that a greenhouse is a structure favoring environment for crop production, there are consequences such as heat excess during the day is absorbed by the ground and during the night it is used to meet the heating needs in enclosed greenhouses [1]. In this way, one of the characteristics of enclosed greenhouses is that they are energy saving compared to greenhouses fully relying on natural ventilation. However, accumulation of energy during the day may become insufficient [2] with higher frequency during the winter. Therefore, night temperature becomes a critical factor in the efficiency of a crop cultivated in a greenhouse. Adequate greenhouse energy management can serve to avoid low night temperatures and reduce condensation phenomena causing dripping process on crops [3–6].

A conventional solution for low-temperature problems is using heating systems inside the greenhouse. Since energy and fuel prices are not cheap [7], their efficient use directly impacts production costs and should be balanced with the risks of crop loss [8,9]. Nonetheless, the amount of heat added to the greenhouse depends on the changing weather conditions, where winter becomes the

critical period [10]. Previous research [10,11] have stated that more attention should be given to the night due to significant heat losses, which should be compensated by means of an artificial heat input.

In addition to conventional heating systems (fossil fuels), there are alternative systems used to heat the interiors of greenhouses, among which are renewable energy source systems. These systems allow the use of biomass, solar, and geothermal energy sources [12–17], with solar energy being the most recommendable, given that it is a clean, abundant, and safe source. One of the greenhouse heating systems that uses solar energy as a main source and that has been studied by many researchers is rock bed storage. This type of system uses underground rocks to store heat during the day and release it at night, generating an increase in air temperature of up to 3 °C, causing improvement of fruit quality by up to 29% [18,19].

In some greenhouse production systems, the energy consumption represents more than 50% of the total cost of production, and it is necessary to calculate its consumption. The more accurate approach is employing mathematical models based on the principle of heat and mass conservation in order to estimate the feasibility of the implementation of control systems during the winter. Numerical models are also used to improve the understanding of convective, radioactive, and conductive phenomena and the environment-plant iteration within the greenhouse [20–23]. These findings have allowed us to deepen our understanding of the dynamics of the microclimate and the energy needed to maintain environmental comfort, achieve a high-performance production, and improve the quality and efficiency of heating systems [24–26].

Modeling by means of Computational Fluid Dynamics (CFD) has achieved an approach to simulate air movement and temperature variation within the greenhouse and the impact of heating systems on the thermal gradient [27–32]. Along with this, it has allowed us to refine sub-systems of the greenhouse such as the heating system to increase its effectiveness and efficiency. Some studies carried out in CFD have allowed us to establish that, by using heating pipes, it was possible to increase the temperature inside the greenhouse by up to 4.5 °C [11]. In 2018, Yilmaz and Selbas [33] investigated the thermal performance of a solar collector, a heat pump, and a boiler for heating a greenhouse. The results showed that the solar collector had a greater impact on the thermal gradient of the greenhouse, with a thermal efficiency of 33.11%. Another work in 2017, Tadj et al. [27] demonstrated that perforated polyethylene duct heating systems generated a uniform temperature compared to other heating systems (hot water pipes and air heaters). These results agreed with what was established in the literature, in which the temperature distribution was more homogeneous in a vertical plane than in a horizontal plane [34].

In regions with mild winters and at specific periods of the year, an emergent heating system is being needed to mitigate occasional frosts. In central Mexico, it is common to place pop-up heaters aiding to stabilize the internal temperature when the outside temperature drops abruptly in specific hours before sunrise. Even though empirical experience has been gained, there is still scarce research about optimal use of electrical heating systems. For instance, recommendations about the position and direction of heaters to optimize amounts of heat that guarantees thermal homogeneity during these critical periods. Nor it is found related research on the energy and economic costs of this emerging heating system.

Then, the aim of this work was to estimate the necessary energy consumption to maintain thermal homogeneity using an electric heater in the greenhouse under winter conditions in central Mexico, using a model of energy balance and CFD to predict the thermal distribution under different heating scenarios.

## 2. Materials and Methods

### 2.1. Experimental Ground Description

The site of the experimental greenhouse was located at Campus Graduate College in the State of Mexico (19°27'45.5" N, 98°54'12.2" W) at 2239 masl, situated on flat ground with no structures around

it. In the region, the minimum monthly temperatures range between 2.49 °C and 11.24 °C throughout the year.

The prototype greenhouse had an area of 1050 m<sup>2</sup>. It was of the zenith type with three spans covered with translucent polyethylene on the floor and sides, polycarbonate on the roof, and anti-insect on the windows. The greenhouse had a natural ventilation system based on the closure and opening of the overhead and front windows and a heating system using an electric heater (CM-VAX, Calelec, Monterrey, Mexico) recommended for enclosed spaces with an area of 96 m<sup>2</sup>. The electric heater was located 3 m above the ground level in span 2 in the windward zone and had a power of 15 kW. Its electrical characteristics were 230/3/60 (Volts/Phases/Cycles), and it had an axial fan with a motor of 1/8 HP that worked with 120 V.

For data acquisition, an Eddy Covariance system 2.4 m away from the windward position with a sonic anemometer (CSAT 3D, Campbell Scientific Ltd., Antony, France), an EC150 gas analyzer (Campbell Scientific Inc., Logan, UT, USA), a temperature and humidity sensor (HMP155A, Campbell Scientific Logan, UT, USA) and four sensors for soil temperature (TCAV thermocouple Campbell Scientific Logan, UT, USA) which were placed inside the greenhouse. Seven temperature sensors (DS18B20, Maxim Integrated, San Jose, CA, USA) and three relative humidity sensors (DHT22, Zhengxinyuan Electronics Co., Ltd., Shenzhen, China) were distributed in the three spans at a height of 3 m (Figure 1).

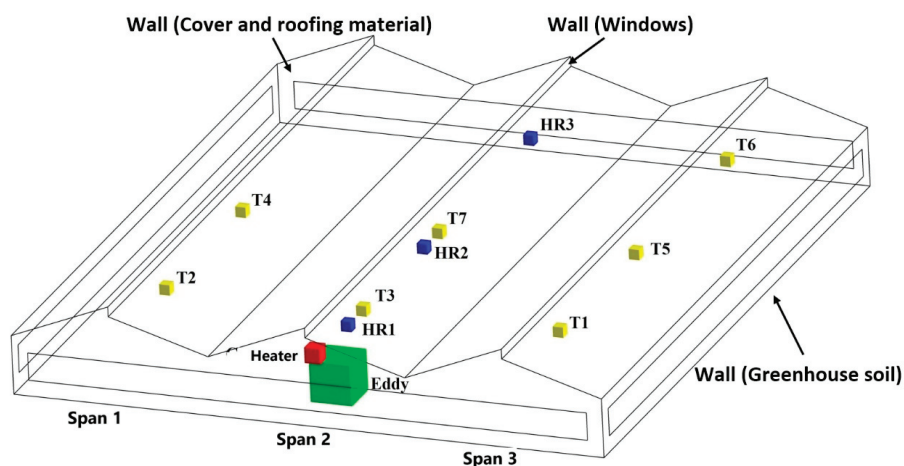


**Figure 1.** Distribution of the temperature (■) and humidity (■) sensors, the heater (■), and the Eddy Covariance System (■) in the three buildings of the experimental greenhouse; border conditions of the computational model.

Data recording and storage were performed every 5 s for the temperature and humidity and every 100 ms for the anemometer. The monitoring period was from February 3 to February 24, 2019, which was enough time to investigate the emergent heater, since the meteorological data recorded minimum temperatures during this month of below 12 °C. The data was stored with a data logger system (CR3000 Micrologger, Campbell Scientific, Inc., Logan, UT, USA) for the Eddy Covariance system and an Arduino data Logger Shield for the DS18B20 and DHT22 sensors. Outside the greenhouse, a weather station (Vantage Pro2 Plus, Davis Instruments, Hayward, CA, USA) was available and used to record data on temperature, humidity, wind direction, and wind speed—these values were used as the initial boundary condition of the computer model. All data was processed in Microsoft Excel to determine the environmental input conditions of the computational model.

## 2.2. Heat Calculation

The greenhouse temperature model was developed based on the energy and mass balances [24,25,35,36] in the completely closed greenhouse without environment-plant iteration, because at the time of data recording there was no crop. The calculation of  $Q_h$  was estimated by establishing the necessary energy consumption transferred by the electric heater to attenuate the thermal gradient, expressed as follows:

$$Q_h = Q_t + Q_i + Q_g - Q_l \quad (\text{W}). \quad (1)$$

The thermal radiation transferred from the inside to the outside of the greenhouse ( $Q_l$ ) depended on the emission of energy into the atmosphere and on the roofing materials.

$$Q_l = S_{sc} \cdot \sigma \cdot \tau_{ter} \cdot (\varepsilon_{atm} \cdot T_{atm}^4 - \varepsilon_{ter} \cdot T_c^4) \quad (\text{W}), \quad (2)$$

where  $S_{sc}$  is the floor area covered ( $\text{m}^2$ ),  $\sigma$  is the Stefan–Boltzmann constant ( $\text{W m}^{-2} \text{K}^{-4}$ ),  $\tau_{ter}$  is the transmittance coefficient of the cover material for thermal radiation,  $\varepsilon_{atm}$  is the emissivity of the atmosphere,  $T_{atm}$  is the temperature of the emission of energy to the atmosphere (K),  $\varepsilon_{ter}$  is the emissivity of the roofing material for thermal radiation, and  $T_c$  is the absolute temperature of the roof (K).

The heat transfer by conduction and convection ( $Q_t$ ) was estimated by the temperature between the inside and outside of the greenhouse.

$$Q_t = S_{dc} \cdot K_{cc} \cdot (t_i - t_e) \quad (\text{W}), \quad (3)$$

where  $S_{dc}$  is the developed area of the greenhouse cover ( $\text{m}^2$ ),  $t_i$  is the interior temperature of the greenhouse (K),  $t_e$  is the exterior temperature of the greenhouse (K), and  $k_{cc}$  is the overall coefficient of heat loss by conduction and convection ( $\text{W m}^{-2} \text{K}^{-1}$ ).

The sensitive and latent heat lost by the renewal of indoor air ( $Q_i$ ) was considered minimal when establishing as an initial condition the closing of the side and overhead windows. However, there is air infiltration through the structure as it is an old construction becoming a partially airtight greenhouse.

$$Q_i = V_{gh} \cdot \frac{R}{3600} \cdot \rho \cdot [c_{pa} \cdot (t_i - t_e) + \lambda_0 \cdot (x_i - x_e) + c_{pv} \cdot (x_i t_i - x_e t_e)] \quad (\text{W}), \quad (4)$$

where  $V_{gh}$  is the volume of the greenhouse ( $\text{m}^3$ ),  $c_{pa}$  is the specific heat of the air ( $\text{J kg}^{-1} \text{K}^{-1}$ ),  $\rho$  is the density of the air ( $\text{kg m}^{-3}$ ),  $c_{pv}$  is the specific heat of the superheated steam ( $\text{J kg}^{-1} \text{K}^{-1}$ ),  $x_i$   $x_e$  is the absolute indoor and outdoor humidity ( $\text{kg kg}^{-1}$ ),  $\lambda_0$  is the latent heat of vaporization ( $\text{J kg}^{-1}$ ), and  $R$  is the air renewal rate ( $\text{h}^{-1}$ ).

The heat transfer through the ground ( $Q_g$ ) is a function of the difference in the indoor and soil temperature.

$$Q_g = K_{ts} \cdot S_{sc} \cdot \frac{(t_i - t_s)}{p} \quad (\text{W}), \quad (5)$$

where  $K_{ts}$  is the coefficient of thermal exchange through the soil ( $\text{W m}^{-1} \text{K}^{-1}$ ),  $t_s$  is the soil temperature (K), and  $p$  is the depth at which the temperature is estimated (m).

The parameters of the energy balance model were analyzed considering the effect of the greenhouse environment, its characteristics, and the roof materials (Tables 1 and 2).

The heat calculation was made using the average weather condition rates of minimum daily temperature. Inside temperature of the greenhouse was established as 12 °C based on the thermal requirement of the tomato (*Solanum Lycopersicum* L.), which, for proper growth, the temperature should be higher than 10 °C at night [40,41].

**Table 1.** Variables for the heat calculation obtained from the literature.

Symbol	Variable	Value	Unit	Source
$\sigma$	Stefan–Boltzmann constant	$5.67 \times 10^{-0.8}$	$\text{W m}^{-2} \text{K}^{-4}$	[37]
$\alpha$	Polycarbonate absorbency	0.09		[37,38]
$\tau_{ter}$	Transmittance coefficient of the polycarbonate	0.025		[37,38]
$\varepsilon_{ter}$	Polycarbonate emissivity	0.935		[37,38]
$C_{pa}$	Specific heat of the air	1008	$\text{J kg}^{-1} \text{K}^{-1}$	[24,25]
$R$	Air renewal rate	4	$\text{h}^{-1}$	[39]

**Table 2.** Characteristics of the greenhouse and its components.

Symbol	Variable	Value	Unit
$S_{dc}$	The developed area of the greenhouse cover	1113	$\text{m}^2$
$S_{sc}$	Floor area covered	1050	$\text{m}^2$
$e_{c1}$	Polycarbonate thickness	0.06	m
$e_{c2}$	Polyethylene thickness	0.000018	m
$V_{gh}$	Greenhouse volume	4,068,076	$\text{m}^3$

### 2.3. Computational Model

Building and simulation of the computational model was carried out in ANSYS® Fluent® (ANSYS, Inc., Canonsburg, PA, USA). The geometry was developed in the design modeler tool. The meshing was done in meshing, and the greenhouse had dimensions of  $30 \times 35 \times 5$  m, with 490,000 average structured elements, an orthogonal quality of 0.98, and a distortion of  $1.935 \times 10^{-0.02}$ .

Model conditions and variables applied to the airflow to solve the transport equations, which were discretized into algebraic equations and calculated by numerical methods, were defined in Table 3.

**Table 3.** Boundary conditions of the computational model.

Boundary Condition	Method
Solver	Pressure-based
State	Steady
Viscosity function	k- $\varepsilon$ Estándar
Energy equation	Activated
Entry	Velocity inlet
Output	Pressure outlet
Air temperature	Constant (12.73 °C)
Wind speed	Constant (0.513 $\text{m s}^{-1}$ )
Heat source	Boussinesq's hypothesis
Soil thermal condition	Temperature (4.7 °C)
Soil	Wall ( $\rho$ :1300, $C_p$ :800, $\lambda$ :1)
Walls and greenhouse padding (Polyethylene PE)	Wall ( $\rho$ :925.5, $C_p$ :1900, $\lambda$ :0.3)
Ceiling (Polycarbonate PC)	Wall ( $\rho$ :1200, $C_p$ :1200, $\lambda$ :0.19)

Heater simulation included a pressure jump and angular velocity. The pressure jump calculation was estimated considering Equation (6):

$$\Delta p = \frac{1}{2} \rho_{air} v^2 \quad (\text{Pa}), \quad (6)$$

where  $\rho_{air}$  is the air density ( $\text{kg m}^{-3}$ ) and  $v$  is the fan speed ( $\text{m s}^{-1}$ ).

### Evaluation of the Computational Models

In order to obtain a reliable computational model, two scenarios were assessed: (I) no heat and (II) with heat. The evaluation was carried out by a statistical analysis of both temperature and wind speed

using simulated and experimental data. The statistic studios were made by an analysis of variance (ANOVA), with a significance level of 0.05 used to contrast the difference of the variables in the different factors parametrically.

#### 2.4. Simulation Scenarios

The analysis of the distribution of heat flow in the greenhouse was performed by comparing the effect of the position and direction of the heaters; two more heaters were included in the computational model, seeking to improve the system with a uniform temperature (Table 4). Simulations were carried out in a stationary state, and the provided energy was modified by the heater based on the assessed computational model's results. The origin of the coordinates (x, y, z) is in the center of the greenhouse, and the flow direction of the evaluated heater is z.

**Table 4.** Simulation scenarios (X transversal, Z longitudinal, Y height).

Sceneries	Heaters	Ubication in Greenhouse (Local Coordinates)	Heater Flow Direction
a	0		
b	1	Span 2 (X: 0 m, Y: 3 m, Z: -16.5 m)	Z
c	1	Span 2 (X: 0 m, Y: 0.5 m, Z: -16.5 m) Span 1 (X: -10 m, Y: 3 m, Z: -16.5 m)	Z Z
d	3	Span 2 (X: 0 m, Y: 3 m, Z: -16.5 m) Span 3 (X: 10 m, Y: 3 m, Z: -16.5 m) Span 1 (X: -10 m, Y: 0.5 m, Z: -16.5 m)	Z Z Z
e	3	Span 2 (X: 0 m, Y: 0.5 m, Z: -16.5 m) Span 3 (X: 10 m, Y: 0.5 m, Z: -16.5 m) Span 1 (X: -10 m, Y: 3 m, Z: -16.5 m)	Z Z Z
f	3	Span 2 (X: 0 m, Y: 3 m, Z: 16.5 m) Span 3 (X: 10 m, Y: 3 m, Z: -16.5 m) Span 1 (X: -10 m, Y: 0.5 m, Z: -16.5 m)	-Z Z Z
g	3	Span 2 (X: 0 m, Y: 0.5 m, Z: 16.5 m) Span 3 (X: 10 m, Y: 0.5 m, Z: -16.5 m)	-Z Z

### 3. Results and Discussion

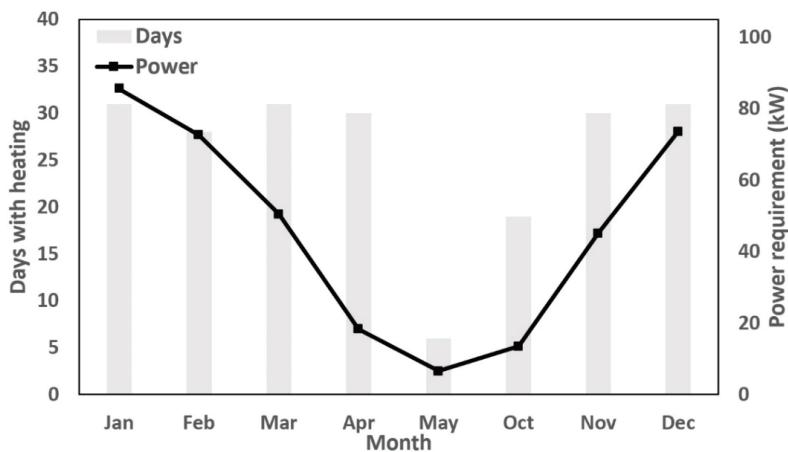
#### 3.1. Energy Consumption

Figure 2 shows the estimation of the necessary heating days and their average power requirement. For their calculation, the results obtained from Equation (1) were used, considering that power requirement is required on days with a temperature below 12 °C inside the greenhouse. The monthly power requirement is the arithmetic average of the air conditioning calculation of the days with heating needs during the year.

Results from Figure 2 show that, during certain hours at night, is necessary to heat the greenhouse's air for 206 days. January was the month with the highest energy requirement, needing an implementation of five more heaters with the same conditions to cover the energy needs and maintain a 12 °C temperature. This means that for thermal comfort in the microclimate of the greenhouse, a device providing 85.56 kW is required.

In Figure 3, a comparison was made between the average minimum monthly temperature in the study area and the energy required to maintain the greenhouse at 12 °C (Equation (1)). The calculation of the monthly energy requirement was carried out by assuming that the period in which the temperature falls below 12 °C during the days with heating needs occurs for an average of three hours per day. The peak of the needs was produced in January and is 13.94% higher than the one in December. During the period from June to September, there is no energetic demand. To cover the annual demand, 32,228.76 kWh is necessary, which represents a cost of MX \$20,626.40 (US \$540.0) according to the nine tariff charges applied to the agriculture in Mexico.





**Figure 2.** Annual variation in the power required to keep the greenhouse at 12 °C during the days with heating needs.

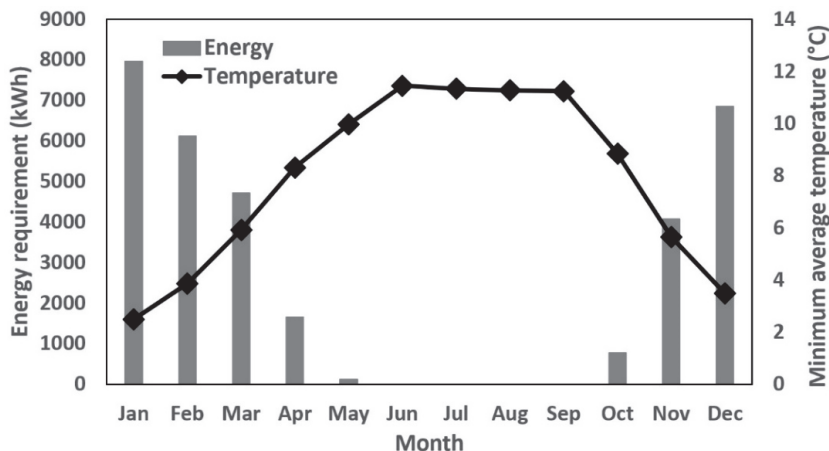


**Figure 3.** Annual variation in energy requirement for three daily hours.

### 3.2. Mesh Sensitivity Analysis of the Computational Model

A sensibility mesh analysis was carried out in the greenhouse by 100 temperature measurements in a location 2 m above the ground. Four scenarios were performed by modifying the number of elements of the inside mesh of the greenhouse. The results showed that there is no meaningful difference between the simulated temperature results with a 490,000 average element mesh.

#### 3.2.1. Validation

The evaluation of the computational model with and without heating was carried out statistically by correlating the values of temperature and wind speed simulated and recorded by the sensors during the nights of February 6th and 7th, 2019, respectively. In Table 5, it can be observed that the recorded and simulated temperature values were approximate. To measure this correlation, the statistical method ANOVA with a significance level of 0.05 was used, considering that if the F statistic test was less than the F critical value ( $F \text{ test statistic} < F \text{ critical value}$ ), there was no significant difference between the measured and simulated variables (Table 6), so the evaluated model can be used in simulations.

**Table 5.** Temperature data (°C) of the evaluated models.

Model without Heating			Heated Model		
Sensor	Experimental	Simulated	Sensor	Experimental	Simulated
T1	11.28	11.42	T1	10.96	11.03
T2	10.28	11.43	T2	10.43	11.05
T3	10.95	11.3	T3	10.94	11.06
T4	10.93	11.33	T4	10.79	10.89
T5	11.52	11.31	T5	10.93	10.86
T6	11.5	11.4	T6	10.86	10.82
T7	11.31	11.29	T7	11.07	10.82
Eddy	11.76	11.85	Eddy	11.08	10.91

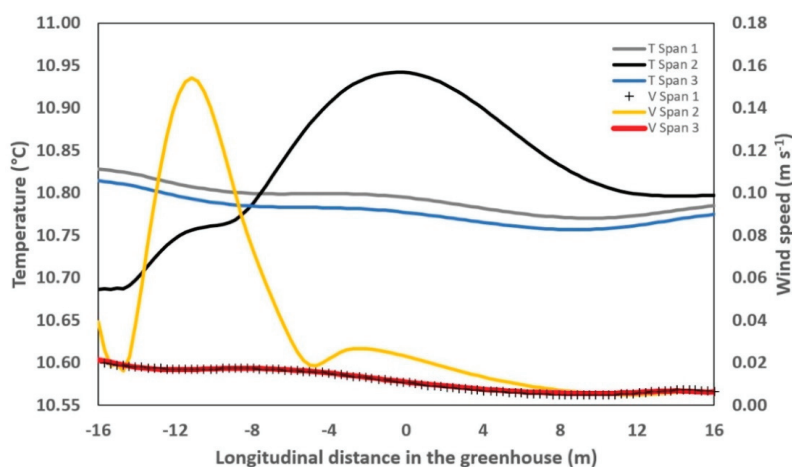
**Table 6.** Comparison between the F test statistic (ANOVA) and its critical value.

	With Heating	Without Heating
Temperature	0.3 < 4.6	1.62 < 4.6
Wind speed	0.005 < 7.7	3.25 < 7.7

### 3.2.2. Environmental Analysis of the Assessed Model

An empty greenhouse was validated to give stability to the variables being analyzed. Once the model was validated, the crop could be modeled, since its thermal and relative humidity requirements were known. In some cases, tomato crop could be modeled as a source or sink of momentum, energy, and mass. The heatless model presented a thermic homogenization at 2 m high inside the three spans of the greenhouse. The speed was not superior to  $0.018 \text{ m s}^{-1}$ , and the number of Rayleigh (Ra) varied around  $2.8 \times 10^8$  for the three greenhouse's spans, with a laminar flow induced by floating forces.

The computational model with heating shows that for span 2, there was an increase in the speed of wind generated by the fan (Figure 4). This rise in speed caused a low on span 2 near the windward. However, in the center of span 2, there was a rise of nearly  $0.15 \text{ °C}$  derived from the energy supply on the part of the heater.

**Figure 4.** Temperature distribution (°C) and wind speed ( $\text{m s}^{-1}$ ) to 2 m high.

On spans 1 and 3 of the model with heat prevailed the laminar flows induced by floating forces with Ra numbers between  $4.09 \times 10^8$  and  $5.98 \times 10^8$ . On span 2 near the fan, the thermic distribution was in accordance with the speed and temperature provided by the heater, causing a transition zone in a turbulent flow ( $10 \times 10^8$  to  $10 \times 10^{10}$ ) with Ra values of  $2.42 \times 10^9$ .

These simulations presented a thermal behavior similar to the one obtained by Chen et al. [24], when greenhouses subjected to non-heating, laminar flows induced by prevailing buoyancy forces. And in greenhouses with heating, there was a turbulent flow transition.

### 3.3. Thermal Spatial Distribution of Simulated Scenarios

Figure 5 shows a top view of the temperatures at 2 m from the ground in the simulated scenarios with initial data from the computational model with and without heating. The results from the simulations present an increase in temperature of  $0.8 \text{ }^\circ\text{C}$  between scenarios a and b, and an increase of  $2 \text{ }^\circ\text{C}$  between scenarios a, d, and e.

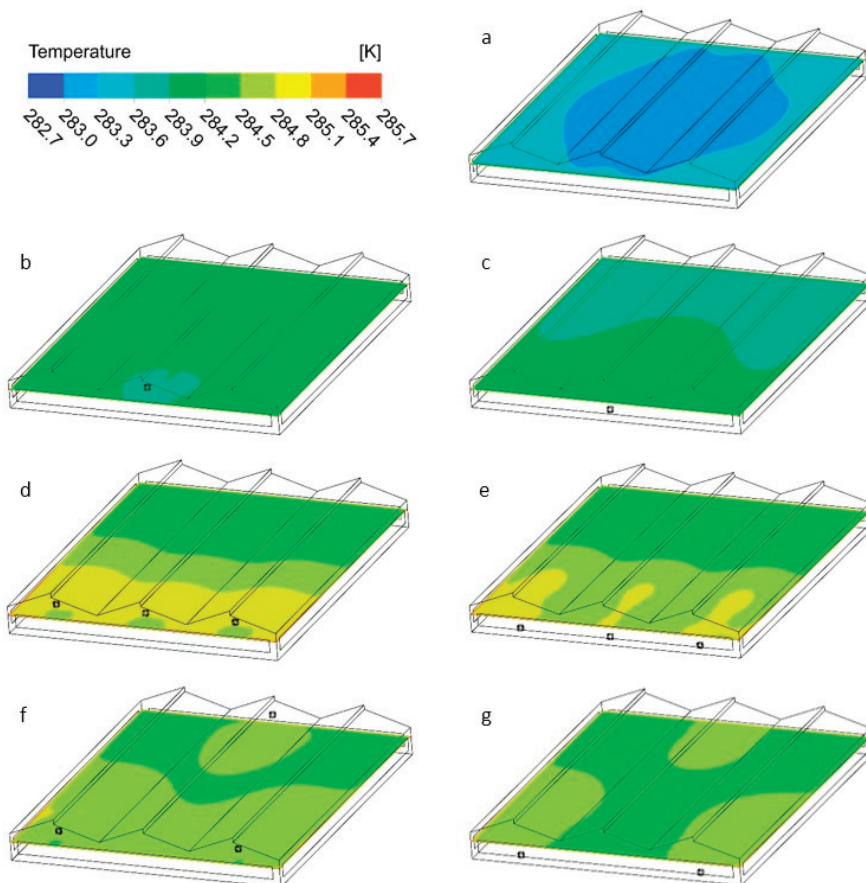


**Figure 5.** Distribution of temperature (K) at 2 m above the ground in the greenhouse under the initial conditions of the heating computational model in the (a–g) sceneries of simulation.

Given that the maximum thermal gradient was  $0.2 \text{ }^\circ\text{C}$  when the heater height was modified (Figure 5b–g), it was determined that if the direction of heat flow was the same, the height has no significant effect on the temperature's distribution at 2 m from the ground under the original conditions of the heater. Unless the heat flow direction was changed (scenarios f and g), in this case, the homogeneity

improved and the buoyancy forces had crucial importance in the heat distribution. The results of the simulations matched those presented in the works of Tadj et al. and Dhiman et al. [27,34], where the air heating was not the most efficient way in which to homogenize the greenhouse's temperature on a horizontal level.

To review the results of Figure 5 and analyze the temperature behavior at 2 m from the ground and its influence on the height and direction of the flow of the heater under different energy supplies, four scenarios were performed (d, e, f, and g) considering a constant supply of air with a temperature of 30 °C by the heater.

Figure 6 shows the relationship of the longitudinal temperature at 2 m high off the ground in span 2 between scenarios d and e ( $\Delta$ ), with a constant temperature supply of 30 °C. The figure shows that if the direction of heat flow remained constant, there was no significant difference in the temperature at 2 m from the ground ( $R^2 = 0.996$ ) between the heater at 0.5 and 3 m. However, this heater position was not adequate to homogenize the vertical temperatures longitudinally 2 m from the ground, since, as the energy provided by the heater increases, the thermal gradient was more significant between the area near the heater and its opposite side. Scenarios d and f (o) showed that in span 2, the direction of heat flow had a more significant impact on the distribution of horizontal temperatures at 2 m high, improving the homogenization and reducing the thermal gradient when mixed heat fluxes are present (scenario f).

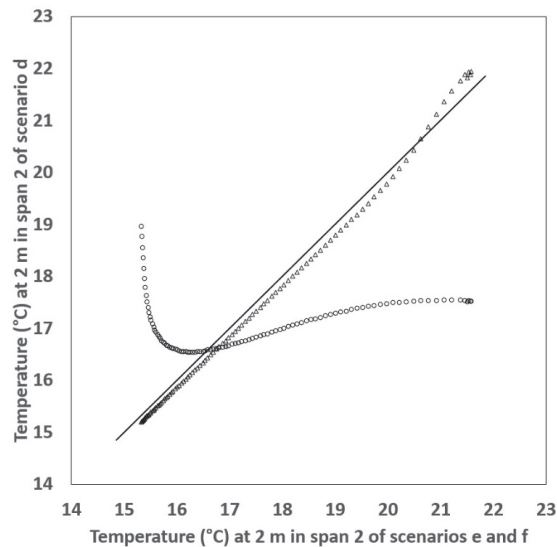


**Figure 6.** Temperature relationship (°C) at a 2 m height in span 2 of the greenhouse with 30 °C constant heating for 4 scenarios: d and e ( $\Delta$ ), and d and f (o).

Through the simulation results of this work, it was possible to assume that the direction of heat flow had a significant impact on thermal homogenization (scenarios d and g), reaffirming the work of Constantinou et al. [27], where the distribution of heat flow was caused by the position of the heating systems and the effect of floating forces created by the thermal gradient between the greenhouse temperature and the energy supplied by the heating system.

When selecting the location of the heater, it was necessary to take into account that the temperature was higher in the area near the heater, as shown in Figure 7. Therefore, to avoid crop damage, the heater must be installed at a height higher than the current crop. In the case of tomatoes, the recommended height was 3 m.

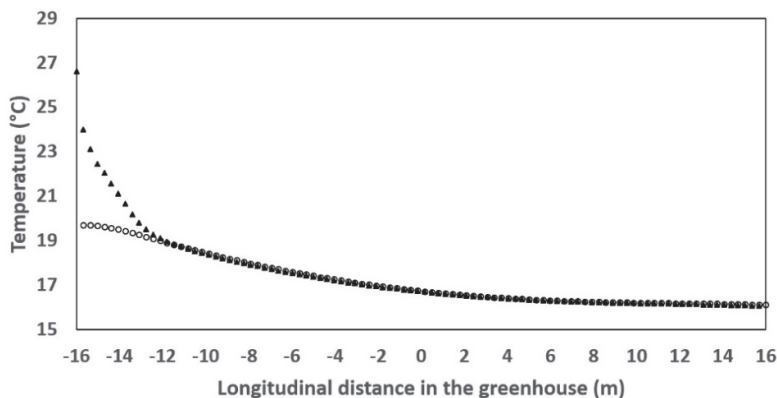


**Figure 7.** Distribution of temperatures (°C) at 0.7 m high in span 1 of the greenhouse for scenarios f (°) and g (▲), with a 30 °C constant temperature supplied by the heater.

The power supplied by the greenhouse heater used in this research was insufficient to mitigate the temperature drop that occurs mainly during the winter period. In addition to the power, it was necessary to consider the distribution of electric heaters, since this type of system, compared to heating systems using pipe networks [34,42,43], was not the best option for homogenizing the temperature in the greenhouse. Currently, there are many techniques used to heat the air in the greenhouse [10,27,44]. However, due to the high investment cost of these systems, they sometimes become unfeasible.

#### 4. Conclusions

During the winter in Central Mexico (December 21 to March 21), energy consumption is around 63% of the total for the year to maintain a temperature of up to 12 °C in the greenhouse during the night period. Such climatic conditions cause an approximate cost of MX \$12,949.7 (US \$540), according to the agricultural tariff in Mexico. Thermal distribution occurs in accordance with the speed and temperature provided by the heater, causing a zone with a turbulent flow and a difference in density between the air near the heater and the rest area of the greenhouse. Thermal homogenization in the greenhouse occurs when there are conditions for opposite heat flows (recirculation), causing an improvement in the greenhouse environment by the distribution of the heaters and reducing the temperature gradient between the area near the heater and its opposite side. This type of heater system, known as aerial, is not ideal for homogenizing the temperature of the greenhouse due to the effect of the buoyancy forces which can be overcome by adding fans at stagnant zones and aid to distribute the heat at all zones of the greenhouse.

**Author Contributions:** Data curation, C.E.A.-R.; formal analysis, C.E.A.-R., J.F.-V., W.O.-B., F.R., and M.I.-C.; investigation, C.E.A.-R., M.I.-C., J.F.-V., and W.O.-B.; methodology, C.E.A.-R., F.R.; supervision, W.O.-B., J.F.-V. and F.R. All authors have read and agreed to the published version of the manuscript.

**Funding:** This research was not funded.

**Acknowledgments:** This study was supported by a PhD thesis of C.E.A.-R in the Water Science and Technology program of the Mexican Institute of Water Technology (IMTA).

**Conflicts of Interest:** The authors declared that they have no conflicts of interest in this work.

#### References

1. Fidaros, D.K.; Baxevanou, C.A.; Bartzanas, T.; Kittas, C. Numerical simulation of thermal behavior of a ventilated arc greenhouse during a solar day. *Renew. Energy* **2010**, *35*, 1380–1386. [CrossRef]
2. Roy, J.C.; Pouillard, J.B.; Boulard, T.; Fatnassi, H.; Grisey, A. Experimental and CFD results on the CO<sup>2</sup> distribution in a semi-closed greenhouse. *Acta Hort.* **2014**, *1037*, 993–1000. [CrossRef]

3. Ali, H.B.; Bournet, P.E.; Danjou, V.; Morille, B.; Migeon, C. CFD simulations of the night-time condensation inside a closed glasshouse: Sensitivity analysis to outside external conditions, heating and glass properties. *Biosyst. Eng.* **2014**, *127*, 159–175. [CrossRef]
4. Salazar-Moreno, R.; Rojano-Aguilar, A.; López-Cruz, I.L. La eficiencia en el uso del agua en la agricultura controlada. *Tecnol. Y Cienc. Del Agua* **2014**, *5*, 177–183.
5. Salazar-Moreno, R.; Mauricio-Pérez, A.M.; López-Cruz, I.L.; Rojano-Aguilar, A. A model of humidity within a semi-closed greenhouse. *Rev. Chapingo Ser. Hortic.* **2016**, *22*, 27–43. [CrossRef]
6. Zeroual, S.; Bougoul, S.; Benmoussa, H. Effect of Radiative Heat Transfer and Boundary Conditions on the Airflow and Temperature Distribution Inside a Heated Tunnel Greenhouse. *J. Appl. Mech. Tech. Phys.* **2018**, *59*, 1008–1014. [CrossRef]
7. Tamimi, E.; Kacira, M. Analysis of climate uniformity in a naturally ventilated greenhouse equipped with high-pressure fogging system using computational fluid dynamics. *Acta Hortic.* **2013**, *1008*, 177–184. [CrossRef]
8. Bakker, J.C. Analysis of Humidity Effects on Growth and Production of Glasshouse Fruit Vegetables. Ph.D. Thesis, Agricultural University of Wageningen, Wageningen, The Netherlands, 1991.
9. Baptista, F.J.; Bailey, B.J.; Meneses, J.F. Effect of nocturnal ventilation on the occurrence of Botrytis cinerea in Mediterranean unheated tomato greenhouses. *Crop. Prot.* **2012**, *32*, 144–149. [CrossRef]
10. Ozgener, O.; Hepbasli, A. Performance analysis of a solar-assisted ground-source heat pump system for greenhouse heating: An experimental study. *Build. Environ.* **2005**, *40*, 1040–1050. [CrossRef]
11. Couto, N.; Rouboa, A.; Monteiro, E.; Viera, J. Computational Fluid Dynamics Analysis of Greenhouses with Artificial Heat Tube. *World J. Mech.* **2012**, *2*, 181187. [CrossRef]
12. Du, J.; Bansal, P.; Huang, B. Simulation model of a greenhouse with a heat-pipe heating system. *Appl. Energy* **2012**, *93*, 268–276. [CrossRef]
13. Zhou, D.; Zhao, C.Y.; Tian, Y. Review on thermal energy storage with phase change materials (PCMs) in building applications. *Appl. Energy* **2012**, *92*, 593–605. [CrossRef]
14. Tian, Y.; Zhao, C.Y. A review of solar collectors and thermal energy storage in solar thermal applications. *Appl. Energy* **2013**, *104*, 538–553. [CrossRef]
15. Joudi, K.A.; Farhan, A.A. Greenhouse heating by solar air heaters on the roof. *Renew. Energy* **2014**, *72*, 406–414. [CrossRef]
16. Zhang, L.; Jiachen, P.X.; Tang, M.X.; Jianguo, Z.L. A low cost seasonal solar soil heat storage system for greenhouse heating: Design and pilot study. *Appl. Energy* **2015**, *156*, 213–222. [CrossRef]
17. Gourdo, L.; Bazgaou, A.; Ezzaeri, K.; Tiskatine, R.; Wifaya, A.; Demrati, H.; Aharoune, A.; Bourirden, L. Heating of an agricultural greenhouse by a reservoir filled with rocks. *J. Mater. Environ. Sci.* **2018**, *9*, 1193–1199. [CrossRef]
18. Gourdo, L.; Fatnassi, H.; Tiskatine, R.; Wifaya, A.; Demrati, H.; Aharoune, A.; Bourirden, L. Solar energy-storing rock-bed to heat an agricultural greenhouse. *Energy* **2018**, *169*, 206–212. [CrossRef]
19. Bazgaou, A.; Fatnassi, H.; Bouhroud, R.; Gourdo, L.; Ezzaeri, K.; Tiskatine, R.; Demrati, H. An experimental study on the effect of a rock-bed heating system on the microclimate and the crop development under Canarian greenhouse. *Sol. Energy* **2018**, *176*, 42–50. [CrossRef]
20. Albright, L.D. Production Solar Greenhouse. *Energy World Agric.* **1991**, *4*, 213–232.
21. Shukla, A.; Tiwari, G.N.; Sodha, M.S. Energy Conservation Potential of Inner Thermal Curtain in an Even Span Greenhouse. *Trends Appl. Sci. Res.* **2006**, *1*, 542–552. [CrossRef]
22. Kumari, N.; Tiwari, G.N.; Sodha, M.S. Thermal Modelling for Greenhouse Heating by Using Packed Bed. *Int. J. Agric. Res.* **2006**, *1*, 373–383. [CrossRef]
23. Rico-Garcia, E.; Lopez-Cruz, I.L.; Herrera-Ruiz, G. Effect of Temperature on Greenhouse Natural Ventilation under Hot Conditions: Computational Fluid Dynamics Simulations. *J. Appl. Sci.* **2008**, *8*, 4543–4551. [CrossRef]
24. Chen, J.; Xu, F.; Tan, D.; Shen, Z.; Zhang, L.; Ai, Q. A control method for agricultural greenhouses heating based on computational fluid dynamics and energy prediction model. *Appl. Energy* **2015**, *141*, 106–118. [CrossRef]
25. Shen, Y.; Wei, R.; Xu, L. Energy consumption prediction of a greenhouse and optimization of daily average temperature. *Energies* **2018**, *11*, 65. [CrossRef]
26. Ahamed, M.S.; Guo, H.; Tanino, K. Development of a thermal model for simulation of supplemental heating requirements in Chinese-style solar greenhouses. *Comput. Electron. Agric.* **2018**, *150*, 235–244. [CrossRef]

27. Tadj, N.; Nahal, M.A.; Draoui, B.; Constantinos, K. CFD simulation of heating greenhouse using a perforated polyethylene ducts. *Int. J. Eng. Syst. Model. Simul.* **2017**, *9*, 3. [CrossRef]
28. Amanowicz, E.; Wojtkowiak, J. Validation of CFD model for simulation of multi-pipe earth-to-air heat exchangers (EAHEs) flow performance. *Therm. Sci. Eng. Prog.* **2017**, *5*, 44–49. [CrossRef]
29. Lekka, T.; Kefalas, P.; Logiakis, M. Energy efficiency analysis in a small greenhouse using computational fluid dynamics. In Proceedings of the 8th International Conference from “Scientific Computing to Computational Engineering” Glyfada, Athens, Greece, 4–7 July 2018.
30. Guo, J.; Liu, Y.; Lü, E. Numerical Simulation of Temperature Decrease in Greenhouses with Summer Water-Sprinkling Roof. *Energies* **2019**, *12*, 2435. [CrossRef]
31. Li, K.; Xue, W.; Mao, H.; Chen, X.; Jiang, H.; Tan, G. Optimizing the 3D Distributed Climate inside Greenhouses Using Multi-Objective Optimization Algorithms and Computer Fluid Dynamics. *Energies* **2019**, *12*, 2873. [CrossRef]
32. Akrami, M.; Javadi, A.A.; Hassanein, M.J.; Farmani, R.; Dibaj, M.; Tabor, G.R.; Negm, A. Study of the Effects of Vent Configuration on Mono-Span Greenhouse Ventilation Using Computational Fluid Dynamics. *Sustainability* **2020**, *12*, 986. [CrossRef]
33. Yilmaz, F.; Selbas, R. Performance assessment of various greenhouse heating systems; a case study in Antalya. *Exergetic Energetic Environ. Dimens.* **2018**, 421–433. [CrossRef]
34. Dhiman, M.; Sethi, V.P.; Singh, B.; Sharma, A. CFD analysis of greenhouse heating using flue gas and hot water heat sink pipe networks. *Comput. Electron. Agric.* **2019**, *163*, 104853. [CrossRef]
35. Reyes-Rosas, A.; Molina-Aiz, F.D.; Valera, D.L.; López, A.; Khamkure, S. Development of a single energy balance model for prediction of temperatures inside a naturally ventilated greenhouse with polypropylene soil mulch. *Comput. Electron. Agric.* **2017**, *142*, 9–28. [CrossRef]
36. Ahamed, M.S.; Guo, H.; Tanino, K. A quasi-steady-state model for predicting the heating requirements of conventional greenhouses in cold regions. *Inf. Process. Agric.* **2018**, *5*, 3–46. [CrossRef]
37. Nisen, A.; Coutisse, S. Modern concept of greenhouse shading. *Plasticulture* **1981**, *49*, 9–26.
38. Nijsskens, J.; Deltour, J.; Coutisse, S.; Nisen, A. Heat transfer through covering materials of greenhouses. *Agric. For. Meteorol.* **1984**, *33*, 193–214. [CrossRef]
39. ASAE. *ASAE D271.2 DEC99 Psychrometric Data*, 1st ed.; American Society of Agricultural Engineers: St. Joseph, MI, USA, 1999; p. 9.
40. Tesi, R. *Medios De Protección Para La Hortoflorofruticultura Y El Viverismo*, 1st ed.; Editorial MundiPrensa: Madrid, Spain, 2001; p. 288.
41. Castilla, N. *Invernaderos De Plástico. Tecnología Y Manejo*, 2nd ed.; Editorial Mundiprensa: Madrid, Spain, 2004; p. 462.
42. Flores-Velázquez, J.; Villarreal-Guerrero, F.; Rojano-Aguilar, A.; Schdmith, U. CFD to analyze energy exchange by convection in a closed greenhouse with a pipe heating system. *Acta Univ.* **2019**, *29*, e2112. [CrossRef]
43. Benli, H. Performance prediction between horizontal and vertical source heat pump systems for greenhouse heating with the use of artificial neural networks. *Heat Mass Transf. Waerme Stoffuebertragung* **2016**, *52*, 1707–1724. [CrossRef]
44. Esen, M.; Yuksel, T. Experimental evaluation of using various renewable energy sources for heating a greenhouse. *Energy Build.* **2013**, *65*, 340–351. [CrossRef]



© 2020 by the authors. Licensee MDPI, Basel, Switzerland. This article is an open access article distributed under the terms and conditions of the Creative Commons Attribution (CC BY) license (<http://creativecommons.org/licenses/by/4.0/>).

Article

# Influence of Soil Particle Size on the Temperature Field and Energy Consumption of Injected Steam Soil Disinfection

Zhenjie Yang <sup>1</sup>, Adnan Abbas <sup>1</sup>, Xiaochan Wang <sup>1,2,\*</sup>, Muhammad Ameen <sup>1</sup>, Haihui Yang <sup>1</sup> and Shakeel Ahmed Soomro <sup>1,3</sup>

<sup>1</sup> College of Engineering, Nanjing Agricultural University, Nanjing 210031, China; 2016212010@njau.edu.cn (Z.Y.); dr\_adnan219@yahoo.com (A.A.); 2016212014@njau.edu.cn (M.A.); 2019212004@njau.edu.cn (H.Y.); ssoomro@sau.edu.pk (S.A.S.)

<sup>2</sup> Jiangsu Province Engineering Laboratory for Modern Facilities Agricultural Technology and Equipment, Nanjing 210031, China

<sup>3</sup> Department of Farm Structures, Sindh Agriculture University, Tandojam 70060, Pakistan

\* Correspondence: wangxiaochan@njau.edu.cn; Tel.: +86-25-58606567

Received: 20 December 2019; Accepted: 17 February 2020; Published: 20 February 2020

**Abstract:** Soil steam disinfection (SSD) technology is an effective means of eliminating soil borne diseases. Among the soil cultivation conditions of facility agriculture in the Yangtze River Delta region of China, the clay soil particles (SPs) are fine, the soil pores are small, and the texture is relatively viscous. When injection disinfection technology is applied in the clay soil, the diffusion of steam is hindered and the heating efficiency is substantially affected. To increase the heating efficiency of SSD, we first discretized the continuum model of Philip and De Vries into circular particle porous media of different sizes and random distribution. Then with Computational Fluid Dynamics (CFD) numerical simulation technology, a single-injection steam disinfection model for different SP size conditions was constructed. Furthermore, the diffusion pattern of the macro-porous vapor flow and matrix flow and the corresponding temperature field were simulated and analyzed. Finally, a single-pipe injection steam disinfection verification test was performed for different SP sizes. The test results show that for the clay soil in the Yangtze River Delta region of China, the test temperature field results are consistent with the simulation results when the heat flow reaches  $H = 20$  cm in the vertical direction, the simulation and test result of the heat flow in the maximum horizontal diffusion distance are  $L = 13$  cm and 12 cm, respectively. At the same disinfection time, the simulated soil temperature change trend is consistent with the test results, and the test temperature is lower than the simulated temperature. The difference between the theoretical temperature and the experimental temperature may be attributed to the heat loss in the experimental device. Further, it is necessary to optimize the CFD simulation process and add the disintegration and deformation processes of soil particle size with the change of water content. Furthermore, the soil pores increase as the SP size increases and that a large amount of steam vertically diffuses along the macropores and accumulates on the soil surface, causing ineffective heat loss. Moreover, soil temperature distribution changes from oval (horizontal short radius/vertical long radius = 0.65) to irregular shape. As the SP size decreases, the soil pore flow path becomes fine; the steam primarily diffuses uniformly around the soil in the form of a matrix flow; the diffusion distance in the horizontal direction gradually increases; and the temperature distribution gradually becomes even, which is consistent with the soil temperature field simulation results. Similar to the energy consumption analysis, the maximum energy consumption for SP sizes  $>27$ mm and  $<2$ mm was 486 and 477 kJ, respectively. Therefore, proper pore growth was conducive to the diffusion of steam, but excessive pores cause steam to overflow, which increased energy consumption of the system. Considering that the test was carried out in an ideal soil environment, the rotary tiller must be increased for fine rotary tillage in an actual disinfection operation. Although large particles may appear during the rotary tillage process, an appropriate number of large particles contributes to the



formation of a large pore flow, under the common effect of matrix flow, it will simultaneously promote greater steam diffusion and heating efficiency. The above theoretical research has practical guiding significance for improving the design and disinfection effect of soil steam sterilizers in the future.

**Keywords:** soil steam disinfection; soil particle size; soil temperature; soil water content; energy consumption

---

## 1. Introduction

Soil borne diseases caused continuous soil cropping problems and affect crop yield and quality. Soil physical disinfection technology is one of the important methods to prevent and control soil-borne diseases [1–4]. As compared to chemical methods, soil physical disinfection methods are clean, efficient, and environment friendly. Soil physical disinfection methods mainly include injected soil steam disinfection (SSD) method, flame disinfection method, solar energy disinfection method, and microwave disinfection method [1–8]. The flame disinfection method can generate a high temperature of 1000 °C in a short time. The high temperature of the flame is then directly sprayed to the ground for disinfection, this avoids the loss of heat during transmission, but does not entirely kill the harmful bacteria in deep soil. At the same time, high temperature eliminates the effective water in the soil and changes the physical properties of the soil. The flame disinfection method can achieve good disinfection effect in sandy soil, but is not appropriate for heavy red, clay and silt soil to heavy red soil, clay soil, and silt soil [1–4]. Furthermore, the solar energy disinfection method is pertinent with the areas having abundant heat resources, it is highly operable and is low in cost, but constrained by external factors such as weather and season [1,2]. The microwave disinfection method has a disadvantage of high operation cost and complicated operations when disinfecting soil [1,2]. The injection SSD method comparatively has a unique “evaporation–condensation” mechanism, which can effectively remove the condensed water blocked in the soil pores, promote the rapid diffusion of steam, and improve the heating efficiency of the soil by steam [6–8]. The injected SSD method can effectively kill harmful bacteria in the deep soil. At the same time, high temperature steam can also humidify the soil to change the pellet structure and restore the pellet activity [6–8]. Earlier the application of soil steam disinfection technology has some problems, like high steam disinfection cost and heavy boiler weight [9], which demoted the wide use of soil steam disinfection technology among the farmers. However, in recent years, the cultivation of high-value-added crops has also encountered problems of continuous cropping, which severely affects its yield and quality, such as *Panax notoginseng* of precious Chinese medicine [10]. Compared with other disinfection methods, the soil steam disinfection method is the most effective and ecological method to overcome the obstacles of continuous cropping of *Panax notoginseng* [10]. Considering this problem and according to the characteristics of greenhouse cultivation of *Panax notoginseng*, Zhu designed a soil steam disinfection machine for *Panax notoginseng* [11]. At the same time, Pan’s optimization and improvement of the soil steam sterilization boiler made the boiler and steam sterilizer smaller and more convenient to move [9]. Therefore, the steam disinfection technology will have more practical development prospects.

Although global experts have done a lot of studies on SSD boilers and machines, and the SSD efficiency has been greatly improved, there is still a need to explore the new methods to improve the disinfection efficiency, and the most essential thing for SSD is that this disinfection technology needs to be adapted to different soil types for disinfection. According to soil scientists, different soils have different contents of clay, silt, and sand. Due to the large sand content, the sandy loam has good gas permeability [12,13]. Clay loam or clay has significant clay contents with fine and small particles, resulting in poor gas permeability [12,13], especially the compacted soil produced after continuous cropping [14,15]. Hence, Gay [6] discovered that when steam is diffused in sandy loam soil, the soil heating rate increases as the soil water content (SWC) increases because sandy loam soil promotes the

diffusion of steam in soil due to its large pores [6,7]. The injected SSD method can reheat and remove condensed water that is blocked in the pores of sandy loam soil to promote the diffusion of steam in the soil [6]. However, most of the soil types of the Yangtze River Delta in China are clay or clay loam due to its high clay content and soil porosity. Small soil pores reduced water permeability and gas permeability [14,15]; removal of the condensed water blocked in the pores is difficult. Therefore, in the case of the injectable disinfection method for soil, the diffusion of steam is hindered, which caused a decrease in the heating efficiency of the soil and an increase in the energy consumption, which affects SSD performance. During the actual cultivation process, the clay produced by the compaction would have aggregates or soil blocks of different sizes, and then form pores of various sizes. Depending on the size of the soil pores, the flow of fluid in the soil can be divided into matrix flow (small pore flow or capillary flow) and large pore flow [16,17], as shown in Figure 1a. When large numbers of large pores exist in soil, fluid rapidly crosses the soil particles (SPs) along the large pore channels to form a large pore flow. In clay or clay loam, which is more viscous, the large pore flow generated by the macropores may help to accelerate the flow of gases and liquids and increase the aeration of the soil relative to the matrix flow [16,17]. Especially in the process of SSD, proper pore growth is beneficial to increase the diffusion speed and range of steam. However, excessive soil pores may cause steam to spread too quickly on the surface of soil and overflow into the atmosphere, which caused ineffective heat loss. Eventually, the interior of the large soil particles or clods cannot be completely heated to the required temperature. Therefore, in the process of steam disinfection, it is necessary to change the compacted large soil clods into small particles to promote the rate and range of soil heating by steam.

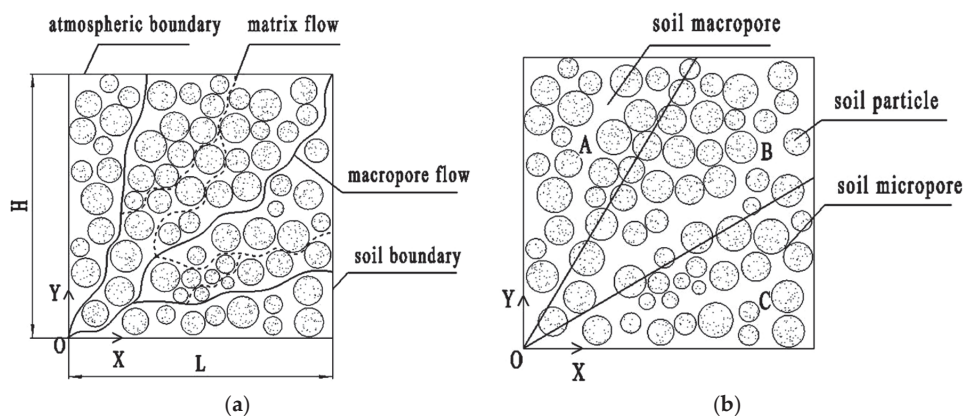


**Figure 1.** Schematic of steam heat transfer in large pores. (a) soil pore diagram; (b) heat transfer zone. Note: Point O is the heat source point of the steam, and L and H represents the horizontal and vertical diffusion distance of the steam heat flow.

When the compacted large soil clods become small soil particles and small clods, the form and direction of the flow during the steam disinfection process will also change. According to previous studies on the flow of liquid water in large pores, it was shown that liquid water mainly used large pores as the diffusion center, and diffused downward in a radial divergence along with small pores. However, for the steam disinfection process, the diffusion and flow direction of steam in large and small pores are uncertain. The areas where steam may diffuse are represented as A, B, and C. Figure 1b depicts the following possible scenarios: if the horizontal velocity is less than the vertical velocity, the steam is concentrated in the A region; if the horizontal velocity is equal to the vertical velocity, the vapor diffusion is concentrated in the B region; and if the horizontal velocity is greater than the vertical velocity speed, the steam is concentrated in the C area.

In order to explore the diffusion direction and range of the steam heat flow under different soil particle size conditions, based on the research by Philip and De Vries, according to the actual soil

particle size and pore width range, the media model is discretized into circular particles of different sizes and randomly distributed porous media. The SP size (<2 mm) after fine soil rotary tillage was used as the control group; and four SP sizes (>27 mm, 17–27 mm, 7–17 mm and 2–7 mm) were set as the test groups. Using CFD numerical simulation technology, a single-pipe injection steam disinfection model under different soil particle sizes was constructed, and the diffusion forms of the large-pore steam flow and matrix flow and the corresponding temperature fields were simulated and analyzed to determine the steam disinfection area. Based on the temperature field simulation, the single-pipe injection type soil steam disinfection test was mainly performed. This paper determined the use of three kinds of steam flow rates under different disinfection durations. The effects of 5 soil particle sizes on soil temperature, water content, and energy consumption were mainly analyzed.

## 2. Theoretical Analysis

### 2.1. Selection of Soil Macropore Model

To facilitate the solution of the soil heat transfer equation, most of the soil models are considered to be continuous homogeneous porous media [18]. However, after actual cultivation, the soil has particle sizes and pores of different sizes. To further explore the variation in the single-injection soil temperature ( $ST$ ) of a field in different SP size conditions, a suitable large pore soil model needs to be selected and determined. Currently, specialists from various countries do not provide a strict definition of large pores in the soil. Beven believes that a preferential flow of large pores exists when the pore width is greater than 0.3 cm [19,20]. Luxmoore and Lamande defined pores with a width greater than 0.1 cm as macropores [21,22], while Singh et al. utilized image processing methods to study soil macropores and set the lower limit width of macropores to 0.16 cm [23]. To determine the range of pore widths that corresponds to SPs and soil block diameters (referred to as SP diameters), first, the compacted soil produced by actual continuous cropping obstacles needs to be smashed by rotary cultivation and the SPs and soil blocks are sieved using a test sieve. According to previous research results [19–23], in this paper, the SP size <2 mm is set as the control group and the soil block particle sizes are divided into four levels (2–7 mm, 7–17 mm, 17–27 mm, and >27 mm) as shown in Figure 2. Each group of soil samples was subjected to five repeated sieving treatments. The collected soil was subjected to an image processing analysis, and the pore widths that corresponded to different particle sizes were counted to determine a large-pore soil model.

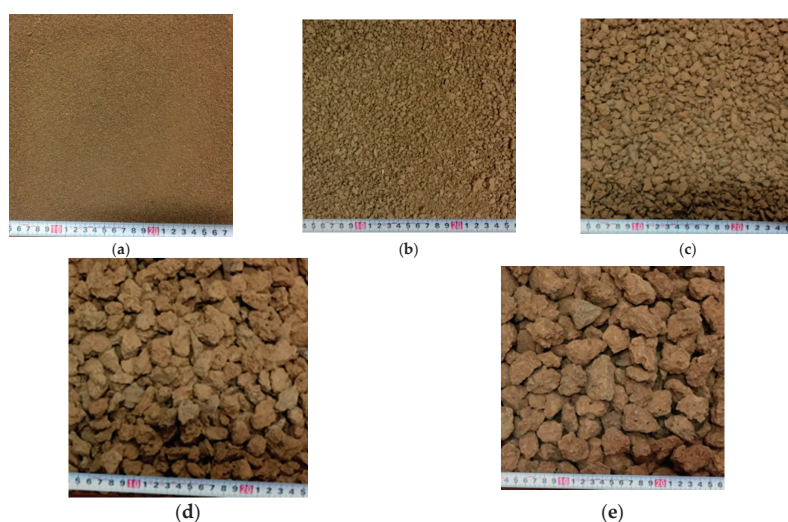


**Figure 2.** Soil pattern. (a) <2 mm; (b) 2–7 mm; (c) 7–17 mm; (d) 17–27 mm; and (e) >27 mm.

This paper uses the set of measurements to analyze particles by Image J software (1.8.0, National Institutes of Health, Bethesda, MD, USA, 2020), obtain and calculate the porosity and pore channel width of the soil layer in the same plane as the steam disinfection pipe (SDP) [24–26]. The morphological characteristics of pores treated with different particle sizes are shown in Table 1 and Figure 3. Some differences exist in the definition of macropores by domestic and foreign experts. According to Singh and Luxmoore et al. [21–23], the width of the pore channel in the particle size section 2–7 mm is between 0.068 and 0.172 cm, and the particle size section is in the transition zone between large pores and small pores. The width of the pore channel in the particle size section 7–17 mm is between 0.13 cm and 0.33 cm, and the particle size section is a large pore area. According to Beven et al.'s definition of the lower limit of soil macropores, pores with a width greater than 0.3 cm are macropores [19,20]. As shown in Table 1, the width of the pore channel in the particle diameter section 17–27 mm is between 0.43 cm and 0.91 cm, and the particle size section is a large pore area. The width of the pore flow channel with a particle size section >27 mm is between 0.46 and 1.56 cm, and the particle size section is in a large pore area.

**Table 1.** Soil porosity and pore width.

SP Diameter/cm	<2 mm	2–7 mm	7–17 mm	17–27 mm	>27 mm
porosity/%	39.02 ± 0.83	40.14 ± 0.56	41.43 ± 1.20	44.02 ± 1.35	47.05 ± 1.52
pore width/cm	0.048 ± 0.024	0.12 ± 0.052	0.23 ± 0.10	0.67 ± 0.24	1.01 ± 0.55

Note: Data are the mean ± standard deviation.

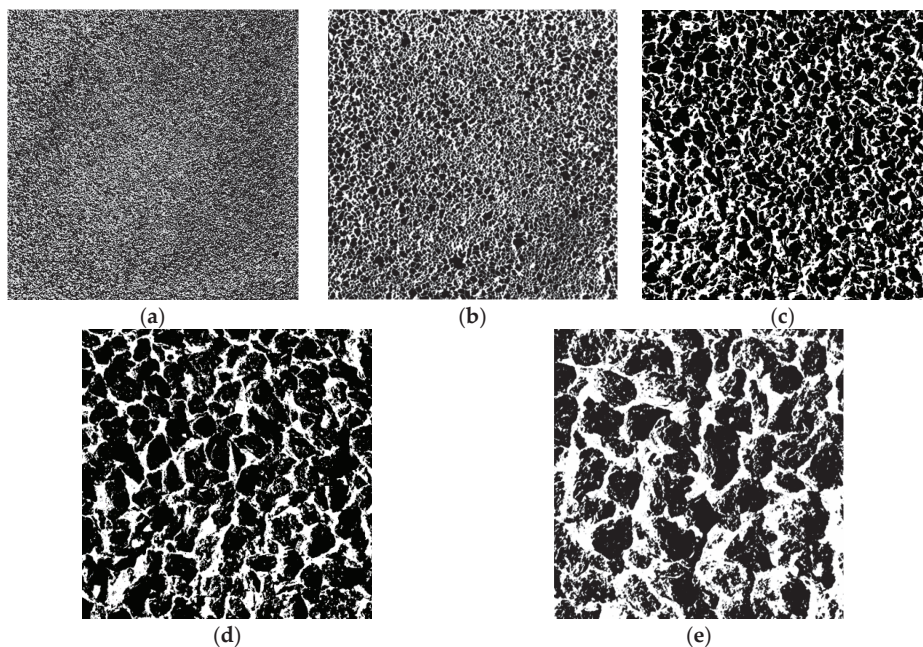


**Figure 3.** Two-dimensional vertical profile of soil pore. (a) <2 mm; (b) 2–7 mm; (c) 7–17 mm; (d) 17–27 mm; and (e) >27 mm. Note: The black parts represent soil particles (SPs) or clods, and the white parts represent pores.

As shown in Table 1 and Figure 3, as the particle size decreases, the soil porosity gradually decreases. However, the number of small pores gradually increases, and the distribution becomes more uniform. With a small particle size and small pores, obtaining a loose and porous soil structure is

beneficial. As the size of the soil clod increases, the width of the soil pore channel gradually increases. Compared with soil with a small particle size and small pores, steam will preferentially flow out of large pores. Although large pores increase the aeration of soil, they also increase the diffusion rate of steam to the soil surface. Excessive soil pores cause steam to diffuse directly to the soil surface, which requires additional steam to heat deep soil during the disinfection process. The steam collected on the soil surface will simultaneously overflow into the air, which causes an ineffective loss of steam heat.

## 2.2. Establishment of a Soil Macropore Model

The shape of the natural SPs extensively varies, and a distinct dividing line among the particles does not exist. In soil science, SPs or soil blocks are generally simplified into spheres. Therefore, in this paper, the homogeneous soil in the study area is separated into equivalent circles of different sizes. The diameter of a circular particle is referred to as the SP diameter, and pore channels of different sizes are formed among particles. A simplified model of discrete soil is established using geometric modeling tools in COMSOL Multiphysics software (5.4, COMSOL Inc, Stockholm, Sweden, 2020). The SDP hole (heat source point) is shown in Figure 4. According to the determination of the soil size and pore width range, particle sizes <2 mm, 2–7 mm, 7–17 mm, 17–27 mm, and >27 mm are randomly generated in a 200 mm × 200 mm square soil area. The atmospheric boundary is set as a thermal insulation layer, and the heat exchange between the soil and outside air can be disregarded, as shown in Figure 4a,c,e,g,i. In this paper, a quadrilateral mesh is created for the model. The number of mesh elements is approximately 280,000, and the number of mesh nodes is approximately 57,000 as shown in Figure 4b,d,f,h,j.

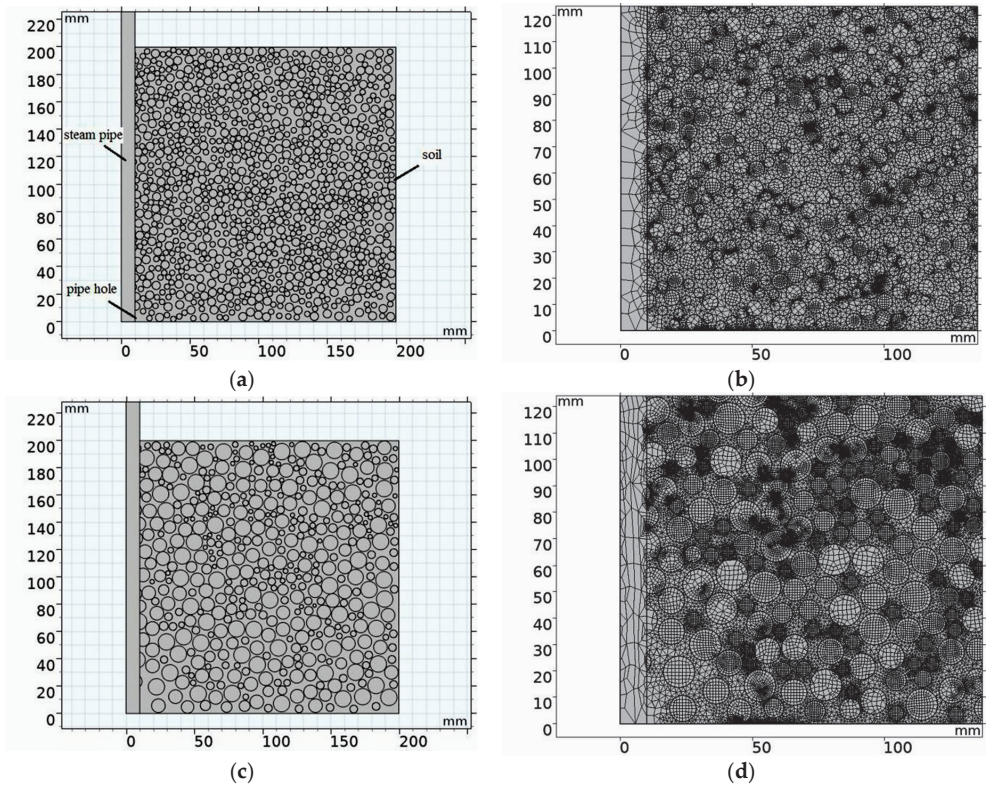
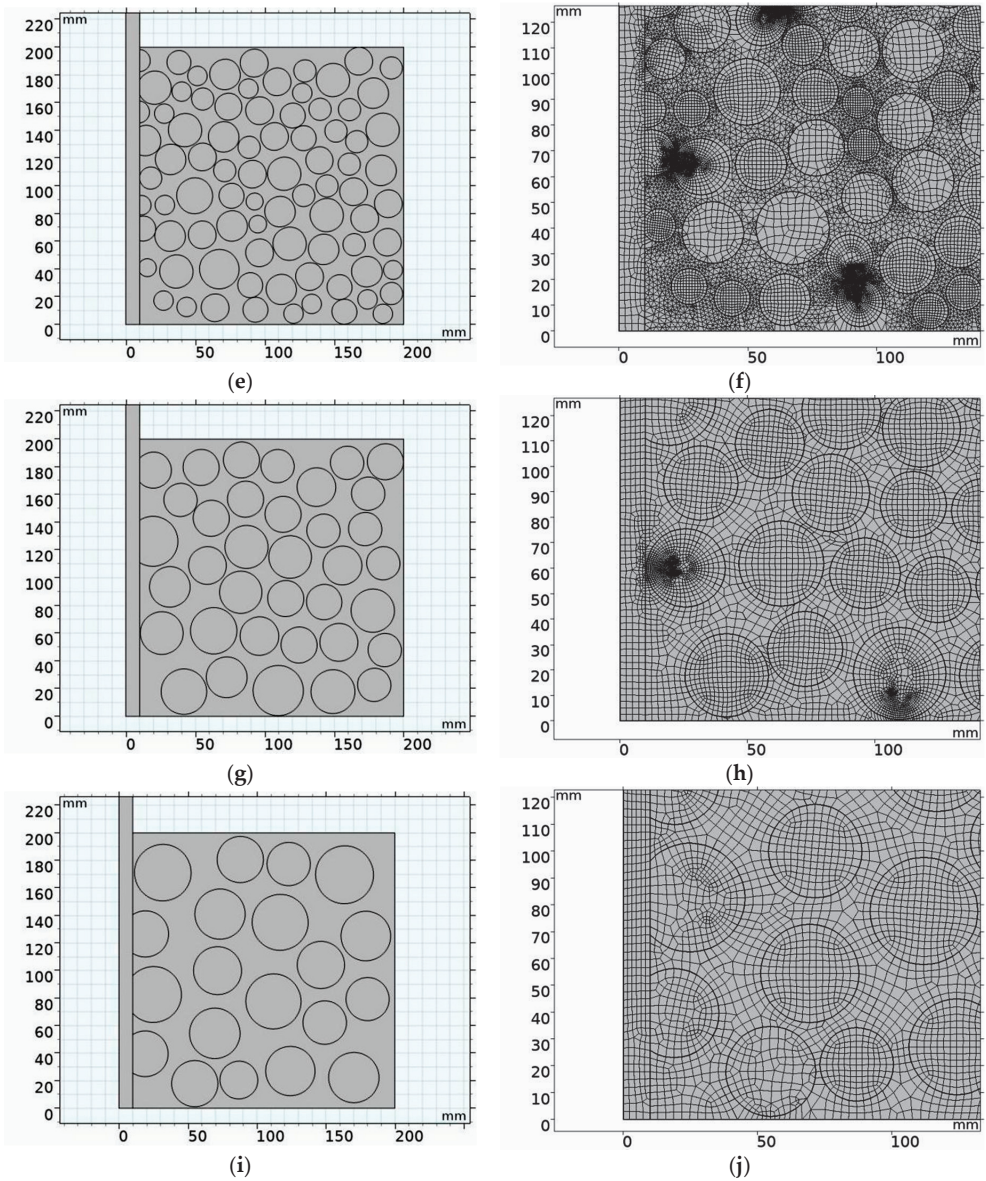


Figure 4. Cont.



**Figure 4.** Steam disinfection model. (a) <2 mm model; (b)<2 mm meshing; (c) 2–7 mm model; (d)2–7 mm meshing; (e) 7–17 mm model; (f) 7–17 mm meshing; (g) 17–27 mm model; (h) 17–27 mm meshing; (i) >27 mm model; and (j) >27 mm meshing. Note: The meshing figures are partially enlarged views.

The heat transfer equation is numerically calculated according to Equations (1) and (2). Refer to Table 2 for the soil physical properties. Due to a large number of disinfected capillary pipes in actual operation, the steam flow rates of single tubes are set to 2, 3, and 4 kg/h. According to previous research, the steam temperature is set to 130 °C; the physical properties of the fluid (air and steam) are shown in Table 3.

**Table 2.** Soil physical parameters.

ST/°C	Soil Bulk Density/(kg/m <sup>3</sup> )	Soil Particle Density/(kg/m <sup>3</sup> )	Specific Heat/(J/(kg·K))	Soil Particle Diameter/mm	Porosity
20	1150	1005	1700	<2 mm	0.39
				2–7 mm	0.41
				7–17 mm	0.42
				17–27 mm	0.45
				>27 mm	0.49

**Table 3.** Fluid parameters.

Air Temperature/°C	Air Density/(kg/m <sup>3</sup> )	Air Specific Heat/(J/(kg·K))	Steam Temperature/°C	Steam Density/(kg/m <sup>3</sup> )	Steam Specific Heat/(J/(kg·K))
20	1.205	1005	130	1.497	2176.3

In this paper, the  $ST$  field is numerically simulated using the heat transfer equation of porous media proposed by De Vries [27]. The expression is as follows:

$$(\rho C_p)_{eff} \frac{\partial T}{\partial t} + \rho C_p \cdot u \cdot \nabla T + \nabla \cdot q = Q \quad (1)$$

$$(\rho C_p)_{eff} = \theta_p \rho_p C_{\rho,p} + (1 - \theta_p) \rho C_p \quad (2)$$

where  $\rho_p$  is the soil bulk density, kg/m<sup>3</sup>;  $C_{\rho,p}$  is the soil specific heat capacity, J/(kg·K);  $C_p$  is the fluid heat capacity at constant pressure, J/(kg·K);  $T$  is the absolute temperature, K;  $u$  is the velocity, m/s;  $q$  is the conducted heat flux (W/m<sup>2</sup>);  $Q$  is the additional heat source (W/m<sup>3</sup>);  $(\rho C_p)_{eff}$  is the effective volumetric heat capacity at constant pressure defined by an averaging model to account for both the solid matrix and the fluid properties, J/(m<sup>3</sup>·K); and  $1 - \theta_p$  is the porosity.

### 2.3. Analysis of Simulation Results

Based on the analysis of the homogeneous soil temperature field in the previous section, the effect of steam temperature on the soil heating rate is small and the effect of steam flow on the soil heating rate is large. Table 4 shows that under the same steam temperature condition, as the steam flow rate increases, the disinfection time used when the steam heat flux reaches the soil surface layer (SS treatment) and when the steam is completely filled with soil (SA treatment) gradually decreases.

**Table 4.** Soil steam disinfection (SSD)time.

Type	Steam Temperature/°C	Steam Flow/(kg/h)	Disinfection Time s
SS treatment	130	2	300
	130	3	220
	130	4	165
SA treatment	130	2	460
	130	3	310
	130	4	230

Note: SS treatment means that the steam just reaches the surface of the soil, and SA treatment means that the steam is completely filled with soil.

This article primarily analyzes the single-SDP injection temperature field, treated with a steam flow of 2 kg/h. As shown in Figure 5a–d, the treatments with particle sizes <2 mm and 2–7 mm are consistent with the shape of the temperature distribution of the homogeneous soil and the range of high temperature (above 80 °C). For disinfection for 300 s, the high-temperature area was distributed

in the middle and lower layers in a 1/4 ellipse. When the diffusion range of the steam heat flow in the vertical direction was  $H = 0\text{--}20$  cm, the diffusion distance in the horizontal direction was  $L = 13$  cm. At the end of the disinfection, the high-temperature area gradually became rectangular, and the surface soil appeared “overheated”. As shown in Figure 5e, during the 300 s disinfection, the high-temperature area with a particle size of 7–17 mm is irregularly distributed in the upper and middle layers of the soil, which differs from the distribution of the high-temperature area with a particle size of <2 mm and 2–7 mm. When Singh and Luxmoore et al. investigated the soil macropores [21–23], all soil pores with a particle size segment <2 mm were small pores, the particle size segment of 2–7 mm was in the transition region between large and small pores, and the particle size segment of 7–17 mm was in the large pore area. Although the particle size section 2–7 mm is in the transition zone between large pores and small pores, as shown in Figure 5a–c, the steam heat flow treated with particle sizes <2 mm and 2–7 mm is uniform in the form of the matrix flow in the horizontal and vertical directions in the soil. The shape and distribution range of the two groups of particle diameters in the high-temperature area are equivalent, while the steam heat flow with particle diameters of 7 to 17 mm primarily diffuses to the soil surface in the form of large pore flows in the vertical direction (Figure 5e).

As shown in Figure 5e,g,i, in the large-pore treatment group with particle sizes of 7–17 mm, 17–27 mm, and >27 mm, larger soil block pores correspond to more irregular heat diffusion of steam, and a higher temperature also corresponds to more irregular heat diffusion of steam. The regular shape is concentrated in the soil pores, and the steam quickly diffuses around the soil large particles to the surface in the form of large pore flows in the vertical direction. When disinfecting for 300s, the diffusion range of the steam heat flow in the vertical direction was  $H = 0\text{--}20$  cm, and the diffusion distance in the horizontal direction was  $L = 10\text{--}13$  cm. Comparing the particle diameters <2 mm and >27 mm, the steam with a particle size of less than 2 mm evenly diffuses around the soil in the form of a matrix flow of small pores, while the steam with a particle size of >27 mm forms a large pore flow. In diffusion to the soil surface, the diffusion rate of the steam heat flow in the vertical direction gradually increases. For example, with a disinfection time of 300 s, the vertical distances in the high-temperature region with a particle size of <2 mm and a particle size of >27 mm are 140 mm and 190 mm, respectively.

Considering that the lethal temperature of the harmful bacteria is 80 °C [6], as shown in Figure 5 with the same disinfection time, the larger the particle size is, the smaller the distribution range of the high-temperature soil area, that is, the smaller the scope of the disinfection area. For example, the soil disinfection area with a particle size >27 mm is the smallest. In the treatment with a particle size >27 mm, the soil pores are the largest, and the steam is primarily diffused to the surface of the soil in the form of a large pore flow. Therefore, with the limited disinfection time (460 s), the temperature inside the soil block is significantly lower than the temperature of the steam in the pores. As the soil clod decreases, the internal temperature of the soil clod gradually approaches the pore temperature. At the end of the disinfection, the heat flow diffusion distance in the horizontal direction of each treatment is less than  $L = 15$  cm.



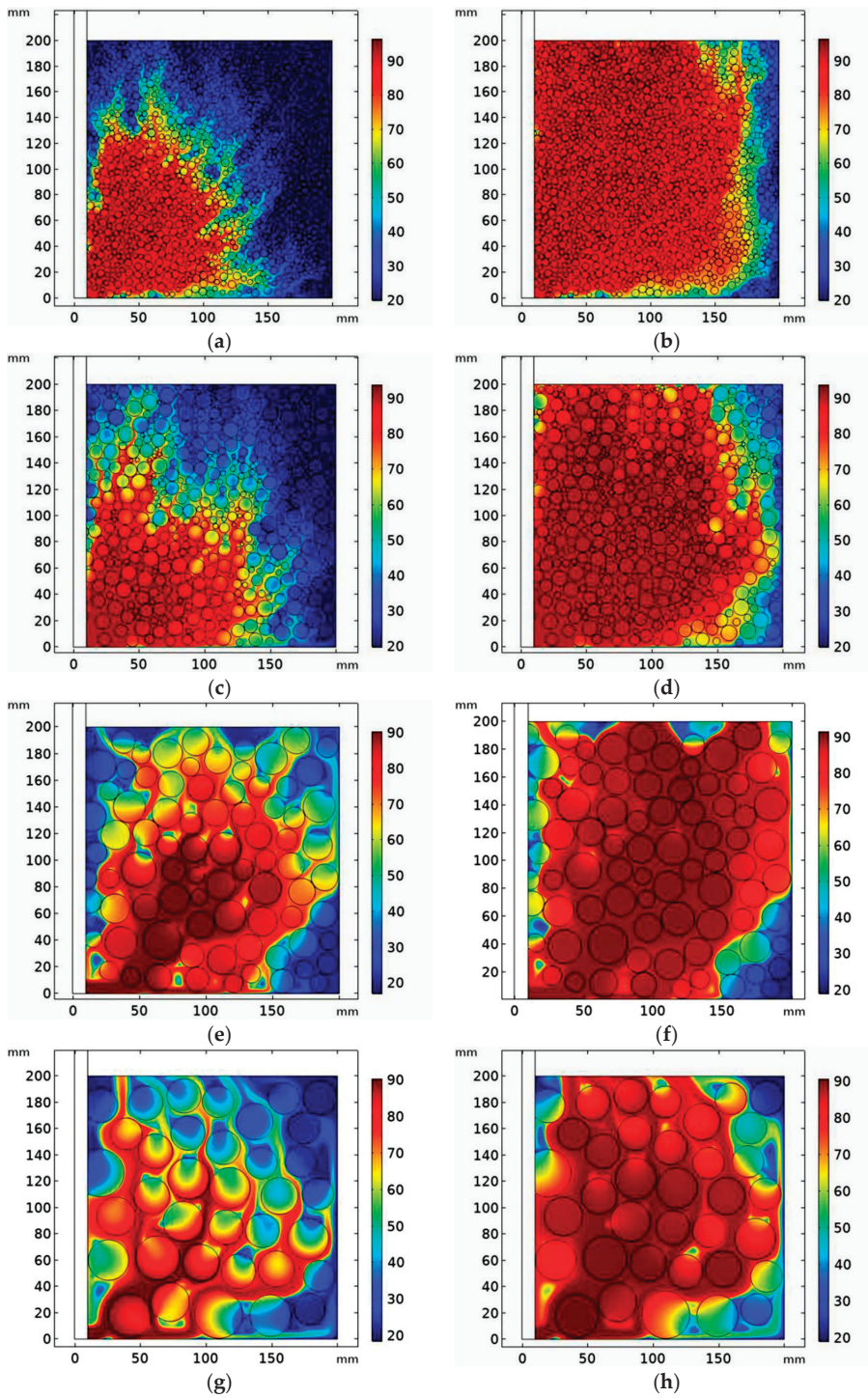
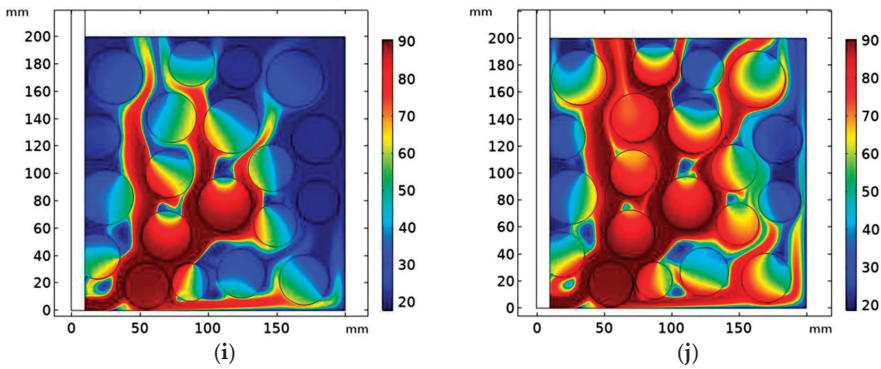
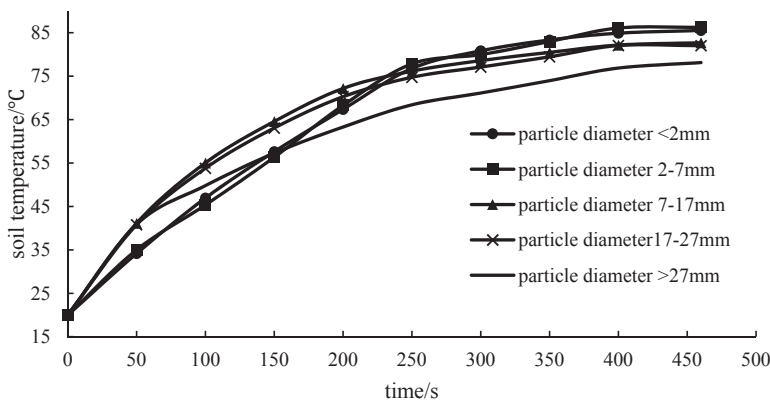


Figure 5. Cont.



**Figure 5.** Soil temperature simulation results: (a) <2 mm, t = 300 s; (b) <2 mm, t = 460s; (c) 2–7 mm model; (d) 2–7 mm meshing; (e) 7–17 mm model; (f) 7–17 mm meshing; (g) 17–27 mm model; (h) 17–27 mm meshing; (i) >27 mm model; and (j) >27 mm meshing. Note: The legend indicates the ST/°C.

The average temperatures of the soil with different particle sizes and times of disinfection are shown in Figure 6. At the beginning of disinfection, the temperature increase rate of the particle sizes of 7–17 mm, 17–27 mm, and >27 mm is faster than that of the particle sizes of <2 mm and 2–7 mm. Because the pores are large, the steam quickly spreads to the various layers of the soil, and results in a higher heating rate. With the progress of disinfection, the heating rate of the particle diameters 7–17 mm, 17–27 mm, and >27 mm is gradually lower than that of the particle sizes for the 2–7 mm and <2 mm treatments. When disinfected for 400 s, the temperature of the particle sizes 2–7 mm and <2 mm exceeds 86 °C; the temperature of the particle sizes 7–17 mm and 17–27 mm can exceed 82 °C, and the minimum temperature of the particle diameter >27 mm is only 78 °C. A larger particle size corresponds to larger pores. Part of the steam heat is concentrated in the pores, and the temperature of the soil block is low. Part of the steam will quickly diffuse along with the large pores to the surface of the soil, which causes an ineffective loss of heat. As a result, the soil temperature is generally low. As shown in the analysis of the soil temperature map in Figure 6, the change in the heating curve of the particle diameters of <2 mm and 2–7 mm is almost constant. The temperature of the particle diameter of 7–17 mm is slightly higher than that of the particle diameter of 17–27 mm.



**Figure 6.** Temperature variation of different soil particle sizes.

According to the analysis of the pore section, with the treatment of the small pore section and the large pore transition section with a particle diameter of <2 mm and 2–7 mm, that is, the treatment of pores less than 0.1 cm in diameter, the temperature field exhibits similar changes. The temperature is 80 °C, disinfection time is 300 s, the temperature of the SP diameters of <2 mm and 2–7 mm can exceed 80 °C, and the range of the effective soil disinfection area is the largest. Due to the different definitions of pores, the particle sizes of 7–17 mm, 17–27 mm, and >27 mm belong to the macropore section. However, the soil temperature rise curve, the particle size >27 mm treatment and the particle size of 7–17 mm reveal a large difference in the change in the temperature rise of the 17–27 mm treatment. The temperature of the particle diameter >27 mm treatment is lower than that of other particle diameter treatments. The pores of the particle diameter >27 mm treatment are excessive—between 0.46 and 1.56 cm. A large amount of steam is unable to collect below the surface of the soil, and heat is lost from the soil surface to the air along with the large pores. For disinfection time =350 s, the temperature of the soil treated with particle sizes of 7–17 mm and 17–27 mm can reach 80 °C, which satisfies the lethal temperature of harmful bacteria [6]. At the end of the disinfection (460s), the temperature of the soil treated with particle size >27 mm is always lower than 80 °C and does not satisfy the lethal temperature of harmful bacteria [6], and the area of effective soil disinfection is the smallest.

### 3. Soil Steam Disinfection Test

#### 3.1. Test Conditions and Materials

One SDP was tested, and it had a length of 300 mm, a diameter of 10 mm, and a wall thickness of 2 mm. One end of the SDP was the inlet end, and the other end was the closed end. Three holes (aperture = 3 mm) were uniformly distributed at a distance of 10 mm from the closed end, and the circumferential direction of the holes was 120°.

The test soil was obtained from the test base of the Yanhai Tractor Factory. The basic properties of the soil are shown in Table 5.

**Table 5.** Physical properties of soil.

Soil Types	Soil Particle Compositions/%		
	Clay (<0.002 mm)	Silt (≥0.002–0.02 mm)	Sand (≥0.02–2 mm)
Clay	53.3%	23.3%	23.3%

The SSD test bench is shown in Figure 7, and the test components and manufacturers are shown in Table 6.

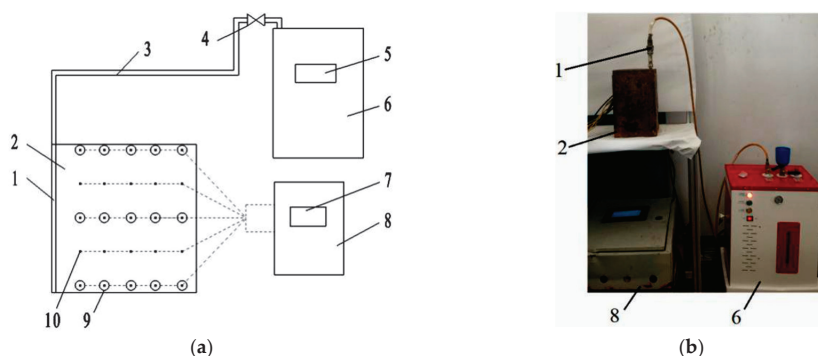


**Figure 7.** Soil steam disinfection (SSD) test bench: 1. steam disinfection pipe; 2. soil trough; 3. steam transport pipe; 4. ball valve switch; 5. boiler pressure controller; 6. boiler; 7. control box screen; 8. soil temperature, water content control box; 9. Soil water content sensor; 10. Soil temperature sensor. (a) components of the SSD test bench; (b) SSD test.

**Table 6.** Test components and manufacturers.

Test Components	Manufacturer
JHD steam generator	Shangrao Jiangxin Boiler Co., Ltd., Shangrao, China
LYK-10 boiler pressure controller	Changzhou Liping Electronic Equipment Co., Ltd., Changzhou, China
Y60 pressure gauge	Hongsheng Instrument Factory Co., Ltd., Fuyang, China
Q911F flow valve	Nanjing Meiyue Valve Co., Ltd., Nanjing, China
LUGB-20 flow meter	Nanjing Lantewan Electronic Technology Co., Ltd., Nanjing, China
ST-SWC control box	/
Steam disinfection pipe	/
Soil bin (20 cm × 20 cm × 30 cm)	/
soil temperature sensor	Jinan Zhengmiao Automation Equipment Co., Ltd., Jinan, China
soil water content sensor	Jinan Zhengmiao Automation Equipment Co., Ltd., Jinan, China

### 3.2. Test Methods

According to the simulation and previous research results [6,13,15], the hardened soil was mashed and then the SP sizes were divided into 6 grades by using sieves of >27 mm, 17–27 mm, 7–17 mm, 2–7 mm, and <2 mm; and then the soil was loaded into the same volume of a test soil bin for the SSD test.

The initial soil temperature was  $(20.1 \pm 2)^\circ\text{C}$ , and the water content was  $(18 \pm 2)\%$ . The temperature sensor selected for the test was a thermocouple soil temperature sensor with a measurement range of 0–200 °C. The soil water content sensor was based on the principle of frequency domain reflection, and the measurement range was 0–100%. According to previous research by Gay [6], the location of the soil temperature sensor and soil water content sensor was shown in Figure 8 and soil temperature and water content control system collected test data every 10s. The following steps were implemented: the residual condensate in the SDP was drained before the test; the boiler pressure was adjusted to 0.3 MPa; the saturated dry steam temperature was increased to 132.88 °C; the flow valve opening through the flow meter was calibrated; and the steam flow was calibrated to 2, 3, and 4 kg/h. The SDP was inserted into test areas (depth = −20 cm) for different particle diameters [6,7], and the surface of the soil bin was sealed with an iron cover to prevent steam overflow. According to the theoretical and simulation calculations, the disinfection times of the flow rates of 2, 3, and 4 kg/h are set to 360, 240, and 180 s, respectively. The disinfection test ends with the statistics of the total amount of steam that flows through the flow meter  $Q_s$ . Each group of experiments was repeated 3 times for a total of 45 groups.

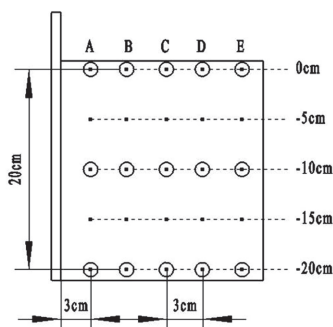


**Figure 8.** ST-SWC test layout. Note: The large circle represents the soil water content(SWC) sensor position, and the small circles represent the soil temperature (ST) sensor position.

### 3.3. Data Analysis

The  $ST$  rise rate is an important indicator used to measure the change in temperature. The rate is expressed as follows:

$$v_T = \frac{T_t - T_{t-1}}{\Delta t} \quad (3)$$

where  $V_T$  is the  $ST$  rise rate,  $^{\circ}\text{C}/\text{s}$ ;  $T_{t-1}$  is the  $ST$  at  $t - 1$ ,  $^{\circ}\text{C}$ ; and  $\Delta t$  is the time interval between  $t$  and  $t - 1$ , s.

The  $ST$  coefficient of variation ( $Cv$ ) can reflect the uniformity of the  $ST$  distribution. The smaller the temperature coefficient of variation is, the better the uniformity of the  $ST$  distribution. The  $Cv$  calculation formula is as follows:

$$Cv = \frac{SD}{\bar{X}} \quad (4)$$

where  $SD$  is the standard deviation of  $ST$ ,  $^{\circ}\text{C}$ , and  $\bar{X}$  is the average  $ST$ ,  $^{\circ}\text{C}$ .

The energy consumption can reflect the degree of utilization of steam heat by the disinfection system. The calculation formula is as follows:

$$W_s = Q_s \cdot H \quad (5)$$

where  $Q_s$  is the cumulative amount of steam, kg;  $H$  is the enthalpy change in steam to liquid water, kJ/kg.

The vertical profiles of  $ST$  and  $SWC$  were plotted using Surfer 12 software (Golden Software, Inc.). The distributions of  $ST$  and  $SWC$  were obtained from the vertical profiles. The area that corresponds to the  $ST$ s below  $60^{\circ}\text{C}$  is the low- $ST$  area; the area that corresponds to the  $ST$ s of  $60\text{--}80^{\circ}\text{C}$  is the moderate- $ST$  area, and the area that corresponds to  $ST$ s  $>80^{\circ}\text{C}$  is the high- $ST$  area. In the figures, red represents the high- $ST$  area; green and yellow represent the moderate- $ST$  area, and blue and black represent the low- $ST$  area. The area that corresponds to  $SWC$ s below 25% is the low- $SWC$  area;  $SWC$ s of 25–30% correspond to the moderate- $SWC$  area; and  $SWC$ s  $>30\%$  correspond to the high- $SWC$  area. In the figures, red represents the high- $SWC$  area; green and yellow represent the moderate- $SWC$  area, and blue and black represent the low- $SWC$  area.

## 4. Results and Analysis

### 4.1. Analysis of the Change in Soil Temperature

The change in the soil average temperature and disinfection time is shown in Figure 9. The temperature of soil heating is gradually accelerated in the initial stage of disinfection because the temperature difference between steam and soil is large at the initial stage of disinfection and the heat transfer is sufficient. In the later stage of disinfection, the soil temperature field tends to be stable. As

indicated by the simulation analysis, the variation law of the temperature rise curve with the particle diameters of <2 mm and 2–7 mm is the same.

Given the same particle size condition, with an increase in the steam flow rate, the soil heating curve shifts to the left; the slope of the curve gradually increases; the temperature of the soil heating increases; and the time required for the soil to heat to the same temperature decreases. Similar to soil remediation techniques, increasing the aeration flow can increase the efficiency of contaminant removal and shorten the soil remediation time. For the same flow rate, with a decrease in the SP size, the largest value of the soil average temperature gradually increases and the temperature for the treatment of <2 mm particles can exceed 80 °C.

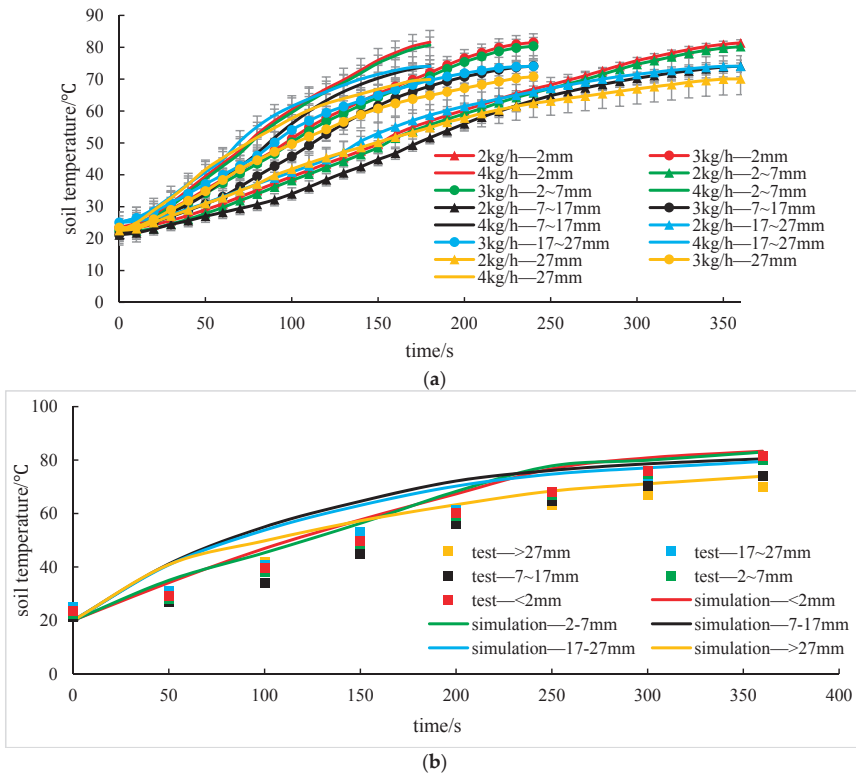


**Figure 9.** Mean ST with time. (a) Soil temperature-time change under different flow and particle size test conditions; (b) Soil temperature-time simulation and experimental comparison of different particle size conditions at a flow rate of 2kg/h. Note: 2 kg/h-2 mm means that the steam flow of the treatment group is 2 kg/h, and the particle size of the soil is <2 mm. The same conditions apply in the following section.

Comparing the results of Figure 9b with the simulated and test temperature, it can be seen that the trend of the soil temperature rise curve is basically the same. At the same disinfection time, the test temperature is lower than the simulated temperature. For example, the theoretical simulation and actual soil temperature of disinfection for 360s, particle size <2mm, flow rate 2kg/h are 85.3 °C and 81.4 °C, respectively, and the test temperature is slightly lower than the theoretical simulation temperature. The difference between the theoretical temperature and the experimental temperature may be attributed to the heat loss in the experimental device.

As shown in Figure 10, the average temperature rise rate and time curve of the soil show a parabolic change, and the slope of the curve before the peak is larger than the slope of the curve

after the peak; that is, the curve rapidly rises to the peak and then gradually decreases and reaches a stable value. At the same flow rate, the peak temperature rise rate in the 27 mm diameter treatment corresponds to a considerably shorter disinfection time than other treatments, because a large particle size corresponds to a large pore width, and the steam quickly fills the entire flow path. Thus, the soil heating rate is faster. However, as the disinfection time is extended, the soil temperature field gradually stabilizes. At the same spacing, the larger is the steam flow rate, the higher is the starting point of the curve, and the higher the peak temperature of the soil heating rate, which is consistent with the trend of the average soil temperature and disinfection time.

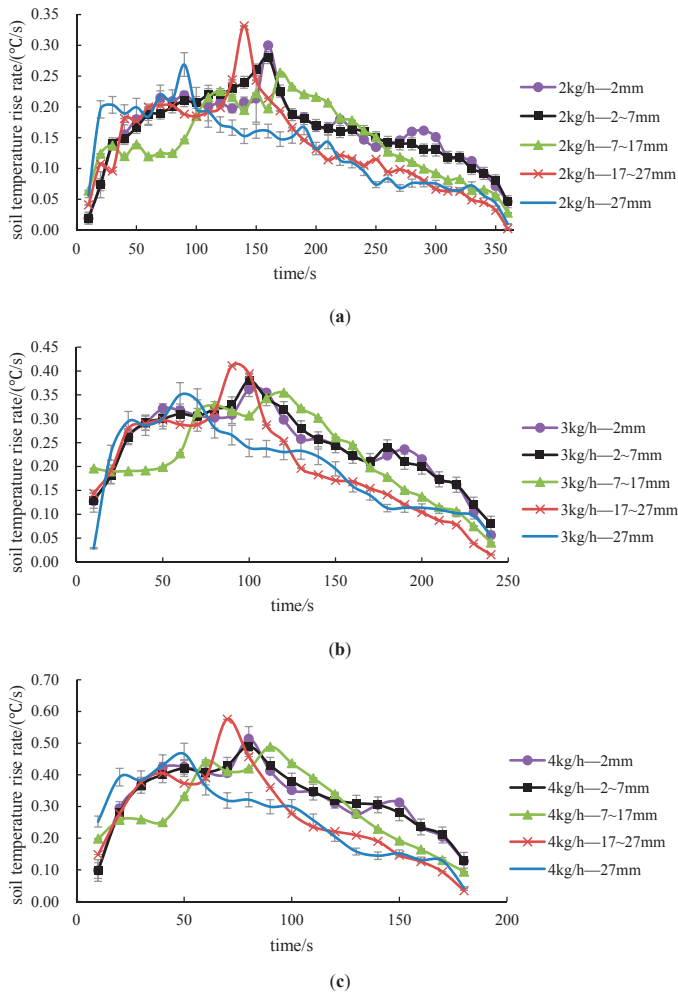
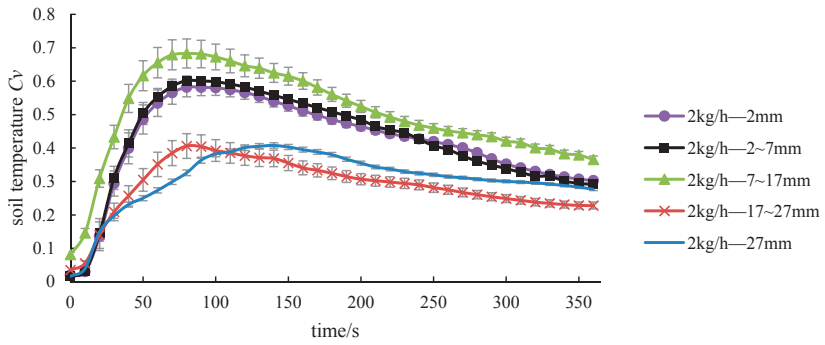


**Figure 10.** Variation in mean *ST* rise rate and disinfection time. (a) 2 kg/h; (b) 3 kg/h; and (c) 4 kg/h.

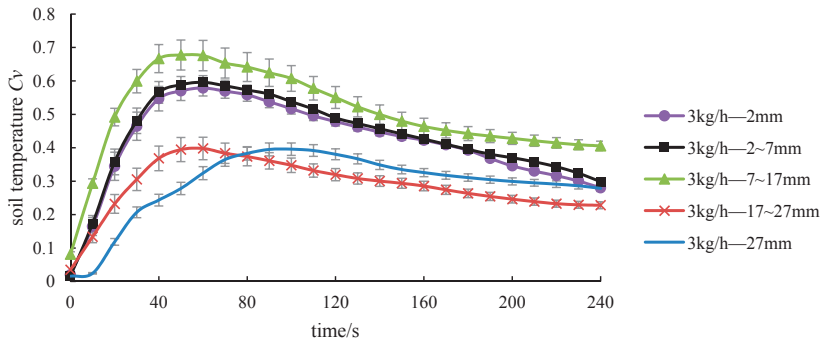
4.2. Soil Temperature Distribution Analysis

As shown in Figure 11, the soil temperature coefficient of variation and the time curve show a parabola change, and the slope of the peak front curve is larger than the slope of the peak curve. The soil temperature at the pipe hole is too high due to the initial stage of disinfection. The total temperature difference is large, and the temperature distribution is not uniform. The soil temperature field tends to be stable in the late stage of disinfection, the temperature difference is gradually reduced,

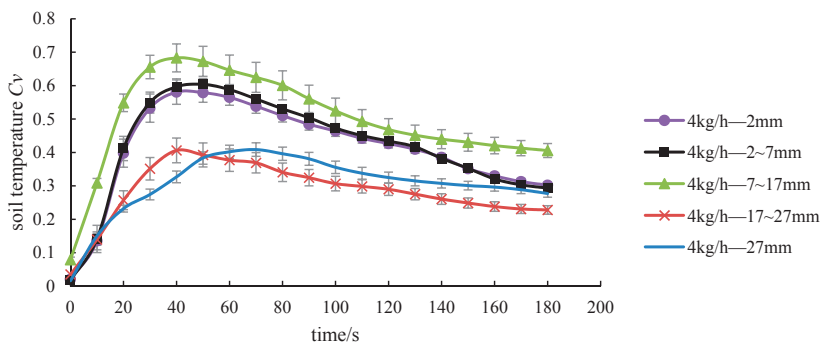
and the temperature distribution is uniform compared with the early of disinfection period. Similar to the analysis of the simulated temperature field, the magnitudes of temperature change with the particle diameters of <2 mm and 2–7 mm are the same.



(a)



(b)



(c)

**Figure 11.** Variation in the mean *ST* variation coefficient with disinfection time. (a) 2 kg/h; (b) 3 kg/h; and; (c)4kg/h.

At the same flow rate, the temperature variation ranges of particles with diameters of 2 mm and 2–7 mm is basically consistent and the curves for particle with sizes >27 and 17–27 mm were lower

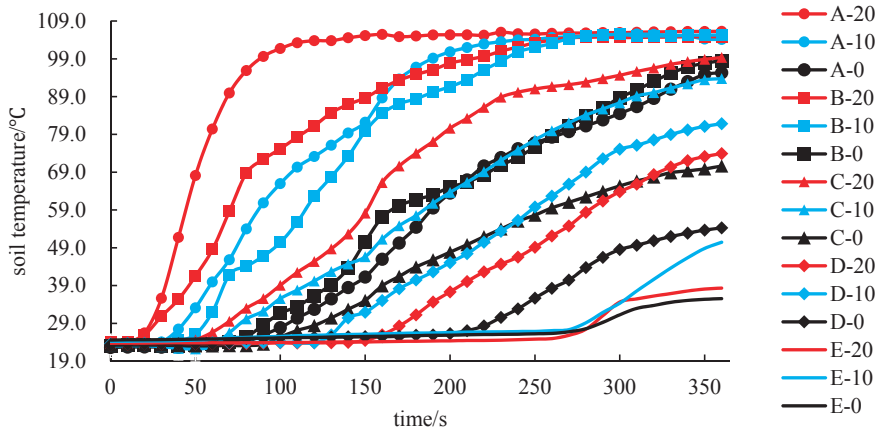


than those for the particle with sizes of 7–17, 2–7 and <2 mm. However, as the disinfection progressed, the curve with a particle size of <2 mm gradually decreased and approached that of the particles with sizes of >27 and 17–27 mm, which was based on an analysis of the rate of temperature increase. When the particle size of the soil is large, the steam quickly fills the soil; thus, the soil temperature distribution is relatively uniform. When the small particle size soil has small pores, the steam slowly spreads around the soil in the initial stage of disinfection. However, with the progress of disinfection, the temperature distribution gradually becomes uniform. For the same particle size conditions, the soil temperature coefficient of variation curves for different flow rates were the same, which indicated that the soil temperature changes of the same particle size treatment were the same for different flow rates.

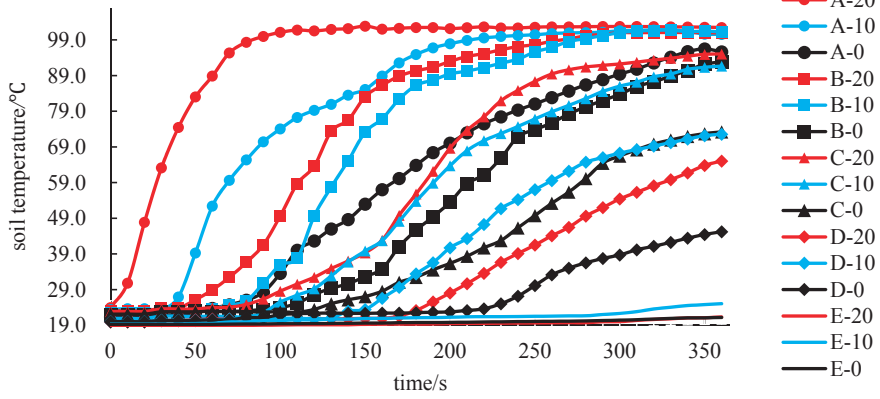
Due to the different flow rates, the soil temperature distribution of the same particle size is the same and the temperature distribution of the particles with sizes of <2 mm and 2–7 mm is basically the same. Therefore, this chapter primarily analyzes the soil layer temperature for the condition of the flow rate of 2 kg/h and particle size treatments of < 2 mm, 7–17 mm, 17–27 mm, and >27 mm.

As shown in Figure 12a,b, the temperature rise curves for the particle sizes <2 and 2–7 mm are similar. The deeper temperature rise rate of the soil is higher than that of the soil surface. The maximum deep temperature of the soil is 105 °C, and the maximum surface temperature is 99 °C, which indicates that the deep layer of the soil is directly heated by high-temperature steam. Further, this finding indicates that the heat transfer method is primarily thermal convection, which is the same as that obtained by Gay in the gas phase [6]. As shown in Figure 12a,b, the temperature of the soil heating at point E is lower than that of other test points at the end of the disinfection, and the temperature is only  $40 \pm 10$  °C, while the temperature of each layer of soil at test points A–C can exceed 70 °C. This finding indicates that the steam level is heated from 0 to 9 cm when the steam is heated to the soil surface (0 cm).

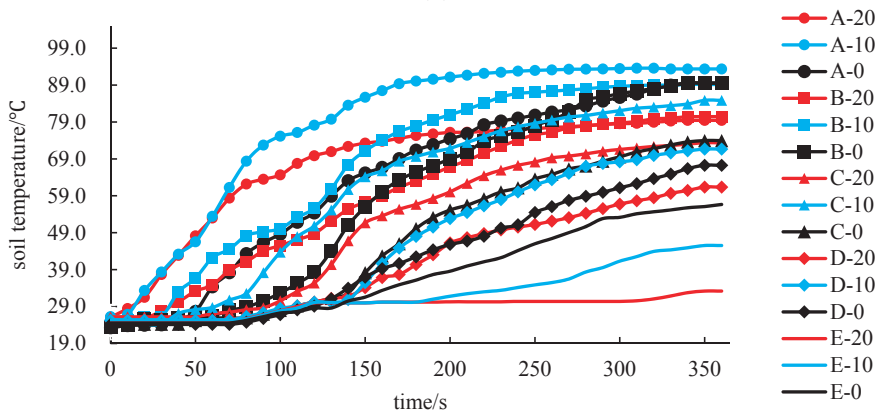
Comparing Figure 12a–d reveal that the temperature rise in the middle and surface layers of the soil is higher than that in deep soil, and the maximum surface temperature of the soil is 90 °C, which indicates that in the large pore flow, the steam directly passes over the soil and the heat transfer method is primarily heat convection. Since the steam heat is concentrated on the surface of the soil to form a superheated area, the temperature of the deep soil will decelerate [6]. As shown in Figure 12c,d, the soil temperature at each test point is sequentially increased, and the soil heating rate at point E at the end of disinfection is lower than that for other test points. This finding indicates that steam can rapidly diffuse around the soil in large pores but the horizontal diffusion range is less than 15 cm.



(a)



(b)



(c)

Figure 12. Cont.

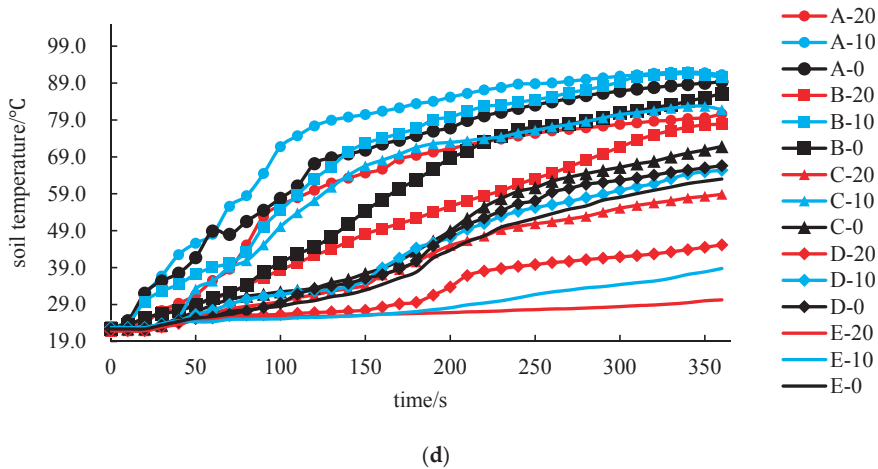


**Figure 12.** Variation diagram of  $ST$  and disinfection time in each layer: (a)  $<2$  mm; (b) 7–17 mm; (c) 17–27 mm; (d)  $>27$  mm. Note: A-20 indicates that A is the test point, and 20 is the test depth ( $-20$ cm). The same conditions apply in the following section.

As shown in soil temperature distribution profile in Figure 13, the particle sizes are 2 and 7–17 mm. At the beginning of the disinfection, the high-temperature region in the soil is  $1/4$  elliptical (horizontal short radius: vertical long radius = 0.63) and is concentrated in the soil. In the deep layer ( $-20$  cm), the soil temperature distribution is uneven; as the disinfection progresses, the steam gradually spreads around the soil, the surface temperature gradually increases, and the soil temperature distribution uniformity is improved. When disinfected for 300 s to 360 s, the soil high-temperature area changes from oval to rectangular distribution that is concentrated in the horizontal direction ( $L$ ) of 0–12 cm and the vertical direction ( $H$ ) of 0–20 cm. For the particle sizes are 17–27 and  $>27$  mm, at the beginning of the disinfection, the high-temperature region in the soil is  $1/2$  elliptical (horizontal short radius: vertical long diameter = 0.41) and primarily distributed in the upper layer of soil ( $-5$ – $14$  cm). When disinfected for 300 s to 360 s, the high-temperature zone of the soil is  $1/4$  elliptical and concentrated in the horizontal direction of  $L = 0$ – $10$  cm and vertical direction of  $H = 0$ – $20$  cm, and the deep layer of the soil is located in the middle and low temperature zone (below  $80$  °C). The thermal range of single-SDP steam is concentrated in the horizontal  $L = 9$ – $12$  cm and vertical  $H = 0$ – $20$  cm, which is consistent with the simulation results.

For the same disinfection time, as the soil pores increase, the high-temperature region gradually migrates to the soil surface. The smaller the particle size of the soil is, the greater the thermal interaction distance of the steam in the horizontal direction. For example, the particle size is 2 mm, and the maximum steam horizontal heat action distance is 12 cm. A larger SP size corresponds to a larger thermal interaction distance of the steam in the vertical direction. For example, when the particle size is  $>27$  mm and the disinfection time is 240 s, the surface layer of the soil gradually appears in the high-temperature region (above  $80$  °C). Therefore, the larger the particle size is, the larger the soil pores, and the steam can be unobstructed along with the large pores. The steam spreads to the surface layer of the soil and accumulates on the surface of the soil to form a high-temperature area, which is consistent with the simulation results.

As shown in Figure 13, when the soil is disinfected for 240 s, the surface temperature that corresponds to the particle size of 2 mm does not exceed  $80$  °C and is primarily located in the middle and low temperature areas. When the soil is disinfected for 300 s, the surface layer of each treated soil begins to appear in the high-temperature area, such that a superficial area is formed in the surface layer of the soil. Due to the late stage of disinfection, the steam of each treatment primarily diffuses

in the vertical direction and accumulates on the surface layer of the soil. Most of the heat begins to accumulate on the surface of the soil, and a small amount of heat may be lost to the air, which is an ineffective loss of heat. At the end of the disinfection, the surface temperature of the soil with the particle sizes >27 and 17–27 mm is lower than that with the particle sizes 7–17 and 2 mm.

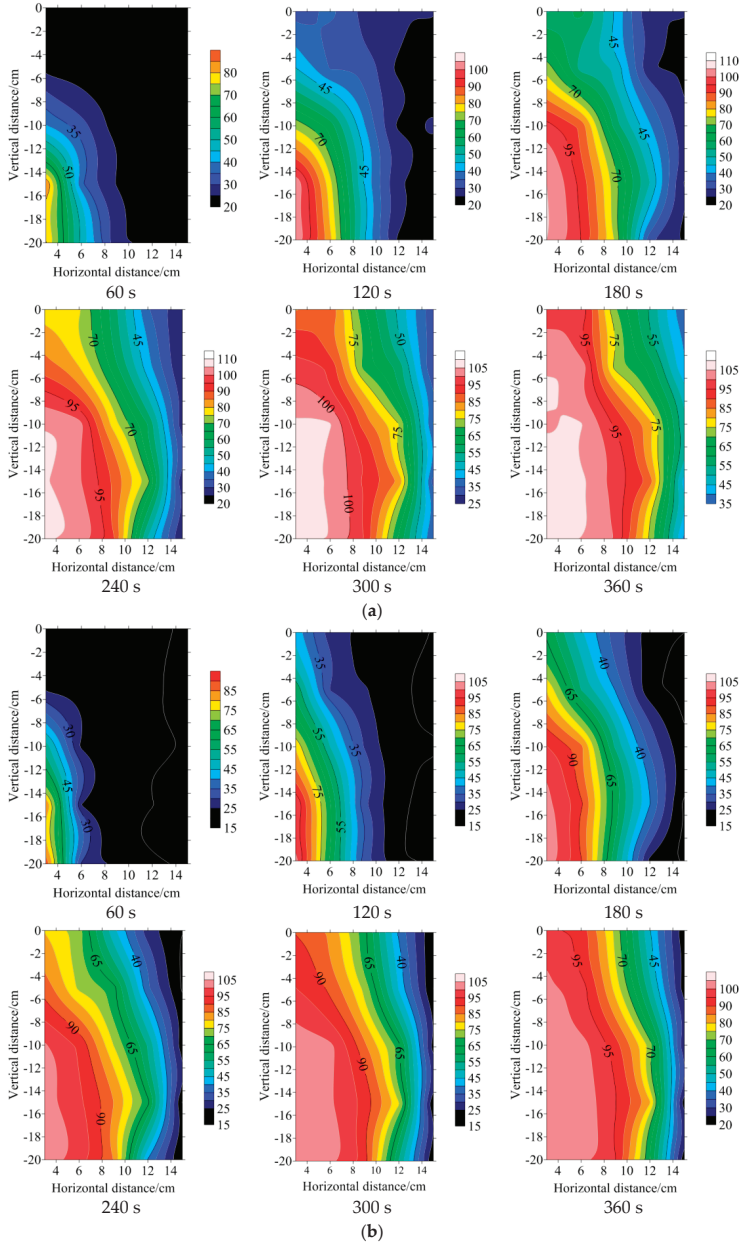
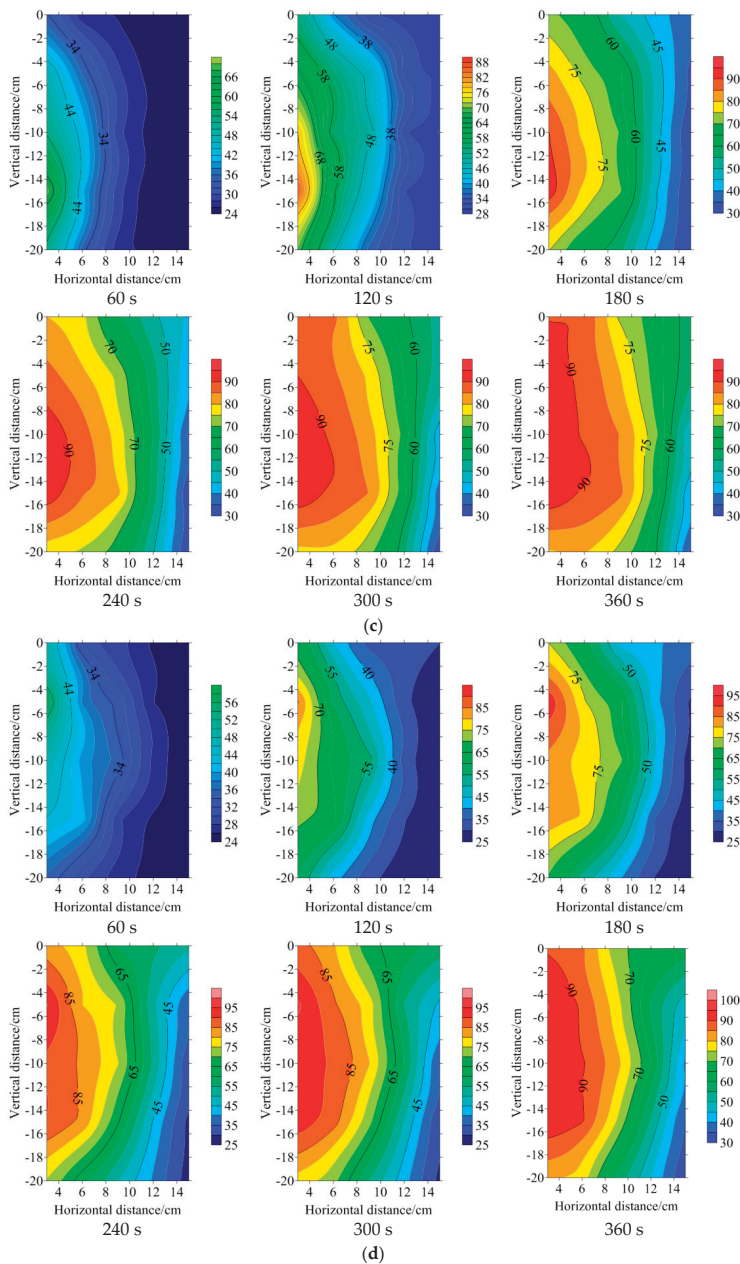


Figure 13. Cont.



**Figure 13.** ST distribution: (a) <2 mm; (b) 7–17 mm; (c) 17–27 mm; (d) >27 mm. Note: The legend indicates the ST/°C and 60 s means that the disinfection time ( $t$ ) is 60 s, 360 s means the disinfection time is 360 s, etc. The same conditions apply in the following section.

#### 4.3. Soil Water Content Distribution Analysis

The soil water content distribution map reveals the diffusion law of steam. The heat transfer mode of each stage in the injection steam disinfection process is investigated in combination with the soil temperature distribution map.

As shown in the wetting front of the soil water content distribution profile 14, the particle sizes are 2 and 7–17 mm. At the beginning of the disinfection, the steam spreads around the soil in the form of a 1/4 oval shape, and the diffusion range is 0 to 11 cm in the horizontal direction. The straight direction is –2–20 cm; at the end of disinfection, the middle and high water content areas are rectangular at the horizontal level of 0–13 cm and vertical level of 0–20 cm; and the high water content area is concentrated in deep soil. When the particle sizes are 17–27 and >27 mm, the steam diffuses in the form of 1/2 ellipse. The diffusion range is 0–10 cm horizontally and 0–20 cm vertically. At the end of disinfection, the medium-high water content area is 1/4 oval. The horizontal level is 0–12.5 cm, and the vertical level is 0–20 cm. The high water content area is concentrated in the upper layer of the soil. The diffusion range of single-SDP steam is concentrated at the horizontal level of 10–13 cm and the vertical level of 0–20 cm.

For the same disinfection time, as the number of soil pores increase, the high water content region gradually migrates to the soil surface. In the initial stage of disinfection, a smaller SP size corresponds to a greater change in the horizontal water content than the vertical water content; thus, the steam primarily diffuses horizontally, such that the soil surface is in the middle and low water content areas. A larger SP size corresponds to greater water changes in the vertical direction; thus, the steam primarily diffuses vertically, and the deep layer of soil is in the middle and low water content area. The larger the particle size is, the larger the soil pores, and the form of steam flow is primarily large pore flow, such that the steam can be unobstructed along the large pores. The steam diffuses to the surface of the soil and accumulates on the surface of the soil. The smaller the particle size is, the smaller the pores of the soil. Consequently, the form of steam flow is primarily the matrix flow and a small part of the large pore flow, and the diffusion ability of steam in the horizontal direction is enhanced.

As shown in Figure 14, when the soil was disinfected for 60 s, the surface soil that corresponds to the particle sizes >27 and 17–27 mm has begun to appear in the middle water content area, while the surface soil that corresponds to the particle sizes 7–17 and 2 mm remains in the low water content area. When the soil was disinfected for 300 s, the steam with the particle sizes of 7–17 and 2 mm began to diffuse into the surface of the soil, such that the vertical diffusion speed was enhanced, and the vapor diffusion gradually became uniform. When the soil was disinfected for 360 s, the surface layer of each treated soil formed a high water-bearing area with a high content of >27 and 17–27 mm particle sizes. The water volume area is larger than that of the area with particle sizes of 7–17 and 2 mm.

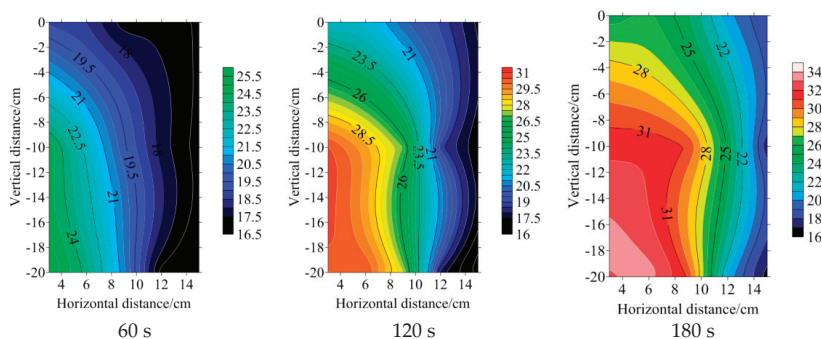


Figure 14. Cont.

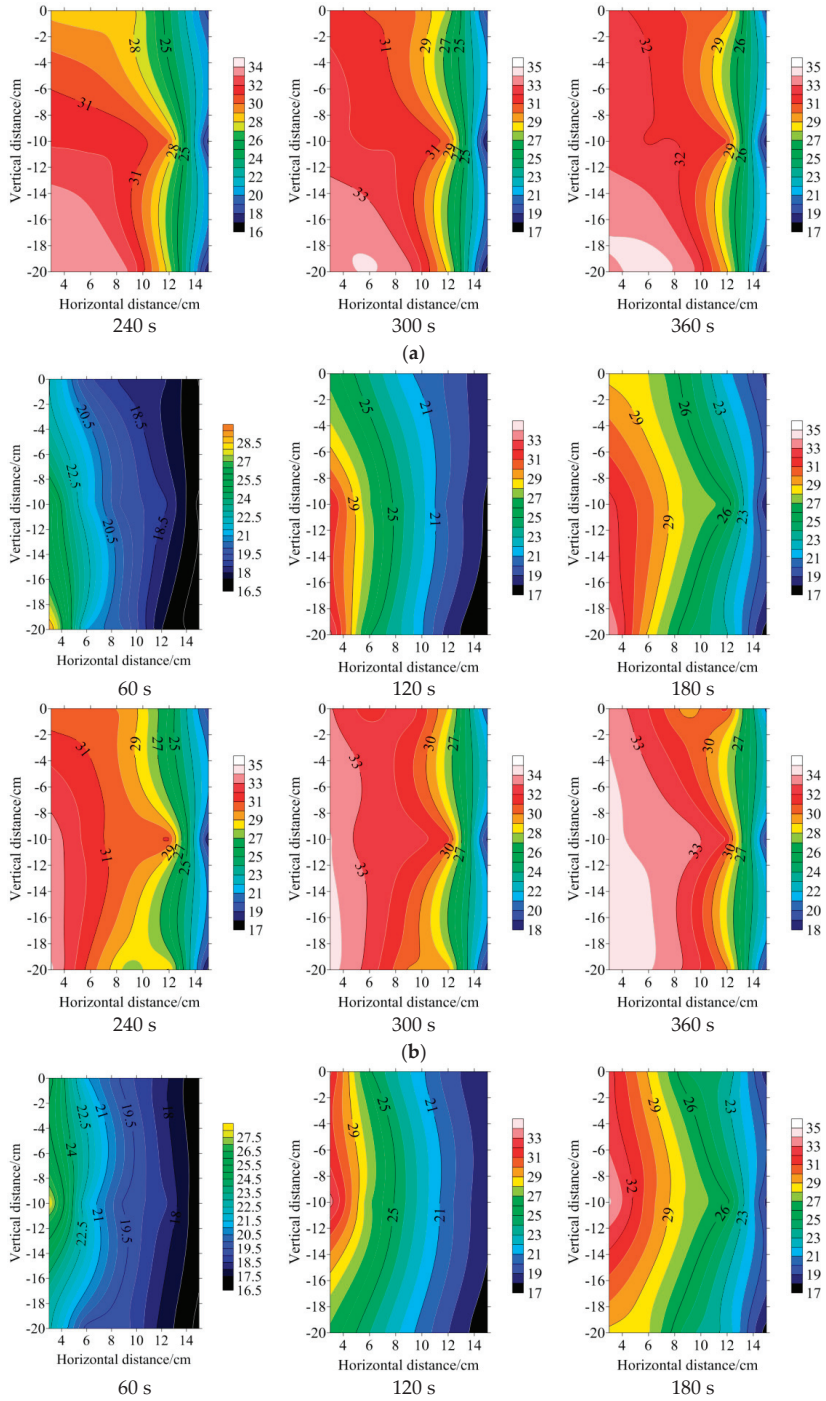
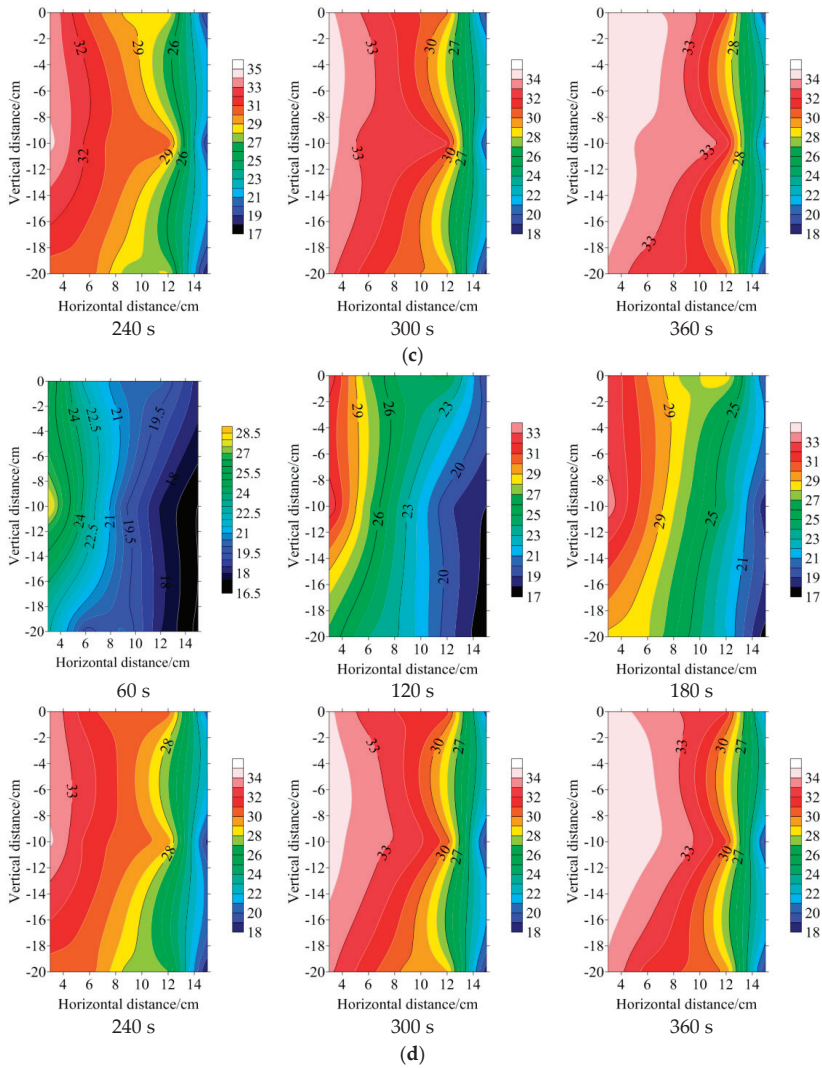


Figure 14. Cont.



**Figure 14.** SWC distribution. (a) <2 mm; (b) 7–17 mm; (c) 17–27 mm; (d) >27 mm. Note: The legend is in SWC, %.

#### 4.4. Energy Consumption Analysis

As shown in Table 7, the particle size has a significant effect on energy consumption, where the energy consumption for the particle size of 2 mm is 477 kJ and the energy consumption for the particle size of >27 mm is 486 kJ. The energy consumption for the particle sizes 7–17, 17–27, and >27 increased by 6.17%, 6.7%, and 9.4%, respectively, compared with that for a particle size of 2 mm. The effect of steam flow on the energy consumption is not significant.



Table 7. Energy consumption.

SP Size (mm)	Flow Rate (kg/h)	Energy Consumption (kJ)
<2	2	476.75 ± 1.33 <sup>b</sup>
	3	476.67 ± 1.30 <sup>b</sup>
	4	476.58 ± 1.37 <sup>b</sup>
7–17	2	482.85 ± 1.6 <sup>ab</sup>
	3	482.90 ± 1.59 <sup>ab</sup>
	4	482.77 ± 1.50 <sup>ab</sup>
17–27	2	483.36 ± 2.79 <sup>a</sup>
	3	483.28 ± 2.81 <sup>a</sup>
	4	483.45 ± 2.80 <sup>a</sup>
>27	2	486.17 ± 4.15 <sup>a</sup>
	3	485.60 ± 4.52 <sup>a</sup>
	4	486.35 ± 4.11 <sup>a</sup>

Note: The data are given as the mean ± standard deviation ( $n = 3$ ); different lowercase letters indicate significant differences in the same flow rate ( $p < 0.05$ ).

## 5. Discussion

Considering the characteristics of Yangtze River Delta soil and to promote the diffusion and heating range of steam in the soil disinfection process, the soil heating rate, temperature distribution, and energy consumption were analyzed by changing the particle and pore size of the soil. Results showed that with an increase in the SP size, the width of the soil pore flow channel gradually increased and the diffusion and the heating rate of steam in the vertical direction is greater than that in the horizontal direction, such that a large amount of steam will overflow the soil surface. Comparing the simulation and test results, it can be seen that the temperature field simulated by CFD is higher than the SSD test at the horizontal diffusion distance  $L$  and the temperature value. This is because the simulation condition is ideal and the heat dissipation is negligible, so the simulation value is greater than the test value. However, there may also be another reason. During the test, due to the continuous flow of steam into the soil, part of the steam will condense into water vapor and liquid water, and some soil particles will disintegrate and aggregate to form larger soil clods [28]. In the later stage of disinfection, the diffusion of steam in the soil will be hindered, which will reduce the diffusion range of the steam and the soil temperature value. Therefore, in future simulation processes, it is necessary to consider the problem of soil particle disintegration and deformation. At the same time, it is also necessary to simulate the impact of water content (steam condensate) changes on soil particles and temperature field during the simulation process.

Although the simulation value is higher than the experimental value, we can still find some new ones. The visualization of simulation process and verification of temperature field of disinfection test indicated that the SP size and pores have a substantial influence on the flow of steam. When the pores are too large, the steam primarily forms a large pore flow in the vertical direction and rapidly diffuses to the surface of the soil to form a high-temperature region [16,17]. A large amount of steam will overflow into the air to cause an ineffective loss of heat, and with a decrease in the SP size, the soil pore flow channel becomes fine and the diffusion velocity of steam in the vertical direction gradually decreases, such that it diffuses around the soil in the form of matrix flow and partial large pore flow. Therefore, appropriately increasing soil pores can help to accelerate the flow of gases and liquids in the soil via the aeration and water permeability of the soil, especially in the soil disinfection process, and promote the diffusion and heat transfer range of the steam. However, the excessive pores in the soil cause the steam to diffuse too quickly to the surface of the soil and overflow into the atmosphere and cause a heat loss such that large particles in the soil cannot be completely heated to the desired temperature [16,17]. Similar to the mobile SSD process, the SDP is continuously pulled to form cracks of different sizes in the soil. Most of the steam will be directly lost from the crack to the air in the form

of large pore flow, and only a small part of the steam will be the substrate flow [7]. The form spreads to both sides of the soil, which prevents the total soil warming from satisfying the temperature required for disinfection, which explains why mobile steam disinfection cannot quickly heat the soil.

Injecting steam disinfection is applied to different soil types. In addition to accelerating the diffusion rate of the soil vapor, the large pore flow can also promote the re-evaporation of condensed water in the pores, which is conducive to gas diffusion. However, this situation is only applicable in sandy loam soils due to the high sand content and relatively large soil pores, which facilitates the diffusion of steam. The findings of Gay et al. indicated that the single-SDP steam has a thermal radius of 15 cm [6]. However, in clay soil, the diffusion of steam in dense soil is difficult. As indicated in the study with a particle size of 2 mm, although the pores have a large pore flow, the maximum horizontal heat transfer distance of single-SDP steam is only 12 cm, which is less than the working distance of sandy loam. Considering that the soil in the Yangtze River Delta is clay or clay loam, when using conventional soil steam sterilizer to inject steam sterilization of compacted clay, there will be problems of difficult steam diffusion and too small effective disinfection area. On the basis of this study, the compacted soil containing large cracks is finely rotated into a loose and porous small-grained soil by adding a rotary tillage device. The combined effects of large-pore steam flow and matrix flow after rotary tillage are more conducive to improving the effective disinfection range of steam. At the same time, according to the heat flow diffusion distance (12 cm) of a single-SDP, it can be determined that the SDP spacing needs to be less than 24 cm. In summary, it can be seen that the soil steam disinfection method will have a better practical disinfection effect than other disinfection methods after the rotary tilling treatment and the optimization of the SDP spacing.

## 6. Conclusions

Based on our findings following conclusions are drawn:

(1) For the clay soil in the Yangtze River Delta region of China, when the heat flow reaches  $H = 20$  cm in the vertical direction, the simulation and test result of the heat flow in the maximum horizontal diffusion distance of single-SDP steam are  $L = 13$  cm and 12 cm, respectively. The test results are basically consistent with the simulation results. At the same disinfection time, the simulated soil temperature change trend is basically consistent with the test results and the test temperature is slightly lower than the simulated temperature. In the future, it is necessary to optimize the CFD simulation process, and add the disintegration and deformation processes of soil particle size with the change of water content.

(2) The larger the soil particle size is, the larger the pore flow path width, and the easier the formation of a large pore flow. Therefore, a large amount of steam will overflow into the air to cause an increase in energy consumption. In the future, it is necessary to add a rotary cultivating device to the soil steam sterilizer to rotate the soil to ensure that the soil can be heated uniformly and quickly.

**Author Contributions:** Conceptualization, Z.Y.; methodology, Z.Y.; software, Z.Y.; validation, Z.Y., X.W., and M.A.; formal analysis, Z.Y.; data curation, Z.Y.; writing—original draft preparation, Z.Y. and A.A.; writing—review and editing, A.A., M.A., S.A.S., and H.Y.; visualization, A.A., M.A., S.A.S., and H.Y.; supervision, X.W.; project administration, X.W.; funding acquisition, X.W. and Z.Y. All authors have read and agreed to the published version of the manuscript.

**Funding:** This research was funded by the Jiangsu Province Science and Technology Support Plan-funded project CX(16)1002 and the Graduate Student Scientific Research Innovation Projects in Jiangsu Province KYCX17\_0648.

**Acknowledgments:** We thank Hongyou Sun and Gang Li for helping with the work.

**Conflicts of Interest:** The authors declare no conflicts of interest.

## Abbreviations

SSD	soil steam disinfection
SP	soil particle
SDP	steam disinfection pipe
ST	soil temperature (°C)
SWC	soil water content (%)
$Q_s$	total amount of steam(kg)
$C_v$	coefficient of variation
$V_T$	soil temperaturerise rate(°C/s)
$W_s$	energy consumption
$L$	horizontal diffusion distance of the steam heat flow (cm)
$H$	vertical diffusion distance of the steam heat flow (cm)
Subscripts	
$T$	temperature
$s$	Steam
$t$	time (s)

## References

- Weiland, J.E.; Littke, W.R.; Browning, J.E.; Edmonds, R.L.; Davis, A.; Beck, B.R.; Miller, T.W. Efficacy of reduced rate fumigant alternatives and methyl bromide against soilborne pathogens and weeds in western forest nurseries. *Crop Prot.* **2016**, *85*, 57–64. [CrossRef]
- Yang, Y.T.; Hu, G.; Zhao, Q.L.; Guo, D.Q.; Gao, Q.S.; Guan, C.S. Research progress of soil physical disinfection equipment. *Agric. Eng.* **2015**, *5*, 43–48. (In Chinese)
- Cao, A.; Zheng, J.; Wang, Q.; Li, Y.; Yan, D. Advances in soil disinfection technology worldwide. *China Veg.* **2010**, *21*, 17–22. (In Chinese)
- Cao, A.; Zheng, J.; Guo, M.; Wang, Q.; Li, Y. Soil disinfection technology and key points. *Vegetables* **2011**, *4*, 41–44. (In Chinese)
- Nishimura, A.; Asai, M.; Shibuya, T.; Kurokawa, S.; Nakamura, H. A steaming method for killing weed seeds produced in the current year under untilled conditions. *Crop Prot.* **2015**, *71*, 125–131. [CrossRef]
- Gay, P.; Piccarolo, P.; Aimonino, D.R.; Tortia, C. A high efficiency steam soil disinfection system, Part I: Physical background and steam supply optimisation. *Biosyst. Eng.* **2010**, *107*, 74–85. [CrossRef]
- Gay, P.; Piccarolo, P.; Aimonino, D.R.; Tortia, C. A high efficiency steam soil disinfection system, part II: Design and testing. *Biosyst. Eng.* **2010**, *107*, 194–201. [CrossRef]
- Peruzzi, A.; Raffaelli, M.; Ginanni, M.; Fontanelli, M.; Frascioni, C. An innovative self-propelled machine for soil disinfection using steam and chemicals in an exothermic reaction. *Biosyst. Eng.* **2011**, *110*, 434–442. [CrossRef]
- Pan, S.P.; Zhou, H.P.; Jiang, X.S.; Chen, Q.; Li, P.P. Design and experiment of soil disinfection steam generator based on pulse combustion technology. *Trans. Chin. Soc. Agric. Mach.* **2018**, *49*, 301–307. (In Chinese)
- Xu, Y.L.; Dai, L.; Zhao, D.; Zhang, Y.J.; Jin, B.H.; Zhang, X.D.; He, X.H. Effect of several soil treatments on seedling growth and root rot disease of *Panax notoginseng*. *J. Yunnan Agric. Univ.* **2016**, *31*, 1006–1011. (In Chinese)
- Zhu, J.F.; Zhao, Y.Q.; Yang, L.Q.; Gao, Z.C.; Zhang, R.K. Design of matrix steam sterilizing machine of *Panax Notoginseng* greenhouse seedling trough. *J. Agric. Mech. Res.* **2017**, *3*, 79–83. (In Chinese)
- Huang, C.Y. *Soil Science*; China Agriculture Press: Beijing, China, 2000; pp. 71–78.
- Lin, D.Y. *Soil Science*; China Forestry Press: Beijing, China, 2002; pp. 61–66.
- Li, D.C.; Zhang, T.L. Fractal features of particle size distribution of soils in China. *Soil Environ. Sci.* **2000**, *9*, 263–265. (In Chinese)
- Ding, R.X.; Liu, Y.Z.; Sun, Y.H. Reference of soil system classification in subtropical humid region of China. *Soils* **1999**, *2*, 97–109. [CrossRef]
- Skopp, J.; Gardner, W.R.; Tyler, E.J. Solute movement in structured Soils: Two-region model with small interaction. *Soil Sci. Soc. Am. J.* **1981**, *45*, 837–842. [CrossRef]

17. Hardie, M.A.; Marcus, A.; Cotching, W.E.; Holz, G.; Lisson, S.; Mattern, K. Effect of antecedent soil moisture on preferential flow in a texture-contrast soil. *J. Hydrol.* **2011**, *398*, 191–201. [CrossRef]
18. Ameen, M.; Xiaochan, W.; Yaseen, M.; Umair, M.; Yousaf, K.; Yang, Z.; Soomro, S.A. Performance Evaluation of Root Zone Heating System Developed with Sustainable Materials for Application in Low Temperatures. *Sustainability* **2018**, *10*, 4130. [CrossRef]
19. Beven, K.; Germann, P. Water flow in soil macropores II. A combined flow model. *Eur. J. Soil Sci.* **1981**, *32*, 15–29.
20. Beven, K.; Germann, P. Macropores and water flow in soils. *Water Resour. Res.* **1982**, *18*, 1311–1325. [CrossRef]
21. Luxmoore, R.J. Micro-, Meso-, and Macroporosity of soil. *Soil Sci. Soc. Am. J.* **1981**, *45*, 671–672. [CrossRef]
22. Wilson, G.V.; Luxmoore, R.J. Infiltration, Macroporosity, and Mesoporosity distributions on two forested watersheds. *Soil Sci. Soc. Am. J.* **1988**, *52*, 329–335. [CrossRef]
23. Singh, P.; Kanwar, R.S.; Thompson, M.L. Measurement and Characterization of Macropores by using Autocad and Automatic Image Analysis. *J. Environ. Qual.* **1991**, *20*, 289–294. [CrossRef]
24. Soille, P.J.; Ansoult, M.M. Automated basin delineation from digital elevation models using mathematical morphology. *Signal Process.* **1990**, *20*, 171–182. [CrossRef]
25. El-Halim, A. Image processing technique to assess the use of sugarcane pith to mitigate clayey soil cracks: Laboratory experiment. *Soil Tillage Res.* **2017**, *169*, 138–145. [CrossRef]
26. Wang, C.; Zhang, Z.Y.; Liu, Y.; Fan, S.M. Geometric and fractal analysis of dynamic cracking patterns subjected to wetting-drying cycles. *Soil Tillage Res.* **2017**, *170*, 1–13. [CrossRef]
27. Yang, Z.J.; Wang, X.C.; Ameen, M. Influence of the spacing of steam-injecting pipes on the energy consumption and soil temperature field for clay-Loam disinfection. *Energies* **2019**, *12*, 3209. [CrossRef]
28. Li, Q.; Zhang, Z.; Xu, H.; Xu, W.Z. A new modified method for calculation of soil disintegration rate. *Res. Soil Water Conserv.* **2015**, *22*, 344–348.



© 2020 by the authors. Licensee MDPI, Basel, Switzerland. This article is an open access article distributed under the terms and conditions of the Creative Commons Attribution (CC BY) license (<http://creativecommons.org/licenses/by/4.0/>).

Article

# Heat Transfer Coefficient Estimation and Performance Evaluation of Shell and Tube Heat Exchanger Using Flue Gas

Xuejun Qian <sup>1,2,\*</sup>, Seong W. Lee <sup>1,2</sup> and Yulai Yang <sup>1,2</sup>

<sup>1</sup> Industrial and Systems Engineering Department, Morgan State University, 1700 East Cold Spring Lane, Baltimore, MD 21251, USA; seong.lee@morgan.edu (S.W.L.); yuyan1@morgan.edu (Y.Y.)

<sup>2</sup> Center for Advanced Energy Systems and Environmental Control Technologies, School of Engineering, Morgan State University, 1700 East Cold Spring Lane, Baltimore, MD 21251, USA

\* Correspondence: xuqia1@morgan.edu; Tel.: +1-443-885-2772

**Abstract:** In the past few decades, water and air were commonly used as working fluid to evaluate shell and tube heat exchanger (STHE) performance. This study was undertaken to estimate heat transfer coefficients and evaluate performance in the pilot-scale twisted tube-based STHE using the flue gas from biomass co-combustion as working fluid. Theoretical calculation along with experimental results were used to calculate the specific heat of flue gas. A simplified model was then developed from the integration of two heat transfer methods to predict the overall heat transfer coefficient without tedious calculation of individual heat transfer coefficients and fouling factors. Performance including water and trailer temperature, heat load, effectiveness, and overall heat transfer coefficient were jointly investigated under variable operating conditions. Results indicated that the specific heat of flue gas from co-combustion ranging between 1.044 and 1.338 kJ/kg·K while specific heat was increased by increasing flue gas temperature and decreasing excess air ratio. The developed mathematical model was validated to have relatively small errors to predict the overall heat transfer coefficient. A flue gas mass flow rate of 61.3–98.8 kg/h, a water flow rate of 13.7–14.1 L/min, and a parallel arrangement of two water-to-air heaters in an empty trailer were found to be optimal conditions for space heating purpose. In addition, a lower poultry litter feeding rate decreased heat loss of flue gas and increased heat gain of water, while a lower water flow rate also provided a lower maximum possible heat transfer rate with a higher actual heat transfer rate to quickly achieve heat equilibrium that ultimately improves the performance. This study demonstrates the possibility of collecting residual heat from the flue gas using the pilot-scale STHE system while outlining a systematic approach and process for evaluating its performance.

**Keywords:** shell tube heat exchanger; poultry litter; natural gas co-combustion; flue gas; specific heat; overall heat transfer coefficient; effectiveness

**Citation:** Qian, X.; Lee, S.W.; Yang, Y. Heat Transfer Coefficient Estimation and Performance Evaluation of Shell and Tube Heat Exchanger Using Flue Gas. *Processes* **2021**, *9*, 939. <https://doi.org/10.3390/pr9060939>

Academic Editor: Alfredo Iranzo

Received: 13 May 2021

Accepted: 24 May 2021

Published: 26 May 2021

**Publisher's Note:** MDPI stays neutral with regard to jurisdictional claims in published maps and institutional affiliations.



**Copyright:** © 2021 by the authors. Licensee MDPI, Basel, Switzerland. This article is an open access article distributed under the terms and conditions of the Creative Commons Attribution (CC BY) license (<https://creativecommons.org/licenses/by/4.0/>).

## 1. Introduction

The shell and tube heat exchanger (STHE) is a common type of exchanger apparatus widely used in several industrial processes and areas, such as chemical engineering, petroleum refining, refrigeration system, food processing, and power generation [1]. They have much lower production costs, robust geometry construction, easy cleaning and maintenance, and flexibility in their utility [1–3]. The STHE system mainly consists of a shell (vessel with different sizes) and a bundle of tubes inside a shell. Heat is transferred from one fluid into the other fluid, either from the tube side to the shell side through the tube walls or vice versa, to equalize the temperature. These fluids can either be liquids or gases on either the shell or tube side [4]. The type of tube plays an important role in heat transfer enhancement and can have a great effect on the overall heat transfer process. There are several types of tubes, such as plain, twisted, spiral, and longitudinally finned, that are currently used in the STHE system [4]. Compared to the round tube bundle with the same arrangement as the crossflow, Li et al. [5] found the twisted tube bundle to be better

convection heat transfer. Tan et al. [6] and Tan et al. [7] investigated and compared the heat transfer performance of the twisted and smooth round tubes. Both results indicated that the twisted tube was better than the round tube in increasing the heat transfer coefficient and the efficiency of heat exchangers.

Besides supporting the tube bundles, the baffle is also responsible for maintaining desirable velocity and creating turbulence for the shell-side working fluid in conjunction with the shell and tube structure [8]. The baffle also resists vibrations to enhance fluid velocity as well as the heat transfer coefficient [2]. The type and inclination angle of the baffle are two important characteristics for influencing the overall performance [2,8]. Various types of baffles, such as segmental, double segmental, helical, disk, and doughnut type, were studied and implemented in the wider applications of STHE systems [9]. The helical baffle serves as a promising technology because of less shell-side pressure drop, better heat transfer performance, and less fluid-induced vibration. However, the helical baffle requires high capital investments to account for costs associated with manufacturing its complex shapes. In contrast, the segmental baffle has been widely adopted and remains the most used baffle in STHE systems because of its ease to fabricate with lower maintenance costs. The segmental baffle forces the shell-side working fluid to pass through in a zigzag manner, thereby improving the heat transfer with acceptable pressure drops. The inclination angle of the baffle is critical for controlling flow velocity and influencing the transfer coefficient. The inclination angle of 90°C may cause a zigzag flow, resulting in a dead zone behind each baffle. This ultimately increases the fouling resistance and decreases the heat transfer rate. Zhang et al. [8] compared the performance of heat exchanger systems at inclination angles of 20°C, 30°C, 40°C, and 50°C, respectively. Results showed that the inclination angle of 40°C was the best performing angle. Duan et al. [3] analyzed the flow and thermal performance of six helical baffle based STHE across three different inclination angles (20°C, 30°C, 40°C) and variable volumetric flow rates. The study indicated that having the inclination angle at 40°C resulted in the highest heat transfer coefficient per unit pressure drop since a larger angle leads to a lower pressure drop. Based on previous findings, the segmental baffle with an inclination angle of 40°C demonstrates the possibility of generating spiral flow while increasing the heat transfer coefficient.

The performance of the STHE system was evaluated in the physical experiments under several operating conditions over the past two decades. Thantharate and Zodpe [10] compared temperature changes and overall heat transfer coefficient for the twisted and plain tube based STHE under four different water flow rates to cover both turbulent and laminar flow ranges. Dubey et al. [4] tested the effectiveness of heat exchangers under variable flow conditions (e.g., 25% opening closed, 50% opening closed, and 75% opening closed) and insulation materials. Kasmir and Joshi [11] investigated the effects of mass flow rate and inlet temperature on the overall heat transfer rate. Emal and Elena [12] studied heat transfer by measuring temperature profiles and the overall heat transfer coefficient under a countercurrent and parallel flow arrangement. Abdulmumuni et al. [13] evaluated heat duty, capacity ratio, general effectiveness, the overall heat transfer coefficient, and the fouling factor under variable water flow rates. Ehyaei et al. [14] also found that extraction mass flow rate was critical to optimize heat transfer and performance of the geothermal power plant. To that end, heat transfer coefficient and its effectiveness are, respectively, two of the most important characteristics used to physically evaluate the performance of the STHE system under variable operating conditions, including water flow rates, tube type, and flow arrangement.

Specific heat of flue gas can be used to calculate enthalpy value, rate of heat flow, and the required surface, as well as overall heat transfer coefficient and the effectiveness of the STHE systems [15]. Thermal and gas properties, such as specific heat, thermal conductivity, density, and viscosity of the common working fluids (e.g., water, air), can be easily found in the thermodynamics table. However, the specific heat of flue gas during the combustion process was not available in the thermodynamic table [16]. Coskun et al. [15] estimated specific heat of flue gas for natural gas, fuel oil, and flame coal, respectively.

Results indicated that specific heat ranged from 1.02 to 1.32 kJ/kg·K for flame coal, 1.08 to 1.38 kJ/kg·K for fuel oil, and 1.11 to 1.43 kJ/kg·K for natural gas, all under variable flue gas temperature. Several similar studies investigated the effects of parameters such as the chemical composition of fuel, excess air (EA) amount, and gas temperature on the specific heat of flue gas from well-known fossil fuel combustion [15–18]. El-shafie et al. [19] estimated thermodynamic properties of flue gases from a glass furnace based on chemical composition analysis measured by the gas analyzer. There has yet to exist a formulation that can calculate the specific heat of flue gas from biomass combustion and co-combustion process, especially poultry litter and natural gas co-combustion process.

Fossil fuel depletion, environmental damages, strict regulation, and policies have collectively shifted energy production from fossil fuels toward using a variety of renewable energy resources, such as biomass. Biomass has been recognized as a major contributor to energy generation because it is abundant, cheap, sustainable, and environmentally friendly. In addition, biomass combustion has a CO<sub>2</sub>-neutral effect during the photosynthesis and combustion process for reducing greenhouse gas emissions [20,21]. Due to the inherent high moisture content and lower heating value of biomass fuels, the co-combustion of biomass and natural gas are adopted to increase combustion temperature and maintain stable combustion conditions [22]. Poultry litter is one type of biomass and animal waste from the poultry farming process [22,23]. Instead of land application of poultry litter, co-combustion of poultry litter and natural gas has been a viable alternative for producing heat and electricity [22,24]. There is the necessity of collecting heat in the hot flue gas using heat exchangers owing to the rapid development and adoption of biomass co-combustion technologies. As shown in Table 1, Qian et al. [22] found that there are various common working fluids, such as air, water, and diesel, used to test the performance of the twisted tube STHE system over the past few decades.

**Table 1.** Investigation of twisted tubes with various tube parameters and working fluids.

Tube Parameters (mm)				Working Fluid		Reference
Thickness	Pitch	A	B	Tube	Shell	
3.0	144, 192, 205	21	-	Diesel	Steam	[5]
2.5	200	29	19.5	Cold water	Hot water	[6]
2.5	230	29	19.5	Cold water	Hot water	[7]
-	90	18.42	12	Water	Air	[10]
2.0	300	33	16	Water	Air	[25]

In more recent studies, computational fluid dynamics (CFD) and numerical simulation tools were also applied to investigate heat transfer mechanisms using the exhaust (or flue) gas, non-Newtonian, and helium as working fluid. El-Shafie et al. [19] used FORTRAN software to compare the overall heat transfer coefficient and pressure drop changes of the compact and STHE heat exchangers using exhaust gas from natural gas combustion. Davarpanah et al. [26] used FLUENT software to study heat transfer mechanism and chemical reactions during the design and simulation of ethylene dichloride thermal cracking reactor. Valizadeh et al. [27] applied CFD and performed a parametric simulation to investigate the influence of non-Newtonian fluids on different parameters, including friction coefficient, shear stress, velocity profiles, and pressure drop on spiral tubes. Wang et al. [28] numerically studied heat transfer performance of the five multi-tube heat exchangers (MTHXs) types, including smooth tubes, identical tube arrangement of transverse corrugated tubes, staggered tube arrangement of transverse corrugated tubes, identical tube arrangement of helically corrugated tubes, staggered tube arrangement of helically corrugated tubes using helium gas. There has been limited research to use flue gas from biomass co-combustion process as working fluid on heat transfer study and performance evaluation of the twisted tube based STHE system.

In the previous study, Qian et al. [29] evaluated the effect of tube shape, flow direction, and water flow rate in the lab-scale STHE system on water and trailer temperature changes using flue gas from the poultry litter and natural gas co-combustion process. As a continuation of the previous study, a pilot-scale STHE system along with the twisted tubes and 40°C segmental baffles were fabricated. The main objectives of this study are to calculate the specific heat of flue gas, develop a mathematical model and estimate heat transfer coefficients, and evaluate the performance of the STHE system using flue gas from the poultry litter and natural gas co-combustion process as working fluid under various operating conditions.

## 2. Materials and Methods

### 2.1. Estimation of Coefficients, Heat Load, and Effectiveness

As shown in Figure 1, theoretical calculations were performed as part of the systematic approach to estimating specific heat of flue gas, heat load, effectiveness, and overall heat transfer coefficient. The specific heat of flue gas during poultry litter and natural gas co-combustion process was calculated based on fuel composition, EA, and flue gas temperature. Fuel composition was assumed to be constant because the study's poultry litter samples were collected from one farm (Bethel Farm, Salisbury, MD, USA), which also maintains a consistent farming process (e.g., bedding materials, cleaning periods, and farming practices) [30]. Co-combustion of 5.76 kg/h poultry litter and 0.69 kg/h natural gas process was assumed to be the ideal case, whereas the complete combustion reaction for carbon, hydrogen, and sulfur in fuels with air was assumed to produce the flue gas and unburned residual products (i.e., ash). Nitrogen in poultry litter is not expected to react with oxygen because flue gas temperature during the co-combustion was less than 1000 °C. It was also generally understood that nitrogen normally reacts with oxygen over 1200 °C [31]. In addition, particulate matter (PM) emission and HCl were disregarded because they exist in relatively lower quantities. Thus, major combustion products of flue gas during the poultry litter and natural gas co-combustion are CO<sub>2</sub>, H<sub>2</sub>O, SO<sub>2</sub>, N<sub>2</sub>, and O<sub>2</sub> [17]. Based on the chemical compositions and feeding rate of the collected poultry litter from fuel analysis and natural gas, the required oxygen amount for the complete combustion of fuels was calculated first [30,31]. Then, the required oxygen amount was divided by 0.21, and the EA ratio was multiplied in the range of 1.0 to 1.5 to calculate the required total air amount. Afterward, the total weight and weight ratio of the major components (in wt.%) in flue gas were calculated. Finally, specific heat was calculated by multiplying the weight ratio and specific heat of individual combustion products at temperatures of 0, 50, 100, 150, 200, 300, 400, 500, and 1000 °C, respectively. The effects of EA and flue gas temperature on the specific heat of flue gas during the co-combustion process were also investigated.

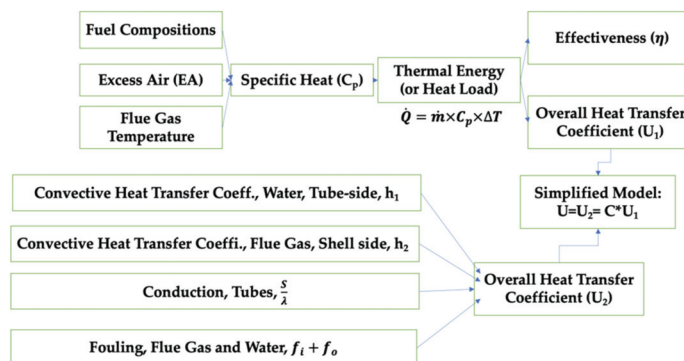


Figure 1. Approach to estimate specific heat and overall heat transfer coefficient.



Heat transfer of the pilot-scale STHE system is determined by the heat load (or thermal energy), also known as heat flow rate, and is calculated as Equation (1):

$$\dot{Q} = \dot{m} \times c_p \times \Delta T, \quad (1)$$

where  $\dot{Q}$  = heat load, in J/s;  $\dot{m}$  = mass flow rate, in kg/s;  $c_p$  = specific heat, in J/g·°C (or kJ/kg·K); and  $\Delta T$  = change in temperature, in °C. The heat load of water ( $\dot{Q}_w$ ) on the tube side was calculated by multiplying mass flow rates of water, the specific heat of water at the average water temperature of inlet and outlet, and water temperature difference between inlet and outlet. The mass flow rate of water was derived from volumetric flow rates and density, while the specific heat of water at various water temperatures was found from the thermodynamics table [16]. The heat load of flue gas ( $\dot{Q}_f$ ) was determined by a function of flue gas mass flow rate, calculated specific heat at average flue gas temperature of inlet and outlet, and the difference in flue temperature between the inlet and outlet of the STHE system. The mass flow rate of flue gas was assumed to be 85% of the total fuel and air amounts because ash content in poultry litter remained after the combustion process, while minor air leakage was observed due to the small holes associated with the combustion chamber's air injection nozzles and temperature sensor holes during the physical combustion experiment.

Then, the effectiveness of the heat exchanger was calculated as Equation (2):

$$\eta_{\text{effectiveness}} = \frac{\dot{Q}_{\text{actual}}}{\dot{Q}_{\text{max}}}, \quad (2)$$

where  $\dot{Q}_{\text{actual}}$  = actual heat transfer rate, in J/s;  $\dot{Q}_w$  = heat load of water, in J/s;  $\dot{Q}_{\text{max}}$  = maximum possible heat transfer rate, in J/s;  $C_{\text{min}}$  = minimum heat capacity rate, in J/s·°C;  $T_{h,\text{in}}$  = inlet temperature of hot fluid, in °C;  $T_{c,\text{in}}$  = inlet temperature of cold fluid, in °C;  $\dot{m}_f$  = mass flow rate of flue gas, in g/s;  $c_{p,f}$  = specific heat of flue gas, in J/g·°C.  $\dot{Q}_{\text{actual}} = \dot{Q}_w$  and  $\dot{Q}_{\text{max}} = C_{\text{min}} (T_{h,\text{in}} - T_{c,\text{in}}) = \dot{m}_f c_{p,f} (T_{h,\text{in}} - T_{c,\text{in}})$  because heat capacity rate of hot fluid (hot flue gas:  $\dot{m}_f c_{p,f}$ ) is smaller than cold fluid (cold water:  $\dot{m}_w c_{p,w}$ ).

In Equation (3), the logarithmic mean temperature difference (LMTD) was determined from two temperature differences  $\Delta t_1$  and  $\Delta t_2$  at each end of the heat exchanger.

$$\text{LMTD} = \frac{\Delta t_1 - \Delta t_2}{\ln \frac{\Delta t_1}{\Delta t_2}}, \text{ where } \Delta t_1 = T_1 - t_2 \text{ and } \Delta t_2 = T_2 - t_1, \quad (3)$$

where  $T_1$  = flue gas temperature at the inlet (°C),  $T_2$  = flue gas temperature at the outlet (°C),  $t_1$  = water temperature at the inlet (°C), and  $t_2$  = water temperature at the outlet (°C). In Equation (4), the LMTD is correlated with a temperature efficiency factor (F) to determine the corrected effective mean temperature difference (CMTD) for multi-pass heat exchangers. According to standards issued by the Tubular Exchanger Manufacturers Association (TEMA), the  $P_z$ ,  $P$ , and  $R$  were determined to jointly calculate the  $F$ , and results showed that  $F = 0.95$  for the pilot-scale STHE system and the CMTD was calculated as Equation (4):

$$\text{CMTD} = F \times \text{LMTD} = 0.95 \text{LMTD}, \quad (4)$$

Based on the calculated heat load (heat transfer rate of flue gas), CMTD, and heat exchanger area of tubes and connections ( $A = 1.034 \text{ m}^2$ ), the overall heat transfer coefficient,  $U_1$ , was calculated using the first method as Equation (5):

$$U_1 = \frac{\dot{Q}}{A \times \text{CMTD}} = \frac{\dot{Q}}{0.9823 \text{LMTD}}, \quad (5)$$

In this study, heat is transferred from flue gas into the tube wall by convection, through the tube wall by conduction, and from the tube wall to cold water again by convection. In addition, deposition of ash deposits (e.g.,  $\text{Na}_2\text{SO}_4$ ,  $\text{K}_2\text{SO}_4$ ) via flue gas on the outer tube wall and calcium-based deposit on the inner tube wall by hard water could cause a fouling effect to increase thermal resistance and deteriorate the heat transfer rate. Thus, the second method was proposed to calculate the overall heat transfer coefficient,  $U_2$  as Equation (6):

$$\frac{1}{U_2} = \frac{1}{h_i} + \frac{1}{h_o} + \frac{S}{\lambda} + f_i + f_o, \quad (6)$$

where  $h_i$  = convective heat transfer coefficient determined by water on the tube side ( $\text{W}/\text{m}^2 \text{K}$ ),  $h_o$  = convective heat transfer coefficient caused by flue gas on the shell side ( $\text{W}/\text{m}^2 \text{K}$ ),  $S$  = tube wall thickness (m),  $\lambda$  = thermal conductivity of the tube material ( $\text{W}/\text{mK}$ ),  $f_i$  = inner fouling factor by water ( $\text{m}^2 \text{K}/\text{W}$ ),  $f_o$  = outer fouling factor by flue gas ( $\text{m}^2 \text{K}/\text{W}$ ). Equations (7)–(9) were used to establish the convective heat transfer coefficient for both tube and shell side. First, the velocity of medium (i.e., flue gas, water) was calculated as Equation (7):

$$V = \frac{\dot{m}}{\rho \times A} = \frac{\dot{m}}{\rho \times \frac{1}{4}\pi D_e^2}, \text{ where } D_e = \frac{4(P_t^2 - \pi d_o^2/4)}{\pi d_o}, \quad (7)$$

where  $V$  = velocity (m/h),  $\dot{m}$  = mass flow rate (kg/h),  $\rho$  = density ( $\text{kg}/\text{m}^3$ ),  $P_t = 29.26$  mm is the distance between centers of two pipes,  $d_o = 15.875$  mm is the outside diameter of the tube, and  $D_e = 52.832$  mm is the equivalent diameter for the square pitch layout of tubes. Based on the average temperature of the inlet and outlet for both flue gas and water, Reynolds number ( $Re$ ) was derived from velocity ( $V$ ), equivalent diameter ( $D_e$ ) with kinematic viscosity ( $\nu$ ,  $\text{m}^2/\text{s}$ ). Herein, kinematic viscosity was also calculated by dividing dynamic viscosity ( $\text{kg}/\text{m s}$ ) by density ( $\text{kg}/\text{m}^3$ ). Based on the calculated  $Re$ , flow conditions of the medium were determined. In the case of laminar flow ( $Re < 2300$ ) on the tube side, the Nusselt number on the tube side of the annular space was derived [32].

In the case of turbulent flow ( $Re > 10,000$ ), the Nusselt number,  $Nu$  was derived as Equation (8):

$$Nu = 0.023 \times Re^{0.8} \times Pr^n = 0.023 \times Re^{0.8} \times Pr^{0.4}, \text{ where } Re = \frac{VD_e}{\nu}, \quad (8)$$

where the exponent of the Prandtl number,  $Pr$  is assumed to be  $n = 0.4$  for heating of the fluid.  $Pr$  number and thermal conductivity are derived from the thermodynamic tables [16]. Then, the convective heat transfer coefficient was calculated as Equation (9):

$$h = \frac{k}{D} Nu \quad (9)$$

where  $k$  = thermal conductivity ( $\text{W}/\text{mK}$ ) and  $D$  = diameter (m).

The total fouling factor at the tube and shell side was assumed to be  $0.0018 \text{ m}^2\text{K}/\text{W}$  because the fouling factor of biomass flue gas played such a major role while fouling of water was relatively small [16]. Conduction through copper tube wall is  $4 \times 10^{-6} \text{ m}^2 \text{K}/\text{W}$  where the thickness was  $0.00159$  m, and heat conductivity was assumed to be  $385 \text{ W}/\text{mK}$ . Results for overall heat transfer coefficient from the first and second method were compared. A correlation was found using the first six sets of overall heat transfer coefficient results. A simplified model was developed to predict the overall heat transfer coefficients. Additionally, two sets of results were used to calculate estimation error and validate the accuracy of our simplified model.

## 2.2. Fabrication of the Pilot-Scale STHE System

As shown in Figure 2, the pilot-scale STHE system consists of one shell, sixteen twisted tubes, and six segmental baffles.

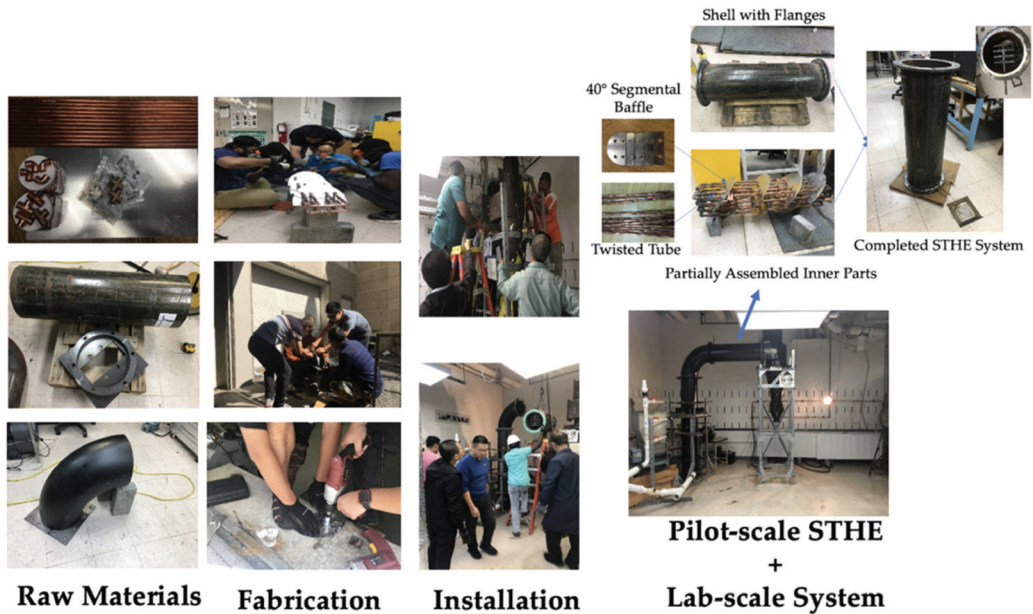


**Figure 2.** Pilot-scale shell and tube heat exchanger (STHE) system, fabrication, and assembly.

In this study, the pilot-scale STHE system integrated the twisted tubes and 40° inclination angle of the segmental baffle to increase heat transfer coefficient and efficiency. The shell has a diameter of 304.8 mm and a length of 1016.0 mm. The tube has a diameter of 12.7 mm and a length of 863.6 mm. The segmental baffle has a diameter of 292.1 mm and a height of 206.6 mm (about 25% area cut). Raw materials for the tube section include copper type L pipes, 90° elbow connections, tees, 4-way copper cross fittings, shell material consisting of schedule 40 carbon steel pipe, and an aluminum plate for the baffle. Twisted tubes and segmental baffles were fabricated by the study's research assistants associated with the Center for Advanced Energy Systems and Environmental Control Technologies (CAESECT) with assistance from the physical plant staff at Morgan State University. Baffle fabrication was also performed by first using a cardboard-based model to then cut the aluminum plate using a 14-gauge swivel head shear (Item 68199, Chicago Electric Power Tools, Calabasas, CA, USA), as well as bi-metal and hole saw set (Items 68,113 and 68,990, Warrior, Camarillo, CA, USA). Fabricated twisted tubes and segmental baffles were preassembled with connections for identifying compatibility between the components. After that, the soldering kit, along with a Bernzomatic Map-Pro gas cylinder and 15% phos-copper silver brazing alloy rod, was acquired to perform the hard-soldering process. Several water leakages tests and hard soldering were performed to seal all small gaps and holes until there was no water leakage in the inner parts of the pilot-scale STHE prototype without the shell. Then, two flanges were welded, and partially assembled inner parts were inserted into the shell to complete the pilot-scale STHE system. Thereafter, the pilot-scale STHE system was installed between the lab-scale swirling fluidized bed combustion (SFBC) system and cyclone system.

### 2.3. Experimental Setup and Evaluation of the STHE System

Figure 3 illustrates the experimental setup for the system analysis and performance evaluation of the pilot-scale STHE system during the poultry litter and natural gas co-combustion process. The pilot-scale STHE system was integrated with the SFBC system, two water-to-air heaters, water circulation pump, heat resistant water rubber hoses, and empty trailer (2438.4 mm width  $\times$  7620.0 mm length  $\times$  2590.8 mm height, Mobile Mini Storage Solutions, Middle River, MD, USA) to simulate the space heating of a typical poultry house. Natural gas was provided at a height of 120.0 mm for ignition and co-combustion with poultry litter [29,30]. Poultry litter as combustion fuel was fed into the SFBC chamber through the fuel feeder. At the same time, the primary and secondary air blowers, along with a voltage regulator, were responsible for controlling and supplying the air. In this study, hot flue gas was produced from co-combustion and used as working fluid in the shell side of the STHE system. Cold water in the twisted tube side served as another working fluid to absorb heat from the hot flue gas and generate hot water. Processed hot water from the pilot-scale STHE system was then sent to the two water-to-air heaters before rejecting heat into the cold air from an empty trailer house to provide space heating. In this study, two water-to-air heaters and the pilot-scale STHE system became a closed-loop connection with a water circulation pump and several water rubbers hoses. Heat gain was achieved from hot flue gas entering cold water by the STHE system. Heat loss was transferred from hot water into cold air using the water-to-air heaters. Insulation materials were applied to water pipes to avoid heat loss and ensure that (a) the outlet temperature of the STHE system was equivalent to the inlet temperature of the heater and (b) the outlet temperature of the heater was equivalent to the inlet temperature of the STHE system. Residual flue gas was emitted to the outside environment via the cyclone and chimney exit of the SFBC system. Vortex flow meters (SV4610, Ifm electronic company, Essen, Nordrhein-Westfalen, Germany), K-type thermocouples (Omega TJ36-CASS-18U-6, OMEGA Engineering, Norwalk, CT, USA) along with a data acquisition system (Omega OMB-DAQ-2416, OMEGA Engineering, Norwalk, CT, USA) were carefully installed to monitor water flow rate, water inlet/outlet temperature, inlet/outlet flue gas, and chamber temperatures. Trailer temperatures were calculated according to the average temperatures across three positions: window side, door side, and middle of the trailer.

Performance indicators, including temperature changes, heat load, effectiveness, CMTD, and overall heat transfer coefficient, were used to investigate and evaluate the fabricated pilot-scale STHE system under variable operating conditions, such as the mass flow rate on the tube side, mass flow rate in the shell side, and the water flow arrangement. Flue gas mass flow on the shell side is influenced by the feeding rate of poultry litter and natural gas and the amount of air being injected [29,30]. In this experiment, the mass flow rate of flue gas was determined by the feeding rate of fuels (including poultry litter and natural gas) and air. The mass flow rate of poultry litter at 5.76 and 6.81 kg/h, natural gas at 0.69 and 0.77 kg/h, and air between 66.00 and 121.00 kg/h were used to investigate the effect of flue gas mass flow rate on the shell side on the performance of the pilot-scale STHE system under constant water flow rates. Then, poultry litter and natural gas co-combustion process was conducted to reach the stable condition of SFBC chamber and STHE system for the first 90 min. Afterward, natural gas was kept at a constant  $2.83 \times 10^{-4} \text{ m}^3/\text{s}$  while poultry litter was fed at a rate of 5.76 kg/h from 90 to 160 min to study the effects of water flow rate on the tube side on its performance. Data collection commenced after 90 min into the co-combustion process, until 160 min in 10-min intervals. The mass flow range on the tube side was controlled by the volumetric flow rate of water at low (13.7 to 14.1 L/min), medium (14.5–14.6 L/min), and high (18.2–18.5 L/min) water flow rates, respectively. In addition, parallel and serial arrangement of the water-to-air heater in the trailer was tested to identify the effects of arrangement on the changes in water temperature and effectiveness of the pilot-scale STHE system.

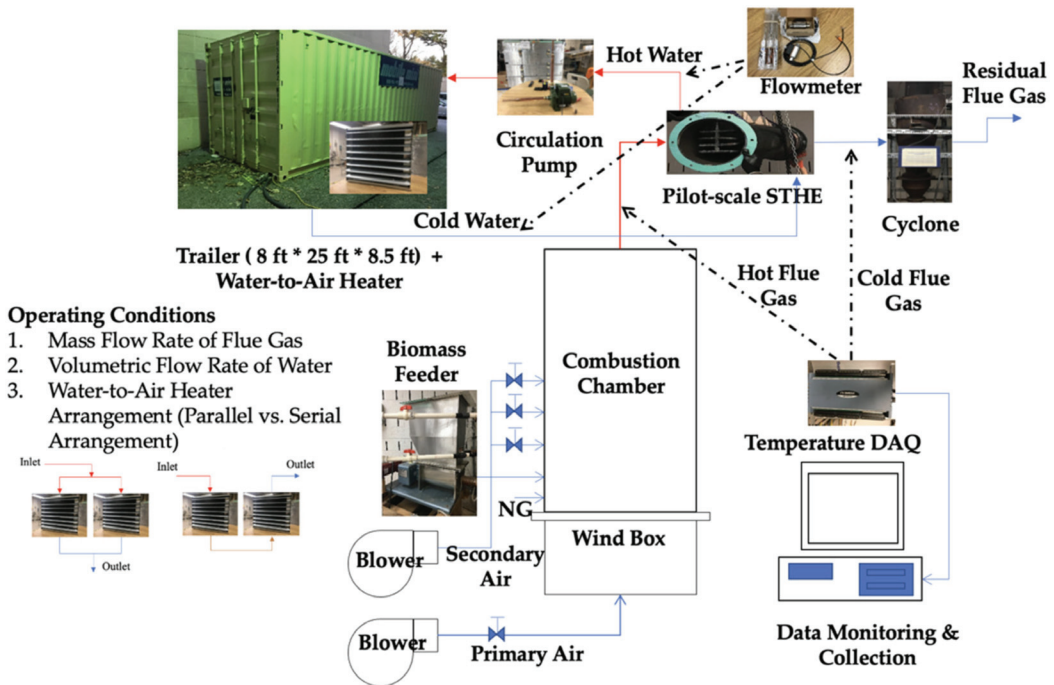


Figure 3. Experimental setup and operating conditions for the pilot-scale STHE system evaluation.

### 3. Results and Discussion

#### 3.1. Estimation of Specific Heat of Flue Gas during Co-Combustion Process

Theoretical co-combustion reaction for carbon, hydrogen, and sulfur in the poultry litter and natural gas under variable EA was calculated using the mass balance equation [15,33]. Theoretically, complete co-combustion of 5.76 kg/h of poultry litter and 0.69 kg/h of natural gas is calculated to require 34.88 kg/h to 52.33 kg/h air to achieve complete combustion and thereby produce 7.74 kg/h carbon dioxide ( $\text{CO}_2$ ), 3.41 kg/h water ( $\text{H}_2\text{O}$ ), and 0.12 kg/h sulfur dioxide ( $\text{SO}_2$ ) along with nitrogen ( $\text{N}_2$ ) in the amount of 27.56 to 41.34 kg/h and oxygen ( $\text{O}_2$ ) in the amount of 0 to 5.49 kg/h. Figure 4 summarizes the composition of major combustion products (in wt. %) during the co-combustion process at EA ratios between 1.0 to 1.5. The composition of  $\text{H}_2\text{O}$  ranged from 5.87% to 8.79%,  $\text{CO}_2$  from 13.32% to 19.93%, and  $\text{SO}_2$  from 0.21% to 0.31%, along with unreacted 70.97 to 71.74%  $\text{N}_2$  and 0 to 9.46%  $\text{O}_2$  in the flue gas. Results showed that changes in  $\text{SO}_2$  and  $\text{N}_2$  were not obvious when EA increased from 1.0 to 1.5. However, weightings of  $\text{CO}_2$  and  $\text{H}_2\text{O}$  were found to decrease while  $\text{O}_2$  weightings increased.

Figure 5 shows specific heat of flue gas during a poultry litter and natural gas co-combustion process range from 1.063 to 1.338 kJ/kg·K, 1.058 to 1.326 kJ/kg·K, 1.054 to 1.315 kJ/kg·K, 1.051 to 1.305 kJ/kg·K, 1.047 to 1.296 kJ/kg·K, and 1.044 to 1.288 kJ/kg·K for EA ratios of 1.0, 1.1, 1.2, 1.3, 1.4, and 1.5, respectively under constant flue gas temperature. It was found that the specific heat of flue gas during the co-combustion process of poultry litter and natural gas decreased with increasing EA ratios. Coskun et al. [15] also investigated the effects of EA ratio between 1.0 to 2.5 on the specific heat of flue gas during the combustion process of fossil fuels, including natural gas, fuel oil, and flame coal. Both studies observed that the specific heat of flue gas decreased when EA was increased across different types of fuel. Combined with the observation from Figure 4, increasing EA decreased the composition of  $\text{H}_2\text{O}$  and  $\text{CO}_2$  while the percentage of  $\text{O}_2$  increased, resulting in lower specific heat values. This is because both  $\text{H}_2\text{O}$  and  $\text{CO}_2$

have a higher specific heat than O<sub>2</sub> [16]. On the contrary, it was found that the specific heat of flue gas during the poultry litter co-combustion process increased by increasing flue gas temperature from 0 to 1000 °C (equivalent to 273.15 to 1273.15 K) at constant EA ratios. As the flue gas reaches higher temperatures, vibrational and kinetic energy also increased, thereby requiring more thermal energy, and ultimately raising specific heat values in the process. It was not surprising that the effect of flue gas temperature and EA on specific heat were inversely related because EA lowers combustion efficiency and flame temperature during co-combustion. Many previous research studies concluded that flue gas temperature and EA had an opposite relationship during the biomass and fossil fuel combustion processes [22,34]. Moreover, it was found that specific heat of poultry litter and natural gas co-combustion had a range of 1.044 to 1.338 kJ/kg·K, which is slightly smaller than the specific heat of natural gas combustion (1.11 to 1.43 kJ/kg·K) due to different chemical compositions of fuels, such as lower carbon and hydrogen contents of poultry litter compared to natural gas. It was also known that specific heat of air was 1.006 kJ/kg·K at 273.15 °K (0 °C) and 1.184 kJ/kg·K at 1,273.15 °K (1000 °C) [16]. This confirmed that the specific heat of flue gas was slightly higher than the specific heat of air because of the difference in composition, whereby flue gas had a higher portion of H<sub>2</sub>O and CO<sub>2</sub> compared to air. These results suggested that one could predict the specific heat of flue gas based on the fuel compositions, EA, and flue gas temperature.

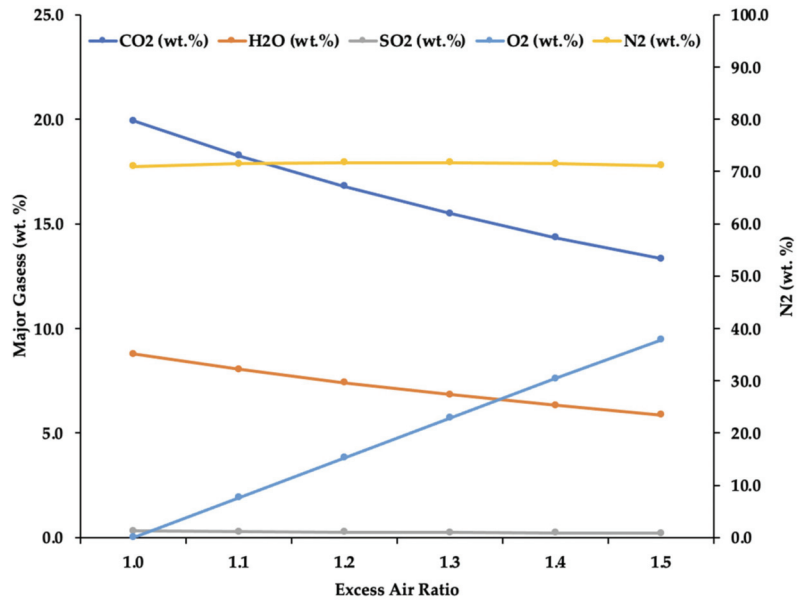


Figure 4. Gas composition in the flue gas under various EA ratios.

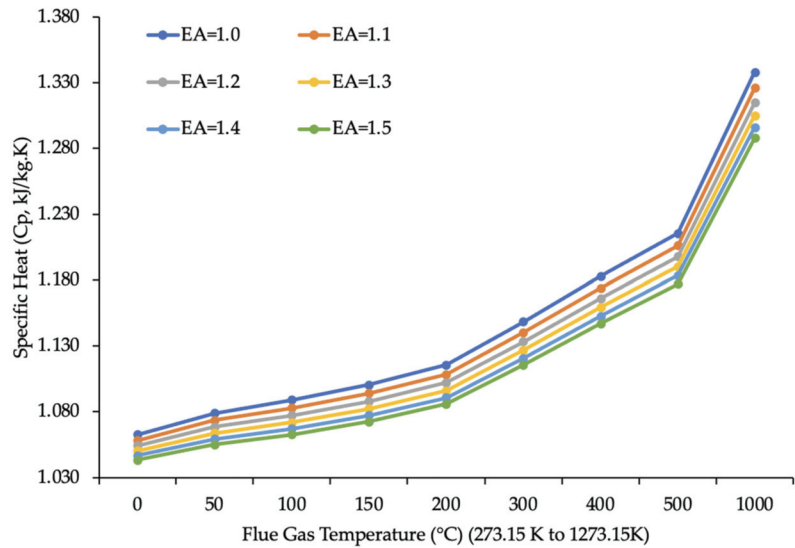


Figure 5. Specific heat of flue gas under various EA ratios and flue gas temperatures.

3.2. Estimation and Comparison of Overall Heat Transfer Coefficient

In the laboratory experiment, co-combustion of 5.76 kg/h of poultry litter and 0.69 kg/h of natural gas under variable EA ratios were performed in the lab-scale SFBC chamber. Table 2 summarizes experimental results of the inlet (entering the SHTE) and outlet (exiting the STHE) flue gas temperature, inlet and outlet water temperature, mass flow rate of flue gas, and calculated specific heat of flue gas at average inlet and outlet temperatures of flue gas during the poultry litter and natural gas co-combustion process. It was found that heat load was between 31.6 to 39.1 MJ/h, CMTD was between 201.8 to 223.6 °C, and overall heat transfer coefficient ( $U_1$ ) for the pilot-scale STHE was between 42.1 to 46.9 W/m<sup>2</sup>K using the first method (Equations (1)–(5)).

Table 2. Estimation of overall heat transfer coefficients ( $U_1$ ) using the first method.

Flue Gas Temp. (°C)		$m_{flue\ gas}$	Water Temp. (°C)		$C_p$ at Avg. Temp.	Heat Load	CMTD	$U_1$
Inlet	Outlet	kg/h	Inlet	Outlet	kJ/kgK	MJ/h	°C	W/m <sup>2</sup> K
479.0	126.0	80.1	42.2	46.7	1.118	31.6	201.8	42.1
489.0	130.0	89.5	43.3	47.8	1.122	36.1	207.0	46.8
492.0	135.0	89.5	44.4	48.9	1.125	35.9	210.9	45.8
474.0	136.0	89.5	45.0	49.4	1.119	33.9	205.7	44.2
489.0	144.0	89.5	46.1	50.6	1.127	34.8	215.8	43.3
499.0	150.0	98.8	46.1	51.1	1.132	39.1	223.6	46.9
489.0	150.0	98.8	46.1	50.6	1.129	37.8	220.7	46.0
481.0	151.0	98.8	46.1	51.1	1.127	36.7	218.9	45.1

Table 3 summarizes the estimation results of the overall heat transfer coefficient ( $U_2$ ) using the second approach (Equations (6)–(9)). It can be observed that convective heat transfer coefficient at shell-side ( $h_1$ ) ranged from 42.7 to 51.0 W/m<sup>2</sup>K and is much smaller than measurements taken at the tube side ( $h_2$ , close to 232 W/m<sup>2</sup>K). This is because the flue gas on the shell side had a lower thermal conductivity than the water on the tube side. It was found that the effects of conduction at the tube wall were  $4.13 \times 10^{-6}$  m<sup>2</sup>K/W, and fouling was estimated to be 0.0018 m<sup>2</sup>K/W. To that end, a combination of these effects

resulted in the overall heat transfer coefficient that measured between 33.9 to 39.0 W/m<sup>2</sup>K using the second method.

**Table 3.** Estimation of overall heat transfer coefficients ( $U_2$ ) using the second method.

$h_i$ (W/m <sup>2</sup> K)	$h_o$ (W/m <sup>2</sup> K)	$U_2$ (W/m <sup>2</sup> K)	$U_1$ (W/m <sup>2</sup> K)	$U_{est.}$ (W/m <sup>2</sup> K)	Errors (%)	
42.73	235.0	33.9	42.1	34.3		
46.8	235.57	36.5	46.8	38.1		
46.87	236.1	36.5	45.8	37.3	ABE <sup>1</sup> = 0.08	AAE <sup>2</sup> = 2.39
46.73	236.37	36.5	44.2	36		
46.92	236.92	36.6	43.3	35.3		
51.0	237.0	39.0	46.9	38.2		
50.84	236.92	38.9	46	37.5		3.73
50.77	237.0	38.9	45.1	36.7		5.60

<sup>1</sup> ABE = average bias error; <sup>2</sup> AAE = absolute bias error.

The values from the second method,  $U_2$ , were slightly lower than the overall heat transfer coefficient from the first method,  $U_1$  (between 42.1 and 46.9 W/m<sup>2</sup>K). Abdulmumuni et al. [13] also found that the overall heat transfer coefficient was 201.0 W/m<sup>2</sup>K when using the first method, thereby exceeding the 98.1 W/m<sup>2</sup>K heat transfer coefficient associated with using the second method. A possible reason for this difference between the two methods is that the first approach makes a rough estimation of the heat transfer area where it only considers the surface area of tubes and connections between the tubes. Other possible heat transfer areas, such as the segmental baffles and shell in the STHE system, were ignored. In addition, heat loss from the shell surface to the environment via radiation was also ignored. The second method, on the other hand, was more comprehensive and required more data, such as density, kinetic viscosity, thermal conductivity at different temperatures for flue gas and water derived from the thermodynamics tables. Therefore, the second method was widely adopted for our heat transfer studies for optimal accuracy with tedious calculations.

Based on results from the first six data sets in Tables 2 and 3, we found that there was a correlation factor of 0.814 between  $U_1$  and  $U_2$ . Therefore, this study suggests an approach that uses a simple calculation process using the first method to estimate the overall heat transfer coefficient,  $U_{est.} = 0.814U_1$ . Absolute average error (AAE) and average bias error (ABE) were also used to evaluate the accuracy and suitability of regression model applications [35]. It was found that this simple model had lower estimation errors, ABE of 0.08% and AAE of 2.39%. The last two data sets were used to validate the results, whereby errors were measured at 3.7% and 5.6%, respectively. This confirms that this simplified model can be used to estimate the overall heat transfer coefficients for a pilot-scale STHE system during a poultry litter and natural gas co-combustion process.

### 3.3. Effect of Flue Gas Mass Flow Rate on the Shell Side

As shown in Figure 6, the overall heat transfer coefficient, heat loss of flue gas, heat gain of water increased from 31.9 to 37.5 W/m<sup>2</sup>K, 18.44 to 37.82 MJ/h, and 11.10 to 20.46 MJ/h, respectively, by increasing the mass flow of flue gas from 61.3 to 98.8 kg/h, for the case of poultry litter at 5.76 kg/h. Similar results were found when the overall heat transfer coefficient, the heat loss of flue gas, heat gain of water was increased from 21.3 to 48.9 W/m<sup>2</sup> K, 21.27 to 48.91 MJ/h, 12.16 to 25.71 MJ/h, respectively, by increasing the mass flow of flue gas from 62.4 to 109.0 kg/h, for the case of poultry litter at 6.81 kg/h. Increments in mass flow rate of flue gas on the shell side increased fluid velocity and the Reynolds number and convective heat transfer on the shell side, which ultimately resulted in the increase in the overall heat transfer coefficient associated with the STHE system. In addition, the heat load of flue gas was increased by increasing the mass flow rate of flue gas because the increasing feeding rates of poultry litter elevated heating values



of fuels while releasing more heat into the flue gas during co-combustion. As a result of heat load increments on the shell side, the heat gain of water from the tube side was also increased. It was found that effectiveness ranged between 48.7% and 77.8% for the case of poultry litter at 5.76 kg/h, while effectiveness ranged between 46.7% to 61.7% for the case of poultry litter at 6.81 kg/h. Effectiveness was slightly lower at higher poultry litter feeding rates because heat loss of flue gas increased between 2.83 to 9.99 MJ/h by increasing feeding rate while heat gain of water was relatively small (about 1.06–5.26 MJ/h) by keeping constant for the water flow rate. It also showed that similar overall heat transfer (between 30 and 40W/m<sup>2</sup> K) with higher efficacy was achieved at a lower feeding rate of poultry litter (5.76 kg/h). These results support the use of a lower feeding rate of poultry litter at 5.76 kg/h and further investigating effect of water flow rate on the tube side on the system performance.

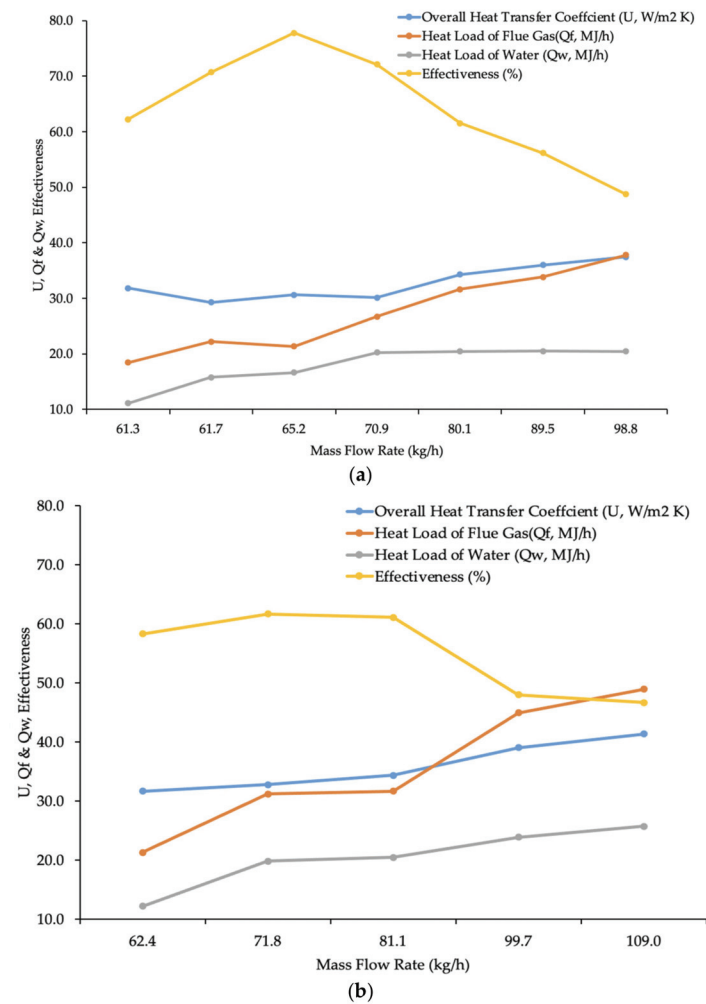


**Figure 6.** Performance of the STHE under various mass flow rates of flue gas on the shell side. (a) Feeding rate of poultry litter at 5.76 kg/h. (b) Feeding rate of poultry litter at 6.81 kg/h.

### 3.4. Effect of Water Flow Rate in Tube Side

As shown in Figure 7, the overall heat transfer coefficient of the pilot-scale STHE system was between 17.9 to 27.0 W/m<sup>2</sup> K, 27.8 to 35.6 W/m<sup>2</sup> K, and 36.9 to 40.1 W/m<sup>2</sup> K for low, medium, and high flow rates, respectively. It was also discovered that higher water flow rates had relatively higher overall heat transfer coefficients. Results also indicated that the CMTD increased from 214.8 to 232.8 °C at lower flow rates, 177.8 to 235.8 °C at medium flow rates, and 161.6 to 218.2 °C at high flow rates, after 160 min of the co-combustion process. Lower CMTD coincides with higher overall heat transfer at a high flow rate (18.2–18.5 L/min) within the same combustion time. In the meantime, higher water flow rates on the tube side generated high velocity and turbulence flow with a high Reynolds number and convective heat transfer coefficients on the tube side, ultimately leading to a higher overall heat transfer coefficient. An interesting trend is observed where the overall heat transfer coefficient was increased at a lower flow rate while overall heat transfer coefficients were decreased at both medium and high flow rate with increasing combustion times. Ultimately, the gap became smaller after 160 min poultry litter and natural gas co-combustion processes.

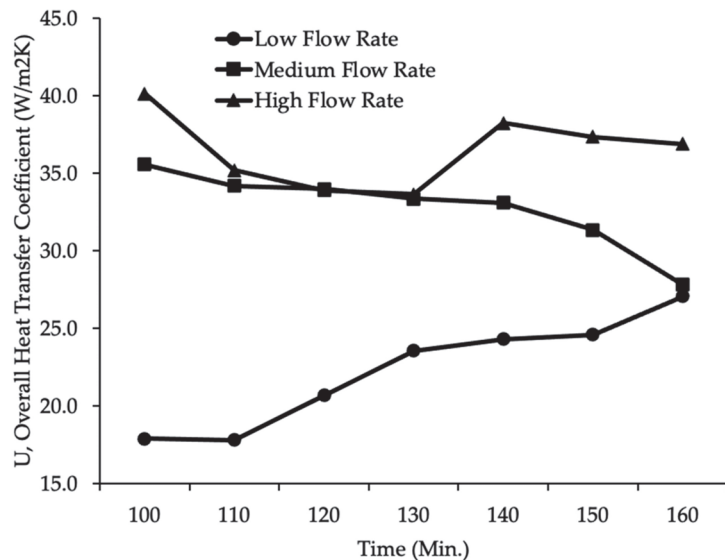
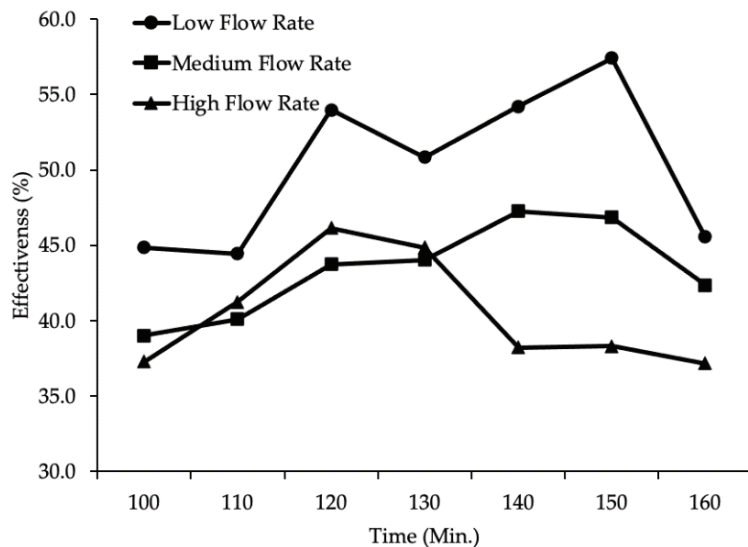


Figure 7. Overall heat transfer coefficients under various water flow rates on the tube side.

As shown in Figure 8, the effectiveness of the pilot-scale STHE system was further analyzed and ranged from 0.444 and 0.574 for low water flow rate, 0.390 to 0.473 for medium water flow rate, and 0.373 to 0.461 for high water flow rate. It was found that the effectiveness of the pilot-scale STHE system decreased when water flow rates were increased. It is postulated that the medium and higher water flow rates reduced the residence time of water on the tube and passed tube sections without effectively gaining heat from hot flue gas on the shell side. Experimental results indicated that inlet temperature of cold water on the tube side increased from 20 to 47.8 °C for low water flow rate, 45.0 °C for medium flow rate, and 45.0 °C for high flow rate, after 160 min co-combustion process. Therefore, the low flow rate achieved a high inlet temperature of the cold fluid (about 2.8 °C higher) and thereby caused a lower temperature difference with an inlet temperature of hot flue gas (around 504 °C), ultimately reducing the maximum possible heat transfer rate ( $Q_{max}$ ). On the other hand, the actual heat transfer rate ( $Q_{actual}$ ) increased by 55.1% (from 13.62 to 21.12), 37.5% (from 16.04 to 22.06), and 35.1% (from 15.05 to 20.34) for low, medium, and high flow rate, respectively. Thus, a low flow rate is the optimal water flow

rate that enabled appropriate velocity and enough residence time of cold water on the tube side to gain heat from hot flue gas in the shell. In the meantime, a low flow rate provided a lower maximum possible heat transfer rate with a higher actual heat transfer rate to quickly achieve heat equilibrium between the two mediums and ultimately increase the effective performance of the pilot-scale STHE system. The current study concluded that the pilot-scale STHE system had an optimal heating performance under the lowest water flow rates (13.7–14.1 L/min), while the lab-scale STHE system experienced optimal performance under different water flow rates (about 6.44 L/min) [28]. Thus, these results infer that optimal water flow rates should be found for different size and capacity STHE systems by controlling mass flow rates on the tube side.



**Figure 8.** Effectiveness under various water flow rates on the tube side.

### 3.5. Effect of Parallel and Serial Arrangement of Water-to-Air Heaters

As shown in Figure 9, it was found that the inlet temperature of the water-to-air heater increased from 20 to 49.4 °C under a parallel arrangement, while it increased to 45.0 °C under serial arrangement after 160 min co-combustion process. In the meantime, the parallel arrangement increased trailer temperature from 10.6 to 82.2 °C, while the serial arrangement increased trailer temperature to 77.9 °C under similar outside temperature (between 8.3 and 9.4 °C). Results show that the parallel arrangement of the water-to-air heaters caused the overall heat transfer coefficient of the STHE to vary from 33.7 to 40.6 W/m<sup>2</sup> K, while a serial arrangement caused the overall heat transfer coefficient of the STHE to range from 28.5 to 34.2 W/m<sup>2</sup>K. To that end, these results indicate that the parallel arrangement performed better than the serial arrangement in terms of the increased inlet temperature of the heater (equivalent to outlet temperature of the STHE), trailer temperature, and the overall heat transfer coefficient. The parallel arrangement of heaters had a slightly faster dynamic response and demonstrated a higher heat transfer rate of 0.5% to 1.9% (about 0.1 to 0.4 MJ/h). Therefore, a parallel arrangement allowed the water-to-air heaters to reject slightly more heat from the hot water into the cold air in the empty trailer and increased trailer temperature by 4.3 °C. Moreover, a parallel arrangement allowed the pilot-scale STHE system to collect more heat from hot flue gas into the cold water being returned.

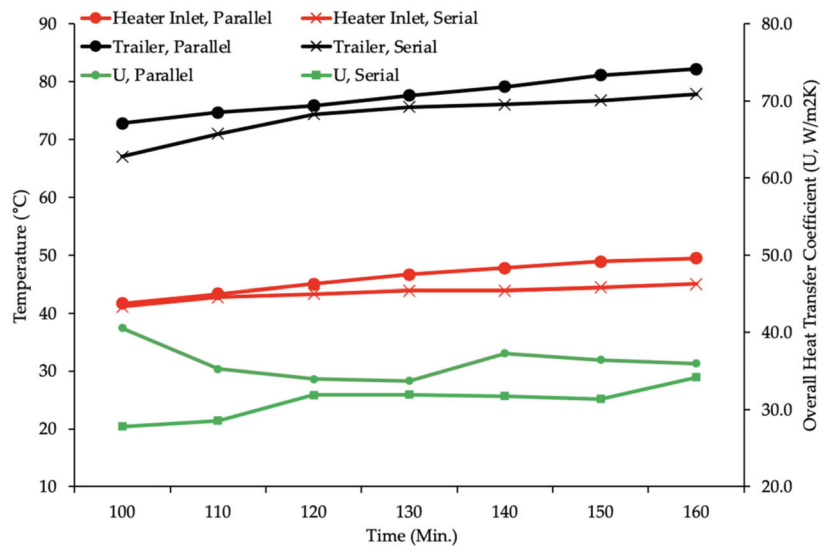


Figure 9. Effect of water-to-air heater arrangement on the system performance.

Limitation of study may include the estimation of flue gas mass flow rate to predict heat transfer rate and assumption of gas compositions during the poultry litter and natural gas co-combustion process to calculate the specific heat of flue gas. In the future study, the mass flow rate of flue gas can be measured using relatively expensive mass flow meters to compare with estimated flue gas mass flow rates and precisely derive heat transfer rate. Real-time gas compositions under various operating conditions of the co-combustion process can also be measured using the emission analyzer and then used to calculate the more accurate specific heat of flue gas that ultimately assist in estimating heat transfer coefficients and evaluate the performance of the STHE system. To reduce a lot of time and vast expenditures on experiment study, CFD and simulation tool can also be adopted to model the STHE system and investigate the heat transfer, pressure drop, velocity distribution using flue gas as one of the working fluids under various operating conditions, such as tube types, tube arrangement, and tube materials.

#### 4. Conclusions

In this study, the pilot-scale shell and tube heat exchanger (STHE) prototype were specially designed and fabricated for the purpose of heat use in the flue gas from the poultry litter and natural gas co-combustion. The pilot-scale STHE prototype implemented twisted tubes and 40-degree segmental baffles to increase the heat transfer coefficient and maximize system performance. A systematic approach was then used to estimate heat transfer coefficients and investigate the performance of the STHE system. First, the specific heat of flue gas was calculated based on fuel properties, EA ratio, and flue gas temperature. Results indicated that the specific heat of flue gas during biomass co-combustion ranging between 1.044 and 1.338 kJ/kg·K was slightly lower than the specific heat of flue gas undergoing fossil fuel combustion. This was because the poultry litter as one of biomass had lower carbon and hydrogen content compared to fossil fuels. Results also indicated that the specific heat of flue gas was increased with decreasing excess air and increasing flue gas temperature. Then, the estimated specific heat was then applied to develop a simplified mathematical model for overall heat transfer coefficient prediction of the pilot-scale STHE system by the integration of two different methods. The developed model was found to have a relatively small average bias error (ABE) of 0.08% and an absolute average error (AAE) of 2.39% to predict the overall heat transfer coefficients. Afterward, the STHE system

performance, including water and trailer temperatures, heat load, effectiveness, and overall heat transfer coefficient, were investigated under the variable operating conditions, such as water flow rates on the shell side, flue gas flow rates on the tube side, and the arrangement of the water-to-air heaters in the trailer. Results showed that the increments in flue gas mass flow rate on the shell side increased fluid velocity and convective heat transfer coefficient, ultimately improving the overall heat transfer coefficient and effectiveness of the STHE system. On the contrary, decreasing the mass flow rate of water on the tube side allowed sufficient residence time and higher actual heat transfer, resulting in a higher overall heat transfer coefficient and effectiveness. Moreover, it was found that a parallel arrangement of the water-to-air heater in the trailer contributed toward an increase in inlet temperature of the heater (equivalent to outlet temperature of the STHE), trailer temperature, and overall heat transfer coefficient when compared to a serial arrangement.

In a future study, analysis of the energy flow and heat transfer from the poultry litter co-combustion into the pilot-scale STHE system, water-to-air heaters, and trailer under variable operating conditions can be performed. In the long-term, hot water production from the STHE using flue gas during the poultry litter and natural gas co-combustion process can contribute to energy savings, reduction in disposal costs and environmental problems, and provide a pathway toward a promising and sustainable waste management option for poultry farmers.

**Author Contributions:** S.W.L. and X.Q. coordinated projects and received grants from the Maryland Industrial Partnerships (MIPS), Maryland Department of Natural Resources (DNR), and Office of Technology Transfer (OTT) at Morgan State University. In conceptualization phase, X.Q. conducted the literature reviews and found the research gaps. X.Q. and Y.Y. designed the approach to set up the testing facility. X.Q. and Y.Y. designed, fabricated, and assembled prototype with major components. X.Q. and Y.Y. collected and performed formal analysis of experimental results. X.Q. wrote the original draft manuscript. S.W.L. and X.Q. reviewed, edited, and provided his constructive comments and suggestions to improve the quality of the article. S.W.L. supervised and coordinated project. All authors have read and agreed to the published version of the manuscript.

**Funding:** This research was supported and partially funded by the Maryland Industrial Partnerships (MIPS), Maryland Department of Natural Resources (DNR), and Office of Technology Transfer (OTT) at Morgan State University on the subject of space heating system development for the poultry house.

**Institutional Review Board Statement:** Not applicable.

**Informed Consent Statement:** Not applicable.

**Acknowledgments:** Authors would like to acknowledge the MIPS office and DNR for an opportunity for the subject research and partial financial support. This research behind it would not have been possible without an efficient collaboration of our industry partner, CyKloburn Technologies, LLC. We are also grateful for the insightful comments offered by the Morgan State University OTT. In addition, the authors would like to appreciate the kind support of the research staff and facilities from the Center for Advanced Energy Systems and Environmental Control Technologies (CAESECT).

**Conflicts of Interest:** The authors declare no conflict of interest.

## Nomenclature

$A$	heat exchanger area ( $\text{m}^2$ )
$c_p$	specific heat ( $\text{J/g}\cdot^\circ\text{C}$ )
$c_{p,f}$	specific heat of flue gas ( $\text{J/g}\cdot^\circ\text{C}$ )
$c_{p,w}$	specific heat of water ( $\text{J/g}\cdot^\circ\text{C}$ )
$C_{min}$	minimum heat capacity rate ( $\text{J/s}\cdot^\circ\text{C}$ )
$CMTD$	corrected effective mean temperature difference ( $^\circ\text{C}$ )

$d_o$	outside diameter of tube (mm)
$D$	diameter (mm)
$D_e$	equivalent diameter (mm)
$\eta_{effectiveness}$	effectiveness (%)
$f_i$	inner fouling factor by water ( $m^2 K/W$ )
$f_o$	outer fouling factor by flue gas ( $m^2 K/W$ )
$F$	temperature efficiency factor
$h$	convective heat transfer coefficient
$h_i$	convective heat transfer coefficient determined by water on tube side ( $W/m^2 K$ )
$h_o$	convective heat transfer coefficient caused by flue gas on shell side ( $W/m^2 K$ )
$k$	thermal conductivity ( $W/m K$ )
$LMTD$	logarithmic mean temperature difference ( $^{\circ}C$ )
$\dot{m}$	mass flow rate (kg/s)
$\dot{m}_f$	mass flow rate of flue gas (kg/s)
$\dot{m}_w$	mass flow rate of water (kg/s)
$Nu$	Nusselt number
$Pr$	Prandtl number
$P_t$	distance between centers of two pipes (mm)
$\dot{Q}$	heat load (J/s)
$\dot{Q}_w$	heat load of water (J/s)
$\dot{Q}_f$	heat load of flue gas (J/s)
$Q_{max}$	maximum possible heat transfer rate (J/s)
$Q_{actual}$	actual heat transfer rate (J/s)
$Re$	Reynolds number
$\rho$	density ( $kg/m^3$ )
$\lambda$	thermal conductivity of the tube material ( $W/m K$ )
$S$	tube wall thickness (m)
$\Delta T$	change in temperature ( $^{\circ}C$ )
$t_1$	water temperature at inlet ( $^{\circ}C$ )
$t_2$	water temperature at outlet ( $^{\circ}C$ )
$T_1$	flue gas temperature at inlet ( $^{\circ}C$ )
$T_2$	flue gas temperature at outlet ( $^{\circ}C$ )
$T_{h,in}$	inlet temperature of hot fluid ( $^{\circ}C$ )
$T_{c,in}$	inlet temperature of cold fluid ( $^{\circ}C$ )
$U_1$	overall heat transfer coefficient, first method ( $W/m^2K$ )
$U_2$	overall heat transfer coefficient, second method ( $W/m^2K$ )
$V$	velocity (m/h)
$\nu$	kinematic viscosity ( $m^2/s$ )

## References

- Master, B.I.; Chunangad, K.S.; Boxma, A.J.; Karl, D.; Stehlik, P. Most frequently used heat exchangers from pioneering research to worldwide applications. *Heat Transf. Eng.* **2006**, *27*, 4–11. [CrossRef]
- Salahuddin, U.; Bilal, M.; Ejaz, H. A review of the advancements made in helical baffles used in shell and tube heat exchangers. *Int. Commun. Heat Mass* **2015**, *67*, 104–108. [CrossRef]
- Duan, Z.; Shen, F.; Cao, X.; Zhang, J. Comprehensive effects of baffle configuration on the performance of heat exchanger with helical baffles. *Nucl. Eng. Des.* **2016**, *300*, 349–357. [CrossRef]
- Dubey, V.V.P.; Verma, R.R.; Verma, P.S.; Srivastava, A.K. Performance analysis of shell and tube type heat exchanger under the effect of varied operating condition. *IOSR J. Mech. Civ. Eng.* **2014**, *11*, 8–17. [CrossRef]
- Li, X.; Zhu, D.; Yin, Y.; Liu, S.; Mo, X. Experimental study on heat transfer and pressure drop of twisted oval tube bundle in cross flow. *Exp. Therm. Fluid Sci.* **2009**, *99*, 251–258. [CrossRef]
- Tan, X.H.; Zhu, D.S.; Zhou, G.Y.; Zeng, L.D. Experimental and numerical study of convective heat transfer and fluid flow in twisted oval tubes. *Int. J. Heat Mass Transf.* **2012**, *55*, 4701–4710. [CrossRef]
- Tan, X.H.; Zhu, D.S.; Zhou, G.Y.; Zeng, L.D. Heat transfer and pressure drop performance of twisted oval tube heat exchanger. *Appl. Therm. Eng.* **2013**, *50*, 374–383. [CrossRef]
- Zhang, J.F.; Li, B.; Huang, W.J.; Lei, Y.G.; He, Y.L.; Tao, W.Q. Experimental performance comparison of shell-side heat transfer for shell-and-tube heat exchangers with middle-overlapped helical baffles and segmental baffles. *Chem. Eng. Sci.* **2009**, *64*, 1643–1653. [CrossRef]

9. Bichkar, P.; Dandgaval, O.; Dalvi, P.; Godase, R.; Dey, T. Study of shell and tube heat exchanger with the effect of types of baffles. *Procedia Manuf.* **2018**, *20*, 195–200. [CrossRef]
10. Thantharate, V.; Zodpe, D.B. Experimental and numerical comparison of heat transfer performance of twisted tube and plain tube heat exchangers. *Int. J. Sci. Eng. Res* **2013**, *4*, 1107–1113.
11. Kasmir, J.; Joshi, S.M. Experimental study of a shell and tube heat exchanger for performance enhancement. In Proceedings of the 2015 International Conference on Technologies for Sustainable Development (ICTSD), Mumbai, India, 4–6 February 2015; pp. 1–3. [CrossRef]
12. Emal, Q.M.; Elena, P. Overall energy balance and heat transfer in a shell and tube heat exchanger. In Proceedings of the ISER 109th International Conference, Ottawa, ON, Canada, 27–28 February 2018.
13. Abdulmumuni, B.; Ayoade, A.; Buhari, O.; Olatunde, A.; Olaniyi, F. Design, fabrication and performance evaluation of a shell and tube heat exchanger for practical application. *Eur. J. Eng. Technol. Res.* **2020**, *5*, 835–845. [CrossRef]
14. Ehyaei, M.A.; Ahmadi, A.; Rosen, M.A.; Davarpanah, A. Thermodynamic Optimization of a Geothermal Power Plant with a Genetic Algorithm in Two Stages. *Processes* **2020**, *8*, 1277. [CrossRef]
15. Coskun, C.; Oktay, Z.U.H.A.L.; Ilten, N. A new approach for simplifying the calculation of flue gas specific heat and specific energy value depending on fuel composition. *Energy* **2009**, *34*, 1898–1902. [CrossRef]
16. Cengel, Y. *Heat and Mass Transfer: Fundamentals and Applications*; McGraw-Hill Higher Education: New York, NY, USA, 2014.
17. Menghini, D.; Marra, F.S.; Allouis, C.; Beretta, F. Effect of excess air on the optimization of heating appliances for biomass combustion. *Exp. Therm. Fluid Sci.* **2008**, *32*, 1371–1380. [CrossRef]
18. Chandok, J.S.; Kar, I.N.; Tuli, S. Estimation of furnace exit gas temperature (FEGT) using optimized radial basis and back-propagation neural networks. *Energy Convers. Manag.* **2008**, *49*, 1989–1998. [CrossRef]
19. El-Shafie, M.; Bassiouny, M.K.; Kambara, S.; El-Behery, S.M.; Hussien, A.A. Design of a heat recovery unit using exhaust gases for energy savings in an absorption air conditioning unit. *Appl. Therm. Eng.* **2021**, 117031. [CrossRef]
20. Patel, M.; Zhang, X.; Kumar, A. Techno-economic and life cycle assessment on lignocellulosic biomass thermochemical conversion technologies: A review. *Renew. Sustain. Energy Rev.* **2016**, *53*, 1486–1499. [CrossRef]
21. Saidur, R.; Abdelaziz, E.A.; Demirbas, A.; Hossain, M.S.; Mekhilef, S. A review on biomass as a fuel for boilers. *Renew. Sustain. Energy Rev.* **2011**, *15*, 2262–2289. [CrossRef]
22. Qian, X. Statistical Analysis and Evaluation of the Advanced Biomass and Natural Gas Co-Combustion Performance. Ph.D. Thesis, Morgan State University, Baltimore, MD, USA, 2019.
23. Lynch, D.; Henihan, A.M.; Bowen, B.; Lynch, D.; McDonnell, K.; Kwapinski, W.; Leahy, J.J. Utilisation of poultry litter as an energy feedstock. *Biomass Bioenergy* **2013**, *49*, 197–204. [CrossRef]
24. Zhu, S.; Lee, S.W. Co-combustion performance of poultry wastes and natural gas in the advanced Swirling Fluidized Bed Combustor (SFBC). *Waste Manag.* **2005**, *25*, 511–518. [CrossRef]
25. Si, Q.; Xia, Q.; Liang, L.H.; Li, D.X. Investigation of heat transfer and flow resistance on twisted tube heat exchanger. *J. Chem. Ind. Eng. (China)* **1995**, *46*, 601–608.
26. Davarpanah, A.; Zarei, M.; Valizadeh, K.; Mirshekari, B. CFD design and simulation of ethylene dichloride (EDC) thermal cracking reactor. *Energ. Sources Part A* **2019**, *41*, 1573–1587. [CrossRef]
27. Valizadeh, K.; Farahbakhsh, S.; Bateni, A.; Zargarian, A.; Davarpanah, A.; Alizadeh, A.; Zarei, M. A parametric study to simulate the non-Newtonian turbulent flow in spiral tubes. *Energy Sci. Eng.* **2020**, *8*, 134–149. [CrossRef]
28. Wang, W.; Shuai, Y.; Li, B.; Li, B.; Lee, K.S. Enhanced heat transfer performance for multi-tube heat exchangers with various tube arrangements. *Int. J. Heat Mass Transf.* **2021**, *168*, 120905. [CrossRef]
29. Qian, X.; Yang, Y.; Lee, S.W. Design and Evaluation of the Lab-Scale Shell and Tube Heat Exchanger (STHE) for Poultry Litter to Energy Production. *Processes* **2020**, *8*, 500. [CrossRef]
30. Qian, X.; Lee, S.; Chandrasekaran, R.; Yang, Y.; Caballes, M.; Alamu, O.; Chen, G. Electricity Evaluation and Emission Characteristics of Poultry Litter Co-Combustion Process. *Appl. Sci.* **2019**, *9*, 4116. [CrossRef]
31. Katsaros, G.; Sommersacher, P.; Retschitzegger, S.; Kienzl, N.; Tassou, S.A.; Pandey, D.S. Combustion of poultry litter and mixture of poultry litter with woodchips in a fixed bed lab-scale batch reactor. *Fuel* **2021**, *286*, 119310. [CrossRef]
32. Kays, W.M.; Perkins, H.C. *Handbook of Heat Transfer*; Rohsenow, W.M., Hartnett, J.P., Eds.; McGraw-Hill: New York, NY, USA, 1972.
33. Moran, M.J.; Shapiro, H.N.; Boettner, D.D.; Bailey, M.B. *Fundamentals of Engineering Thermodynamics*; John Wiley & Sons: New York, NY, USA, 2010.
34. Houshfar, E.; Skreiberg, Ø.; Løvås, T.; Todorović, D.; Sørum, L. Effect of excess air ratio and temperature on NO<sub>x</sub> emission from grate combustion of biomass in the staged air combustion scenario. *Energy Fuels* **2011**, *25*, 4643–4654. [CrossRef]
35. Qian, X.; Lee, S.; Soto, A.-M.; Chen, G. Regression model to predict the higher heating value of poultry waste from proximate analysis. *Resources* **2018**, *7*, 39. [CrossRef]

## Article

# Numerical Investigation of the Flow and Infrared Radiation Characteristics of Nozzles with Transverse Jets of Different Shapes

Bo Zhang \*, Ziqiang Lin, Jun Zhang, Sheng Yang and Honghu Ji

Jiangsu Province Key Laboratory of Aerospace Power System, College of Energy and Power, Nanjing University of Aeronautics and Astronautics, Nanjing 210016, China; lzq2002063@nuaa.edu.cn (Z.L.); zhangjun5563@nuaa.edu.cn (J.Z.); yang\_s@nuaa.edu.cn (S.Y.); jhhpe@nuaa.edu.cn (H.J.)

\* Correspondence: zhangbo\_pe@nuaa.edu.cn

**Abstract:** The hot jet of an aero engine is one of the main radiation sources of infrared detectors in 3–5 microwave bands. Transverse jets were introduced into a hot jet to enhance mixing and reduce the infrared radiation characteristics. This proved to be a high-efficiency and low-resistance infrared suppression technology. The steady-state distribution of temperature data was simulated, which was needed in the thermal radiation calculation. The radiation characteristics were calculated based on the anti-Monte Carlo method in 3–5 microwave bands. The mechanics of enhanced mixing by a rectangular nozzle or transverse jets was investigated with the LES simulation. Compared with an axisymmetric nozzle, a rectangular nozzle induced abundant counter-rotating vortex pairs (CVP), hairpins, shears, and helical vortexes, which resulted in significant mixing enhancement and infrared radiation decrease of the hot jets. Further, circumferential transverse jets of different types were introduced downstream of the nozzle. These jets enhanced the mixing and reduced the infrared radiation in the 3–5  $\mu\text{m}$  band. The mixing characteristics of these different schemes were studied in detail. Large-scale vortices formed on the windward portion of the hot jet boundary under the effect of the transverse jets, which caused strong CVP structures. They also resulted in hairpin vortexes, shear vortexes, and helical vortexes appearing earlier and occurring more frequently than with nozzles without transverse jets. The enhanced mixing caused by the transverse jets led to an increase in temperature decay and a decrease in infrared radiation in the 3–5  $\mu\text{m}$  band. Further, transverse jets of different geometrical shapes (rectangular, cube, and circular schemes) achieved different mixing characteristics, and the rectangular transverse jets allowed the most significant mixing for the largest Q criterion value.

**Citation:** Zhang, B.; Lin, Z.; Zhang, J.; Yang, S.; Ji, H. Numerical Investigation of the Flow and Infrared Radiation Characteristics of Nozzles with Transverse Jets of Different Shapes. *Processes* **2022**, *10*, 763. <https://doi.org/10.3390/pr10040763>

Academic Editor: Alfredo Iranzo

Received: 3 March 2022

Accepted: 8 April 2022

Published: 13 April 2022

**Publisher's Note:** MDPI stays neutral with regard to jurisdictional claims in published maps and institutional affiliations.



**Copyright:** © 2022 by the authors. Licensee MDPI, Basel, Switzerland. This article is an open access article distributed under the terms and conditions of the Creative Commons Attribution (CC BY) license (<https://creativecommons.org/licenses/by/4.0/>).

**Keywords:** circular to rectangular; transverse jets; infrared radiation; mixing enhancement

## 1. Introduction

With the rapid development of the detection technology of infrared (IR), the IR signature of aero engine has become a serious problem. From the point of view of aircraft survivability, IR signatures within two atmospheric windows, 3–5 and 8–14  $\mu\text{m}$ , are the most important. In the waveband of 3–5  $\mu\text{m}$ , the hot components (including nozzles, turbine blades, cones, afterburners) of an aero engine exhaust system and the hot plume are the major sources of IR emission.

Aero engines are the main infrared radiation aircraft sources in the 3–5  $\mu\text{m}$  band, while the thermal components and exhaust plumes are the main infrared radiation sources of aero engines. The hot components have large infrared radiation, which can mainly be detected in relatively small backward angular regions of the nozzle. Due to the omnidirectional radiation of the plumes, they can be detected from almost any angle in the hemispherical space [1].



When a plume travels downstream, its high temperature region spreads in both axial and radial directions through the exchanging process of heat and momentum between the plume and the nearby gas. Thermal radiation increases with the enlarged surface and volume of the high-temperature region [2,3]. By increasing the mixing of the plume and the ambient air, temperature attenuation becomes larger, and the thermal radiation of the plume significantly decreases [4].

Jet mixing enhancement methods can be classified in two major categories: passive flow control and active flow control technologies. The passive flow control methods include solid tab, lobe nozzle, and chevron nozzle [5–11]. These techniques can effectively alter the primary jet shear layers, but the performance of the engine exhaust system will decrease with these off-design conditions. The passive flow control methods also have a thrust penalty on the exhaust system.

Based on passive flow control technologies, active flow control technologies were gradually developed [12–15]. Mature active flow control methods of jet mixing enhancement include steady and pulsed jet technologies. Behrouzi and McQuirk compared the mixing effects of solid small tab, steady state, and pulse transverse jets on the near-field jet of an axis-symmetric nozzle [16]. Their results indicated that the pulse transverse jet showed the best effect. Knowles and Saddington summarized these approaches in [3].

Gevorkyan et al. and Kamran et al. carried out several experiments on jets [17,18]. Their results showed that the mixing characteristics of the plume could be effectively improved by transverse jets. In addition, they preliminarily examined the mixing mechanics. Active flow control methods were based on the local energy of transverse jets into the main flow. These techniques disturbed the jet flow shear layers and then generated large-scale structures which promoted jet mixing [19,20].

Many scholars focused on the influence of the shape and configuration parameters of transverse jets, which greatly affect the mixing characteristics. McClinton experimentally investigated the influence of the injection angle and concluded that, with the decrease of the injection angle, the penetration height becomes larger, and the mixing rate increases [21]. Greta [6] drew different conclusions from McClinton [21] through numerical research on the 2-D slot injection. That paper showed that, with the decrease of the injection angle, the penetration height becomes smaller, and both the mixing rate and the total pressure loss decrease.

Gruber et al. experimentally investigated the penetration and mixing characteristics in a Mach 2 flow field with three different injection schemes including the vertical injection of a circular hole, the oblique injection of a circular hole, and the vertical injection of an elliptical hole [22]. Zhang Bo numerically investigated the mixing characteristics in supersonic primary flow and subsonic secondary flow and revealed the influence of waves on the mixing layer between supersonic primary flow and subsonic secondary flow from circle injectors [23,24]. Kan Kobayashi carried out research on mixing of the scramjet model with a diamond-shaped injector [25]. Yang carried out investigations on the influence of circular and elliptical transverse-hole jets on the vortex structure [26]. The results showed that the vortex structures in the far field of the two schemes were similar, while the leading-edge vortex pulsation of the elliptic jet in the near field was more intense in the shear layer. The transverse pulsing frequency also plays an important role. Eri carried out a study of the effect of the mixing efficiency and coherent structures by using a large eddy simulation and suggested that the optimal mixing enhancement corresponded to an effective balance between the number and the size of vortex structures [27]. The formation of the counter-rotating vortex pair in the near field of transverse jets and its development in the far field have drawn much attention. However, few studies focusing on the effect of transverse jets on the generation and evolution of downstream vortex structures have been published.

Recently, more and more studies have tended to use the anti-Monte Carlo method in radiation characteristics simulation for its high accuracy and efficiency; this method has gradually replaced the traditional ray-tracing method [28,29].

A circular to rectangular nozzle with an exit with a width-to-height ratio of 2 was designed in this paper, based on the axisymmetric convergent nozzle. Four transverse jets were arranged in the circumferential direction of the rectangular exit. The effects of transverse jets on the mixing and the infrared suppressing characteristics of a hot jet in the 3–5  $\mu\text{m}$  bands were investigated. In addition, the mixing mechanisms were preliminarily analyzed.

## 2. Physical Models

Figure 1 presents the physical models of all CASEs studied in this paper. CASE A (axis-symmetrical nozzle) is shown in Figure 1a. The specific parameters are marked as following:  $D_n$  (Diameter of the nozzle entrance) was 0.1 m,  $D$  (Diameter of the nozzle exit) was  $0.8 D_n$ , and the length  $L$  was  $1.5 D_n$ . CASE A was set as the basic design. Figure 1b shows CASE B (Circular to rectangular nozzle), with a rectangular exit having an aspect ratio of 2. It has the same length, entrance, and exit area as CASE A. Further, CASE B1 was formed at the base of CASE B, after introducing transverse jets. The diameters of the transverse jets ( $D$ ) were  $0.1 D_n$ , with the same length of  $0.3 D_n$ , and the center of the jets hole was  $0.08 D_n$  downstream of the nozzle exit. Then, the transverse jets' shapes were optimized for the equivalent square and rectangular holes (named CASE B2 and CASE B3, respectively); the specific scheme are shown in Table 1.

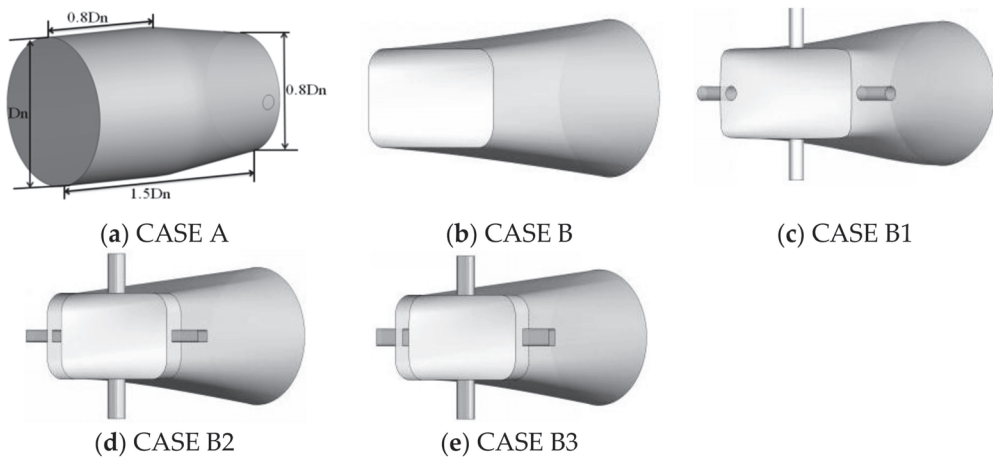


Figure 1. Physical models of CASEs.

Table 1. Illustration of the models.

Model-A	Model-B	Model-B1	Model-B2	Model-B3
Asymmetrical nozzle	Circular-rectangular nozzle	Model-B with Round transversers jets	Model-B With square transversers jets	Model-B With rectangular transversers jets

## 3. Computational Domain and Boundary Conditions

Figure 2 shows the cylindrical computational domain used in this paper. Its diameter was  $16 D_n$ , and the length was  $30 D_n$ . The flow direction was along the x-axis, the wide side was in the y-direction, and the narrow side was in the z-direction.

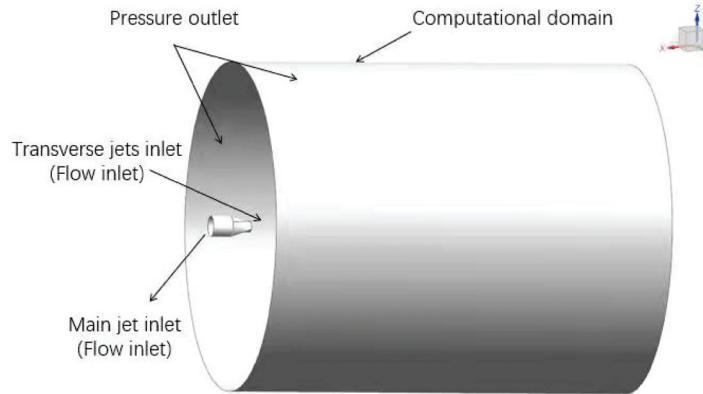


Figure 2. Computational domain.

The calculated boundary conditions were as follows: the mass flow rate of the inlet was 1 kg/s, the pressure was 1.5 bar, the temperature was 600 K, and the mass fractions of CO<sub>2</sub>, CO, and H<sub>2</sub>O were 6.6%, 0.1%, and 2.7%, respectively. The ambient pressure was 100 kPa, and the temperature was 300 K. The wall of the nozzle was gray, with an emissivity of 0.9. The transverse jets had 4 uniform inlets set in the circumferential direction. These jets had a flow rate of 0.01 kg/s each, whose pressure was 210 kPa, and the temperature was 350 K.

#### 4. Meshes Generation and Independence

The software ANSYS ICEM-CFD was used to generate the computational meshes, and ANSYS FLUENT was used as the flow solver. The domain meshes were hexahedral, including four layers close to the nozzle wall. There were about 5.6 million elements in total (Figure 3), which allowed performing a sufficiently precise analysis. A mesh independent test was carried out with different meshes for CASE B, and the results are shown in Figure 4. It was observed that, when the mesh number increased to 5.6 million, the difference of the results was less than 2%. Thus, the meshes used in CASE B proved to be suitable and can be used as a reference for mesh generation in other cases.

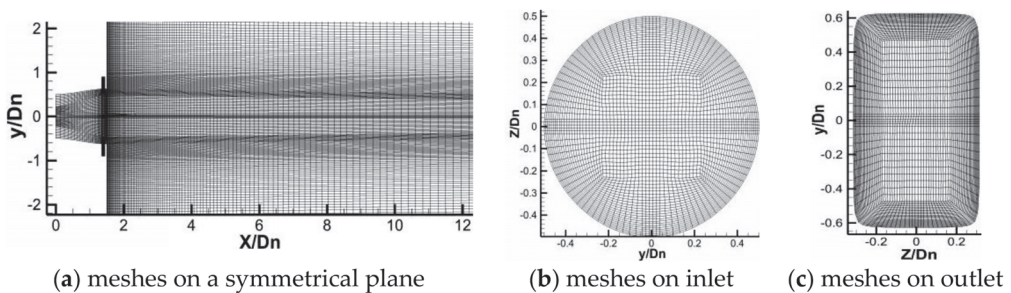
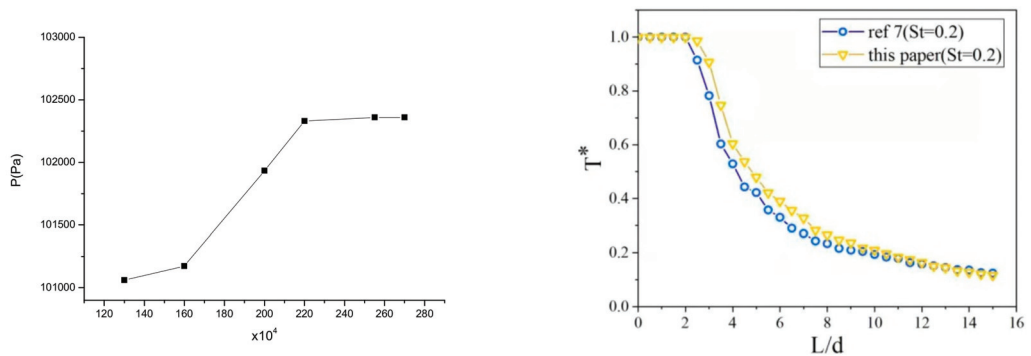


Figure 3. Meshes for flow computation.

In this paper, the numerical simulation method was verified with the data of Ref [7], and the comparative result (Stanton number  $St$  ( $St = Nu / (Pr \cdot Re)$ ) = 0.2 is shown in Figure 4b, which proves the validity of the numerical simulation method.

In Figure 4b,  $T^*$  is a dimensionless parameter to assess the cooling efficiency, which is defined as  $T^* = \frac{T_h - T_\infty}{T_c - T_\infty}$ .  $T_h$  is the temperature of the plume,  $T_c$  is the temperature of the transverse flow, and  $T_\infty$  is the ambient temperature.



(a) Sensitivity as a function of the meshes

(b) Validity of the method in the paper

**Figure 4.** Validity of the meshes and numerical simulation method.

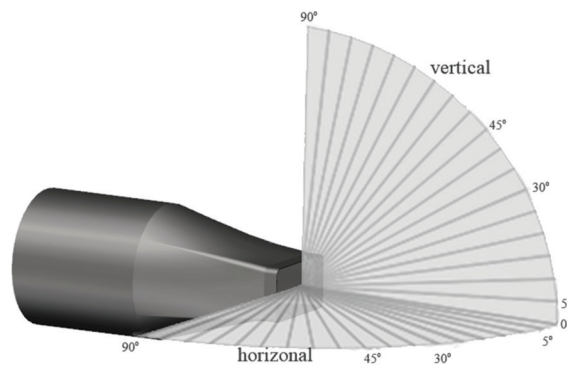
### 5. Numerical Simulation Method

This paper is divided into two parts: the study of the flow field and the study of infrared radiation characteristics. The time-averaged temperature data of different models were simulated by using Reynolds stress equation model (RSM), which were needed for thermal radiation calculation. The radiation characteristics in 3–5  $\mu\text{m}$  bands were calculated based on the anti-Monte Carlo method as in [30].

In order to reveal the mechanism of enhanced mixing with a rectangular nozzle and transverse jet, the flow field was calculated using the Large Eddy Simulation method and the dynamic Smagorinsky model. Instantaneous mixing and the vortex evolution characteristics were simulated, and the evolution of the vortex structure from the two dimensions of time and space was analyzed through Ansys Fluent.

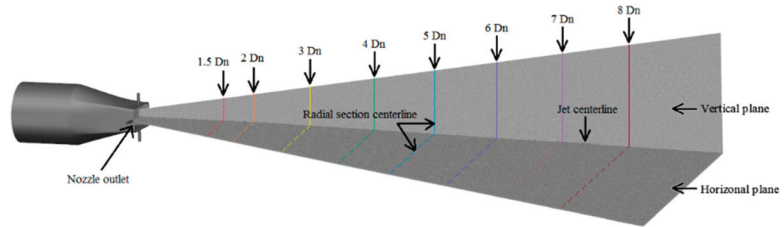
The detection distance was set at 35 m as in previous experiments. The walls are treated as grey walls with an emissivity of 0.9. The HTEMP2000 database was adopted to calculate the atmospheric absorption and emission.

Figure 5 shows the distribution of the infrared radiation detection surfaces. The infrared radiation could be detected from the horizontal detection surface (XOY) and the vertical detection surface (XOZ). The detection points were located at 5° intervals;  $\alpha = 0^\circ$  is the direction of the nozzle axis, and  $\alpha = 90^\circ$  is the direction perpendicular to the nozzle axis.

**Figure 5.** Sketch of the detecting orientations.

## 6. Analysis of the Calculation Results

Figure 6 shows the location of the typical axial sections downstream of the horizontal plane and vertical plane, and the intersections of the axial sections are marked from 1.5 Dn to 8 Dn.



**Figure 6.** Typical downstream sections.

### 6.1. The Distribution of the High-Temperature Zone

Figure 7 shows the distribution of instantaneous temperature contours on different planes of the CASEs, simulated with LES models. The instantaneous temperature contour maps in symmetrical plane of CASE A is shown in Figure 7a, and those in horizontal and vertical planes of CASE B are shown in Figure 7b,c. The temperature contours of the three figures have similar distribution.

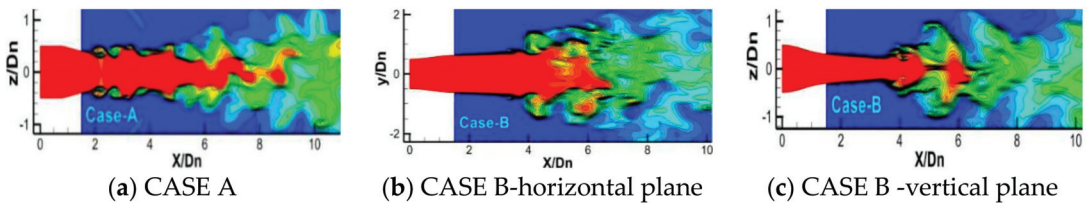


**Figure 7.** Transient temperature contour on planes.

In Figure 7, it can be seen in the field near the hot jet that the jet column remained stable and that the boundary layer of the jet formed an obvious shear vortex structure. With the development of the jet, the jet column became unstable, and the larger vortex structure dissipated into smaller and richer small vortices. The vortices dissipated shorter jet columns and obvious pulsation characteristics.

In order to compare the time-averaged temperature characteristics of different cases, Figure 8a–e show the temperature distributions of CASE A, B, B1, B2, and B3 obtained with the Reynolds stress equation model (RSM). The range of high-temperature zones ( $T > 540$  K) are marked by black vertical lines.

Figure 8a presents the temperature contour distribution for CASE A. Figure 8b presents the temperature contour distribution on the vertical plane for CASE B. The results show agreement with CASE A, while the length of the high-temperature zone decreased.

Figure 8c–e show the influence of the configurations on the transverse jets. The circular transverse jets of CASE-B1 resulted in a compressing influence on the hot jet in the vertical plane. The mixing between transverse jets and hot jet increased, which led to the decay of the high-temperature zone and shortened it. Further, when comparing the different transverse jets, the cube jet (CASE B2) and the rectangular jet (CASE B3) showed similar distributions as that of the circular jet (CASE B1). On the other hand, the lengths of the temperature zones decreased. This was caused by the stronger mixing between the hot jets and the non-axis-symmetrical transverse jets.

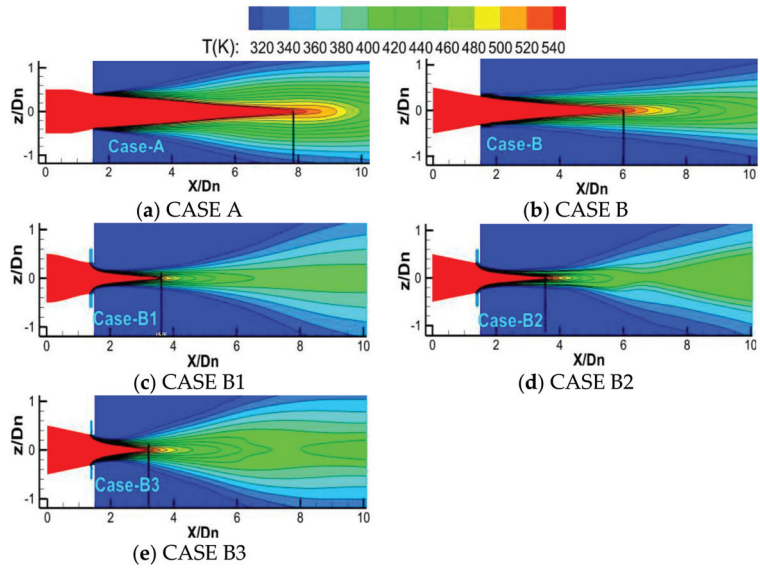


Figure 8. Temperature contour on the vertical plane.

Figure 9a–e present the temperature distributions of the horizontal planes of CASE A–CASE B3. The results are obviously different from those of vertical planes. In Figure 9b, CASE B shows a contour profile of double peaks, which is different from that of CASE A. This observation shows that the mixing area was enlarged, and the mixing between the ambient and the hot jet was strengthened. This mixing led to a decrease in the high-temperature zone. The length of the high-temperature zone on the vertical and horizontal planes are marked with dotted and continuous lines, respectively. CASE B1 and CASE B2 also showed similar distributions, while CASE B3 showed a reduced high-temperature zone on both vertical and horizontal planes.

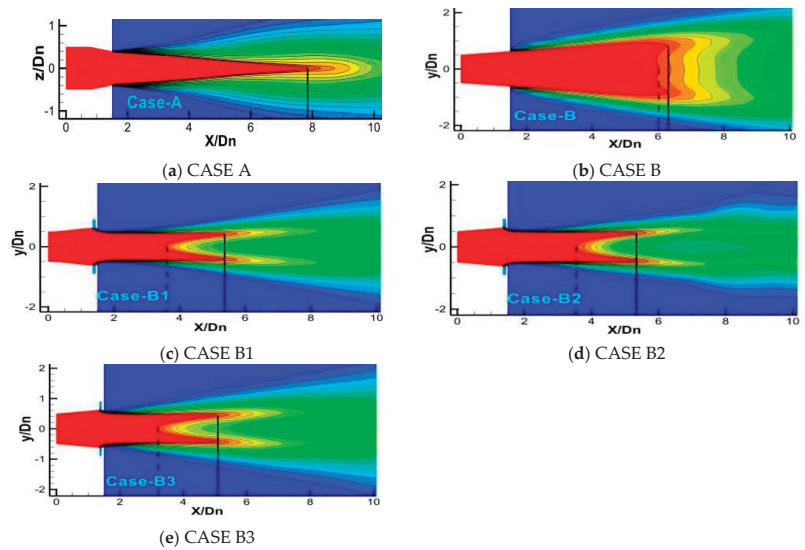
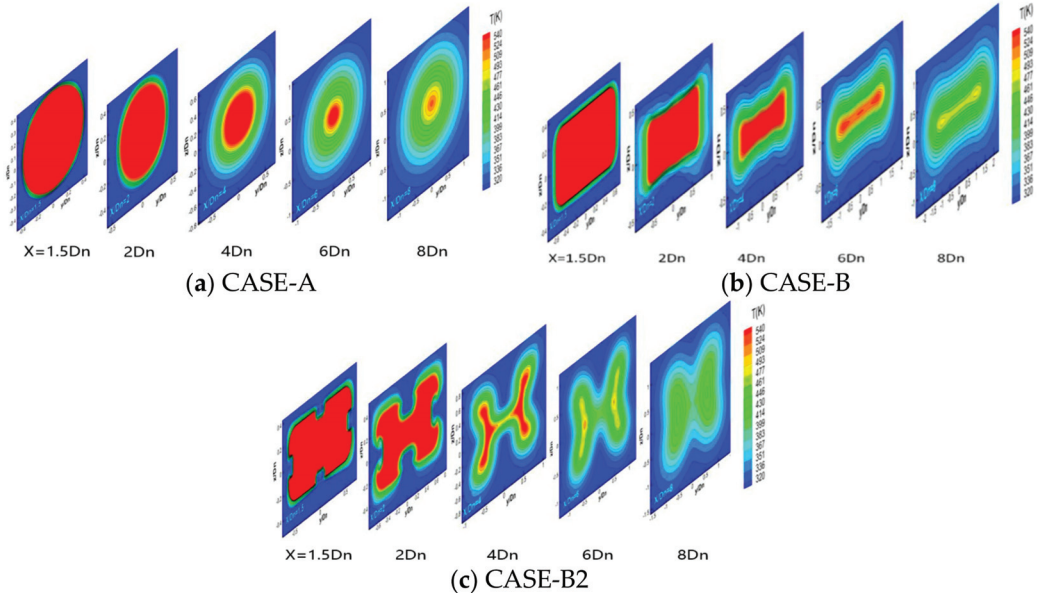


Figure 9. Mean temperature contour on the horizontal plane.

Figure 10 shows the time-averaged temperature distribution of the axial sections for different cases. Compared with CASE A (Figure 10a), the temperature contour map of CASE B (Figure 10b) showed a flatter, rectangular profile, which resulted in a larger contacting area with ambient gas and a stronger mixing ability for the ambient gas.



**Figure 10.** Mean temperature contours on the radial plane.

In Figure 10c, circumferential four-strand transverse jets are introduced. The high-temperature zones in CASE B1 showed four concave zones in the middle of four edges near the nozzle exit, and in the downstream field, the hot jet expanded in both the vertical and the horizontal plane under the extrusion of the transverse jets. The transverse jets significantly increased the mixing between hot jet and ambient gas, which truncated the high-temperature zone downstream, on the vertical and horizontal planes.

### 6.2. Analysis of the Mixing Mechanism of Flow Field

In this paper, the jet mixing process was numerically investigated by the LES simulation method. For the vortex kernel analysis, the widely used Q criterion was adopted to identify the vortex structures [19].

$$Q_{Dim} = \frac{1}{2}(u_{ij}^2 - u_{ij}u_{ji}) = \frac{1}{2}(\|\Omega\|^2 - \|S\|^2) \quad (1)$$

$Q_{Dim}$  represents the vorticity amplitude, indicating rotation,  $S$  represents the strain rate amplitude, indicating deformation.

$$\Omega = \sqrt{2\omega_{i,j}\omega_{i,j}} \quad S = \sqrt{2S_{i,j}S_{i,j}} \quad \omega_{i,j} = \frac{1}{2}\left(\frac{\partial u_i}{\partial x_j} - \frac{\partial u_j}{\partial x_i}\right) \quad S_{i,j} = \frac{1}{2}\left(\frac{\partial u_i}{\partial x_j} + \frac{\partial u_j}{\partial x_i}\right) \quad (2)$$

Figure 11 shows the instantaneous coherent structure distributions of the jet vortex Q in downstream regions for each of the CASES. The vortex structures were mainly composed of a vortex ring, a vortex braid, a hairpin vortex, and a helical vortex. Compared with CASE A, CASE B showed a greatly enhanced strength of shear vortex rings, with abundant vortex braids and hairpin vortices. These structures appeared earlier in position than similar structures in CASE A.

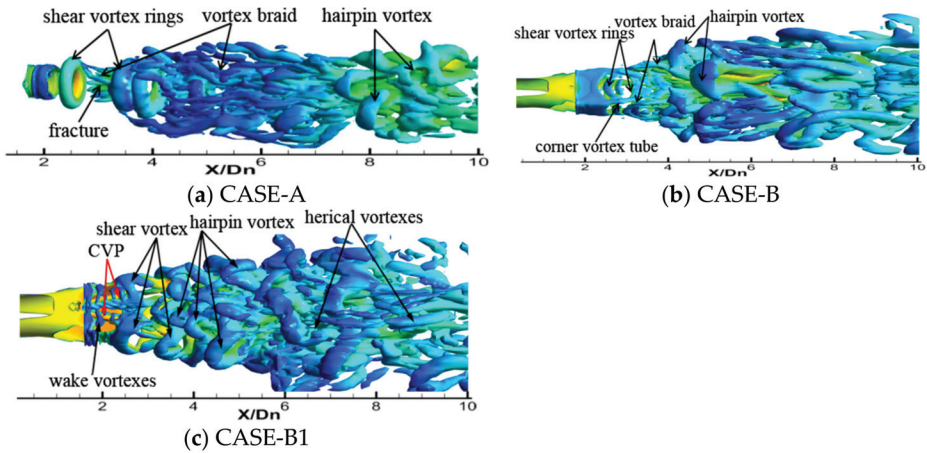


Figure 11. Distribution of dimensionless core areas along the axial direction at  $t = 0.02$  s.

In Figure 11c, the discontinuity of the velocity for the transverse jets and the hot jet in CASE-B1 resulted in strong reverse rotating vortex pairs (CVP) that showed inward entrainment in the shear layer. A series of shear vortex structures were introduced, and weak wake vortices were also produced on the leeward surface, which induced an extensive mixing, increasing near the nozzle exit. Downstream, helical vortices appeared, resulting in stronger mixing. The variation of the injection shape mainly affected the near-field mixing degree, and among the three different transverse jets schemes studied in the present paper, Case B3 appeared to be the optimal one. The rectangular jet increased the mixing area, leading to a stronger CVP.

### 6.3. Infrared Radiation Intensity Distribution

Figure 12 presents the infrared radiation intensity spectrum of the hot jet in the  $3\text{--}5\ \mu\text{m}$  bands, which was measured at  $60^\circ$ . In the  $4.16\text{--}4.6\ \mu\text{m}$  band, the absorption and emission of  $\text{CO}_2$  and  $\text{H}_2\text{O}$  induced wave peaks and troughs. The distribution of spectral radiation in CASE-B was similar to that of CASE-A, while the radiation intensity magnitude of CASE-B was smaller. When the transverse jets were applied, the infrared spectrum radiation intensity was clearly reduced for both detective planes. This is illustrated for CASE B1, CASE B2, and CASE B3, while the magnitude of the three decreased in the  $4.16\text{--}4.6\ \mu\text{m}$  band.

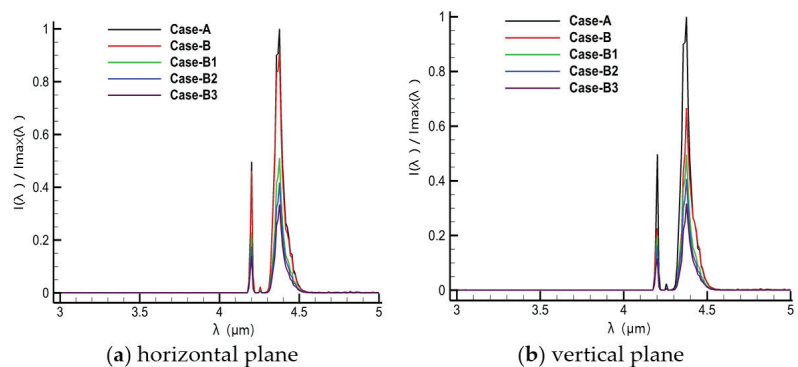


Figure 12. Dimensionless spectral radiant intensity of a hot jet at a detective angle  $\alpha = 60^\circ$ .



The infrared radiation intensity is defined as:

$$I = \int_{\lambda_1}^{\lambda_2} I_{\lambda} d\lambda \quad (3)$$

In formula (1), the infrared radiation intensity can be integrated in the infrared spectrum radiation.  $I_{\lambda}$  is the spectral radiation intensity, while  $\lambda_1$  is the lower and  $\lambda_2$  is the upper limit of the 3–5 microwave band. The results are dimensionless and based on the maximum radiation intensity  $I_{\max}$  of CASE-A. The results for the horizontal and the vertical planes are shown in Figure 13a,b.

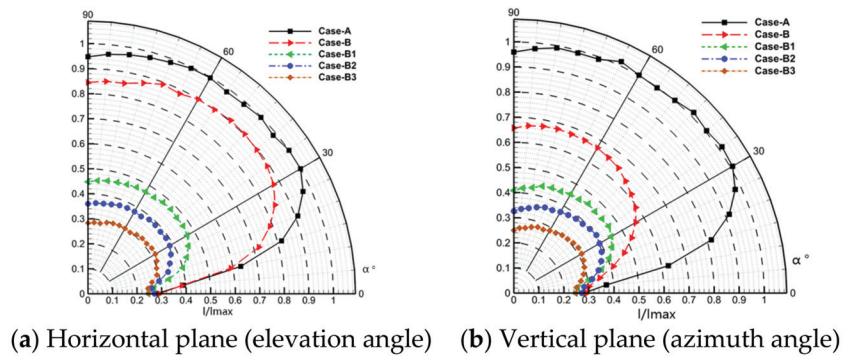


Figure 13. Dimensionless radiation intensity.

Figure 13 presents the infrared radiation intensity of the hot jet in the 3–5 microwave regions for detected angles from 0 to 90°. The infrared radiation intensity,  $I$ , of the hot jet increased first and then decreased in all CASEs. The infrared radiation intensity reached a high value between 30 and 60°.

The infrared radiation intensity of CASE-A was consistent on the horizontal and vertical planes because of its symmetrical geometrical characteristics. For CASE-B, the infrared radiation intensity distribution was in good agreement with that of CASE-A, while the intensity was lower for both planes. Further, the intensity on the horizontal plane was slightly higher than that on the vertical plane. The infrared radiation intensity distribution for CASE-B1, CASE B2, and CASE B3 was also in good agreement with that of CASE B. The intensity on both planes was also lower than those observed for CASE-B and decreased on both the horizontal and the vertical plane.

## 7. Conclusions

In this paper, a circular convergent nozzle and a circular-rectangular nozzle were designed. Using the latter nozzle, three different circumferential transverse jets were introduced. The heat transfer and infrared radiation characteristics in subsonic situations were numerically investigated. The main conclusions of the research presented in this paper are the following:

- (1) Compared with the axisymmetric nozzle, the circular-to-rectangular nozzle induced great mixing and led to a decrease of the high-temperature zone. The induced transverse jets resulted in a mixing enhancement of the hot jet. The high temperature-zones were shortened.
- (2) By changing from a circular to a rectangular nozzle, abundant vortices occurred in the near field of the hot jet. Shear vortices near the corners developed rapidly. Hairpin vortices, which formed near the nozzle exit, dissipated quickly.
- (3) The transverse jets induced CVP structures, resulting in abundant near-field vortices, increased vortex development speed, and enhanced pulsation of the mainstream boundary layer. They even expanded the penetration range, which led to the insta-

bility of the hot jet. Furthermore, the lap winding frequency was higher, large-scale hairpin vortices formed earlier, and the influenced range was wider.

- (4) As the transverse jets were introduced into the circular-rectangular nozzle, the infrared radiation significantly decreased. For all angles, when circular transverse jets were introduced, the infrared radiation decreased on the horizontal and vertical planes. Furthermore, when cube and rectangular transverse jets were introduced, the infrared radiation decreased by 28.2% on the horizontal plane and by 25.3% on the vertical plane.

**Author Contributions:** Introduction: B.Z., Z.L.; Physical Model: B.Z., Z.L., J.Z.; Computational Domain and Boundary Conditions: Z.L., J.Z., S.Y.; Meshes Generation and Independence: J.Z., S.Y.; Numerical Simulation Method: B.Z., Z.L., Analysis of the Calculation Results: B.Z., Z.L., H.J. All authors have read and agreed to the published version of the manuscript.

**Funding:** This research was funded by National Science and Technology Major Project (J2019-III-0009-0053) and Aeronautical Science Foundation of China (20200027052002).

**Institutional Review Board Statement:** Not applicable.

**Informed Consent Statement:** Not applicable.

**Data Availability Statement:** Some or all data, models, or code generated or used during the study are available from the corresponding author by request.

**Conflicts of Interest:** The authors declare no conflict of interest.

## References

- BAE Systems. *Stealth Technology*; BAE Systems: Farnborough, UK, 2004.
- Freund, J.B.; Moin, P. Jet mixing enhancement by high-amplitude fluidic actuation. *AIAA J.* **2000**, *38*, 1863–1870. [CrossRef]
- Knowles, K.; Saddington, A.J. A review of jet mixing enhancement for aircraft propulsion applications. *Proc. Inst. Mech. Eng. Part G J. Aerospace Eng.* **2006**, *220*, 103–127. [CrossRef]
- Parekh, D.E.; Kibens, V.; Glezer, A.; Wiltse, J.M.; Smith, D.M. Innovative jet flow control: Mixing enhancement experiments. In Proceedings of the 34th Aerospace Sciences Meeting and Exhibit, Reno, NV, USA, 15–18 January 1996; pp. 96–308.
- Mahjoub, S.N.; Habli, S.; Bournot, H.; Le Palec, G. The near field in the mixing of a three-dimensional inclined pollutant jet with a crossflow. *J. Enhanc. Heat Transf.* **2012**, *19*, 161–178. [CrossRef]
- Gretta, W.J.; Smith, C.R. The Flow Structure and Statistics of a Passive Mixing Tab Transactions of the Asme. *J. Fluids Eng.* **1993**, *115*, 255–263. [CrossRef]
- Behrouzi, P.; McQuirk, J.J. Jet Mixing Enhancement Using Fluid Tabs; AIAA-2004-2401. In Proceedings of the 2nd AIAA Flow Control Conference, Portland, OR, USA, 28 June–1 July 2004.
- Du, L.W.; Liu, Y.H.; Li, T. Numerical Predictions of Scarfing on Performance of S-Shaped Nozzle with Asymmetric Lobe. *J. Propuls. Power* **2015**, *31*, 604–618. [CrossRef]
- Sheng, Z.Q.; Chen, S.C.; Wu, Z.; Huang, P.L. High mixing effectiveness lobed nozzles and mixing mechanisms. *Sci. China Technol. Sci.* **2015**, *58*, 1218–1233. [CrossRef]
- Callender, B.; Gutmark, E.J.; Martens, S. Flow field characterization of coaxial conical and serrated (chevron) nozzles. *Exp. Fluids* **2010**, *48*, 637–649. [CrossRef]
- Suvagiya, M.; Sharma, S.D. Numerical investigation on the effect of geometric parameters of chevron nozzle on generation of streamwise vortices in high subsonic jets. *J. Aerosp. Sci. Technol.* **2019**, *71*, 225–230.
- Eri, Q.; Hong, L.; Li, T.; Wang, Q.; Wang, M. Numerical Simulations of Mixing Enhancement in Subsonic Jet Using High-Momentum Synthetic Jets. *J. Propuls. Power* **2016**, *32*, 1095–1103. [CrossRef]
- Karagozian, A.R. Transverse jets and their control. *Prog. Energy Combust. Sci.* **2010**, *36*, 531–553. [CrossRef]
- Kamran, M.A.; McQuirk, J.J. Subsonic Jet Mixing via Active Control Using Steady and Pulsed Control Jets. *AIAA J.* **2015**, *49*, 712–724. [CrossRef]
- Andreopoulos, J. On the structure of jets in a crossflow. *J. Fluid Mech.* **2006**, *157*, 163–197. [CrossRef]
- Behrouzi, P.; McQuirk, J. Effect of Tabs on Rectangular Jet Plume Development. *J. Propuls. Power* **2009**, *25*, 930–939. [CrossRef]
- Gevorkyan, L.; Shoji, T.; Getsinger, D.R.; Smith, O.I.; Karagozian, A.R. Transverse jet mixing characteristics. *J. Fluid Mech.* **2016**, *790*, 237–274. [CrossRef]
- Kamran, M.A. Manipulation of High Mach Number Shear Layers Using Control Jets. Ph.D. Thesis, Loughborough University, Loughborough, UK, 2009.
- Kelso, R.M.; Lim, T.; Perry, A.E. New experimental observation of vortical motions in transverse jets. *Phys. Fluids* **1998**, *10*, 2427–2429. [CrossRef]

20. Bidan, G.; Nikitopoulos, D.E. On steady and pulsed low-blowing-ratio transverse jets. *J. Fluid Mech.* **2013**, *714*, 393–433. [CrossRef]
21. McClinton, C.R. *The Effect of Injection Angle on Interaction between Sonic Secondary Jets and a Supersonic Free Stream*; NASA TND-6669; NASA: Washington, DC, USA, 1972.
22. Gruber, M.R.; Nejadt, A.S.; Chen, T.H.; Dutton, J.C. Mixing and Penetration Studies of Sonic Jets in a Mach 2 Free stream. *J. Propuls. Power* **2012**, *11*, 315–323. [CrossRef]
23. Zhang, B.; Hong, Q.; Bai, Y.; Li, J.; Ji, H. Numerical Investigation of Heat Transfer in Film Layer under Supersonic Condition. *Ther. Sci.* **2020**, *24*, 2279–2288. [CrossRef]
24. Zhang, B.; Chen, Y.X.; Wang, Z.G.; Li, J.Q.; Ji, H.H. Influence of Mach number of Main Flow on Film Cooling Characteristics under Supersonic Condition. *Symmetry* **2021**, *13*, 127. [CrossRef]
25. Kobayashi, K.; Bowersox, R.D.; Srinivasan, R.; Tichenor, N.R.; Carter, C.D.; Ryan, M.D. Experimental and Numerical Studies of Diamond-Shaped Injector in a Supersonic Flow. *J. Propuls. Power* **2010**, *26*, 373–376. [CrossRef]
26. Yang, H.; Li, G.N.; Zhou, H.; Cen, K.F. Large eddy simulation of transverse elliptic jet. *J. Zhejiang Univ.* **2007**, *41*, 1181–1185.
27. Kong, B.; Li, T.; Eri, Q. Large eddy simulation of turbulent jet controlled by two pulsed jets: Effect of forcing frequency. *Aerospace Sci. Technol.* **2019**, *89*, 356–369. [CrossRef]
28. Zhou, Y.; Wang, Q.; Li, Y. A new model to simulate infrared radiation from an aircraft exhaust system. *Chin. J. Aeronaut.* **2017**, *30*, 651–662. [CrossRef]
29. Liu, L.H. Backward Monte Carlo Method Based on Radiation Distribution Factor. *J. Thermophys. Heat Transf.* **2004**, *18*, 151–153. [CrossRef]
30. Niu, Q.L.; Fu, D.B.; Dong, S.K.; Tan, H.P. A simplified model for fast estimating infrared thermal radiation of low-altitude under-expanded exhaust plumes. *Int. J. Heat Mass Transf.* **2019**, *136*, 276–287. [CrossRef]

## Article

# Modification of Meso-Micromixing Interaction Reaction Model in Continuous Reactors

Junan Jiang <sup>†</sup>, Ning Yang <sup>†</sup>, Hanyang Liu, Jianxin Tang, Chenfeng Wang, Rijie Wang \* and Xiaoxia Yang

School of Chemical Engineering and Technology, Tianjin University, Tianjin 300350, China; xxy@tju.edu.cn

\* Correspondence: rjwang@tju.edu.cn

<sup>†</sup> These authors contributed equally to this work.

**Abstract:** The yields of chemical reactions are highly dependent on the mixing pattern between reactants. Herein, we report the modification of a meso-micromixing interaction reaction model which is applied in batch reactors by leveraging the flow characteristics in the continuous reactors. Both experimental and model-predicted yields were compared using the classical Villermaux–Dushman method in a self-designed split and recombination reactor. This modified model significantly reduced the error in predicted product yields from approximately 15% to within 3%, compared to a model containing the micromixing term only. The effects of flow rates and reactor structure parameters on mixing performance were analyzed. We found that increasing flow rates and the degree of twist in the mixing element's grooves, as well as decreasing the cross-sectional area of grooves, improved mixing performance. The optimization of reactor flow rates and structural parameters was achieved by combining Gaussian process regression and Bayesian optimization with the modified model. This approach provided higher target product yields for consecutive reactions, while simultaneously achieving a lower pressure drop in the reactor. Corresponding combinations of reactor parameters were also identified during this process. Our modified model-based optimization methodology can be applied to a diversity of reactors, serving as a reference for the selection of their structure and operational parameters.

**Keywords:** mesomixing; micromixing; continuous reactors; optimization

**Citation:** Jiang, J.; Yang, N.; Liu, H.; Tang, J.; Wang, C.; Wang, R.; Yang, X. Modification of Meso-Micromixing Interaction Reaction Model in Continuous Reactors. *Processes* **2023**, *11*, 1576. <https://doi.org/10.3390/pr11051576>

Academic Editor: Alfredo Iranzo

Received: 25 April 2023

Revised: 15 May 2023

Accepted: 16 May 2023

Published: 22 May 2023



**Copyright:** © 2023 by the authors. Licensee MDPI, Basel, Switzerland. This article is an open access article distributed under the terms and conditions of the Creative Commons Attribution (CC BY) license (<https://creativecommons.org/licenses/by/4.0/>).

## 1. Introduction

Consecutive reactions are extensively employed in the chemical process industry (CPI), such as in the synthesis of pharmaceuticals and high-performance polymers [1–3]. Studying consecutive reaction yields is crucial for assessing the reactions' performance and designing synthetic routes [4]. In cases where the reaction rate is less than or equal to the mixing rate, mixing within the reactor governs the contact pattern of the various species involved, thereby influencing their distributions. Consider the following consecutive reactions:



These reactions are second-order, where the yield of the desired product S is:

$$Y_S = \frac{2c_S}{c_{A0}} \quad (2)$$

Proper control of mixing quality is essential to maximize the yield of the target product S when  $k_1 > k_2$ , and has been extensively studied [5–10]. Christy et al. investigated the reaction between 1,2 diphenyl ethane (B) and  $\text{NO}_2\text{BF}_4$  (A) [8]. They found that the yield of the polynitro product (S) decreased from 78% to 54% upon increasing the stirring intensity then improving mixing uniformity. This decrease in yield can be attributed to different distribution states of the nitrifying agent (A) in the reactor [11]. Enhancing mixing homogeneity

resulted in a uniform distribution of A and a rapid decrease in its local concentration within the reactor after the formation of R. This can lead to the continuous accumulation of R, less subsequent reactions taking place, and, finally, a decrease in  $Y_S$ . However, these studies merely qualitatively evaluated the effect of mixing performance on consecutive reaction yields without analyzing yields governed by mixing processes quantitatively.

The quantitative relationship between mixing and yields can be described using a reaction model containing parameters characterizing mesomixing and micromixing. Baldyga and Bourne proposed a model in terms of the influence of meso- and micromixing on reactions and applied it to a semi-batch reactor with an extremely high flow ratio of two mixing streams [12]. The simulation results had a good prediction accuracy with a yield error of  $\pm 2\%$  compared to experimentally measured yields. Samant et al. studied consecutive reactions in a stirred batch reactor based on this model [13]. They found that structural parameters, such as the stirring paddle shape and the number of feed points, had significant effects on mixing rate-limited steps and reaction yields. Then they provided empirical correlations of mixing characteristic times at each scale controlled by these parameters to guide the reactor design.

Continuous reactors have many parameters that can significantly affect the internal fluid flow and mixing pattern, which, in turn, affect the yield of consecutive reactions [14–18]. Baldyga and Bourne used the aforementioned model to forecast the yield in a Kenics tubular reactor with a flow ratio of 3000:1 [12]. However, the yield was mainly influenced by the mixing pattern of the stream with the extremely low flow rate, which does not hold true for two streams with comparable flow rates in tubular reactors. Thus, the model requires modification based on the flow and mixing characteristics in such cases. Nevertheless, no model modification work has been conducted for meso-micromixing interaction reaction models in tubular reactors, which could ascertain the ambient fluid concentration of the reagents and the volume change of the fluid due to mixing.

The structural parameters of tubular reactors not only influence the mixing pattern and target product yield of reactions but are also closely related to the pressure drop in reactors. Maximizing the target product yield while keeping the pressure drop within a reasonable range is a valuable pursuit of study [19]. However, optimizing numerous parameters of reactors based on the reaction model can be computationally challenging [20]. Multidimensional regression and optimization required for this process are difficult to carry out. Gaussian process regression combined with Bayesian optimization can provide a general optimal solution for nonlinear optimization problems with fewer iterations and higher calculation speed [21–23]. Zuhail et al. [24] and Seongeon Park [25] employed CFD to conduct a series of Bayesian optimization designs to optimize the structure of the airfoil and stirred batch reactor based on minimum pressure drop criteria. However, there are currently no relevant studies on the structural design of continuous reactors that link reaction models with optimization methods to evaluate the relationship between target product yields and the pressure drop in reactors.

In this study, we analyze the flow characteristics and mixing pattern in continuous reactors and modify the meso-micromixing interaction reaction model which had been used in batch conditions in previous work. We use the Villermaux–Dushman method in a self-fabricated split and recombination reactor to verify the model's accuracy by comparing the results obtained by experiments with the model. We analyze the changes in mixing performance due to parameter variations from a flow field perspective. We use this modified model combined with Gaussian process regression and Bayesian optimization to obtain higher yields of target products in consecutive reactions while maintaining a lower pressure drop in the reactor. Such a design method can be applied to the optimization of various types of reactors.

## 2. Modified Meso-Micromixing Interaction Reaction Model

### 2.1. Initial Mixing-Related Reaction Model

According to Baldyga and Bourne's theory [12], a meso- and micromixing interaction reaction model can be characterized by the following equation:

$$\frac{dc_i}{dt} = E \left( 1 - \frac{X_B}{X_u} \right) (c_i - c_i) + r_i \quad (3)$$

The symbols in this equation are defined as follows: The rate of engulfment,  $E$ , describes the micromixing of fluid elements, which will be explained in detail in Section 3.4.  $X_u$  represents a fraction of the fluid volume. This part of the fluid contains partially segregated fluid as islands embedded in a sea, where the reagents are coarsely mixed and concentration fluctuations still exist.  $X_u$  can be derived by statistical method:

The variance of composition of the

$$X_u = \frac{X_0}{X_0 + (1 - X_0) \exp\left(-\frac{t}{t_d}\right)} \quad (4)$$

The initial volume fraction in the reactor where the reagents are present is  $X_0$ . For tubular reactors,  $X_0$  can be considered as the ratio of the initial flow rates. As  $X_u$  tends to 1, it signifies that the reagents spread everywhere from the mesomixing perspective, although without being completely micromixed.

$X_B$  refers to the volume of micromixed fluid relative to the whole fluid. According to the engulfment model, the rate of engulfment from  $E$  model is:

$$\frac{dX_B}{dt} = EX_B \left( 1 - \frac{X_B}{X_u} \right) \quad (5)$$

This equation describes the micromixing pattern when mesomixing is incomplete. Initially the islands, whose initial volume fraction is  $X_0$ , only consist of pure B-rich feed, so that the initial value of  $X_B$  is also  $X_0$ . As the flow enters the reactor, eddy breakup increases  $X_u$ , which initiates micromixing.

### 2.2. Comparison of Batch and Continuous Conditions

In batch reactors, the limited reagents are added dropwise. The chemical reaction occurs only in the droplets. The ambient fluid concentration  $\langle c_i \rangle$  outside the micromixing region can be assumed to be a constant concentration of excess fluid in the reactor. Additionally, when the flow rate in one of these streams is extremely low, the volume of fluid that has been fully micromixed will be present only in the other excessive stream.

In the case of two comparable flow rates in the continuous reactors, chemical reactions can occur in both streams after achieving micromixing. This implies that each stream contains a significant concentration of reagents and products, as was shown in Figure 1. As a result, the ambient fluid concentration  $\langle c_i \rangle$  is no longer a changeless concentration, which is the case in batch reactors. Furthermore, when the flow rates are comparable, both flows experience reciprocal engulfment effects and micromixing. Consequently, the volume of fluid that is completely micromixed in both streams changes (in Figure 1, the total volume of each stream is  $V_A + \Delta V_A$  or  $V_B + \Delta V_B$ ), which ultimately impacts the concentration of species in each stream.

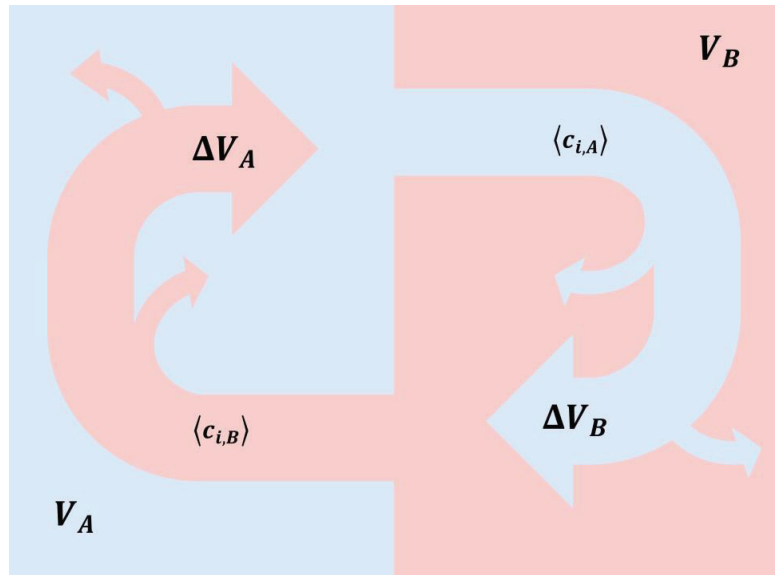


**Figure 1.** Diagram of mixing between two streams with comparable flow rates under continuous conditions. Each stream serves as the reciprocal environmental fluid and their volume flow rates change a lot. (The amount of  $\Delta V_A$  and  $\Delta V_B$  cannot be ignored).

### 2.3. Model Modification

We have modified the model after accounting for the differences between the above two conditions.

Firstly, since both streams, 1 and 2, exhibit self-engulfment behavior and undergo chemical reactions, we considered the ambient species' concentration outside the micromixing region of stream 1 as that of the corresponding species in stream 2, and vice versa. In other words, these two streams are treated as reciprocal environmental fluids, as was shown in Figure 1.

Secondly, since the change in fluid volume resulting from the mesomixing and micromixing in these two streams is not negligible, we took stream 1 as the reference and switched from the concentration change due to the volume change of stream 2 to the volume-based concentration of stream 1. To describe this behavior, we introduced a fluid volume change rate  $\varphi_B$ , which essentially represents the fluid volume change induced by mixing at the mesoscopic and microscopic scales. This rate can be calculated using the following integrated equation:

$$\varphi_B = e^t + \left(1 - \frac{1}{e^{-Qt}}\right)Q \quad (6)$$

Here,  $Q$  is the ratio of the micromixing characterized time and the mesomixing characterized time.

Based on these, the model can be modified as (taking concentrated reagent A in stream 1 for instance):

$$\frac{dc_{A1}}{dt} = E \left(1 - \frac{X_{B1}}{X_{uA}}\right) (c_{A2} - c_{A1}) + r_A \quad (7)$$

$$\frac{dc_{A2}}{dt} = \left[ E \left(1 - \frac{X_{B2}}{X_{uA}}\right) (c_{A1} - c_{A2}) + r_A \right] \frac{\frac{V_{total} V_A}{(V_A + V_B)} \varphi_B}{\left( V_{total} - \frac{V_{total} V_A}{(V_A + V_B)} \varphi_B \right)} \quad (8)$$

where  $\frac{V_{total} V_A}{(V_A + V_B)}$  is the inlet flow rate of stream 1.

By analogy, each species is governed by two ordinary differential equations that control its concentration in each of these two fluid environments (stream 1 and stream 2). In Equation (7), the subscript 1 represents the fluid that has undergone micromixing, while the subscript 2 represents the ambient fluid surrounding stream 1. For Equation (8), the opposite is true of what was explained above.

### 3. Methods and Materials

#### 3.1. 3D-Printed Split-and-Recombine Millimeter-Scale Reactor

The equipment for studying the modified model is a tubular split and recombination reactor, whose physical model is illustrated in Figure 2a,b. A central annular tube with an outer diameter of 6 mm ( $R_O$ ) and an inner diameter of 3 mm ( $R_I$ ) comprises the reactor. It has a series of split and recombination mixing elements with a diameter of 6 mm and a length of 10 mm ( $L_M$ ), distributed uniformly at intervals of 10 mm ( $L_G$ ) along the circular tube. The structure has four twisted grooves uniformly rotating along the circumference for fluid passage. Two adjacent twisted grooves are separated at 90 degrees on the cross-section of the tube. The physical structure of the reactor can be obtained using 3D printing technology, with a processing accuracy less than 0.05 mm.

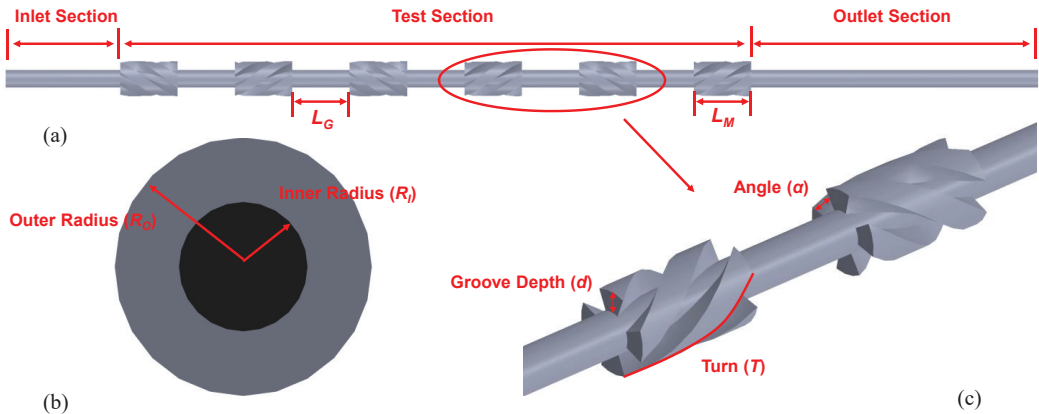


**Figure 2.** Physical model of SAR reactors: (a) Front view of SAR reactor; (b) Schematic diagram of the annular structure; (c) Geometrical parameters of mixing elements.

The tubular reactor consists of three sections: inlet, test, and outlet. The inlet section, 20 mm long, is designed to ensure the complete development of the fluid. These two mixing streams are introduced at equal velocity there, with one entering the reactor through a 3 mm central tube, and the other entering through the remaining annular tube. Thus, the initial flow ratio of these two streams will be 1:3. The test section is 110 mm long, an adequate length to achieve various mixing patterns. The outlet section is 40 mm long, sufficient to stabilize the outlet flow.

Based on the results obtained from the pre-experiments, the angle ( $\alpha$ ), groove depth ( $d$ ), turn ( $T$ ), and flow rate ( $F$ ) of the reactor significantly affect the flow field and mixing performance in the reactor. These parameters are shown in Figure 2c. Angle denotes the rotation angle of the groove in the mixing element; groove depth represents the depth of the groove; turn refers to the degree of one groove twist. If  $T = 1$ , the groove rotates  $360^\circ$  in a single mixing element. We selected these parameters for numerical simulation and experimental study and set several discrete points for each parameter, which are listed in Table 1.



**Table 1.** Geometrical parameters and flow rate of the tube and inserts.

$\alpha, ^\circ$	$d, \text{mm}$	$T$	$F, \text{mL/min}$
15, 30, 45, 60, 75	0.5, 1, 1.5, 2, 2.5	0.2, 0.4, 0.6, 0.8, 1	100, 150, 200, 250, 300, 350, 400

### 3.2. Numerical Simulation

To investigate the influence of different structural parameters and inlet flow rates on pressure drop and the energy dissipation rate in the reactor, we conducted 3D steady-state numerical simulations. Water was chosen as the working medium and modeled as a Newtonian, incompressible fluid. The simulations were performed at 20 °C and it is assumed that physical properties, such as viscosity, remain constant. Since the mixing element is placed horizontally in a tube with an inner diameter of 6 mm, we assume that the effect of gravity is negligible. With these assumptions, the momentum governing equations of the fluid are as follows.

$$\frac{\partial u_i}{\partial x_i} = 0 \quad (9)$$

$$\rho \frac{\partial u_i}{\partial x_i} + \rho \frac{\partial u_i u_j}{\partial x_j} = -\frac{\partial p}{\partial x_i} + \frac{\partial}{\partial x_j} \left( \mu \frac{\partial u_i}{\partial x_i} + p \tau_{ji} \right) \quad (i = 1 \sim 3) \quad (10)$$

where  $\rho$  is the density of mixture fluid;  $u$  is the internal velocity field;  $p$  is the local pressure field;  $\mu$  is the viscosity of the mixture fluid; and  $\tau_{ji}$  is the Reynold stress tensor. Here, the SST k- $\omega$  model was applied. The range of the Reynold number in this study was from 658 to 5821. The SST k- $\omega$  model can be applied to the cases with relatively lower Reynold numbers, which can reproduce the transition from laminar to turbulent flow regimes. Furthermore, for the flow ejected from the curved grooves of the mixing elements, where the fluid has a high-velocity gradient within the boundary layer, the SST k- $\omega$  model will be more applicable.

In this study, ANSYS fluent 2020R1, a commercial software based on the finite volume method, was used for the numerical simulations and CFD-Post for post-processing. The SIMPLE algorithm was applied for pressure–velocity coupled solution calculations while the PRESTO! method was used to perform gradient and pressure discretization. The second-order upwind algorithm spatially discretized the momentum, turbulent kinetic energy, and turbulent dissipation rate. The convergence criteria are less than  $10^{-6}$  for the continuity and momentum equations.

In the simulations, there is difficulty calculating the turbulent kinetic energy, energy dissipation rate, etc., accurately, so, obtaining these results requires higher quality discrete meshes. Therefore, the grid independence test and algorithm reliable verification are necessary to be carried out, which are shown in the Supplementary Materials.

### 3.3. Mixing Performance Experiments

To quantitatively evaluate mixing performance, classical Villermaux–Dushman experiments [26–28] were conducted. We considered the approximate micromixing time range in this case and used the concentration groups of substances provided by J.M. Commenge’s study [29–31]. The concentrations of each reagent are presented in Table 2.

**Table 2.** Concentration recipe of reagents for Villermaux–Dushman method.

Materials	Concentration [mol/L]
H <sub>2</sub> BO <sub>3</sub>	0.09
NaOH	0.09
KIO <sub>3</sub>	0.006
KI	0.032
H <sub>2</sub> SO <sub>4</sub>	0.0026

The experimental setup diagram is depicted in Figure 3. Iodide-iodate-borate buffer solution and sulfuric acid solution were supplied to the reactor through two HPLC pumps from the outer and central tubes, respectively. The outer and central tubes were connected by commercial T-connectors. To minimize error, three independent samples were taken in each experiment and analyzed by UV-VIS. Finally, the concentration of each species was obtained by subsequent data processing, then  $X_S$  (segregation index) was calculated. For further details on the Villiermaux–Dushman method [32–34], please refer to the Supplementary Materials.

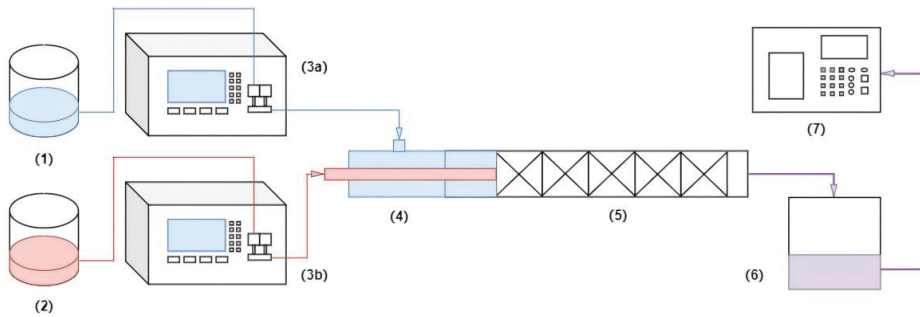


**Figure 3.** Schematic overview of the experimental setup: (1) Sulfuric acid solution container; (2) Buffered solution container; (3a) HPLC pump for sulfuric acid solution; (3b) HPLC pump for buffered solution; (4) Commercial T-joint; (5) SAR reactor; (6) Outflow container; (7) UV–VIS spectrometer. The blue solution represents sulfuric acid solution, the red buffered solution, and the purple the solution after the reaction.

### 3.4. Data Reduction

Based on the set of ordinary differential equations given in Section 2, the independent variables that need to be imported to the reaction model include the inlet flow rate, reaction kinetics, flow time, micromixing characteristic time and mesomixing characteristic time. Apart from the inlet flow rate and reaction kinetics, the calculation of the remaining three variables is given below.

The flow time can be calculated by dividing the reactor length by the average flow velocity in the reactor as follows:

$$t = \frac{L}{u_m} \quad (11)$$

In such SAR reactors, additional attention needs to be taken with respect to  $D$ , because the shape of the flow channels in the circular cross section is not regular and the reactor characteristic sizes cannot be determined by conventional methods. Therefore, the hydrodynamic diameter calculation method was used [35]:

$$D = \frac{4V}{S} \quad (12)$$

where  $V$  is the fluid domain volume in the reactor and  $S$  is the area which contacts with the fluid in the reactor.

The Reynolds number represents the relative relationship between the inertial and viscous forces in the fluid and is expressed as follows:

$$Re = \frac{\rho u_m D}{\mu} \quad (13)$$

where  $u_m$  is the average velocity along the flow direction.

Baldyga and Bourne [36–39] proposed an engulfment model to describe micromixing behavior, which is based on the premise that the engulfment of small-scale eddies generates interlaced laminar structures between the micromixing fluid and the environment. These

structures promote the deformation of fluid layers that accelerates the aggregate size reduction up to the diffusion scale then intensifies the molecular diffusion between the fluid layers. Based on this theory, the micromixing characteristic time can be determined from numerical simulation using the following equation [40]:

$$t_m = E^{-1} = 17.3(v/\varepsilon)^{0.5} \quad (14)$$

Here, the engulfment rate,  $E$ , is the inverse of  $t_m$ , which is related to the energy dissipation rate  $\varepsilon$  and the dynamic viscosity  $\nu$ . It is important to note that this empirical formula (Equation (11)) for calculating the micromixing characteristic time requires more validation through comparison with experimental results, which are detailed in the Supplementary Materials.

Additionally, the energy dissipation rate is directly related to the evaluation index of mesomixing [11,41]. According to the theory of inertial-convective disintegration of large-scale eddies, the fluid element's intermediate scale shrinks from the initial  $\Lambda_c$  to the Kolmogorov scale through turbulence dispersion. The whole process constitutes mesomixing [38,41–43]. Based on this theory, the mesomixing characteristic time can be estimated using statistical method [12]:

$$t_d = 2 \left( \frac{\Lambda_c^2}{\varepsilon} \right)^{\frac{1}{3}} \quad (15)$$

The initial scale of mesoscopic mixing,  $\Lambda_c$ , for two streams with the same inlet flow velocity can be calculated by the following equation [11]:

$$\Lambda_c = \left( \frac{V_B}{\pi u} \right)^{0.5} \quad (16)$$

where  $V_B$  is the volume flow rate of the stream that has a relatively lower flow rate.

The energy dissipation rate refers to energy loss in the fluid due to its essential viscosity and the turbulence induced. The turbulent energy dissipation rate can be related to the velocity strain rate tensor by:

$$\varepsilon = \frac{1}{2} \nu \left( \frac{\partial u_i}{\partial x_j} + \frac{\partial u_j}{\partial x_i} \right)^2 \quad (17)$$

This tensor can be obtained directly from CFD simulations.

### 3.5. Optimization Procedure

The optimization method for reactors using GPR, BO, and the modified model is presented in the flowchart shown in Figure 4. In this study, 100 initial design points about the reactor were obtained using the Latin hypercube sampling method. CFD simulations were carried out to determine parameters such as the energy dissipation rate. The reaction kinetics and modified models were then incorporated into a self-programmed 4th-order Runge–Kutta MATLAB program for calculations, acquiring 100 sets of yield and pressure drop data for fitting. These yield and pressure drop data, as performance functions, were mapped to performance metrics by a specific design. This design was defined by a set of structural and operating parameters and subjected to regression validation and optimization in the next step.

In each iteration, a surrogate model was calculated using the known correspondence between the four reactor parameters and the three dependent variables (two product yields plus pressure drop). The next set of parameters, whose mapping value will get closer to the maximum yield and the lowest pressure drop, was chosen by the acquisition function. This parameter set was further used for numerical simulation to obtain the new pressure drop and yields. The cycle of updating the model was repeated. An evaluation index  $K$  was defined to determine the final multi-objective optimization results.

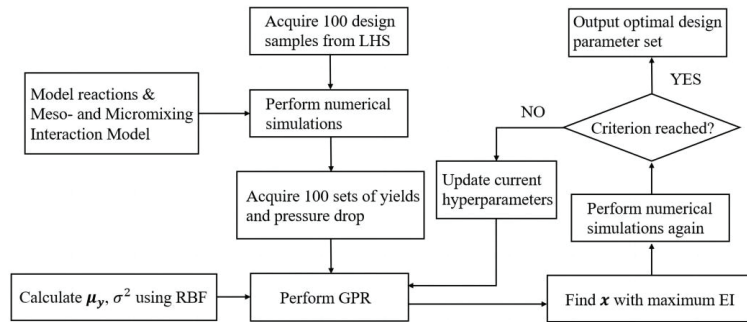


Figure 4. Algorithm of CFD-GPR-BO.

$$K = \frac{\frac{Y_B - Y_A}{Y_A}}{\frac{\Delta P_B - \Delta P_A}{\Delta P_A}} \quad (18)$$

Specifically,  $K$  is calculated as the ratio of the percentage yield improvement to the percentage pressure drop improvement between two adjacent iteration points,  $A$  and  $B$ . This metric indicates the amount by which the yield improves when the unit pressure drop increases. If  $K$  is less than 5%, we select the current design point as the final multi-objective optimization result based on the optimization principle of GPR-BO.

## 4. Results and Discussion

### 4.1. Validation of Modified Model Accuracy

The present study acquired experimental and simulated yields using parallel competing reactions in the classical Villermaux–Dushman method. The yields obtained from both the modified meso-micromixing interaction reaction model and the reaction model containing only the micromixing time term were compared with the experimental results. The results are presented in Figure 5.

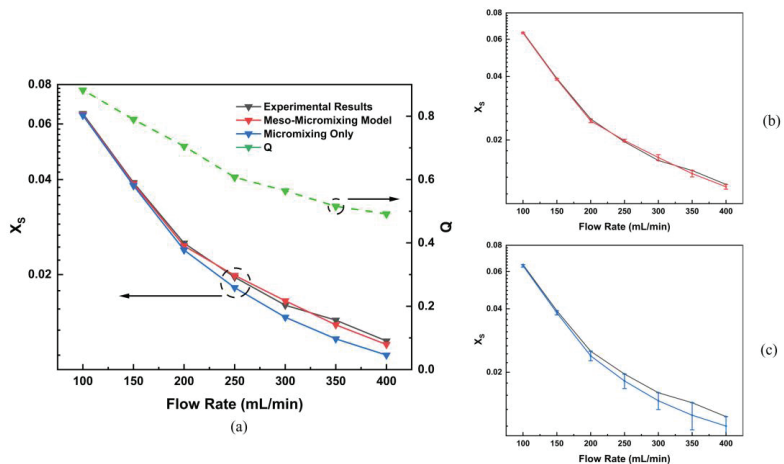


Figure 5. (a) Comparison of the yields obtained by the Villermaux–Dushman method with those obtained by the meso-micromixing interaction reaction model and the model which only consists of micromixing time. (The green dashed line represents the ratio of micromixing time to mesomixing time,  $Q$ , as a function of the inlet flow rate); (b) Error lines of yields obtained by experiments and meso-micromixing model; (c) Error lines of yields obtained by experiments and the model only with micromixing term.

The figure shows that the yields obtained from the modified meso-micromixing interaction reaction model are in good agreement with the experimental results, with a maximum relative error of only 3% (Figure 5b). This indicates the accuracy of this modified model for yield prediction. However, the reaction model with the micromixing time term only has a much larger error in the experimental results, particularly at high flow rates, where the relative error can reach up to 14.7% (Figure 5c). This can be attributed to mesomixing becoming the rate-limited step gradually, which is evident from Figure 5, showing that the ratio of micromixing time to mesomixing time,  $Q$ , decreases with increasing flow rates. Growing flow rates increase the overall energy dissipation. However, the rate of mesomixing triggered by turbulent dispersion cannot catch up with that of micromixing, and, thus, becomes the rate-limited step [44]. In conclusion, this modified meso-micromixing interaction reaction model is an accurate approach for obtaining yields and can subsequently be used for the optimization in Section 4.3.

#### 4.2. Effect of Parameters on Mixing

##### 4.2.1. Effect of Turn

In Figure 6, the reactor's full domain energy dissipation rate and segregation index were evaluated at various turns for a fixed groove depth of 1.5 mm and angle of  $45^\circ$ , while the inlet flow rates were also varied. The results indicated a decreasing trend in energy dissipation rate and segregation index with an increase in  $T$ , which was found to be more pronounced at lower flow rates. At a flow rate of 150 mL/min,  $X_S$  for a  $T$  of 0.4 was 0.03911, which was 40.4% lower than that for a  $T$  of 0.4 with an  $X_S$  value of 0.06564. However,  $X_S$  variation at higher  $T$  did not become that significant, especially when  $T = 0.4$  and 0.6, as there was almost no difference, with a maximum difference of less than 5%.

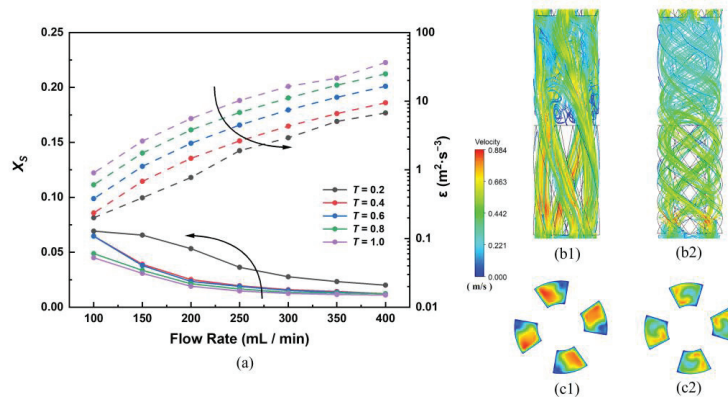


**Figure 6.** (a) Variation in segregated index ( $X_S$ , a series of solid lines) and volume-average energy dissipation rate in the reactor ( $\epsilon$ , a series of dashed lines) under different flow rates and skewness at  $d = 1.5$  mm and  $\alpha = 45^\circ$ ; (b) Streamline in a mixing unit set; (c) Velocity contours of cross-sections at  $z = 42$  mm in the twisted grooves. Here, (1) represents the cases with  $S = 0.2$ , while (2) with  $S = 0.8$ .

The helical motion of the fluid caused by the increased radial velocity component and extended flow path, both in the empty annular space between the two mixing elements and the twisted grooves in the mixing elements, was responsible for this trend (Figure 6b2). At the same time, the strong rotational effect increased the contact area between relatively high and low flow velocity zones in the twisted grooves (Figure 6c2). However, although further increase in  $T$  indeed lengthened the flow path, excellent mixing could be achieved right in the middle of the path due to more frequent contact with the fluid. Therefore, extending the flow path or increasing the radial velocity more significantly had a limited effect on improving mixing performance [45]. Overall, these findings highlight the importance of selecting the appropriate turn for optimal reactor performance.

#### 4.2.2. Effect of Inlet Flow Rates

Figure 5 illustrates the decreasing trend of  $X_S$  with increasing inlet flow rates, from a maximum of 0.05331 to 0.01911. For  $T > 0.4$  and at lower flow rates ( $F < 200$  mL/min),  $X_S$  decreased significantly with increasing flow rate, from 0.06464 to 0.02352, representing a change of 63.6%. However, at higher flow rates, the change in  $X_S$  leveled off until it concentrated around 0.0123 at a flow rate equal to 400 mL/min.

This trend was mainly attributed to the increasing energy dissipation rate in the annular space between the two mixing elements as the flow rates increased. As shown in Figure 7a1,a2, the flow pattern remained largely unchanged with increasing flow rates, but the overall velocity was significantly affected. This increased velocity leads to a higher degree of turbulence and contact frequency with the fluid, thereby substantially increasing the energy dissipation rate in the annular space (Figure 7b1,b2). However, the effect of higher flow rates on the energy dissipation rate in the annular space is minimal, resulting in a slow improvement in mixing performance. Overall, high flow rates are beneficial for enhancing mixing performance in the reactor.

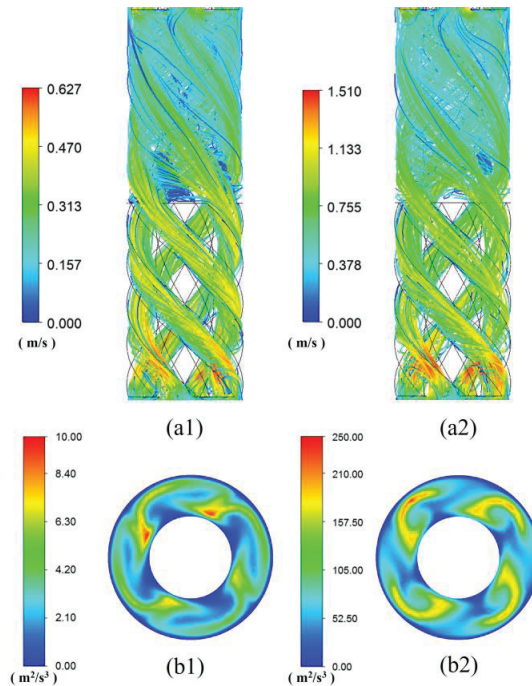


**Figure 7.** Flow pattern information with different flow rates: (a1,a2) Streamline in a mixing unit set; (b1,b2) EDR contours of cross-sections at  $z = 53$  mm. Here, (1) represents the cases with  $F = 150$  mL/min, while (2) with  $F = 350$  mL/min.

#### 4.2.3. Effect of Cross-Sectional Area of the Grooves

Angle and groove depth are important factors that determine both the width and depth of grooves in the mixing element, respectively. These two factors together determine the cross-sectional area of grooves, which affects the flow pattern and mixing performance in the annular space and twisted grooves.

Given  $T = 0.4$ ,  $F = 300$  mL/min, the reactor's energy dissipation rate and segregation index varied with groove depth and angle, as presented in Figure 8. Decreasing the cross-sectional area of the groove led to a significant reduction in  $X_S$ . The maximum  $X_S$  of 0.0258

was obtained at  $\alpha = 75^\circ$  and  $D = 2.5$  mm, while a minimum  $X_S$  of 0.00426 was observed at  $\alpha = 30^\circ$  and  $D = 1$  mm, overall resulting in an 83.5% decrease in  $X_S$ .

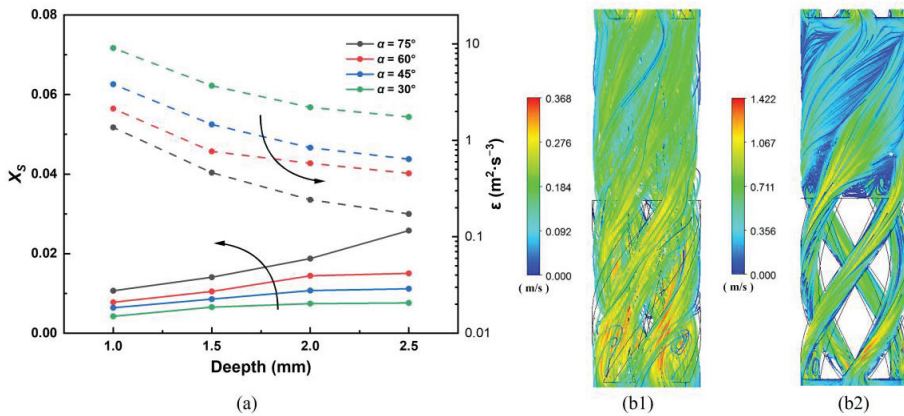


**Figure 8.** (a) Variation in segregated index ( $X_S$ , a series of solid lines) and volume-average energy dissipation rate in the reactor ( $\epsilon$ , a series of dashed lines) under different  $D$  and  $\alpha$  at  $F = 300$  mL/min and  $S = 0.4$ ; (b1,b2) Streamline in a mixing unit set; Here, (1) represents the cases with  $\alpha = 75^\circ$  and  $D = 2.0$  mm, while (2) with  $\alpha = 30^\circ$  and  $D = 1.0$  mm.

Reducing the cross-sectional area of the groove leads to a jet with higher velocity, which spreads out into the annular space to form a rotating plume flow. As this plume moves away from its source, its edges entrain the surrounding fluid, causing the plume to expand further then promoting mixing (Figure 8b2). The energy dissipation rate increased significantly when the cross-section area of the groove became small, from  $1.46 \text{ m}^2/\text{s}^3$  at  $\alpha = 45^\circ$  and  $D = 1.5$  mm to  $8.39 \text{ m}^2/\text{s}^3$  at  $\alpha = 30^\circ$  and  $D = 1$  mm. This can be explained by the fact that the flow area is reduced by a factor of 2.25 and the velocity of the ejected plume increases exponentially, leading to an accelerated improvement in mixing performance. In conclusion, reducing the cross-sectional area of the groove improves the mixing performance of the reactor.

#### 4.3. Optimization Calculations

##### 4.3.1. Optimization Objectives

The objective of this work is to maximize the target product yield and minimize pressure drop by optimizing the reactor parameters. The information about the relevant consecutive reaction is presented in Table 3. The reactor is fed with two streams, A and B, which enter from a 3 mm diameter center tube and annular space with a 6 mm outer diameter and 3 mm inner diameter, respectively. To satisfy the demand for different products in the consecutive reaction, the yields  $Y_1$  and  $Y_2$  of product C and product E, as well as the pressure drop, were chosen as the optimization objectives, while the angle, groove depth, turn and flow rate were selected as the corresponding optimization parameters.

**Table 3.** Kinetic and operational information about the competitive consecutive reaction.

Information about the Reactions		
$A + B \rightarrow C$	$r_1 = k_1 c_A c_B$	
$C + B \rightarrow D$	$r_2 = k_2 c_C c_B$	
$D + B \rightarrow E$	$r_3 = k_3 c_D c_B$	
$k_1 = 50 \text{ m}^3/(\text{mol}\cdot\text{s})$	$k_2 = 20 \text{ m}^3/(\text{mol}\cdot\text{s})$	$k_3 = 100 \text{ m}^3/(\text{mol}\cdot\text{s})$
$V_A : V_B = 1 : 3 \quad V_{MA} = V_{MB} = 5 \text{ mol}/\text{m}^3$		

BO is applied to obtain the local minimum value [46]. Therefore, the yields of both products in the consecutive reaction were multiplied by  $(-1)$  to transform the optimization problem into a maximization problem, as shown in the following expression:

$$\text{Objectives : } f_1(\alpha, d, T, F) = \{\Delta P_{SAR}, -Y_1\} \text{ and } f_2(\alpha, d, T, F) = \{\Delta P_{SAR}, -Y_2\}$$

$$\text{Subjected to : } \alpha \in [15,75]; d \in [0.5,2]; S \in [0,1]; F \in [100,400]$$

#### 4.3.2. Results of Gaussian Process Regression

Two commonly used metrics to evaluate a data regression are the mean square error (*MSE* for short) and the coefficient of determination ( $R^2$  for short), which are defined as:

$$MSE = \frac{1}{N} \sum_{i=1}^N (Y_{i, GPR} - Y_i)^2 \quad (19)$$

$$R^2 = 1 - \frac{\sum_{i=1}^N (Y_{i, GPR} - Y_i)^2}{\sum_{i=1}^N (\bar{Y}_i - Y_i)^2} \quad (20)$$

A GPR that has a smaller *MSE* and a larger  $R^2$  is considered more reliable and accurate. Three separate GPRs were utilized to fit the data of  $\Delta P_{SAR}$ ,  $Y_1$ , and  $Y_2$ . To assess the effectiveness of GPR for the regression, an additional analysis was conducted using an artificial neural network (ANN) with multilayer perceptron (MLP). The tanh function was employed as the activation function in the ANN, which has been widely used in this context [19,47–49]. The final trained ANN had a configuration of 5:14:12:2 after double hidden layers were used. Both the regression results of ANN and GPR were compared with results obtained by the reaction model (short for RM), whose normalized values are presented in Figure 9 and Table 4.

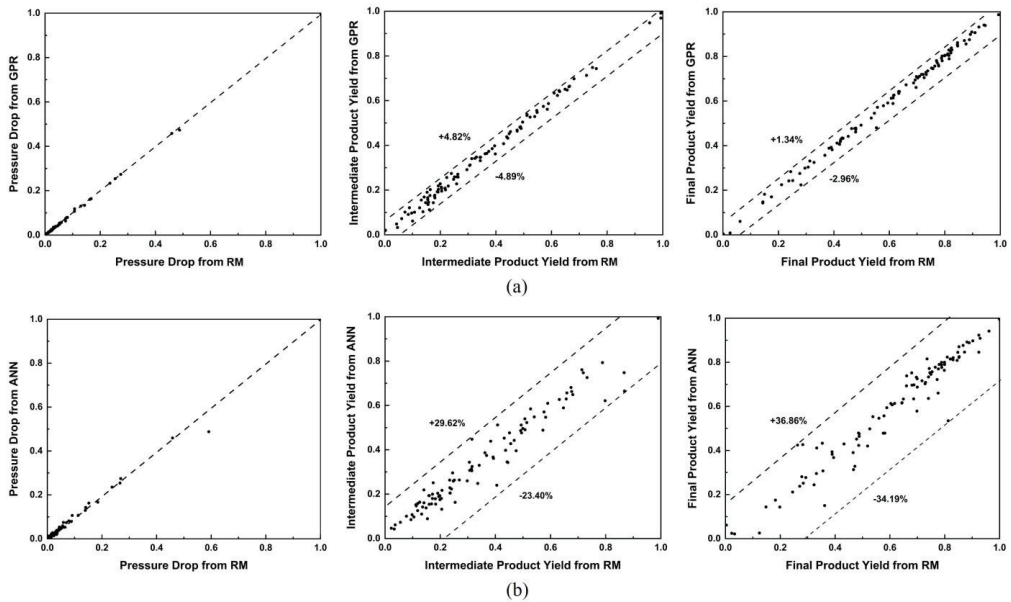


**Figure 9.** Deviations and maximum relative errors between RM and the two regression methods: (a) results between RM and GPR; (b) results between RM and ANN. Each dot in the figures represents the simulated value and the fitted value. Each dashed line represents the maximum positive or negative relative error of the fitted value.



**Table 4.** MSE and  $R^2$  of three optimization objectives for GPR and ANN.

	GPR		ANN	
	MSE	$R^2$	MSE	$R^2$
$\Delta P_{SAR}$	$1.40880 \times 10^{-4}$	0.94593	$8.51216 \times 10^{-5}$	0.99670
$Y_1$	$3.38565 \times 10^{-3}$	0.78948	$2.87026 \times 10^{-4}$	0.97674
$Y_2$	$3.85881 \times 10^{-3}$	0.96288	$1.45477 \times 10^{-4}$	0.99972

In Figure 9, the deviations of three dependent variables for RM, ANN, and GPR are presented. The maximum relative errors for  $Y_1$  and  $Y_2$  were 3.52% and 5.75%, respectively, when using GPR. On the other hand, while ANNs generally meet accuracy requirements, there were several outliers that deviated significantly from the CFD calculations, resulting in maximum errors of 29.62% and 36.86% for  $Y_1$  and  $Y_2$ , respectively.

Table 4 shows that both the MSE and  $R^2$  values in GPRs were significantly better than those in ANNs, indicating that GPR can provide more accurate data and is, therefore, more suitable for fitting in this case. This is because GPR can quantitatively predict uncertainty in a more principled way than ANN, which is particularly relevant for conditions with excessive degrees of freedom. Moreover, by selecting a specific kernel function, GPR can be considered equivalent to an ANN with an infinite number of hidden nodes [50]. However, high accuracy requires more computational resources, although, for just 100 design points, the computational time remains relatively short.

#### 4.3.3. Results of Bayesian Optimization

After obtaining regression results for GPRs, Bayesian optimization was subsequently performed to optimize the reactor parameters.

The optimization process is determined as a multi-objective optimization when the target product is the intermediate product C. To improve the yield of C, the mixing performance needs to be enhanced to disperse the reagent B in the reactor quickly, which reduces its local concentration and slows down the second and third reactions, thereby accumulating product C and reducing the formation of subsequent products, D and E. However, improving the mixing performance requires a higher energy dissipation rate of the fluid, resulting in a higher pressure drop in the reactor. Therefore, a compromise solution between higher intermediate product yields and a relatively lower reactor pressure drop needs to be achieved.

Using Bayesian optimization, a series of Pareto front points were obtained, as shown in Figure 10. These optimization points were evaluated using the metric  $K$  presented in Section 3.5. The desired points with  $K = 2.92\%$  were identified with a red circle in Figure 10. Therefore, for the intermediate product C, the maximum yield was 92.5% with a pressure drop in the reactor of 510.50 Pa, where  $\alpha = 32.8^\circ$ ,  $d = 2.36$  mm,  $T = 0.215$ , and  $F = 145.7$  mL/min.

When the target product is the product in the last reaction, E, the process becomes a single-objective optimization. To increase the yield of E, the mixing performance needs to be worsened, resulting in the intermediate product C being diffused to the enriched B region, further reacting with it. This is particularly significant when the residence time of the species becomes longer, as it leads to a higher selectivity of E. A lower energy dissipation rate results in poorer mixing, but also keeps the pressure drop low. Therefore, there is no trade-off or coordination required between the product yield in the last reaction and the pressure drop in the reactor. Optimization is straightforward in that the solution containing both the lowest pressure drop and the highest yield is desired.

A series of optimal points were obtained by Bayesian optimization, as shown in Figure 11. The three leftmost points in the figure are indeed close in value, with a relative difference of less than 0.2%, indicating that the single-objective optimization has reached the limit of iterations. The point identified with the red circle is the desired point, where we acquired the lowest pressure drop and the highest yield. Thus, for the product in the

last reaction, the highest yield was 94.3%, with a pressure drop in the reactor of 253.81 Pa, where  $\alpha = 48.3^\circ$ ,  $d = 2.04$  mm,  $T = 0.344$ , and  $F = 120.37$  mL/min.

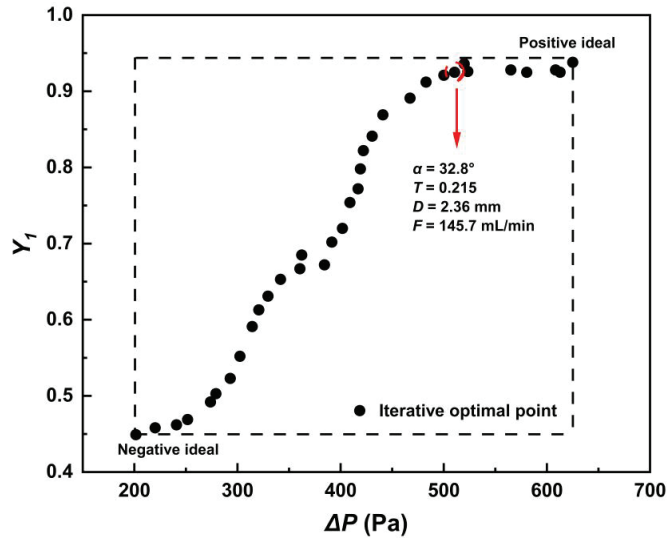


**Figure 10.** Pareto front for intermediate product yield obtained by BO and a solution that meets the criteria.

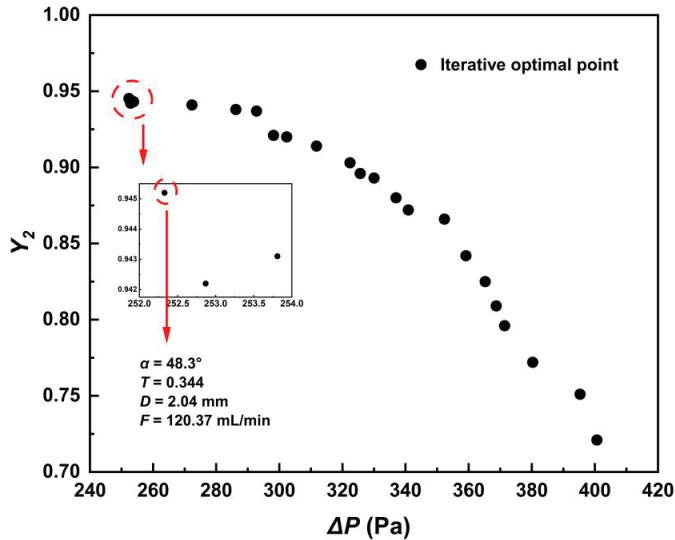


**Figure 11.** Results of single-objective optimization for the yield of product in the last reaction obtained by BO and a solution which meets the error criteria.

We have developed an active reactor design method based on CFD-GPR-BO that is applicable to the analysis of different types of reactions, accounting for a meso-micromixing interaction reaction model. In practice, it may be acceptable for a reactor to have a higher pressure drop to achieve the most desired yields as long as the pressure drop is within a reasonable and allowable range. Nevertheless, this method still provides valuable guidance

for practical applications, including reactor development for different types of reactions, significantly reducing the reactor design time.

## 5. Conclusions

In summary, the present study has led to the following conclusions:

1. A modified meso-micromixing interaction reaction model was developed based on the flow characteristics in continuous reactors. The model was validated by comparing experimentally obtained yields with those predicted by this model. The modified model significantly reduced error in predicted product yields from approximately 15% to within 3%, compared to the model containing the micromixing term only.
2. Mixing performance in the reactor was improved by characterizing the decreasing  $X_S$  with increasing flow rate, the degree of twist in the mixing element's grooves, and the decreasing cross-sectional area of grooves. A high flow rate intensifies the energy dissipation of the fluid in the annular space between two mixing elements; high turn extends the flow path and increases the contact area between the areas with high and low flow velocities in the twisted grooves. When the cross-sectional area in the grooves becomes small, a significant plume flow can be formed in the annular space, improving mixing performance.
3. The optimization, in which the yields of target products and pressured drop in the reactors were chosen as the optimization objectives, was based on the modified model and performed by BO along with GPR. We obtained the highest product yield while keeping the pressure drop low. For the intermediate product, the yield was 92.5%, while the pressure drop in the reactor was 510.50 Pa. For the product in the last reaction, the yield was 94.3%, while the pressure drop in the reactor was 253.81 Pa. The corresponding combinations of reactor parameters were obtained. This kind of optimization method can be applied to the design of various reactors, providing a reference for structural selection and operational parameter determination.

**Supplementary Materials:** The following supporting information can be downloaded at: <https://www.mdpi.com/article/10.3390/pr11051576/s1>. Supporting information is available on model accuracy verification, mesh independence test, and the principles of the Villermaux–Dushman method, Gaussian process regression and Bayesian optimization.

**Author Contributions:** Conceptualization, methodology, CFD simulation, validation, formal analysis, writing—original draft preparation, writing—review and editing, J.J.; CFD simulation, formal analysis, supervision, N.Y.; Conceptualization, methodology, H.L. and J.T.; validation, C.W.; supervision, R.W. and X.Y. All authors have read and agreed to the published version of the manuscript.

**Funding:** This research is funded by the Jiangsu Seven Continents Green Chemical Co., Ltd.

**Institutional Review Board Statement:** Not applicable.

**Informed Consent Statement:** Not applicable.

**Data Availability Statement:** The data can be found in the supporting information.

**Conflicts of Interest:** The authors declare no conflict of interest.

## Nomenclature

ANN	Artificial neural network, for short
BO	Bayesian optimization, for short
$c_i$	The mole concentration of component $i$ , mol/m <sup>3</sup>
$d$	Groove depth, mm
$D$	The hydrodynamic diameter of the reactor cross-section, m
$E$	The engulfment rate in terms of micromixing, s <sup>-1</sup>
EDR	Energy dissipation rate, for short
$F$	Flow rate, mL/min

GPR	Gaussian process regression, for short
K	Criteria for multi-objective optimization
$L_G$	Distance between two mixing elements, mm
$L_M$	Length of a mixing element, mm
MSE	Mean square error, for short
P	Local pressure field, Pa
$\Delta P_{SAR}$	Pressure drop in the full domain of reactors
$r_i$	Intrinsic reaction rate of component i, mol/(m <sup>3</sup> ·s)
$R_I$	Outer radius of tube-in-tube reactors, mm
$R_O$	Inner radius of tube-in-tube reactors, mm
$R^2$	Coefficient of determination
Re	Reynold number
S	Skewness of curved grooves
SAR	Split-and-recombine reactor, for short
$t_d$	Mesomixing characteristic time, s
$t_m$	Micromixing characteristic time, s
u	Local velocity field, m/s
$u_m$	Average velocity along the flow direction, m/s
V	Volume of the reactor fluid domain
$X_0$	Ratio of initial flow rates in a tubular reactor
$X_B$	Volume of micromixed fluid relative to the whole fluid
$X_u$	Volume fraction which contains the partially segregated fluid as islands, embedded in a sea
$Y_1$	Intermediate product yield
$Y_2$	Final product yield
z	Axial position of the reactors, m
<b>Greek symbols</b>	
$\alpha$	Circulation angle, °
$\varepsilon$	Energy dissipation rate, m <sup>2</sup> /s <sup>3</sup>
$\Lambda_c$	Average from the integral scale of concentration fluctuations to Kolmogorov scale
$\mu$	Dynamic viscosity of the fluid, Pa·s
$\nu$	Kinematic viscosity of the fluid, Pa·s
$\rho$	Density of the fluid, kg/m <sup>3</sup>
$\varphi_B$	Ratio of fluid volume change after micromixing

## References

- Berton, M.; de Souza, J.M.; Abdiaj, I.; McQuade, D.T.; Snead, D.R. Scaling continuous API synthesis from milligram to kilogram: Extending the enabling benefits of micro to the plant. *J. Flow Chem.* **2020**, *10*, 73–92. [CrossRef]
- Hughes, D.L. Applications of Flow Chemistry in the Pharmaceutical Industry—Highlights of the Recent Patent Literature. *Org. Process. Res. Dev.* **2020**, *24*, 1850–1860. [CrossRef]
- Nagaki, A.; Yoshida, J.-I. Controlled Polymerization in Flow Microreactor Systems. In *Controlled Polymerization and Polymeric Structures: Flow Microreactor Polymerization, Micelles Kinetics, Polypeptide Ordering, Light Emitting Nanostructures*; Abe, A., Lee, K.-S., Leiber, L., Kobayashi, S., Eds.; Springer: Berlin/Heidelberg, Germany, 2013; pp. 1–50.
- Parua, S.; Sikari, R.; Sinha, S.; Chakraborty, G.; Mondal, R.; Paul, N.D. Accessing Polysubstituted Quinazolines via Nickel Catalyzed Acceptorless Dehydrogenative Coupling. *J. Org. Chem.* **2018**, *83*, 11154–11166. [CrossRef] [PubMed]
- Paul, E.L.; Treybal, R.E. Mixing and product distribution for a liquid-phase, second-order, competitive-consecutive reaction. *AIChE J.* **1971**, *17*, 718–724. [CrossRef]
- Bourne, J.R.; Ravindranath, K.; Thoma, S. Control of product distribution in mixing-controlled reactions. *J. Org. Chem.* **1988**, *53*, 5166–5168. [CrossRef]
- Rys, P. The Mixing-Sensitive Product Distribution of Chemical Reactions. *Chimia* **1992**, *46*, 469. [CrossRef]
- Christy, P.F.; Ridd, J.H.; Stears, N.D. Nitration of bibenzyl by nitronium tetrafluoroborate. Comments on the mechanism of nitration by nitronium salts. *J. Chem. Soc. B Phys. Org.* **1970**, 797–801. [CrossRef]
- Cox, S.M. Chaotic mixing of a competitive–consecutive reaction. *Phys. D Nonlinear Phenom.* **2004**, *199*, 369–386. [CrossRef]
- Baldyga, J.; Bourne, J.R.; Dubuis, B.; Etechells, A.W.; Gholap, R.V.; Zimmermann, B. Jet Reactor Scale-Up for Mixing-Controlled Reactions. *Chem. Eng. Res. Des.* **1995**, *73*, 497–502.

11. Bourne, J.R. Mixing and the Selectivity of Chemical Reactions. *Org. Process. Res. Dev.* **2003**, *7*, 471–508. [CrossRef]
12. Bałdyga, J.; Bourne, J.; Hearn, S. Interaction between chemical reactions and mixing on various scales. *Chem. Eng. Sci.* **1997**, *52*, 457–466. [CrossRef]
13. Samant, K.D.; Ng, K.M. Development of liquid-phase agitated reactors: Synthesis, simulation, and scaleup. *AIChE J.* **1999**, *45*, 2371–2391. [CrossRef]
14. Chin, P.; Barney, W.S.; A Pindzola, B. Microstructured reactors as tools for the intensification of pharmaceutical reactions and processes. *Curr. Opin. Drug Discov. Dev.* **2009**, *12*, 848–861.
15. Hessel, V.V.; Gursel, I.V.; Wang, Q.Q.; Noel, T.; Lang, J. Potential Analysis of Smart Flow Processing and Micro Process Technology for Fastening Process Development: Use of Chemistry and Process Design as Intensification Fields. *Chem. Eng. Technol.* **2012**, *35*, 1184–1204. [CrossRef]
16. Movsisyan, M.; Delbeke, E.I.P.; Berton, J.K.E.T.; Battilocchio, C.; Ley, S.V.; Stevens, C.V. Taming hazardous chemistry by continuous flow technology. *Chem. Soc. Rev.* **2016**, *45*, 4892–4928. [CrossRef] [PubMed]
17. Morse, P.D.; Beingessner, R.L.; Jamison, T.F. Enhanced Reaction Efficiency in Continuous Flow. *Isr. J. Chem.* **2017**, *57*, 218–227. [CrossRef]
18. Schlüter, M.; Herres-Pawlis, S.; Nieken, U.; Tuttlies, U.; Bothe, D. Small-Scale Phenomena in Reactive Bubbly Flows: Experiments, Numerical Modeling, and Applications. *Annu. Rev. Chem. Biomol. Eng.* **2021**, *12*, 625–643. [CrossRef]
19. Lira, J.O.; Riella, H.G.; Padoin, N.; Soares, C. Computational fluid dynamics (CFD), artificial neural network (ANN) and genetic algorithm (GA) as a hybrid method for the analysis and optimization of micro-photocatalytic reactors: NO<sub>x</sub> abatement as a case study. *Chem. Eng. J.* **2022**, *431*, 133771. [CrossRef]
20. Gambella, C.; Ghaddar, B.; Naoum-Sawaya, J. Optimization problems for machine learning: A survey. *Eur. J. Oper. Res.* **2021**, *290*, 807–828. [CrossRef]
21. Stulp, F.; Sigaud, O. Many regression algorithms, one unified model: A review. *Neural Netw.* **2015**, *69*, 60–79. [CrossRef]
22. Ryan, E.G.; Drovandi, C.C.; McGree, J.M.; Pettitt, A.N. A Review of Modern Computational Algorithms for Bayesian Optimal Design. *Int. Stat. Rev.* **2015**, *84*, 128–154. [CrossRef]
23. Greenhill, S.; Rana, S.; Gupta, S.; Vellanki, P.; Venkatesh, S. Bayesian Optimization for Adaptive Experimental Design: A Review. *IEEE Access* **2020**, *8*, 13937–13948. [CrossRef]
24. Zuhail, L.R.; Amalinadhi, C.; Dwianto, Y.B.; Palar, P.S.; Shimoyama, K. Benchmarking multi-objective Bayesian global optimization strategies for aerodynamic design. In Proceedings of the 2018 AIAA/ASCE/AHS/ASC Structures, Structural Dynamics, and Materials Conference, Kissimmee, FL, USA, 8–12 January 2018.
25. Park, S.; Na, J.; Kim, M.; Lee, J.M. Multi-objective Bayesian optimization of chemical reactor design using computational fluid dynamics. *Comput. Chem. Eng.* **2018**, *119*, 25–37. [CrossRef]
26. Guichardon, P.; Falk, L. Characterisation of micromixing efficiency by the iodide–iodate reaction system. Part I: Experimental procedure. *Chem. Eng. Sci.* **2000**, *55*, 4233–4243. [CrossRef]
27. Guichardon, P.; Falk, L.; Villermaux, J. Characterisation of micromixing efficiency by the iodide–iodate reaction system. Part II: Kinetic study. *Chem. Eng. Sci.* **2000**, *55*, 4245–4253. [CrossRef]
28. Gobert, S.R.L.; Kuhn, S.; Braeken, L.; Thomassen, L.C.J. Characterization of Milli- and Microflow Reactors: Mixing Efficiency and Residence Time Distribution. *Org. Process. Res. Dev.* **2017**, *21*, 531–542. [CrossRef]
29. Feng, Y.; Zhang, H.; Wang, J.; Yang, Y. Performance Evaluation and Scale-Up Behavior of an Engineered In-Line Mixer for 3D Printing. *Ind. Eng. Chem. Res.* **2021**, *60*, 11568–11578. [CrossRef]
30. Martínez, A.N.M.; Chaudhuri, A.; Assirelli, M.; van der Schaaf, J. Effects of increased viscosity on micromixing in rotor–stator spinning disk reactors. *Chem. Eng. J.* **2022**, *434*, 134292. [CrossRef]
31. Commenge, J.-M.; Falk, L. Villermaux–Dushman protocol for experimental characterization of micromixers. *Chem. Eng. Process. Process. Intensif.* **2011**, *50*, 979–990. [CrossRef]
32. Arian, E.; Pauer, W. A comprehensive investigation of the incorporation model for micromixing time calculation. *Chem. Eng. Res. Des.* **2021**, *175*, 296–308. [CrossRef]
33. Wenzel, D.; Assirelli, M.; Rossen, H. On the reactant concentration and the reaction kinetics in the Villermaux–Dushman protocol. *Chem. Eng. Process.-Process Intensif.* **2018**, *130*, 332–341. [CrossRef]
34. Fournier, M.C.; Falk, L.; Villermaux, J. A new parallel competing reaction system for assessing micromixing efficiency—Experimental approach. *Chem. Eng. Sci.* **1996**, *51*, 5053–5064. [CrossRef]
35. Khalde, C.M.; Ramanan, V.; Sangwai, J.S.; Ranade, V.V. Passive Mixer cum Reactor Using Threaded Inserts: Investigations of Flow, Mixing, and Heat Transfer Characteristics. *Ind. Eng. Chem. Res.* **2020**, *59*, 3943–3961. [CrossRef]
36. Bałdyga, J.; Bourne, J. A fluid mechanical approach to turbulent mixing and chemical reaction part II micromixing in the light of turbulence theory. *Chem. Eng. Commun.* **1984**, *28*, 243–258. [CrossRef]
37. Bałdyga, J.; Bourne, J. Interactions between mixing on various scales in stirred tank reactors. *Chem. Eng. Sci.* **1992**, *47*, 1839–1848. [CrossRef]
38. Bałdyga, J.; Bourne, J. Simplification of micromixing calculations. I. Derivation and application of new model. *Chem. Eng. J.* **1989**, *42*, 83–92. [CrossRef]
39. Bałdyga, J.; Pohorecki, R. Turbulent micromixing in chemical reactors—A review. *Chem. Eng. J. Biochem. Eng. J.* **1995**, *58*, 183–195. [CrossRef]

40. Ghanem, A.; Lemenand, T.; Valle, D.D.; Peerhossaini, H. Static mixers: Mechanisms, applications, and characterization methods—A review. *Chem. Eng. Res. Des.* **2014**, *92*, 205–228. [CrossRef]
41. Baldyga, J.; Bourne, J.; Yang, Y. Influence of feed pipe diameter on mesomixing in stirred tank reactors. *Chem. Eng. Sci.* **1993**, *48*, 3383–3390. [CrossRef]
42. Villermaux, J.; Falk, L. A generalized mixing model for initial contacting of reactive fluids. *Chem. Eng. Sci.* **1994**, *49*, 5127–5140. [CrossRef]
43. Ertesvåg, I.S.; Magnussen, B.F. The Eddy Dissipation Turbulence Energy Cascade Model. *Combust. Sci. Technol.* **2000**, *159*, 213–235. [CrossRef]
44. Martínez, A.N.M.; Jansen, R.; Walker, K.; Assirelli, M.; van der Schaaf, J. Experimental and modeling study on meso- and micromixing in the rotor–stator spinning disk reactor. *Chem. Eng. Res. Des.* **2021**, *173*, 279–288. [CrossRef]
45. Woldemariam, M.; Filimonov, R.; Purtonen, T.; Sorvari, J.; Koiranen, T.; Eskelinen, H. Mixing performance evaluation of additive manufactured milli-scale reactors. *Chem. Eng. Sci.* **2016**, *152*, 26–34. [CrossRef]
46. Shields, B.J.; Stevens, J.; Li, J.; Parasram, M.; Damani, F.; Alvarado, J.I.M.; Janey, J.M.; Adams, R.P.; Doyle, A.G. Bayesian reaction optimization as a tool for chemical synthesis. *Nature* **2021**, *590*, 89–96. [CrossRef] [PubMed]
47. Lv, J.; Liu, Z.; Liu, W. Active design for the tube insert of center-connected deflectors based on the principle of exergy destruction minimization. *Int. J. Heat Mass Transf.* **2020**, *150*, 119260. [CrossRef]
48. Ofman, P.; Struk-Sokołowska, J. Artificial Neural Network (ANN) Approach to Modelling of Selected Nitrogen Forms Removal from Oily Wastewater in Anaerobic and Aerobic GSBP Process Phases. *Water* **2019**, *11*, 1594. [CrossRef]
49. Abdollahi, A.; Shams, M. Optimization of shape and angle of attack of winglet vortex generator in a rectangular channel for heat transfer enhancement. *Appl. Therm. Eng.* **2015**, *81*, 376–387. [CrossRef]
50. Neal, R.M. *Bayesian Learning for Neural Networks*; Springer Science & Business Media: Berlin/Heidelberg, Germany, 2012; Volume 118.

**Disclaimer/Publisher’s Note:** The statements, opinions and data contained in all publications are solely those of the individual author(s) and contributor(s) and not of MDPI and/or the editor(s). MDPI and/or the editor(s) disclaim responsibility for any injury to people or property resulting from any ideas, methods, instructions or products referred to in the content.

*Perspective*

# CFD Applications in Energy Engineering Research and Simulation: An Introduction to Published Reviews

**Alfredo Iranzo**

Energy Engineering Department, University of Sevilla, 41092 Sevilla, Spain; airanzo@us.es; Tel.: +34-954-487471

Received: 17 October 2019; Accepted: 21 November 2019; Published: 26 November 2019

**Abstract:** Computational Fluid Dynamics (CFD) has been firmly established as a fundamental discipline to advancing research on energy engineering. The major progresses achieved during the last two decades both on software modelling capabilities and hardware computing power have resulted in considerable and widespread CFD interest among scientist and engineers. Numerical modelling and simulation developments are increasingly contributing to the current state of the art in many energy engineering aspects, such as power generation, combustion, wind energy, concentrated solar power, hydro power, gas and steam turbines, fuel cells, and many others. This review intends to provide an overview of the CFD applications in energy and thermal engineering, as a presentation and background for the Special Issue “CFD Applications in Energy Engineering Research and Simulation” published by Processes in 2020. A brief introduction to the most significant reviews that have been published on the particular topics is provided. The objective is to provide an overview of the CFD applications in energy and thermal engineering, highlighting the review papers published on the different topics, so that readers can refer to the different review papers for a thorough revision of the state of the art and contributions into the particular field of interest.

**Keywords:** computational fluid dynamics; energy engineering; modelling; simulation; renewable energy; combustion; turbulence; heat transfer; thermal radiation

---

## 1. Introduction

Since the early contributions from D.B. Spalding and co-workers at Imperial College London and CHAM (Concentration Heat and Momentum) [1–3], Computational Fluid Dynamics has become a powerful tool for engineers and researchers of a wide range of applications. With the increasing computing power and development of both physical models and numerical and discretization techniques, CFD is nowadays considered to be a highly valuable must-have tool in the investigation of fluid flow. The main reasons are that CFD allows for the systematic analysis and optimization of the fluid flow field without the need for interfering with the flow itself, which is not always possible with conventional experimental techniques. CFD also allows the (virtual) observation of flow variables at locations that may not be accessible to measuring instruments.

Computational Fluid Dynamics has a wide variety of applications in energy engineering and research, namely the modelling of combustion, heat transfer, and multiphase flow, and in the simulation of gas and steam turbines, wind turbines, or tidal and wave devices. A very significant widespread of CFD has been observed during the last two decades in terms of users and number of applications, and indeed the CFD business reached a value of \$1.0 billion in 2013, with around a 10% annual growth rate in industry.

However, CFD is not yet at the level where it can be used by designers or analysts without a working knowledge of the numerical algorithms involved, and despite the increasing computational resources, CFD has not yet evolved to a level where it can be straightforward to use. Numerical

analyses still require significant effort to be set up, run, and analyzed. Therefore, CFD is in fact an aid to other analysis and experimental tools and must be used in conjunction with them.

## 2. Computational Fluid Dynamics (CFD)

Computational fluid dynamics, commonly known as CFD, consists of the resolution of the fluid flow governing equations by using numerical techniques implemented in a computer code. The domain of interest is divided into small volumes using a mesh, where the set of partial differential equations are discretized into algebraic equations and then solved in an iterative fashion. The basic fluid flow simulation involves the Navier–Stokes equations for the transport and conservation of mass and momentum. Additional physical and chemical phenomena can be included in the model by adding the correspondent transport equations: Chemical species conservation, heat transfer, and other coupled phenomena such as electrochemistry, magneto-hydrodynamics, and others.

The methodology for a CFD analysis comprises a pre-processing stage, a solver stage, and a post-processing stage. During pre-processing, the geometry for the domain of interest is generated. The corresponding fluid volume is divided into discrete cells in the mesh generation process. The physical model is then setup by defining fluid properties, physical models, and boundary conditions. For transient problems, the initial conditions are defined, and the time continuum is discretized into time steps. The equations are solved iteratively using appropriate discretization and numerical algorithms, and finally during the post-processing stage, the results analysis and flow visualization is performed.

The Navier–Stokes equations, also known as conservation or transport equations, which govern the fluid flow motion, can be written in its general form as:

$$\frac{\partial}{\partial t} \int_V \rho \varnothing dV + \oint_A \rho \varnothing V \cdot dA = \oint_A \Gamma \nabla \varnothing \cdot dA + \int_V S_{\varnothing} dV \quad (1)$$

where  $\varnothing$  is the transported quantity,  $t$  is the time,  $A$  the superficial area,  $V$  the volume,  $\Gamma$  is transported quantity diffusivity, and  $S_{\varnothing}$  is the source of  $\varnothing$ . The first term in the equation corresponds to the transient transport of  $\varnothing$ , the second term to the transport by convection mechanism, the third term represents the transport of  $\varnothing$  by diffusion, and the fourth term represents the source (or sink) of  $\varnothing$ . The different transport equations are assembled by using the appropriate variables, as shown in Table 1.

**Table 1.** Main transport equations used in Computational Fluid Dynamics (CFD) analysis.

Equation	Variable $\varnothing$
Continuity	1
x-momentum	u (velocity in x-direction)
y-momentum	v (velocity in y-direction)
z-momentum	w (velocity in z-direction)
Energy	h (enthalpy)
Chemical specie i	yi (mass fraction of i)

## 3. CFD Applications in Energy Engineering Research and Simulation

This section will cover the main CFD applications in energy and thermal engineering. A thorough review of such a wide variety of different applications is however not feasible within one single publication. Instead, a brief introduction to the most significant reviews that have been published on the particular topics related to CFD in energy and thermal engineering is provided. The objective of the review is thus to provide an overview of the CFD applications in energy and thermal engineering, highlighting the review papers published on the different topics, so that readers can refer to the different review papers for a thorough revision of the state of the art and contributions into the particular field of interest. The applications covered are depicted in Figure 1.



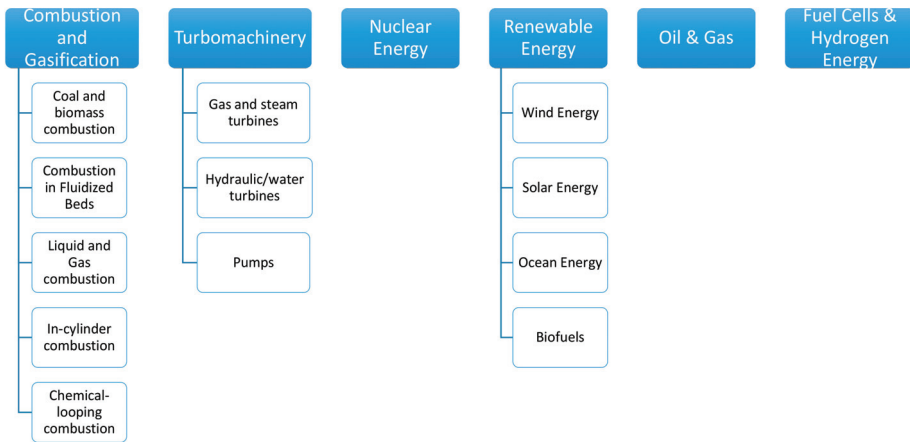


**Figure 1.** CFD applications related to energy and thermal engineering covered in this review.

To date, there has been a significant scientific production regarding CFD application in the areas indicated in Figure 1. The number of publications identified for each particular field are presented in Figure 2.

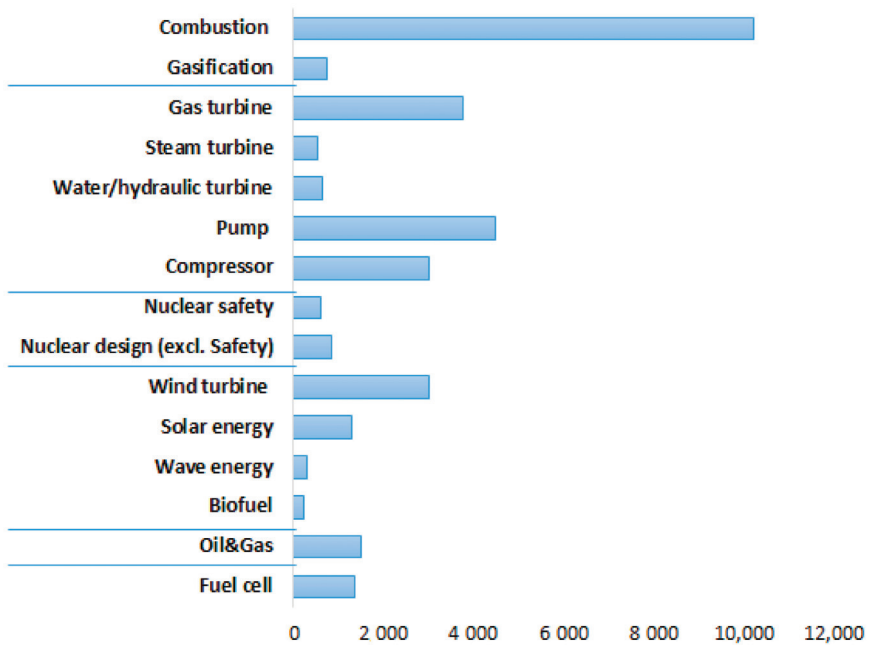


**Figure 2.** Bibliometric study: Number of scientific publications in the areas indicated in Figure 1.

### 3.1. Combustion and Gasification

Combustion is one of the major fields of application of CFD, where the wide variety of combustion types have been deeply explored (coal and biomass, liquids, gas, oxy-combustion, and others). The basic models for turbulent combustion initially developed for very high or very low Damköhler numbers

(reaction rate limited by reactants mixing or by chemical kinetics) were the eddy break up (EBU, also known as eddy dissipation model—EDM) and the finite rate chemistry (FRC) model. Both basic models were further developed and refined, and additional models have been progressively developed, such as the flamelet model for non-premixed combustion describing the interaction of chemistry with turbulence.

### 3.1.1. Coal and Biomass Combustion

CFD simulation of coal combustion in boilers has attracted much attention during the last decades as it has been typically one of the main technologies for power generation. Coal combustion involves many different modelling issues such as multiphase modelling, chemical reactions, heat transfer, and radiation or emissions modelling (Figure 3). Pulverized coal particles tracked within a Lagrangian integration framework is the most typical simulation method to compute the multiphase flow, that must be coupled to heat and mass transfer models to account for devolatilization.

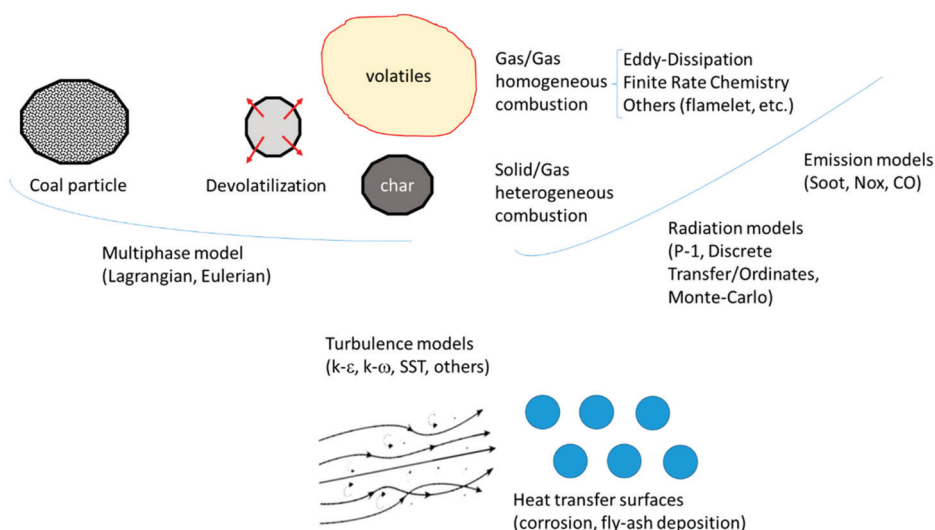


**Figure 3.** Main processes and models involved in coal combustion.

One of the first reviews on the topic was published by Phil Stopford [4] in 2002, when AEA Technology was owner of the CFX-4 code. The review focuses on coal-fired low-NO<sub>x</sub> burner design, furnace optimization, over-fire air, gas re-burn, and laminar flames. CFD modelling of pulverized coal boilers has been also reviewed by Diez et al. [5] and Sankar et al. [6], as well as by Kurose et al. [7]. Other applications such as pulverized coal in blast furnaces were reviewed by Shen et al. [8]. A particular focus on modelling of poly-dispersed particles in reactive flows by population balance models (PBM) was done by Rigopoulos [9] with applications not only on coal combustion, but also many others such as soot formation or spray combustion. Finally, the coupling of CFD simulation of equipment with process simulation codes have been reviewed by Zitney [10]. Overall, the major challenges in pulverized coal combustion are the modelling of chemical kinetics (both devolatilization and char combustion), radiation, and the overall furnace modelling. The current trends in devolatilization generally involve multi-step kinetic models [6]. In any case, it is crucial that an appropriate coal characterization is carried out. Regarding radiation, not only the adequate radiation model must be selected (that will depend on the optical thickness, where the effect of flying-ash should be considered), but also the gas radiation properties model.

Although most of the considerations above are applicable to biomass combustion, such a process presents particular modelling issues, and modelling approaches were reviewed by Dernbecher et al. [11] or Haberle et al. [12] and Chaney et al. [13] for small-scale grate furnaces and boilers. A particular focus on CFD modelling of biomass gasification was reviewed by Mazaheri et al. [14]. Gasification is a particularly complex process involving chemical kinetics, heat and mass transfer, and thermochemical equilibrium, that in addition can take place in a wide range of gasifier designs currently being investigated [14], and with very different types of biomass feedstock. All this complexity makes biomass gasification particularly challenging for CFD modelling, and it is generally recognized that there is still a lack of accurate gasification models and procedures for assessing the different types of gasifiers [14].

Co-firing of coal and biomass in industrial boilers and furnaces has been covered in recent reviews by Tabet et al. [15] or Bhuiyan et al. [16], focusing as well on slagging issues when co-firing is used.

Oxy-fuel combustion of pulverized coal is also a topic of major interest (as a promising technology for CO<sub>2</sub> capture) and its CFD modelling has been specifically addressed by Chen et al. [17], Yin et al. [18], or Edge et al. [19]. CFD is expected to play a vital role for the oxy-fuel combustion technology development as it played for conventional combustion processes. Research efforts are particularly put on modelling how oxy-fuel conditions are affecting combustion physics and chemistry such as turbulent gas–solid flow, heat and mass transfer, pyrolysis, or char reactions [19].

Finally, there are specific issues and challenges associated to coal combustion and its CFD modelling, such as slagging [20] or erosion modelling [21].

### 3.1.2. Combustion in Fluidized Beds

Fluidized beds (FBs) are widely used in the chemical and process industry and are also used for the combustion of solids and gasification. Simulations (Figure 4) are involving transient multiphase flows with particular treatments for very dense particulate flows (mostly based on the kinetic theory of gases) and, in general, small time-step sizes are required to achieve convergence. This makes CFD unsuitable to address large 3D industrial cases within the commonly available computing power.

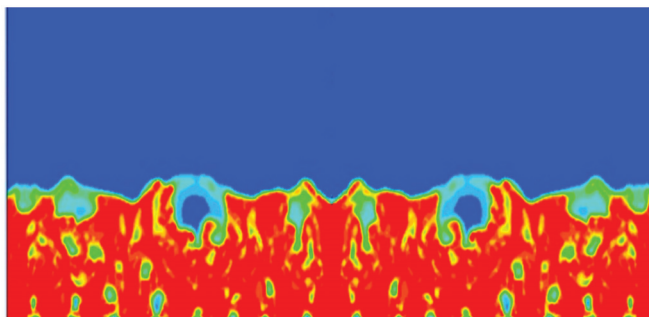


**Figure 4.** Time snapshot of a CFD simulation of fluidized bed (gas volume fraction in blue, sand particles volume fraction in red).

CFD modelling of fluidized bed combustion for biomass and co-firing was reviewed by Kumar et al. [22], Kuffa [23], and Singh [24], whereas the particular application of CFD simulation of FBs in waste-to-energy plants was discussed by Ravelli et al. [25]. The reviews demonstrate that CFD has been extensively used to analyze the distributions of chemical species, temperature and heat fluxes, ash deposition, and pollutants concentrations in both combustion and gasification in fluidized beds [24]. It is, however, clear that simulation models are still approximations and many assumptions are required, such as when considering Eulerian–Eulerian approaches with variation in particle sizes.

### 3.1.3. Liquid and Gas Combustion

Roslyakov et al. [26] very recently published a review on CFD modelling of liquid and gaseous fuel combustion in power generation installations. An in-depth review on the modelling of turbulent burning rates for gaseous fuels was published by Bradley [27]. The atomization and transport of liquid fuel droplets during the evaporation process is of particular importance when modelling burners and combustion of liquid fuels, whereas the subsequent combustion in gas phase is typically modelled with the eddy break up model (EBU, also known as eddy dissipation model—EDM).

### 3.1.4. In-Cylinder Combustion

Combustion in engines has been of major importance for the automotive industry and for other propulsion systems, aiming at developing low-fuel-consumption and low-emissions internal combustion engines. Review papers were published already in the 1990s such as by Reitz and Rutland [28] on diesel engines or Gosman [29]. CFD modelling of diesel combustion engines was reviewed by Barths et al. [30], and dual fuel diesel-CNG (Compressed Natural Gas) engines by Shah et al. [31]. A focus on turbulence modelling able to represent different combustion regimes and detailed chemical kinetics was carried out in the review of Haworth [32], while the application of Large-Eddy Simulation (LES) models represents a significant contribution to the topic [33]. The Engine Combustion Network (ECN) provided a review on the methodology to properly characterize and control ambient and fuel-injector boundary conditions [34], which is of major importance for accurate results. CFD combustion modelling in engines is a mature application, but there is a need for model improvements in some areas such as spray modelling (break-up, atomization) and other related phenomena such as wall films and wall heat transfer in such conditions. Some of the problems requiring a particular accuracy on flow unsteadiness such as cyclic variation and design sensitivity can be probably better studied with LES [33], but appropriate submodels must be carefully used.

### 3.1.5. Chemical-Looping Combustion

Chemical-looping combustion (CLC) consists of a two-step process interconnecting two fluidized beds reactors (circulating fluidized bed for air reactor and bubbling fluidized bed for fuel reactor). Oxygen is carried from air to fuel by means of a carrier (a highly reactive metal particle) thus avoiding direct contact between air and fuel and resulting in a flameless combustion with pure CO<sub>2</sub> exhaust stream suitable for sequestration. Multiphase modelling is one of the fundamental issues in chemical-looping combustion (apart to reacting flow), and thus different drag models to account for the solid–gas interaction can be found in the review by Banerjee and Agarwal [35] or Jung and Gamwo [36]. A better knowledge of the multiphase reactive gas–solid flow is fundamental for the simulation of CLC combustors.

## 3.2. Turbomachinery

CFD is playing a major role in the aerodynamic design of turbomachines, and currently all modern designs are being aided by the use of CFD, with clear reductions in the costs and design cycles. Denton and Dawes [37] published one of the earliest reviews devoted to computational fluid dynamics for turbomachinery design in 1999, while Moore and Moore [38] reviewed methods and models related to in two-equation turbulence models applied to compressors and turbine cascades. The state of the art of the use of open-source CFD software was analyzed by Casartelli and Mangani [39], and Pinto et al. [40] reviewed the work carried out in the CFD analysis for turbines, compressors, and centrifugal pumps, also discussing parallelization issues and strategies.

### 3.2.1. Gas and Steam Turbines

Predicting flow field and heat transfer in the cooling passages and cavities of gas turbines and jet engines is of major importance for the design of more efficient and robust machines. Flow is strongly

turbulent along the intricate passages, with the aim to achieve higher heat transfer coefficients. Flow separation, rotation and curvature, and impingement, are some of the challenges to the advanced turbulence modelling currently being applied. For the particular application of blade cooling in gas turbines, Iacovides and Launder [41] published a review in 1995 and have later also been addressed together with additional modelling issues such as hot gas path modelling by Dawes [42] and Horlock and Denton [43]. Steam turbines were particularly addressed by Tominaga and Tanuma [44]. Multistage and unsteady predictions have become common practice in the last decade as the increased computer power has enabled such simulations. Among the significance of unsteady calculations, it is relevant to mention the simulation of two-way fluid–structure interaction (FSI) for investigations such as unsteady blade loading and the assessment of mechanical aspects in the turbine blades. The consequences of unsteady flows on the loss generation are also being explored. Secondary gas paths are also significantly being analyzed, such as leakage flows, cooling flows, and cavity flows (as in shroud leakage flows in turbines). Such flows are highly turbulent and, thus, their simulation is very reliant on the turbulence modelling capabilities [43], where Scale Adaptive Simulation (SAS) has been applied with success.

### 3.2.2. Hydraulic/Water Turbines

CFD modelling and simulation of hydraulic turbomachines has been the objective of review articles such as in Sick and Wilson [45], Keck and Sick [46], or Trivedi et al. [47]. A particular focus was put on horizontal axis turbines by Lain et al. [48], while the state of the art in CFD modelling of Pelton turbines was discussed by Židonis and Aggidis [49]. Both steady-state and transient simulation of hydraulic turbines are widely carried out, where steady-state conditions include the calculation of the best efficiency point, high load, and part load conditions. Transient simulations focus on load variation, startup, shutdown, and total load rejection [47]. Such simulations are challenging due to the time-dependent movement of the guide vanes, requiring dynamic/moving meshes (or overset or “chimera” meshes). Off-design conditions are also challenging as the flow field is usually unstable.

The simulation domain considered ranges from component modelling (which is the most common for example in Francis and Kaplan turbines), to the complete turbine modelling and passage modelling. When simulating a turbine component, accurate boundary conditions are crucial for ensuring reliable results [47]. Two-way FSI is also being applied to water turbines to analyze the mechanical behavior of the turbine components.

### 3.2.3. Pumps

CFD is commonly applied to the investigation and design of centrifugal pumps, typically for the performance prediction at design and off-design conditions, cavitation analysis, diffuser design, parametric studies, or pump performance when running in turbine mode. Besides diffuser and impeller flows, the analysis of volute flow and the impeller–volute interaction is also being investigated for further improvement of the pump performance. Centrifugal pumps have been addressed by Shah et al. [50], and Niedzwiedzka et al. [51] reviewed the specific topic of CFD modelling of cavitating flows. The particular applications in pumps that can be likewise used as turbines (reverse running pumps) were discussed by Nautiyal et al. [52]. Some active research fields are two phase flow in pumps, fluid–structure interaction, and non-Newtonian fluids [50].

### 3.3. Nuclear

The use of CFD in nuclear power generation has been traditionally focused on safety analysis, for modelling different scenarios such as loss-of-coolant, and the related safety measures. The results and progresses of the benchmark case proposed by the Organization for Economic Co-operation and Development (OECD)/Nuclear Energy Agency to assess the predictive capabilities of (CFD) codes were reported by Kelm et al. [53]. The Korea Institute of Nuclear Safety (KINS) is auditing calculation activities on the applicability of CFD software to nuclear safety problems and discussed checking whether valid CFD software is used for nuclear safety problems [54]. Many other works investigate

multiphase flow and boiling, involving critical heat flux (CHF) simulations [55–58]. Indeed, the thermal hydraulics of the reactor core is one of the key issues for safety. The complex geometry and non-uniform heating make thermal-hydraulics and CHF predictions in light water reactors (LWR) particularly challenging. Abrupt transients caused by sudden flow regime transition and their implications in CHF events have also been analyzed [57]. CFD modelling include additional challenges such as coupling of single and two-phase turbulent flow over a wide range of thermal-hydraulic conditions, and flow boiling, for both natural and forced convection [57].

Fuel bundle analysis and thermo-hydraulic design (spacers, etc.) have also been modelled, and reviews were published by Moorthi et al. [59] or Verman et al. [60]. The developments of AREVA S.A. on predicting flow field and thermal mixing within fuel bundles and fuel assembly components were discussed in [61], focusing as well on validation.

### 3.4. Renewable Energies

#### 3.4.1. Wind

Wind energy is progressively increasing its share in electricity production worldwide, and major research efforts have been made for enhancing turbine blade aerodynamics [62–66]. Hybrid methods combining CFD with BEM (blade element momentum) have some advantages such as reducing the computational time required for the aerodynamic load analysis of turbine blades [63]. In addition, optimization methods such as GA (genetic algorithms) have been widely applied in the optimization of wind turbines [63]. It is fully recognized that CFD is enabling the achievement of better aerodynamic designs and larger turbine efficiencies [64], where CFD is primarily focused not only on blade optimization, but also on micro-siting, wind modelling and prediction, or noise prediction.

Flow aerodynamics around turbine blades is complex and challenging, and typically two approaches are used to account for the blades rotation: One being the multiple frames of reference (where steady-state simulations are possible), the second being the use of dynamic meshes where a transient simulation is defined to accurately capture the flow around the rotating blade (with obviously a much higher computational effort). CFD and blade aero-elasticity was discussed by Hansen et al. [67]. CFD for the particular design of horizontal-axis wind turbines (HAWT) has been discussed together with experimental approaches [68] transition modelling [69], and review of CFD, FE codes, and experimental practices [70]. It can be determined that the accuracy of the simulations is, overall, determined by the turbulence model, where for turbine wake modelling, LES is generally applied [68].

Darrieus vertical axis wind turbines were reviewed by Ghasemian et al. [71]. Similarly, wind farm aerodynamics is a significant contribution to CFD to wind energy [72], and wind flow around buildings for urban wind energy exploitation has also been recently reviewed by Toja-Silva et al. [73]. Some relevant physics such as wake meandering, effect of atmospheric stratification on wake development, or the response of the turbine to partial wake interaction can only be addressed currently by CFD [72]. Wind farms are also modelled with LES, and particularly with advanced SGS models. The correct modelling of the atmospheric boundary layer and its interaction with turbines is crucial for guaranteeing accurate results.

Further developments in CFD modelling for wind energy will be covering topics such as advanced atmospheric boundary layer simulation in complex terrains such as cliffs or wake–wake interactions [64].

#### 3.4.2. Solar

CFD has been widely and successfully used for optimizing the heat transfer in solar collectors and for components design, enhancing the efficiency of the collectors and receivers. Solar air heaters have been thoroughly investigated with aid of CFD modelling and simulations [74–78] for heat transfer enhancement. The thermal performance of solar air heaters has been extensively investigated, and optimum values of relative roughness pitch ( $P/e$ ) and relative roughness height ( $e/D$ ) in roughened

solar air heater duct obtained by different researchers are summarized and tabulated in the review work by Manjunath et al. [75].

Solar drying systems [79] and solar receivers in central receiver systems have been reviewed recently [80]. Heliostats are an additional field of CFD work in order to assess aerodynamic wind loads for a suitable design of the related mechanical and tracking systems [81].

#### 3.4.3. Ocean Energy

Wave energy converters (WECs) are attracting a significant attention with progresses achieved within several development programs. Numerical tools such as CFD of numerical wave tanks (NWTs) provide an excellent and cost-effective tool. A comprehensive review on NWTs based on CFD approaches was published by Windt et al. [82] including best practice guidelines for CFD in the field of wave energy. CFD studies on axial flow turbines for WECs were reviewed by Cui et al. [83], whereas the particular case of numerical modelling of tidal stream turbines was discussed by Masters et al. [84]. CFD work on WECs started on 2004 [82] and has shown a clear progression in model fidelity and capabilities, although there are known shortcomings to be tackled, such as the accurate modelling of the power take-off (PTO) system dynamics for a better analysis of WEC performance, loading, or control strategies [82].

#### 3.4.4. Biofuels

Although biofuels production is not one of the most extensive application of CFD, many works can be found in the literature both for liquid biofuels (bioethanol, biodiesel, green diesel) [85] and biogas [86]. Thermochemical conversion of biomass to provide gaseous, liquid, and solid fuels was reviewed by Wang et al. [87]. It can be determined that biodiesel production has attracted much of the CFD activities in biofuel production simulation, while others (biogasoline or aviation biojet fuels) are not currently found in the literature [85]. Moreover, there is a significant potential for further refining the modelling of the chemical reactions involved, together with a need for the use of multi-physics modelling involving also heat and mass transfer and development of more accurate interfacial mass transfer for equipment involving multi-phase reactions [85].

#### 3.5. Oil & Gas

The oil and gas industry represents one of the major contributors to energy engineering (and it is slowly re-orienting some of its activities in order to increasingly become global players in the renewable energy industry in the medium term). Oil and gas has extensively been applying CFD during the last decades [88], including liquid loading phenomena in gas wells [89] and piping systems [90]. Liquefied natural gas production has become likewise a relevant technology and CFD applications for heat exchangers have been discussed by Samokhvalov et al. [91]. Overall, a very large number of different applications are increasingly being simulated in oil and gas, involving different flow configurations, single-phase, or gas–liquid, gas–solid, and also gas–liquid–solid. The coupling of multi-phase flow with mass and heat transfer and with chemical reactions is one of the major challenges in CFD modelling in such applications [88]. Future developments are required in order to develop more accurate interaction laws between phases (involving momentum transfer and heat and mass transfer), particularly for the complex flows commonly found in oil and gas.

#### 3.6. Fuel Cells and Hydrogen Energy

In fuel cells, not only fluid flow and heat and mass transfer must be modelled, but also additional phenomena such as electrochemistry, in order to compute the reactants oxidation and reduction rates. The overpotential or difference between the solid and electrolyte/membrane potential is the driving force for the reactions, and therefore, potential equations are solved in these models (one equation describing the electron transport inside the solid materials such as current collectors, and a second potential equation representing the ionic transport inside the electrolyte). A comprehensive review on

the fundamental models for fuel cells was published by Wang [92], including discussion for validation requirements, with additional reviews published afterwards [93–97]. Aman et al. [98] addressed the particular case of solid-oxide fuel cells. The numerical models for PEM (Polymer Electrolyte Membrane) fuel cell cold start were reviewed by Guo et al. [99]. Apart from the investigation of reactants distributions in bipolar plates and electrodes (Figure 5), it is well known that liquid water management is a fundamental research field in PEM-type fuel cells, and its CFD modelling has been the focus of several reviews [100–105]. Future developments in Fuel Cell CFD modelling will surely be devoted to the challenging water transport and multi-phase physics involved in the different cell components: Dissolved water for membrane hydration, phase change (evaporation, condensation), water transport in the porous media of both the catalyst and gas diffusion layers, and the different gas–liquid flows regimes occurring in the bipolar plate channels, also influenced by surface tension and wall adhesion, as well as further refinements of electrode models (cathode particle or agglomerate models).

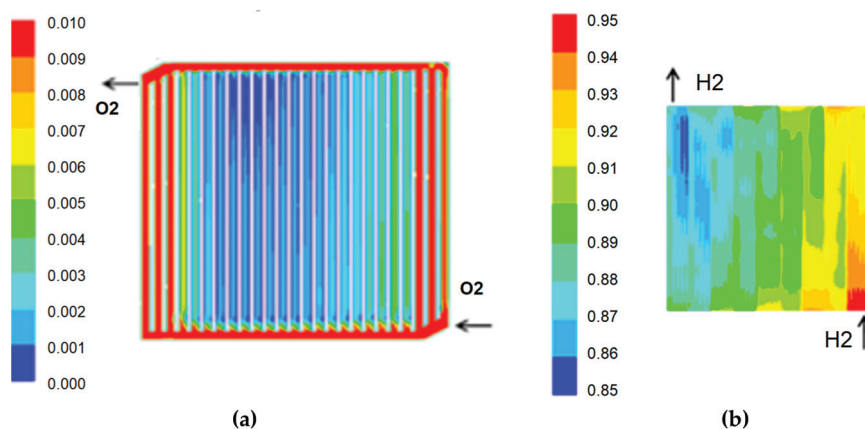


**Figure 5.** PEM fuel cell CFD simulation showing (a) velocity distribution in the cathode channels of a parallel bipolar plate; (b) hydrogen distribution over the anode electrode with a serpentine bipolar plate.

Regarding hydrogen production, Tapia et al. [106,107] reviewed a general CFD methodology for the design and analysis of solar reactors based on thermochemical cycles. The modelling of solar reactors requires the use of a radiation model, where, in general, surface-to-surface radiation is modelled as volumetric absorption in the media and can be neglected. However, in case the radiation direction is important (such as concentrated radiation coming from a heliostat field), the Monte-Carlo model is recommended in order to achieve a correct representation of the incoming radiation (Figure 6).



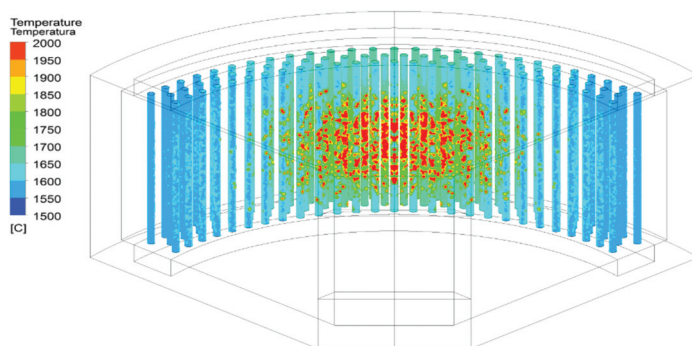


**Figure 6.** Temperature distribution over a multi-tubular solar reactor for hydrogen production.

### 3.7. Heat Transfer Processes and Other Applications

Other additional applications of CFD in energy engineering that have been thoroughly discussed are thermal energy storage, both for latent [108] and phase change materials [109]. Electronics cooling is also a field with a significant growth [110]. CFD analysis of heat exchangers was addressed by Aslam Bhutta et al. [111], and applications of for the design of thermal processes in the food industry by Norton et al. [112] and Zhao et al. [113].

## 4. Software Tools

There is currently a broad choice of CFD solvers, mesh generation software, and visualization tools. Both commercial and free or open source software is available, where the most common software tools currently being used are indicated in Table 2.

**Table 2.** Main software tools used in CFD analysis on energy engineering.

Software Vendor	Software Name	Purpose
ANSYS Inc	ANSYS-FLUENT	Meshing/Solver/Visualization
	ANSYS-CFX	
Siemens Industry Software Inc.	STAR-CCM+	Meshing/Solver/Visualization
COMSOL Group	COMSOL Multiphysics	Meshing/ Solver/Visualization
AVL List GmbH	AVL Fire	Meshing/ Solver/Visualization
NUMECA International	AutoMesh / FINE	Meshing/ Solver/Visualization
ESI Group	OpenFOAM <sup>1,2</sup>	Meshing/ Solver/Visualization
CHAM Ltd.	PHOENICS <sup>3</sup>	Meshing/ Solver/Visualization
Mentor Graphics (Siemens PLM)	FloTHERM / FloEFD	Meshing/ Solver/Visualization
Pointwise Inc.	Pointwise	Meshing
ANSYS Inc.	ANSYS-ICEM CFD	Meshing
Tecplot Inc	Tecplot	Visualization
ANSYS Inc.	Ensign	Visualization

<sup>1</sup> freeware/shareware; <sup>2</sup> open source; <sup>3</sup> older versions available as shareware.

Most solvers are general-purpose CFD codes, whereas others are focused on particular applications (such as AVL Fire, focused on internal combustion engines, or FloTHERM, focused on electronics cooling). PHOENICS was the very first commercially available CFD code (released in 1981), but currently ANSYS is the most widely used CFD software nowadays (over 40% market share), with both major codes CFX (acquired in 2003) and FLUENT (acquired in 2006). Among the open source CFD software, OpenFOAM from ESI Group is the most widely used.

## 5. Conclusions

This brief review has covered the main CFD applications in energy and thermal engineering. A brief introduction to the most significant reviews that have been published on the particular topics related to CFD in energy and thermal engineering has been provided, so that readers can refer to the different review papers for a thorough revision of the state of the art and contributions into the particular field of interest. This has been intended as a presentation and background for the Special Issue “CFD Applications in Energy Engineering Research and Simulation” published by Processes in 2020. Overall, it has been shown that CFD is covering all major processes and equipment involved in energy engineering, with applications increasingly achieving more complex phenomena and simulations. The increase in the available computing power is allowing simulations with larger mesh sizes and increasing resolution. Nevertheless, regarding turbulence modelling, RANS modelling is currently still much more present than LES for most applications. It has been shown that CFD use in industry and academia continues to grow with a yearly rate of around 10%, with North America and Asia as major users. The strong competition among CFD software vendors will ensure further efforts on model developments to enhance accuracy and even cover new applications and novel technologies. Industry will continue to increase its reliance and trust on CFD to improve their product designs and reduce design cycles and associated costs. The expected transition towards an energy system mostly based on renewable energies that will (sooner or later) take place, will require major efforts in technology development that will surely be supported by CFD in energy engineering research. Based on the above, it can be thus ensured that CFD will continue to grow and expand, and it will be necessary to ensure that quality and trust is maintained among users, by further developing, refining, and using CFD best practice guidelines.

**Funding:** This research received no external funding.

**Conflicts of Interest:** The authors declare no conflict of interest.

## References

1. Artemov, V.; Beale, S.B.; de Vahl Davis, G.; Escudier, M.P.; Fueyo, N.; Launder, B.E.; Leonardi, E.; Malin, M.R.; Minkowycz, W.J.; Patankar, S.V.; et al. A tribute to D.B. Spalding and his contributions in science and engineering. *Int. J. Heat Mass Transf.* **2009**, *52*, 3884–3905. [CrossRef]
2. Runchal, A.K. Brian Spalding: CFD and reality—A personal recollection. *Int. J. Heat Mass Transf.* **2009**, *52*, 4063–4073. [CrossRef]
3. Patankar, S.V. *Numerical Heat Transfer and Fluid Flow*; Taylor & Francis: Abingdon, UK, 1980; ISBN 978-0891165224.
4. Stopford, P.J. Recent applications of CFD modelling in the power generation and combustion industries. *Appl. Math. Model.* **2002**, *26*, 351–374. [CrossRef]
5. Díez, L.I.; Cortés, C.; Campo, A. Modelling of pulverized coal boilers: Review and validation of on-line simulation techniques. *Appl. Therm. Eng.* **2005**, *25*, 1516–1533. [CrossRef]
6. Sankar, G.; Kumar, D.S.; Balasubramanian, K.R. Computational modeling of pulverized coal fired boilers—A review on the current position. *Fuel* **2019**, *236*, 643–665. [CrossRef]
7. Kurose, R.; Watanabe, H.; Makino, H. Numerical simulations of pulverized coal combustion. *KONA Powder Part. J.* **2009**, *27*, 144–156. [CrossRef]
8. Shen, Y.; Yu, A.; Zulli, P. CFD modelling and analysis of pulverized coal injection in blast furnace: An overview. *Steel Res. Int.* **2011**, *82*, 532–542. [CrossRef]
9. Rigopoulos, S. Population balance modelling of polydispersed particles in reactive flows. *Prog. Energy Combust. Sci.* **2010**, *36*, 412–443. [CrossRef]
10. Zitney, S.E. Process/equipment co-simulation for design and analysis of advanced energy systems. *Comput. Chem. Eng.* **2010**, *34*, 1532–1542. [CrossRef]
11. Dernbecher, A.; Dieguez-Alonso, A.; Ortwein, A.; Tabet, F. Review on modelling approaches based on computational fluid dynamics for biomass combustion systems: Focus on fixed bed and moving grate systems. *Biomass Convers. Biorefin.* **2019**, *9*, 129–182. [CrossRef]

12. Haberle, I.; Skreiberg, Ø.; Łazar, J.; Haugen, N.E.L. Numerical models for thermochemical degradation of thermally thick woody biomass, and their application in domestic wood heating appliances and grate furnaces. *Prog. Energy Combust. Sci.* **2017**, *63*, 204–252. [CrossRef]
13. Chaney, J.; Liu, H.; Li, J. An overview of CFD modelling of small-scale fixed-bed biomass pellet boilers with preliminary results from a simplified approach. *Energy Convers. Manag.* **2012**, *63*, 149–156. [CrossRef]
14. Mazaheri, N.; Akbarzadeh, A.H.; Madadian, E.; Lefsrud, M. Systematic review of research guidelines for numerical simulation of biomass gasification for bioenergy production. *Energy Convers. Manag.* **2019**, *183*, 671–688. [CrossRef]
15. Tabet, F.; Gökalp, I. Review on CFD based models for co-firing coal and biomass. *Renew. Sustain. Energy Rev.* **2015**, *51*, 1101–1114. [CrossRef]
16. Bhuiyan, A.A.; Blichlau, A.S.; Naser, J. Co-firing of biomass and slagging in industrial furnace: A review on modelling approach. *J. Energy Inst.* **2017**, *90*, 838–854. [CrossRef]
17. Chen, L.; Yong, S.Z.; Ghoniem, A.F. Oxy-fuel combustion of pulverized coal: Characterization, fundamentals, stabilization and CFD modeling. *Prog. Energy Combust. Sci.* **2012**, *38*, 156–214. [CrossRef]
18. Yin, C.; Yan, J. Oxy-fuel combustion of pulverized fuels: Combustion fundamentals and modeling. *Appl. Energy* **2016**, *162*, 742–762. [CrossRef]
19. Edge, P.; Gharebaghi, M.; Irons, R.; Porter, R.; Porter, R.T.J.; Pourkashanian, M.; Smith, D.; Stephenson, P.; Williams, A. Combustion modelling opportunities and challenges for oxy-coal carbon capture technology. *Chem. Eng. Res. Des.* **2011**, *89*, 1470–1493. [CrossRef]
20. Bhuiyan, A.A.; Naser, J. Modeling of slagging in industrial furnace: A comprehensive review. *Procedia Eng.* **2015**, *105*, 512–519. [CrossRef]
21. Lyczkowski, R.W.; Bouillard, J.X. State-of-the-art review of erosion modeling in fluid/solids systems. *Prog. Energy Combust. Sci.* **2002**, *28*, 543–602. [CrossRef]
22. Kumar, H.; Mohapatra, S.K.; Singh, R.I. Review on CFD Modelling of Fluidized Bed Combustion Systems based on Biomass and Co-firing. *J. Inst. Eng. (India) Ser. C* **2018**, *99*, 449–474. [CrossRef]
23. Kuffa, M.; Paul, M.C.; Janicka, J. Combustion processes of biomass in a fluidized bed: A review and results of CFD modelling. In *Soot: Sources, Formation and Health Effects*; Nova Science Publishers: Hauppauge, NY, USA, 2012; pp. 243–280.
24. Singh, R.I.; Brink, A.; Hupa, M. CFD modeling to study fluidized bed combustion and gasification. *Appl. Therm. Eng.* **2013**, *52*, 585–614. [CrossRef]
25. Ravelli, S.; Perdicchizzi, A.; Barigozzi, G. Description, applications and numerical modelling of bubbling fluidized bed combustion in waste-to-energy plants. *Prog. Energy Combust. Sci.* **2008**, *34*, 224–253. [CrossRef]
26. Roslyakov, P.V.; Khudyakov, I.V.; Khokhlov, D.A.; Zaichenko, M.N. Experience Gained with CFD-Modeling of Liquid and Gaseous Fuel Combustion Processes in Power Installations (Review). *Therm. Eng.* **2019**, *66*, 599–618. [CrossRef]
27. Bradley, D. Problems of predicting turbulent burning rates. *Combust. Theory Model.* **2002**, *6*, 361–382. [CrossRef]
28. Reitz, R.D.; Rutland, C.J. Development and testing of diesel engine CFD models. *Prog. Energy Combust. Sci.* **1995**, *21*, 173–196. [CrossRef]
29. Gosman, A.D. State of the art of multi-dimensional modeling of engine reacting flows. *Oil Gas Sci. Technol.* **1999**, *54*, 149–159. [CrossRef]
30. Barths, H.; Hasse, C.; Peters, N. Computational fluid dynamics modelling of non-premixed combustion in direct injection diesel engines. *Int. J. Engine Res.* **2000**, *1*, 249–267. [CrossRef]
31. Shah, A.; Thipse, S.S.; Tyagi, A.; Rairikar, S.D.; Kavthekar, K.P.; Marathe, N.V.; Mandloi, P. Literature review and simulation of dual fuel diesel-CNG engines. *SAE Tech. Pap.* **2011**. [CrossRef]
32. Haworth, D.C. A review of turbulent combustion modeling for multidimensional in-cylinder CFD. *SAE Tech. Pap.* **2005**, 899–928. [CrossRef]
33. Rutland, C.J. Large-eddy simulations for internal combustion engines—A review. *Int. J. Engine Res.* **2011**, *12*, 421–451. [CrossRef]
34. Meijer, M.; Somers, B.; Johnson, J.; Naber, J.; Lee, S.Y.; Malbec, L.M.C.; Bruneaux, G.; Pickett, L.M.; Bardi, M.; Payri, R.; et al. Engine Combustion Network (ECN): Characterization and comparison of boundary conditions for different combustion vessels. *At. Sprays* **2012**, *22*, 777–806. [CrossRef]

35. Banerjee, S.; Agarwal, R.K. Review of recent advances in process modeling and computational fluid dynamics simulation of chemical-looping combustion. *Int. J. Energy Clean Environ.* **2017**, *18*. [CrossRef]
36. Jung, J.; Gamwo, I.K. Multiphase CFD-based models for chemical looping combustion process: Fuel reactor modeling. *Powder Technol.* **2008**, *183*, 401–409. [CrossRef]
37. Denton, J.D.; Dawes, W.N. Computational fluid dynamics for turbomachinery design. *Proc. Inst. Mech. Eng. Part C J. Mech. Eng.* **1999**, *213*, 107–124. [CrossRef]
38. Moore, J.G.; Moore, J. Realizability in turbulence modelling for turbomachinery CFD. In Proceedings of the ASME Turbo Expo 1, ASME 1999 International Gas Turbine and Aeroengine Congress and Exhibition, Indianapolis, IN, USA, 7–10 June 1999.
39. Casartelli, E.; Mangani, L. Object-oriented open-source CFD for turbomachinery applications: A review and recent advances. In Proceedings of the ASME Turbo Expo 6 B, San Antonio, TX, USA, 3–7 June 2013. GT2013–95285.
40. Pinto, R.N.; Afzal, A.; D'Souza, L.V.; Ansari, Z.; Mohammed Samee, A.D. Computational Fluid Dynamics in Turbomachinery: A Review of State of the Art. *Arch. Comput. Methods Eng.* **2017**, *24*, 467–479. [CrossRef]
41. Iacovides, H.; Launder, B.E. Computational fluid dynamics applied to internal gas-turbine blade cooling: A review. *Int. J. Heat Fluid Flow* **1995**, *16*, 454–470. [CrossRef]
42. Dawes, W.N. Turbomachinery computational fluid dynamics: Asymptotes and paradigm shifts. *Philos. Trans. R. Soc. Math. Phys. Eng. Sci.* **2007**, *365*, 2553–2585. [CrossRef]
43. Horlock, J.H.; Denton, J.D. A review of some early design practice using computational fluid dynamics and a current perspective. *J. Turbomach.* **2005**, *127*, 5–13. [CrossRef]
44. Tominaga, J.; Tanuma, T. The application of computational fluid dynamics to the technologies on steam turbine efficiency enhancement. *Nihon Enerugi Gakkaishijf. Jpn. Inst. Energy* **2004**, *83*, 348–353.
45. Sick, M.; Wilson, A. CFD for water turbines: Review of the state of the art. *Int. J. Hydropower Dams* **2005**, *12*, 52.
46. Keck, H.; Sick, M. Thirty years of numerical flow simulation in hydraulic turbomachines. *Acta Mech.* **2008**, *201*, 211–229. [CrossRef]
47. Trivedi, C.; Cervantes, M.J.; Dahlhaug, O.G. Numerical Techniques Applied to Hydraulic Turbines: A Perspective Review. *Appl. Mech. Rev.* **2016**, *68*, 010802. [CrossRef]
48. Laín, S.; Contreras, L.T.; López, O. A review on computational fluid dynamics modeling and simulation of horizontal axis hydrokinetic turbines. *J. Braz. Soc. Mech. Sci. Eng.* **2019**, *41*, 375. [CrossRef]
49. Židonis, A.; Aggidis, G.A. State of the art in numerical modelling of Pelton turbines. *Renew. Sustain. Energy Rev.* **2015**, *45*, 135–144. [CrossRef]
50. Shah, S.R.; Jain, S.V.; Patel, R.N.; Lakhera, V.J. CFD for centrifugal pumps: A review of the state-of-the-art. *Procedia Eng.* **2013**, *51*, 715–720. [CrossRef]
51. Niedzwiedzka, A.; Schnerr, G.H.; Sobieski, W. Review of numerical models of cavitating flows with the use of the homogeneous. *Arch. Thermodyn.* **2016**, *37*, 71–88. [CrossRef]
52. Nautiyal, H.; Kumar, A. Reverse running pumps analytical, experimental and computational study: A review. *Renew. Sustain. Energy Rev.* **2010**, *14*, 2059–2067. [CrossRef]
53. Kelm, S.; Müller, H.; Allelein, H.-J. A Review of the CFD Modeling Progress Triggered by ISP-47 on Containment Thermal Hydraulics. *Nucl. Sci. Eng.* **2019**, *193*, 63–80. [CrossRef]
54. Lee, G.-H. Review of audit calculation activities on the applicability of CFD software to nuclear safety problems. *MATEC Web Conf.* **2018**, *240*, 05016. [CrossRef]
55. Habib, M.A.; Nemitallah, M.A.; El-Nakla, M. Current status of CHF predictions using CFD modeling technique and review of other techniques especially for non-uniform axial and circumferential heating profiles. *Ann. Nucl. Energy* **2014**, *70*, 188–207. [CrossRef]
56. Bestion, D.; Anglart, H.; Caraghiaur, D.; Péturaud, P.; Smith, B.; Andreani, M.; Niceno, B.; Krepper, E.; Lucas, D.; Moretti, F.; et al. Review of available data for validation of nuresim two-phase CFD software applied to CHF investigations. *Sci. Technol. Nucl. Install.* **2009**, *2009*, 214512. [CrossRef]
57. Yang, B.-W.; Han, B.; Liu, A.; Wang, S. Recent challenges in subchannel thermal-hydraulics-CFD modeling, subchannel analysis, CHF experiments, and CHF prediction. *Nucl. Eng. Des.* **2019**, *354*, 110236. [CrossRef]
58. Murallidharan, J.S. A review of openfoam-based CFD investigations of component-scale subcooled flow boiling phenomena using the two-fluid model. *Multiph. Sci. Technol.* **2018**, *30*. [CrossRef]

59. Moorthi, A.; Kumar Sharma, A.; Velusamy, K. A review of sub-channel thermal hydraulic codes for nuclear reactor core and future directions. *Nucl. Eng. Des.* **2018**, *332*, 329–344. [CrossRef]
60. Verma, S.K.; Sinha, S.L.; Chandraker, D.K. A Comprehensive Review of the Spacer Effect on Performance of Nuclear Fuel Bundle using Computational Fluid Dynamics Methodology. *Mater. Today Proc.* **2017**, *4*, 10030–10034. [CrossRef]
61. Hatman, A.; Chatelain, A.; Goodheart, K.; Martin, M.; Keheley, T. A review of AREVA'S experimental validation of state-of-the-art single-phase CFD methods with application to PWR fuel analysis and design. *Int. Top. Meet. Nucl. React. Therm. Hydraul. Nureth* **2015**, *9*, 7792–7805.
62. Li, Z.; He, D. Reviews of fluid dynamics researches in wind energy engineering. *Adv. Mech.* **2013**, *43*, 472–525.
63. Shourangiz-Haghighi, A.; Haghnegahdar, M.A.; Wang, L.; Mussetta, M.; Kolios, A.; Lander, M. State of the Art in the Optimisation of Wind Turbine Performance Using CFD. *Arch. Comput. Methods Eng.* **2019**, 1–9, in press. [CrossRef]
64. Miller, A.; Chang, B.; Issa, R.; Chen, G. Review of computer-aided numerical simulation in wind energy. *Renew. Sustain. Energy Rev.* **2013**, *25*, 122–134. [CrossRef]
65. Sumner, J.; Watters, C.S.; Masson, C. CFD in wind energy: The virtual, multiscale wind tunnel. *Energies* **2010**, *3*, 989–1013. [CrossRef]
66. Sandeise, B.; Van Der Pijl, S.P.; Koren, B. Review of computational fluid dynamics for wind turbine wake aerodynamics. *Wind Energy* **2011**, *14*, 799–819. [CrossRef]
67. Hansen, M.O.L.; Sørensen, J.N.; Voutsinas, S.; Sørensen, N.; Madsen, H.A. State of the art in wind turbine aerodynamics and aeroelasticity. *Prog. Aerosp. Sci.* **2006**, *42*, 285–330. [CrossRef]
68. Bai, C.-J.; Wang, W.-C. Review of computational and experimental approaches to analysis of aerodynamic performance in horizontal-axis wind turbines (HAWTs). *Renew. Sustain. Energy Rev.* **2016**, *63*, 506–519. [CrossRef]
69. Lanzafame, R.; Mauro, S.; Messina, M. Evaluation of the radial flow effects on micro HAWTs through the use of a transition CFD 3D model—Part I: State of the art and Numerical model review. *Energy Procedia* **2015**, *82*, 156–163. [CrossRef]
70. O'Brien, J.M.; Young, T.M.; O'Mahoney, D.C.; Griffin, P.C. Horizontal axis wind turbine research: A review of commercial CFD, FE codes and experimental practices. *Prog. Aerosp. Sci.* **2017**, *92*, 1–24. [CrossRef]
71. Ghasemian, M.; Ashrafi, Z.N.; Sedaghat, A. A review on computational fluid dynamic simulation techniques for Darrieus vertical axis wind turbines. *Energy Convers. Manag.* **2017**, *149*, 87–100. [CrossRef]
72. Mehta, D.; van Zuijlen, A.H.; Koren, B.; Holierhoek, J.G.; Bijl, H. Large Eddy Simulation of wind farm aerodynamics: A review. *J. Wind Eng. Ind. Aerodyn.* **2014**, *133*, 1–17. [CrossRef]
73. Toja-Silva, F.; Kono, T.; Peralta, C.; Lopez-Garcia, O.; Chen, J. A review of computational fluid dynamics (CFD) simulations of the wind flow around buildings for urban wind energy exploitation. *J. Wind Eng. Ind. Aerodyn.* **2018**, *180*, 66–87. [CrossRef]
74. Manjunath, M.S.; Madhwesh, N. A review of CFD investigations on heat transfer augmentation of forced convection solar air heater through enhanced fluid turbulence levels. *Int. J. Mech. Prod. Eng. Res. Dev.* **2019**, *9*, 1309–1322.
75. Gawande, V.B.; Dhoble, A.S.; Zodpe, D.B.; Chamoli, S. A review of CFD methodology used in literature for predicting thermo-hydraulic performance of a roughened solar air heater. *Renew. Sustain. Energy Rev.* **2016**, *54*, 550–605. [CrossRef]
76. Yadav, A.S.; Bhagoria, J.L. Heat transfer and fluid flow analysis of solar air heater: A review of CFD approach. *Renew. Sustain. Energy Rev.* **2013**, *23*, 60–79. [CrossRef]
77. Tagliafico, L.A.; Scarpa, F.; De Rosa, M. Dynamic thermal models and CFD analysis for flat-plate thermal solar collectors—A review. *Renew. Sustain. Energy Rev.* **2014**, *30*, 526–537. [CrossRef]
78. Sharma, S.K.; Kalamkar, V.R. Computational Fluid Dynamics approach in thermo-hydraulic analysis of flow in ducts with rib roughened walls—A review. *Renew. Sustain. Energy Rev.* **2016**, *55*, 756–788. [CrossRef]
79. Singh Chauhan, P.; Kumar, A.; Tekasakul, P. Applications of software in solar drying systems: A review. *Renew. Sustain. Energy Rev.* **2015**, *51*, 1326–1337. [CrossRef]
80. Avila-Marin, A.L.; Fernandez-Reche, J.; Martinez-Tarifa, A. Modelling strategies for porous structures as solar receivers in central receiver systems: A review. *Renew. Sustain. Energy Rev.* **2019**, *111*, 15–33. [CrossRef]

81. Bendjebbas, H.; Abdellah-ElHadj, A.; Abbas, M. Full-scale, wind tunnel and CFD analysis methods of wind loads on heliostats: A review. *Renew. Sustain. Energy Rev.* **2016**, *54*, 452–472. [CrossRef]
82. Windt, C.; Davidson, J.; Ringwood, J.V. High-fidelity numerical modelling of ocean wave energy systems: A review of computational fluid dynamics-based numerical wave tanks. *Renew. Sustain. Energy Rev.* **2018**, *93*, 610–630. [CrossRef]
83. Cui, Y.; Liu, Z.; Zhang, X.; Xu, C. Review of CFD studies on axial-flow self-rectifying turbines for OWC wave energy conversion. *Ocean Eng.* **2019**, *175*, 80–102. [CrossRef]
84. Masters, I.; Williams, A.; Croft, T.N.; Togneri, M.; Edmunds, M.; Zangiabadi, E.; Fairley, I.; Karunarathna, H. A comparison of numerical modelling techniques for tidal stream turbine analysis. *Energies* **2015**, *8*, 7833–7853. [CrossRef]
85. Quiroz-Pérez, E.; Gutiérrez-Antonio, C.; Vázquez-Román, R. Modelling of production processes for liquid biofuels through CFD: A review of conventional and intensified technologies. *Chem. Eng. Process-Process Intensif.* **2019**, *143*, 107629. [CrossRef]
86. Wang, J.; Xue, Q.; Guo, T.; Mei, Z.; Long, E.; Wen, Q.; Huang, W.; Luo, T.; Huang, R. A review on CFD simulating method for biogas fermentation material fluid. *Renew. Sustain. Energy Rev.* **2018**, *97*, 64–73. [CrossRef]
87. Wang, Y.; Yan, L. CFD studies on biomass thermochemical conversion. *Int. J. Mol. Sci.* **2008**, *9*, 1108–1130. [CrossRef] [PubMed]
88. Raynal, L.; Augier, F.; Bazer-Bachi, F.; Haroun, Y.; Pereira Da Fonte, C. CFD Applied to Process Development in the Oil and Gas Industry—A Review. *Oil Gas Sci. Technol.* **2016**, *71*, 42. [CrossRef]
89. Adaze, E.; Al-Sarkhi, A.; Badr, H.M.; Elsaadawy, E. Current status of CFD modeling of liquid loading phenomena in gas wells: A literature review. *J. Pet. Explor. Prod. Technol.* **2019**, *9*, 1397–1411. [CrossRef]
90. Hamad, A.A.; Aftab, S.M.A.; Zahari, R.; Aziz, F.A.; Ahmad, K.A. Application of computational fluid dynamics in piping distribution system and special focus on the Arabian peninsula: A review. *Int. Rev. Mech. Eng.* **2019**, *13*. [CrossRef]
91. Samokhvalov, Y.; Kolesnikov, A.; Krotov, A.; Parkin, A.; Navasardyan, E.S.; Arkharov, I.A. Heat transfer in the structure of a spiral-wound heat exchanger for liquefied natural gas production: Review of numerical models for the heat-transfer coefficient of condensation for a hydrocarbon mixture in a horizontal tube. *J. Enhanc. Heat Transf.* **2018**, *25*, 109–120. [CrossRef]
92. Wang, C.-Y. Fundamental models for fuel cell engineering. *Chem. Rev.* **2004**, *104*, 4727–4765. [CrossRef]
93. Ma, L.; Ingham, D.B.; Pourkashanian, M.; Carcadea, E. Review of the computational fluid dynamics modeling of fuel cells. *J. Fuel Cell Sci. Technol.* **2005**, *2*, 246–257. [CrossRef]
94. Biyikoğlu, A. Review of proton exchange membrane fuel cell models. *Int. J. Hydrog. Energy* **2005**, *30*, 1181–1212. [CrossRef]
95. Cheddie, D.; Munroe, N. Review and comparison of approaches to proton exchange membrane fuel cell modeling. *J. Power Sources* **2005**, *147*, 72–84. [CrossRef]
96. Shah, A.A.; Luo, K.H.; Ralph, T.R.; Walsh, F.C. Recent trends and developments in polymer electrolyte membrane fuel cell modelling. *Electrochim. Acta* **2011**, *56*, 3731–3757. [CrossRef]
97. Sousa, R., Jr.; Gonzalez, E.R. Mathematical modeling of polymer electrolyte fuel cells. *J. Power Sources* **2005**, *147*, 32–45. [CrossRef]
98. Aman, N.A.M.N.; Mcuhtar, A.; Somalu, M.R.; Rosli, M.I.; Baharuddin, N.A.; Kalib, N.S. A short review on the modeling of solid-oxide fuel cells by using computational fluid dynamics: Assumptions and boundary conditions. *Int. J. Integr. Eng.* **2005**, *10*, 87–92.
99. Guo, X.; Peng, X.; Xu, S. Numerical Models for PEMFC Cold Start: A Review. *SAE Int. J. Altern. Powertrains* **2017**, *6*, 151–164. [CrossRef]
100. Jarauta, A.; Ryzhakov, P. Challenges in Computational Modeling of Two-Phase Transport in Polymer Electrolyte Fuel Cells Flow Channels: A Review. *Arch. Comput. Methods Eng.* **2018**, *25*, 1027–1057. [CrossRef]
101. Andersson, M.; Beale, S.B.; Espinoza, M.; Wu, Z.; Lehnert, W. A review of cell-scale multiphase flow modeling, including water management, in polymer electrolyte fuel cells. *Appl. Energy* **2016**, *180*, 757–778. [CrossRef]
102. Ferreira, R.B.; Falcão, D.S.; Oliveira, V.B.; Pinto, A.M.F.R. Numerical simulations of two-phase flow in proton exchange membrane fuel cells using the volume of fluid method—A review. *J. Power Sources* **2015**, *277*, 329–342. [CrossRef]

103. Gurau, V.; Mann, J.A. A critical overview of computational fluid dynamics multiphase models for proton exchange membrane fuel cells. *SIAM J. Appl. Math.* **2009**, *70*, 410–454. [CrossRef]
104. Zhang, G.; Jiao, K. Multi-phase models for water and thermal management of proton exchange membrane fuel cell: A review. *J. Power Sources* **2018**, *391*, 120–133. [CrossRef]
105. Wu, H.-W. A review of recent development: Transport and performance modeling of PEM fuel cells. *Appl. Energy* **2016**, *165*, 81–106. [CrossRef]
106. Tapia, E.; Iranzo, A.; Pino, F.J.; Rosa, F.; Salva, J.A. Methodology for thermal design of solar tubular reactors using CFD techniques. *Int. J. Hydrog. Energy* **2016**, *41*, 19525–19538. [CrossRef]
107. Tapia, E.; González-Pardo, A.; Iranzo, A.; Romero, M.; González-Aguilar, J.; Vidal, A.; Martín-Betancourt, M.; Rosa, F. Multi-tubular reactor for hydrogen production: CFD thermal design and experimental testing. *Processes* **2019**, *7*, 31. [CrossRef]
108. Al-Abidi, A.A.; Bin Mat, S.; Sopian, K.; Sulaiman, M.Y.; Mohammed, A.T. CFD applications for latent heat thermal energy storage: A review. *Renew. Sustain. Energy Rev.* **2013**, *20*, 353–363. [CrossRef]
109. Liu, S.; Li, Y.; Zhang, Y. Mathematical solutions and numerical models employed for the investigations of PCMs' phase transformations. *Renew. Sustain. Energy Rev.* **2014**, *33*, 659–674. [CrossRef]
110. Tucker, P.G. CFD applied to electronic systems: A review. *IEEE Trans. Compon. Packag. Manuf. Technol. Part A* **1997**, *20*, 518–529. [CrossRef]
111. Bhutta, M.M.A.; Hayat, N.; Bashir, M.H.; Khan, A.R.; Ahmad, K.N.; Khan, S. CFD applications in various heat exchangers design: A review. *Appl. Therm. Eng.* **2012**, *32*, 1–12. [CrossRef]
112. Norton, T.; Tiwari, B.; Sun, D.W. Computational Fluid Dynamics in the Design and Analysis of Thermal Processes: A Review of Recent Advances. *Crit. Rev. Food Sci. Nutr.* **2013**, *53*, 251–275. [CrossRef]
113. Zhao, C.-J.; Han, J.-W.; Yang, X.-T.; Qian, J.-P.; Fan, B.-L. A review of computational fluid dynamics for forced-air cooling process. *Appl. Energy* **2016**, *168*, 314–331. [CrossRef]



© 2019 by the author. Licensee MDPI, Basel, Switzerland. This article is an open access article distributed under the terms and conditions of the Creative Commons Attribution (CC BY) license (<http://creativecommons.org/licenses/by/4.0/>).

MDPI AG  
Grosspeteranlage 5  
4052 Basel  
Switzerland  
Tel.: +41 61 683 77 34

*Processes* Editorial Office  
E-mail: [processes@mdpi.com](mailto:processes@mdpi.com)  
[www.mdpi.com/journal/processes](http://www.mdpi.com/journal/processes)



Disclaimer/Publisher's Note: The statements, opinions and data contained in all publications are solely those of the individual author(s) and contributor(s) and not of MDPI and/or the editor(s). MDPI and/or the editor(s) disclaim responsibility for any injury to people or property resulting from any ideas, methods, instructions or products referred to in the content.







Academic Open  
Access Publishing

[mdpi.com](https://www.mdpi.com)

ISBN 978-3-7258-2222-5